NATO Science for Peace and Security Series - A:
Chemistry and Biology

Nanoscience Advances in CBRN Agents Detection, Information and Energy Security

Edited by
Plamen Petkov
Dumitru Tsiulyanu
Wilhelm Kulisch
Cyril Popov

Springer

NATO OTAN

This publication is supported by:

The NATO Science for Peace and Security Programme

Nanoscience Advances in CBRN Agents Detection, Information and Energy Security

NATO Science for Peace and Security Series

This Series presents the results of scientific meetings supported under the NATO Programme: Science for Peace and Security (SPS).

The NATO SPS Programme supports meetings in the following Key Priority areas: (1) Defence Against Terrorism; (2) Countering other Threats to Security and (3) NATO, Partner and Mediterranean Dialogue Country Priorities. The types of meeting supported are generally “Advanced Study Institutes” and “Advanced Research Workshops”. The NATO SPS Series collects together the results of these meetings. The meetings are co-organized by scientists from NATO countries and scientists from NATO’s “Partner” or “Mediterranean Dialogue” countries. The observations and recommendations made at the meetings, as well as the contents of the volumes in the Series, reflect those of participants and contributors only; they should not necessarily be regarded as reflecting NATO views or policy.

Advanced Study Institutes (ASI) are high-level tutorial courses intended to convey the latest developments in a subject to an advanced-level audience

Advanced Research Workshops (ARW) are expert meetings where an intense but informal exchange of views at the frontiers of a subject aims at identifying directions for future action

Following a transformation of the programme in 2006 the Series has been re-named and re-organised. Recent volumes on topics not related to security, which result from meetings supported under the programme earlier, may be found in the NATO Science Series.

The Series is published by IOS Press, Amsterdam, and Springer, Dordrecht, in conjunction with the NATO Emerging Security Challenges Division.

Sub-Series

A.	Chemistry and Biology	Springer
B.	Physics and Biophysics	Springer
C.	Environmental Security	Springer
D.	Information and Communication Security	IOS Press
E.	Human and Societal Dynamics	IOS Press

http://www.nato.int/science
http://www.springer.com
http://www.iospress.nl

Series A: Chemistry and Biology

Nanoscience Advances in CBRN Agents Detection, Information and Energy Security

edited by

Plamen Petkov
Department of Physics
University of Chemical Technology and Metallurgy
Sofia, Bulgaria

Dumitru Tsiulyanu
Department of Physics
Technical University of Moldova
Chisinau, Moldova

Wilhelm Kulisch
Department of Mathematics and Natural Sciences
University of Kassel
Kassel, Germany

and

Cyril Popov
Institute of Nanostructure Technologies and Analytics
University of Kassel
Kassel, Germany

Published in Cooperation with NATO Emerging Security Challenges Division

Proceedings of the NATO Advanced Study Institute on
Nanoscience Advances in CBRN Agents Detection,
Information and Energy Security
Sozopol, Bulgaria
29 May 2014–6 June 2014

Library of Congress Control Number: 2015931518

ISBN 978-94-017-9699-6 (PB)
ISBN 978-94-017-9696-5 (HB)
ISBN 978-94-017-9697-2 (e-book)
DOI 10.1007/978-94-017-9697-2

Published by Springer,
P.O. Box 17, 3300 AA Dordrecht, The Netherlands.

www.springer.com

Printed on acid-free paper

Preface

Nanotechnology has a strong potential to effect substantial changes in different fields of our life, including ***security*** and ***safety***. The ever increasing requirements towards different aspects of security, for example in ***information technology***, in ***biotechnology***, in ***energy management***, etc. demand the latest achievements of ***nanoscience and nanotechnology***. Novel functional materials, devices and systems allowing the control of matter on atomic and molecular levels, i.e. at the level of the matter building blocks, have to face the challenges of the security of the modern society. The nanostructured materials possess unique properties – mechanical, electrical, optical, magnetic, biological, etc. – entirely different from those of the conventional micro- or millimeter sized materials, due to their distinctive sizes and shapes, and predominant surface and quantum effects determining their behavior. In such a sense, ***nanoscience*** is the main driving force in the development of ***new concepts for security***. It concerns not only the preparation and investigation of smart nanosized materials for different applications, like quantum dots, nanotubes, nanowires, nanoparticles and nanocomposites, but also combination of their performance with ICs, micro- and nanooptics, MEMS and NEMS, leading to a higher level of integration and effective processing and transmission. Only the common efforts of scientists from different fields of research – chemistry, physics, biology, materials science and engineering – and from different countries can bring the complimentary expertise in the development of reliable security conceptions taking the advantages of ***nanoscience and nanotechnology***. An important issue related to the security and safety that has to be also addressed is the possible adverse effects of nanoscience on humans and environment.

The first objective of the ***NATO ASI on Nanoscience Advances in CBRN Agents Detection, Information and Energy Security*** held between 29 May and 6 June 2014 in Sozopol, Bulgaria, was to present to the participants the up-to-date nanotechnological achievements for applications in different fields of security and safety and the future perspectives. The second objective was the teaching and training of the participants in the scientific and technological background of nanostructures and nanostructured materials used in fields like quantum cryptography, nanobiotechnology, energy conversion and storage, new generation of

advanced sensors and systems for early detection of CBRN agents, etc. The third objective addressed the initiation of trans-border and interdisciplinary collaborations between young scientists towards the implementation of the recent nanotechnological achievements in security. The overall objective of the ASI was the transfer of competence in nanoscience and nanotechnological advances in different fields of security in order to meet one of the key priorities of the ***NATO Science for Peace and Security Programme***.

The ASI covered topics connected with the recent achievements in different fields of security taking the advantages of nanotechnology and nanomaterials. The ***lectures*** were given by outstanding scientists from universities and research institutes who are experts in nanoscience-related fields. Eleven ***thematic seminars*** on specific topics, not covered by the lectures, were also included in the programme. During three ***poster sessions*** the participants could present their results, establish closer contacts and discuss in a less formal atmosphere.

Seventy seven participants from 14 NATO countries (Bulgaria, Canada, Croatia, Czech Republic, Germany, Greece, Hungary, Poland, Portugal, Romania, Slovakia, Spain, Turkey, USA) and 6 partner countries (Algeria, Belorus, Egypt, FYR Macedonia, Moldova, Ukraine) insured that the overall objective of transfer of competence and technology in the field of nanostructured materials and nanotechnologies was reached on a high level.

We, the members of the Organizing Committee, would like to thank the NATO Science Committee for the financial support for the organisation of the ASI. The local organisation and the publicity of the ASI in the media (TV, newspapers and information websites) was actively supported by Mr. Panayot Reyzi, Mayor of Sozopol, whom we gratefully acknowledge.

Sofia, Bulgaria — Plamen Petkov
Chisinau, Moldova — Dumitru Tsiulyanu
Kassel, Germany — Wilhelm Kulisch
Kassel, Germany — Cyril Popov
October 2014

Group photo of NATO Advanced Study Institute on Nanoscience Advances in CBRN Agents Detection, Information and Energy Security

Contents

Part I
Introduction

Chapter 1
Nanoscience Advances in CBRN Agent Detection, Information and Energy Security: An Introduction

P. Petkov, D. Tsiulyanu, C. Popov, and W. Kulisch

Abstract The present volume comprises the most important contributions to the NATO ASI "Nanoscience advances in CBRN agent detection, information and energy security" held on 29.5.–6.6.2014 in Sozopol, Bulgaria. This short introduction aims to give an overview of the topics of the ASI and to relate them to the presently actual state of the art, but also to future fields of research in nanosciences and nanotechnology. Another aim of this introduction is to hint the reader to the most important contributions of these proceedings. Although nanotechnological products can presently be found in a wide range of application fields, in the ASI the topics were restricted to a number of fields which are related to the future well-being and safety of planet earth. This may sound exaggerated but the future of our planet will indeed rely on the ability to detect dangerous agents (chemical, biological and radionuclear = CBRN) as well as to provide a clean environment, health, and energy and information safety. With other words: The topics of this ASI are at the leading edge to solve many of the currently most important questions to be tackled by science and technology.

Keywords Nanosciences • Nanotechnology • CBRN agents • Energy security • Information security

P. Petkov
Department of Physics, University of Chemical Technology and Metallurgy, 8 "Kl. Ohridski" blvd., Sofia 1756, Bulgaria

D. Tsiulyanu
Department of Physics, Technical University, bd. Dacia 41, Chisinau 2060, Moldova

C. Popov
Institute of Nanostructure Technologies and Analytics, University of Kassel, Kassel, Germany

W. Kulisch (✉)
Department of Mathematics and Natural Sciences, University of Kassel, Kassel, Germany
e-mail: wilhelm.kulisch@yahoo.de

P. Petkov et al. (eds.), *Nanoscience Advances in CBRN Agents Detection, Information and Energy Security*, NATO Science for Peace and Security Series A: Chemistry and Biology, DOI 10.1007/978-94-017-9697-2_1

1.1 Introduction

In the past decades, nanosciences and nanotechnology experienced a tremendous development, making them to one of the present key technologies. The main reason is that materials and devices render their properties or function sometimes completely if one or more of their dimensions is nanoscaled thus opening up new possibilities to solve a given problem even in cases of problems not solvable with standard macroscopic solutions. There are at least three major reasons for these changes [1, 2].

- The surface to volume ratio of a material increases drastically if it is nanoscaled. This has an tremendous effect of the working e.g. of sensors and detectors utilizing nanoscaled materials.
- Many physical relationships routinely used in macroscopic physics are in fact approximations. Many of them are based on the assumption that the dimensions of the body are larger than some characteristic length playing a decisive role in the physical description of the process under discussion. If the dimensions of the structures are smaller than this characteristic length, completely new properties of the materials and devices may arise [3].
- For nanoscaled structures and devices, quantum mechanics applies. Prior to the development of nanotechnology, quantum physical effects could only be studied in systems already existing in nature, e.g. atoms and molecules and the bodies formed by them. The development of nanotechnology opened for the first time the possibility to realize nanoscaled quantum systems and to utilize the sometimes strange quantum properties of nanoscaled materials in man-made devices.

In the contributions to this volume, all three of these points will play decisive roles. The large surface to volume ratio is decisive for many detectors. The decrease of the dimensions below a characteristic length is decisive e.g. for the mechanical properties of nanoscaled materials [3]. Finally, quantum mechanics plays a role e.g. in quantum dots, carbon nanotubes and other types of zero- and one-dimensional structures.

1.2 Preparation and Characterization Techniques

The techniques to prepare nanostructures can be divided into two principally different classes[1]:

- Top-down approaches: The materials of interest are first produced as macroscopic bodies and then – by more or less destructive methods – reduced to the nanoscale.

[1] The paper of Paunović et al. on page 239 provides some insight into the differences between top-down and bottom-up approaches.

- Bottom-up methods: The desired materials are produces in nanoscale by adding atoms or other building units to a growing structure from the beginning of the process. In many cases some kind of self-assembly [4] takes place, i.e. the fact is utilized that the building units form a defined structure if they are brought together.

In this volume, many techniques are described to produce nanoscaled materials either by top-down or by bottom-up methods. They are too numerous to mention each of them here. At this point, two techniques will be highlighted which are not standard, i.e. laser techniques which can be used in top-down as well as bottom-up approaches and ion implantation as a typical example for top-down techniques.

1.2.1 Laser Techniques

Lasers can be used for top-down as well as in bottom-up techniques.[2] A prominent example of the former is pulsed laser deposition, in which a pre-fabricated target is exposed to laser pulses leading to the evaporation of material, sometimes in nanoscaled form, which is collected on a substrate. Several examples of such processes can be found in this volume. Laser beams can also be used for the patterning of nanostructures.[3]

However, laser beams can also assist to bottom down techniques. One of these techniques is called laser printing. Gold [5] or silver [6] nanoparticles are printed onto a substrate utilizing the electromagnetic fields of a laser beam to position the particle on the substrate.

1.2.2 Ion Implantation

It has already been pointed out that top-down approaches are essentially based on the partial destruction of previously produced macroscopic materials. This destruction can be rough and violently as in grinding and milling techniques or sophisticated as is the case of the extremely successful present semiconductor technology which essentially relies on etching processes of pre-deposited layers to prepare nanoscale structures [7].

An interesting alternative to these well established techniques is ion implantation. Ion implantation uses the bombardment of a substrate with medium or high energy ions. Ion implantation is routinely used in semiconductor industry to incorporate a chemical element into a certain depth of a material. However, as

[2] This question is to some extent addressed in the contribution of Vasileiadis and Yannopoulos on page 17.

[3] An example can be found in the paper of Meinl et al. on page 29.

high energy particles are use in ion implantation, the process is also more or less destructive to the target used. These destructive effects can also be used to create nanostructures in the target of which the ions used may be a part.[4] By proper choice of the energy, the depth of the nanostructures in the target can be selected.

1.2.3 Characterization

One of the major problems of nanotechnology is the characterization of the nanostructures and nanomaterials realized. According to the Rayleigh criterium, characterization based on visible light is limited to structures larger than approximately one quarter of the wavelength used, which is on the order of 200 nm or above, i.e. well above the typical structure size of nanoobjects. There are at least two solutions of this problem:

- The use of particle beams, especially electron beams utilizing the small de Broglie wavelength of the electrons. Techniques based on this approach are scanning electron microscopy (SEM) and transmission electron microscopy (TEM). Especially with high resolution TEM (HRTEM) atomic resolution is possible.
- The use of scanning probe microscopy techniques (SPM) in which a tip with a sharp end in the nanometer range is scanned over a surface and one or more properties (depending on the technique) are recorded with nanometer or even atomic resolution [8]. Examples are the scanning tunnelling microscopy [9] and the atomic force microscopy [10] but since their invention many more techniques such as scanning near-field optical microscopy (SNOM) or magnetic force microscopy (MFM) have been developed.

It has been pointed out that the tips used in SPMs are nanostructures themselves and have to be fabricated by the methods of nanotechnology [11]. Thus there is some kind of synergetic effect: On the one hand, improved characterization on the nanoscale helps to improve the properties of the materials and structures used for the techniques. On the other hand, improved components may result in improved characterization.

Another method based on sharp tips but only loosely related to SPM techniques is nanoindentation [12]. Here, the tip is not rastered over the surface but impressed into it in order to determine mechanical properties such as hardness, Young's modulus or plasticity. There are several contributions to this volume on this topic.[5]

[4] The preparation of nanostructures by ion implantation is discussed in detail in the contribution of Kavetskyy and Stepanov on page 35.

[5] See, for example, the paper of Harea et al. on page 53.

Finally, in this context it is noteworthy that the 2014 Nobel prize for chemistry was awarded for the development of a super-resolved fluorescence microscopy [13, 14]. With this technique, resolutions on the order of a few nm are possible.

1.3 Materials

Two of the most important questions for every researcher in the field of nanosciences and nanotechnology are:

- Which material should be used for a desired application?
- Which type of nanostructure should be used for a desired application?

Generally speaking, all contributions to this ASI and also in this volume are addressing one, if not both of these questions. Thus at this point it is useful to introduce some classification of the various types of nanostructures.

An object is considered as nanoscaled if at least one of its dimensions is below 100 nm [15]. From this definition, a classification can easily be inferred:

- Zero-dimensional nanostructures have nm sizes in all three dimensions. Typical examples are buckyballs and quantum dots but also the numerous nanoparticles addressed in this book.
- Nanowires, nanotubes and nanofibers are structures with two dimensions in the nm range while the third is in the μm or even the mm range. The aspect ratio of such structures can be astonishingly high. Typical examples are nanotubes and nanowires.
- Two-dimensional structures possess nm dimensions in one direction only, while the other two are macroscopic. Typical examples are thin films but also single graphene sheets.

In this volume, numerous examples of all these types of nanostructures can be found.

Besides this classification, the possibilities to realize nanostructures are more than numerous. The materials addressed in the contributions to the ASI and to this volume can roughly be divided into six groups, which will be introduced shortly in the following.

1.3.1 Nanocarbon: Nanotubes, Graphene und Nanodiamond

The development of nanosciences and nanotechnology got important kicks by the invention of several new carbon-based nanostructures and nanomaterials [16]:

- Zero-dimensional structures such as fullerenes [17].
- One-dimensional structures such as carbon nanotubes [18].
- Two-dimensional structures such as graphene [19].

There are several reasons for the prominent role carbon-based materials play in nanotechnology:

- Carbon materials can be realized in a wide range of allotropes depending on the state of hybridisation of the carbon atoms and the crystalline order of the materials.
- Carbon atoms may be sp^3, sp^2 or sp hybridised allowing each atom to undergo four, three or two bonds with neighboring atoms.

As a consequence carbon nanostructure with a wide range of properties can be realized. Besides the well-known nanostructures mentioned above, even simple diamond nanocrystals can be used for several promising applications.[6] In addition, diamond nanostructures can be realized by top-down techniques to achieve structures such as diamond nanopillars as discussed below.

1.3.2 Nanowires and Nanofibers

One-dimensional nanostructures possess nanoscale dimension in two directions while the third is in the μm or even in the mm range. As a result, the aspect ratio of such structures can be impressively high.

The most prominent of this type of structures are of cause carbon nanotubes, but ZnO or Ag are meanwhile following very closely.[7] Other types of structures are nanowhiskers and nanofibers. If the two dimensions with nanometer sizes are really small, the situation may arise that quantum mechanics applies in two directions but not in the third. This means for example that the nm directions of a nanostructure can be used to tune the wavelength of light emission (e.g. in a quantum wire) while the long direction is used to guide this light.

1.3.3 Nanoparticles

Nanoparticles are nanostructures in the very sense of the word. They are nanoscaled in all three dimensions. The most famous nanoparticles are the fullerenes or buckeyballs [17] which, however, play no role in this volume. On the other hand, the list of nanoparticles already used in industrial applications is almost endless. Silver nanoparticles are very often used but in this case questions concerning the environmental and health compatibility has arisen [20].

[6] Blue light emitting diamond nanostructures are discussed in the contribution of Himics et al. on page 93.

[7] The article of K. Govatsi, A. Chrissanthopoulos, and S.N. Yannopoulos on page 129 gives a good overview about the growth and properties of ZnO nanowires.

One major problem of nanoparticles is the difficulty to isolate them as they tend to aggregate. This problem can be overcome by using nanocomposites as will be discussed in the next section.

1.3.4 Nanocomposites

As nanoparticles and other nanostructures are hard to be prepared in pure form and tend to aggregate, they are often used as one component of a nanocomposite, the other component being often, but not exclusively a polymer or glass. But there is yet another reason to use nanocomposites: In general, to prepare nanoparticles is expensive. Thus, a mixture of high-cost nanostructures with a low cost filler is an appropriate solution as long as the special properties of the nanostructures are not obscured. (By the way, this is a reason for the use of many composites, may they be nanoscaled or not.),[8,9] All this also holds for other nanostructures such as nanotubes which are often used in nanocomposites to achieve materials with excellent mechanical properties.

1.3.5 Thin Films

Generally speaking thin films are – irrespective of their thickness – used to render the surface properties of a body different from its bulk properties, mainly for two reasons: The first may be simply cost aspects, if materials with the desired surface properties are too expensive. The second is that some properties of the thin film, e.g. the mechanical strength are insufficient to form the whole body of the system [21]. Thus the bulk is responsible for the mechanical properties and the thin film on top of it for specially desired characteristics. Thin films may consist of one monolayer only but the thickness can reach several microns. It is interesting to note that the thickness of gate insulators in modern semiconductor devices is down to 4–5 nm [22] (in the beginning it was on the order of 100 nm) causing serious problems with tunnelling currents which has led to the replacement of the standard SiO_2 by other (so-called high-k) materials.

According to the above definition, thin films are regarded as nanostructures if their thickness does not exceed 100 nm. Moreover, thin films may consist of structures which themselves are of nanometer size. If such films do not exceed

[8] The contribution of Kukhta on page 207 reports on the preparation and properties of organic–inorganic nanocomposites. The article of Telegeev et al. on page 185 addresses the properties of silver nanoparticles covered by methyl methacrylate oligomers.

[9] The paper of Costa on page 227 discusses the microwave electrical properties of nanocomposites.

100 nm, they are nanostructures in a double sense. There are several examples of such kinds of thin films in the contributions to this volume.[10]

1.3.6 Glasses and Polymers

On a first view it may be astonishing to find a chapter on glasses and polymers in a book on nanosciences and nanotechnology. With both classes the imagination of smooth, structureless materials is closely connected. So if their thickness exceeds 100 nm one would not expect such materials to be nanosized. However, both classes can serve as one of the components of nanocomposites. Due to the high number of contributions on glasses and polymers to the ASI we decided to devote an own chapter to these materials. Much of what was said in the previous section on nanocomposites also holds for nanocomposites based on glasses and polymers.[11]

1.4 Applications

Today, there are many applications of nanomaterials and nanosized devices. They span from every day products such as sun screams, textiles and even food[12] over modern high-end products in the fields of computer and data storage devices to the fields addressed in this ASI.

According to the topics of this ASI, the contributions to this volume concentrate on the following applications, which are, as has been pointed out above, on the forefront of developments urgently required to render life on planet earth more save, more healthy and more reliable:

- Sensors and detectors for CBRN agents.
- Energy security
- Information security.

1.4.1 Sensors and Detectors

It has been pointed out above that one of the most prominent features of nanoscaled materials is the large, sometimes extremely large, surface to volume ratio. This

[10] The structural, optical and electrical properties of nanostructured ZnO films are discussed in the paper of Lovchinov et al. on page 289.

[11] Harizanova et al. discuss the magnetic and dielectric properties of oxide-glass ceramics with nanosized crystals (page 359).

[12] See in this context the paper of Kharlamova et al. on page 461.

makes nanoscaled materials excellent candidates for detectors and other sensors in which surface reactions play a decisive role. First of all it is important to distinguish between the two terms:

- A detector is a device aimed to prove the existence of a certain agent above a given level in the material or environment to be investigated. In the ideal case, it is also able to quantify the amount of this agent in a certain range.[13]
- A sensor is a device to measure a certain physical (or chemical) properties within a certain range exactly. Examples are acceleration sensors, sensors for magnetic fields or such for certain kinds of radiation.[14]

Especially for detectors, the large surface to volume ratio of nanomaterials plays a decisive role for the use of nanomaterials for this purpose. Several contributions on this topic can be found in this volume.

1.4.2 Health, Water Treatment and Environment

One of the most exciting topics concerning the applications of nanostructures is their use to solve medical and environmental problems. On the one hand, great advances have already been achieved in the use of nanostructures in these fields:

- Nanostructures can be used as markers in medical applications.
- Nanostructures may have protective effects on the human health.[15]
- Nanostructures can also be used to deliver drugs to the very point where they are needed.
- Nanostructures can be used for the cleaning of water or air, making use of the very large surface to volume ratio.[16]

On the other hand, the question arises whether nanostructures are adversary to the health of humans or the environment. The debate of these topics is currently carried out very controversially. It is the opinion of the present authors that this question has to be clarified for each nanoproduct to be introduced on the market. It makes no sense to state categorically "Nanotechnology is dangerous" or "Nanotechnology is harmless".

[13] The article of Tsiulianu and Moraru on page 389 addresses the gas sensing properties of nanocrystalline tellurium films.

[14] The paper of Tonchev et al. on page 347 reports on sensors for X-ray radiation.

[15] The article of V.V. Vasilieva, M. Alyakov, and M.D. Apostolova on page 423 addresses the possibility to use nanoparticles for protection against gamma radiation.

[16] Boycheva et al. discuss nanocrystalline zeolites for environmental protection in their article on page 443.

1.4.3 Energy

Among the presently most intensively discussed topics concerning the future of planet earth is to provide every man with sufficient energy. Currently the energy resources used can be divided into three groups (omitting some very special techniques):

- Burning of fossil fuel such as gas, oil or coal or even renewable fuels such as wood or biomaterials. In the former case, the resources are limited and cannot be replaced. In any cases, burning of materials causes environmental damages.
- The use of nuclear energy. The recent catastrophy of Fukushima after the Tsunami in Japan (and the previous catastrophes in Chernobyl and elsewhere) has caused several governments to give up this type of energy production. Besides, the question of the nuclear waste has not been finally solved in any country.
- The use of renewable energies such as wind, water and sun.

In the context of this volume, the sun energy plays an important role. Currently, the harvesting of sun energy is mainly based on photovoltaic devices (solar cells), produced by means of the methods of semiconductor technology which meanwhile itself is a nanotechnology. However, the energy or cost balances of solar cells are far from being perfect.

Therefore it makes sense to investigate other approaches to harvest sun light. One possibility may be to mimic nature. The most important natural process to harvest sun energy is photosynthesis. One current research topic is to mimic photosynthesis making use of nanostructures[17] [22].

But there is another important problem. Power plants working with fossil fuels or on a nuclear basis are able to produce power with a predictable rate, i.e. energy per time. With wind, water and sun the situation is not so easy. For each of them there are high times and low times. The best solution for this problem would be energy storages (some type of large scale batteries or fuel cells) which allow to store energy in large amounts from the high times for the low times. For this reasons, systems able to store large amounts of energy for certain times are a very actual topic in present research. There is a good chance that the final solution will be of nanotechnological nature, as in this situation again the large surface to volume ration of nanostructures can be utilized.[18]

[17] The paper of Pehlivanova et al. on page 479 addresses the use of nanostructures for the conversion of sun energy into electrical energy by the line given by natural photosynthesis.

[18] The use of perovskite materials for solid oxide fuel cells is discussed in the contribution of Koleva et al. on page 487.

1.4.4 Quantum Information Technology

One of the most exciting and promising but also most mysterious applications of nanotechnology concerns quantum information technology (QIT) and quantum key distribution [23, 24]. These technologies implement the so-called qubits (quantum bits) representing a quantum two-level system. Several material platforms for realization of qubit devices exist, including ions in traps, local defect states in crystal lattices, superconducting junctions, etc. One of the most promising (and maybe the most studied) defects are the so-called nitrogen-vacancy (NV) centers in diamond, which are perspective candidates for a number of applications, including quantum computation and cryptography.[19]

References

1. Gleiter H (2000) Acta Mater 48:1
2. Bonnell DA (2003) J Vac Sci Technol A 21:194
3. Kassing R, Kulisch W (2006) In: Kassing R, Petkov P, Kulisch W, Popov C (eds) Functional properties of nanostructured materials. Springer, Berlin, p 3
4. Zhang K, Jiang M, Chen D (2012) Prog Polym Sci 37:445
5. Urban AS, Luttich AA, Stefani FD, Feldmann J (2010) Nano Lett 11:4794
6. Rapp L, Ailuno J, Alloncle AP, Delaporte P (2011) Opt Express 19:21563
7. Xiao H (2012) Introduction to semiconductor manufacturing technology. SPIE Press, Bellingham
8. Meyer E, Jarvis SP, Spencer ND (2004) MRS Bull 29:443
9. Binnig G, Rohrer H (1982) Helv Phys Acta 55:726
10. Binnig G, Quate CF, Gerber C (1986) Phys Rev Lett 56:930
11. Kassing R, Oesterschulze E, Kulisch W (2003) Surf Coat Technol 169/170:237
12. Oliver WC, Pharr GM (2004) J Mater Res 19:3
13. Hell SW, Wichmann J (1994) Opt Lett 19:780
14. Betzig E, Patterson GH, Sougrat R, Lindwasser OW, Olensuych S, Bonifacino JS, Davidson MW, Lippincott-Schwartz J, Hess HF (2006) Nature 313:1642
15. Auffan M, Rose J, Bottero J-Y, Lowry GV, Jolivet JP, Wiesner MR (2009) Nat Nanotechnol 4:634
16. Krüger A (2010) Carbon materials and nanomaterials. Wiley-VCH, Weinheim
17. Kroto HW, Heath JR, O'Brien SC, Curl RF, Smalley RE (1985) Nature 318:162
18. Iijima S (1991) Nature 354:56
19. Castro Neto AH, Guinea F, Peres NMR, Novoselov KS, Geim AK (2009) Rev Mod Phys 81:109
20. Tran QH, Nguyen VQ, Le A-T (2013) Adv Nat Sci: Nanosci Nanotechnol 4:033001
21. Lüth H (2010) Solid surfaces, interfaces and thin films. Springer, Berlin
22. Grätzel M (2001) Nature 414:338
23. Childress L, Hanson R (2013) MRS Bull 38:134
24. Greentree AD, Fairchild BA, Hossain FM, Prawer S (2008) Mater Today 11:22

[19] The contribution of Popov et al. on page 519 provides an instructive overview on this exciting topic.

Part II
Preparation Techniques

Chapter 2
Laser-Assisted Growth and Processing of Functional Chalcogenide Nanostructures

Thomas Vasileiadis and Spyros N. Yannopoulos

Abstract A novel method for the laser-assisted, template-free and surfactant-free fabrication of low-dimensional nanomaterials, i.e. nanotubes, nanowires, nanospheres, of elemental Te, hybrid Te/TeO_2 and GeTe structures is presented. Owing to the high light absorption at visible wavelengths and the low melting points of chalcogen-based materials, simple cw lasers operating from near-UV to near-IR can be used for the controlled growth of such nanostructures; this method can be generalized to other narrow bandgap semiconductors. Raman scattering and electron microscopies are used to explore the dependence of the morphology and size of the nanostructures grown on the irradiation time and fluence. Preliminary results on the binary GeTe phase-change material reveal that lasers can offer a simple and fast method for nanostructuring materials used in phase-change memories. One of the main merits of a laser-assisted method is that it can provide a means of simultaneous growing and integrating tailored nanostructures into an optoelectronic or photonic device.

Keywords Tellurium nanostructures • Laser nanofabrication • Raman scattering

2.1 Introductory Remarks

During the last two decades considerable efforts have been undertaken towards the development of rational synthesis methods for the controlled growth of low-dimensional nanostructures [1]. Decreasing the size and the dimensionality

T. Vasileiadis
Foundation for Research and Technology – Hellas, Institute of Chemical Engineering Sciences, (FORTH/ICE–HT), P.O. Box 1414, Rio-Patras GR-26504, Greece

Department of Materials Science, University of Patras, Rio-Patras GR-26504, Greece

S.N. Yannopoulos (✉)
Foundation for Research and Technology – Hellas, Institute of Chemical Engineering Sciences, (FORTH/ICE–HT), P.O. Box 1414, Rio-Patras GR-26504, Greece
e-mail: sny@iceht.forth.gr

P. Petkov et al. (eds.), *Nanoscience Advances in CBRN Agents Detection, Information and Energy Security*, NATO Science for Peace and Security Series A: Chemistry and Biology, DOI 10.1007/978-94-017-9697-2_2

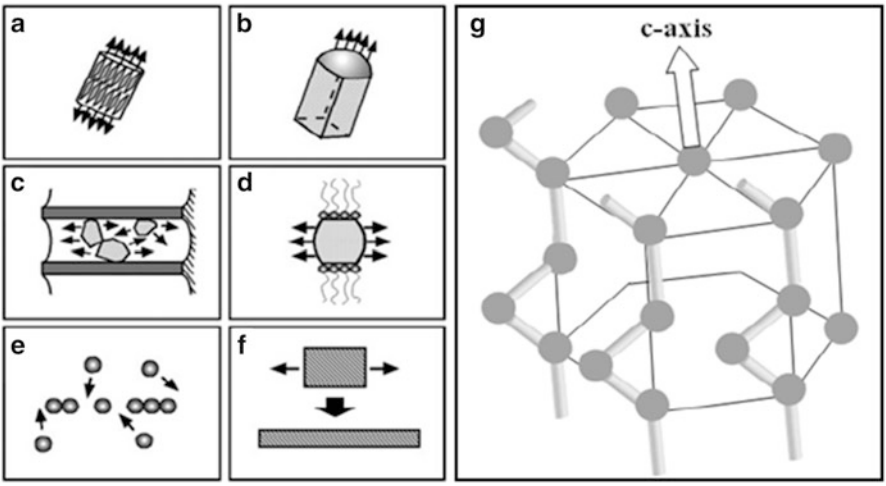

Fig. 2.1 (**a–f**) Schematics of the various methods for growing anisotropic 1D nanostructures (Taken from Xia et al. [3] with permission). (**g**) Hexagonal lattice showing how the *t*-Te chains are arranged along the c-axis, which is the principal symmetry axis of the crystal

of a structure causes drastic modification of the material's physicochemical properties. Various strategies have been adopted for this purpose. One-dimensional (1D) nanostructures have gained broad interest and have been the subject of extensive investigations [2]. Xia et al. [3] proposed an elegant classification of the most frequently employed synthesis strategies as illustrated in Fig. 2.1a–f. Six main paths for the development of linear 1D structures are envisaged: (**a**) Exploiting the anisotropic crystal structure and the preferential crystal growth towards certain crystallographic directions; this is the case for *t*-Se and *t*-Te. (**b**) Using the vapor-liquid-solid method where a liquid droplet of a catalyst (usually an Au nanoparticle) absorbs gaseous molecules forming an eutectic composition. When the liquid mixture becomes supersaturated precipitation takes place leading to the growth of 1D structures. (**c**) Utilizing hollow nanostructures or porous materials as templates for growing 1D structures inside the cavities. (**d**) Deactivating (or neutralizing) the side surfaces with appropriate molecules to permit growth primarily in one direction. (**e**) Self-organization of nanoparticles into larger 1D structures. (**f**) Degradation of larger structures into smaller ones by top-down processes. It is worth noting that all other approaches (**a**) to (**e**) are bottom-up processes.

As to be expected, the rational synthesis and advanced characterization of low-dimensional nanostructures have boosted the field of nanotechnology and materials science during the last two decades. Among low-dimensional materials 1D nanostructures with high aspect ratios (>10) emerge as high-added-value materials. Apart from offering a framework for understanding phenomena at the nanoscale, 1D materials have been extensively explored in regard to a wide variety

of potential applications in sectors related to energy conversion and storage (solar cells, batteries supercapacitors, etc.), nano- and opto-electronic devices, sensors, biomedicine, and so on [1–5]. Carbon nanotubes, ZnO nanorods/nanowires and silicon nanowires are considered as the most representative actors in the family of 1D nanostructures [6].

2.2 Tellurium Nanostructures Growth by Conventional Methods

The elemental chalcogens (group VI of the periodic table) trigonal Selenium (*t*-Se) and trigonal Tellurium (*t*-Te) exhibit a tendency to form 1D nanostructures due to their highly anisotropic crystal structure and the preference of the crystal to grow along a certain direction, as is depicted in Fig. 2.1g. Se and Te show a strong tendency to form 1D nanostructures as their crystal lattices consist of parallel polymeric chains – helices with three atoms as the repeat unit – arranged in an hexagonal form. The much stronger intra-molecular covalent interactions (each Se/Te bonds to its two first nearest neighbors in the same chain) as compared to the inter-molecular, mostly van der Waals bonding (each Se/Te interacts with four second-nearest neighbors in neighboring chains) endows a molecular-like character to elemental Se and Te where the single long chain plays the role of the molecule.

The kinetics of vapor-grown *t*-Te whiskers was studied by Furuta et al. [7] more than 40 year ago. In general, two methods are employed for the controlled synthesis of 1D *t*-Te nanostructures, mainly nanotubes (NTs): the solution chemistry approach [8, 9] and vapor deposition at high temperatures [10, 11]. Several interesting properties, such as photoconductivity, photoelectricity, thermoelectricity, piezoelectricity, and a nonlinear optical response characterize bulk *t*-Te. In addition, a number of possible applications have recently been reported for *t*-Te nano-structures. These include ammonia gas sensors at room temperature [12], Hg (II) sensors in aqueous media [13], and an antibacterial activity better than that of silver nanoparticles, while maintaining their toxicity lower than silver's [14].

The above methods cannot be considered as "green" approaches as they require the use of hazardous chemicals and elaborate high temperature processes. Alternatively, we have demonstrated a novel laser-assisted method for photo-processing of bulk *t*-Te that leads to a fast, one step controlled fabrication of *t*-Te NTs, which grow by irradiating elemental bulk Te with visible continuous wave lasers either under inert atmosphere or at ambient conditions for short exposure times [15]. The presence of oxygen controls the conversion of *t*-Te NTs via photo-oxidation, towards the formation of ultrathin core-Te/sheath-TeO_2 nanowires (NWs). In addition, we show that the growth parameters can be tuned to provide nanostructures with spherical shapes and sizes that depend upon the substrate distance from the irradiated target.

2.3 Tellurium Nanostructures Growth by Laser Irradiation

2.3.1 Experimental Details

Polished *t*-Te pieces were used as targets and placed inside a special cell that allows to control the atmosphere i.e. ambient (presence of oxygen) or inert (argon). Large-area or selective-area growth of Te nanostructures can be realized by changing the irradiation conditions. (i) To achieve large-scale production of Te nanostructures, a laser beam (514.5 or 488.0 nm) with a high intensity (~0.5 W) on a relatively large focusing area (ca. 100 μm.) is used. In this way, large quantities of Te vapors are produced which subsequently condensate either onto the Te piece used as target, Fig. 2.2a, or onto a Si substrate which is placed at various distances (2–10 mm) away from the target, Fig. 2.2b. (ii) For selective-area nanostructuring the 441.6 nm line is focused through a microscope objective (50×) on an area with a diameter of ca. 1–2 μm. Various neutral density filters are used to control the power density, i.e. 10^5, 10^4 or 10^3 W cm^{-2}.

In this set-up, the microscope is a component of a micro-Raman spectrometer, thus allowing the *in situ* accumulation of Raman spectra [15] and the monitoring of the evolution of photoinduced structural changes with time (Fig. 2.2c). In this case, the evaporated material condenses at the periphery of the focusing spot. In the center of the focusing spot a large crater is formed while at the periphery, Te vapors condense forming *t*-Te NTs, as shown in Fig. 2.3. The obtained nanostructures are characterized by Raman scattering, scanning and transmission electron microscopy (SEM, TEM) and high-resolution TEM (HRTEM).

2.3.2 Growth Mechanism of t*-Te Nanotubes*

Figure 2.4 presents typical *t*-Te NTs obtained when the target was irradiated with a power density of 10^5 W cm^{-2}. These structures grow at the periphery of the crater, shown in Fig. 2.3. Depending on the irradiation conditions, the average internal NT

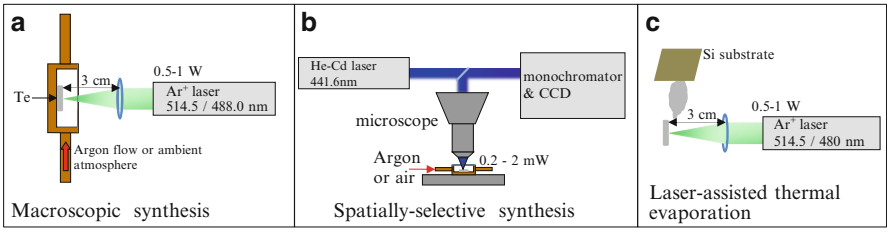

Fig. 2.2 Schematics of the various set-ups employed for the laser-assisted synthesis of chalcogen nanostructures

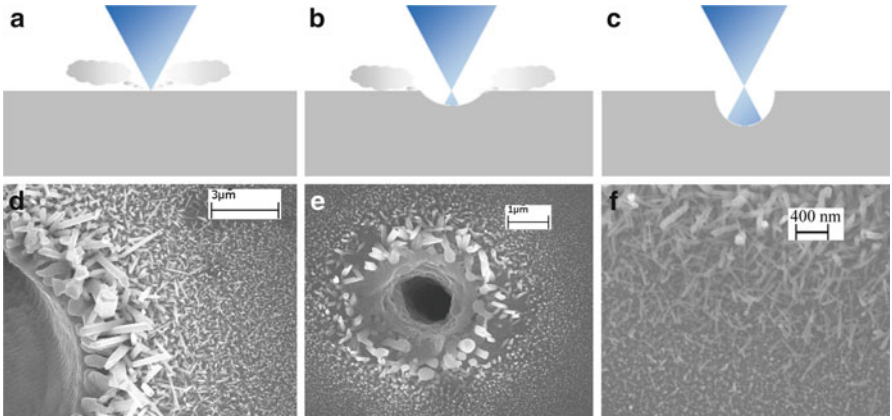

Fig. 2.3 Schematics of the laser beam focusing (*upper row*) in the course of irradiation of a polished Te surface and SEM images (*bottom*) of the crater formed and the nanostructures grown

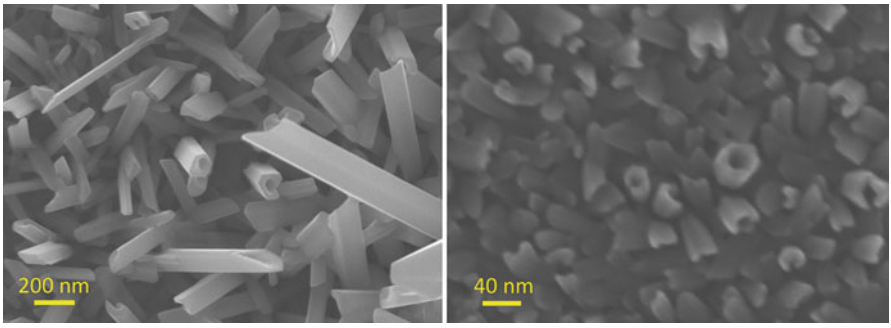

Fig. 2.4 Typical *t*-Te Nts grown by laser-assisted thermal evaporation

diameter can vary from 50 to 10 nm. The growth mechanism is based on the laser-assisted thermal evaporation of Te. For all visible wavelengths used here, the photon energy is much higher than the optical bandgap of *t*-Te (0.33 eV). The penetration depth of the light can be calculated from the imaginary part of the refractive index based on literature data [16]. Table 2.1 shows that for the laser energies used in the current work the penetration depth is in the range 8.5–9.5 nm, which implies that the first ~10 nm of the Te surface absorb the major part of the radiation causing a drastic temperature rise. As a low melting point solid ($T_m = 459$ °C) Te will considerably evaporate under focused illumination with the high power density of 10^5 W cm^{-2}.

The growth mechanism of *t*-Te NTs has been discussed elsewhere for tubes grown by solution-phase synthesis [17]. In the case of thermal evaporation, which applies here, the supersaturation of Te vapors plays an important role, analogous to the concentration of Te atoms in the solution-phase synthesis. The condensation of

Table 2.1 Optical constants of *t*-Te at selected visible wavelengths

Wavelength (nm)	Imaginary part of refractive index		Average penetration depth
	$k^{\parallel}$	$k^{\perp}$	$\mu = \left(\lambda/4\pi k^{\parallel} + \lambda/4\pi k^{\perp}\right)/2$ (nm)
441.6	4.42	3.63	8.8
488.0	4.85	3.76	9.2
514.5	5.08	3.77	9.5

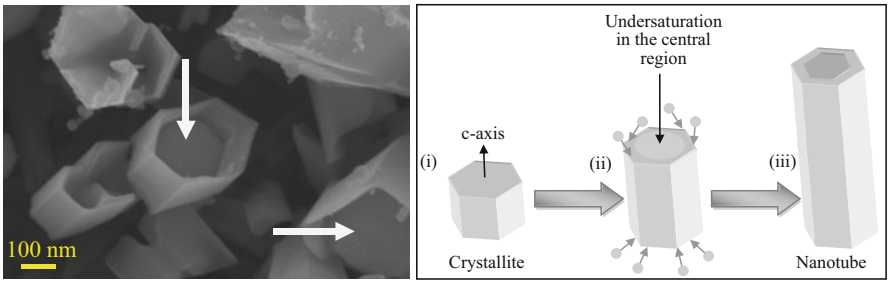

Fig. 2.5 Growth mechanism of t-Te nanotubes. *Left*: SEM image of *t*-Te nanotubes at the initial growth stage. *Right*: Schematic illustration of the growth mechanism

Te vapors leads to the creation of crystallites with a hexagonal shape. These crystallites act as nucleation centers for Te atoms condensating at the circumference of the seeds, driven by the free energy minimization requirement. The high mobility of Te atoms is essential for their localization to the periphery of the hexagonal crystal. The SEM image in Fig. 2.5 (left panel) provides evidence of the initial steps of the Te nanotube growth. The white arrows show the surfaces of the originally grown hexagonal crystallites perpendicular to the [0001] direction, which provides a template for incoming atoms to form the nanotube. A schematic diagram of the process is shown in Fig. 2.5 (right panel).

2.3.3 Growth of Tellurium Nanospheres

To investigate the effect of a cold substrate on the morphology of the nanostructures grown, the large-scale synthesis set-up (Fig. 2.2b) was used to irradiate the Te target, while the vapors condensate on a Si substrate. In the previous case the Te target was also used as the substrate to collect the vapors. Condensation of the vapor very near to the irradiated area implies that the crystal grown takes place on a substrate held at elevated temperature. In contrast, placing the substrate a few mm away from the target and collecting the Te vapors ensures that the substrate is at ambient temperature. As illustrated in Fig. 2.6, the effect of growing the Te

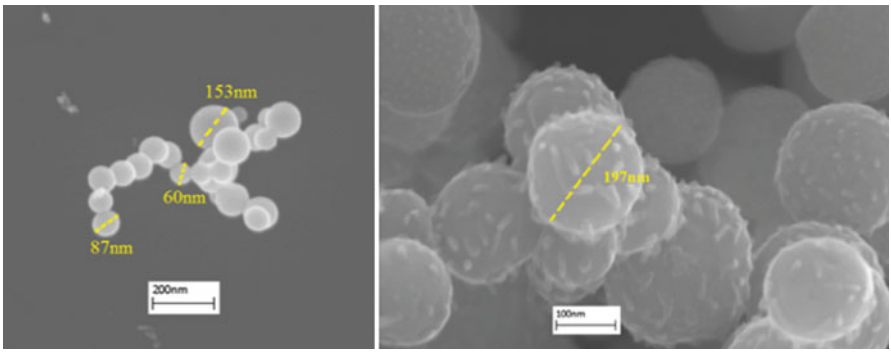

Fig. 2.6 Representative SEM images of Te nanospheres grown by the large-area growth set-up shown in Fig. 2.2 for target-substrate distances 4 (*left*) and 3 mm (*right*), respectively

nanostructures on a "cold" substrate is that only spherically shaped nanoparticles are observed. Preliminary experiments reveal that the particle size distribution depends on the distance between the target and the substrate. In general, shorter target-substrate distances result in particle size distributions centered at larger values.

The conditions of this experiment resemble those of the standard conditions for the preparation of amorphous Te thin films where a cold substrate is imperative for keeping Te in the amorphous phase. In the present experiment the vapors condense on a Si substrate held at ambient temperature. The kinetics of crystal growth in this case is different than that of condensing the vapor on a warmer substrate in an area very near to the target; as a result the morphology of the initial seeds formed do not allow the growth of anisotropic 1D structures.

2.3.4 *Te/TeO_2 Hybrid Nanostructures and the Kinetics of Photo-Oxidation*

Photo-induced processing of *t*-Te at ambient conditions (in the presence of oxygen) and with low light fluences (less than 5×10^4 W cm^{-2}) does not cause material evaporation. Instead, *in situ* recorded Raman spectra show that the photo-processed volume undergoes simultaneous photo-induced oxidation and amorphization as is illustrated in Fig. 2.7a [18]. Raman spectra reveal the appearance of a broad peak at ca. 170 cm^{-1} whose intensity increases systematically with irradiation time. The band profile indicates the development of an amorphous component in the illuminated volume, and in particular the formation of non-crystalline Te. In addition, vibrational modes appear at higher frequencies, in the spectral range of 350–800 cm^{-1}, demonstrating the formation of amorphous TeO_2 (a-TeO_2).

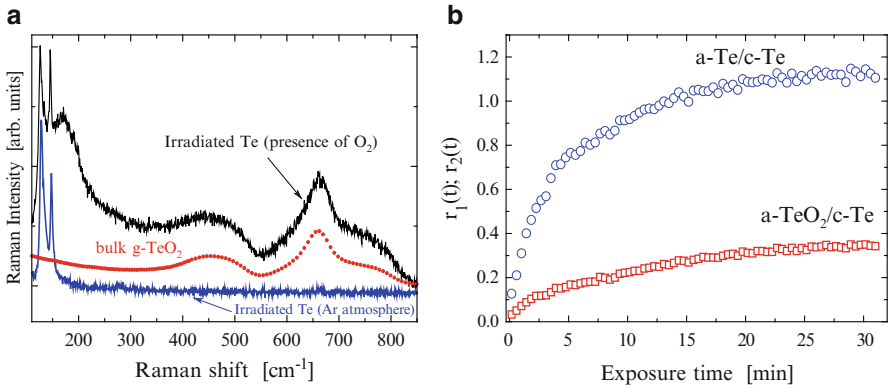

Fig. 2.7 (**a**) Raman spectra of *t*-Te irradiated at ambient and controlled (Ar) atmosphere. The Raman spectrum of bulk glassy TeO_2 is also shown for comparison. (**b**) Kinetics of the photo-induced oxidation and amorphization of *t*-Te under illumination. The *solid curves* represent the best fit results with exponential dependence on the illumination time

The kinetics of photo-amorphization and photo-oxidation are monitored by the change of the time-dependent intensity ratios $r_1(t) = I^{a-Te}(t)/I^{t-Te}$ and $r_2(t) = I^{a-TeO_2}(t)/I^{t-Te}$, respectively. $I^{t\text{-Te}}$, $I^{a\text{-Te}}$, and I^{a-TeO_2} denote the intensities of the Raman peaks centered at 144, ~165 and ~660 cm^{-1}, respectively, as shown in Fig. 2.7b for a light fluence of 5×10^3 W cm^{-2}. A rather abrupt increase of the intensity ratios seen at short times is followed by a saturation trend at longer times. More intense illumination speeds-up both photo-induced effects. The saturation (plateau) value which is reached for long enough times also depends upon the illumination power; higher saturation values are observed when increasing illumination power. The behavior of the intensity ratios $r_{1,2}(t)$ indicates an exponential-like increase for the process related to the power density 5×10^3 W cm^{-2}, while it turns out to be non-exponential at higher light fluences [18]. Prolonged irradiation leads to the crystallization of the thin amorphous TeO_2 film formed at early stages and drives the structure through all known crystalline phases of the oxide.

Direct evidence that controlled irradiation results in hybrid Te/TeO_2 structures such as core/shell nanospheres or core/sheath nanowires, as evidenced in the TEM images in upper panel of Fig. 2.8a, b, respectively. The coexistence of *t*-Te and a-Te peaks in the Raman spectrum indicates that the thickness of the a-Te layer, sandwiched between TeO_2 and *t*-Te, is of the order of few nm. This is clearly demonstrated in the HRTEM image shown in Fig. 2.8c, taken from nanowire. The core/sheath structure is evident, manifesting the growth of an amorphous layer around the tellurium nanowire spatially confined within a few nanometers. Photo-oxidation can be used to engineer *t*-Te nanowires and nanospheres towards the formation of hybrid nanostructures. The present findings may have far-reaching implications to various applications since the interface of Te and TeO_2 has been found to exhibit strong potential for applications in UV photoconductivity [19].

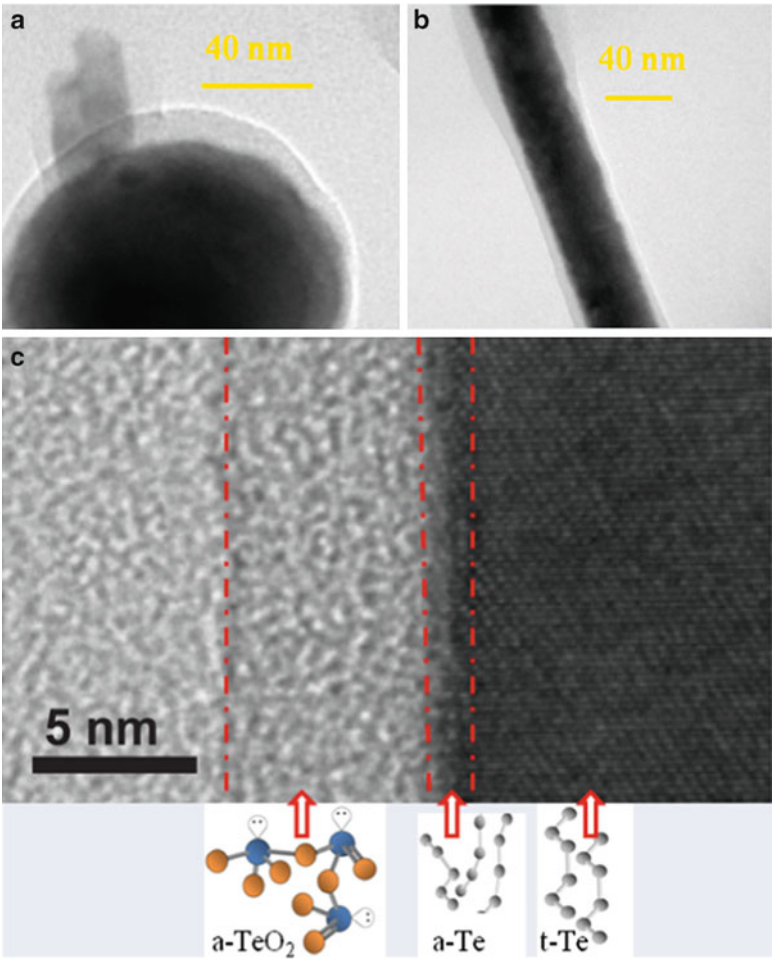

Fig. 2.8 TEM images of hybrid *t*-Te/aTeO_2 structures: (**a**) nanospheres and (**b**) nanowires. (**c**) HRTEM image of the interface showing single crystalline *t*-Te coated by an amorphous TeO_2 layer. A buffer layer of amorphous Te exists between these two regions. Schematics of the atomic arrangement of the three regions are shown at the bottom of panel (**c**)

2.4 Laser-Assisted Nanostructuring of Phase-Change Materials

The laser-assisted phenomena presented above are essentially based on the high tendency of elemental Te to crystallization. Indeed, it is practically impossible to prepare bulk glassy elemental Te by melt quenching. In the search of other chalcogen-based materials that allow laser-assisted nanostructuring, preliminary investigations on elemental Se did not show promising results. This is explained by the good glass-forming ability of Se. Therefore, the laser-assisted nanostructuring

phenomena should be sought in telluride materials which are known to be poor glass formers. The binary system GeTe fulfills this condition; in addition it is a material of high interest since it is the basic ingredient of the phase change Ge-Sb-Te alloy used for data storage (phase-change memories, PCMs). Materials used as PCMs have the ability to switch between two different phases which can be easily distinguished either by light (refractive index contrast) or by electrical signals (resistance contrast). Recent trends in Ge-Sb-Te materials to be used as PCMs are directed towards miniaturizing the memory cell size down to few tens of nm, i.e. less than 40 nm [20]. Reducing the cell size is essential to achieve high switching speed and low operating power of the memory device. Fabrication of low-dimensional Sb-doped Te NTs nanotubes by thermal evaporation and study of their memory switching properties have been reported [21]. These nanostructures showed significantly improved phase-change characteristics desirable for power-efficient memories, which was explained based on the intrinsic material properties and the geometric contribution from the hollow structures being more effective with regard to heat confinement and localization [21].

SEM images of nanostructures obtained by laser-assisted processing of crystalline GeTe are shown in Fig. 2.9. Image (a) is representative of the structures formed near the irradiated area, which are characterized by a fractal-like morphology. Large grains of ca. 100–150 nm are decorated by smaller particles with sizes of ~20–30 nm. Higher resolution images reveal that the surface of these smaller particles are also textured decorated by even smaller ones with dimensions less than 5 nm. A few tens of microns away from the irradiated area the morphology of the grown structures is different, as shown in Fig. 2.9b. Ultrathin nanowires grow in this area whose composition is different than the target. In particular, it is found that these nanowires are Te-rich structures, which is explained by the higher thermal evaporation rate of Te during irradiation of the binary GeTe.

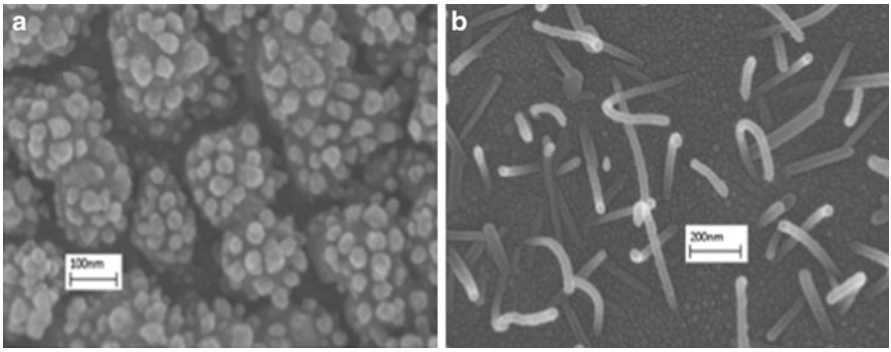

Fig. 2.9 (**a**) Fractal-like nanocrystals of GeTe and (**b**) Te-rich nanowires grown by GeTe irradiation with 441.6 nm for 60 s

2.5 Conclusions

The current method involves an all-laser, solid state materials processing which is fast and environmentally friendly since no hazardous substances are used and no post-fabrication treatment is needed to remove chemical byproducts, thus resulting in high purity nanostructures. The method demonstrates the feasibility of using focused laser beams for selectively inscribing the desired nanostructures on the surface of pre-deposited films, thus providing a means of simultaneous growth and integrating the nanostructures into an optoelectronic or photonic device.

References

1. Vajtai R (ed) (2013) Springer handbook of nanomaterials. Springer, Berlin
2. Xu S, Wang ZL (2011) Nano Res 4:1013
3. Xia Y, Yang P, Sun Y, Wu Y, Mayers B, Gates B, Yin Y, Kim F, Yan H (2003) Adv Mater 15:353
4. Yang PD, Yan R, Fardy M (2010) Nano Lett 10:15296
5. Yan R, Park J, Choi Y, Heo C, Yang S, Lee LP, Yang P (2012) Nat Nanotechnol 7:191
6. Wang ZL (2009) Mater Sci Eng R 64:33
7. Furuta N, Ohasi Y, Itinose H, Igarashi I (1975) Jpn J Appl Phys 14:929
8. Mo M, Zeng J, Liu X, Yu W, Zhang S, Qian Y (2002) Adv Mater 14:1658
9. Zhu H et al (2011) J Phys Chem C 115:6375
10. Geng BY, Lin Y, Peng XS, Meng GW, Zhang LD (2003) Nanotechnology 14:983
11. Hawley CJ, Beatty BR, Chen G, Spanier JE (2012) Cryst Growth Des 12:2789
12. Wang Z, Wang L, Huang J, Wang H, Pan L, We X (2010) J Mater Chem 20:2457
13. Wei TY, Chang HY, Lee YF, Hung Y, Huang C (2011) J Chin Chem Soc 58:732
14. Lin ZH, Lee CH, Chang HY, Chang HT (2012) Chem Asian J 7:930
15. Vasileiadis T, Dracopoulos V, Kollia M, Yannopoulos SN (2013) Sci Rep 3:1209
16. Palik ED (ed) (1985) Handbook of optical constants of solids. Academic, Orlando
17. Mayer B, Xia Y (2002) Adv Mater 14:279
18. Vasileiadis T, Yannopoulos SN (2014) J Appl Phys 116:103510
19. Oishi K, Okamoto K, Sunada J (1987) Thin Solid Films 148:29
20. Loke D, Shi L, Wang W, Zhao R, Yang H, Ng L-T, Lim K-G, Chong T-C, Yeo Y-C (2011) Nanotechnology 22:254019
21. Jung Y, Agarwal R, Yang C-Y, Agarwal R (2011) Nanotechnology 22:254012

Chapter 3
Material Processing of Dielectrics via Temporally Shaped Femtosecond Laser Pulses as Direct Patterning Method for Nanophotonic Applications

Tamara Meinl, Nadine Götte, Yousuf Khan, Thomas Kusserow, Cristian Sarpe, Jens Köhler, Matthias Wollenhaupt, Arne Senftleben, Thomas Baumert, and Hartmut Hillmer

Abstract Dielectric materials are of great interest for optical applications since they are transparent in the UV, visible and IR spectral range. That makes them very suitable for optical filters, polarizer, waveguides or even reflectors. When dielectrics are processed with conventional techniques based on electron or ion bombardments, they suffer from severe charging effects. For this reason, we present temporally shaped femtosecond laser pulses as a novel direct patterning method of wide band gap materials with very high precision to create photonic crystal structures in dielectrics. Material processing with temporally shaped femtosecond laser pulses overcomes the charging problems. Fabrication of structures well below the diffraction limit is feasible with temporally shaped asymmetric pulse trains due to nonlinear ionisation effects like multiphoton ionisation and avalanche ionisation. For the implementation as optical filters, a thin-film waveguide with a 2D periodic pattern of photonic crystals with circular base elements is investigated. The wave guiding layer consists of a material with a higher refractive index than the surrounding materials, in our case SiO_2. Although the refractive index contrast is low, numerical design results prove that light with normal incidence to the plane of

T. Meinl (✉) • Y. Khan • T. Kusserow • H. Hillmer
Institute of Nanostructure Technologies and Analytics, Technological Electronics and CINSaT, University of Kassel, Heinrich-Plett-Str. 40, Kassel 34132, Germany
e-mail: meinl@ina.uni-kassel.de

N. Götte • C. Sarpe • J. Köhler • A. Senftleben • T. Baumert
Institute of Physics and CINSaT, University of Kassel, Heinrich-Plett-Str. 40, Kassel 34132, Germany

M. Wollenhaupt
Institute of Physics and CINSaT, University of Kassel, Heinrich-Plett-Str. 40, Kassel 34132, Germany

Institute of Physics, Carl von Ossietzky University of Oldenburg, Carl-von-Ossietzky-Straße 11, Oldenburg 26111, Germany

P. Petkov et al. (eds.), *Nanoscience Advances in CBRN Agents Detection, Information and Energy Security*, NATO Science for Peace and Security Series A: Chemistry and Biology, DOI 10.1007/978-94-017-9697-2_3

periodicity couples to waveguide modes and Fano resonances are excited. This makes the device extremely interesting as a compact narrow-band optical filter.

Keywords Photonic crystal • Fano resonance filter • Low refractive index contrast • Dielectrics • Shaped femtosecond laser pulse

3.1 Introduction

Dielectric materials offer great potential for applications in photonic devices since they are transparent in the UV, visible and near infrared spectral range. A vast variety of dielectric materials is available with good chemical and mechanical stability and processing properties, especially oxide and nitride compounds. The implementation of nanophotonic structures like photonic crystals with dimensions smaller than the targeted wavelength enables the utilization of strong interaction or other specific effects.

On the one hand, dielectrics offer low-cost fabrication when compared to semiconductors, but in contrast to them they underlie severe charging effects when processed with conventional techniques based on electron beam lithography or focused ion beams as already presented in a previous work [1]. Material processing with temporally shaped femtosecond laser pulses avoids these charging effects. Additionally, it provides very fast processing times, while no additional sample treatments and no vacuum conditions are required.

The interaction between laser irradiation and transparent materials is mainly based on the deposition of energy into the medium. This enables the ablation of the material by plasma formation and the expansion of the plasma into the material [2–4]. The free electron density is controlled in this case by temporally shaped femtosecond laser pulses. The two main ionization processes involved are multiphoton ionization and avalanche ionization [5, 6]. The utilization of these effects allows the generation of reproducible structures with dimensions being an order of magnitude below the diffraction limit [5, 7, 8].

Our design consists of a photonic crystal (PhC) array and a wave guiding layer with dimensions smaller than the target wavelength. We utilize the guided-mode resonance effect from light with normal incidence to the surface, which is based on the interference between the resonant waveguide modes and free space modes. Thus, externally propagating fields from direct transmission or reflection, respectively, couple to modes of the waveguide [9]. Hessel and Oliner [10] gave the first model in 1965 to describe these resonance types. Since then, different approaches using this effect as well as possible photonic applications have been reported [1, 9, 11–14].

3.2 Design and Fabrication

We generate a periodic grating of photonic crystal structures with circular base elements via shaped femtosecond laser pulses into a silicon oxide (SiO_2) substrate with a refractive index of $n_{Low} = 1.5$. The deposition of a thin Nb_2O_5 layer with a

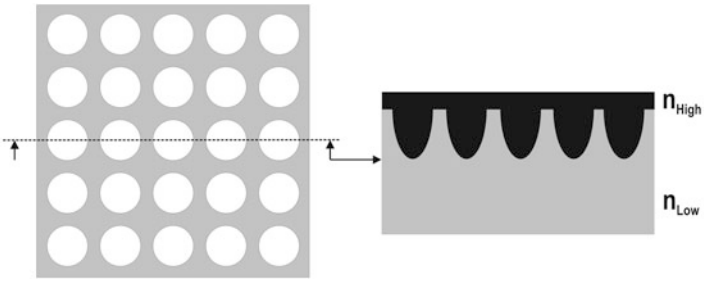

Fig. 3.1 *Left*: A photonic crystal structure array generated into a fused silica substrate (n_{Low}). *Right*: Sectional view with added waveguide layer (n_{High})

higher refractive index $n_{High} = 2.2$ completes this guided-mode resonance filter device. A schematic of this design is depicted in Fig. 3.1. The Nb_2O_5 layer acts as slab waveguide and enables the coupling of incident light to discrete slab modes. Although the refractive index contrast is low, we prove this device to be suitable as narrowband filter. We achieved asymmetric Fano resonances in the near infrared spectral region for base element structure sizes of typically a couple hundred nanometers. By simple scaling down, this kind of devices are also applicable in the visible or UV spectral range.

The laser setup for material processing consists of an amplified Ti:Sapphire laser system which provides linearly polarized laser pulses with a full width at half maximum (FWHM) duration of 35 fs at the central wavelength of 800 nm. Laser pulses are temporally shaped with a self-built pulse shaper [15] and focused onto the substrate with a microscope setup. The lateral spot diameter is 1.4 µm ($1/e^2$ value of the intensity profile). During the experiment, the energy of the pulses is controlled and monitored with a neutral density gradient filter and a photodiode, respectively. The sample is moved via a 3-axis piezo stage which provides an accuracy of 10 nm.

PhC profiles were produced by means of bandwidth-limited and modulated femtosecond laser pulses by introducing a third order dispersion (TOD) of $\varphi_3 = +6 \times 10^5$ fs^3. TOD shaped pulses with positive φ_3 were applied which show a temporally asymmetric profile. This specific pulse profile consists of a high energy sub-pulse followed by a long pulse train of lower energies with a constant instantaneous frequency throughout the entire pulse. Different focal positions of the laser beam relative to the substrate surface are investigated. They vary in vertical direction from a few micrometers below the substrate surface to a few micrometers above in steps of $\Delta z = 1$ µm, with the total energy of the pulses remaining constant.

The characterization of the inner profiles of the generated PhC structure was carried out after focused ion beam (FIB) preparation. Cross-sections were performed at the center of the elements to evaluate specifically the diameter D and depth h. A thin platinum layer was sputtered onto the entire substrate as conductive layer to avoid charging of the dielectric material while operating with FIB and SEM. Additionally, a platinum layer was deposited locally on the

PhC elements to protect the structure during the milling process. After cross-sectioning, the PhC profile parameters were measured in the SEM mode.

3.3 Results

The numerical simulation in Fig. 3.2 demonstrates a suitable conical PhC shape for implementation as narrowband optical filter. The parameters for the calculation are diameter $D = 500$ nm, depth $h = 900$ nm, lattice constant $a = 1$ µm and waveguide layer thickness $d_{wgl} = 330$ nm. Two sharp narrowband resonances are observed at wavelengths around $\lambda = 1.52$ µm and $\lambda = 1.82$ µm.

As first experimental result,[1] shown in Fig. 3.3, we compare the PhC profiles fabricated with a bandwidth-limited pulse and a TOD shaped pulse with the same focal position (on the substrate surface) and same energies (2.5 times above the damage threshold). In comparison, the diameter at the surface is similar for both types of pulses: for bandwidth-limited pulses $D = 956$ nm and for TOD pulses $D = 985$ nm. The profile created by the bandwidth-limited pulse is restricted in depth to around 340 nm, while the result created by the TOD pulse shows a

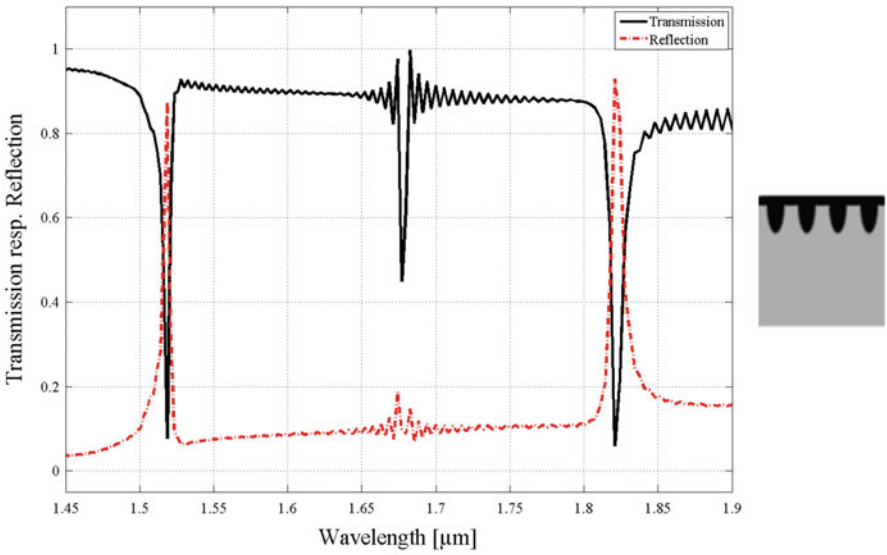

Fig. 3.2 Numerical simulation performed with the parameters: diameter $D = 500$ nm, depth $h = 900$ nm, lattice constant $a = 1$ µm and waveguide layer thickness $d_{wgl} = 330$ nm. Two sharp narrowband resonances appear at wavelengths around $\lambda = 1.52$ µm and $\lambda = 1.82$ µm

[1] All measured values underlie an error of ±20 nm due to analyzing software.

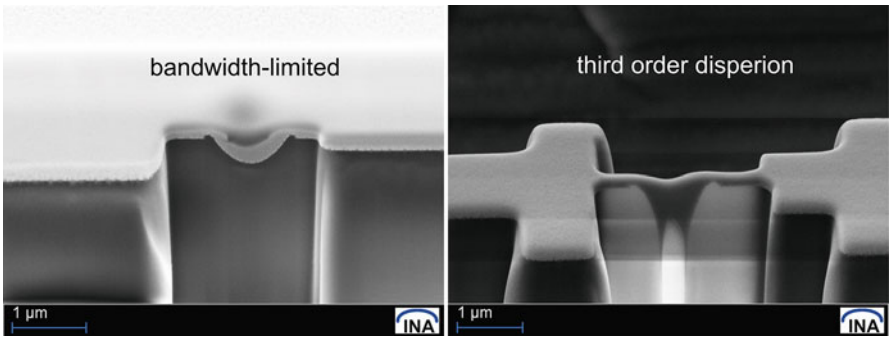

Fig. 3.3 Resulting hole profiles from a bandwidth-limited pulse (*left*) and a TOD shaped pulse with $\varphi_3 = +6 \times 10^5$ fs^3 (*right*) at the same focal position $z = 0$ µm with energies 2.5 times above damage threshold. The difference in penetration depth is clearly observable

funnel-shaped hole with an increased depth of more than 2 µm. Hence, the aspect ratio of PhC elements created by bandwidth-limited pulses is not sufficient to achieve strong guided-mode resonances, whereas the PhC structures created by TOD show a promising profile. Additionally, for the same energy values less than 250 nm of the inner diameter were achieved, which is well below the diffraction limit (1.4 µm).

3.4 Conclusions

We demonstrated numerically that our PhC designed structures show great potential for application as narrowband optical filters due to guided-mode resonances. The characterization of the PhC profiles confirms that direct material processing via temporally shaped femtosecond laser pulses is a very promising tool for nanophotonic device fabrication in dielectric materials. We compared PhC profiles fabricated with bandwidth-limited laser pulses and TOD shaped laser pulses. TOD shaped pulses provide a very promising aspect ratio.

Acknowledgments The financial support by the German Research Foundation (DFG) in the priority program SPP1327 is gratefully acknowledged. The authors thank D. Gutermuth, J. Krumpholz and A. Dück for their technical support and R. Tahir for scientific contributions.

References

1. Kusserow T, Khan Y, Zamora R, Messow F, Hillmer H, Optical MEMS and Nanophotonics (OMN) (2012) 2012 International Conference, Technical digest, pp 170–171
2. Balling P, Schou J (2013) Rep Prog Phys 76:036502

3. Mao SS, Quéré F, Guizard S, Mao X, Russo RE, Petite G, Martin P (2004) Appl Phys A 79:1695–1709
4. Vogel A, Venugopalan V (2003) Chem Rev 103:577–644
5. Englert L, Rethfeld B, Haag L, Wollenhaupt M, Sarpe-Tudoran C, Baumert T (2007) Opt Express 15:17855–17862
6. Sarpe C, Köhler J, Winkler T, Wollenhaupt M, Baumert T (2012) New J Phys 14:1367–2630
7. Wollenhaupt M, Englert L, Horn A, Baumert T (2009) J Laser Micro/Nanoeng 4:144–151
8. Englert L, Wollenhaupt M, Sarpe C, Otto D, Baumert T (2012) J Laser Appl 24:042002
9. Magnusson R, Wang SS (1992) Appl Phys Lett 61:1022–1024
10. Hessel A, Oliner AA (1965) Appl Opt 4:1275–1297
11. Boutami S, Bakir B, Hattori H, Letartre X, Leclercq J-L, Rojo-Romeo P, Garrigues M, Seassal C, Viktorovitch P (2006) IEEE Photon Technol Lett 18:835–837
12. Zamora R, Benes M, Kusserow T, Hillmer H, Akcakoca U, Witzigmann B (2011) Proc IEEE Conf Opt MEMS and Nanophotonics, pp 83–84
13. Nazirizadeh Y, Lemmer U, Gerken M (2008) Appl Phys Lett 93:261110
14. Crozier K, Lousse V, Kilic O, Kim S, Fan S, Solgaard O (2006) Phys Rev B 73
15. Köhler J, Wollenhaupt M, Bayer T, Sarpe C, Baumert T (2011) Opt Express 19:11638–11653

Chapter 4
Fabrication of Nanoporous Silicon by Ion Implantation

T.S. Kavetskyy and A.L. Stepanov

Abstract Ion implantation is an advanced new technological method for the fabrication of nanoporous silicon material with metal nanoparticles. The methodology of this technique is developed by Ag^+-ion implantation with an energy of 30 keV and a dose of $1.5 \cdot 10^{17}$ ion/cm^2 into a polished monocrystalline silicon substrate. By using Raman spectroscopy, SEM and AFM measurements it is found that amorphous layers of porous silicon (PSi) with an average size of the porous holes on the order of 150–180 nm, a depth of about 100 nm and a wall thickness of about 30–60 nm are formed on the Si surface as a result of ion irradiation. Ion implantation is also applied to locally modify the surface of Si to create periodic plasmonic PSi microstructures with Ag nanoparticles with a diameter of 5–10 nm. The results obtained clearly demonstrate how low-energy ions can be used for the fabrication of photonic microstructures on Si surfaces in a single-step process, similarly as it was recently done for Cu^+-ion implanted silica glass.

Keywords Ion implantation • Nanoporous silicon • Silver nanoparticles

4.1 Introduction

Porous silicon (PSi) is one of the most widely studied modern structured materials whose application in micro, nano, and optoelectronics, as well as in sensorics, biosensorics, and solar cells, is very promising [1]. Such PSi layers were first obtained in the mid-1950s at Bell Labs [2], but it were not seriously used until

T.S. Kavetskyy (✉)
Drohobych Ivan Franko State Pedagogical University, Drohobych 82100, Ukraine

John Paul II Catholic University of Lublin, Lublin 20-718, Poland
e-mail: kavetskyy@yahoo.com

A.L. Stepanov
Kazan Physical-Technical Institute of Russian Academy of Sciences, Kazan 420029, Russia

Kazan National Research Technological University, Kazan 420015, Russia

Kazan Federal University, Kazan 420008, Russia

P. Petkov et al. (eds.), *Nanoscience Advances in CBRN Agents Detection, Information and Energy Security*, NATO Science for Peace and Security Series A: Chemistry and Biology, DOI 10.1007/978-94-017-9697-2_4

the discovery of their strong luminescent properties in 1990 [3]. Prior to this discovery, PSi was almost exclusively considered as insulating layer devices in the microelectronics industry. The detail advantages of PSi vs. silicon are observed in literature very well [4, 5]. Therefore, searching for new techniques to obtain PSi and improving the corresponding methods, existing for synthesis of such structures, is a topical problem now.

In the past, there were only two main technological methods for the production of PSi structures: electrochemical etching and chemical stain etching [4, 5]. Thus, PSi could be chemically created on silicon under appropriate conditions with porous sizes of a few nanometers to micrometers [1, 6]. Both the porosity and the pore morphology of PSi are greatly influenced by the electrochemical and chemical stain etching parameters such as temperature, current density, light illumination and so on.

The use of ion implantation with ions of rare gases to obtain nanodimensional PSi layers at the surface of monocrystalline silicon is also known. The solubility of rare gases in solids is very low and does not exceed a level of 10^{16} ions/cm^2. The gettering of gas bubbles from the matrix gas ions in irradiated polymer materials leads to the formation of nanopores (free volumes, nanovoids) [7]. In the case of silicon the implanted silicon wafers are subjected to thermal annealing in order to stimulate the nucleation and growth of pores from implanted gas ions [8]. This technique for the formation of pores at the surface of silicon was demonstrated earlier for implantation with ions such as He^+ [9], H^+ [10], Ne^+ [11], Ar^+ [12] and Kr^+ [11, 13].

Additionally, recently interest for silicon nanostructures containing noble metal nanoparticles has developed. It was initiated since metal nanoparticles with localized surface plasmon modes demonstrate a specific option to enhance the recombination rate of silicon light emitters to increase the efficiency of photoluminescence and internal quantum yield effectively, etc. [6, 14–16]. Silver nanoparticles (AgNPs) are the subject of increasing interest due to their strong plasmon resonance in the visible spectrum [17, 18]. For example, PSi samples coated with a layer of AgNPs showed after their electrochemical etching that the photoluminescence intensity remarkably increases [19], and the reflection of incident light with wavelengths below 1,100 nm can be reduced to use them for antireflection devices [20] or surface-enhanced Raman scattering of some organic molecules adsorbed on AgNP-PSi structures [15].

Instead of using simple silicon as the substrate for AgNPs deposition on the top of a sample, the ion implantation technique can be used to form AgNPs in the silicon volume as in the case of ion-irradiated silica glasses or polymers [18, 20–24]. Earlier, in experiments described [25, 26] Ag-ion implantation into crystalline silicon wafers and nanocrystalline silicon layers with an energy of 30–35 keV and a rather low dose of $5.0 \cdot 10^{15}$ ions/cm^2 was performed. Then AgNPs in the silicon matrix were synthesized after thermal annealing of the implanted samples at 500 °C. In another work [27], Ag^+-ion implantation of silicon using a conventional metal vapor vacuum arc (MEVVA ion source, which produces a mixture of Ag^{n+} ions) was applied with a higher dose of $2.0 \cdot 10^{17}$ ions/cm^2 to create AgNPs.

As will be discussed here and was shown in the literature [28], the physical technique of metal-ion implantation was not used before 2013 in practice for the fabrication of PSi [29]. A successful experiment of synthesis of PSi with implanted Ag nanoparticles was demonstrated, for the first time, in [29, 30]. A detailed description of the technological approach and new results obtained for AgNP-PSi structures are presented and explained in this contribution.

4.2 Experimental Procedure

Single crystalline p-type (100)-oriented silicon wafers were used as substrates for Ag^+-ion implantation to create PSi structures. Before implantation the substrates were cleaned by a wet chemical etching process. The silicon wafers were implanted with Ag^+ ions at the energy of 30 keV and an ion current density of 4 μA/cm^2 with doses in the range from $7.5 \cdot 10^{16}$ to $1.5 \cdot 10^{17}$ ions/cm^2 using the ion accelerate "ILU-3" at a residual pressure of 10^{-5} Torr and room temperature.

In an additional experiment, in order to reveal effects of sputtering or swelling of the surface, some silicon substrates were implanted through a mask consisting of a nickel mesh grid with square holes and a bar width of 20 μm. The mask was imposed onto the substrate during implantation to form a structure of irradiated and non-irradiated parts of the silicon surface. In this way, selectively implanted regions were prepared next to unimplanted ones in order to perform step-height profilimetry.

The depth distribution profiles of the Ag atoms and the damage level in the implanted silicon were modeled using the simulation-program "Stopping and Range of Ions in Matter" (SRIM-2013) [31].

The morphology of the implanted structured silicon surfaces were characterized in plan-view by scanning electron microscopy (SEM) using a high-resolution microscope (Merlin Carl Zeiss) combined with ASB (angle selective backscattering) and SE InLens (secondary electrons energy selective backscattering) detectors; in addition it was also equipped with a AZTEC X-MAX energy-dispersion spectrometer from Oxford Instruments for energy-dispersive X-ray spectroscopy (EDX) analysis.

The crystallinity of the implanted silicon structure was estimated from Raman spectra recorded with a DFS-52 spectrometer at room temperature, excited by a continuous argon laser LGN-502 with a wavelength of 448 nm and a radiation power of 50 mW.

Surface morphology observations and measurements of the profile and depth of pores (cross sections) in PSi were carried out by an Innova Bruker atomic-force microscope (AFM). A quantitative evaluation of the size of the pores was carried out by histograms with the size distribution using the Axio Vision computer software for processing SEM images according to the method described in [32].

The focused ion beam technique (FIB) was applied to provide milling of the implanted silicon surface for analyzing the sample depth by Auriga CrossBeam

Workstation Carl Ziess (FIB-SEM) with a 30 keV Ga liquid metal ion source at normal incidence. By this approach a square of 2×2 μm^2 on a PSi surface was written with a ion current density of 50 nA/cm^2 that did not heat the sample but effectively sputtered the implanted surface.

4.3 Results and Discussion

4.3.1 Vacancies and Ion Depth Distribution

Ion implantation is a widely applied technique used for controlled in-depth doping of various metals, dielectrics, and semiconductors by embedding into them energetically accelerated ions of various chemical elements [1]. According to SRIM simulations, during ion bombardment a vacancy-rich region and an accumulation of implanted ions can be formed close to the surface in the irradiated matrix (Fig. 4.1). The mean penetration range R_p^{Ag} of 30 keV accelerated Ag^+-ions in a silicon substrate is about 26 nm with a longitudinal straggling ΔR_p^{Ag} of 8 nm with a Gaussian depth distribution (Fig. 4.1a). Thus, the predicted thickness of the modified silicon surface layer $R_p + 2\Delta R_p$ is about 42 nm.

Wang and Birtcher [33] assumed that during ion implantation porous structures in various semiconductors can result from nucleation of small voids in the irradiated materials by vacancy generation. Therefore the vacancy depth distribution for silicon implanted with Ag^+ ions was also simulated by SRIM (Fig. 4.1b), which shows a profile similar to the ion distribution for such low energies. Analyzing the SRIM modeling, however, should take in account that the depth distribution of Ag-ions and vacancies obtained correspond to an implantation process in an

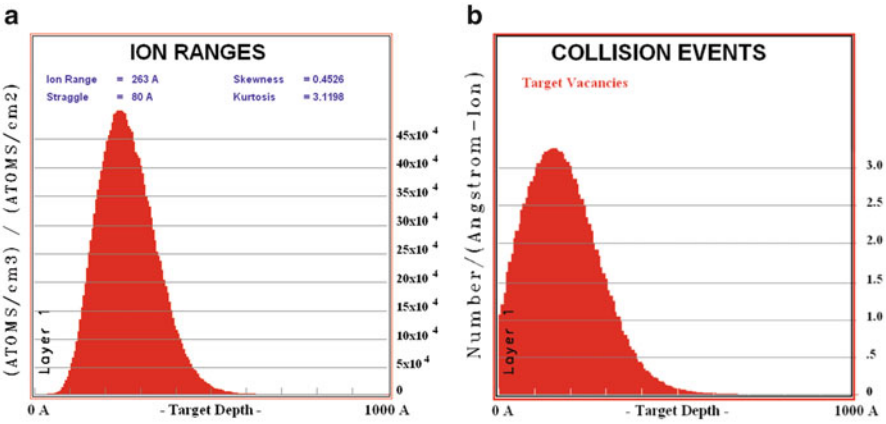

Fig. 4.1 Depth ion distribution of Ag-ions implanted (**a**) and generated vacancy profiles (**b**) in silicon with energy of 30 keV calculated using the SRIM code

uniform silicon matrix before nucleation and growth of PSi (for ion doses less than $1.0 \cdot 10^{16}$ ions/cm^2). As will be shown below, a prolonged irradiation results, simultaneous with the formation of PSi and the segregation of silver near the surface, in silicon sputtering.

4.3.2 SEM Study of PSi Structure

Figure 4.2a shows a plane-view SEM image of unimplanted silicon, which looks very smooth without any surface structural inhomogeneity.

The results of the creation of pores on the silicon samples are observed by plan-view SEM images (Fig. 4.3). In contrast to unimplanted silicon (Fig. 4.2) the characteristic PSi surface structures show the appearance of black holes in the implanted silicon region. They consist of nearly cellular features separated by rather thin walls with thicknesses about 30–60 nm. Such features are clearly resolved for all samples formed by various Ag-ion dose irradiations: $7.5 \cdot 10^{16}$, $1.0 \cdot 10^{17}$ and $1.5 \cdot 10^{17}$ ions/cm^2. Uniform pore distributions with distinguished sharp holes were observed for all implanted surfaces on silicon-implanted samples. The size of the pores was measured by counting the number of holes in several micrographs, taking into account all visible holes boundaries and subtracting those holes that intersects an edge of the SEM image. From this, the size of the pores was estimated. It can be seen that mean pore size (black holes) increase in magnitude with increasing Ag-ion doses. White spots in these SEM figures correspond to a material with a higher density compared to silicon which suggests them to be AgNPs.

Figures 4.2b and 4.4 present EDX spectra recorded on the examined unimplanted silicon and on PSi structures with AgNPs fabricated with the highest

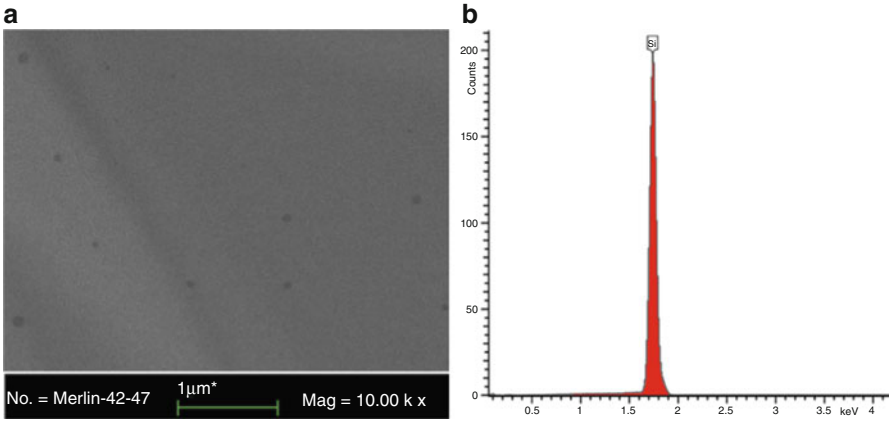

Fig. 4.2 SEM image (**a**) and EDX characteristic spectrum (**b**) of unimplanted silicon

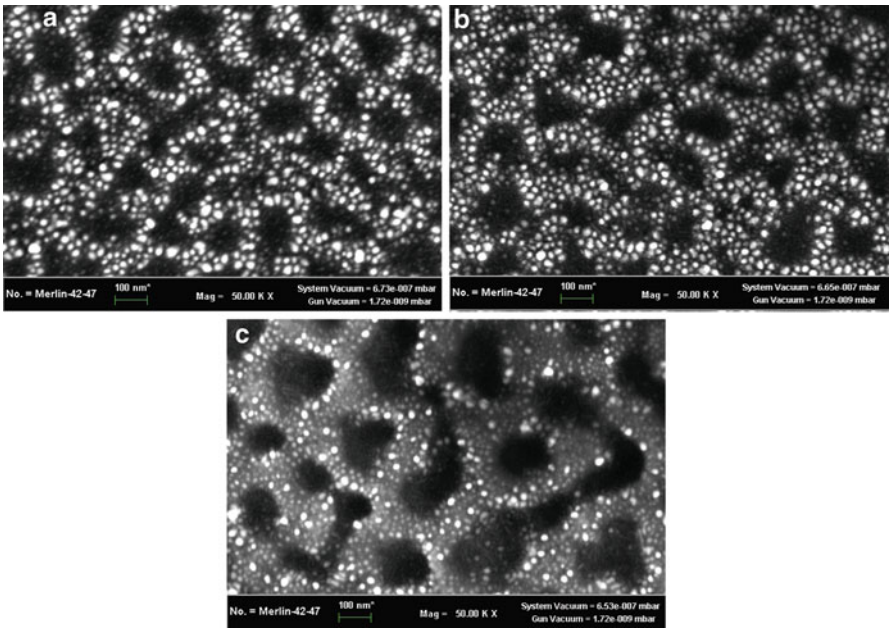

Fig. 4.3 SEM images of PSi fabricated by Ag^+-ion implantation into silicon with various doses: (**a**) $7.5 \cdot 10^{16}$; (**b**) $1.0 \cdot 10^{17}$ and (**c**) $1.5 \cdot 10^{17}$ ions/cm^2

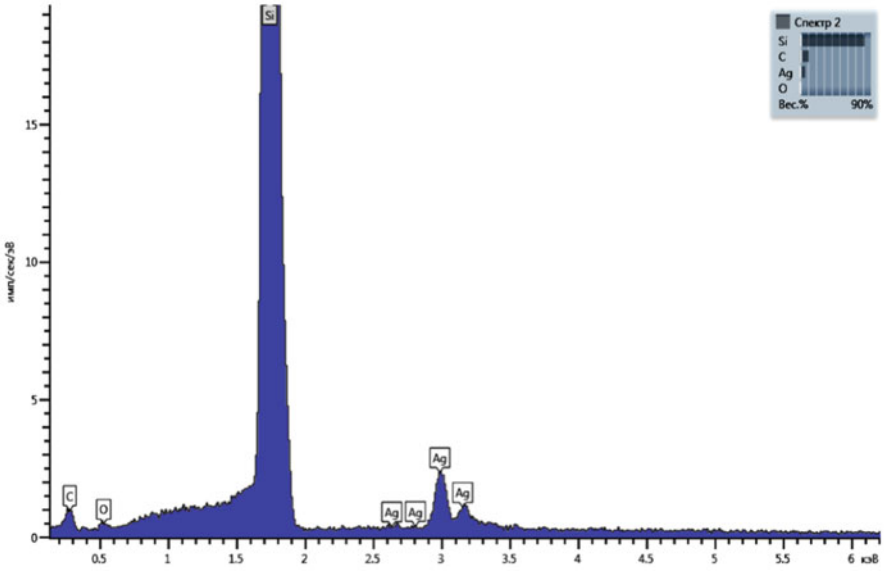

Fig. 4.4 EDX characteristic spectrum of PSi fabricated with an ion dose of $1.5 \cdot 10^{17}$ ions/cm^2. The visible EDX peaks confirm the presence of Ag in the synthesized PSi structures

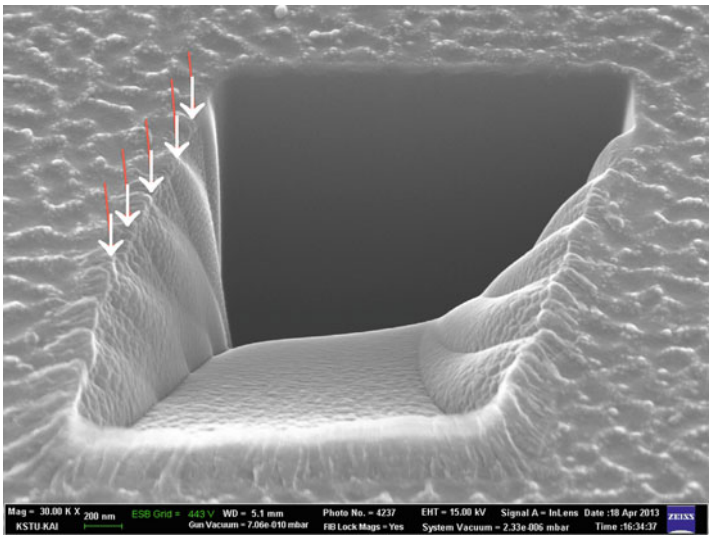

Fig. 4.5 SEM image of a sample surface with PSi structures (as in Fig. 4.3a) fabricated with an Ag^+-ion dose of $1.5 \cdot 10^{17}$ ions/cm^2 after FIB treatment with Ga ions. The *arrows* show the top positions of vertically continued structures on the walls of the FIB-milled cross-section

ion dose, respectively. Such EDX spectra for implanted samples were recorded in the surface area outside the black holes of the silicon pores. In contrast to the EDX data for unimplanted silicon, in the middle part of the presented spectrum of PSi four peaks located between 2.5 and 3.5 keV are clearly seen. These maxima are characteristic for Ag. It was observed that the intensity of the EDX Ag peaks increases with increasing implantation dose which means a growing Ag concentration in the silicon samples. The appearance of Ag peaks is in consistence with the white spots in the SEM images of the PSi (Fig. 4.3), which correspond to AgNPs synthesized in PSi during ion implantation. As shown in the present study, using selected conditions for low-energy Ag-ion irradiation of silicon, AgNPs can be fabricated without post-implantation thermal annealing, which was earlier done in [25, 26].

For the applied FIB conditions of PSi treatment, the mean penetration depth of Ga^+-ions implanted into silicon was obtained by SRIM calculation, which gives a value $R_p^{Ga} = 28$ nm with a straggling ΔR_p^{Ga} of 10 nm in the Gaussian depth distribution. Figure 4.5 shows a SEM image of a FIB-milled cross-section of an irradiated area of the surface with PSi from Fig. 4.3c. The whole thickness of the affected layer is about 1 μm. On the walls short columnar structures (shown by arrows) with an approximate size of several tens of nanometers could be recognized, which is expends from the surface to the depth of the sample.

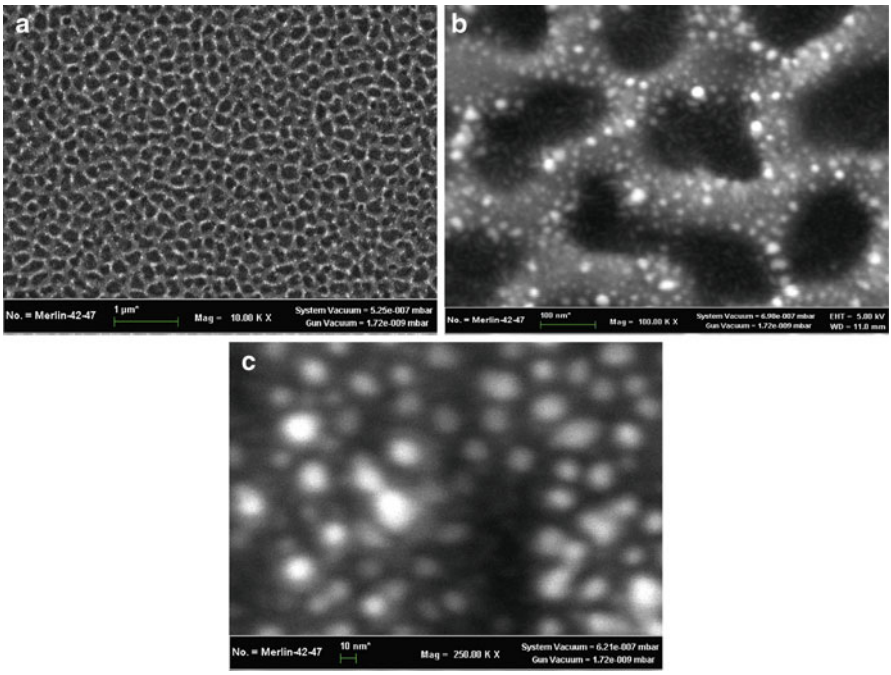

Fig. 4.6 SEM images of a PSi structure fabricated with a dose of $1.5 \cdot 10^{17}$ ions/cm^2 presented with different scales: (**a**) 1 μm; (**b**) 100 nm; (**c**) 10 nm

Figure 4.6 shows SEM images with various scales of the silicon surface implanted with silver ions. In contrast to the initial polished substrate, the morphology of the irradiated silicon surface is determined by the typical PSi structure. As can be seen from Fig. 4.6a, the PSi layer formed by implantation looks very homogeneous on a rather large scale (tens of microns). Reducing the scale (Fig. 4.6b) allows to estimate the average diameter of the pore holes (black in the image) to about 150–180 nm, as follows from the histogram of the pore size distribution presented in Fig. 4.7. The thickness of pore walls is estimated to be on the order of 30–60 nm. A further decrease of the scale (Fig. 4.6c) indicates the formation of implantation nanoinclusions (white) in the structure of the PSi walls with an average size on the order of ~5–10 nm. Since heavier chemical elements recorded by the detector of backscattered electrons are shown in the SEM microphotographs in a lighter tone, for a composite material composed of silicon atoms and implanted silver, it is possible to conclude that the white regions observed on a dark background (signals from silicon) are due to metallic silver in the form of nanoparticles (Fig. 4.6c). In this case it should be noted that silver atoms do not form any chemical compounds with silicon, similar to silicides of metals (cobalt, iron, etc.).

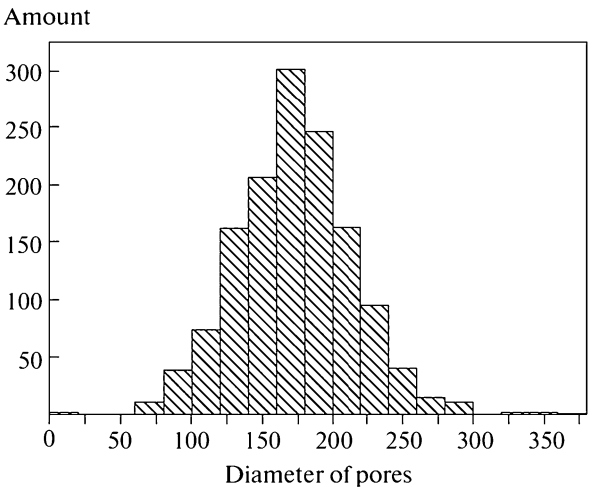

Fig. 4.7 Histogram of the pore size distribution in a PSi structure (Fig. 4.6b) formed by implantation of silicon with silver ions

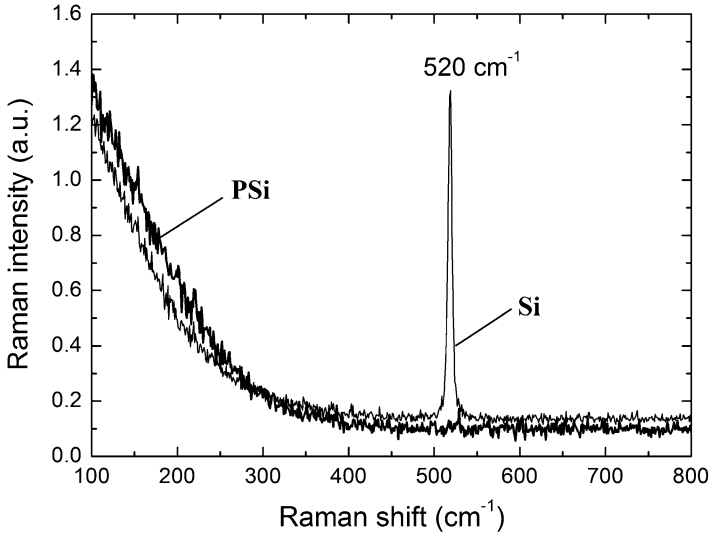

Fig. 4.8 Raman spectra of a polished monocrystalline Si substrate and a PSi structure fabricated at a dose of $1.5{\cdot}10^{17}$ ions/cm^2

Figure 4.8 shows Raman spectra of the polished monocrystalline Si substrate and a PSi structure fabricated with a dose of $1.5 \cdot 10^{17}$ ions/cm^2. By using Raman measurements of Ag^+-irradiated and non-irradiated silicon, it is demonstrated that the peak at a frequency of ~520 cm^{-1}, associated with scattering of optical phonons in the crystalline silicon matrix [34], disappears after ion implantation completely, thus characterizing the formed PSi layer as amorphous [35].

4.3.3 AFM Study of PSi Formation

Additional information proving the formation of PSi by implantation of silicon with Ag ions was obtained by AFM measurements. Figure 4.9a shows the AFM image observed from a fragment of the PSi surface, looking typically for porous structures in the case of AFM experiments [13]. Figure 4.9b gives the profiles of cross sections of individual pores measured in the directions shown in Fig. 4.9a, they allow an estimation of the depth of pores amounting to a value on the order of 100 nm. Thus, we can conclude that, as a result of silicon implantation with silver ions, characteristic pores are formed comparable with the relatively shallow pores in PSi obtained by an electrochemical method in highly diluted solutions of hydrofluoric acid [4].

4.3.4 PSi Structure Fabricated Through Mask

In order to estimate the steps formed at the interface between irradiated and non-irradiated regions of silicon by surface swelling or its sputtering during the ion implantation, in particular by the formation of pores in semiconductors, for example in germanium by irradiation with germanium ions, implantation through a mask is commonly suggested [28]. The formation of periodic plasmonic microstructures with metal nanoparticles with a diameter of 5–10 nm due to low-energy ion implantation in a single-step process was recently demonstrated in the case of Cu^+-ion implanted silica glass with different sizes of the grid mask [36, 37].

SEM images of a silicon surface containing fragments of PSi microstructures formed in this work by implantation with silver ions with a dose of $1.5 \cdot 10^{17}$ ions/cm^2 through a mask are shown in Fig. 4.10. As can be seen from the Fig. 4.10a, b, rectangular light-gray PSi regions were formed at the surface of silicon as a result of the implantation, which were confined by dark strips of non-irradiated crystalline silicon. A 3D reconstruction of a part of the sample close to an edge of the mask is presented in Fig. 4.10c, giving direct evidence for sputtering of the Ag^+-ion implanted silicon surface. In a first approximation, it can be speculated that the volume expansion is related to a mechanism simply governed by the nuclear energy deposition, which is usually measured in displacements per atom [33]. An AFM image of a fragment of a sample comprising a region of several square holes of the mask in 3D projection is shown in Fig. 4.11. As can also be seen from these figures, an efficient sputtering of the silicon-substrate surface takes place during the implantation of silicon with silver ions and the formation of a porous structure. Earlier, sputtering and erosion of silicon surfaces were observed by their irradiation with argon ions in an energy range of 50–140 keV [38]. However, there was no information about the formation of pores in this publication. As a result of implantation with Ag ions, holes and steps are formed at the interface between silicon and PSi in the irradiated part of silicon.

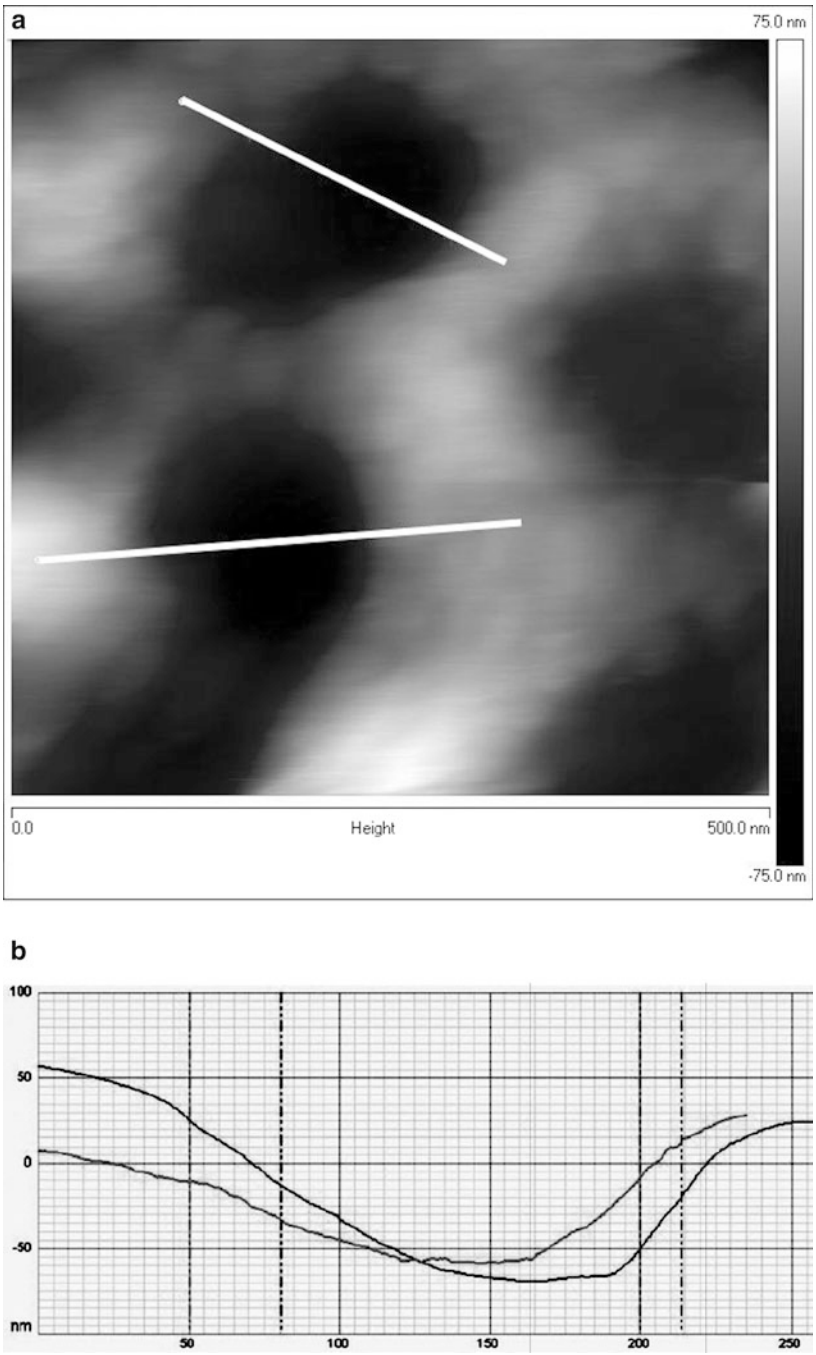

Fig. 4.9 (**a**) AFM images of the PSi surface obtained by silicon implantation with Ag ions and (**b**) profiles of individual pores measured on the directions shown in (**a**)

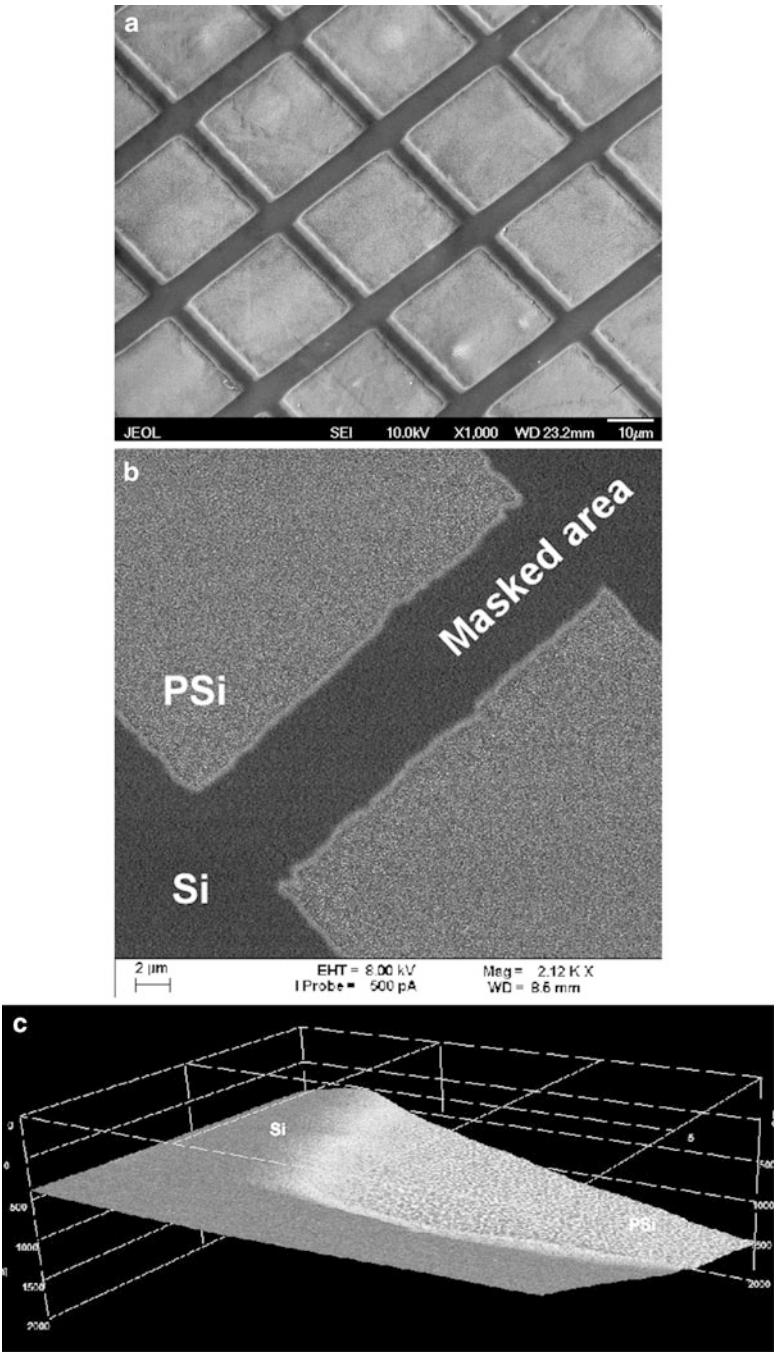

Fig. 4.10 (**a**) and (**b**) SEM images (with different scales) of structures with PSi (*light gray*) fabricated with an Ag^+-ion dose of $1.5 \cdot 10^{17}$ ions/cm^2 through a nickel mesh mask. (**c**) 3D SEM reconstruction of a step area that demonstrating sputtering of the silicon surface during Ag-ion implantation

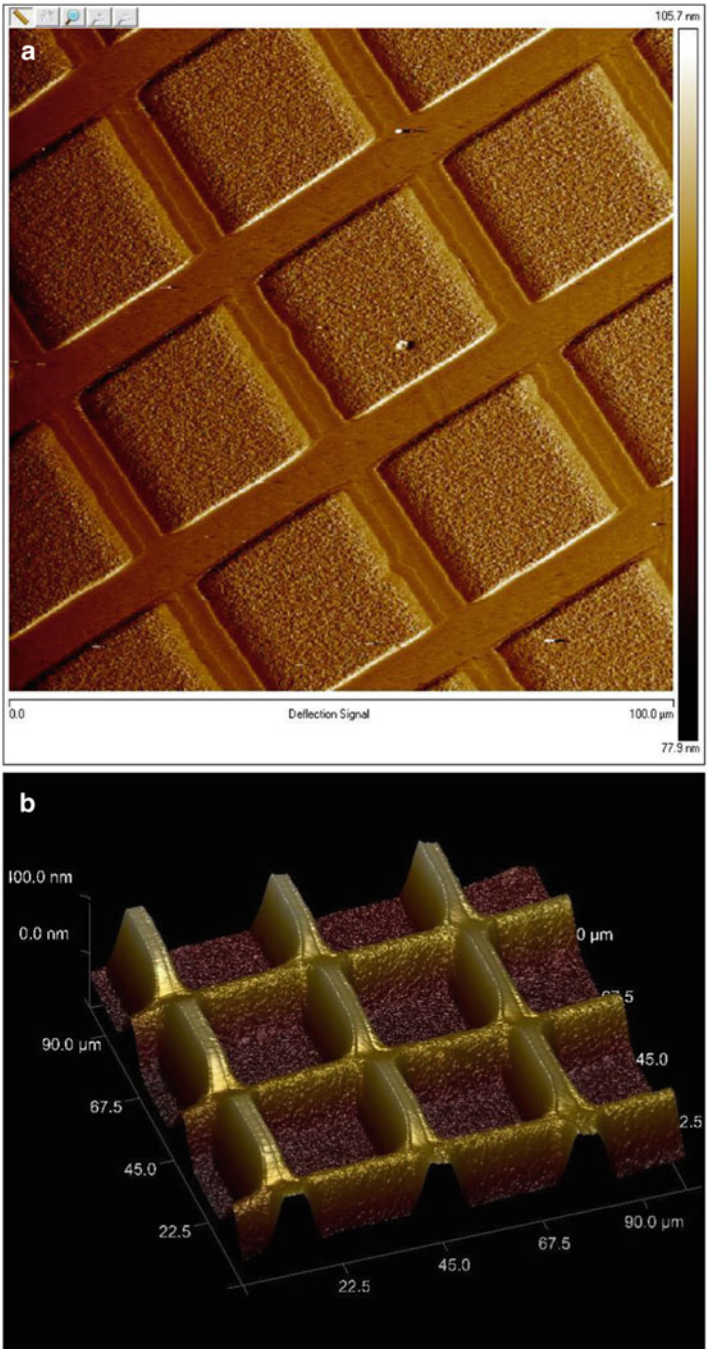

Fig. 4.11 (**a**) and (**b**) 3D fragments of an AFM image of the surface in the mask region, which demonstrates the sputtering of silicon

It is known that for a critical, rather low implantation dose, silicon undergoes a phase transition from a crystalline to the amorphous [39, 40]. As seen from the results reported in this work, at higher doses the amorphous silicon layer transforms to a porous structure with AgNPs. Thus, for the first time in practice it is demonstrated by the present experiments that PSi growth is stimulated by high-dose metal-ion implantation. This new result for silicon can be considered to be consistent with published data for porous semiconductors, in particular for germanium fabricated during an ion implantation process [28, 41–43] and, thus, a similar suited possible method for PSi structuring can be considered also. Sputtering effects (Figs. 4.10 and 4.11) seem to be important to determine the mechanism of PSi formation; this is somewhat unexpected, since it is known that by formation of pores in implanted semiconductors (germanium), an opposite phenomenon was observed: the swelling of the surface [28]. Therefore, the proposed mechanism of pore formation in implanted germanium based on the generation of vacancies in the irradiated semiconductor, which join the pores, cannot be merely transferred to the matrix of Si implanted with silver ions.

Despite PSi creation by metal-ion implantation of silicon, in the case of germanium there was a great debate over the past 30 years regarding the mechanisms governing the formation of porous semiconductor structures in ion-implanted germanium [44]. Currently, there are two main theories of void formation for germanium: vacancy clustering and the so-called “microexplosions”. The vacancy clustering theory involves an inefficient recombination of germanium point defects during ion implantation, where, once a critical point defect density is created by ion implantation, excess vacancies cluster into pores in order to minimize the dangling bond density. In contrast, the microexplosion theory is based on the creation of voids through pressure waves and thermal spikes caused by the overlap of ion cascades [44].

Therefore, in principle, it is possible to determine which theory better models the formation of voids and pores in silicon by selecting appropriate implant conditions and observing the resulting microstructure after ion implantation.

4.4 Conclusions

In this work a completely new technique used to obtain PSi layers with silver nanoparticles at the surface of monocrystalline silicon by a low-energy high-dose implantation was demonstrated. Ion implantation is one of the basic techniques used in industrial semiconductor microelectronics for the formation of various types of silicon nano- and microdevices. Therefore, the proposed new physical technique for the formation of PSi, in contrast to the well-known chemical approaches, has the advantage of being rather easily integrated into a modern industrial process for improving the technologies of the fabrication of microcircuits.

As follows from the results presented in this work, in our experiments PSi structures with silver nanoparticles were successfully obtained without a chemical technique in solution. Evidently, the further steps in improving this type of composite materials must consist of an optimization of the fabrication processes and, in particular, searching for correlation features between structural parameters and the characteristics of optical, plasmon, photoluminescence, and sensor properties of the new porous structures.

Acknowledgments T.S. Kavetskyy acknowledges the SAIA (Slovak Academic Information Agency) for scholarships in the Institute of Physics, Slovak Academy of Sciences within the National Scholarship Program of the Slovak Republic. A.L. Stepanov thanks for financial support by the Russian Scientific Foundation (No. 14-13-00758). This work was also partly supported by the State Fund for Fundamental Researches of Ukraine (No. F52.2/003). The authors are grateful to V.I. Nuzhdin and V.F. Valeev for help with the ion implantation procedure.

References

1. Torres-Costa V, Martin-Palma RJ (2010) J Mater Sci 45:2823
2. Uglir A (1956) Bell Syst Tech J 35:333
3. Canham LT (1990) Appl Phys Lett 57:1046
4. Feng ZC, Tsu R (1994) Porous silicon. World Scientific Publications, New York
5. Sallor MJ (2011) Porous silicon in practice. Willey-VCH, Weinheim
6. Oskam G, Long JG, Natarajan A, Searson PC (1998) J Phys D Appl Phys 31:1927
7. Kavetskyy T, Tsmots V, Kinomura A, Kobayashi Y, Suzuki R, Mohamed HFM, Šauša O, Nuzhdin V, Valeev V, Stepanov AL (2014) J Phys Chem B 118:4194
8. Kozlovskii VV, Kozlov VA, Lomasov VN (2000) Semiconductors 34:123
9. Stein HJ, Myers SM, Follstaedt DM (1993) J Appl Phys 73:2755
10. Cerofolini GF, Meda L, Balboni R, Corni F, Frabboni S, Ottaviani G, Tonini R, Anderle M, Canteri R (1992) Phys Rev B 46:2061
11. Wittmer M, Roth J, Revesz P, Mayer JM (1978) J Appl Phys 49:5207
12. Revesz P, Wittmer M, Roth J, Mayer JM (1978) J Appl Phys 49:5199
13. Galyautdinov MF, Kurbatova NV, Buinova EY, Shtyrkov EI, Bukharaev AA (1997) Semiconductors 31:970
14. Amran TS, Hashim MR, Al-Obaidi NK, Yazid H, Adnan R (2013) Nanoscale Res Lett 8:35
15. Chan S, Kwon S, Koo T-W, Lee LP, Berlin AA (2003) Adv Mater 15:1595
16. Wang M, Wang X, Ghoshal S (2013) Micro & Nano Lett 8:465
17. Kreibig U, Vollmer M (1995) Optical properties of metal clusters. Springer, Berlin
18. Stepanov AL (2010) Ion-synthesis of silver nanoparticles and their optical properties. Nova Scientific Publications, New York
19. Cao DT, Ngan LTQ, Anh CT (2013) Surf Interface Anal 45:762
20. Wang Y, Liu YP, Liang HL, Mei ZX, Du XL (2013) Phys Chem Chem Phys 15:2345
21. Ganeev RA, Ryasnyansky AI, Stepanov AL, Usmanov T (2004) Phys Status Solidi B 241:R1
22. Stepanov AL, Abdullin SN, Petukhov VY, Osin YN, Khaibullin IB (2000) Philos Mag B 80:23
23. Stepanov AL, Popok VN (2004) Surf Sci 566:1250
24. Stepanov AL (2010) Rev Adv Mater Sci 26:1
25. Sing AK, Gryczynski KG, McDaniel FD, Park SY, Kim M, Neogi A (2010) Appl Phys Express 3:102201
26. Sing AK, Gryczynski KG, Neogi A (2012) Opt Mater Express 2:501

27. Seo HW, Chen QY, Rusakova IA, Zhang ZH, Wijesundera D, Yeh SW, Wang XM, Tu LW, Ho NJ, Wu YG, Zhang HX, Chu WK (2012) Nucl Instrum Methods Phys Res B 292:50
28. Romano L, Impellizzeri G, Tomasello MV, Giannazzo F, Spinella C, Grimaldi MG (2010) J Appl Phys 107:84310
29. Stepanov AL, Trifonov AA, Osin YN, Valeev VF, Nuzhdin VI (2013) Optoelectron Adv Mater Rapid Commun 7:692
30. Stepanov AL, Osin YN, Trifonov AA, Valeev VF, Nuzhdin VI (2014) Nanotechnol Russia 9:163
31. Ziegler JF, Biersack JP, Littmark U (1985) The stopping and range of ions in solids. Pergamon Press, New York. http://www.srim.org/
32. Peckham J, Andrews GT (2013) Semicond Sci Technol 28:105027
33. Wang LM, Birtcher RC (1989) Appl Phys Lett 55:2494
34. Tyschenko IE, Popov VP, Talochkin AB, Gutakovskii AK, Zhuravlev KS (2004) Semiconductors 38:107
35. Trifonov AA, Osin YN, Valeev VF, Nuzhdin VI, Kavetskyy TS, Stepanov AL (2013) Nanotekhnologii: Nauka i Proizvodstvo 4(25):46
36. Stepanov AL, Evlyukhin EA, Nuzhdin VI, Valeev VF, Osin YN, Evlyukhin AB, Kiyan R, Kavetskyy TS, Chichkov BN (2013) Appl Phys A Mater Sci Process 111:261
37. Kavetskyy TS, Galyautdinov MF, Valeev VF, Nuzhdin VI, Osin YN, Evlyukhin AB, Stepanov AL (2013) Tech Phys Lett 39:591
38. Chini TK, Sanyal MK, Bhattacharyya SR (2002) Phys Rev B 66:153404
39. Chason E, Picraux ST, Poate JM, Borland JO, Current MI, Diaz de la Rubia T, Eaglesham DJ, Holland OW, Law ME, Mayer CW, Melngails J, Tasch AF (1997) J Appl Phys 81:6513
40. Williams JS (1998) Mater Sci Eng A 253:8
41. Romano L, Impellizzeri G, Bosco L, Ruffino F, Miritello M, Grimaldi G (2012) J Appl Phys 111:113515
42. Donovan TM, Heinemann K (1971) Phys Rev Lett 27:1794
43. Steinbach T, Wemecke J, Kluth P, Ridgway MC, Wesch W (1987) Phys Rev B 35:104108
44. Darby BL, Yates BR, Rudawski NG, Jones KS, Kontandos A, Elliman RG (2011) Thin Solid Films 519:5962

Part III
Characterization Techniques

Chapter 5
Cyclic Nanoindentation for Examination of the Piezoresistivity and the Strain-Sensor Behavior of Indium-Tin-Oxide Thin Films

E.E. Harea, K.E. Aifantis, K.M. Pyrtsac, and L. Ghimpu

Abstract The piezoresistivity of indium-tin-oxide (ITO) thin films was investigated using the three point bending method combined with cyclic indentation. The 500 nm thick ITO films were deposited on glass slides using magnetron sputtering. The resistance variation of the resulting ITO/glass based sensors during cyclic indentation showed a good sensitivity and fast response to mechanical strain, with the gauge factor ranging from −1.4 to −3.7.

Keywords Cyclic nanoindentation • Strain sensor • Thin films

5.1 Introduction

Sensors based on ITO films have been intensively studied over the past two decades. They belong to the class of ceramic sensors with outstanding physical properties such as: thermal, electrical and chemical stability, adhesion, transparency, thermo-electricity, conductivity, piezoresistivity. The applications of ITO films range from transparent contacts for solar cells [1] to active elements in temperature measurements [2], as well as pressure sensors [3] and promising gauge sensors which work at elevated temperatures (up to 1,500 °C) [4]. The present article is concerned with examining the piezoresistive and strain sensor behavior of ITO thin films using cyclic indentation. This is important to understand the speed of the electrical response of the sensor versus repeated mechanical action.

E.E. Harea (✉) • K.M. Pyrtsac
Institute of Applied Physics, ASM, Chisinau, Moldova
e-mail: evg2000@mail.md

K.E. Aifantis
Aristotle University of Thessaloniki, Thessaloniki, Greece

University of Arizona, Tucson, AZ, USA

L. Ghimpu
Ghitu Institute of Electronic Engineering and Nanotechnologies, Chisinau, Moldova

P. Petkov et al. (eds.), *Nanoscience Advances in CBRN Agents Detection, Information and Energy Security*, NATO Science for Peace and Security Series A: Chemistry and Biology, DOI 10.1007/978-94-017-9697-2_5

The sensitivity of strain sensors is determined by the gauge factor G, and it represents the ratio of the relative change in the electrical resistance $\Delta R_g/R_g$ to the strain ε:

$$G = \frac{\Delta R_g}{R_g} \cdot \frac{1}{\varepsilon} \tag{5.1}$$

where R_g is the initial resistance of the gauge system and ΔR_g the variation of the resistance introduced by the strain ε. Various load-bending tests on ITO strain sensors have revealed that the gauge factor ranges between −0.3 [5] and 24.9 [4]. In this contribution, instead of using conventional load-bending tests, cyclic nanoindentation will be employed in order to bend ITO/glass strips with a constant rate and to analyze their sensitivity and electrical response. The method employed here was similar to that used in [6] for measuring the elastic modulus of thin films using nanoindentation of bending systems.

5.2 Experimental

Glass slices were used as substrates for depositing the ITO films. Before deposition the glass substrates (area 1.4 cm^2) were cleaned in a mixed solution of 7 g $K_2Cr_2O_7$, 10 ml H_2O, and 100 ml H_2SO_4 at room temperature, and then they were rinsed abundantly with distilled water. Then they were mounted on a rotatable substrate holder equipped with a resistive heater. The distance between the substrate and the ITO target was 8 cm. The target was 5 cm in diameter, with a composition of In_2O_3: $SnO_2 = 9{:}1$ in weight and a purity of 99.95 %. The chamber was first pumped to a background pressure of 1.2×10^{-6} Torr. The argon working gas pressure was regulated to maintain a constant vacuum pressure of 5×10^{-3} Torr. The substrate temperature T_s was 400 °C. The magnetron power was set to 300 W. The film thickness d_f was determined using a MTM-10/10A High Resolution thickness monitor quartz microbalance and was found to be ~500 nm.

After the deposition the ITO/glass slice was cut in equal strips with dimensions 1 mm × 2 mm × 30 mm; indium contacts were prepared on the ITO film.

Strain in the ITO film was induced by ITO/glass strip bending during cyclic indentation of sample placed on two glass blocks. The conductivity variation during nanoindentation was measured using an unbalanced Wheatstone bridge circuit as shown in Fig. 5.1b. The unbalanced bridge method for strain gauge measurements [7] allowed to increase the accuracy of the measurements of the variation of the sample resistance. If we define the unstrained value of the gauge resistance as R_g and the change due to strain as ΔR_g, the strained value of the gauge resistance is $R_g + \Delta R_g$.

$$\frac{\Delta R_g}{R_g} = \frac{4V_r}{1 + 2V_r} \tag{5.2}$$

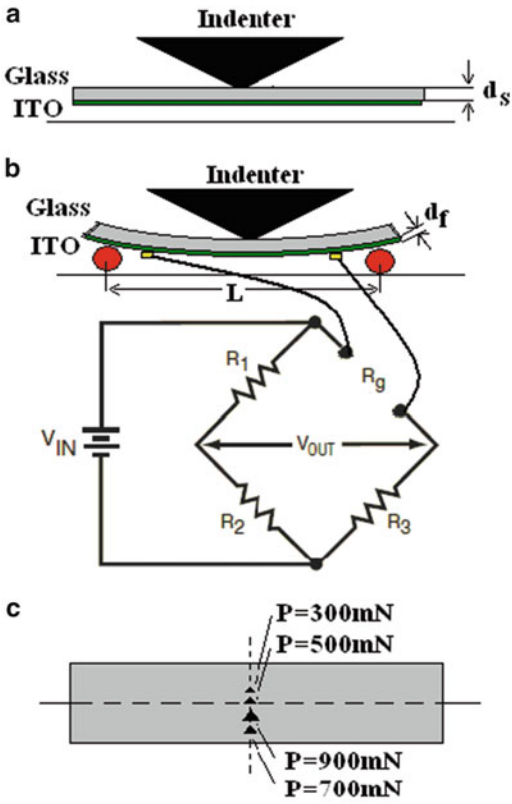

Fig. 5.1 (**a**) Scheme of the experimental set-up for nanoindentation of a fixed glass substrate; (**b**) scheme of the experiment to study the strain-sensor behavior using cyclic indentation; (**c**) imprints arrangement depending on the maximum applied load and the sample center (the distance between the imprints is 100 μm)

where the term V_r is defined as the difference of the ratios of V_{OUT} to V_{IN} from the unstrained to the strained state of the sample studied. V_{OUT} is the bridge output signal, and V_{IN} is the input voltage to the bridge,

$$V_r = \left[\left(\frac{V_{OUT}}{V_{IN}}\right)_{strained} - \left(\frac{V_{OUT}}{V_{IN}}\right)_{unstrained}\right] \tag{5.3}$$

and

$$\frac{V_{OUT}}{V_{IN}} = \left[\frac{R_2}{R_2 + R_g} - \frac{R_2}{R_1 + R_2}\right] \tag{5.4}$$

The bridge resistances shown in Fig. 5.1b were set equal to each other as $R_1 = R_2 = R_3 = 100\ \Omega$, the unstrained value of the gauge resistance was $R_g = 98.9\ \Omega$. A constant voltage power supply furnished $V_{IN} = 1.5$ V, and a digital voltmeter was used to measure the bridge output V_{OUT} under unstrained and strained conditions.

The flexural strain on a thin film in the case of a bilayer material can be calculated taking into consideration that the Young's modulus is different for film

and substrate and that the neutral axis of the sample shifts towards the layer of higher modulus. Consequently, the flexural properties depend on the ratio of the Young's modulus and the thicknesses of film and substrate. In the present case the equation for the strain of the film has been solved in [8] as:

$$\varepsilon_{\text{film}} = \left(\frac{d_f + d_s}{2R}\right) \cdot \frac{1 + 2\eta + \chi\eta^2}{(1+\eta)(1+\chi\eta)} \tag{5.5}$$

where R is the radius of curvature and d_f and d_s are the thicknesses of film and substrate, respectively. $\eta = d_f/d_s$ and $\chi = E_f/E_s$, where $E_f \approx 126$ GPa and $E_s \approx 68$ GPa are the Young's modulus of film and substrate, respectively. These parameters were automatically calculated by the nanotester software using the method of Oliver and Pharr [9]. ITO film measurements were done with a maximum penetration depth of $h_c \approx 50$ nm in accordance with ISO 14577- 4 [10], where the surface roughness R_a should be < 5 % of the indentation depth h_c and $h_c < 10$–15 % of the coating thickness. $R_a \approx 5$ nm was measured by AFM.

The radius of curvature R can be expressed in terms of the length span, L = 22,000 μm and the bending deflection D [8]:

$$2R = \frac{4D^2 + L^2}{4D} \tag{5.6}$$

A nanotester PMT-3-NI-02 was used for applying a cyclic stress on the sample (Fig. 5.1a, b) in the bending direction. Five cyclic indentations were performed at the centre of the tested strip with a 30 s loading stage, 10 s holding time at the maximum load and 30 s unloading stage. The maximum applied load for each set of five indents was 300, 500, 700 and 900 mN, and the distance between imprints was 100 μm (see Fig. 5.1c). Figure 5.2a, b display the load-displacement curves obtained under the aforementioned conditions for the case when the sample was indented while the glass was flat on the sample stage (Fig. 5.1a), and for the case

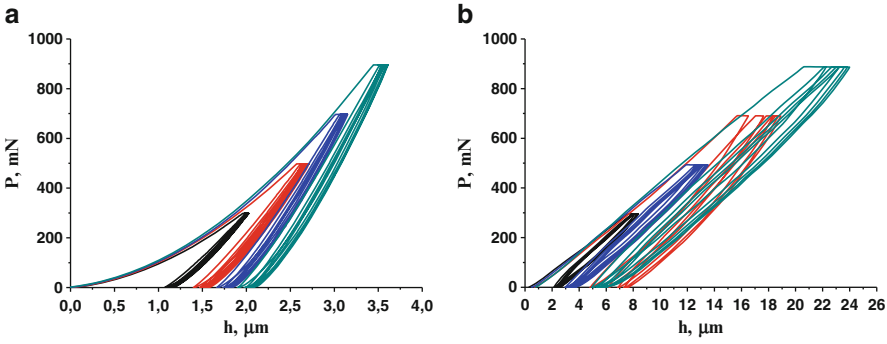

Fig. 5.2 Load-displacement curves: (**a**) for a flat sample (configuration of Fig. 5.1a), (**b**) for bending systems (configuration of Fig. 5.1b)

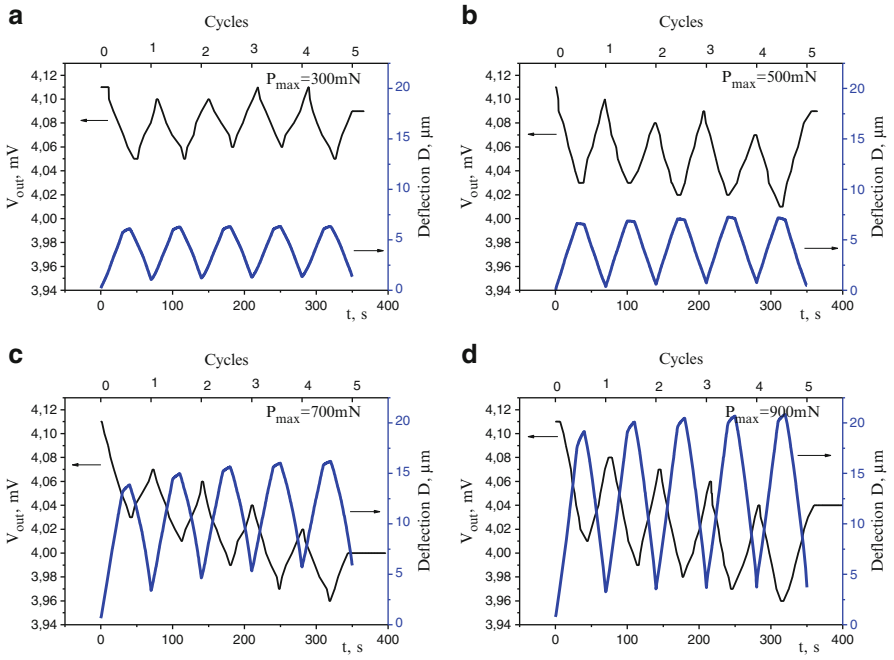

Fig. 5.3 Sample conductivity variation during cyclic bending under a maximum applied load of (**a**) P = 300 mN, (**b**) P = 500 mN, (**c**) P = 700 mN, (**d**) P = 900 mN

when the bending system was subjected to indentation (Fig. 5.1b). The real bending deflection of the sample in Fig. 5.1b can be calculated by subtracting the results for the two cases. The results are shown in Fig. 5.3.

5.3 Results and Discussion

In Fig. 5.3 two curves are shown in each diagram which represent the bridge output signal V_{out} (left axes) versus time (bottom axes), and the magnitude of sample deflection (right axes) versus number of cycles of the indentation (upper axes).

Figure 5.3 depicts the results of the variation of the sample conductivity during cyclic bending at different magnitudes of the flexural deflection (calculated from Eq. 5.5), depending on the maximum applied load: (a) P = 300 mN with a maximum flexural deflections between 6 and 6.3 µm, (b) P = 500 mN with maximum flexural deflections between 6.6 and 7.1 µm, (c) P = 700 mN with maximum flexural deflections between 13 and 16 µm and (d) P = 900 mN with maximum flexural deflections between 19 and 20 µm, depending on the cycle number. Combined cyclic indentation and the three point bending method for strain-sensor analysis are interesting tools for the in-situ characterization of the

Table 5.1 Gauge factor variation depending on cycling deflection and maximal applied load

Cycle Nr:	Gauge factor G ($P_{max} = 300$ mN)	Gauge factor G ($P_{max} = 500$ mN)	Gauge factor G ($P_{max} = 700$ mN)	Gauge factor G ($P_{max} = 900$ mN)
1	−3.23	−3.74	−2.24	−1.69
2	−3.28	−3.23	−1.46	−1.53
3	−2.26	−2.75	−1.76	−1.55
4	−2.69	−3.09	−1.74	−1.52
5	−3.28	−2.81	−1.49	−1.40

electrical variation versus mechanical deformation. In strain sensor manufacturing the choice of the substrate and the active thin film element is crucial. More than that, the mechanical properties of the film/substrate structure are decisive for the sensor accuracy. The high sensitivity indentation method allows us to determine the flexural deflection of the sample for different numbers of cycles, maximum applied loads, speed of deflection and magnitude of sensor recovering. All these parameters can affect the sensor precision. For example in Fig. 5.3 it can clearly be seen that the sample does not fully recover between the cycles. This is most probably due to torsion forces that develop in the sample during indentations performed above or below the sample's geometric center (Fig. 5.1c). It should be noted that this effect is more visible with increasing indentation distance from the sample center. Figure 5.3d shows better recovery (the sample's deflection recovers incomplete after the unloading stage as compared to the flat sample) between the cycles for a maximum applied load of P = 900 mN than for a maximum load of P = 700 mN (Fig. 5.3c) due to the fact that the distance of the indent from the center of the sample is two times shorter for first than for the second case. The recovery deficiency between the cycles, the magnitude of the applied load and consequently the flexural deflection of the sample lead to sensor resistivity variations expressed by the Wheatstone bridge output signal $V_{out.}$ An increase in the sensor resistivity is observed during cyclic loading and the magnitude of this effect increases when the flexural deflection increases, while it disappears several minutes after the indenter is removed from the sample. A more probable explanation is that stress accumulates in the substrate and the piezoresistive film during the applied cyclic stress, and there is not sufficient time for it to relax. As a result the gauge resistivity between the first and subsequent cycles changes.

This strongly affects the gauge factor of sensor. In Table 5.1 the gauge factor variation depending on cyclic load application and the magnitude of the applied load are presented.

5.4 Conclusions

Combined cyclic indentation and the three point bending method open large possibilities for studying piezoresistive phenomena in gauge sensors. Due to high precision measurements of the indenter displacement, and the possibility to apply

different ratios and magnitudes of stress to the studied samples we can simulate various modes of sensors loading, measure the value of the deflection and analyze the variation of the electrical signal.

References

1. Simashkevich AV, Sherban DA, Bruk LI, Kharya EE, Usatii I (2011) Surf Eng Appl Electrochem 47:266
2. Chen YZ, Jiang HC, Jiang SW, Liu XZ, Zhang WL (2014) Adv Mater Res 873:420
3. Yeung KW, Ong CW (2007) Sensors Actuators A 137:1
4. Gregory OJ, You T (2004) J Electrochem Soc 151:198
5. Miller TM, Fang H, Magruder RH III, Weller RA (2003) Sensors Actuators A 104:162
6. Hsu C, Tsou C, Fang W (2007) J Micro/Nanolith MEMS MOEMS 6:033011
7. Agilent Technologies Application note (1999) Practical strain gauge measurements. 94
8. Suo Z, Ma EY, Gleskova H, Wagner S (1999) Appl Phys Lett 74:1177
9. Oliver WC, Pharr GM (2004) J Mater Res 19:3
10. ISO 14577- 4: Test method for metallic and non-metallic coatings

Chapter 6
Positron Annihilation Study of the Juniperus Communis Based Biomaterial NEFROVIL

T.S. Kavetskyy, S.Ya. Voloshanska, I.V. Komar, O. Šauša, and A.L. Stepanov

Abstract The results of positron annihilation lifetime (PAL) measurements of the Juniperus communis based biomaterial NEFROVIL are reported for the first time. Three- and four-component fittings were applied to deconvolute the PAL spectrum. In order to determine which fitting procedure is most suited, a maximum entropy lifetime (MELT) analysis was also performed. It was found that the nanovoid topology of this biomaterial is constructed by small and large free-volume holes identified by the *ortho*-positronium lifetime parameters in the most suitable four-component fitting procedure.

Keywords Positron annihilation • Positronium • Biomaterial • Nanovoids

6.1 Introduction

Positron annihilation spectroscopy is a powerful experimental tool to study the defect structure (vacancies, unsaturated bonds, clusters, etc.) of materials in the nanometric and sub-nanometric range [1]. The concept of the free-volume structure of materials and its interpretation is a very useful and actual idea in the physics and chemistry of disordered systems and especially of organic polymers [2].

T.S. Kavetskyy
Drohobych Ivan Franko State Pedagogical University, Drohobych 82100, Ukraine

John Paul II Catholic University of Lublin, Lublin 20-718, Poland

S.Ya. Voloshanska • I.V. Komar (✉)
Drohobych Ivan Franko State Pedagogical University, Drohobych 82100, Ukraine
e-mail: bioddpu@ukr.net

O. Šauša
Institute of Physics, Slovak Academy of Sciences, Bratislava 84511, Slovak Republic

A.L. Stepanov
Kazan Physical-Technical Institute, Russian Academy of Sciences, Kazan 420029, Russia

Kazan National Research Technological University, Kazan 420015, Russia

Kazan Federal University, Kazan 420008, Russia

P. Petkov et al. (eds.), *Nanoscience Advances in CBRN Agents Detection, Information and Energy Security*, NATO Science for Peace and Security Series A: Chemistry and Biology, DOI 10.1007/978-94-017-9697-2_6

Biomaterials based on Juniperus communis (JC) are organic molecular media for potential use in advanced applications in biotechnology and medicine (see, e.g., [3]). A suitable technique to directly measure of the free-volume entities is positron annihilation lifetime spectroscopy (PALS). In the present work we performed a PALS study of the JC based biomaterial NEFROVIL.

6.2 Experimental Procedure

The investigated NEFROVIL biomaterials were obtained in form of pressed tablets as commercial product from the company "Roslyna Karpat" (Ukraine) [4]. The positron annihilation lifetime (PAL) measurement of the samples was carried out at the Institute of Physics, Slovak Academy of Sciences (IPSAS, Slovakia).

The PAL spectrum was taken by the conventional fast-fast coincidence method using plastic scintillators coupled to photomultiplier tubes as detectors. The radioactive ^{22}Na positron source (0.6 MBq activity) was placed in an envelope of Kapton films (8 μm thick) and then sandwiched between two identical samples. The time resolution (FWHM) of the positron lifetime spectrometer was about 0.32 ns, measured using a defect free Al sample as a standard. More than three million counts were recorded for the PAL spectrum to allow statistical analysis of the lifetime spectrum, which was conducted using the PATFIT-88/POSITRONFIT software package [5] with proper source corrections.

Three- and four-component fitting procedures of the PAL data were applied. The lifetimes (τ_3, τ_4) and their relative intensities (I_3, I_4) of *ortho*-positronium (*o*-Ps) pick-off annihilation in free-volume spaces were finally taken into consideration, in accordance with the conventional interpretation [6]. In order to determine which of the fitting procedures is suited best, a maximum entropy lifetime (MELT) analysis was also performed [7].

6.3 Results and Discussion

Figure 6.1 shows a photograph of Juniperus communis from the Carpathian region (Ukraine) and schematically its berries and their cross-section. Such biomaterials have complex a molecular structure hardly to be investigated by using direct structural techniques on the nanoscale level. It has been suggested that some important information on the structure of these materials may be extracted on the nanoscale void level using positron annihilation spectroscopy. In the present work a PAL measurement was performed with a sample of the JC based biomaterial NEFROVIL, which is commercially produced as potential candidate for biomedical applications [4]. As the molecular structure of NEFROVIL is based on the JC matrix, which contain grains of different sizes in the complex structure of the berries (Fig. 6.1), it is supposed that the results obtained for the nanovoid topology

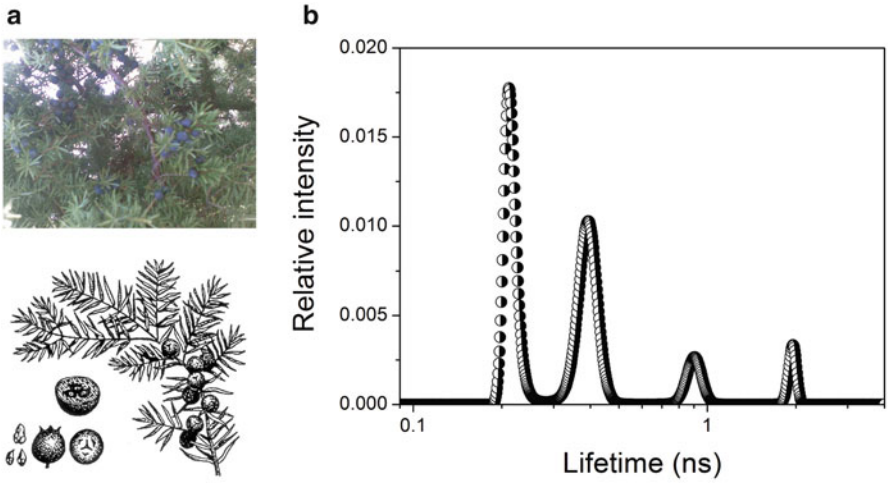

Fig. 6.1 (**a**) Photograph of Juniperus communis of Carpathian region (Ukraine) with schematically presentations of its berries and their cross-section, and (**b**) MELT results obtained for the investigated biomaterial showing lifetime distribution with four peaks

Table 6.1 Positron annihilation lifetimes τ_i (ns) and their relative intensities I_i (%) ($i = 1...4$) for the investigated biomaterial

Three-component fitting (fit variance = 1.0)			
$\tau_1 = 0.230 \pm 0.004$	$\tau_2 = 0.504 \pm 0.017$	$\tau_3 = 1.736 \pm 0.034$	
$I_1 = 61.8 \pm 2.2$	$I_2 = 30.9 \pm 2.0$	$I_3 = 7.3 \pm 0.3$	
Four-component fitting (fit variance = 1.0)			
$\tau_1 = 0.181 \pm 0.031$	$\tau_2 = 0.327 \pm 0.049$	$\tau_3 = 0.761 \pm 0.150$	$\tau_4 = 1.937 \pm 0.121$
$I_1 = 28.7 \pm 16.5$	$I_2 = 53.7 \pm 12.0$	$I_3 = 12.3 \pm 4.5$	$I_4 = 5.3 \pm 1.0$

of the material will be important for further experiments with Juniperus communis of different history, e.g., as freshly received, after prolonged physical aging, as dry and moist, in the form of powder and oil samples, etc.

Table 6.1 presents the PAL results obtained for the investigated biomaterial with applied deconvolution using three- and four-component fitting procedures.

As mentioned above, it is of interest to analyse the *ortho*-positronium (a bound electron-positron state with parallel particle spins) parameters, which are related with the size and distribution of free volume in the material structure (see, e.g., [1, 6, 8] for a review). The *o*-Ps parameters (lifetime and intensity) found in this study were (Table 6.1):$\tau_3 \approx 1.74$ ns, $I_3 \approx 7$ % for the three-component fitting procedure and $\tau_3 \approx 0.76$ ns, $I_3 \approx 12$ % and $\tau_4 \approx 1.94$ ns, $I_4 \approx 5$ % for the four-component fitting (a fit variance = 1.0 was attained).

The MELT results obtained are presented in Fig. 6.1, giving four peaks (lifetime components) and the following *o*-Ps lifetime data: $\tau_3 \approx 0.91$ ns and $\tau_4 \approx 1.96$ ns.

These data are found to be in a good agreement with the τ_3 and τ_4 values obtained by the four-component fitting. Thus the four-component deconvolution of the PAL spectrum shows that the nanovoid topology of the investigated biomaterial consists of the smaller and larger free-volume holes identified by the *o*-Ps lifetimes τ_3 and τ_4. The numerical values of size of the voids with a radius R in spherical approximation ($R = 1.2 \pm 0.3$ Å for $\tau_3 = 0.76 \pm 0.15$ ns, and $R = 2.8 \pm 0.1$ Å for $\tau_4 = 1.94 \pm 0.12$ ns) are estimated using the equation [9–11] $\tau_{o\text{-Ps}} = 0.5 \times [1 - (R/(R + \Delta R)) + 1/2\pi \times \sin(2\pi R/(R + \Delta R))]^{-1}$, where $\Delta R = 1.656$ Å.

6.4 Conclusions

Results of a positron annihilation lifetime measurement of the Juniperus communis based NEFROVIL are reported in this work for the first time. It is established that the nanovoid topology of the investigated biomaterial in pressed tablets is constructed by the smaller and larger free-volume holes identified by the *o*-Ps lifetimes τ_3 and τ_4, respectively, in the most suitable four-component fitting procedure. No large pores over 1 nm in radius were detected in the tablets. The spaces between the grains of crushed seeds are probably filled by oil substances from the pressing, large pores are not observed by positrons.

Acknowledgments T.S. Kavetskyy acknowledges the SAIA for scholarships at the IPSAS within the NSP of the Slovak Republic. S.Ya. Voloshanska is grateful to the EU PL-BY-UA project. O. Šauša wishes to thank the Slovak Grant Agency VEGA (Nos. 2/0099/10 and 2/0164/14). This work was also partly supported by the SFFR of Ukraine (No. F52.2/003) and the MESU (No. 0114U002617). A.L. Stepanov thanks for the financial support by the RSF (No. 14-13-00758) in Russia.

References

1. Dupasquier A, Mills AP Jr (eds) (1993) Positron spectroscopy of solids. Proceedings of the international school of physics "Enrico Fermi", course CXXV. Ios Press, Amsterdam
2. Krištiak J, Bartoš J, Krištiaková K, Šauša O, Bandžuch P (1994) Phys Rev B 49:6601
3. Brezhneva YB, Kolomiyets VI, Refitsky VI, Brezhneva AV (2008) Ukr Rheumatol J 4:78
4. http://amrita.club/shop/90/katalog/nefrovil-forte
5. Kirkegaard P, Eldrup M, Mogensen OE, Pedersen NJ (1981) Comput Phys Commun 23:307
6. Schrader DM, Jean YC (eds) (1988) Positron and positronium chemistry: studies in physics and theoretical chemistry. Elsevier, New York
7. Shukla A, Peter M, Hoffmann L (1993) Nucl Instr Meth Phys Res A 335, 310; Hoffmann L, Shukla A, Peter M,. Barbiellini B, Manuel AA (1993) ibid. 335, 276
8. Schultz PJ, Lynn KG (1988) Rev Mod Phys 60:701
9. Tao SJ (1972) J Chem Phys 56:5499
10. Eldrup M, Lightbody D, Sherwood JN (1981) Chem Phys 63:51
11. Nakanishi N, Wang SJ, Jean YC (1988) In: Sharma SC (ed) International symposium on positron annihilation studies of fluids. World Scientific, Singapore, p 292

Chapter 7
The Influence of Low Dose Ion-Irradiation on the Mechanical Properties of PMMA Probed by Nanoindentation

T.S. Kavetskyy, J. Borc, Y.Y. Kukhazh, and A.L. Stepanov

Abstract The results of investigations of the influence of low dose B^+-ion-irradiation (6.25×10^{14} ion/cm^2) on the mechanical properties (hardness and elastic modulus) of polymethylmethacrylate (PMMA) using the nanoindentation tests with an ultra nano hardness tester are reported for the first time. It is established that the dependences of hardness and elastic modulus on the maximum indentation depth show major differences between pristine and ion-implanted samples in the range up to about 400 nm which is consistent with the maximum penetration depth of B^+-ions into the PMMA matrix determined earlier by slow positron beam spectroscopy and SRIM simulation (stopping and range of ions in matter).

Keywords Ion irradiation • Polymethylmethacrylate • Nanoindentation

7.1 Introduction

In general, indentation or depth-sensing indentation, also called nanoindentation, means an instrument which possesses the ability to measure the indenter penetration depth h under an applied force F throughout the testing cycle [1]. This method

T.S. Kavetskyy
Drohobych Ivan Franko State Pedagogical University, Drohobych 82100, Ukraine

John Paul II Catholic University of Lublin, Lublin 20-718, Poland

J. Borc
Lublin University of Technology, Lublin 20-618, Poland

Y.Y. Kukhazh (✉)
Drohobych Ivan Franko State Pedagogical University, Drohobych 82100, Ukraine
e-mail: juljakhj@mail.ru

A.L. Stepanov
Kazan Physical-Technical Institute, Russian Academy of Sciences, Kazan 420029, Russia

Kazan National Research Technological University, Kazan 420015, Russia

Kazan Federal University, Kazan 420008, Russia

P. Petkov et al. (eds.), *Nanoscience Advances in CBRN Agents Detection, Information and Energy Security*, NATO Science for Peace and Security Series A: Chemistry and Biology, DOI 10.1007/978-94-017-9697-2_7

gives information about the contact parameters and mechanical properties, which are calculated from the indenter load and the depth measured continuously during loading and unloading (see e.g. [1–7]). The advantages are very low loads and only minor depths with no special demands on the test specimens. It is capable of measuring both the plastic and elastic deformation of the material under test. The method was originally developed for testing the hardness and elastic modulus from indentation load-displacement data in elastic-plastic materials including fused silica, soda-lime glasses, and single crystals of aluminum, tungsten, quartz, and sapphire in 1992 [8] and further reviewed in 2004 with advances in understanding the mechanics governing elastic-plastic indentation [9]. Nanoindentation of polymers [2], polymer nanocomposites [10], thin films [3], hybrid polymer/metal thin films [11], metals [12], glasses [13], metallic glasses [14], crystals [15], ion-implanted crystalline materials [16], and others may serve as typical examples of hardness test applications in materials science.

By using a nanoindentation technique we paid attention to polymers. Polymethylmethacrylate (PMMA) was selected for the study as one of the most widely used commercial polymers. Indeed, nanoindentation tests of PMMA have already been carried out (see e.g. [2, 4, 6, 7]). However, ion-implanted PMMA samples, which are of interest from a practical point of view [17, 18], have not been studied yet by depth-sensing indentation as far as we know.

Thus, the present work is aimed to study, for the first time, the influence of low-dose ion-irradiation (6.25×10^{14} ion/cm^2) on the mechanical properties (hardness and elastic modulus) of 40 keV B^+-ion implanted PMMA (B:PMMA) by nanoindentation tests. Recent investigation of such samples implanted with ion doses from 6.25×10^{14} to 5.0×10^{16} ion/cm^2 by slow positron beam spectroscopy and SRIM simulation (stopping and range of ions in matter) [19] clearly confirmed the concept of the occurrence of two processes upon ion implantation – scission of polymer chains and appearance of free radicals preceding the aggregation of carbon clusters resulting in the formation of network of conjugated bonds for lower ion doses ($< 10^{16}$ ion/cm^2) and carbonization for higher doses ($>10^{16}$ ion/cm^2). Thus, in the present work the first process of the modification of the polymer structure will be examined by indentation.

7.2 Experimental Procedure

As substrates for ion implantation, optically transparent PMMA plates were used. The B^+-ion implantation with an energy of 40 keV, a dose of 6.25×10^{14} ion/cm^2 and a current density < 2 μA/cm^2 was performed under a pressure of 10^{-5} Torr at room temperature at the ILU-3 ion accelerator at the Kazan Physical-Technical Institute (Russia) [20]. The nanoindentation tests of the investigated materials (PMMA and B:PMMA) were carried out using an ultra nano hardness tester (UNHT) with a diamond Berkovich indenter at the Lublin University of Technology (Poland).

There are some advantages in the new UNHT design for nanoindentation tests compared to the conventional nano indenter (or NHT) design, both developed by CSM Instruments (Switzerland) [1]. The main improvements are a new tip and reference fixing system introduced in the ultra indenter head and the use of active top referencing (very low loads applied by the reference, less than 1 g), the possibility of depth and load measurements, one order less noise level, etc.; they allow us to make measurements using the UNHT with high performance.

In the present work, the results of our first nanoindentation tests of PMMA and B:PMMA with maximum indentation depths in the range of 300–1,100 nm are reported. The thickness of the implanted layer was determined to ~400 nm by slow positrons and SRIM simulation [19].

It must be noted here that in principle on a coated surface, the maximum indentation penetration should be less than 10 % of the total film thickness to avoid substrate influences [1]. That is, for the ultra-thin film in our case, the maximum indentation depth should be less than 40 nm to estimate the mechanical properties of the implanted layer. Unfortunately, the maximum indentation depths lower than 40 nm were not achieved in these experiments (the load-depth and load/depth-time curves are given below). In order to achieve maximum indentation depths less than 40 nm and to analyze the mechanical properties of the implanted layers, separate measurements will be carefully performed in the further work. Therefore, taking into account the substrate influence within the maximum indentation depth range examined, the reported values of hardness and elastic modulus should be only considered as those of a composite (layer + matrix), but not as hardness and elastic modulus of the implanted layer.

The main parameters in the UNHT experiment were used [1]: 20 progressive cycles, an acquisition rate of 10 Hz, linear loading, unload to 20 nm, contact force 0.05 mN, maximum depth 1,040 nm, loading rate 20 mN/min, unloading rate 20 mN/min, delay 120 s, delay between the cycles 10 s. Each measurement was repeated 3 times, and, finally, about 60 indentations were made to average values of the indentation hardness and the indentation elastic modulus.

7.3 Results and Discussion

The theory and models of nanoindentation tests of materials are well described in literature (see e.g. [2, 4, 6, 7] for PMMA and references therein). Figure 7.1 shows the typical load-depth and load/depth-time curves obtained in the present measurements for pristine PMMA and implanted B:PMMA samples in the multicycle mode for 20 cycles. For each cycle the hardness and elastic modulus (with a Poisson ratio of the specimen of $\nu = 0.3$) values were calculated by the method of Oliver and Pharr with the software of CSM Instruments for the UNHT [1].

The averaged values of indentation hardness and elastic modulus versus maximum indentation depth for PMMA and B:PMMA are plotted in Fig. 7.2. It can be seen that the hardness and elastic modulus dependences on the maximum

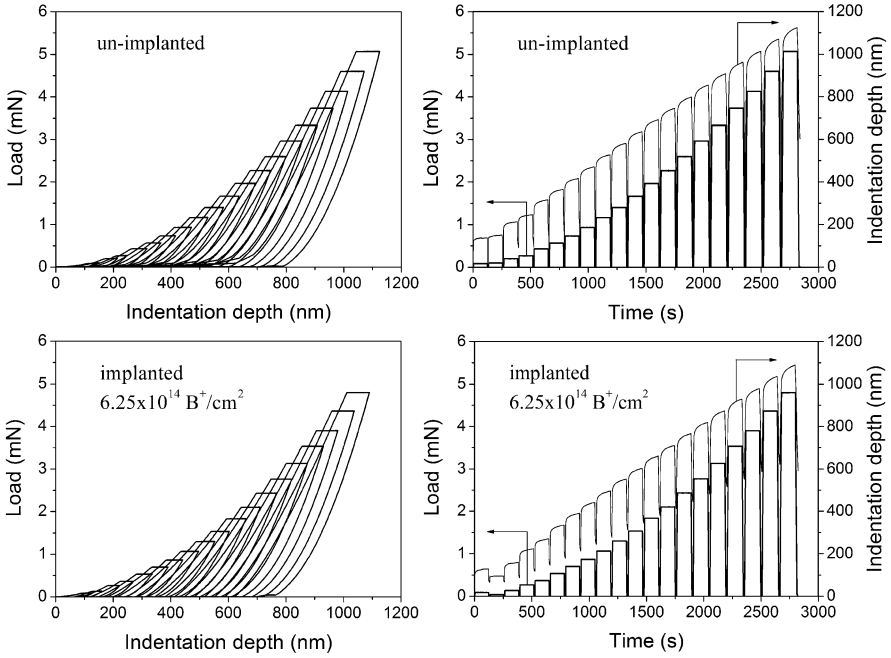

Fig. 7.1 Typical load-depth and load/depth-time curves for un-implanted PMMA (*top*) and implanted B:PMMA (*bottom*) samples

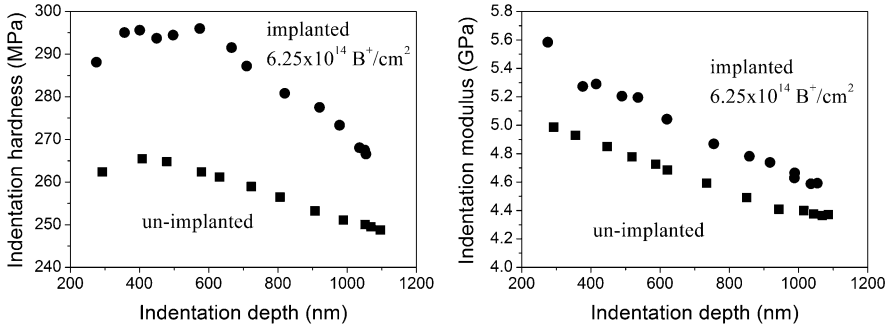

Fig. 7.2 Indentation hardness and elastic modulus versus maximum indentation depth for un-implanted PMMA (*squares*) and implanted B:PMMA (*circles*) samples

indentation depth illustrate the difference between pristine PMMA and B:PMMA samples in the entire range investigated up to 1,100 nm with the largest changes at about 400 nm, in consistence with the maximum penetration depth of B^+-ions into PMMA matrix obtained earlier by slow positron measurements and SRIM [19]. For clarity, the distribution of 40 keV B^+-ions implanted into PMMA calculated by SRIM [21] is presented in Fig. 7.3, showing the maximum depth of ~400 nm.

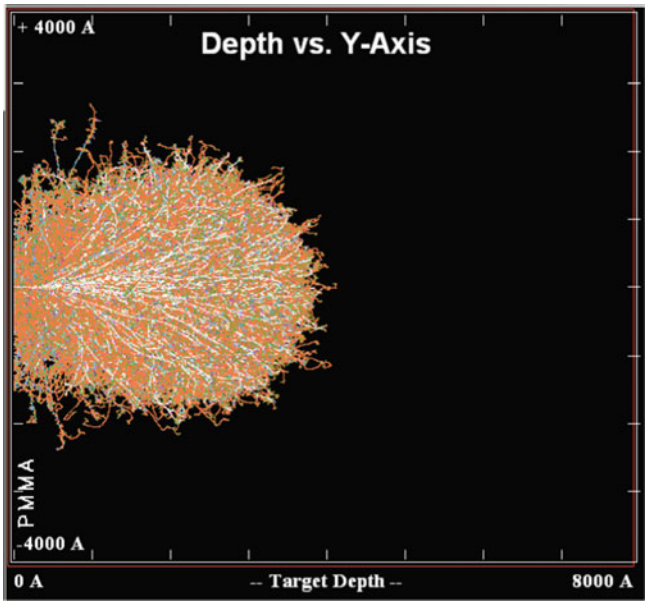

Fig. 7.3 Distribution of 40 keV B^+-ions implanted into PMMA after SRIM code [21]

The observed increased hardness of PMMA irradiated with B^+ ions is in good agreement with the increasing microhardness of a polystyrene surface irradiated with Ar^+ ions and Kapton irradiated with He^+, B^+, and Si^+ ions according to Lee et al. [22]. In the case of microindentation test, the hardness increase was more pronounced for higher ion doses and energies.

Sviridov [23] noted the increased microhardness in ion-implanted polymeric materials is determined by the degree of interconnectivity within the carbon cluster aggregates and presented some suggestions to explain the increase of the microhardness with ion dose and ion energy. Namely, an increase in the microhardness correlates with the increase of the relative energies transferred from the incident ions to the polymer by electronic excitations and by nuclear collisions, respectively; a high microhardness requires that the incident ions deposit their energy mainly in electronic excitations, leading to the formation of carbon clusters, while the contribution of energy losses by nuclear collisions is rather small. Thus, a general trend towards increasing microhardness with ion dose and ion energy is most probably due to energy losses by electronic excitations. This may explain in our case the observed increase of the composite hardness and elastic modulus in the whole range tested up to 1,100 nm. But, according to Sviridov [23], nuclear collisions are responsible for the formation of random links between the carbon clusters, leading to a gradual accumulation of domains with predominant sp^3-hybridisation of the carbon atoms and an increased microhardness of the implanted layer. Thus, the largest increase of hardness and elastic modulus detected

in the vicinity of 400 nm (i.e., the boron ion-implanted layer) can be interpreted by the energy loss by nuclear collisions.

Finally, it has to be mentioned that after Lee et al. [22] ion beam processing possesses a high potential for improving surface-sensitive mechanical properties of polymeric materials to render them suitable for hard-materials applications. In this respect, the results of nanoindentation tests of this study are important for further progress.

7.4 Conclusions

The first results of an investigation of the influence of low dose B^+-ion-irradiation (6.25×10^{14} ion/cm^2) on the mechanical properties (hardness and elastic modulus) of PMMA using nanoindentation tests with the UNHT device are reported. It was established that the dependences of hardness and elastic modulus on the maximum indentation depth show the main difference between the pristine and ion-implanted samples in the range up to about 400 nm, in good agreement with the maximum penetration depth of B^+-ions into PMMA matrix obtained by slow positrons and SRIM simulation.

Acknowledgments The authors are indented to E. Harea (Institute of Applied Physics, Academy of Sciences of Moldova) for useful discussions. T.S. Kavetskyy thanks the SFFR of Ukraine (No. F52.2/003) and the MESU (Nos. 0114U002616 and 0114U002617). A.L. Stepanov was supported by the RSF (No. 14-13-00758) in Russia.

References

1. Introduction on Instrumented Indentation, http://www.csm-instruments.com
2. Bushby AJ, Ferguson VL, Boyde A (2004) J Mater Res 19:249
3. Chowdhury S, Laugier MT, Rahman IZ, Serantoni M (2004) Surf Coat Technol 177–178:537
4. Menčik J, Rauchs G, Bardon J, Riche A (2005) J Mater Res 20:2660
5. Beegan D, Chowdhury S, Laugier MT (2008) Thin Solid Films 516:3813
6. Menčik J, Beneš L (2008) J Optoelectron Adv Mater 10:3288
7. Menčik J, He LH, Němeček J (2011) Polym Test 30:101
8. Oliver WC, Pharr GM (1992) J Mater Res 7:1564
9. Oliver WC, Pharr GM (2004) J Mater Res 19:3
10. Chafidz A, Ali I, Mohsin MEA, Elleithy R, Al-Zahrani S (2012) J Polym Res 19:9906
11. Nunes J, Piedade AP (2013) Appl Surf Sci 284:792
12. Jauberteau I, Nadal M, Jauberteau JL (2008) J Mater Sci 43:5956
13. Chorfa A, Madjoubi MA, Hamidouche M, Bouras N, Rubio J, Rubio F (2010) Ceramics – Silikáty 54:225
14. Yang F, Geng K, Liaw PK, Fan G, Choo H (2007) Acta Mater 55:321
15. Gogotsi YG, Domnich V, Dub SN, Kailer A, Nickel KG (2000) J Mater Res 15:871
16. Oliver DJ, Ruffell S, Bradby JE, Williams JS, Swain MV, Munroe P, Simpson PJ (2009) Phys Rev B 80:115210

17. Wang J, Zhu F, Zhang B, Liu H, Jia G, Liu C (2012) Appl Surf Sci 261:653
18. Gupta R, Kumar V, Goyal PK, Kumar S (2012) Appl Surf Sci 263:334
19. Kavetskyy T, Tsmots V, Kinomura A, Kobayashi Y, Suzuki R, Mohamed HFM, Šauša O, Nuzhdin V, Valeev V, Stepanov AL (2014) J Phys Chem B 118:4194
20. Stepanov AL, Abdullin SN, Petukhov VY, Osin YN, Khaibullin IB (2000) Phil Mag B 80:23
21. http://www.srim.org
22. Lee EH, Rao GR, Lewis MB, Munsur LK (1993) Nucl Instrum Meth Phys Res B 74:326
23. Sviridov DV (2002) Rus Chem Rev 71:315

Chapter 8
Nanoindentation Measurements of Cu Films with Different Thicknesses Deposited on a Single Crystalline Si Substrate

Constantin Pyrtsac

Abstract Thin films of various types are key components of modern microelectronics. By use of the dynamic nanoindentation method, Cu/Si structures with different thicknesses of the Cu film (t = 85, 470 and 1,000 nm) were investigated. It is shown that the film thickness and the wide range of maximum loads applied are some of the main factors influencing the deformation peculiarities and mechanical properties (Young's modulus E and hardness H) of the film/substrate structures.

Keywords Thin films • Nanoindentation • Hardness • Young modulus

8.1 Introduction

The increasing development of nanotechnology tends to reduce the component sizes of micro/nanoelectromechanical system devices (MEMS/NEMS). Thin films of various types are key components of modern microelectronics. Usually, the electronic properties are very important for the thin films. However, the mechanical features are also of interest for long time operation of MEMS/NEMS. During the process of growth and exploitation of films strong internal tensions can occur which after relaxation may cause deformation and destruction. Thin films imply the existence of a substrate from another material with different properties. The mechanical properties of thin films also depend on the features of substrate [1].

The study of the mechanical properties of thin films is done by the nanoindentation method that allows the identification of elastic and plastic deformations. For the determination of Young's modulus E and hardness H of thin films the method proposed by Oliver and Pharr is most often used [2]. This method was intensely applied for bulk materials. On the other hand, for investigations of the

C. Pyrtsac (✉)
Institute of Applied Physics, Academy of Sciences of Moldova, Chisinau, Republic of Moldova
e-mail: pirtac@phys.asm.md

P. Petkov et al. (eds.), *Nanoscience Advances in CBRN Agents Detection, Information and Energy Security*, NATO Science for Peace and Security Series A: Chemistry and Biology, DOI 10.1007/978-94-017-9697-2_8

mechanical properties of thin films it is necessary to take the influence of other factors into account which depend on the substrate features. The determination of the contact surface between indenter and films using the method of Oliver-Pharr is imperfect due to "pile-up" extrusion or "sink-in" deepening of the material around the indentation imprints. With increasing indenter penetration in the material the mechanical properties are determined not only by the films but also by the substrate.

In the case of hard/soft coated systems the elastic and plastic deformation of the substrate also plays a relevant role. For soft/hard coated systems, it is necessary to exclude the influence of the substrate by keeping the penetration depth of the indenter to about 10–20 % of the film thickness. Due to the restricted capacity of the equipment this requirement cannot always be kept due to the very small indentation depths necessary. Thus, it is impossible to exclude the influence of substrate in the final measurements stage [3].

In this paper we study the mechanical properties of Cu thin films deposited on Si substrates. Copper, having a higher conductivity and better electromigration properties is today replacing aluminum in integrated circuits. It is also beneficial to use a material with a low dielectric constant (low-k) to fill the space between Cu interconnect lines in order to reduce the amount of cross talk between the lines and to place them closer to each other. Basically, the entire systems of devices has been changed with the introduction of Cu metallization.

For the mechanical durability mentioned above, the following features of the investigated complex structures are important: elastic modulus, yield stress, fracture toughness, etc. All these characteristics can be obtained applying the nanoindentation method.

8.2 Experimental Techniques

As a substrate, single crystals of *n*-type Si(100) with a resistivity $\rho = 4{,}5$ Ωcm doped with phosphorus have been used. The Cu films were obtained by magnetron sputtering at room temperature using a RF sputter apparatus. The thickness of Cu films was equal to $t = 85$ (1), 470 (2), and 1000 (3) nm (see Table 8.1).

The topology of the surface of the thin films was estimated using atomic force microscopy and optical microscopy. Areas of 20×20 μm dimensions were scanned; the roughness R_a values are shown in Table 8.1.

Table 8.1 The thickness t and roughness R_a of the Cu films

Sample		Thickness t, nm	Roughness R_a, nm
Cu	1	85	7
	2	470	9
	3	1000	12.2
Si	4	–	1.95

Nanoindentation was carried out with a Nanotester-PMT-3-NI-02 using the dynamical range of penetration.

A diamond Berkovich indenter with a tip radius of 150 nm was used in these tests. The indentation followed a trapezoidal loading profile with 20 s loading time, 5 s holding time under the load and 20 s unloading time. The loads of the Berkovich indenter varied in the limits $P_{max} = 2$–900 mN. The H and E values were evaluated as the mean of five indentations applied with the same load. Figure 8.1 shows the dependences of H and E as a function of the applied force.

8.3 Results and Discussions

The hardness of sample 1 for the maximum loads $P_{max} < 300$ mN is close to that of the Si sample 4. The increase of H with decreasing load is caused by the appearance of indentation size effects. The influence of the Si substrate on the hardness value of Cu/Si structures is confirmed by the load-displacement curves analysis, where the 'pop-in', 'pop-out' and 'elbow' effects can be noticed (Figs. 8.2 and 8.3).

The influence of P_{max} on the modification of the load-displacement curves is as follows (see Figs. 8.2 and 8.3). In the loading parts of the curves slight oscillations of the indenter displacement are observed for $P_{max} = 10$ mN and 20 mN, even the "pop-in" effect is taking place (indicated by arrows). For the unloading parts the situation is reverse, for $P_{max} = 10$ mN, the shape of curves differs from conventional ones.

Two different effects appear for decreasing loads: the "elbow" effect at 20–40 mN and "pop-out" for $P_{max} = 50$–300 mN. The "pop-in" effect for small loads appears due to pronounced plastic flow of the Cu film when the indenter penetrates in material. The effects of 'pop-out' and 'elbow' in the curves of Cu/Si systems for $P_{max} > 300$mN occur due to phase transformations in the bulk Si [4].

Comparing the curves in Fig. 8.4a, d one observes the existence of the "pop-out" effect in the unloading curves of the bulk Si (indicated by arrows). The effect of the Si substrate becomes apparent for indentations with maximum loads smaller than 10 mN ($P_{max} = 7$ mN), when the indentation depth is approximately equal to the with films thickness ($t = 85$ nm), which is in accordance with Ref. [3]. This effect was confirmed also by our investigations for the Cu films of 470 and 1,000 nm. The "pop-out" effect cannot be observed when $h_{max}/t = 0.5$, here h_{max} is maximal indentation depth (nm) and t is the film thickness (nm) (see Fig. 8.4b, c).

We observed that the hardness of Cu/Si structure 1 approaches a saturation value for loads $P_{max} > 300$ mN. In this interval hardness value of the Si substrate 4 is smaller than the hardness of Cu/Si 1. This phenomenon takes place due to a protection effect by the Cu film against fragile destruction, i.e. due to the fact that the Cu film changes the geometry of the Berkovich pyramid by rounding the indenter tip a little. As a result, the indenter with its rounded tip more softly acts on the sample.

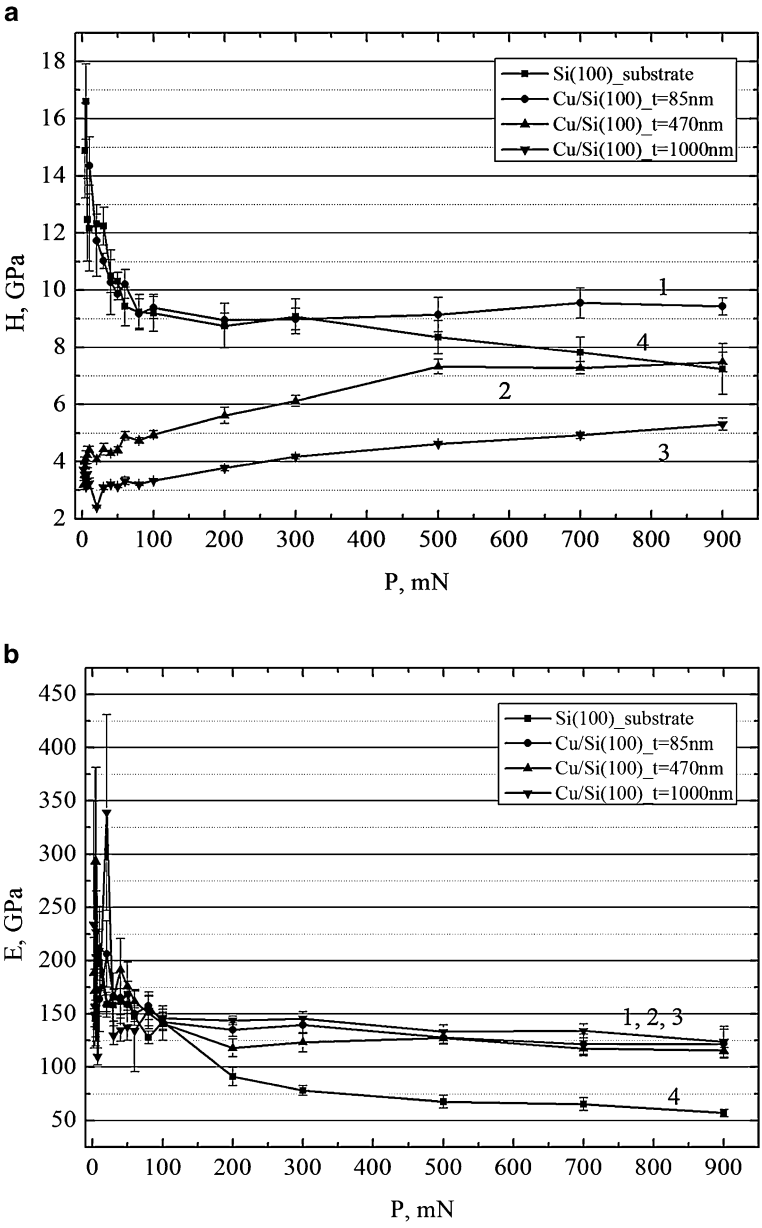

Fig. 8.1 Dependences *H(P)* (**a**) and *E(P)* (**b**) for the Cu/Si structures (*1*), (*2*), (*3*) and for the Si substrate (*4*)

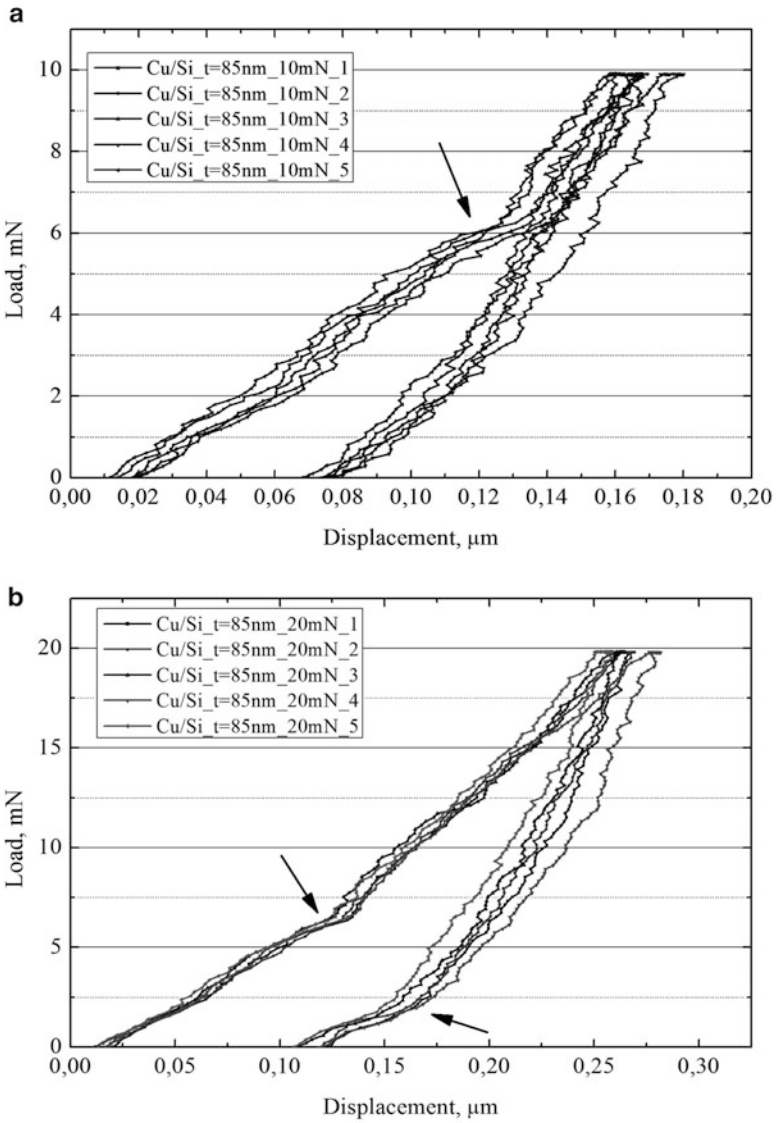

Fig. 8.2 Evolution of the for a Cu/Si structure (t = 85 nm) on the maximum applied load: (**a**) 10, (**b**) 20, (**c**), 50 mN for 5 indentations at each P_{max}

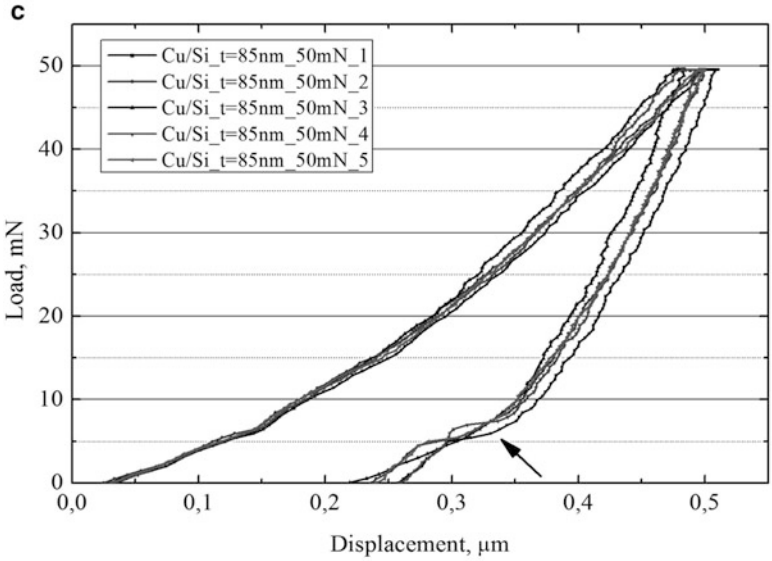

Fig. 8.2 (continued)

To confirm this idea, the Cu film was dissolved by chemical etching and the indentation images of Cu/Si, bulk Si and the residual indentation shapes after chemical etching were compared with each other. The results obtained are presented in Fig. 8.5.

When comparing the indentation images in Fig. 8.5b, c one can see that the cracks and destruction on the bulk Si surface are larger than the cracks on the Si substrate after chemical etching of the Cu film. This leads to an increase of the indentation dimensions; as a result a lower value of H is obtained for bulk Si.

As was mentioned above, the hardnesses of the Cu films 2 and 3 are on the same order of magnitude as described in [3]. The hardness of the Cu/Si structures is two times less than the hardness of bulk Si for small values of P_{max}. One can see from Fig 8.2c, d that the "pop-out" effect does not appear in the curves when the indenter penetrates to a depth of 50 % of the film thickness.

Figure 8.1a shows that in the case of the Cu/Si sample 2 for increasing P_{max} the hardness of the structure also increases reaching the hardness value of bulk Si. On the other hand, the hardness of the Cu/Si system 3 doesn't reach the hardness of bulk Si. The plastic indentations have been observed on the Si substrate after dissolution of the Cu film from the Cu/Si structures 2 ($P_{max} > 100$mN) and 3 ($P_{max} > 200$mN) by chemical treatment. It was concluded that the elastic action of the Si substrate has a dominant influence for $P_{max} < 100$mN. On the other hand, the influence of Si substrate is increasing for $P_{max} > 100$mN, and plastic deformation also takes place during the indentation. This conclusion is confirmed by the E (P) dependence (Fig. 8.1b). So, the Young's moduli E for both the system Cu/Si and bulk Si ($P_{max} < 100$mN) show a similar behavior. However, for $P_{max} > 100$mN the elastic modulus of bulk Si has a 50 % lower value than the system Cu/Si. The reason of such a behavior can be attributed to the destruction of crystal in the indentation neighbourhood.

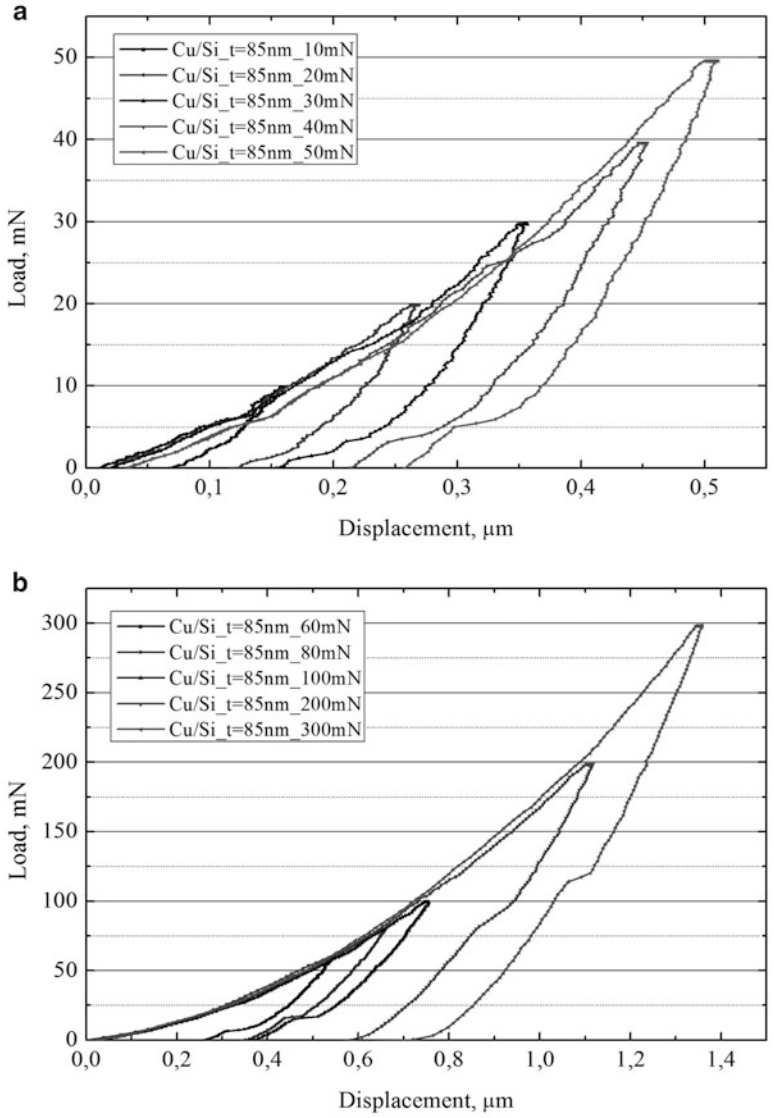

Fig. 8.3 Evolution of the load-displacement curves for Cu/Si structure (t = 85 nm) as function of the maximum applied load: (**a**) 10, 20,30, 40 50, (**b**) 60 80 100, 200, 300 mN

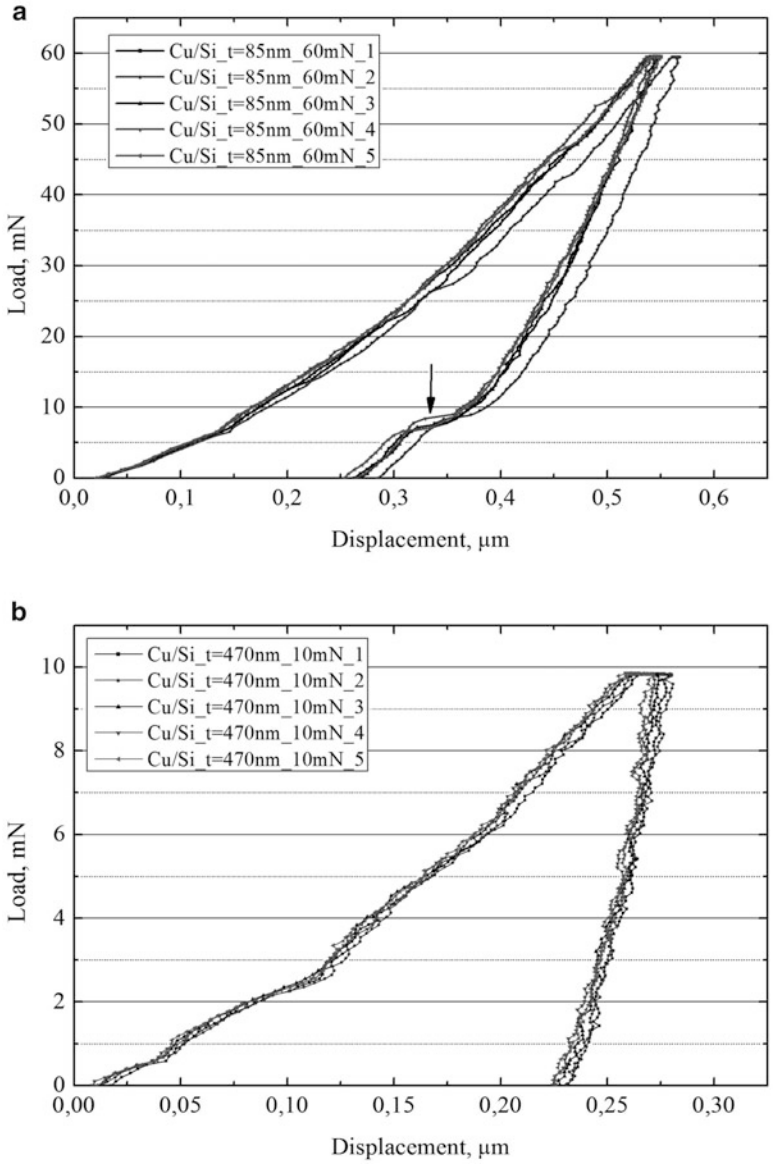

Fig. 8.4 Load-displacement curves for Cu/Si structures: (**a**) t = 85 nm, (**b**) t = 470 nm, (**c**) t = 1,000 nm and (**d**) of the Si substrate

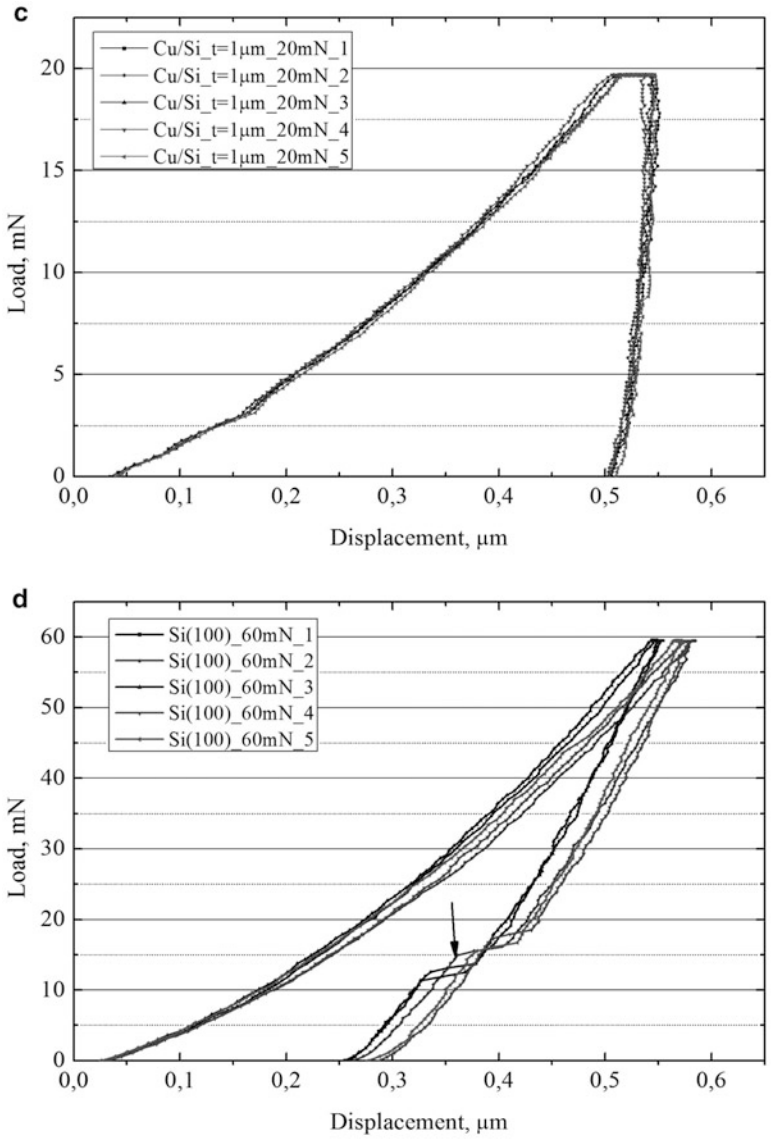

Fig. 8.4 (continued)

8.4 Conclusion

The mechanical properties of Cu thin films grown on Si(100) substrates using the magnetron sputtering method have been studied in the work. By use of the dynamic nanoindentation method, Cu/Si structures with different thicknesses of the Cu film

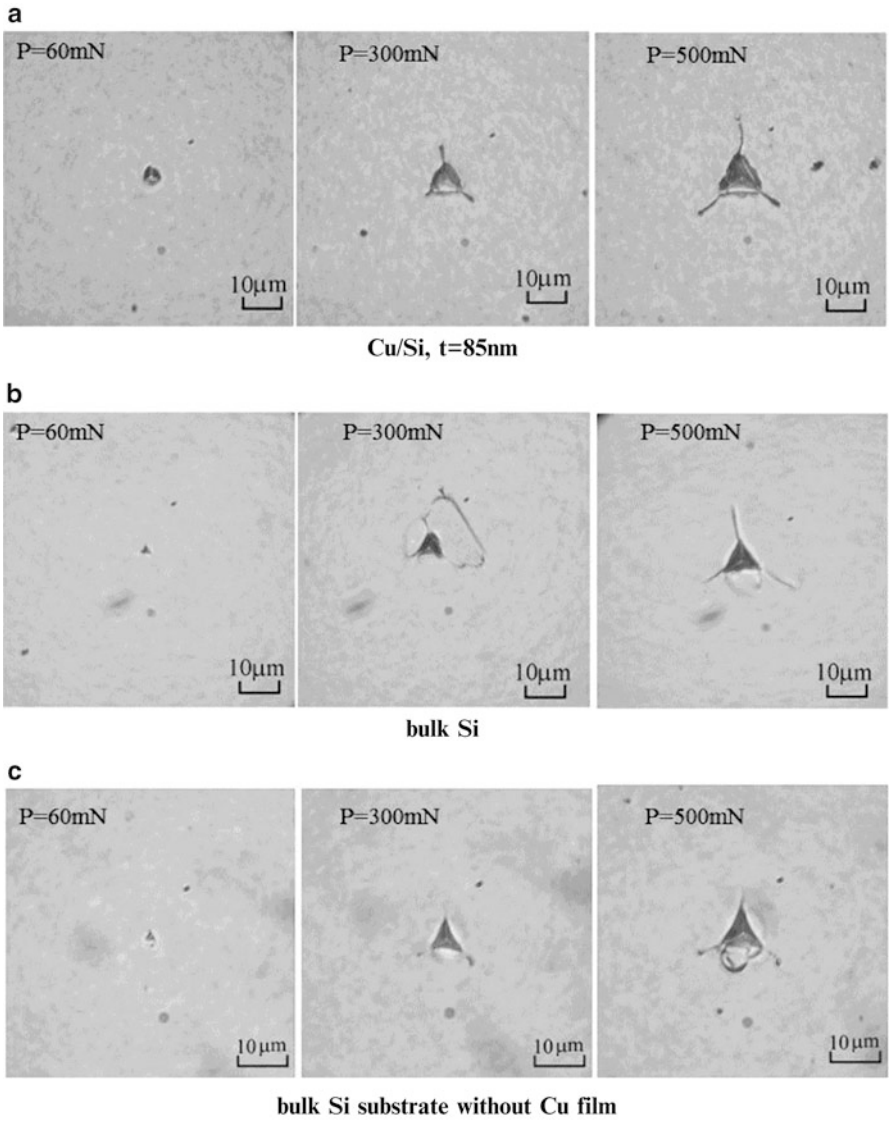

Fig. 8.5 Shape of indentations made on the Cu/Si structure (**a**), bulk Si (**b**) and the residual indentation images on the Si substrate after chemical etching of Cu film (**c**)

(t = 85, 470 and 1,000 nm) were investigated. It was shown that the Cu film thickness and the range of maximum loads applied are some of the main factors influencing the deformation peculiarities and the mechanical properties (Young modulus and hardness) of the film/substrate structures.

Acknowledgments The author thanks Dr. Lidia Ghimpu for the help with preparation of the Cu/Si structures by use of the magnetron sputtering method.

References

1. Read DT, Volinsky AA (2007) Micro- and Opto-electronic materials and structures: physics, mechanics, design, reliability, packaging, vol 1, A135
2. Oliver WC, Pharr GM (1992) J Mater Res 7:1564
3. Shugurov AR, Panin AV, Oskomov KV (2008) PSS 50:1050
4. Shikimaka O et al (2010) 5th International conference on materials science and condensed matter physics. Book of abstracts, Chisinau, 13–17 Sept 2010, p 127

Chapter 9
Doppler Broadening of the Annihilation Line Study of Organic-Inorganic Hybrid Ureasil-Based Composites

T.S. Kavetskyy, O. Šauša, T. Petkova, V. Boev, P. Petkov, A.V. Kukhta, and A.L. Stepanov

Abstract The organic-inorganic hybrid ureasil-based composites, containing polyether chains covalently linked to a silica framework through urea bridges, referred as ureasilicates or ureasils, and semiconducting As_2S_3 clusters, are investigated using Doppler broadening of annihilation line technique. It is established that the Doppler *S* and *W* parameters show significant structural difference between the pure ureasil and the As_2S_3-ureasil composites, the effect is more essential as the loading fraction of As_2S_3 increases. The new Doppler broadening results obtained in this work are found to be in consistent with the earlier reported results of positron annihilation lifetime measurements of the same materials.

Keywords Organic-inorganic composites • Annihilation line study

T.S. Kavetskyy (✉)
Drohobych Ivan Franko State Pedagogical University, Drohobych 82100, Ukraine

John Paul II Catholic University of Lublin, Lublin 20-718, Poland
e-mail: kavetskyy@yahoo.com

O. Šauša
Institute of Physics, Slovak Academy of Sciences, Bratislava 84511, Slovak Republic

T. Petkova • V. Boev
Institute of Electrochemistry and Energy Systems, Bulgarian Academy of Sciences, Sofia 1113, Bulgaria

P. Petkov
University of Chemical Technology and Metallurgy, 1756 Sofia, Bulgaria

A.V. Kukhta
Institute for Nuclear Problems, Belarusian State University, Minsk 220030, Belarus

Tomsk State University, Tomsk 634050, Russia

A.L. Stepanov
Kazan Physical-Technical Institute, Russian Academy of Sciences, Kazan 420029, Russia

Kazan National Research Technological University, Kazan 420015, Russia

Kazan Federal University, Kazan 420008, Russia

P. Petkov et al. (eds.), *Nanoscience Advances in CBRN Agents Detection, Information and Energy Security*, NATO Science for Peace and Security Series A: Chemistry and Biology, DOI 10.1007/978-94-017-9697-2_9

9.1 Introduction

In general, the micro-/nanocomposite materials bring together the polymer matrix (organic or inorganic) and filler, which could be metal, semiconductor, ceramic, etc. A combination between the inorganic siloxane framework and organic polymers results in enhanced resistance against cracking and processability. Typical representatives of organic-inorganic hybrid materials are so-called ureasilicates or ureasils. They are characterized by high optical transparency and high degree of flexibility, which allow them to be positioned on non-planar surfaces and to be used as perspective materials for information and energy security applications.

Recently, positron annihilation lifetime spectroscopy (PALS) and scanning electron microscopy (SEM) techniques have been applied for investigation of the organic-inorganic hybrid polymer network ureasil and semiconducting As_2S_3-ureasil composites [1]. It has been established that incorporation of the As_2S_3 clusters into ureasil influences on the *ortho*-positronium (*o*-Ps) intensity or positronium formation probability and micro-/nanoscopic structure compared to the pure polymer, the effect is more essential as the loading fraction of As_2S_3 increases. Also, incorporation of the As_2S_3 clusters into ureasil assists at ion-synthesis of Ag nanoparticles in polymer matrix, more effectively at higher doses of ion-implantation and for silver containing $(As_2S_3)_{95}Ag_5$-ureasil composite as revealed from SEM measurements [2]. Early Ag-nanoparticles were synthesized by ion implantation only in conventional polymers, for instance, in PMMA [3]. The goal of the present work is to study the organic-inorganic ureasil-based composites with Doppler broadening of annihilation line (DBAL) technique in positron annihilation spectroscopy (see, e.g., [4, 5]).

9.2 Experimental Procedure

The ureasil-based composites were prepared in the Institute of Electrochemistry and Energy Systems, Bulgarian Academy of Sciences (IEES-BAS, Bulgaria) [1]. The pure ureasil matrix was synthesized as follows. O,O′-bis (2-aminopropyl)-polypropylene glycol-block-polyethylene glycol-block-polypropylene glycol-500 (Jeffamine ED-600, Fluka) was dried under vacuum for 30 min. 3-isocyanatepropyltriethoxysilane (ICPTES, Aldrich), tetraethoxysilane (TEOS, 98 %, Aldrich) and n-butylamine were used as received. 0.875 mmol of Jeffamine (535 μL) was added to 1.76 mmol of ICPTES (464 μL) in order to obtain a liquid ureasil monomer. Thereupon 1.05 mmol of TEOS (251 μL) and 300 μL of n-butylamine were added to the mixture, which was kept under stirring for more than 10 min. The mixture was transferred into a plastic Petri dish and jellified under appropriate conditions. The gels were heated in a vacuum furnace at 60 °C at 0.1 Pa. A non-rigid, homogeneous and transparent stiff gel in form of a disk with a diameter of 40 mm and a thickness of 0.25 mm was obtained within 1 day.

To prepare the As_2S_3-ureasil composites the next synthesis procedure was applied. The starting materials for the preparation of As_2S_3 ingots were As (5 N) and S (5 N). The melting of the components was carried out in sealed quartz ampoules at 650 °C and a residual pressure of 0.1 Pa. The melt was quenched to room temperature, and the obtained glassy samples were finely grounded in powder form and dissolved in n-butylamine. Solutions with two different concentrations of the As_2S_3 clusters were prepared by dissolving 0.1 g (sample I) and 0.3 g (sample II) As_2S_3 in 3 ml of n-butylamine. The final concentrations of the As_2S_3 clusters containing solutions were about 0.13 M and 0.4 M, respectively. Incorporation of the chalcogenide phase was realized by mixing the preliminary obtained ureasil monomer with the chalcogenide clusters, dispersed in the organic solvent. For this purpose 300 μL of freshly prepared As_2S_3 in n-butylamine solution was added drop by drop to the mixture under vigorous stirring. The stiff gel was obtained as described above.

The DBAL experiment was done in the Institute of Physics, Slovak Academy of Sciences (IPSAS, Slovakia) [6]. The DBAL spectra were recorded using a HPGe detector with a resolution of 1.9 keV (FWHM) at 1,274 keV. The investigated samples, sandwiched between appropriately 8 μm Kapton foils, were placed on both sides of the ^{22}Na positron source with activity of 0.6 MBq. The DBAL spectrum was recorded 24 times with elapsed time 1 h and, consequently, the total time per measurements was 24 h. Finally, more than 10^6 counts at annihilation peak 511 keV were achieved. The annihilation line was deconvoluted with Gold iterative algorithm [7], permitting the measurement of small changes of the annihilation peak (e.g., *S* and *W* parameters) with high confidence. The typical example of deconvoluted DBAL spectrum is shown in [8]. The Doppler *S* and *W* parameters were defined as the ratio of the central area to the total area of the 511 keV annihilation peak and as the ratio of wings area to the total area, respectively [9].

9.3 Results and Discussion

The DBAL spectroscopy measures the projection p_L of electron momentum on the direction of photon emission, i.e. a one dimensional distribution of momentum of the positron-electron annihilating pairs. This quantity is related to the detected broadening ΔE of the 511 keV line (i.e., the energy of the annihilation ray is shifted by the Doppler broadening due to the kinetic momentum of annihilated electron) by relation $\Delta E = p_L c/2$, where c is the speed of light. The principle of this technique is to record the energy spectrum of γ rays. The sum of annihilation events, registered by γ detector, leads to a peak which is broadened symmetrically to both sides of its maximum. Large values of p_L contribute to a high momentum distribution part, affecting the wings of the peak (core electrons), whereas small values of p_L contribute mainly to a low momentum distribution part, affecting the center of the peak (valence and conductivity electrons). Due to their low momentum, the annihilations with valence electrons fall predominantly in the region of the

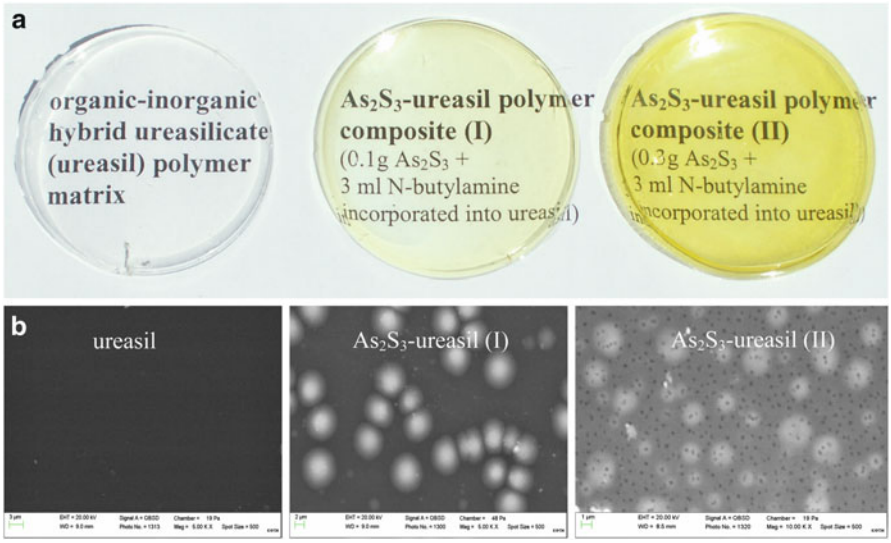

Fig. 9.1 (**a**) Photographs and (**b**) SEM images for the pure ureasil matrix and ureasil-based composites with two loading fractions of As_2S_3 (samples I – 0.1 g and II – 0.3 g)

S parameter (shape of the peak), while mainly core electrons have momentum values high enough to contribute to the *W* parameter (wings of the peak). Thus *S* and *W* are often called as valence and core annihilation parameters, respectively.

Figure 9.1 shows the investigated ureasil-based polymeric materials with two loading fractions of As_2S_3. As an example, the morphology of these samples is also given in this figure as revealed by SEM measurements [1]. A good homogeneity, with randomly distributed As_2S_3 clusters of about 1–5 μm size, and optical transparency of the composite samples are observed. It confirms a perfect synthesis procedure performed as well as a suitability of the ureasil matrix used for fabrication of organic-inorganic composite materials.

The results of DBAL study of the samples are demonstrated in Fig. 9.2. It is established that the Doppler *S* and *W* parameters show significant structural difference between the pure ureasil and the As_2S_3-ureasil composites. Likely to PALS results [1], in the DBAL experiment conducted the effect is more essential as the loading fraction of As_2S_3 increases. The Doppler broadening results obtained (i.e., *S* increases and *W* decreases with increasing of As_2S_3 quantity in ureasil matrix) could be plausibly explained by the formation of vacancy-type voids in the As_2S_3 clusters, taking into account that the increase in *S* and decrease in *W* implies an increase in the concentration of vacancy-like defects in the material structure (see, e.g., [10–12]). But it should be considered only as suggestion because of impact of some inhomogeneity in the hybrid As_2S_3-ureasil structure as well as possible changes at the border of matrix-grain (As_2S_3 chalcogenide cluster) are hardly to be estimated in the DBAL experiment. In order to support this local conclusion as revealed from the measurements carried out, the *S* and *W* data for the As_2S_3 glass,

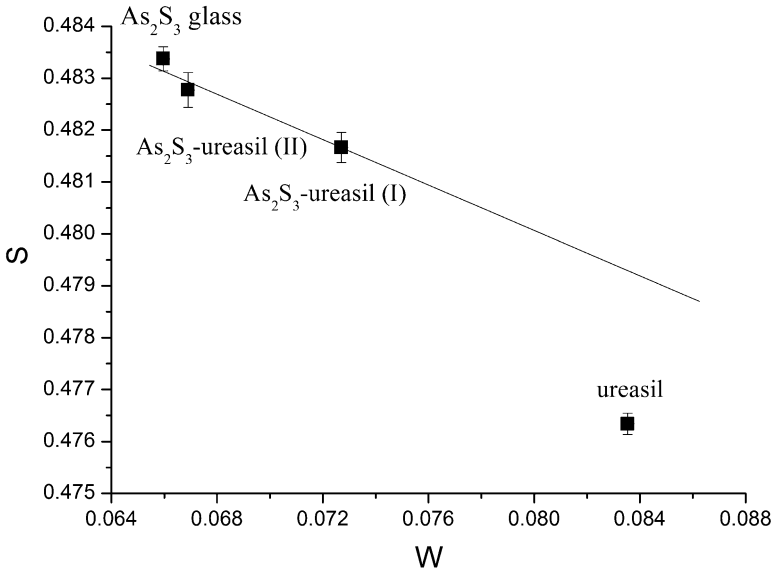

Fig. 9.2 Doppler *S* versus *W* parameters for the pure ureasil matrix as well as ureasil-based composites with two loading fractions of As_2S_3. The samples are marked as shown in Fig. 9.1. The *S* and *W* data for As_2S_3 glass are taken from the work [6] for comparison. The *solid line* is drawn as a guide for the eye (see text for details)

taken from the work [6] for the same activity of ^{22}Na positron source (0.6 MBq), geometry and thickness of Kapton films (8 μm), are also plotted in Fig. 9.2. It is clear seen that the *S*-*W* data for the As_2S_3 glass and for the As_2S_3-ureasil composites are located under the same straight line far away from the *S*-*W* data for the pure ureasil, indicating that the same defect structure (voids) in the chalcogenide glass may exist in the chalcogenide clusters (see, e.g., [13, 14] for *S*-*W* slope).

Why the Doppler lineshape parameters for the pure ureasil exhibit the lowest *S* and the highest *W* values (Fig. 9.2)? To answer on this question the role of positronium (an electron-positron bound state) formation should be taken into account. Indeed, the PALS experiment [1] showed that the *ortho*-positronium (*o*-Ps) intensity or positronium formation probability is significantly larger for the pure ureasil matrix compared to the As_2S_3-ureasil composites. It should be noted here that the *o*-Ps formation undergoes the pick-off annihilation process, i.e. to encounter an electron with the appropriate "opposite" spin to the positron, and annihilate into 2 *annihilation photons* than by the 3 *annihilation photons* in the vacuum, reducing the *o*-Ps lifetime from about 142 ns (in vacuum) to a few nanoseconds in solid (see, for instance, review [4] and references therein). Two-photon pick-off *o*-Ps decay creates photons with energies within the 511 keV photopeak, which are evenly distributed [15] and may impact on the wings of the annihilation peak, resulting in *W* increases (*S* decreases). Thus, the lowest *S* and the highest *W* values obtained are probably connected with the largest value of *o*-Ps intensity for the pure ureasil matrix among other ureasil-based composites under study [1].

9.4 Conclusions

The original results on the DBAL study of organic-inorganic hybrid ureasil-based composites, containing polyether chains covalently linked to a silica framework through urea bridges and As_2S_3 clusters, are reported. It is established that the Doppler *S* and *W* parameters show significant structural difference between the pure ureasil and the As_2S_3-ureasil composites, the effect is more essential as the loading fraction of As_2S_3 increases. These new findings are in consistent with the previous results of positron annihilation lifetime measurements for the same samples. The DBAL results obtained are plausibly explained by the formation of specific vacancy-type voids in the As_2S_3 clusters incorporated into ureasil matrix.

Acknowledgments T.S. Kavetskyy is grateful to the SAIA for scholarships in the IPSAS. O. Šauša wishes to thank the Slovak Grant Agency VEGA (Nos. 2/0099/10 and 2/0164/14). T. Petkova and V. Boev were supported by the project BG051PO001/07/3.3-02/58/17.06.2008. This work was also partly supported by the SFFR of Ukraine (Nos. F40.2/019 and F52.2/003) and the MESU (No. 0114U002616). A.L. Stepanov thanks for the financial support by the RSF (No. 14-13-00758) in Russia.

References

1. Kavetskyy T, Љ ауљ а O, Kriљtiak J, Petkova T, Petkov P, Boev V, Lyadov N, Stepanov A (2013) Mater Sci Forum 733:171
2. Kavetskyy T, Lyadov N, Valeev V, Tsmots V, Petkova T, Boev V, Petkov P, Stepanov AL (2012) Phys Status Solidi C 9:2444
3. Stepanov AL, Abdullin SN, Petukhov VY, Osin YN, Khaibullin IB (2000) Philos Mag B 80:23
4. Schultz PJ, Lynn KG (1988) Rev Mod Phys 60:701
5. Grafutin VI, Prokop'ev EP (2002) Adv Phys Sci 45:59
6. Kavetskyy TS, Tsmots VM, Љ ауљ а O, Stepanov AL (2014) Semiconductors 48:9
7. Bandžuch P, Morháč M, Krištiak J (1997) Nucl Inst Methods Phys Res A 384:506
8. Kavetskyy T, Tsmots V, Љ ауљ а O, Stepanov AL (2012) Phys Status Solidi C 9:2420
9. Priesmeyer HG, Bokuchava G (2006) Mater Sci Eng A 437:54
10. Saarinen K, Hautojärvi P, Keinonen J, Rauhala E, Räisänen J, Corbel C (1991) Phys Rev B 43:4249
11. Kerbiriou X, Barthe MF, Esnouf S, Desgardin P, Blondiaux G, Petite G (2006) Mater Sci Forum 527–529:571
12. Huang Y-Y, Chen Z-Y, Wei Y-Q, Li Y-X, Deng W (2009) Mater Sci Forum 607:149
13. Misheva MA, Djourelov N, Margaca FMA, Miranda Salvado IM, Passage G (1996) J Phys Condens Matter 8:6313
14. Misheva M, Djourelov N, Kotlarova T, Elenkov D, Passage G (1996) Thin Solid Films 283:26
15. Adhikari S, Chumbley LS, Chen H, Jean YC, Geiculescu AC, Hillier AC, Hebert KR (2010) Electrochim Acta 55:6093

Part IV
Materials: Carbon Nanotubes, Graphene and Nanodiamond

Chapter 10
Creation of Blue Light Emitting Color Centers in Nanosized Diamond for Different Applications

L. Himics, S. Tóth, M. Veres, A. Czitrovszky, A. Nagy, D. Oszetzky, A. Kerekes, Sz. Kugler, I. Rigó, A. Tóth, and M. Koós

Abstract Plasma immersion ion implantation and focused ion beam treatment techniques were used to create nitrogen-related complex defect centers in detonation nanodiamond crystals. Helium implantation was used to produce vacancies in the crystal structure, which was followed by the introduction of nitrogen ions (with the same method). Heat treatment at 1,023 K was applied to initiate vacancy diffusion and formation of complex defect centers. The sp^2 carbon content of the samples formed during the implantation and the high-temperature annealing was decreased by oxidation at 723 K in air. Changes in the bonding structure were monitored by Raman and infrared spectroscopic measurements after each step of the defect creation process. It was found that the photoluminescence of nanosized diamond changes remarkably as a consequence of different treatments and a new, narrow, intense emission band develops in the deep blue wavelength region. The N3 nitrogen-related complex defect center was considered as source of this fine structured emission band in the luminescence spectrum.

Keywords Nanodiamond • Nitrogen-related complex color centers • Ion implantation • Photoluminescence

L. Himics • S. Tóth • M. Veres (✉) • A. Czitrovszky • A. Nagy • D. Oszetzky • A. Kerekes
Sz. Kugler • I. Rigó • M. Koós
Wigner Research Centre for Physics, Hungarian Academy of Sciences, P.O.B. 49,
H-1525 Budapest, Hungary
e-mail: veres.miklos@wigner.mta.hu

A. Tóth
Institute of Materials and Environmental Chemistry, Research Centre for Natural Sciences,
Hungarian Academy of Sciences, H-1525 Budapest, Hungary

P. Petkov et al. (eds.), *Nanoscience Advances in CBRN Agents Detection, Information and Energy Security*, NATO Science for Peace and Security Series A: Chemistry and Biology, DOI 10.1007/978-94-017-9697-2_10

10.1 Introduction

Due to its unique properties, which provide a good basis for many important applications and technologies now and in future, nanodiamond (ND) gained much scientific attention from many research groups in the last decades. Particular interest is devoted to the light emitting properties of different color centers in diamond [1–3]. Most of these emit in the green-red wavelength region, but some, like the so-called "N3" optically active defect, detected first in natural diamond, emit in the UV or near-UV range. The N3 center has excellent emission properties, which make it a good candidate as a active laser material for color center lasers, for example. It was shown that the N3 center is thermally stable up to temperatures above 800 K and exhibits no photobleaching even at extremely high power densities (up to 100 MW/cm^2) [4]. It consists of three substitutional nitrogen atoms situated in the (111) plane around a carbon vacancy in the diamond crystal and has $C_{3\nu}$ point symmetry [5]. In the case of the optically active N3 defect the zero phonon line (ZPL) (characteristic parameter of different color centers allowing also the identification of luminescent point defects in diamond) appears at 2.985 eV (415 nm) in the photoluminescence (PL) spectrum. This center was observed earlier in artificial single crystal CVD diamond films and also after intentional nitrogen ion implantation of IIa type diamonds [4]. The situation for nanosized diamond, more actual for nanotechnological applications, is not so auspicious. Except some literature data on the detection of optically active N3 defect centers [6] theirintentional creation in ND was not demonstrated earlier.

In this paper we report on the formation of N3 color center ins detonation nanodiamond crystals with average grain size below 20 nm using ion implantation and subsequent heat treatments.

10.2 Experimental Details

10.2.1 Preparation of the ND Samples

"Layers" were prepared from nanodiamond powders in order to eliminate handling difficulties of the samples during the different treatments and investigations. Commercially available detonation ND powder (Neomond Ltd.) was mixed with distilled water and subjected to ultrasonication for 3 h. The concentration of ND in the suspension was 1.5 mg/ml. After sonication 1,500 ml of ND slurry was dripped into a 10 mm hole of a stainless steel ring placed on a silicon substrate. The ring was used to limit the surface covered by the ND suspension. The samples were dried in air for at least 48 h at room temperature. After removal of the ring a circular stain of ND "film" was left on the silicon surface.

10.2.2 Treatments

Samples were implanted using two different implantation methods: Plasma Immersion Ion Implantation (PIII) and Focused Ion Beam (FIB) treatment with different energies and fluences.

An acceleration voltage of $U = 20$ kV and a fluence of $F = 10^{15}$ ion/cm^2 were used during the PIII treatment. The samples were implanted first with He^+ ions, followed by the N^+_2 treatment.

For the FIB technique the acceleration voltage was $U = 2$ kV, and fluences of $F = 1.8 \times 10^{15}$ ion/cm^2 and $F = 1.5 \times 10^{15}$ ion/cm^2 were used during He^+ and N^+_2 ion bombardment, respectively. The implanted samples were heat treated at 1,023 K for 2 h in vacuum, then annealed at 723 K for 5 h in air.

10.2.3 Characterization Techniques

Raman spectra of the samples were recorded in the 1,000–2,000 cm^{-1} region with a Renishaw 1,000 Raman spectrometer equipped with a Leica microscope. The 488 nm line of an argon ion laser served as excitation source. After baseline correction all spectra were normalized to the maximal intensity in the D-band region and shifted along the ordinate for better visibility.

Fourier-transform infrared spectroscopic measurements were performed in the 1,000–2,000 cm^{-1} wavenumber region using a Bruker IFS28 FTIR spectrometer attached to a microscope. The samples were tilted in order to eliminate interference effects in the spectra.

Steady state photoluminescence was measured at room temperature in front face geometry using a Horiba Jobin Yvon Fluorolog FL3-22 fluorimeter with a 450 W xenon lamp as an excitation source. The spectral luminescence distribution of was analyzed in the 1.8–4.25 eV photon energy range using 4.597 eV excitation. The measured spectra were corrected for the spectral response of the system and for the excitation intensity. The spectral resolution was between 4 and 17 meV.

10.2.4 SRIM Calculations

The Stopping and Range of Ions in Matter (SRIM) [7] computer program, a widely used Monte-Carlo-simulation based software for the prediction of the stopping depth of different ions in different structures of solid materials, was used to estimate the depth distributions of the implanted ions and generated vacancies for 20 keV / (PIII) and 2 keV (FIB) ions. Modelling parameters were: 3.15 g/cm^3 for the density of nanodiamond, 45 eV for the displacement energy and 4.3 eV for the surface binding energy [8–10] in both cases.

10.3 Results and Discussion

10.3.1 SRIM Calculations

Figure 10.1 shows the result of SRIM calculations. Since the fluences used with PIII and FIB were similar, the acceleration voltage is the main parameter being different for the two treatments. It can be seen that helium ion implantation with 20 keV energy creates vacancies in the 2–160 nm range with a maximum around 80 nm, while a ten times lower ion energy results in a five times shallower vacancy distribution (2–30 nm). The results for the nitrogen ion distributions are similar. While for 20 keV the nitrogen ion distribution is in the range of 1–60 nm, the lower ion energy resulted in a five times shallower implantation region (1–11 nm). The formation of nitrogen-vacancy complexes is expected to be of highest probability in the depth region where the vacancy and nitrogen distributions overlap. However, the maximum of the distribution of complexes is slightly shifted to lower depths, since vacancies are also generated by the nitrogen implantation (black curve on Fig. 10.1) which can take part in the formation of complex centers too.

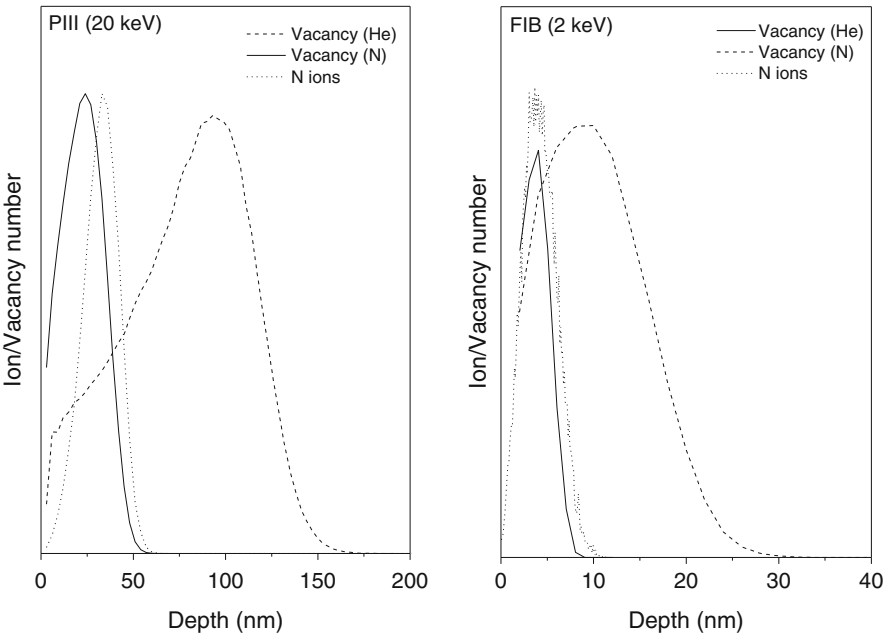

Fig. 10.1 The calculated depth distribution of vacancies generated by helium and nitrogen ions, and of nitrogen-vacancy complex centers during 20 keV PIII and 2 keV FIB treatments

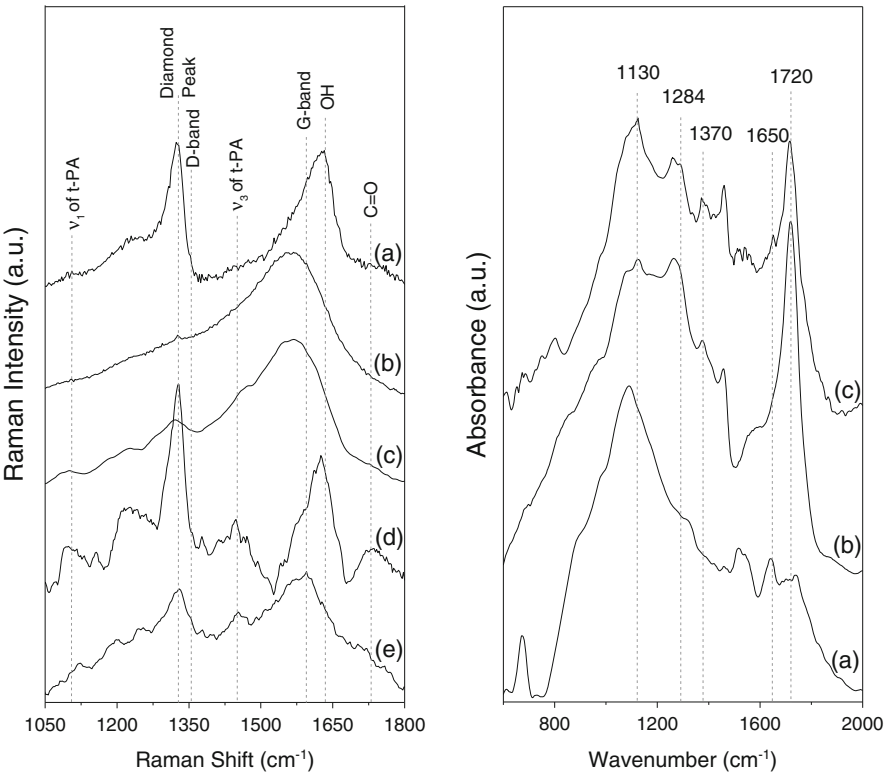

Fig. 10.2 *Left*: Raman spectra of nanodiamond samples measured after different treatments: (**a**) untreated, after He^+ and N_2^+ ion implantation by (**b**) PIII and (**c**) FIB techniques and after complex heat treatment of the (**d**) 20 keV and (**e**) 2 keV samples. *Right*: FTIR spectra of nanodiamond samples measured after different treatments: (**a**) untreated, after He^+ and N_2^+ ion implantation and complex heat treatment by the (**b**) PIII and (**c**) FIB techniques

10.3.2 Raman and FTIR Investigations

The Raman spectrum of an untreated sample is typical for small crystallite size ND ((a) in the left panel of Fig. 10.2). Due to the confinement effect the characteristic diamond peak is shifted to lower wavenumbers and it is located at 1,324 cm^{-1}. Following the algorithm described in Ref. [11] and fitting the peak, the average grain size was estimated to be around 12 nm for our sample. D and G bands characteristic for amorphous carbon material can be seen around 1,355 and 1,590 cm^{-1} respectively. Other types of impurities assigned to surface functional groups like OH (peak at 1,640 cm^{-1}) and oxygen (peak at 1,740 cm^{-1}) were also detected in the spectrum of the sample. The weak so called "nanodiamond finger-print" peaks (attributed to the υ_1 and υ_3 modes of trans-polyacetylene (t-PA)) can be seen at 1,120 and 1,455 cm^{-1}, respectively [12].

Both ion implantation techniques affect the character of the Raman spectra remarkably ((b) and (c) in the left panel of Fig. 10.2). The spectrum of the PIII sample is now dominated by the G band of graphitic carbon.

Due to the increased, broad background in the D band region the diamond peak is very weak, but still detectable. This finding indicates that the PIII treatment causes graphitization of the diamond structure and the surface of the diamond crystallites is transformed into graphitic amorphous carbon. The FIB implantation has less impact on the bonding structure of the diamond sample, mainly because of the ion energy one order of magnitude lower. The Raman spectrum of the FIB implanted sample also contains the characteristic D and G bands, but compared to the PIII case they contribute less to the scattering.

As a result of the complex heat treatments, performed at 1,023 K in vacuum and at 723 K in air, the bonding structure of both types of samples has changed remarkably ((d) and (e) on the left panel of Fig. 10.2). It is known that high temperature annealing initiates vacancy migration and induces relaxation of the implanted structure, while the oxidation in air at lower temperatures removes the sp^2 hybridized carbon content. After the treatments the diamond peak has become more pronounced, especially in the PIII treated sample. The oxidation reduced the non-diamond content in both samples, as is indicated by the remarkable decrease of G band intensity. The "fingerprint" peaks can also be seen again in the spectra recorded after the heat treatments.

FTIR spectroscopy was used to prove the presence of nitrogen impurities in the nanodiamond structure [13]. New features were observed in the spectra recorded after different treatments (right panel in Fig. 10.2), compared to the untreated sample. The appearance of characteristic bands at 1,130, 1,284 and 1,370 cm^{-1} after both PIII and FIB implantation evidences the introduction of nitrogen into the nanodiamond structure. Peaks at 1,130 and 1,284 cm^{-1}, appearing as weak shoulders of a broad band, can be attributed to substitutional nitrogen and the more complex N2 center consisting of two neighboring nitrogen atoms, respectively. The third peak at 1,370 cm^{-1} is observable as an individual band, but has a lower intensity than the former two. This band can be assigned to the N3 center, containing three or more adjacent nitrogen atoms. Detection of the above described nitrogen complexes in the implanted diamond structures is in good agreement with the SRIM calculations predicting a relatively narrow depth distribution of the nitrogen ions, which means a relatively high nitrogen concentration in the implanted regions.

10.3.3 Photoluminescence

From the results of the SRIM calculations and the significant differences between the Raman and FTIR spectra of untreated and ion implanted ND samples remarkable changes can be expected also in the electronic structure of the investigated nanodiamond samples. Its can be studied optically by photoluminescence spectroscopy, which is widely used for the characterization of impurities and defects in

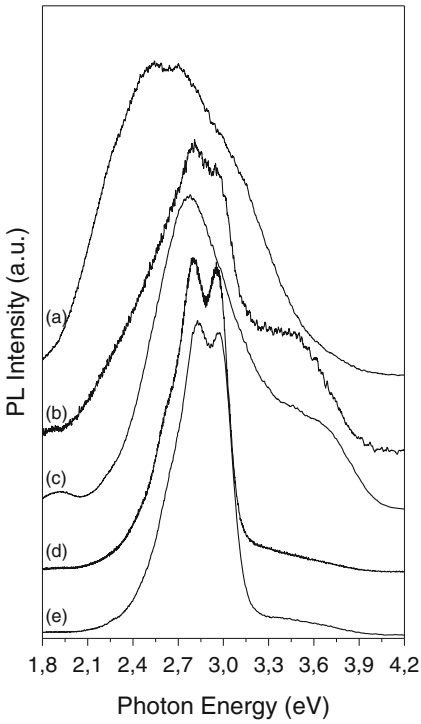

Fig. 10.3 Photoluminescence spectra of (**a**) untreated, (**b**) PIII and (**c**) FIB implanted samples. Curves (**d**) and (**e**) are PL spectra taken after complex heat treatment of PIII and FIB treated samples, respectively. All spectra were normalized to the maximal peak intensity and shifted along ordinate for clarity

diamond structures [14]. Due to the well-defined structure of optically active point defects, the strong carbon-carbon bond and the relatively weak electron-phonon interaction, PL allows easy identification of color centers in the diamond structure [15].

Figure 10.3 shows the evolution of the PL spectra after different treatments. The PL spectrum of the untreated material excited with by $E_{ex} = 4.597$ eV photons (Fig. 10.3a) has a wide broad feature typical for small size nanocrystalline diamond and was observed by many research groups [16, 17]. This broad band is explained as a result of overlapping of narrow peaks attributed mainly to different functional groups on crystallite surfaces and to structural defects created during the detonation process [17].

Curves (b) and (c) in Fig. 10.3 show the effect of He^+ and N_2^+ ion implantations on the PL spectra for the PIII and FIB cases. PIII implantation causes considerable modification of the PL band; at least three spectral components became distinguishable near 2.85, 3.09 and 3.6 eV photon energies. A small enhancement on the low energy side near 2.3 eV can also be observed. In addition, the emission intensity is decreased remarkably, as it can be seen from the signal-to-noise ratio. The unresolved components around 3.6 eV are related to different types and combinations of nitrogen defects and vacancies [4] and indicate the formation of nitrogen-related defects during the implantation. The emission band in the 2.7–3.0 eV range can be assigned to the well known N3 color center. The enhancement around 2.3 eV is due to non-diamond carbon structures created by the implantation.

The FIB treatment causes similar changes in the PL spectrum as PIII (Fig. 10.3c), but the dramatic decrease of the signal-to-noise ratio was not observed. Since the lower ion energy used in FIB implantation is less destructive, less sp^3 hybridized carbon atoms transform into emission-quenching sp^2 ones compared to PIII. This is also supported by the Raman measurements (Fig. 10.2). A well pronounced broad luminescence band with a maximum around 2.75 eV appears in the spectrum of the FIB implanted sample overlaps with a broad band at higher energies. This band can be related to substitutional nitrogen and other nitrogen-related defects in the structure [18].

PL spectra recorded with the implanted samples show that both implantation techniques are suitable for the introduction of nitrogen into the ND structure, but the formation of "good quality" complex centers requires further treatments. Curves (d) and (e) in Fig. 10.3 represent the PL spectra after heat treatments of the PIII and FIB samples. Well defined emission bands developed in both cases, the detailed analysis of which proves the formation of N3 defect centers: the zero phonon line at 2.98 eV and the phonon side bands at lower photon energies, partially resolved at 2.83 and 2.71 eV, are characteristic for this type of defect in diamond. The phonon replica with 150 and 120 meV spacings are slightly different from those observed for large diamond crystals, but this is due to the differences in local phonon modes of nanocrystalline and macroscopic diamond.

10.4 Conclusions

A relatively intense deep blue light emission band, attributed to the N3 complex defect center was obtained in nanosized diamond with average grain sizes below 20 nm by He^+ and N_2^+ implantation using 20 keV and 2 keV ion energies and subsequent heat treatments. Raman and infrared spectroscopies show remarkable changes in the bonding configuration of the samples after the different treatments and proved the introduction of nitrogen and the formation of complex nitrogen-related defect centers in the diamond structure, the light emission properties of which were examined by PL measurements. Our results demonstrate the effectiveness of low-energy implantation methods for the formation of light emitting centers in nanodiamonds.

References

1. Aharonovich I, Castelletto S, Simpson DA, Su C-H, Greentree AD, Prawer S (2011) Rep Prog Phys 74:076501. doi:10.1088/0034-4885/74/7/076501
2. Fu C-C, Lee H-Y, Chen K, Lim T-S, Wu H-Y, Lin P-K, Wei P-K, Tsao P-H, Chang H-C, Fann W (2007) Natl Acad Sci 104:727
3. Aharonovich I, Greentree AD, Prawer S (2011) Nat Photonics 5:397
4. Zaitsev AM (2001) Optical properties of diamond. Springer, Berlin/New York

5. Stephen C, Rand L, DeShazer G (1987) US Patent US4638484 A, 20 Jan 1987
6. Mikov SN, Igo AV, Gorelik VS (1999) Phys Solid State 41:1012
7. Ziegler JF, Ziegler MD, Biersack JP (2010) Nucl Inst Methods B 268:1818
8. Vereshchagin AL, Sakovich GV (2001) Mendeleev Commun 11:39
9. Koike J, Parkin DM, Mitchell TE (1992) Appl Phys Lett 60:1450
10. Ullmann J, Delan A, Schmidt G (1993) Diam Relat Mater 2:266
11. Osswald S, Mochalin VN, Havel M, Yushin G, Gogotsi Y (2009) Phys Rev B 80:075419
12. Ferrari AC, Robertson J (2001) Phys Rev B 63:121405
13. Hsiao-Chi L, Bing-Ming C (2011) Anal Chem 83:6539–6544
14. Zaitsev AM, Melnikov AA, Denisenko AV, Varichenko VS, Job R, Fahrner WR (1996) Mater Res Soc Symp Proc 416:113
15. Collins AT (1992) Diam Relat Mater 1:457
16. Mochalin VN, Shenderova O, Ho D, Gogotsi Y (2012) Nat Nanotechnol 7:11
17. Schrand AM, Ciftan Hens SA, Shenderova OA (2009) Crit Rev Solid State Mater Sci 34:18
18. Eaton-Magana S, Post JE, Heaney PJ, Walters RA, Breeding CM, Butler JE (2007) Gems Gemol 43:332

Chapter 11
Characterization of Graphene Produced by Electrolysis in Aqueous Electrolytes

Aleksandar Petrovski, Aleksandar Dimitrov, Anita Grozdanov, Beti Andonović, and Perica Paunović

Abstract This work is concerned with the production of graphene using electrolysis in aqueous electrolytes with a reverse change of the potential. As electrodes and precursors for the graphene production highly oriented graphite was used. The electrolytes used were: H_2SO_4 (pH = 0.5); $H_2SO_4 + KOH$ (pH = 1.2) and $H_2SO_4 + NaOH$ (pH = 1.2). The produced graphene samples were characterized by means of scanning and transmission electron microscope (SEM and TEM) and Raman spectroscopy. The size of the crystallites and the number of layers of the studied graphene samples was determined. It was found that by the proposed electrochemical method graphene with few layers only can be produced.

Keywords Graphene • Graphene layers • Crystallite size • Electrolysis • Reverse voltage

11.1 Introduction

Graphene is the last discovered graphitic material consisting of sp^2-bonded carbon atoms packed into a two-dimensional (2D) honeycomb lattice [1]. It exhibits superior physical properties such as electrical conductivity, mechanical characteristics, elasticity, thermal conductivity, optical transparency and a high specific surface area (2,630 $m^2 \cdot g^{-1}$) [2, 3] as well as environmental stability. Therefore, graphene can be used in electronics for the fabrication of transistors or integrated circuits, computer chips, in optoelectronics for light-emitting devices (LED), as sensor in various fields such as medicine, photo-detection, environmental monitoring etc., as photocatalyst in solar cells, as electrochemical supercapacitors, and in biomedicine and biotechnology, etc. [3–5].

The short history of graphene includes an intensive research and numerous publications focused on the study of its structure and properties, the development

A. Petrovski (✉) • A. Dimitrov • A. Grozdanov • B. Andonović • P. Paunović
Faculty of Technology and Metallurgy, University "Ss Cyril and Methodius", Skopje, Republic of Macedonia
e-mail: aleksandar_mec69@yahoo.com

P. Petkov et al. (eds.), *Nanoscience Advances in CBRN Agents Detection, Information and Energy Security*, NATO Science for Peace and Security Series A: Chemistry and Biology, DOI 10.1007/978-94-017-9697-2_11

of methods for its production and application in many different fields of modern life. There are several well-developed methods for graphene production such as mechanical exfoliation, among them chemical vapor deposition (CVD), chemical exfoliation, liquid phase exfoliation of graphite or thermal decomposition of SiC etc. [6]. Particular attention was paid to the development of methods for production of high quality graphene (monolayerd or few layers only) with increased production yield and low production costs. Electrochemical approaches are a suitable alternative for a high-yield production of graphene since electrolysis is simple, environmentally friendly, economic (taking place at ambient conditions) and flexible (the thickness can be controlled by potential or current adjusting). From the electrode reaction's point of view, there are two basic approaches to produce graphene: (i) anodic oxidation of graphite to produce graphene oxide (GO) and further cathodic reduction to graphene and (ii) direct cathodic reduction to for produce non-oxidized graphene [7–9]. From the electrolyte's point of view the electrochemical procedures can be divided in electrolysis in (i) aqueous and (ii) non-aqueous solutions. The mostly used aqueous electrolytes are sulfuric [10] and perchloric acids [11]. Non-aqueous electrolytes used for the electrochemical production of graphene are organic solvents, ionic liquids or molten salts. Ionic liquids have the added advantage of being non-volatile; they are also biodegradable [12].

The aim of this work is to produce graphene using a reverse potential in a sulfuric acid electrolyte.

11.2 Experimental

Electrolytic exfoliation of highly-oriented graphite electrodes in an aqueous electrolyte with reverse change of the voltage between anode and cathode was performed in order to produce graphene. The electrochemical setup is schematically shown in Fig. 11.1.

As electrodes, two types of commercial graphite were used (M1 and M2). The reverse voltage was changed from +15 V to −15 V. Before the electrolysis, all electrodes were pretreated at constant reverse voltages of +5 V to −5 V for 5 min. The electrolytes used were (i) pure sulfuric acid (pH = 0.5), (ii) sulfuric acid with KOH (pH = 1.2) and (iii) sulfuric acid with NaOH (pH = 1.2), prepared using chemicals of high purity.

During the electrolysis, as a result of exfoliation of graphite electrode, sheets of graphene are suspended into the electrolytic solution. After electrolysis, the solutions were filtered through vacuum-filter; thereafter, the fine graphene sheets were washed several times with distillated water.

The studied graphene samples were observed by scanning electron microscopy (JEOL 6390) and transmission electron microscopy (FEI Tecnai G2 Spirit TWIN equipped with LaB6). Structural characterisation as well as an estimation of the crystallite size and the number of layers were performed by Raman spectroscopy (micro-Raman multichannel spectrometer Horiba JobinYvon LabRam 300 Infinity).

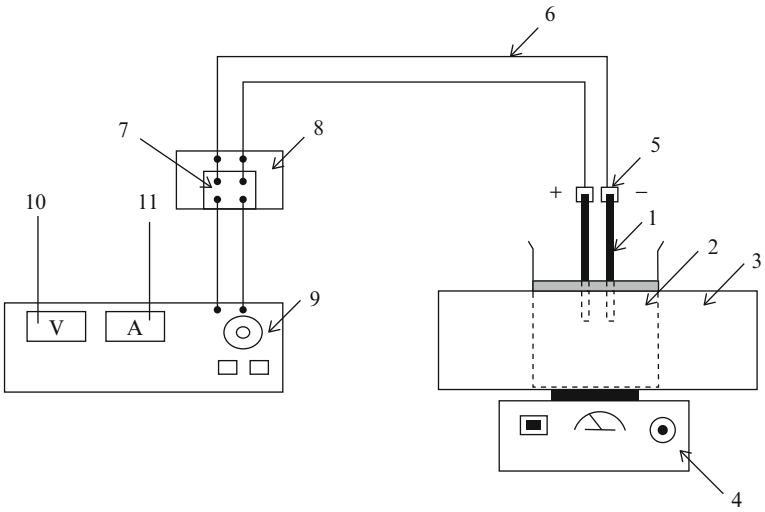

Fig. 11.1 Electrochemical setup for the production of graphene in aqueous electrolytes. *1*. Graphite electrodes; *2*. Electrolyte; *3*. Cooling water bath; *4*. Magnetic stirrer; *5*. Contacts; *6*. Electrical conductors; *7*. Electronic timer; *8*. Power switch; *9*. AC rectifier; *10*. Voltmeter; *11*. Ampermeter

11.3 Results and Discussion

For preliminary estimation of the produced graphene quality and selection of the samples for further investigation, SEM observation was performed. SEM images of the studied graphene are shown in Fig. 11.2.

The morphology of the samples corresponds to graphene material with a transparency characteristic for this type of material. According to literature, graphene shows a high transparency (97,7 %) [13]. Due to strong acidic medium, the sample produced in pure sulfuric acid (pH = 0.5, Fig. 11.2a, d) are highly defective, with large aggregates (around 30 μm) and the lowest transparency. With addition of alkalis the produced material is less damaged, with smaller aggregates (10 μm) and higher transparency. The improvement of the sample quality as result of the addition of alkalis can be explained by the lower aggressivity of the electrolyte (lower acidity, higher pH), causing lower concentrations of defects. Na^+ and K^+ ions also improve the exfoliation process. Na^+ ions show better effects than K^+ due to the smaller atomic radius ($r_{Na} = 186$ pm vs $r_K = 227$ pm). Generally, at the applied voltage, the material produced has an appropriate quality and show a high yield of graphene. Comparing the samples produced from the graphites M1 and M2, one can conclude that better morphology and transparency, i.e. better exfoliation was observed for the samples originating from graphite M2 as a result of the more oriented structure and quality.

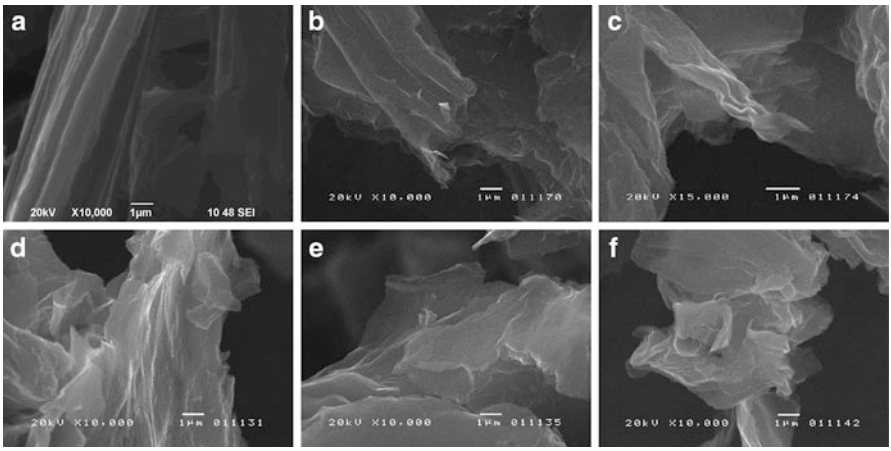

Fig. 11.2 SEM images of the studied samples: (**a**) M1, H_2SO_4; (**b**) M1, $H_2SO_4 + KOH$; (**c**) M1, $H_2SO_4 + NaOH$; (**d**) M2, H_2SO_4; (**e**) M2, $H_2SO_4 + KOH$; (**f**) M2, $H_2SO_4 + NaOH$

In Fig. 11.3 TEM images of some samples are shown. Generally, one can say that the morphology of the graphene produced by reverse electrolysis in aqueous electrolytes is similar to graphene published elsewhere. The graphene sheets are broken and intertwined. There is a low amount of impurities, fibers, non-exfoliated graphite and amorphous carbon. The thickness of the samples varies from a few nanometers to 20 nm.

Also, according to the TEM analysis, the graphene produced from graphite M2 in sulfuric acid with NaOH shows the best characteristics: the lowest thickness and the least number of layers (4–6). According to the TEM images, the graphene sheets are monolayered, few-layered and multilayered in different parts of the sample. This is obvious from the graphene transparency in some parts and is in accordance with Raman analysis for the determination of the number of layers.

Raman spectroscopy is an appropriate technique for a structural study of graphene which provides a lot of information such as a qualitative identification of graphene, the level of ordered and disordered structure, the presence of defects, the number of layers, the size of crystallites etc. Raman spectra of the studied graphene samples are shown in Fig. 11.4. The main peaks characteristic for graphene are the D, G and 2D bands. The G band (near 1,580 cm^{-1}) is the primary mode in graphene and graphite and attributed to the ordered crystalline structure [14]. Samples 4 and 6 produced from the second type of graphite M2 show a higher degree of crystallinity. The D band (near 1,350 cm^{-1}) is attributed to disorder in the graphene structure, i.e. to the defects present in the graphene plane. It is result of one-phonon vibrational lattice processes [14]. This band is typically less pronounced in graphite and graphene. If it is pronounced one can conclude that the tested material contains a lot of defects. The studied samples, especially those originating from graphite M1 show D bands higher than the G band, which is

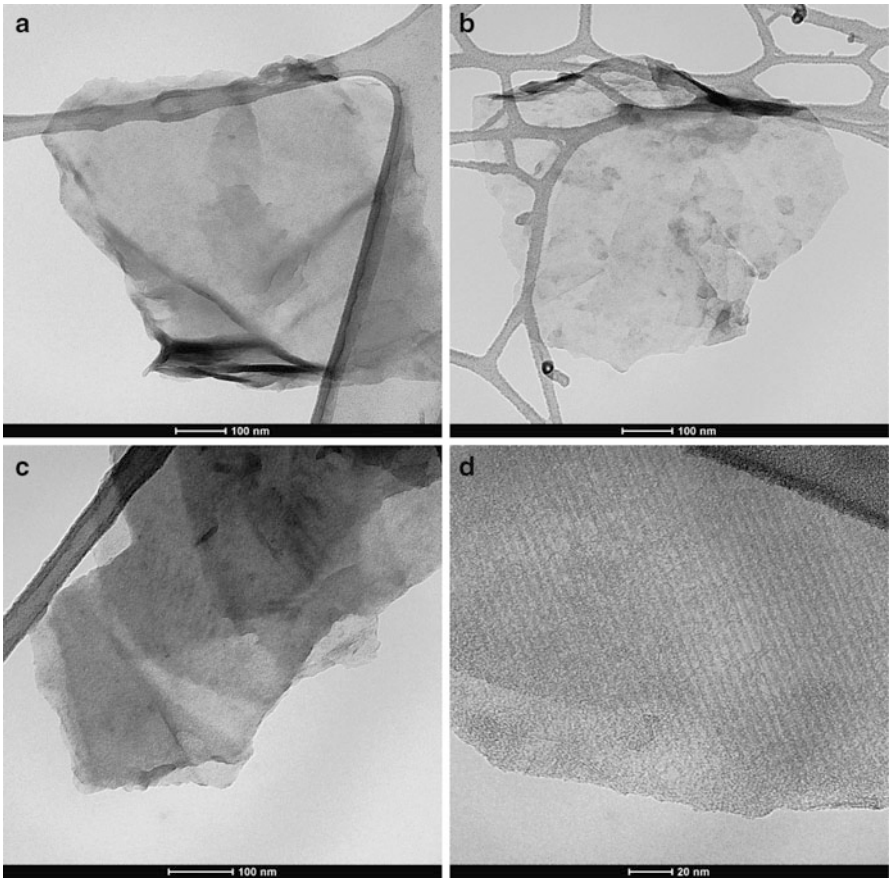

Fig. 11.3 TEM images of the studied samples: (**a**) M1, H_2SO_4; (**b**) M1, H_2SO_4 + NaOH; (**c**) M2, H_2SO_4; (**d**) M2, H_2SO_4 + NaOH

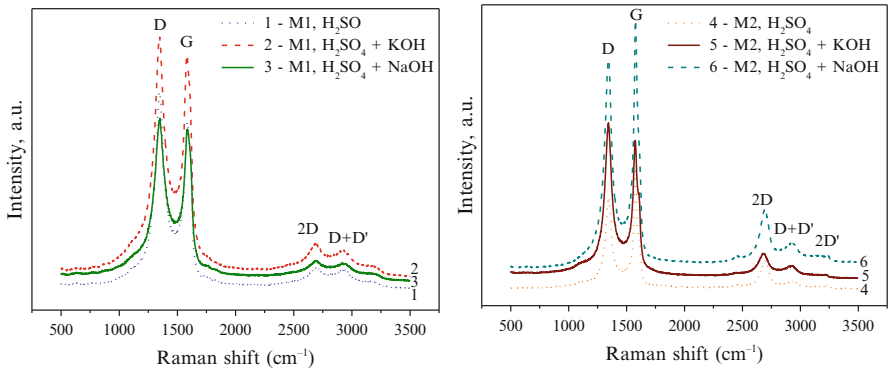

Fig. 11.4 Raman spectra of the graphene samples studied

characteristic for an ordered structure. There is a similar situation in sample 5 originating from graphite M2.

The ratio of intensities the of the D and G peaks I_D/I_G is a measure for the order/disorder of the graphene structure. Also, this ratio can be used to estimate the average crystallite size of the sp^2 domains. The relation between I_D/I_G and the average crystallite size of the sp^2 domains L_a is given by the equation of Tuinstra and Koenig [15]:

$$\frac{I_D}{I_G} = \frac{C(\lambda)}{L_a} \tag{11.1}$$

$C(\lambda)$ is a wavelength dependent prefactor: $C(\lambda) = -12.6 + 0.33 \cdot \lambda$ [15]. λ is the laser wavelength at which the Raman spectra were recorded, i.e. in this case 532 nm. Therefore, for the studied samples $C(\lambda) = 4.956$. The intensities of the D and G peaks can be expressed by the height of the peak, the surface area of the peak measured from the base-line, or by the full width at half maximum (FWHM). Mostly, the full width at half maximum is used [16]. The I_D/I_G ratio expressed by FWHM and the calculated crystallite size L_a of the studied samples are shown in Table 11.1. The crystallite size varies from 3.26 nm for sample 6 produced from graphite M2 in sulfuric acid with NaOH to 4.16 in sample 1 produced from graphite M1 in sulfuric acid.

The 2D band is the second order peak of the D band; it appears as result of vibrational lattice processes. Although the 2D peaks of the samples studied are not so pronounced, they indicate the presence of graphene rather than graphite. The 2D band is not attributed to defects in the structure, but depends on the number of graphene layers. Thus, analyzing the intensity ratio of the 2D and the G peak I_{2D}/I_G the number of layers can be estimated [9, 17]. For the samples produced

Table 11.1 Raman analysis of studied graphene samples

	D	G	2D		
	Position, cm^{-1}	Position, cm^{-1}			
Sample	I_D (FWHM), cm^{-1}	I_G (FWHM), cm^{-1}	Position, cm^{-1}	I_D/I_G	L_a, nm
1	1345.8	1591.9	2683.2	1.20	4.16
	75.74	63.22			
2	1345.67	1585.77	2678.5	1.48	3.35
	97.45	66.01			
3	1346.27	1592.12	2682.5	1.26	3.93
	78.20	62.07			
4	1354.1	1578.48	2683.5	1.26	3.93
	50.48	39.91			
5	1343.04	1576.6	2678.4	1.20	4.13
	68.24	56.81			
6	1341.05	1581.01	2692.4	1.52	3.26
	72.59	47.67			

from graphite M1 (Fig. 11.4 left), the 2D peak is less pronounced indicating the presence of multilayered graphene (more than 8 layers). For the samples produced from graphite M2 (Fig. 11.4 right), the 2D peak is more sharp and intensive. This and the fact that the G band of these samples is shifted to wave numbers lower than 1,582 cm^{-1} indicate that these samples have fewer layers (4–6 layers) and a better quality than the previous ones. According to the Raman analysis, it is evident that the sample 6 produced from graphite M2 in sulfuric acid with NaOH shows the most appropriate structure characteristics of all studied graphene samples.

11.4 Conclusions

This work presents a method for high-yield graphene production by electrolysis in aqueous solutions using reverse potential. Several techniques were used to characterize the obtained graphene samples.

- SEM images have shown that the graphene samples produced at reverse voltage of 15 to −15 V have the high transparency characteristic for graphene material. Graphene produced from graphite M2 has shown better transparencies than those produced from graphite M1, indicating less defects and less number of layers.
- Morphology testing was done by TEM. Generally, it was found that the morphology of graphene produced by the reverse electrolysis in aqueous electrolytes is similar to graphene produced by other methods. The graphene sheets are broken and intertwined. There is a low amount of impurities, fibers, non-exfoliated graphite and amorphous carbon. The thickness of the samples varies from few nanometers to 20 nm.
- Using the Raman spectroscopy, structural parameters were determined. The crystallite size varies from 3.26 nm for the sample 6 (graphite M2) in H_2SO_4 with NaOH to 4.16 nm for sample 1 (graphite M1). The obtained values for I_{2D}/I_G from the FWHM of the corresponding peaks indicate that the obtained samples consist of 4 to 6 layers.

Acknowledgments This research was done within the FP7 Project "Cost-effective sensors, interoperable with international existing ocean observing systems, to meet EU policies requirements" (Project reference 614155) and the Project "Research and development of new nanostructured sensors aimed for protection and development of environment and nature" financed by the Ministry of Environment and Physical Planning of the R. Macedonia.

References

1. Novoselov KS, Geim AK, Morozov SV, Jiang D, Zhang Y, Dubonos SV, Grigorieva IV, Firsov AA (2004) Science 306:666
2. Rocha CG, Rümmeli MH, Ibrahim I, Sevincli H, Börrnert F, Kunstmann J, Bachmatiuk A, Pötschke M, Li W, Makharza SAM, Roche S, Büchner B, Cuniberti G (2011) In: Choi W, Lee J-W (eds) Graphene: synthesis and applications. CRC Press, Boca Raton, p 1
3. Cooper DR, D'Anjou B, Ghattamaneni N, Harack B, Hilke M, Horth A, Majlis N, Massicotte M, Vandsburger L, Whiteway E, Yu V (2012) International Scholarly Research Network ISRN, condensed matter physics, vol 2012, Article ID 501686, doi:10.5402/2012/501686
4. Bonaccorso F, Sun Z, Hasan T, Ferrari AC (2010) Nat Photonics 4:611
5. Zhou X, Liang F (2014) Curr Med Chem 21:855
6. Bonaccorso F, Lombardo A, Hasan T, Sun Z, Colombo L, Ferrari AC (2012) Mater Today 15:564
7. Low CTJ, Walsh FC, Chakrabarti MH, Hashim MA, Hussain MA (2013) Carbon 54:1
8. Alanyahoğlu M, Segura JJ, Oró-Solè J, Casañ-Pastor N (2012) Carbon 50:142
9. Morales GM, Schifani P, Ellis G, Ballesteros C, Martinez G, Barbero C, Salvagione HG (2011) Carbon 49:2809
10. Su CY, Lu AY, Xu Y, Chen FR, Khlobystov AN, Li LJ (2011) ACS Nano 5:2332
11. Schnyder B, Alliata D, Kötz R, Siegenthaler H (2001) Appl Surf Sci 173:221
12. Liu N, Luo F, Wu H, Liu Y, Zhang C, Chen J (2008) Adv Funct Mater 18:1518
13. Zhu Y, Murali S, Cai W, Li X, Suk JW, Poots JR, Ruoff RS (2010) Adv Mater 22:3906
14. Matthews MJ, Pimenta MA, Dresselhaus G, Dresselhaus MS, Endo M (1999) Phys Rev B 59: R6585
15. Tuinstra F, Koenig JL (1970) J Chem Phys 53:1126
16. Zickler GA, Smarsly B, Gierlinger N, Peterlik H, Paris O (2006) Carbon 44:3239
17. Gupta A, Chen G, Joshi P, Tadigadapa S, Eklund PC (2006) Nano Lett 6:2667

Chapter 12
Simultaneous CVD Growth of Nanostructured Carbon Hybrids

N.F. Santos, A.J.S. Fernandes, T. Holz, R.F. Silva, and F.M. Costa

Abstract In this work the MPCVD (microwave plasma chemical vapour deposition) conditions for the growth of nanocarbon hybrids were studied. Using a single run MPCVD procedure, nanocrystalline diamond (NCD) and carbon nanotubes (CNTs) hybrids were obtained using a continuous delivery of catalytic Fe particles. The grown films were characterized by Scanning Electron Microscopy (SEM) and μ-Raman spectroscopy, proving the coexistence of sp^2 and sp^3 bonded phases, either in a dense multi-layer arrangement or in a porous 3-D like morphology. Without the addition of a catalyst, NCD/carbon nanowalls (CNWs) hybrids were also synthesized. High quality and well intercalated hybrid carbon forms were successfully obtained in a simultaneous growth procedure.

Keywords Carbon nanotubes • Carbon nanowalls • Nanocrystalline diamond • Hybrid • Simultaneous growth

12.1 Introduction

Despite some decades have passed since the discovery of NCD, CNTs and CNWs, these carbon nanostructures (CNs) are still a matter of intense scientific and technologic research worldwide [1]. The scale reduction to the nanometre size and their different spatial arrangements, combined with distinct physical and chemical properties arising from each type of C-C bond hybridization, results in

N.F. Santos (✉)
I3N, Physics Department, University of Aveiro, Aveiro 3810-193, Portugal

CICECO, Materials Engineering Department, University of Aveiro, Aveiro 3810-193, Portugal
e-mail: nfsantos@ua.pt

A.J.S. Fernandes • T. Holz • F.M. Costa
I3N, Physics Department, University of Aveiro, Aveiro 3810-193, Portugal

R.F. Silva
CICECO, Materials Engineering Department, University of Aveiro, Aveiro 3810-193, Portugal

P. Petkov et al. (eds.), *Nanoscience Advances in CBRN Agents Detection, Information and Energy Security*, NATO Science for Peace and Security Series A: Chemistry and Biology, DOI 10.1007/978-94-017-9697-2_12

rather diverse mechanical, electronic, thermal and chemical properties of the different carbon allotropes.

NCD material (sp^3 hybridization) is characterized by conserving the superior hardness and wear resistance observed for single crystal diamond [2, 3]. Additionally, it is dimensionally stable with temperature, chemically inert and biocompatible, accepting functionalization and allowing a wide range of electrical conduction tunability by incorporation of n or p dopants (N and B, respectively) [4–6]. Distinctly, CNTs and other sp^2 coordinated CNs provide exquisite mechanical, thermal and electronic properties such as a high tensile strength, very high geometric aspect ratios, superior thermal and electrical conductivities and the possibility of bandgap tuning, among others [7]. Hence, a lot of efforts have been spent for the development of nanostructured carbon hybrids, aiming at synergistically combining specific carbon allotropes (and thus their properties) in the form of a hybrid thin film. In fact, a sp^2-on-sp^3 technology is a currently debated item among the scientific community [8–10]. However, the formation of a truly hybrid material implies a high interfacial area and strongly bonded CNs. In order to obtain a good intercalation and strong linkage between the NCD and CNT phases, a simultaneous growth mechanism is highly desirable. This growth mode is possible with the CVD technique, assisted by a continuous delivery of catalytic particles, enabling also the synthesis of multi-layered hybrid films [8, 11]. If properly combined, these carbon nanostructured hybrids could form a framework for the development of a new class of efficient and high-performance microelectronic and electrochemical systems such as low noise THz-frequency transistors, stable microelectromechanical systems (MEMS) with superior Q factors, efficient high-current cold cathodes for field emission devices (FEDs), high selectivity/sensibility gas and biomolecule sensors, and high surface area electrodes for supercapacitors, among others [12–15].

In this work, the routes for single-run MPCVD synthesis of two types of well-intercalated nanocarbon hybrids are presented. The first is composed of linked NCD and CNT phases, while the second is formed by vertically aligned CNWs (also known as carbon nanoplatelets) covered by a thin layer of NCD. The development of the two hybrid nanostructures depends on the MPCVD growth parameters and on the use of catalytic phases.

12.2 Experimental

The substrates used for nanocarbon hybrid synthesis consisted of 1.25×1.25 cm^2 squares cut from a <100> oriented p-type Si single crystal wafer. The substrates were mechanically abraded using a BUEHLER Microfloc® cloth impregnated with diamond powder (Saint-Gobain, <500 nm) ultrasonically dispersed in ethanol (1.5 g/l). This procedure is used for both abrading the Si surface, leaving active

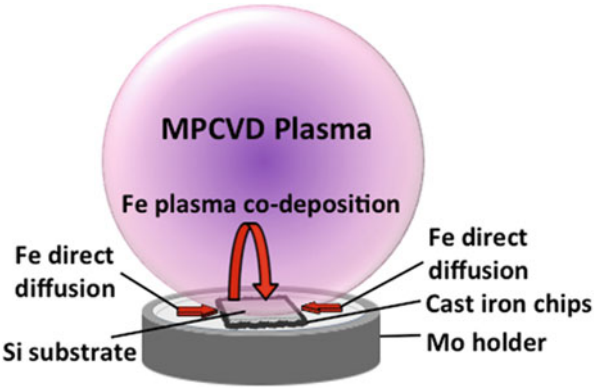

Fig. 12.1 Scheme of the experimental arrangement used for continuous catalyst delivery

nucleation 'scars', and for enhancing the production of nanodiamond fragments adhered to the scratched substrate. Both effects are known to play important roles if a high diamond nucleation density is to be attained [16]. The scratched substrates were then thoroughly rinsed in ethanol and dried under a low-pressure N_2 flow. A continuous delivery of Fe catalyst impurities for CNT formation was accomplished via a dual-mechanism method developed by Fernandes et al. [8]. Sub-millimetric cast iron chips were placed in the surroundings of the Si square substrates, on a cooled Mo holder (Fig. 12.1). The migration of catalytic particles is achieved both by (i) Fe direct diffusion to the nearby growing film surface and (ii) plasma co-deposition, which involves etching of the Fe chip by the harsh plasma conditions and subsequent deposition via a solid-gas-solid mechanism.

The NCD/CNT hybrid growth was carried in a 2.45 GHz MPCVD reactor (ASTeX PDS18). The samples were exposed to a range of parameters, namely the microwave (MW) power and the total gas pressure (1.75–3.5 kW, 75–100 Torr, respectively) were varied. The weight amount of Fe chips was fixed to 400 mg in all growths. A gas composition of 5 vol.% CH_4 and 1 vol.% N_2 diluted in H_2 was used for 40 min to promote an initial nucleation of the NCD phase and the formation of a first thin layer in which the hybrid material is to develop. Next, a modulation of the gas composition to 15 vol.% CH_4 and 1 vol.% N_2 diluted in H_2 for 20 min was performed to induce the CNT formation and hybrid phase development. This modulation of the gas composition results in a temperature increase as methane dissociation releases more energy than hydrogen's counterpart. This temperature change was detected by a thermocouple in contact with the backside of the cooled Mo holder. Although the setup does not allow the accurate determination of the temperature of the synthesis surface, the iron chips acquired a red/orange colour during growth characteristic of temperatures above 700 °C. The same parameters were applied to pre-treated substrates without the presence of the catalyst for growing the NCD/CNWs hybrids. The resulting samples were characterized by scanning electronic microscopy (SEM, Hitachi SU70) and μ-Raman spectroscopy (Horiba JY HR800) using a 442 nm laser (~1 μm diameter laser spot).

12.3 Results and Discussion

The range of MPCVD parameters used in this work produced samples with different morphologies and phase contents. The parameter modulation during growth is a complex task as many variables are mutually dependent. Additionally, the presence of nearby iron compounds during the NCD/CNT hybrid growth added to the complexity. In the high power/pressure regime the films obtained have a dark greyish colour, which is typical for NCD films. The presence of NCD is further depicted in the corresponding SEM micrographs (Fig. 12.2a), where a network of CNTs (region 2) is clearly distinguishable, partially embedded in micrometre-sized NCD clusters (region 1), which tend to coalesce. Also visible is an underlayer beneath the NCD/CNT hybrid structure, consisting in NCD with mixed Fe catalytic particles. In fact, some of the CNTs arise from that layer and are often found to be linked to the upper NCD clusters, suggesting a strong mechanical interlock. The CNTs either penetrate or wrap the NCD clusters, in agreement with previous observations using the same catalyst-delivery technique [8]. The high aspect-ratio MWCNTs have diameters with an appreciable dispersion but are smaller than 70 nm, while their lengths range from one to several tens of μm.

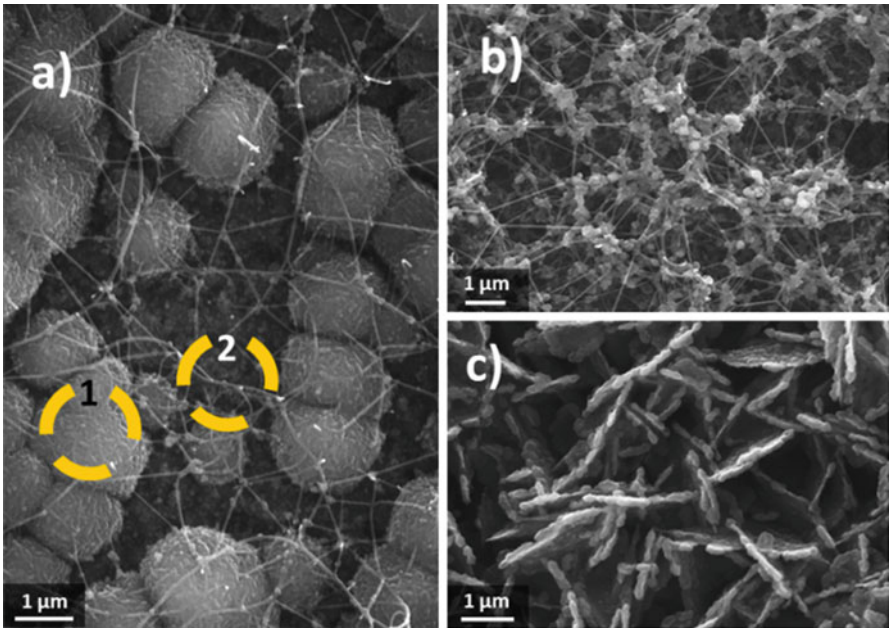

Fig. 12.2 SEM micrographs of as-grown samples: (**a**) with the presence of Fe catalyst at high MW power regime, (**b**) with the presence of Fe catalyst at low MW power regime, and (**c**) without the presence of Fe catalyst

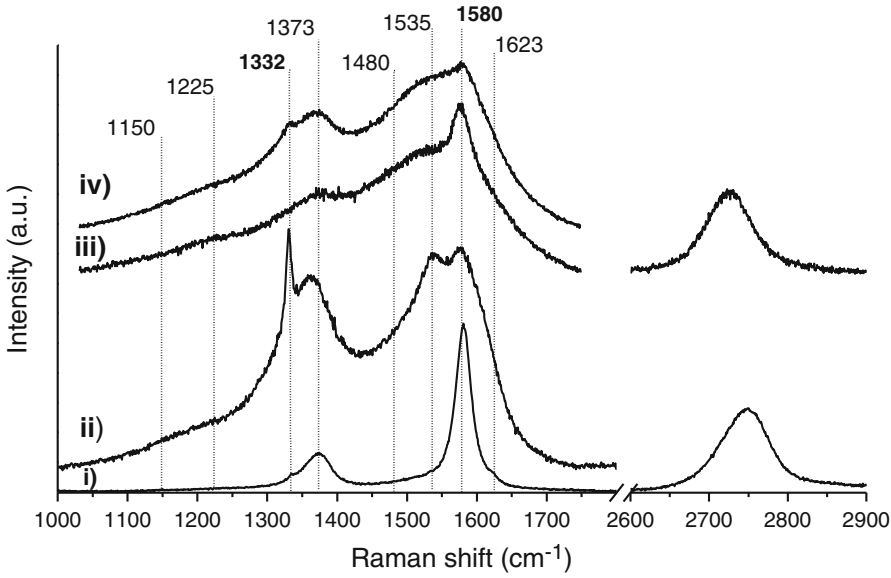

Fig. 12.3 Raman spectra of as-grown samples, normalized to the G-band and shifted in intensity for clarity. (*i*) and (*ii*) with the presence of Fe catalyst at high MW powers, acquired in region 2 and 1 (see Fig. 12.2a), respectively, (*iii*) with the presence of Fe catalyst at low MW powers (see Fig. 12.2b), and (*iv*) without the presence of Fe catalyst (see Fig. 12.2c)

The Raman data (Fig. 12.3) collected from the NCD clusters in region 1 exhibits a strong and narrow peak, corresponding to the T_2g mode of sp^3 bonded diamond at 1,332 cm^{-1}. Furthermore, the presence of the bands at ~1,150 cm^{-1} and ~1,480 cm^{-1}, corresponding to trans-polyacetylene (TPA) at the NCD grain boundaries (GB), is an unequivocal signature of the nanoscale nature of the film. In fact, these features appear only when the GB density reaches extremely high values, since the TPA contribution to the overall Raman signal is only moderate. Additionally, a broad band at ~1,225 cm^{-1} is also present. Although the origin of this feature in NCD films is not yet fully understood, it may correspond to a peak in the VDOS due to the relaxation of the $q = 0$ rule occurring in small-grain NCD. Also present in the spectrum of region 1 is the disorder-induced dispersive D-band (~1,370 cm^{-1}) corresponding to the breathing modes of sp^2 coordinated defective graphitic phases at GBs. Along with it, the graphite G-band (1,580 cm^{-1}) appears, assigned to the sp^2 C-C stretching E_{2g} mode. The band at 1,535 cm^{-1} is probably due to "G-like" vibrational modes in graphitic materials displaying some disorder, leading to the observed redshift. In addition, a small shoulder at ~1,620 cm^{-1} (D' band) related to surface defects activated modes is also detected.

A rather distinct Raman spectrum is obtained in region 2. Here, the typical features of CNTs, namely the D, G and D' bands, are dominant, while those related to the diamond phase are almost absent. The presence of the 2D symmetric band

with a fair intensity, typical of well-structured MWCNTs, confirms the good quality of the CNTs. The small shoulder at 1,332 cm^{-1} indicates that the excited volume contains a fraction of sp^3 bonded carbon, most likely due to signal arising from the underneath layer.

Regarding the films grown in the presence of Fe chips at lower MW power/pressure regime (Fig. 12.2b), the samples presented a dark appearance for the naked eye. Under higher magnification, one can see that a porous, 3D-like network of interconnecting CNT agglomerates is formed. The corresponding Raman spectrum (Fig. 12.3) depicts the signature of CNTs, super-imposed to a background similar to that of ultra-nanocrystalline diamond, characterized by a strongly convoluted spectrum where the diamond peak is often absent. It has also to be noted that the cross-section for Raman scattering of both sp^3/sp^2 phases is wavelength dependent and the concentration of NCD phase on this sample is clearly lower when compared with the sample grown at a higher power regime.

By removing the Fe catalytic particles during MPCVD growth another distinctive structure is obtained, consisting in vertically aligned graphitic platelets covered by a NCD film (Fig. 12.1c). The Raman spectra show the typical features of a mixture of sp^2 carbon phases with NCD (Fig. 12.3), as seen in the previous samples. However, here the sp^2-related bands are mostly due to the inner graphitic nanoplatelets. In fact, the platelet-like NCD structure is only possible due to the formation of an initial underlaying graphitic structure, since the growing habits of pure NCD films are completely distinct than the observed. Although reported elsewhere [17–19], this structure presents a good NCD phase crystallinity in a fast synthesis routine.

12.4 Conclusions

A well-defined NCD/(NCD + CNTs) multilayer structure was successfully synthesized in a single MPCVD run without the need for other time and resource consuming steps, which often imply deposition of metallic catalytic films and annealing processes. The intimate mixture of these two phases was also achieved in a porous network of CNTs interconnecting NCD clusters. Additionally, a catalyst-free and fast route to produce CNWs fully covered by a NCD layer is presented.

The apparent strong linkage between the allotropes and the expected enhanced properties of the hybrids are yet to be confirmed via appropriate techniques. If so, the presented variety of nanocarbon hybrids might find applications in structural layers for MEMS as well as electrodes for FEDs and gas/biomolecule sensors.

Acknowledgments The authors gratefully acknowledge the financial support from the SFRH/BD/90017/2012, PTDC/CTM-NAN/117284/2010 and PEst-C/CTM/LA0025/ 2013–14.

References

1. Dresselhaus MS (2012) Phys Scr T146:014002
2. Kulisch W et al (2004) Diam Relat Mater 13:1997
3. Catledge S et al (2002) J Appl Phys 91:5347
4. Geis MW et al (1996) Appl Phys Lett 68:2294
5. Iakoubovskii K et al (2000) J Phys Condens Matter 12:L519
6. Catledge SA et al (1999) J Appl Phys 86:698
7. Jorio A, Dresselhaus M, Dresselhaus G (eds) (2007) Carbon nanotubes: advanced topics in the synthesis, structure, properties and applications. Springer, Berlin
8. Fernandes AJS et al (2009) Diam Relat Mater 18:160
9. Shankar N et al (2008) Diam Relat Mater 17:79
10. Varshney D et al (2010) Carbon N Y 48:3353
11. Varshney D et al (2013) Carbon N Y 63:253
12. Zou Y et al (2012) J Appl Phys 112:044903
13. Cheng CY et al (2012) Diam Relat Mater 27–28:40
14. Pandey S et al (2012) Appl Phys Lett 100:043104
15. Wade TC et al (2012) Diam Relat Mater 22:29
16. Lee ST et al (1999) Mater Sci Eng R Rep 25:123
17. Raina S et al (2008) Diam Relat Mater 17:896
18. Wong YM et al (2009) Diam Relat Mater 18:563
19. Tzeng Y et al (2014) Sci Rep 4:4531

Chapter 13
Wetting and Photoactive Properties of Laser Irradiated Zinc Oxide – Graphene Oxide Nanocomposite Layers

A. Datcu, A. Pérez del Pino, C. Logofatu, A. Duta, and E. György

Abstract Laser irradiation of zinc oxide (ZnO) – graphene oxide (GO) nanocomposite layers obtained by the drop-casting method has been carried out using a frequency quadrupled Nd:YAG ($\lambda = 266$ nm, $\tau_{FWHM} \cong 4$ ns, $\nu = 10$ Hz) laser source in air at atmospheric pressure or in controlled nitrogen atmosphere. The dependence of the morphology and chemical composition of the layers on the incident laser fluence, the number of accumulated laser pulses, and the ambient atmosphere has been studied. A significant improvement of the wetting and photoactive properties of the laser processed layers was attributed to nitrogen incorporation. The kinetics of the variation of the water contact angle when the samples are submitted to laser irradiation in nitrogen atmosphere is faster than that of the samples irradiated in air, the surfaces becoming super-hydrophilic under UV light irradiation.

Keywords Zinc oxide-graphene oxide nanocomposite layers • Laser irradiation • Superhydrophilicity • Wettability • Photoactive properties

A. Datcu (✉)
National Institute for Lasers, Plasma and Radiation Physics,
P. O. Box MG 36, Bucharest 76900, Romania
e-mail: datcu.angela@inflpr.ro

A.P. del Pino
Consejo Superior de Investigaciones Científicas, Instituto de Ciencia de Materiales de Barcelona (CSIC-ICMAB), Campus UAB, Bellaterra 08193, Spain

C. Logofatu
National Institute for Materials Physics, P. O. Box MG. 7, Bucharest 77125, Romania

A. Duta
Transilvania University of Brasov, Eroilor 29, Brasov 500036, Romania

E. György
National Institute for Lasers, Plasma and Radiation Physics,
P. O. Box MG 36, Bucharest 76900, Romania

Consejo Superior de Investigaciones Científicas, Instituto de Ciencia de Materiales de Barcelona (CSIC-ICMAB), Campus UAB, Bellaterra 08193, Spain

P. Petkov et al. (eds.), *Nanoscience Advances in CBRN Agents Detection, Information and Energy Security*, NATO Science for Peace and Security Series A: Chemistry and Biology, DOI 10.1007/978-94-017-9697-2_13

13.1 Introduction

For industrial applications, one of the most exciting sub-fields of nanotechnology is nanocatalysis focused on the photoactive properties of materials [1]. Much attention has been paid to the development of novel materials displaying more than one interesting property. Among the photoactive materials, those based on zinc oxide (ZnO) have deserved special attention due to its potential ability to form multifunctional materials, combining its semiconducting features (ZnO is a wide band-gap semiconductor) with a high thermal and chemical stability, and good transparency in the infrared-visible spectral region [2]. Due to these attractive properties ZnO is widely investigated, being a promising material for many applications in optoelectronics, gas sensors, transducers, filters, catalysts, as well as in biomedical fields due to its biocompatible properties [3]. Furthermore, transition metal oxides, and in particular ZnO, have peculiar wetting and photoactive properties [4]. It was found that their typical hydrophobic or slightly hydrophilic character changes to highly hydrophilic upon UV light irradiation [5]. Several products have already been designed based on this phenomenon, e.g. self-cleaning construction materials or anti-fogging surfaces [6]. As reported, the original hydrophobic character of the films recovers after storage in the dark [4]. Thus, the control of wetting contact angle even in the absence of UV light presents a challenge of this field, providing the possibility to wash the surface contaminants where UV light cannot be ensured. An option to obtain highly hydrophilic ZnO nano-composite is to combine it with other highly hydrophilic materials, such as graphene oxide (GO) [7] which offer the possibility to tailor the water contact angle. Motivated by this idea, we herein report on a study of UV laser irradiation in air and controlled nitrogen atmosphere, the incident laser fluence and the number of subsequent laser pulses, on the surface morphology and photoactive properties of ZnO/GO nanocomposite thin films by monitoring the water wetting angle evolution under UV light irradiation.

13.2 Experimental

Preparation of ZnO/GO Nanocomposites Films A 100 µl dispersions of 1 wt.% ZnO nanoparticles (NPs) and 0.5 wt. % GO plates in distilled water was deposited by the drop-casting method on the surface of 10×10 mm^2 (001) SiO_2 quartz substrates and dried in air at atmospheric pressure and at 60 °C during 30 min.

Irradiation of the Obtained Sample The reaction chamber where the sample was placed was evacuated down to a residual pressure of 10^{-4} Pa. The laser irradiation of the films was performed with a Nd:YAG ($\lambda = 266$ nm, $\tau_{FWHM} = 4$ ns, $\nu = 10$ Hz) laser source. The number of subsequent laser pulses was chosen in the range of 10–2,000. The incident laser fluence was set at 10, 30, 50 or 100 J/cm^2. The irradiations were performed in air at atmospheric pressure or nitrogen at a pressure of 2×10^4 Pa.

Characterizations Morphological properties of the deposited thin films were investigated by field emission scanning electron microscopy (FE-SEM) with the aid of a QUANTA FEI 200 FEG-ESEM system. Energy dispersive X-ray spectroscopy (EDX) analyses were carried out using an EDS Thermo Scientific Ultra Dry silicon drift X-ray detector controlled by NORAN System 7 software. The hydrophilic properties of the films were determined by measuring the contact angle of distilled water using an OCA-20 contact angle system from DataPhysics Instruments. A 3 μL volume liquid drop was placed in 0.5 μL/s steps on the surface of the ZnO/GO composite thin films. Contact angles were measured during 5 min time interval, the data were recorded with one second step.

13.3 Results and Discussion

SEM images of a ZnO/GO composite reference thin film obtained by the drop-cast method are shown in Fig. 13.1. The ZnO NPs partially cover the micro sized GO sheets (Fig. 13.1a). The higher amplification FE-SEM image (Fig. 13.1b) reveals that the ZnO NPs have a homogeneous size distribution with an average diameter around 20 nm (Fig. 13.1b).

The drop-cast samples were submitted to laser irradiation in air at atmospheric pressure (Fig. 13.2) and in controlled nitrogen atmosphere at a pressure of 2×10^4 Pa (Fig. 13.3). In air, at the lowest laser fluence value of 10 mJ/cm^2, and 1,000 pulses a melting of the ZnO NPs takes place followed by the formation of hundreds of nm sized interconnected grains (Fig. 13.2a), while for the GO sheets no morphological changes can be observed in the FE-SEM images (Fig. 13.2b) under the same irradiation conditions. Inter-connected molten aggregates of ZnO NPs can also be observed at a higher laser fluence of 30 mJ/cm^2 but a lower number of pulses

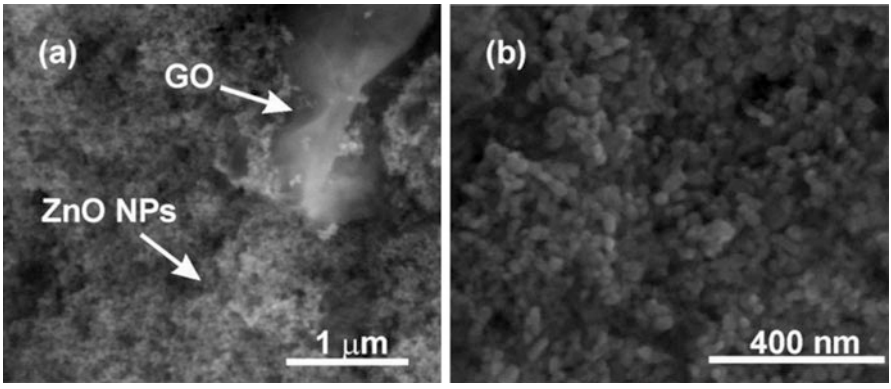

Fig. 13.1 FE-SEM images of a composite reference thin film consisting of ZnO NPs and GO plates

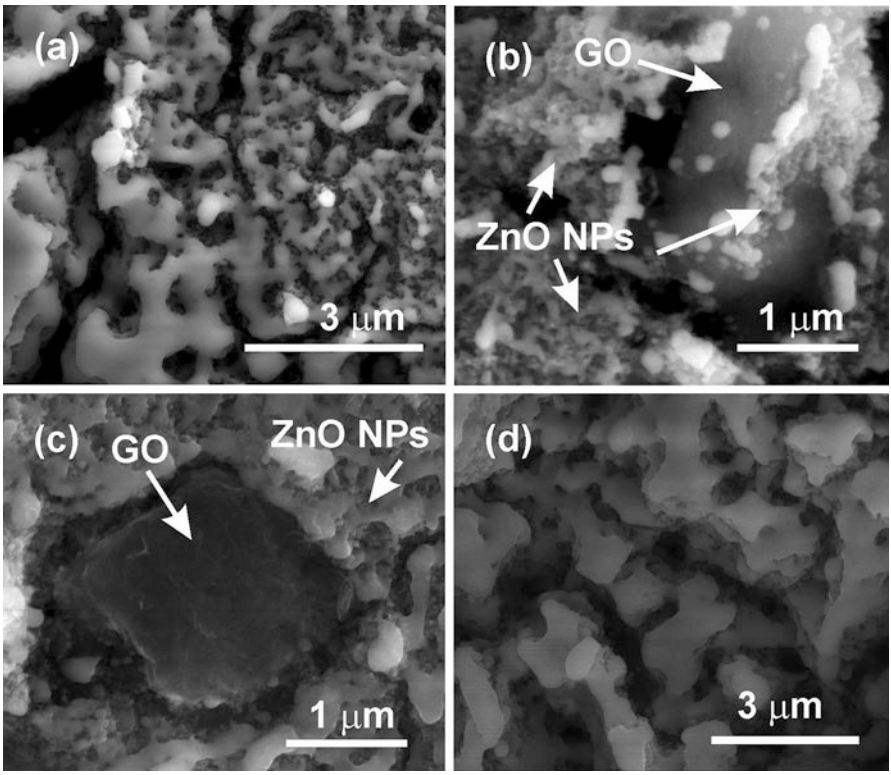

Fig. 13.2 FE-SEM images of ZnO/GO composite thin films irradiated in air at (**a**, **b**) 10 mJ/cm^2 laser fluence and 1,000 subsequent laser pulses, and 30 mJ/cm^2 laser fluence with (**c**) 100 or (**d**) 1,000 subsequent laser pulses

(Fig. 13.2c). With the accumulation of the laser pulses the dimensions of the inter-connected molten aggregates increases (Fig. 13.2d). However, with the increase of the laser fluence value to 50 mJ/cm^2 vaporization of the irradiated material takes place even at 10 subsequent pulses only.

It is well-known that laser-induced melting and vaporization thresholds are significantly reduced for multi-pulse irradiation as compared to single-shot thresholds. This interesting phenomenon, in the literature referred to as incubation effect, can be explained by the changes in absorption of the incident laser radiation caused by the creation of radiation-induced defects on the surface of the irradiated material [8].

In parallel experiments the ZnO/GO drop-cast samples were irradiated in controlled nitrogen atmosphere (Fig. 13.3). In nitrogen atmosphere both the incident laser fluence and the number of laser pulses necessary for the onset of the melting process are higher as compared to the experiments performed in air. For an irradiation with 50 mJ/cm^2 fluence and 2,000 subsequent pulses the melting of ZnO NPs takes place followed by the formation of inter-connected structures (Fig. 13.3a) similar to those observed when the irradiations were conducted in air.

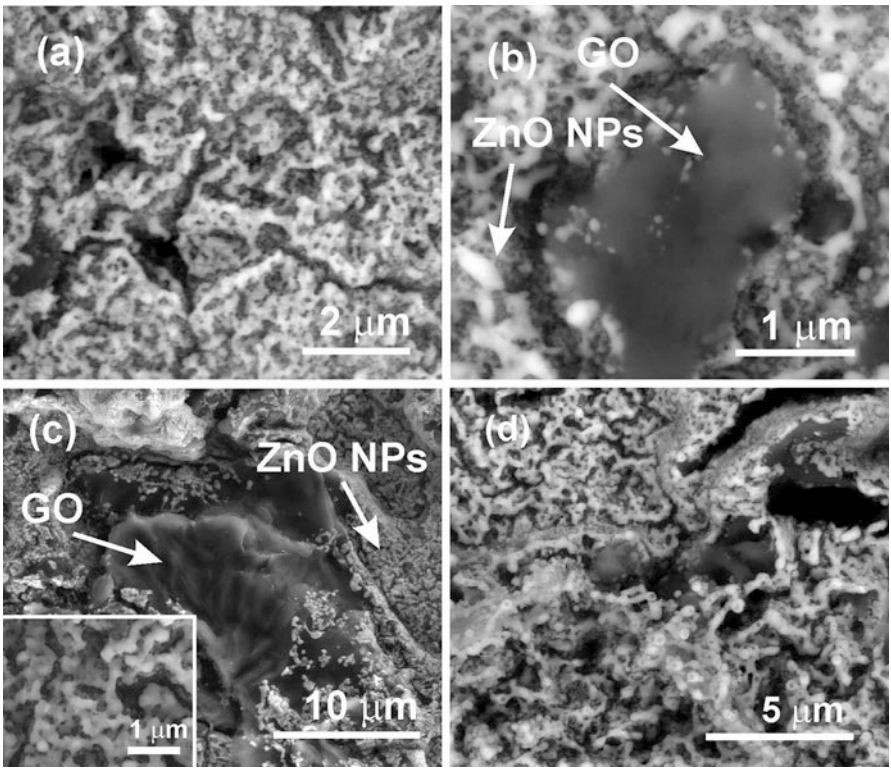

Fig. 13.3 FE-SEM images of ZnO/GO composite thin films irradiated in 2×10^4 Pa nitrogen atmosphere at (**a**) 50 mJ/cm^2 laser fluence and 2,000 subsequent laser pulses and 100 mJ/cm^2 laser fluence and (**b**) 10, (**c**) 1,000, or (**d**) 2,000 subsequent laser pulses

At a laser fluence of 100 mJ/cm^2 melting of the ZnO NPs can be observed even at 10 subsequent laser pulses (Fig. 13.3b). An increase of the number of pulses leads to a network-like structure consisting of large, hundreds of nm sized particles (Fig. 13.3c, d) formed most probably by the coalescence of molten ZnO NPs.

Figure 13.4 shows a FE-SEM image of a ZnO/GO composite thin film irradiated in 2×10^4 Pa nitrogen with 100 mJ/cm^2 laser fluence and 1,000 subsequent pulses, and the corresponding EDX mapping of the element distribution (Zn, C, O, N) on a surface.

The difference of the surface composition is clearly visible in the C and Zn maps; the regions with more intense C signals corresponding to GO plates surrounded by ZnO NPs visible in the Zn signal. The O signal contains contributions both from the GO sheets and ZnO NPs as well as from the SiO_2 quartz substrate. On the other hand, the less intense N signal belongs to nitrogen incorporated during laser processing.

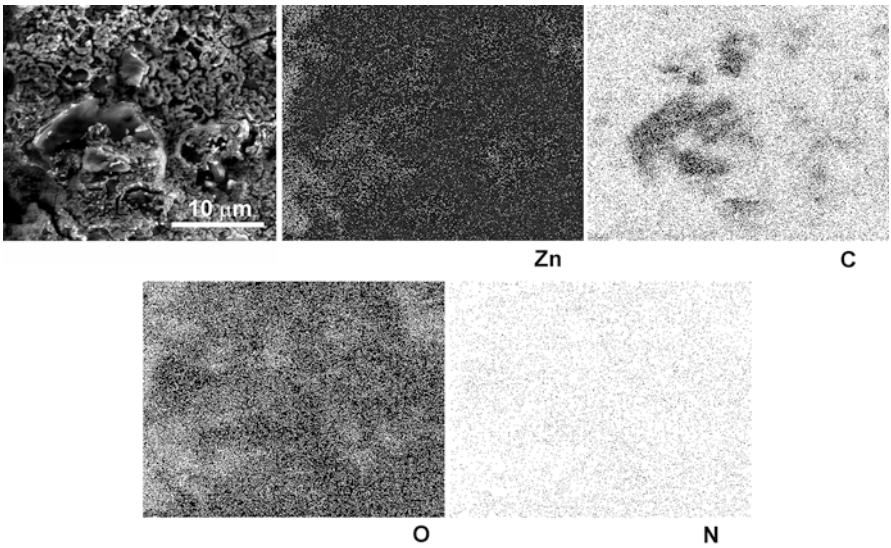

Fig. 13.4 FE-SEM image of a ZnO/GO composite thin film irradiated in 2×10^4 Pa nitrogen atmosphere with a fluence of 100 mJ/cm^2 and 1,000 subsequent pulses, and the corresponding EDX maps of the elements Zn, C, O, and N. The surface area of the FE-SEM image is 30×30 µm^2

The static contact angle values of ZnO/GO composites measured in the absence of UV light irradiation in air as well as nitrogen atmosphere are much lower than those characteristic for pure ZnO reported in the literature [4c, 8]. The reduction kinetics of the contact angle is approximately five times faster in the case of the samples irradiated in nitrogen as compared to those obtained in air, the surface becoming super-hydrophilic after only 1 min of UV light irradiation. The better performance of the samples submitted to laser treatment in nitrogen as compared to those irradiated in air is attributed to nitrogen inclusion in the films. The contact angle decrease on the UV illuminated surfaces is attributed to dissociative adsorption of water molecules on the photogenerated surface defective oxygen vacancy sites [4c]. It is known that N doping of metal oxides enhances the formation of oxygen vacancies [9].

13.4 Conclusions

The based ZnO/GO nanocomposite thin films were deposited by the drop-cast method using ZnO/GO aqueous dispersions. The drop-cast samples were submitted to laser irradiations using a frequency quadrupled Nd:YAG laser source in air and controlled nitrogen atmosphere. The results obtained for the laser processed composite layers for the water wetting angle evolution suggest that the incorporation of

GO in the ZnO thin films improves the photoactive properties after irradiation atmosphere in air and in nitrogen. A better performance is obtained in the case of thin film nano-composite ZnO/GO irradiated in nitrogen.

Acknowledgements The authors acknowledge the financial funding of the Executive Unit for Financing Higher Education, Research, Development, and Innovation of the Romanian Ministry of Education, Research, Youth, and Sports, under the contracts PN-II-PT-PCCA-2011-3.2-1235. and PNII-ID-PCE-2012-4-0292.

References

1. (a) Cendrowski K, Jedrzejczak M, Peruzynska M, Dybus D, Drozdzik M, Mijowska E (2014) J Alloys Compd 605:173; (b) Obregón S, Colón G (2014) Appl Catal B Environ 328:152; (c) Saif M, El-Molla SA, Aboul-Fotouh SMK, Ibrahim MM, Ismail LFM, Dahn Douglas C (2014) J Mol Struct 1067:120
2. Lide DR (1991) Handbook of chemistry and physics, 71st edn. CRC Press, Boca Raton
3. Wang ZL (2004) Mater Today 7:26
4. (a) Wang R, Hashimoto K, Fujishima A, Chinkuni M, Kojima E, Kitamura A, Shimohigoshi M, Watanabe T (1997) Nat 388:431; (b) Fujishima A, Rao TN, Tryk DA (2000) J Photochem Photobiol C Photochem Rev 1:1; (c) Sun R, Nakajima A, Fujishima A, Watanabe T, Hashimoto K (2001) J Phys Chem B 105:1984; (d) Borras A, Lopez C, Rico V, Garcia F, Gonzalez-Elipe AR, Richter E, Battiston G, Gerbasi R, McSporran N, Sauthier G, György E, Figueras A (2007) J Phys Chem C 111:1801 (e) Pan X, Yang M.-Q, Xu Y-J (2014) Phys Chem Chem Phys 16:5589; Fateh R, Dillert R, Bahnemann D (2014) ACS Appl Mater Interfaces 6:2270
5. Fujishima A, Hahimoto K, Watanabe T (1999) TiO_2 photocatalysis: fundamentals and applications. BKC. Inc., Tokyo
6. Dreyer DR, Park S, Bielawski CW, Ruoff RS (2010) Chem Soc Rev 39:228
7. (a) György E, Mihailescu IN, Serra P, Perez del Pino A, Morenza JL (2002) Appl Phys A Mater Sci Process 74:755; (b) Bäuerle D (2011) Laser processing and chemistry. Springer, Berlin, p 268; (c) Xiao S, Gurevich EL, Ostendorf A (2012) Appl Phys A Mater Sci Process 107:333
8. Lin LY, Kim HJ, Kim DE (2008) Appl Surf Sci 254:7370
9. (a) Prokes SM, Gole JL, Chen X, Burda C, Carlos WE (2005) Adv Funct Mater 15:161; (b) Wang J, Tafen DN, Lewis SP, Hong Z, Manivannan A, Zhi M, Li M, Wu N (2009) J Am Chem Soc 131:12290

Part V
Materials: Nanowires and Nanofibers

Chapter 14
ZnO Nanowires: Growth, Properties and Advantages

Katerina Govatsi, Athanassios Chrissanthopoulos, and Spyros N. Yannopoulos

Abstract One-dimensional anisotropic nanostructures, and in particular nanowires, are under intensive investigations over the last decade owing to their unique physical properties and their documented performance in a wide range of opto-electronic and nano-photonic devices. Here, we present a short overview of the main assets of nanowire arrays with particular emphasis as materials for solar energy harvesting and conversion. A brief survey on the main growth techniques of ZnO nanowires, i.e. chemical vapor deposition and solution chemistry is also presented.

Keywords Nanowires • Zinc Oxide • Energy conversion

14.1 Introduction – Remarks on Nanomaterials

The nature of a number of physicochemical effects changes drastically as the size of the system decreases down to the nanometer scale. Two main categories of changes occur, i.e. those which include quantum mechanical effects and those which arise

K. Govatsi
Foundation for Research and Technology – Hellas, Institute of Chemical Engineering Sciences, (FORTH/ICE–HT), P.O. Box 1414, Rio-Patras GR-26504, Greece

Department of Chemistry, University of Patras, Rio-Patras GR-26504, Greece

A. Chrissanthopoulos
Foundation for Research and Technology – Hellas, Institute of Chemical Engineering Sciences, (FORTH/ICE–HT), P.O. Box 1414, Rio-Patras GR-26504, Greece

Department of Chemistry, National and Kapodistrian University of Athens, Athens GR-15771, Greece

S.N. Yannopoulos (✉)
Foundation for Research and Technology – Hellas, Institute of Chemical Engineering Sciences, (FORTH/ICE–HT), P.O. Box 1414, Rio-Patras GR-26504, Greece
e-mail: sny@iceht.forth.gr

P. Petkov et al. (eds.), *Nanoscience Advances in CBRN Agents Detection, Information and Energy Security*, NATO Science for Peace and Security Series A: Chemistry and Biology, DOI 10.1007/978-94-017-9697-2_14

from the enhanced surface area to volume ratio. Quantum-size and confinement effects prevail when the particle size r becomes comparable to the Bohr radius, i.e. when r is smaller than ca 5–10 nm. In this case, the optical and electronic properties of solids are significantly altered; the bandgap increases and strong modifications of the electrical properties occur. For larger sizes, but still at length scales well below 100 nm, surface effects play a dominant role, while quantum-size and confinement effects are not important. The main changes observed pertain to the thermal, mechanical, and chemical (catalytic) properties of the material in question.

Nanomaterials or nanostructured materials are usually classified into three categories depending on their shape, i.e. zero-dimensional (0D), one-dimensional (1D) and two-dimensional (2D). Quantum dots and nanowires/nanorods are typically used to describe 0D and 1D materials, respectively [1]. Quantum dots are perhaps the most common example of semiconductor nanostructures confined in all three dimensions; their hallmark is the tunability of their optical properties used for *in vivo* imaging and diagnostics [2]. However, over the last two decades, another important class of 1D semiconductor nanostructures aroused considerable interest. Such structures have cross-sections in the range 10–100 nm and lengths extending to several micrometers. Although the term "nanowhiskers" was originally used [3] to describe the growth of ultrafine InAs whiskers with diameters less than 20 nm on GaAs substrates, the term nanowires (NWs) has prevailed [4]. The merit of these anisotropic nanosized objects is that confinement – with its availing consequences in the material's properties – occurs only in two dimensions while the third micrometer-sized dimension makes the manipulation of NWs in technological applications feasible. The long dimension also provides a pathway for the fast and lossless transport of electrons, holes and photons, rendering NWs favorable candidates for micro/nano-electronics and nano-photonics.

14.2 Why Nanowires?

As mentioned above, NWs combine spatial confinement effects in 2D with the ability of feasible manipulation (long dimension). The majority of the current investigations concerning applications of NWs pertain to the field of renewable energy sources and in particular to solar energy harvesting and conversion. In this context, the unique electrical and optical properties of NWs render these 1D objects important energy conversion materials with applications in solar and photoelectrochemical cells. Perhaps, the major advantages of NWs nanowires are the integrity and qualities of their structure. Their single-crystalline nature ensures very small defect density and the absence of other structural irregularities within the NW. In addition, the growth of NWs is not only limited to semiconducting oxides. A wide class of materials, including superconductors, metals, insulators, semiconductors and so on, can be produced as NWs. Rational growth methods have been developed allowing today the fabrication of arrays/assemblies of nanowires of various geometries and orientations as shown in Fig. 14.1. Oriented NWs perpendicular (vertical, Fig. 14.1a) and parallel (in-plane, Fig. 14.1b) to the substrate, as

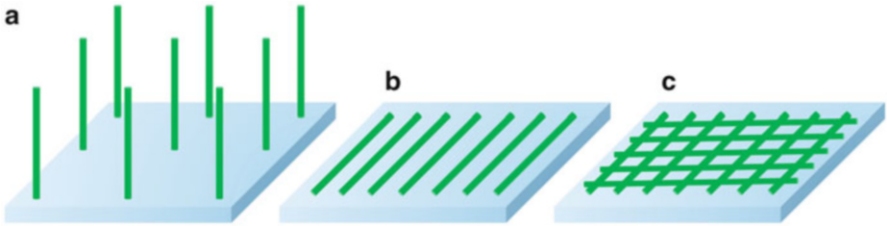

Fig. 14.1 Arrays of NWs: (**a**) Vertical growth, (**b**) in-plane growth, (**c**) ordered mesh of in-plane grown NWs

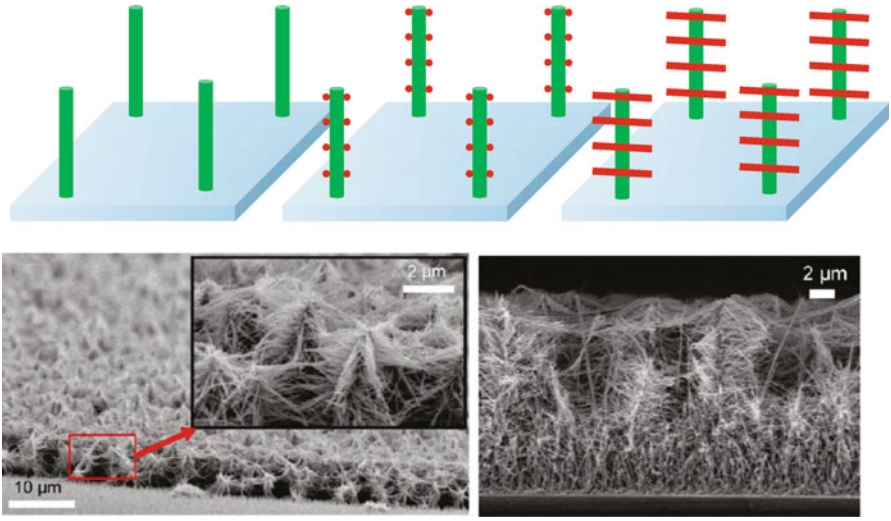

Fig. 14.2 *Upper row*: Schematic illustration of the growth of branched NWs. *Bottom*: Scanning electron microscopy images of branched NWs: tilted view (*left*) and cross section (*right*) (Adapted with permission from Ref. [5], copyright (2011) American Chemical Society)

well as meshes of ordered NWs can be fabricated, which depending on the aspect ratio of NWs and the pitch of the array, provide tunable physical properties, such as optical, electrical, magnetic, and so on. More complex nanostructures, called nanoforests, have been envisaged to provide enhancement of the surface area, in comparison to simple NWs, where hierarchical growth results in tree-like morphologies, as illustrated in Fig. 14.2. Such hierarchical structures have been shown to result in a 5-fold increase of the solar cell efficiency compared to simple upstanding ZnO NWs [5]. The efficiency increase was assigned to the enhanced surface area, which made higher dye loading and light harvesting possible. In addition, the branched geometry offers direct conduction pathways resulting in the reduction of charge recombination.

14.3 Nanowire-Based Solar Cells

Several merits of NW-based solar cells have been considered to demonstrate their superiority over planar photovoltaic devices (based on wafers and thin-films). Improved optical and electrical properties, less semiconducting material, different charge separation mechanisms and strain relaxation effects, less demand on crystallinity purity, cheap and flexible substrates are some of the advantages of the NW-based solar cell devices with efficiencies (1–10 %) comparable, but still inferior, to those of their planar counterparts. A number of materials has been employed to fabricate NW-based solar cells including ZnO, TiO_2, SnO_2, ZnS, CdTe, CdSe, Si, Ge, CuO, GaN, InGaN, GaAs, InAs, and so on. Several steps are involved in the process of light-to-energy conversion. Minimizing the losses in each step is essential for increasing the efficiency. These steps include: **(i)** absorption of the incident light, **(ii)** light-induced generation of electron-hole pairs (excitons), **(iii)** separation of excitons which is caused by the electric potential gradient generated within the structure, and **(iv)** collection of the carriers at the electrodes [6, 7]. It should be noted here that NWs exhibit significant efficiency in trapping light, if they are properly configured, for an effective exciton generation. In addition, the dimensions of NWs fall in the range of the carrier diffusion length and hence the collection of free carriers is highly facilitated in the separation process. Both features render NWs ideal candidates for solar energy conversion.

14.3.1 Light Harvesting Advantages of Nanowires

Two main factors may affect (limit) light absorption by active photovoltaic materials: reflection, where not all photons enter into the active material and transmission, where the active thickness of the material is not optimal to trap enough photons. Therefore, activities are directed towards the development of both anti-reflection coatings and nanostructures that offer enhanced light trapping.

Regarding the decrease of light reflection, the main approach is to develop coatings with refractive index intermediate between the refractive indices of the material and the air. This approach works well to prevent reflection of a given wavelength only, thus being not so useful taking into account the broad solar spectrum. More than one layer can be used to achieve better anti-reflective performance. However, an arrangement with a continuously-graded refractive index would tackle the problem of reflection losses. Such a possibility for an effective gradually changing refractive index is provided by tapered or nanocone-shaped nanowire geometries. To this end, solution-grown ZnO nanorods were investigated as effective anti-reflective coatings for Si solar cells and were compared to conventional single layer (SiN) anti-reflective coatings [8]. It was found that in comparison to the single anti-reflective layer, ZnO nanorod arrays exhibited

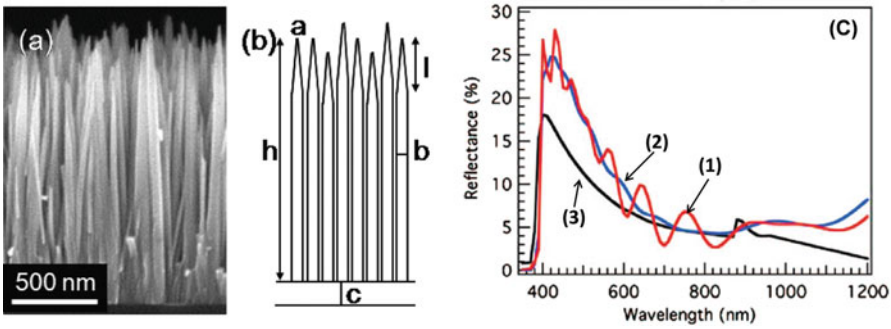

Fig. 14.3 Array of highly tapered ZnO NWs: (**a**) side view SEM image, (**b**) schematic illustration of the NW parameters. (**c**) Effect of the ZnO NW morphology on the (calculated: *red* and *blue*) reflectance spectra of the array: highly tapered array with uniform length (*1*), 10 % length variation (*2*), and experimental data (*3*) (Adapted with permission from Ref. [8], copyright (2008) American Chemical Society) (Color figure online)

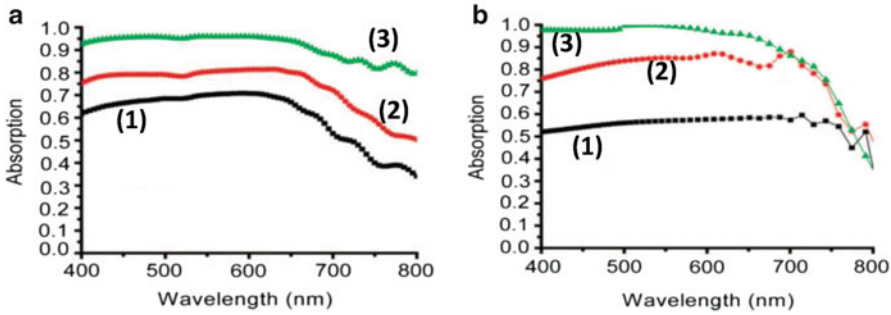

Fig. 14.4 Experimental (**a**) and calculated (**b**) absorption for a-Si:H samples at normal incidence for thin film (*1*); nanowire (*2*) and nanocone (*3*) morphologies (Adapted with permission from Ref. [11], copyright (2009) American Chemical Society)

broadband reflection suppression over a wide spectral range, i.e. from 400 to 1,200 nm. It was shown that a tapered geometry of the nanorods with an average tip diameter of 10 nm are able to provide a weighted reflectance of ~6.6 %, which is better than an optimized SiN single anti-reflective layer (Fig. 14.3). Similar effects were exhibited by nanowires of other materials, i.e. Si [9] and GaP [10]. Similar results were obtained for amorphous hydrogenated silicon (a-Si:H) nanowire and nanocone arrays [11] where a good agreement between experimental and calculated results was found as shown in Fig. 14.4. It was demonstrated that more than 90 % of light is absorbed at angles of incidence up to 60° for a-Si:H nanocone arrays, which was higher than NW arrays (70 %) and thin films (45 %).

Regarding optimum trapping of the incident light, it should be kept in mind that the size of the nanostructures is a key parameter, as particles with sizes considerably

smaller (i.e. <50–100 nm) than the wavelength of the visible light appear "transparent" to light. Increasing the effect of light scattering within nanoparticle films has been considered as a mean to increase the photon-capture efficiency. The increase of light scattering can be achieved by adding submicron-sized particles into a nanoparticle film [12]. Although this effect might be compromised by the decreased surface area of the larger particles, it has been shown that polydisperse aggregates of ZnO particles with a broad size distribution can enhance the optical absorption and hence the light-harvesting efficiency of solar cells [13]. This enhancement is attributed to the increased light scattering, which originates from submicron sized particles with dimensions comparable to the wavelength of the incident light. Multiple scattering, due to light trapping, practically extends the travelling distance of light within the nanoparticle film.

Anisotropic NWs grown with lengths of the order of few microns offer also a viable solution towards increasing photon absorption through enhanced light scattering. Nanoparticle/nanowire composites of TiO_2 combining the advantages of both structures (the high surface area of the nanoparticles and the fast transport rate and the light scattering effect of single-crystalline nanowires) were employed in solar cells demonstrating a notable increase of the energy conversion efficiency [14].

14.3.2 Exciton Generation Advantages of Nanowires

Apparently, light absorption, and hence the solar cell device efficiency, depends upon the ratio of the energy of the incident photons E^{ph} to the optical bandgap energy E_g of the active photovoltaic material. Photons with sub-bandgap energy are not able to excite electron-hole pairs, while photons with super-bandgap energy produce excitons. When the exciton binding energy is strong, the electron-hole pair constitutes a bound exciton state. On the contrary, if the exciton energy is weak the carriers will "cool down" or relax to the band edges as free carriers by transmitting their surplus energy E^{ph}-E_g to the crystal lattice in the form of phonons. This part of energy is dissipated as heat and does not contribute to electricity production. This loss represents presumably 30–40 % of the overall losses in a solar cell.

To overcome this problem and to exploit the surplus energy, current attempts are concentrated on devices based on multi-junction configurations and other multiple energy-level approaches such as intermediate band solar cells [15]. Such systems are designed to have structures within the cell able to absorb photons with various energies, thus minimizing the surplus energy E^{ph}-E_g. Another common approach is to synthesize the active photovoltaic material by multicomponent (e.g. ternary mixtures $In_xGa_{1-x}N$) systems, which can provide a fine tuning of the optical bandgap [16]. The exceptional composition tunability of the above ternary system was mainly assigned to the ability of the NWs to relax high strains developed due to large lattice mismatch in planar single crystalline films.

14.3.3 Carrier Collection Efficiency Advantages of Nanowires

Collecting efficiently the photo-induced generated carriers is a major issue yet to be solved in photovoltaics. Crystalline Si is still the dominant material in the photovoltaics market outperforming its current rivals, i.e. CdTe, CuInGaSe and amorphous Si. Convectional *c*-Si solar cells are constructed employing planar p-n junctions, where the electrostatic potential developed at the interface is responsible for charge separation. The collection efficiency of the photogenerated charge carriers near the p-n junction depends on the diffusion length of the minority carrier in the n- and p-type regions. Various recombination mechanisms limit the carrier diffusion length in the Si lattice. Defect-free single-crystalline Si is thus necessary to achieve a large carrier diffusion length, which poses limits to practical applications due to high costs. The employment of 1D nanostructures in solar cells alleviates the above requirement. Indeed, it was almost 10 years ago when a device physics model was developed for radial p-n junction nanowire solar cells. In this model, densely packed nanowires, each having a p-n junction in the radial direction, are oriented with their long axis parallel to the incident light direction. The high-aspect-ratio of NWs makes it possible to use a sufficient thickness of material to obtain good optical absorption while at the same time it provides short collection lengths for excited carriers in a direction normal to the light absorption [17].

The above ideas have now been expanded; recent investigations focus on the application of three main architectures [7]: (a) radial heterostructures with junctions along the NW radius, (b) axial heterostructures with junctions along the NW long axis, and (c) substrate junctions where NWs of either p- or n-type are grown on substrates of the opposite type, such as those illustrated in Fig. 14.5. The pros and cons of these three NW array configurations have been discussed in detail elsewhere [7].

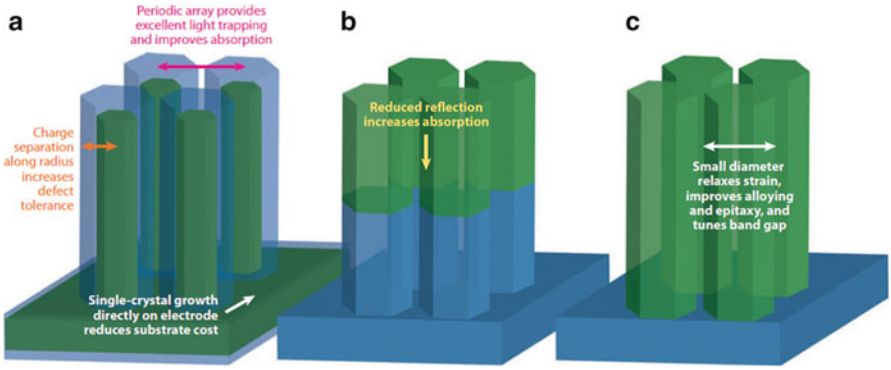

Fig. 14.5 Various types of periodic arrays of NW heterojunctions. (**a**) NWs with radial junctions, (**b**) NWs with axial junctions, (**c**) NWs with substrate junctions (Adapted with permission from Ref. [7])

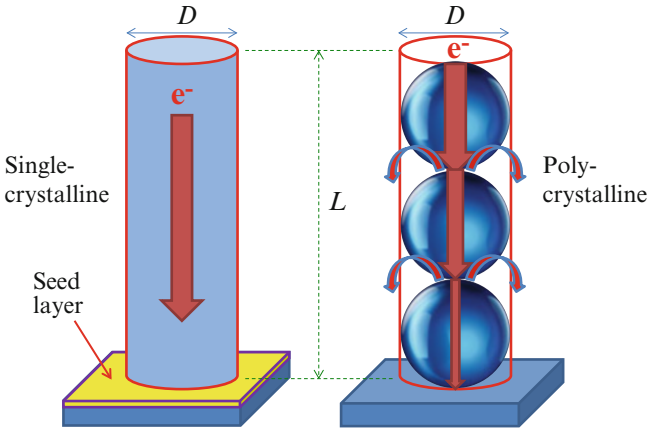

Fig. 14.6 Schematic representations of the electron transport in a photoanode based on single-crystalline NWs and nanoparticles

Finally, as shown schematically in Fig. 14.6, NWs offer the possibility of fast electron conduction along the NW axis. This promotes the collection of electrons by decreasing the collection time in comparison to nanoparticles, where scattering of electrons of the grain boundaries lead to trap-limited diffusion and deteriorate the device performance. Indeed, the defect-free, single-crystalline nature of the NWs constituting the photoanode, with fewer sites for electron trapping, ensures a fast electron transport owing to the direct pathway to the conductive glass electrode. Therefore, electron transport in single-crystalline NWs is expected to be several orders of magnitude faster than the percolated random walk diffusion through a polycrystalline nanoparticles film. In addition, electrical measurements have demonstrated barrier-free contacts between ZnO nanowires and the substrate [18]. Measurements of the mobility properties of individual ZnO NWs yielded values in the range 1–5 $cm^2\ V^{-1}\ s^{-1}$, which implies an electron diffusivity of about 0.05–0.5 $cm^2\ s^{-1}$ for single dry nanowires [18]. This value is almost two to three orders of magnitude larger than the highest reported diffusivity for TiO_2 or ZnO nanoparticle films in photovoltaic cells.

A major concern in the comparison between NW arrays and nanoparticle thin films relates to the surface area of the active material which is a key parameter for dye absorption in dye-sensitized solar cells. Nanoparticle films are considered to provide a few times higher surface area in comparison to NW arrays. Low temperature, simple and cost-effective chemistry has demonstrated that dense arrays, up to 35 billion wires per cm^2, can be grown on arbitrary substrates of any size [18]. The schematic shown in Fig. 14.6 reveals that the side surface of a nanowire of length L and diameter D, $S_{NW} = \pi\ D\ L$ is equal the surface of an arrangement of nanospheres occupying the same volume, i.e. $S_{sp} = \pi\ D^2\ *\ L/D = \pi\ D\ L$, where L/D stands for the number of spheres over a length equal of L. This shows that the surface area of a dense array of well-aligned NWs can approach or even surpass the

surface area of equally order arrays of spheres of the same diameter. Closing this section, it is worth mentioning that NW films exhibit better mechanical properties than their nanoparticles-based counterparts. The solution growth process involving the growth from a seed layer ensures also a much stronger attachment to the substrate in the case of NW arrays.

14.4 ZnO Nanostructures

According to Wang [19] there are three main types of 1D nanostructures that are being actively studied in nanotechnology: carbon nanotubes, silicon NWs, and ZnO NWs. ZnO, a wide bandgap semiconductor (3.37 eV) having a high electron-hole binding energy (60 meV), is an important transparent material [20]. ZnO exhibits a dazzling variety of nanostructure configurations (Fig. 14.7) [21], thus having a wide range of applications in optics, optoelectronics, spintronics, sensors, actuators, the energy sector, biomedical sciences, etc. ZnO nanocrystals are non-toxic, biosafe, and their large-scale production does not present environmental and health hazards [22]. Early work on semiconductor nanowhiskers [3] was followed by systematic studies in the area of inorganic NWs [23]. In the late 1990s, the field of semiconductor NWs underwent a significant expansion and became one of the most active research areas in nanoscience [24]. A boost in the study of ZnO nanostructures was

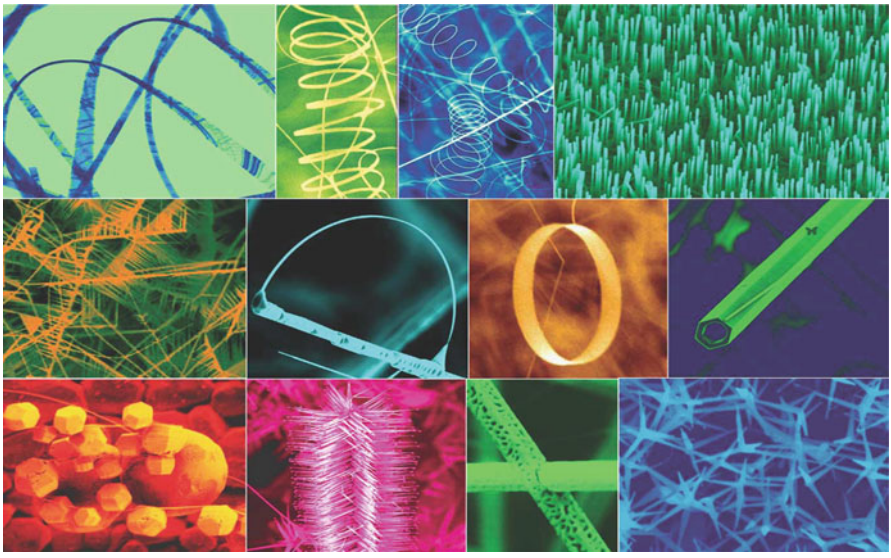

Fig. 14.7 Typical morphologies of ZnO nanostructures grown under controlled conditions by thermal evaporation of solid powders (Adapted with permission from Ref. [21])

given by the discovery of ZnO nanobelts [25] and the demonstration of ultra-violet lasing properties of ZnO NWs at room temperature [26]. These two articles [25, 26] have been the most influential in the development of the research focused on ZnO nanostructures. Actually, more than 28,000 articles appear in the "Web of Science™" since 2001 when searching with the keywords "ZnO" and "nano"; hence it is practically impossible to present here a well-balanced survey on ZnO growth and properties. In brief, the latest representative breakthroughs in the field of ZnO nanostructures include:

(a) The development of the first examples of logic gates based on ZnO NW arrays which can be switched simply by bending the substrate, exploiting the piezotronic effect [27]. Using only ZnO NWs, the first piezoelectric triggered mechanical-electronic logic operation using the piezotronic effect was demonstrated.
(b) The realization of self-powered ZnO NW devices [28]. It was shown that the vertical and lateral integration of ZnO nanowires into arrays are capable of producing sufficient power to operate real devices. A lateral integration of 700 rows of ZnO NWs could produce a peak voltage of 1.26 V at a low strain of 0.19 %, which is potentially sufficient to recharge an AA battery.
(c) The fabrication of optical fiber/ZnO-NW hybrid structures for efficient 3D dye-sensitized solar cells (DSSC) [29]. The ZnO NWs were grown normal to the optical fiber surface in order to enhance the surface area for the interaction of light with dye molecules. In this arrangement, the light illuminates the fiber from one end along the axial direction, and its internal reflection within the fiber creates multiple opportunities for energy conversion at the interfaces.
(d) The use of aligned ZnO-NWs in photovoltaic devices [18]. The authors introduced a version of the DSSC in which the traditional nanoparticle film was replaced by a dense array of oriented, crystalline ZnO nanowires, facilitating the rapid collection of carriers generated throughout the device. Later, ZnO NWs grown hydrothermally into nanoforest formations have yielded energy conversion efficiencies up to 2.6 % [5].
(e) The doping of ZnO nanorods with transition metal ions in order to fabricate diluted magnetic semiconductors with intrinsic ferromagnetism offering great potential in spintronics [30].

14.4.1 Synthesis of ZnO Nanowires

A large number of physical and chemical methods have been applied for the growth of ZnO NWs. The majority of the approaches make use of bottom-up synthetic routes offering the possibility for a controlled growth of NWs with the desired aspect ratio, areal density and positional order on the substrate, enabling also the possibility for heterostructure growth. ZnO nanowires can be either grown as free

standing particles in a solution or on specific substrates. As has been discussed in the previous sections, the aligned vertical-to-the-substrate growth of NWs entails certain advantages for energy conversion as well for photonic applications. The wurtzite structure of ZnO has two essential features, i.e. the non-central symmetry and the polar surfaces. The atomic arrangement in ZnO is described as a number of alternating planes composed of tetrahedrally coordinated Zn^{2+} and O^{2-} ions, stacked successively along the c-axis. The unit cell of ZnO is neutral; however, the ion distribution is such that some surfaces can be terminated entirely with cations or anions, resulting in positively or negatively charged surfaces, the so-called polar surfaces. The basal plane is the most common polar surface. Zn-(0001) and the O-(000-1) are the positively and negatively polar surfaces, respectively. These polar surfaces result in a normal dipole moment and a spontaneous polarization along the c-axis. Energetic reasons for maintaining a stable structure demand that the polar surfaces have facets or undergo considerable surface reconstructions. Below, we focus on two techniques most commonly employed for nanowires growth: chemical vapor deposition (CVD) and solution phase growth (or chemical bath deposition).

14.4.1.1 Chemical Vapor Deposition of ZnO Nanowires

In the CVD method, chemical precursors are introduced as vapors into the hot zone of a furnace. Their reaction (mainly) onto a substrate heated at a selected temperature often takes place in the presence of a nanostructured metal catalyst which has been predeposited on the substrate. Vapor–liquid–solid (VLS) and the vapor–solid–solid (VSS) are the two main mechanisms for the growth of ZnO NWs. In the VLS mechanism a metal catalyst (in the form of nanoparticles) forms a liquid eutectic with the desired nanowire material [31]. The gaseous reactants dissolve progressively into the liquid eutectic droplet, which leads to a supersaturated solution facilitating nucleation and growth. The nucleated material precipitates; continuous feeding of the liquid catalyst droplet leads to further precipitation and nanowire growth, as shown schematically in Fig. 14.8. The VLS method is quite flexible allowing the growth of heterostructures by changing the source reactants. Nanowires with superlattice arrangements can be grown by the periodic introduction of different reactants. Furthermore, selecting appropriate experimental conditions, epitaxial layers on the side walls can also grow. In general, both axial and radial heterostructures can be synthesized by VLS. The first demonstration of ZnO NWs growth with perfect vertical alignment to the substrate (single crystalline sapphire) was achieved by Huang et al. [26] where the NWs array was shown to exhibit room-temperature ultraviolet lasing.

The growth of well-aligned ZnO NWs requires a rather low growth rate. Since the ZnO sublimation temperature (~1,300 °C) is quite high, an alternative method to provide the reactants for ZnO growth is to adopt the carbothermal reduction by

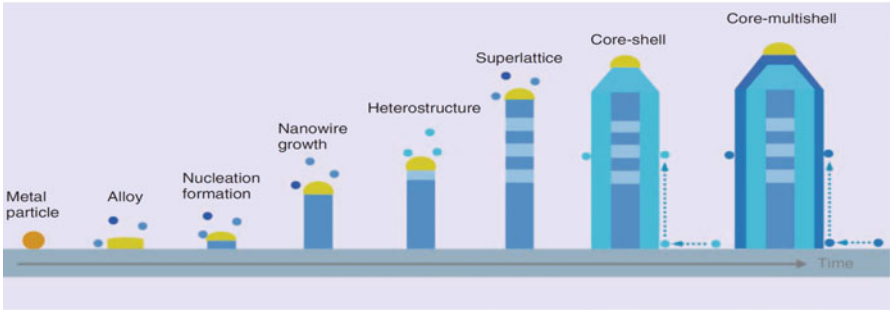

Fig. 14.8 Schematic representation of metal nanoparticle-catalyzed VLS growth of heterostructured (axially and radially) nanowires (Adapted with permission from Ref. [32])

mixing ZnO and carbon powders. In this case, the reaction temperature can be reduced to 900 °C. The overall reaction (reduction) of ZnO can be written as:

$$\mathrm{ZnO(s) + C(s) \leftrightarrow Zn(g) + CO(g)} \tag{14.1}$$

The main intermediate reactions are the:

$$\mathrm{ZnO(s) + CO(g) \leftrightarrow Zn(g) + CO_2(g)} \tag{14.2a}$$

$$\mathrm{C(s) + CO_2(g) \leftrightarrow 2CO} \tag{14.2b}$$

The zinc can be fully or partially oxidized in the air stream leading to the formation of stoichiometric ZnO or suboxides (ZnO_x, $x < 1$). Both Zn and ZnO_x are volatile; after being transferred by an inert gas they reach the substrate. Since reaction (14.1) is reversible at somewhat lower temperatures than the carbothermal reduction, the vapors merge in the Au liquid droplet and react to form ZnO.

The alignment of the ZnO NWs depends to a large extent on the epitaxial relationship between ZnO and the substrate. The very small lattice mismatch between ZnO and various materials has made it possible to produce well aligned ZnO NWs on sapphire [26] and various nitrides (GaN, AlGan, AlN) [33]. The issue of NW orientation to the substrate has recently been put under a more rigorous base. Cao and Yang [34] have worked out a theoretical model for the quantitative description of the temperature-dependent nanowire orientation in the VLS process, based on thermal fluctuations. Their main outcome is that there is a critical temperature, T_{cr}, which depends upon on the Gibbs free energy of the NW precipitated nucleus. At $T > T_{cr}$ NWs tend to align horizontally to the substrate. At $T < T_{cr}$ NWs can grow either vertically aligned on the substrate or inclined at various angles in the range 40–90° (see Fig. 14.9).

Although the VLS growth mechanism is considered as one of the simplest methods for NW growth, a number of externally controlled experimental parameters

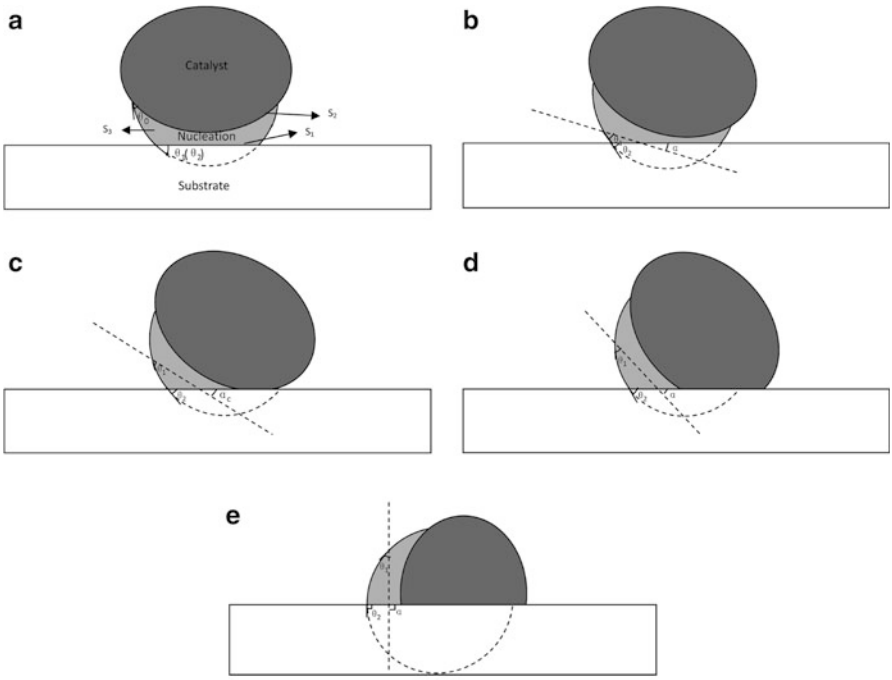

Fig. 14.9 Schematic illustration of the various directions which the NW nucleus can adopt. (**a**) Vertical growth. The *dashed* line in (**b**–**e**) denotes the angle α between the substrate and the growth direction. In (**e**) the NW displays in-plane growth. The angle α_c (**c**) is the critical angle, if it is exceeded the morphology of the nucleus would change dramatically (Adapted with permission from Ref. [34], copyright (2012) American Chemical Society)

render this method quite inextricable. In particular, the reaction temperature, the temperature gradient (between the source and the substrate), the growth time, the vapor pressure of Zn or ZnO, the inert gas and oxygen partial pressures, the gas concentration and flow rate, the type of the substrate, and the catalyst details (predominantly Au films deposited by sputtering and annealed to form NPs) are among the parameters that should be optimized for a controlled growth of ZnO NWs. The chamber total pressure, the oxygen partial pressure and the thickness of catalyst layer are the most important parameters.

An exhaustive investigation of the influence of the oxygen partial pressure and the chamber pressure on the quality and growth behavior of ZnO NWs has been presented by Song et al. [35]. Conducting more than 100 experiments under different growth conditions, a quantitative definition of the best combination of the O_2 partial pressure and the chamber pressure for growing well-aligned ZnO NWs was achieved (Fig. 14.10a). The results were used to construct a kind of "phase diagram" of the controlled NW growth as shown in Fig. 14.10b. Light color regions represent the best growth conditions in terms of NWs with perfect

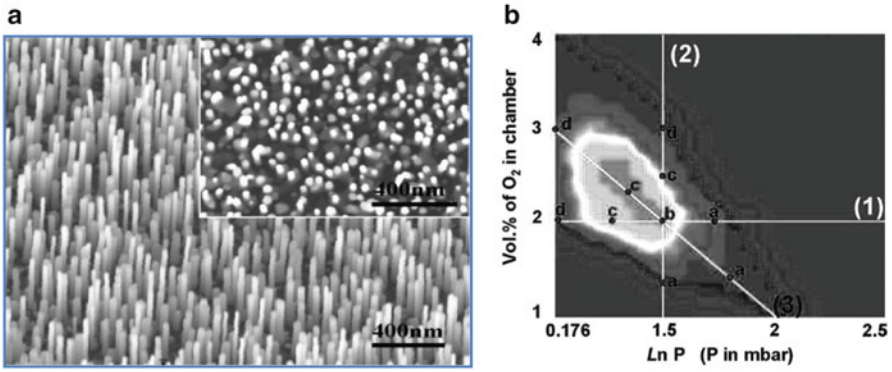

Fig. 14.10 (**a**) SEM images of aligned ZnO nanorods on a GaN substrate. (**b**) "Phase diagram" correlating the O_2 partial pressure and the growth chamber pressure. *Lines* (*1*), (*2*), and (*3*) represent growth with constant O_2 pressure, constant system pressure, and linearly varying O_2 percentage and system pressure (Adapted with permission from Ref. [35], copyright (2005) American Chemical Society)

alignment, high areal density and uniform length and diameter. No growth of ZnO NWs was detected in the dark region.

The thickness of the catalyst layer that is pre-deposited on the substrate plays a dominant role for the morphology of the NWs. It is a general perception that the size of the catalyst particles determines the width of nanowires. However, it was shown that this condition is practically valid as long as the catalyst nanoparticle sizes do not exceed 40 nm [36]. While Au is the most frequently used catalyst for growing ZnO nanowires, its morphological features on the substrate, which determine the size and shape of the nanostructures grown, were not put into focus until recently. In a recent detailed study [37] we investigated the details of the solid state thermal dewetting of Au films into nanoparticles on Si substrates.

Au films of various thicknesses ranging from 2 to 15 nm were annealed withslow and fast rates at various temperatures, and the morphological details of the nanoparticles formed were investigated. Typical SEM images of dewetted Au films of various thicknesses and their respective particle size distributions (PDS) are shown in Fig. 14.11. It was revealed that efficient and high throughput growth of ZnO nanowires, for a given growth time, was realized in cases of thin Au films, Fig. 14.12 (upper left), i.e. when the thickness is lower than 10 nm. Based on experimental findings, a two-step mechanism is proposed to account for the growth of ZnO nanowires ending in a tapered geometry with ultrathin (~30 nm), micron long tips, Fig. 14.12 (right). The ZnO NW arrays with the dispersed Au nanoparticles which remain on top of them after the growth process (Fig. 14.12; bottom left) could be used as substrates for surface enhanced Raman scattering, exploiting the plasmon properties of Au nanoparticles.

From a different point of view, remnants of catalyst particles on the NW arrays might be detrimental for the performance of a NW-based device. To alleviate this problem other growth methods such as the catalyst-free metal organic CVD

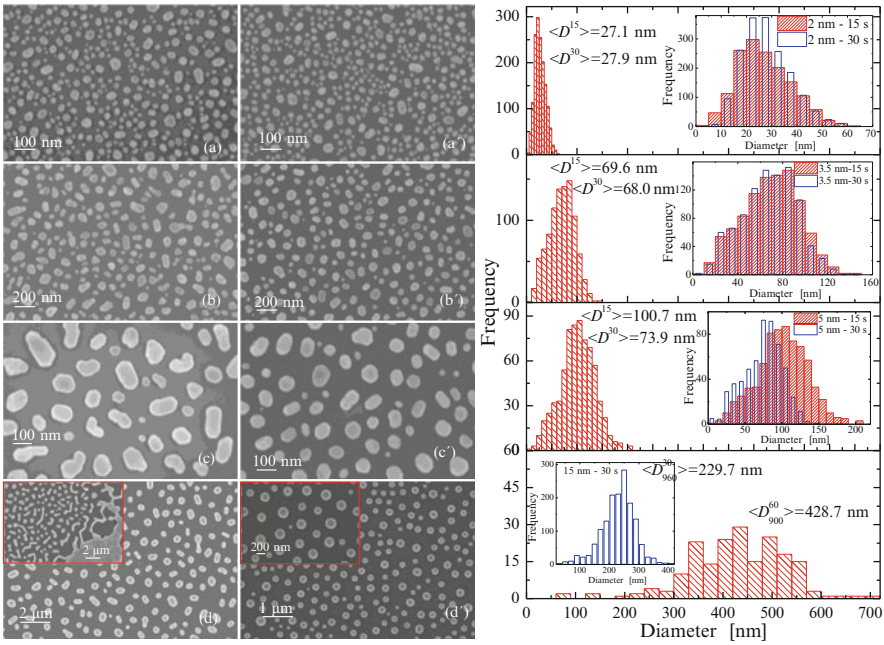

Fig. 14.11 *Left*: SEM images of dewetted Au films. Nominal Au film thickness, annealing temperature and time are as follows: (**a**) 2 nm, 900 °C, 15 s; (**a´**) 2 nm, 900 °C, 30 s; (**b**) 3.5 nm, 900 °C, 15 s; (**b´**) 3.5 nm, 900 °C, 30 s; (**c**) 5 nm, 900 °C, 15 s; (**c´**) 5 nm, 900 °C, 30 s; (**d**) 15 nm, 900 °C, 60 s (*inset*: 15 nm, 900 °C, 30 s); (**d´**) 15 nm, 960 °C, 30 s (*inset*: magnification). *Right*: Particle size distributions of the Au nanoparticles shown in the *left* panel. The insets show the comparison between the PSDs obtained for the two different annealing times (Adapted with permission from Ref. [37])

(MOCVD) method are employed. Shi et al. [38] investigated the possibility of controlling the morphology and crystallinity of ZnO nanostructures by optimizing the MOCVD growth parameters. This led to the control of ZnO nanostructures from a 3D NWs form to a 2D nanowall network-like form, and then to a 2D dense film form, as is schematically illustrated in Fig. 14.13.

14.4.1.2 Solution Chemistry Growth of ZnO Nanowires

The high temperature techniques for the controlled growth of ZnO NWs discussed above entail some disadvantages in the direction of integrating such NW arrays onto flexible organic substrates, which could lead to the fabrication of foldable devices. Several methods have been currently implemented for the growth of ZnO NWs in solutions [39]. ZnO can crystallize by the hydrolysis of Zn salts in a basic solution. As mentioned above, Zn^{2+} is tetrahedrally coordinated forming the respective complexes. Solution temperature and pH determine the number of Zn^{2+}

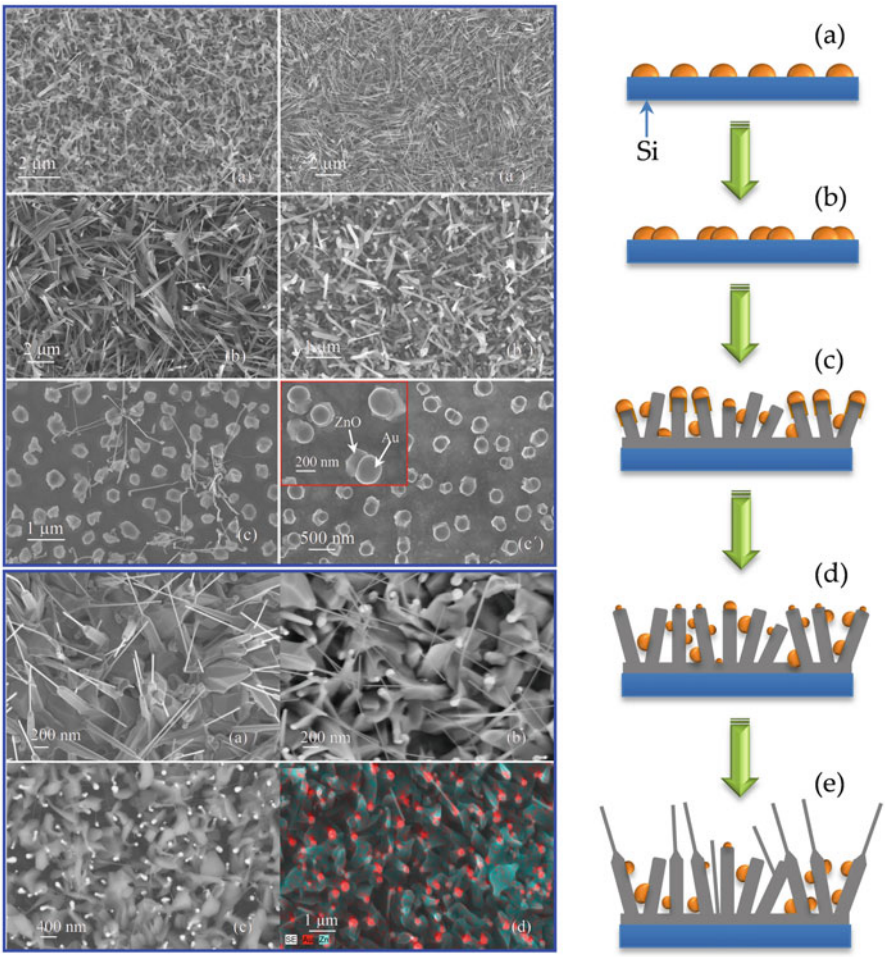

Fig. 14.12 *Upper Left*: SEM images of ZnO nanostructures grown by VLS on Si substrates covered by Au films with thicknesses (**a**) 2 nm, (**b**) 5 nm, and (**c**) 15 nm. *Bottom Left*: (**a**) SEM magnification of the ZnO nanostructures shown in the *upper left* image (**b**). (**b, c**) Images of the same nanostructures recorded with the BSE detector at 5 kV (**b**) and 15 kV 7 (**c**). (**d**) EDS mapping of the elements Au and Zn. *Right*: Schematic representation of the two-step growth mechanism of ZnO. (**a**) Initial Au morphology after dewetting of Au films. (**b**) Partial coarsening of Au NPs after heating the substrate into the reaction tube, just before the growth starts. (**c**), (**d**) Growth of ZnO nanostructures via VLS; the different wettability of Au on ZnO surfaces causes the fragmentation of Au NPs. Smaller Au NPs on *top* of ZnO nanorods impede the further growth of these large diameter nanorods. (**e**) Smaller Au NPs act as catalytic sites for additional growth of ultrathin nanowires (Adapted with permission from Ref. [37])

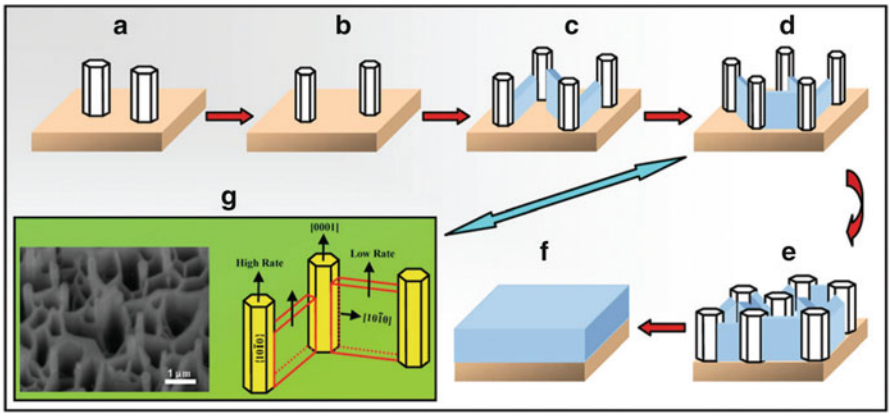

Fig. 14.13 Schematic representation of the morphological progress of ZnO nanostructures by properly adjusting the MOCVD growth parameters (Adapted with permission from Ref. [38])

intermediates whose dehydration will finally lead to the formation of ZnO. The energy minimization of the reaction system is generally considered as the driving force for crystal growth, while a reversible equilibrium is considered to dictate the chemical reactions in an aqueous system. The high-energy polar surfaces (0001) have a high tendency to attract and adsorb the incoming ions, and alternating Zn and O terminated surfaces are formed during the reactions. This mechanism gives rise to anisotropic growth which leads to NW formation. Since solution chemistry growth takes place mostly in aqueous media, the term hydrothermal method is frequently used.

The growth of ZnO NWS has been achieved in alkaline solutions, in hexamethylenetetramine (HMTA) aqueous solution, by electrochemical deposition on conductive substrates, via templated growth in combination with electrodeposition, and by epitaxial growth where various metals such as Au, Pt, and Cu have been used as seeds on the substrate since they provide a lower lattice mismatch with ZnO [39]. The typical steps of the hydrothermal growth method of well-aligned ZnO NWs are illustrated in Fig. 14.14.

The seed layer can be formed by depositing ZnO nanoparticles onto the substrate. More frequently, droplets from a dispersion of a Zn-containing precursor (e.g. ZnAc dihydrate) are deposited by spin coating onto the substrate followed by thermal decomposition at >200 °C to form ZnO islands. The seeds facilitate nucleation of ZnO NWs due to lowering of thermodynamic barrier. An aqueous solution mixture of an alkaline reagent (e.g. HMTA or NaOH) and a Zn^{2+} precursor (e.g. ZnAc dihydrate, zinc nitrate etc.) is prepared as the nutrient solution. The solution may also contain a capping agent (e.g. polyethyleneimine, PEI) which prevents lateral growth of NWs to maximize their aspect ratio. The seeded substrate is kept (frequently face-down) into the solution over a certain period (e.g. 2–48 h) at constant temperatures (70–90 °C). Post-growth annealing (e.g. 300 °C for 30 min)

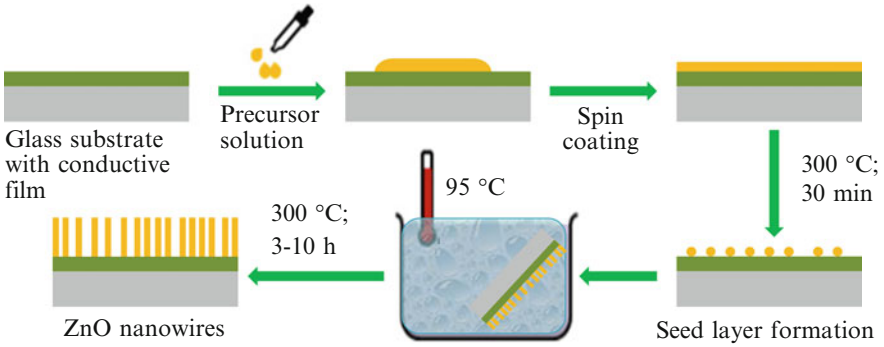

Fig. 14.14 Schematic illustration of the various steps followed for the growth of ZnO NWs using the hydrothermal method

takes place to remove organic matter from the ZnO NW surfaces. In analogy with the VLS method, a number of parameters involved in the hydrothermal growth of ZnO NWs must be properly optimized in order to obtain NW arrays with the desired morphology, i.e. orientation, areal density and aspect ratio. The reactants concentrations, the details of the seed layer, the growth time, the bath temperature, the position of the substrate, the solution pH, the present of capping agents, mechanical stirring, etc. are among the parameters that affect the morphology of ZnO NWs.

The density of ZnO NW arrays on smooth surfaces in the absence of seeds has been achieved by optimizing the precursor concentration [40]. Studying also the effect of growth time it was found that the growth process can be divided into three stages: (i) lateral growth, (ii) axial growth, and (iii) proportional growth. The optimum growth temperature was found to be 70 °C. In a more detailed study, Xu et al. [41] adopted a systematic statistical design and analysis to optimize the aspect ratio of ZnO NWs [41] (Fig. 14.15). Reaction temperature, growth time, precursor concentration and capping agent were the reaction parameters which were controlled. It was found that for precursor concentration ~1 mmol/L, at a reaction temperature ~80 °C, and growth time of about 30 h, the aspect ratio of the ZnO NWs achieved their highest value of nearly 23.

14.5 Conclusions and Outlook

We have attempted in this article to provide a brief overview of the main advantages of 1D nanostructures and in particular of nanowires over other low-dimensional structures. NWs represent a class of nanomaterials the confinement of which in two dimensions (radially) can be exploited to benefit from changes in electronic and other physical properties, while, at the same time, their micron-sized long axis makes their manipulation for easy integration in optoelectronic and photonic devices possible. Thus, both their absolute size and their

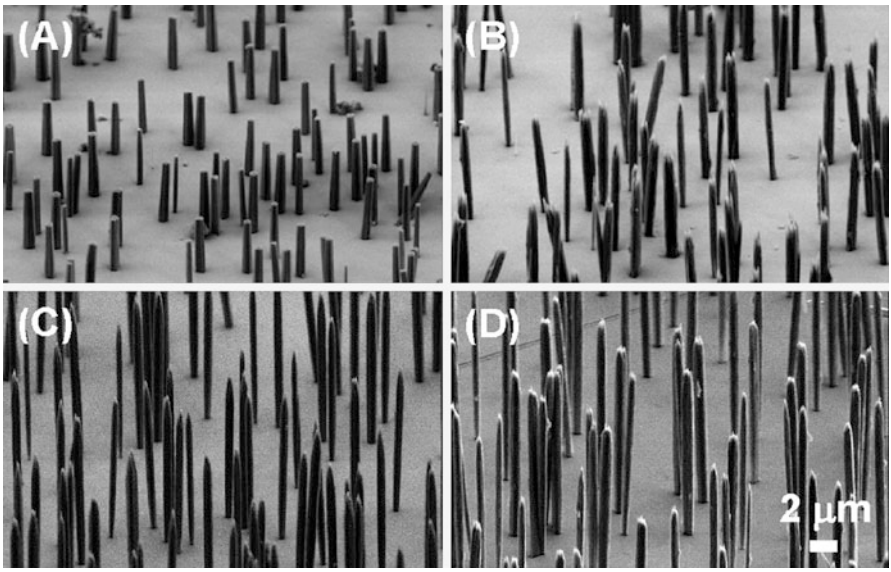

Fig. 14.15 SEM images of ZnO NWs with aspect ratio of (**a**) 7.7, (**b**) 12.4, (**c**) 14.5, and (**d**) 22.3 (Adapted with permission from Ref. [41], copyright (2009) American Chemical Society)

aspect ratio are important features. In addition, the geometry of NWs assists strain relaxation which in turn facilitates hetero-epitaxial growth even in the case of high lattice mismatch. A short description on the main applications and growth methods of ZnO NWs has been presented, where the pros and cons of the vapor deposition and solution chemistry synthesis approaches have been discussed. Both synthesis methods are multiparametric problems and fine tuning of the experimental parameters must be first conducted in order to achieve optimization of the NW growth, including location control, high aspect ratio and areal density, and vertical orientation to the substrate. Hierarchical or hybrid 1D nanostructures have also been developed to improve and provide tuning of the electrical and optical properties of NWs; considerable increase of the photovoltaic efficiency has been observed in hierarchically growth ZnO nanotree arrays.

Despite the progress in the field, NWs are not yet in the verge of commercialization, especially in the sector of photovoltaics where power conversion efficiency is still lower than offered by the thin film technology. However, this is not true for light emitting diode applications where 1D structures outperform in relation to their traditional rivals.

It should be born in mind that the nature of the research conducted in the field of ZnO NWs is much more interdisciplinary than presented here, involving a diverse range of activities of highly collaborative character between chemists, physicists, biologists, engineers, pharmacologists, etc. In parallel, the elaborate synthetic methods of novel NW architectures have boosted the development of unique nanotechnology-enabling investigative tools which are now capable of providing

to the desired spatial and time resolution information on the electronic, optical, structural, etc. properties of these structures. This development made it possible to gain insights from *in situ* growth studies and during device operation.

Acknowledgements This research has been co-financed by the European Union (European Social Fund – ESF) and Greek national funds through the Operational Program "Education and Lifelong Learning" of the National Strategic Reference Framework (NSRF) – Research Funding Program: Thales. Investing in knowledge society through the European Social Fund.

References

1. Vajtai R (ed) (2013) Springer handbook of nanomaterials. Springer, Berlin
2. Michalet X, Pinaud FF, Bentolila LA, Tsay JM, Doose S, Li JJ, Sundaresan G, Wu AM, Gambhir SS, Weiss S (2005) Science 307:538
3. Yazawa M, Koguchi M, Hiruma K (1991) Appl Phys Lett 58:1080
4. Xia Y, Yang P, Sun Y, Wu Y, Mayers B, Gates B, Yin Y, Kim F, Yan H (2003) Adv Mater 15:353
5. Ko SH, Lee D, Kang HW, Nam KH, Yeo JY, Hong SJ, Grigoropoulos CP, Sung HJ (2011) Nano Lett 11:666
6. Hochbaum AI, Yang PD (2010) Chem Rev 110:527
7. Garnett EC, Brongersma ML, Cui Y, McGehee MD (2011) Ann Rev Mater Res 41:269
8. Lee Y-J, Ruby DS, Peters DW, McKenzie BB, Hsu JWP (2008) Nano Lett 8:1501
9. Garnett E, Yang PD (2010) Nano Lett 10:1082
10. Diedenhofen SL, Vecchi G, Algra RE, Artsuiker A, Muskens OL, Immink G, Bakkers EPAM, Vos WL, Gomez Rivas J (2009) Adv Mater 21:973
11. Zhu J, Yu Z, Burkhard GF, Hsu C-M, Connor ST, Xu Y, Wang Q, McGehee M, Fan S, Cui Y (2009) Nano Lett 9:279
12. Ferber J, Luther J (1998) Sol Energy Mater Sol Cells 54:265
13. Zhang Q, Chou TP, Russo B, Jenekhe SA, Cao G (2008) Adv Funct Mater 18:1654
14. Tan B, Wu Y (2006) J Phys Chem B 110:15932
15. Kφnig D, Casalenuovo K, Takeda Y, Conibeer G, Guillemoles JF, Patterson R, Huang LM, Green MA (2010) Phys E 42:2862
16. Kuykendall T, Ulrich P, Aloni S, Yang PD (2007) Nat Mater 6:951
17. Kayes BM, Atwater HA, Lewis NS (2005) J Appl Phys 97:114302
18. Law M, Greene LE, Johnson JC, Saykally R, Yang PD (2005) Nat Mater 4:455
19. Wang ZL (2009) Mater Sci Eng R 64:33
20. Jagadish J, Pearton SJ (eds) (2006) Zinc oxide bulk, thin film and nanostructures. Elsevier, Amsterdam
21. Wang ZL (2004) Mater Today 7:26
22. Li Z, Yang R, Yu M, Bai F, Li C, Wang ZL (2008) J Phys Chem C 112:20114
23. Yang PD, Lieber CM (1996) Science 273:1836
24. Dasgupta NP, Sun J, Liu C, Brittman S, Andrews SC, Lim J, Gao H, Yan R, Yang P (2014) Adv Mater 26:2137
25. Pan ZW, Dai ZR, Wang ZL (2001) Science 291:1947
26. Huang MH, Mao S, Feick H, Yan H, Wu Y, Kind H, Weber E, Russo R, Yang PD (2001) Science 292:1897
27. Wu WZ, Wei Y, Wang ZL (2010) Adv Mater 22:4711
28. Xu S, Qin Y, Xu C, Wei Y, Yang R, Wang ZL (2010) Nat Nanotechnol 5:366
29. Weintraub B, Wei YG, Wang ZL (2009) Ang Chem Int Ed 48:1
30. Zhang ZH, Wang X, Xu JB, Muller S, Ronning C, Li Q (2009) Nat Nanotechnol 4:523

31. Wagner RS, Ellis WC (1964) Appl Phys Lett 4:89
32. Zhang G, Tateno K, Gotoh H, Sogawa T (2010) NTT Tech Rev 8:1
33. Wang XD, Song JH, Li P, Ryou JH, Dupuis RD, Summers CJ, Wang ZL (2005) J Am Chem Soc 127:7920
34. Cao YY, Yang GW (2012) J Phys Chem C 116:6233
35. Song JH, Wang XD, Riedo E, Wang ZL (2005) J Phys Chem B 109:9869
36. Wang X, Song J, Summers CJ, Ryou J-H, Li P, Dupuis RD, Wang ZL (2006) J Phys Chem B 110:7720
37. Govatsi K, Chrissanthopoulos A, Dracopoulos V, Yannopoulos SN (2014) Nanotechnology 25:215601
38. Shi Z-F, Zhang Y-T, Cai X-P, Wang H, Wu B, Zhang J-X, Cui X-J, Dong X, Liang H-W, Zhang B-L, Dua G-T (2014) CrystEngComm 16:455
39. Xu S, Wang ZL (2011) Nano Res 4:1013
40. Xu S, Lao C, Weintraub B, Wang ZL (2008) J Mater Res 23:8
41. Xu S, Adiga N, Ba S, Dasgupta T, Jeff Wu CF, Wang ZL (2009) ACS Nano 7:1803

Chapter 15
Structural and Optical Properties of Electrochemically Deposited Nanostructured ZnO Arrays on Different Conductive Substrates

M. Petrov, K. Lovchinov, H. Nichev, D. Karashanova, and D. Dimova-Malinovska

Abstract In this paper we report results of a study of the structural and optical properties of ZnO nanostructured (NS) array layers electrochemically deposited on different conductive substrates. The following types of substrates have been used: (i) conductive multilayer stack structures glass/ZnO:Al/Ag/ZnO:Al and glass/Ag/ZnO:Al/Ag/ZnO:Al, (ii) conductive multilayer stack structures glass/ZrO_2/Ag/ZrO_2, and (iii) ITO on the front side of Si heterojunction solar cells (SHJ). An analysis of the surface morphology of ZnO NS layers was performed by means of scanning electron microscopy (SEM). It was observed that the morphology of the deposited ZnO structures strongly depends on the type of the substrate used. It was also found that ZnO NS array with different shapes such as nanorods (NRs) or nanowhiskers (NWs) are grown. Reflection spectra of ZnO NS have been recorded. It was found that the deposited ZnO NS layers on the conductive multilayer stacks lead to decreasing reflectance but increasing diffuse reflection. In the case of ZnO NS growth on ITO on the front side of SHJ both direct and diffuse reflection decrease. Possible applications of ZnO NR or NW structures for production of advanced Si-based solar cells are discussed.

Keywords ZnO nanostructures • Optical properties • Reflection spectra • ARC

M. Petrov (✉) • K. Lovchinov • H. Nichev • D. Dimova-Malinovska
Central laboratory of Solar Energy and New Energy Sources, Bulg. Acad. Sci., bulv., Tzarigradsko chaussee, 72, Sofia 1784, Bulgaria
e-mail: petrov80@abv.bg

D. Karashanova
Institute of Optical Materials and Technologies, Bulgarian Academy of Sciences, Acad. G., Bonchev str., bl. 109, Sofia 1113, Bulgaria

P. Petkov et al. (eds.), *Nanoscience Advances in CBRN Agents Detection, Information and Energy Security*, NATO Science for Peace and Security Series A: Chemistry and Biology, DOI 10.1007/978-94-017-9697-2_15

15.1 Introduction

ZnO based nano-structured (NS) layers with nanometer-sized features have very large surface areas per unit volume, which offers a possibility to improve the light harvesting properties of solar cells when such layers are used as a substrate for the deposition of thin film solar cells or as antireflection coatings (ARC) on the top side of the solar cells. One of the methods of fabrication of ZnO layers with nanostructures is electrochemical deposition [1–3]. It offers some advantages: it is a low cost non-vacuum method and is suitable for industrial application.

This paper reports a study of the optical and structural properties of electrochemically deposited ZnO nanolayers on different conductive substrates: (i) -conductive multilayer stack structures glass/ZnO:Al(20 nm)/Ag(20 nm)/ ZnO:Al(20 nm) (in the following: three-layer stack), glass/Ag(100 nm)/ZnO:Al(20 nm)/Ag(20 nm)/ZnO:Al(20 nm) (in the following: four-layer stack), (ii) conductive multilayer stack structures glass/ZrO_2(9 nm)/Ag(20 nm)/ZrO_2(9 nm); and (iii) ITO covered front sides of Si heterojunction (SHJ) solar cells. Multilayer stacks with Ag nanograins as substrates for ZnO NS deposition are due to their plasmonic properties of great interest for application as a back reflector in thin film solar cells for advanced light trapping concepts [4, 5]. Nanostructured ZnO arrays deposited on the front (top) side of thin film solar cells with appropriate optical properties can be used as ARC. The optical properties of ZnO NS arrays (direct reflectance and diffuse reflection) are demonstrated and discussed.

15.2 Experimental

ZnO layers were deposited by mean of an electrochemical process in an aqueous solution of $ZnCl_2$ and KCl using a electrochemical three-electrode cell with a saturated calomel electrode (SCE) as reference electrode [6, 7]. The electrolyte contents $ZnCl_2$ (5×10^{-4} M) and KCl (1 M) with pH ~ 5. The deposition temperature was 80 °C. The deposition was carried out controlling the potential by a high power potentiostat system WENKING HP 96. Since the potential of Zn in the electrolyte is −1.05 V vs. SCE, the deposition process of ZnO was carried out at −1.0 V vs. SCE to prevent deposition of metallic Zn. Good quality ZnO films were obtained at a redox potential within the range between +0.30 and +0.40 V vs. SCE. At a redox potential higher than +0.4 V zinc peroxide (ZnO_2) was formed on the samples with a poor adhesion to the substrate. A spectrally pure graphite plate was used as an anode. The electrolyte was agitated by a magnetic stirrer. Different kind of materials were used as conductive substrates for ZnO layer growing: as described above. The duration of the process was 1.5 min in the case of the deposition on ITO on solar cells and 60 min for the deposition on the other substrates. The method of SHJ solar cells fabrication was described in [8]. The sheet resistance of the three-layers stack and the ZrO_2/Ag/ZrO_2 stacks was 7 and 3 Ω/sq, respectively, that of ITO 60 Ω/sq (measured on an ITO/glass substrate). The electrical contact to the substrates during the electrochemical

deposition was made to the Ag films in the four-layer stacks and to the frontal Ag grid of the SHJ solar cells.

The surface morphology of the deposited films were studied by scanning electron microscopy (SEM) Philips 515. The optical spectra were measured by a spectrophotometer Shimadzu UV-3,600 in the range of 320–1,200 nm employing a 60 mm integrating sphere in the case of diffuse reflection spectra measurements.

15.3 Results and Discussion

15.3.1 Three-and Four-Layer Ag/ZnO Stacks

The SEM micrographs of the ZnO NS layers deposited on seeding three- and four-layers stack structures are shown in Fig. 15.1b, d. For comparison the micrographs of the corresponding seeding stacks are presented in Fig. 15.1a, c, as well, where Ag nanograins with sizes of about 10–20 nm are seen. In the four-layer seeding stack the Ag nano-grains are slightly larger and closer situated as compared to the three-layer stack as reported earlier [4]. The pictures of the electrodeposited ZnO layers exhibit the view of the films surface which consists of planar hexagonal ZnO nanowhickers (NW) with thicknesses of about 500 nm and different lengths in the range 5–6 μm, stacked with the narrow side to the substrate surface. In the case of deposition on the four-layer stack a slightly denser distribution of the whiskers on the surface area is observed as compared to the layers on three-layer stack substrates, probably due to the better homogeneity of the applied electrical field due to the thicker Ag layer in the seeding stacks.

Figure 15.2 shows reflectance and diffuse reflection spectra and the haze ratio in reflection of the ZnO layer deposited on a three-layer seeding stack substrate glass/ZnO:Al/Ag/ZnO:Al. For comparison the corresponding spectra of the seeding stack structure are presented as well. After ZnO NW deposition the values of the specular reflectance of the sample decreases while those of the diffuse reflection and the haze ratio increase. The maximum of the diffuse reflection of 30 % is observed for wavelengths >750 nm. The haze ratio in reflection is higher than 90 % in the wavelength range 400–800 nm and is >60 % for wavelengths >800 nm. The presence of weak plasmonic bands at about 370–380 nm in the spectra of diffuse reflection of the seeding stack structures and also in the electrochemically grown ZnO NW layers should be noted. The reflectance diffuse reflection spectra and the haze ratio in reflection of the ZnO layers on four-layer-stacks are displayed in Fig. 15.3. Similar to the case of ZnO NW layers deposited on three-layer seeding stacks, the values of reflectance decrease compared to the reflectance of the seeding steak while those of diffuse reflection and the haze ratio in reflection increase in the whole spectral region investigated. The values of diffuse reflection are higher than those in the case of deposition on three-layer stacks and are between 60 and 70 % in the spectral range 500–1,200 nm probably due to the presence of larger Ag nanograins as SEM demonstrated by SEM.

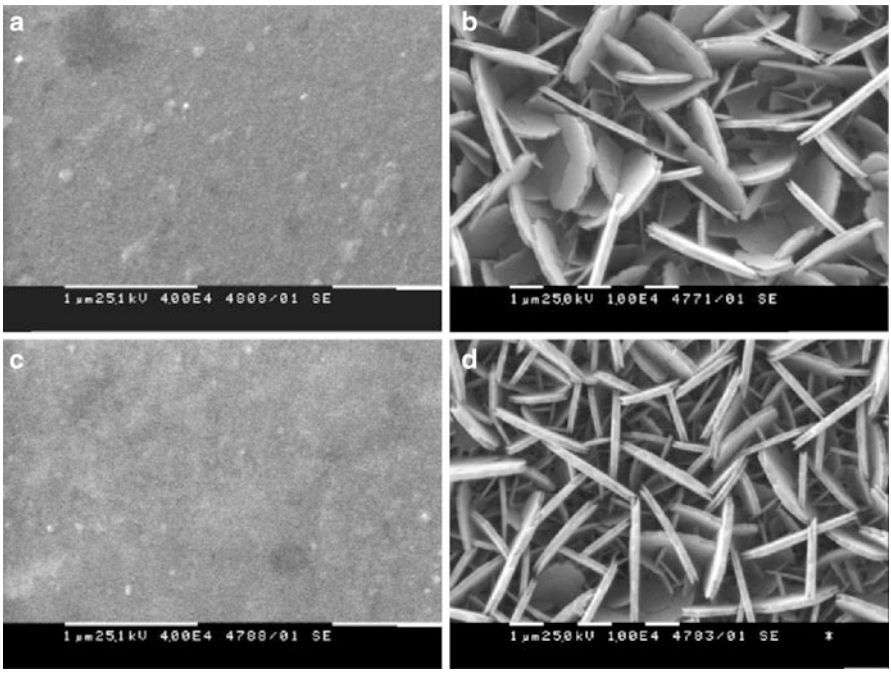

Fig. 15.1 SEM micrographs of ZnO layers deposited on three- (**b**) and four-layer seeding stacks (**d**). For comparison the micrographs of the corresponding seeding stacks are presented too: (**a**) and (**c**). The bars correspond to 1 μm

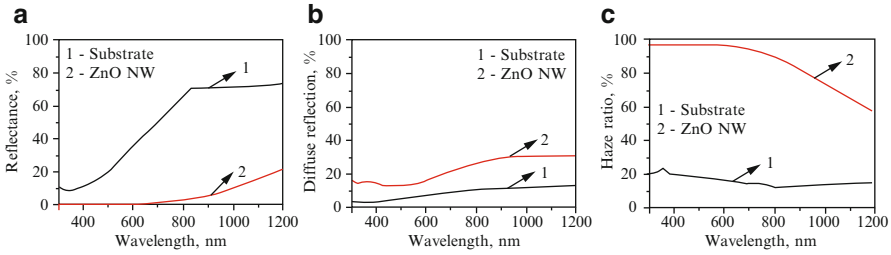

Fig. 15.2 Spectra of reflectance (**a**) and diffuse reflection (**b**) and the haze in reflection (**c**) of ZnO layers electrochemically deposited on glass/ZnO:Al/Ag/ZnO substrates. For comparison the corresponding spectra of the seeding stack structures (curves 1) are presented, as well

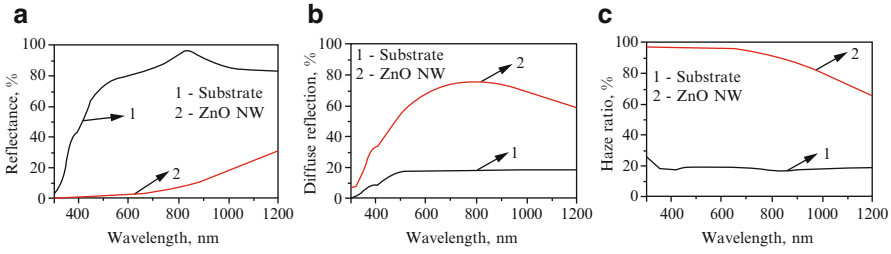

Fig. 15.3 Spectra of reflectance (**a**) and diffuse reflection (**b**) and the haze in reflection (**c**) of ZnO layers electrochemically deposited on glass/Ag/ZnO:Al/Ag/ZnO substrates. For comparison the corresponding spectra of the seeding stack structures (curves 1) are presented, as well

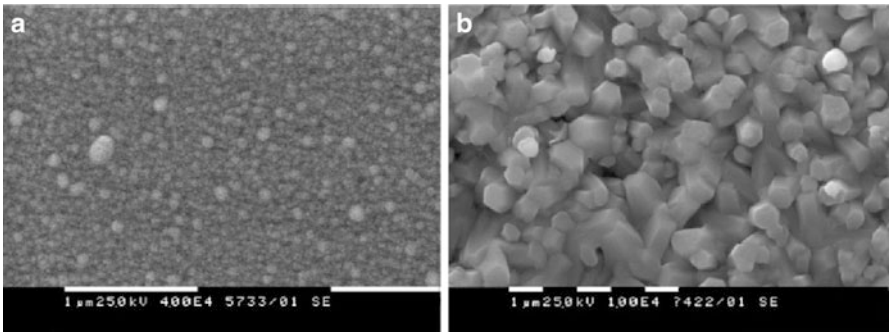

Fig. 15.4 SEM of a ZrO_2/Ag/ZrO_2 seeding stack (**a**) and of the ZnO NS array layer deposited thereon (**b**). The markers in both pictures correspond to 1 µm

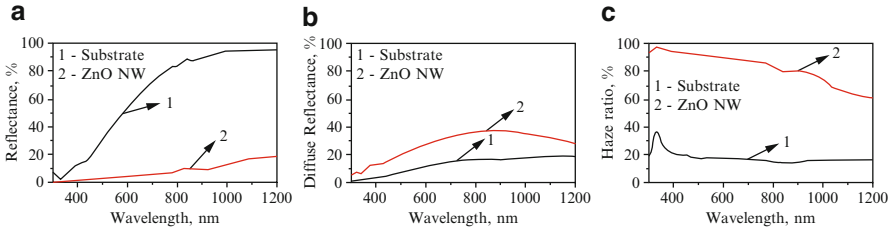

Fig. 15.5 Spectra of reflectance (**a**), diffuse reflection (**b**) and haze in reflection (**c**) of ZnO layers electrochemically deposited on glass/ZrO_2/Ag/ZrO_2 substrates. For comparison the corresponding spectra of the seeding stack structures (*curves 1*) are presented as well

15.3.2 *ZnO NS Deposited on Seeding Three-Layer Stacks ZrO_2/Ag/ZrO_2*

A SEM image of a ZnO NS array deposited on highly conductive seeding films glass/ZrO_2/Ag/ZrO_2 is presented in Fig. 15.4. Deposition and properties of the seeding layers are described in reference [9]. Ag grains about 90–100 nm sizes are seen on the surface of the seeding stack. As a result of the electrochemical deposition ZnO nanorods about 0.8–1 µm thickness with a hexagonal shape are grown almost perpendicular to the substrate. Probably the presence of large Ag metal grains in the seeding stack favorites the growth of rod-like nanostructures. Reflectance and diffuse reflection spectra and the haze ratio of the ZnO NS are shown in Fig. 15.5 and compared with the optical spectra of the seeding stack. As in the case of the ZnO:Al-based stacks the values of reflectance decrease, while the diffuse reflection and the haze ratio increase. The diffuse reflection is higher than 30 % in the spectral range 600–1,200 nm with a maximal value of 40 % at about 800 nm; it is higher than in the case of ZnO:Al three-layer stacks probably due to the presence of the nanorod array with size lower than the wave length. The band about 380 nm in reflection spectra due to the Plasmon effect is seen, as well.

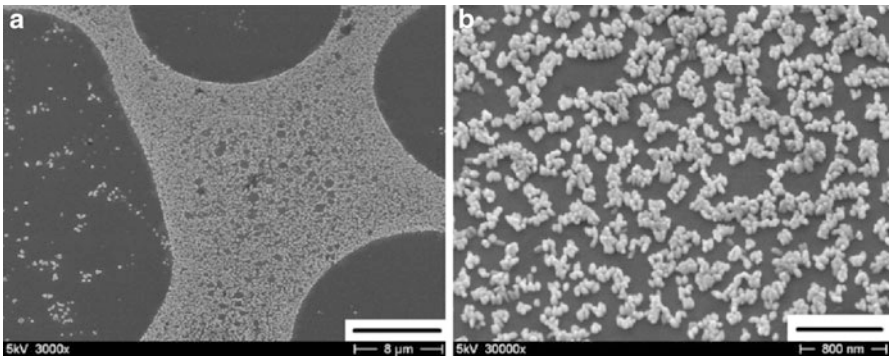

Fig. 15.6 SEM of ZnO NS deposited on the ITO front side of SHJ solar cells. The markers correspond to 8 µm (**a**) and 800 nm (**b**)

15.3.3 ZnO NS Deposited on the ITO Front Contact of SHJ Solar Cells

Nanostructured ZnO films were electrochemically deposited on the surface of the ITO antireflection coating on the front side of SHJ solar cells. In this case the deposition time was 1.5 min. SEM micrographs with different magnifications of the deposited arrays are shown in Fig. 15.6. The ZnO nanograins are very inhomogenously distributed. Large areas of several μm^2 with denser grains are seen (Fig. 15.6a). The grains have sizes of about 100–150 nm and are inhomogeneous scattered leaving uncovered spaces between 50 and 400 nm (Fig. 15.6b).

Figure 15.7 shows reflectance, diffuse reflection and total reflection spectra of the ZnO NS. After deposition of ZnO NS the values of reflectance, diffuse reflection and total reflection decrease. The haze ratio in reflection increases in the whole spectral region. This result demonstrates good antireflection properties of the deposited ZnO NS arrays.

The preliminary results of a study of the characteristics of a SHJ solar cell before and after deposition of ZnO NS array show a increase in of the short circuit current and the efficiency by about 12.5 % and 14.2 %, respectively, after deposition of ZnO NS array due to the decreasing reflection from the front side of the solar cell [10]. The results demonstrate that the shape of the ZnO nanostructures grown by electrochemical deposition is influenced by the material of the substrate. Nanostructures in the shape of whiskers are grown on seeding stacks with ZnO: Al. Nanostructured arrays with nanorods are deposited on ITO surfaces. ZnO nanostructures leading to an increased diffuse reflection of the substrate can be applied as substrates for thin film solar cells with an increased effective area and improved short circuit current. The ZnO nanostructures leading to decreasing in diffuse and total reflection have good antireflection properties and can be applied as ARC in solar cells for increasing light harvesting.

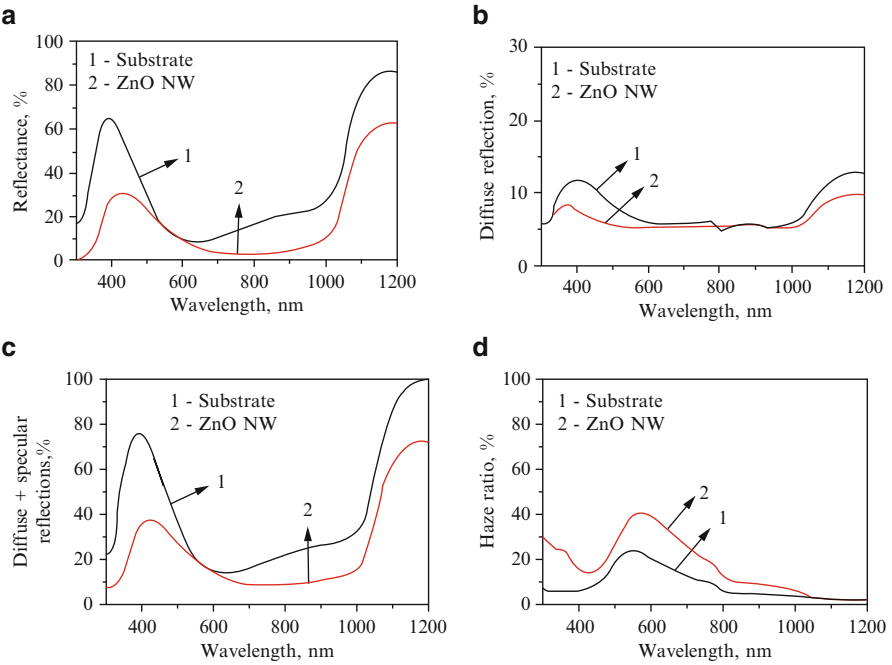

Fig. 15.7 Spectra of reflectance (**a**), diffuse reflection (**b**), total reflection $R + R_{dif}$, (**c**) and the haze ratio in reflectance (**d**) of a ZnO NS array layer deposited on the front side of a SHJ solar cell. The corresponding spectra of the substrate before ZnO NS deposition are shown as well for comparison

15.4 Conclusions

In this work the surface morphology and the optical properties of electrochemically deposited ZnO films on different conductive substrates were studied. The shape of the nanostructures in ZnO layers depends on the structure and the nature of the substrate material used. The ZnO NS layers consist of nano-whiskers in the case of growing on multilayer stacks ZnO:Al/Ag/ZnO:Al or hexagonal nanorods in the case of growth on ZrO_2/Ag/ZrO_2 stacks and ITO. The deposition of ZnO NS on conductive multilayer stacks results in an increase of the diffuse reflection due to the presence of nanosized features and a rough surface. It was shown that electrochemically deposited ZnO NS on ITO/SHJ leads to a decrease of the reflectance and the diffuse reflection and demonstrates good antireflecting properties. As the preliminary experiments show the electrochemically deposited ZnO nanostructures (nanowiskers and nanorods) can be applied for increased light harvesting and improvement of the parameters of solar cells.

Acknowledgements This work has been funded by the 7 European FP (project NanoPV № 24331) and the Bulgarian National Scientific Fund (project № 859/2012). The authors thank Dr. O. Angelov for the deposition of the multilayer stack substrates.

References

1. Kopenkamp R, Boedecker K, Lux-Steiner MC, Poschenrieder M, Zenia F, Levy Clement C, Wagner S (2000) Appl Phys Lett 77:2575
2. Dimova-Malinovska D, Lovchinov K, Ganchev M, Angelov O, Graff JS, Ulyashin A (2013) Phys Status Solidi A 210:737
3. Lovchinov K, Nichev H, Angelov O, Mikli V, Dimova-Malinovska D (2012) Adv Nat Sci: Theory Appl 1:61
4. Lovchinov K, Petrov M, Angelov O, Nitchev H, Karachanova D, Dimova-Malinovska D (2013) Procc. 28 EUPVSEC E, 26–30 Sept, Paris, France, 408:12
5. Tan H, Santbergen R, Smets AHM, Zeman M (2012) Nano Lett 12:4070
6. Mews M, Schulze TS, Mingirulli N, Korte L (2013) Energy Procedia 38:855
7. Dimova-Malinovska D, Nichev H, Angelov O, Grigorov V, Kamenova M (2007) Superlattice Microst 42:123
8. Lovchinov K, Ganchev M, Petrov M, Nichev H, Rachkova A, Angelov O, Mikli V, Dimova-Malinovska D (2013) Phys Status Solidi A 210:743
9. Dimova-Malinovska D, Lovchinov K, Petrov M, Karashanova D, Angelov O (2014) Phys Status Solidi A. doi: 10.1002/pssa201431492 (in press)
10. Petrov M, Lovchinov K, Ganchev M, Lendeetz C, Dimova-Malinovska D (2013) Proc Sci Stud 38:157

Chapter 16
Nanofibers for the Detection of VOCs

Nimet Bölgen, Didem Demir, and Ashok Vaseashta

Abstract Volatile organic compounds (VOCs) are significant environmental pollutants and have harmful effects on the human health. In order to detect VOCs, nanofibrous materials received considerable attention due to their unique chemical/physical properties and their high surface area/volume ratio. Electrospun fibers with polyelectrolyte components, conducting polymer composites, and semiconductors were successfully applied as gas sensing interfaces. Increasing the thermal and electrical conductivity of typical insulating polymers, such as nylon-6,6 will allow the development of new and improved ultrasensitive sensors for detection of VOCs. In this study, we report our preliminary results for the production of electrospun Nylon-6,6 nanofibrous matrices after combination with a conductive component for a possible VOC sensor platform. Three dimensional nonwoven nanofibers with various compositions (5,10,15 and 20 wt%) were fabricated by the electrospinning method from Nylon-6,6 polymer solutions dissolved in a 4:1 weight ratio formic acid/acetic acid solution. Chemical and morphological structure of the electrospun matrices were studied by FT-IR and SEM, respectively. The electrospun Nylon-6,6 membranes demonstrated nanofibrous structures with fiber sizes ranging between 32 and 103 nm. By varying the polymer concentration and the conductivity of the polymer solution, changes of the size and the morphology of the final structures are observed.

Keywords VOCs • Gas sensor • Electrospinning • Polymeric nanofibers • Nylon-6,6

N. Bölgen (✉) • D. Demir
Chemical Engineering Department, Engineering Faculty, Mersin University, Mersin, Turkey
e-mail: nimet@mersin.edu.tr

A. Vaseashta
Institute for Advanced Sciences Convergence, and Int'l Clean Water Institute, NUARI, 13873 Park Center Rd., Ste: 500, Herndon, VA, USA

P. Petkov et al. (eds.), *Nanoscience Advances in CBRN Agents Detection, Information and Energy Security*, NATO Science for Peace and Security Series A: Chemistry and Biology, DOI 10.1007/978-94-017-9697-2_16

16.1 Introduction

Volatile organic compounds (VOCs), such as methanol (CH_3OH), ethanol (C_2H_5OH), toluene ($C_6H_5CH_3$), chloromethane (CH_3Cl_3), hydrazine (N_2H_4), dimethylformamide (C_3H_7NO) are harmful as the vapors of these VOCs are flammable, harmful to human and animal health or detrimental to the ozone layer even in very low concentrations [1]. The amount of these compounds in the atmosphere must be controlled not to reach a standard exposure limit [2]. Therefore, much research is ongoing to develop gas sensors which can detect the different toxic gases to monitor environmental chemical pollution.

Gas sensors based on nanofibers that are fabricated from polymers possess considerable advantages when compared with other types of sensors: among them are room temperature operation, the use of low cost materials, sensitivity, selectivity, rapid response and flexibility of chemical structure, durability and reproducibility [3, 4]. Electrospinning is a well known process to produce continuous polymer fibers with diameters ranging from several nanometers to a few micrometers through the action of a strong electrostatic field [5]. The parameters affecting the morphology, nanofiber size, mechanical integrity, surface area and porosity of the electrospun matrices are the type and concentration of the polymer, the viscosity and conductivity of the polymeric solution, the voltage applied and the feeding rate of the syringe pump [3, 6]. Electrospun nanofibers with their porous structure and high surface-to-volume ratio can not only be used for sensors for VOC detection, but are highly promising materials that can be used in studies for various applications such as controlled drug delivery, enzyme immobilization, as scaffolds in tissue engineering, wound dressings, protective clothing, military wear with chemical and biological toxin-resistance, filtration, biosensors, cosmetics, etc. [7].

Nylon-6,6 (a polyamide) is one of the most widely used engineering thermoplastic due to its excellent physical and mechanical properties [8]. The significant properties of Nylon-6,6 are its toughness, fatigue resistance, low friction, abrasion resistance, resistance to oils and solvents, stability at high temperature, fire resistance, creep resistance, drawability, good appearance, good molding economics, low density and ease of fabrication [9]. In this study electrospun nanofibers made from Nylon-6,6 are produced by using an electrospinning technique for a possible future application as a VOC sensor.

16.2 Materials and Methods

16.2.1 Preparation of Electrospun Nylon-6,6 Nanofibers

Nylon-6,6 was dissolved in glacial acetic acid (100 %, v/v) (Merck, Germany) and formic acid (98 %, v/v) (Panreac, Spain) at different polymer concentrations (5,10,15 and 20 wt%). The ratio of acetic acid to formic acid was kept constant at 4:1 (v/v). The polymer solutions were stirred at room temperature by a magnetic stirrer during 2 h at 1,000 rpm to obtain a clear and homogeneous solution.

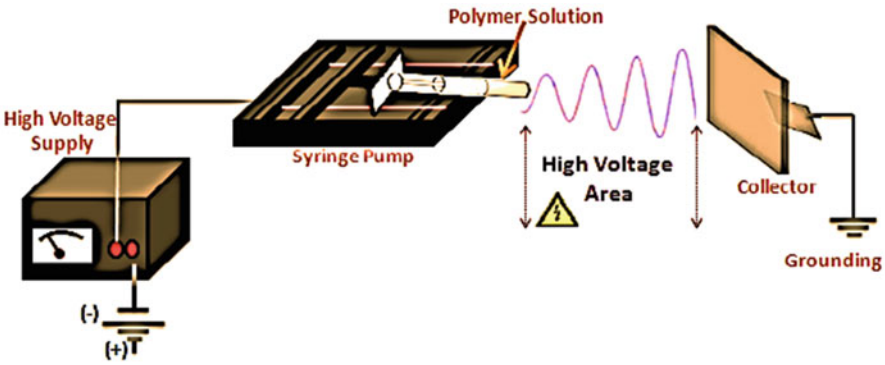

Fig. 16.1 Schematic illustration of the electrospinning set up

A generic electrospinning apparatus and the process used are shown in Fig. 16.1. It consists of a plastic syringe, a syringe pump (New Era, NR-300, USA), a high voltage power supply (Gamma High Voltage Research, ES50, USA) and a metal collector covered by aluminum foil. A solution consisting of 2 mL of desired composition was loaded in a 2.5 ml syringe with a metallic needle of 0.2 mm inside diameter. The syringe was placed in a horizontal position on a syringe pump; an electric field was supplied from the high voltage power supply to the needle of the syringe. The polymer solutions were electrospun at 20 kV, the needle-tip to collector distance was 15 cm and feed rate of the polymer solution was ~0.6 mLh^{-1}. After the electrospinning process was completed, the nanofibers were dried overnight. All experiments were carried out at room temperature.

16.2.2 Characterization of Nylon-6,6 Nanofibers

16.2.2.1 Fourier Transform Infrared Spectroscopy (FTIR)

A FTIR spectrometer (Perkin-Elmer Spectrum 1000, USA) was used to determine the chemical compositions of the produced materials. The spectra were recorded in the range of 550–4,000 cm^{-1} with automatic signal gain with 10 scans at a resolution of 4 cm^{-1}.

16.2.2.2 Scanning Electron Microscopy (SEM)

The morphology of the nanofibrous structure of the materials were investigated by SEM (SEM, Quanta 400 F Field Emission, Supra 55, Zeiss, Germany) at an accelerating voltage of 5 kV. The specimens were coated with platinum before SEM analysis. The diameters of the nanofibers were identified by using Lucia 32G image analysis software. The fiber diameters given were the average of 10 nanofibers.

16.3 Results and Discussion

Nylon-6,6 nanofibrous materials were prepared by using an electrospinning technique. Polymer solutions were prepared with at concentrations of 5, 10, 15 and 20 wt%. The polymer concentration has a significant effect on the production of homogeneously distributed nanofibrous membranes by electrospinning. If the polymer concentration is lower than the optimal value, the viscosity of the solution decreases, the solvent or solvent mixture does not evaporate before reaching the collector and neither nanofibers nor a nanofibrous membrane can be obtained. Contrarily, if the polymer concentration is higher than the optimal value, the viscosity of the solution increases and the voltage applied is not able to push the solution across the collector. In this study, opaque films were obtained on the collector at each concentration, however in the case of 5 wt% polymer concentration, drops formed on the collector and a powder like structure was obtained which could not be removed from the surface of aluminium collector (Fig. 16.2a). In the case of the electrospun material prepared from 10 wt%. Nylon-6,6, a very thin film was formed on the collector, while drops and the powder like structure was not observed. However, it was not possible to remove the film from the collector; therefore, this material was found not to be suited for future application (Fig. 16.2b). It was possible to produce a membranous structure which could be easily removed from the collector in the case of materials produced from 15 % and 20 wt% polymer solutions (Fig. 16.2c, d).

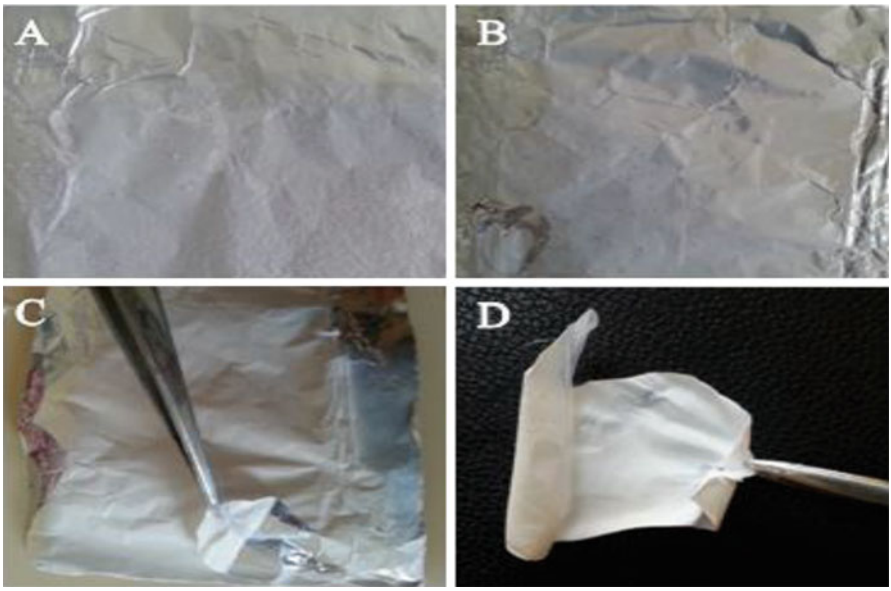

Fig. 16.2 The images of electrospun matrices prepared at different Nylon-6,6 concentrations: (**a**) 5 %, (**b**) 10 %, (**c**) 15 %, (**d**) 20 wt%

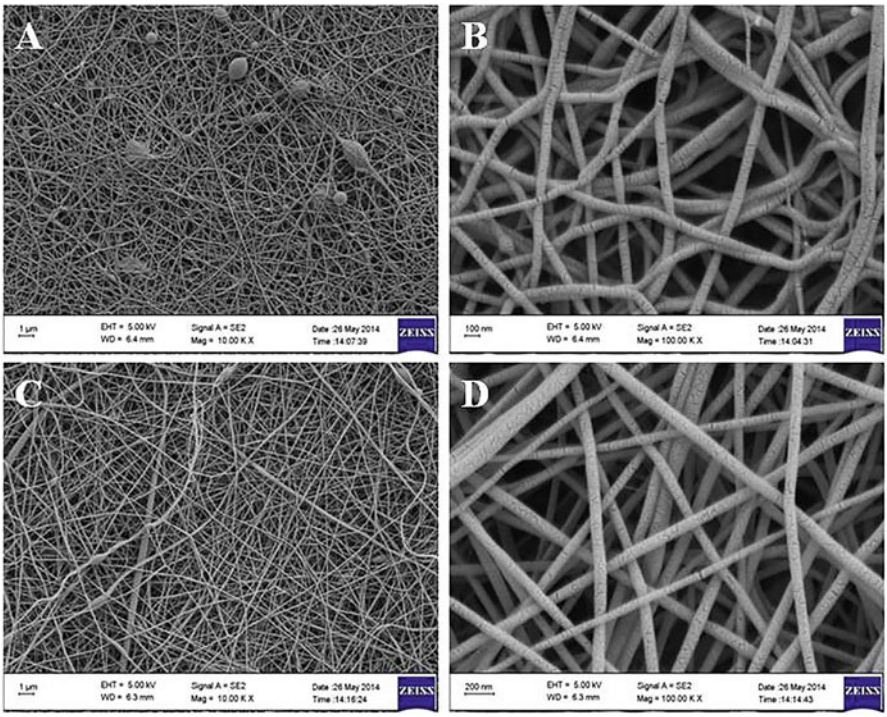

Fig. 16.3 SEM photographs of the fabricated nanofibrous samples with different Nylon-6,6 polymer concentrations and magnifications: (**a**) 15 %, 10,000× (**b**) 15 % 100,000×, (**c**) 20 % 10,000×, (**d**) 20 %, 100,000×

Since the nanofibers prepared from Nylon-6,6 with concentrations of 15 % or 20 wt% were more suited for future applications, SEM image of these samples were recorded; they are presented in Fig. 16.3, which demonstrates the morphology of the Nylon-6,6 nanofibers at low and high magnifications (10,000× and 100,000×, respectively). Beads are present in the membranes prepared at 15 % polymer concentration (Fig. 16.3a). Increasing the polymer concentration to 20 % enhanced the uniformity of the nanofibers, while the amount of beads decreased significantly (Fig. 16.3c). In addition, the increase in the polymer concentration affected the fiber diameters (Fig. 16.3b, d). The range of the diameter of the nanofibers was between 32–90 nm and 54–103 nm, with average fiber diameter of 66.228, 72.056 nm, for the nanofibrous membranes prepared from solutions with a polymer concentration of 15 % and 20 %, respectively. Our previous studies supported that the nanofiber diameter increases as the polymer concentration increases [10].

FTIR spectra of Nylon-6,6 nanofibrous materials are presented in Fig. 16.4. The chemical structure of Nylon-6,6 is evident; the FTIR diagram shows the characteristic peaks of Nylon-6,6 which are listed in Table 16.1 [11]. The spectra did not change after applying the electrospinning process [12].

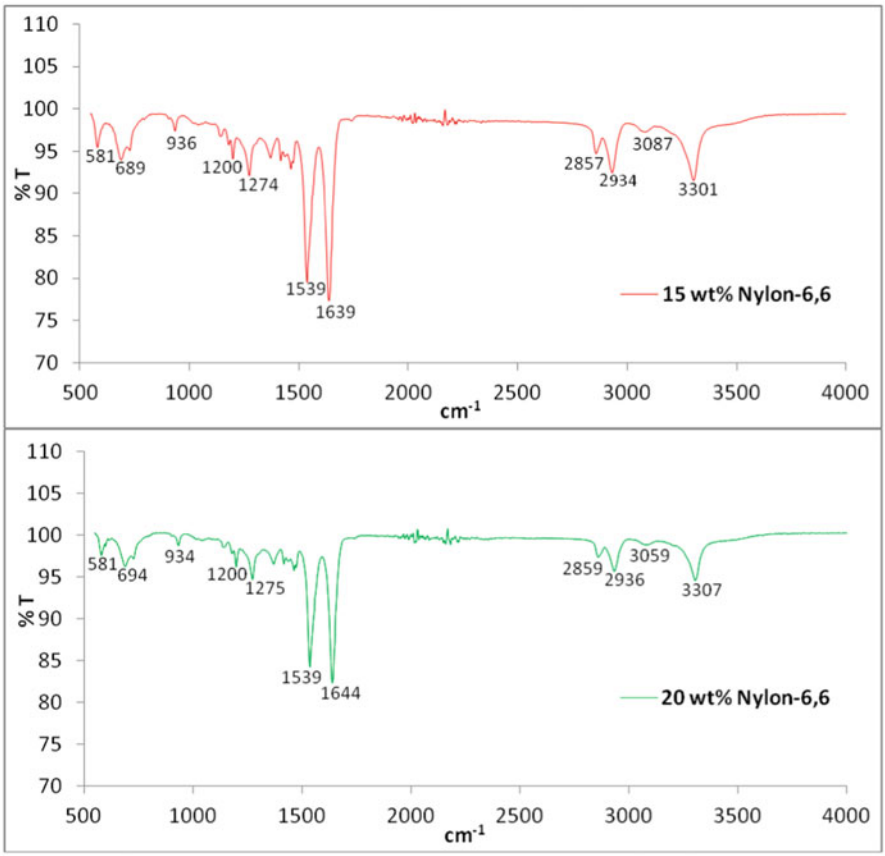

Fig. 16.4 FTIR spectra of nanofibrous Nylon-6,6 materials prepared at different polymer concentrations

Table 16.1 Characteristic FTIR peak assignment of Nylon-6,6

Wave number, cm^{-1}	Transmission, % T	Assignment
3,301–3,307	91.64–94.62	N – H stretching
3,059–3,087	99.02–97.33	C – H stretching (asymmetric)
2,934–2,936	92.51–95.70	CH_2 stretching (asymmetric)
2,857–2,859	94.83–97.36	CH_2 stretching (asymmetric)
1,639–1,644	77.38–82.74	Amide – I stretching
1,539	84.24	Amide – II stretching
1,274–1,275	92.13–94.69	Amide – III stretching
1,200	96.16	CCH bending/CH_2 twisting
934–936	98.76–97.44	C – C stretching
689–694	94.00–96.33	C – C bending
581	97.55	C – C deformation

16.4 Conclusions

As a conclusion, in this study Nylon-6,6 nanofibrous materials were prepared by electrospinning at different polymer concentrations. The polymer concentration affects on the uniformity and fiber diameter of the samples, which would in turn affect the surface area and the sensing capability of the final material produced. Template synthesis, self-assembly, phase separation and electrospinning are some of the various techniques used to produce nanofibers. Among them, electrospinning is an efficient, relatively simple and cost-effective technique to produce polymer and composite fibers with diameters ranging from several nanometers to a few micrometers by applying a high voltage to a polymer solution or melt. Many kinds of materials such as polymers, semiconductors and organic/inorganic composites have been used to produce high performance sensing materials to detect the targeted gases. A variety of electrospun nanofibrous materials were produced from a variety of polymers including polyacrylic acid, polyaniline, polyethyleneoxide, nylon, polyacrylonitrile, polymethyl methacrylate, to be used as gas sensors. Electrospun fibers with polyelectrolyte components, conducting polymer composites, and semiconductors are successfully applied as gas sensing interfaces. The types of gas sensors prepared mainly include acoustic wave, resistive, photoelectric, and optical gas sensors. This manuscript presents our preliminary studies on the production of Nylon-6,6 nanofibers by electrospinning, for possible preparation of a sensor to detect VOCs, after combining with a conductive component such as polyaniline. Further studies are ongoing.

References

1. Huang ZM, Zhang YZ, Kotaki M, Ramakrishna S (2003) Compos Sci Technol 63:2223
2. Ding B, Wang M, Yuand J, Sun G (2009) Sensors 9:1609
3. Bai H, Shi G (2007) Sensors 7:267
4. Jin M, Zhang X, Pu H, Nishimoto S, Murakami T, Fujishima A (2011) J Colloid Interface Sci 362:188
5. Jorgensen RB (2007) Build Environ 42:1913
6. Nam K, Pant HR, Jeong J, Pant B, Kim B, Kim H (2011) Polym Degrad Stab 96:1984
7. Ding B, Kim J, Miyazaki Y, Shiratori S (2004) Sensors Actuators B 101:373
8. Ristolainen N, Heikkila P, Harlin A, Seppala J (2005) Macromol Mater Eng 291:114
9. Li Y, Huang Z, Lü Y (2006) Eur Polym J 42:1696
10. Bölgen N, Menceloğlu YZ, Acatay K, Vargel I, Pişkin E (2005) J Biomater Sci-Polym Ed 16:1537
11. Mahdi HA, Ibn al-Haitham (2011) J Pure Appl Scı 24
12. Charles J, Ramkumaar GD, Azhagiri S, Gunasekaran S (2009) E-J Chem 6:22

Chapter 17
Electrophysical Characteristics of Polystyrene/MWCNTs Composites Ordered by a Magnetostatic Field

G.S. Gunko, C. Pandis, Yu.M. Bolbukh, G.P. Prikhod'ko, P. Pissis, and V.A. Tertykh

Abstract Polymeric films based on polystyrene filled with multiwalled carbon nanotubes, either pristine, oxidized, or chemically (or adsorption) modified with vinyltriethoxysilane have been studied. An external magnetic field with different orientations of the force lines with respect to the film surface was applied to regulate the filler orientation within the polymer matrix during preparation. The effect of the nature of the filler surface layer on the electrophysical characteristics of the nanocomposites was investigated below the percolation point.

Keywords Carbon nanotubes • Polystyrene films • Conductivity • Dielectric permittivity

17.1 Introduction

Application of carbon nanotubes (CNTs) as a filler for polymers allows to synthesize nanocomposites with principally new properties and to significantly improve their electrical, thermal and mechanical characteristics [1]. The electrical conductivity and the sensitivity of CNTs to external influences (electromagnetic fields, radiation, etc.) can be used effectively in the development of different conductive materials, in particular based on biocompatible polymers [2, 3].

Carbon in the tubular form possesses also unusual magnetic properties. The abnormal high value of the diamagnetic susceptibility of graphite at perpendicular orientation of a magnetic field to the graphite surface is well-known. In such systems the orientation of the nanotubes (nanotube to nanotube and nanotube to the

G.S. Gunko (✉) • Yu.M. Bolbukh • G.P. Prikhod'ko • V.A. Tertykh
Chuiko Institute of Surface Chemistry, National Academy of Sciences of Ukraine,
17 General Naumov Str., Kyiv 03164, Ukraine
e-mail: gunko_galyna@ukr.net

C. Pandis • P. Pissis
Department of Physics, National Technical University of Athens, Athens 15780, Greece

P. Petkov et al. (eds.), *Nanoscience Advances in CBRN Agents Detection, Information and Energy Security*, NATO Science for Peace and Security Series A: Chemistry and Biology, DOI 10.1007/978-94-017-9697-2_17

macromolecules of the polymer matrix) is highly important. Often the desired formation of the composite materials is achieved due to self-organization of the nanotubes. Structures of a required architecture can also be formed by mechanical influence which, however, causes additional production costs. Due to the unique properties of nanotubes the direct formation of a "polymer-nanotubes" system is possible by means of magnetic fields. This approach was realized for the synthesis of composites based on polystyrene [4], epoxide polymers [5] and polyethyleneterephtalate [6].

The chemical activity of nanotubes is caused by the presence of structural defects on the walls and ports mainly by oxygen-containing groups, which are formed during the synthesis and purification of CNTs. The conditions of the purification step determine the type of the oxygen-containing groups and their arrangement. The presence of oxygen-containing groups improves the dispersion of the nanotubes and makes a further modification of their surface possible.

It has to be noted that for successful applications of nanotubes as fillers their fine distribution within the polymeric matrix is highly important. The tendency of nanotubes to aggregate complicates dispersion in liquids. Modification of nanotubes facilitates a more uniform distribution of the filler within matrix; in some cases it provides a chemical interaction between filler and polymer.

The aim of this work was to determine the dependence of the electrophysical properties of composites on their structure. The investigations were carried out with materials based on polystyrene filled with pristine, oxidized or chemically (or adsorption) modified carbon nanotubes. In order to regulate the filler orientation within the polymer matrix the synthesis was carried out in the presence of an external magnetic field with different orientations of the force lines with respect to the surface of polymeric film.

17.2 Experimental

Multiwalled carbon nanotubes (MWCNTs) synthesized by pyrolytic decomposition of propylene over an iron-containing catalyst with further purification in a mixture of HCl and HF [7] and with a specific surface area of 180 m^2/g were used in this work. Functionalization with simultaneous opening of the nanotube ports was performed by oxidation in hydrogen peroxide (50 wt%). under continuous stirring for 40–47 h at 80–90 °C [8]. Under these treatment conditions phenol groups are formed on the nanotube surface predominantly with higher concentration on ports.

Adsorption modification of the pristine and oxidized nanotubes was carried out in solution of vinyltriethoxysilane in toluene. A homogeneous distribution of the nanotubes in the solution was achieved by ultrasonication at a frequency of 22 kHz for 30 min; then the required quantity of alkoxysilane was added in order to modify the nanotube surface. Modification was carried out for 5 h with continuous stirring at 80 °C. Silane chemisorption was carried out in the presence of a polycondensation initiator. The samples obtained were washed out and dried at 60 °C. Composites were obtained by means of filling polystyrene (dissolved in toluene) with of pristine or modified MWCNTs. During the synthesis an external magnetic field

Table 17.1 Samples used in this study

No	Sample
1	Polystyrene
2	Polystyrene with pristine MWCNTs
3	Polystyrene with pristine MWCNTs, horizontally oriented
4	Polystyrene with pristine MWCNTs, vertically oriented
5	Polystyrene with oxidized MWCNTs
6	Polystyrene with oxidized MWCNTs, horizontally oriented
7	Polystyrene with oxidized MWCNTs, vertically oriented
8	Polystyrene with pristine MWCNTs with adsorbed vinyltriethoxysilane
9	Polystyrene with pristine MWCNTs with adsorbed vinyltriethoxysilane, horizontally oriented
10	Polystyrene with pristine MWCNTs with adsorbed vinyltriethoxysilane, vertically oriented
11	Polystyrene with oxidized MWCNTs with adsorbed vinyltriethoxysilane
12	Polystyrene with oxidized MWCNTs with adsorbed vinyltriethoxysilane, horizontally oriented
13	Polystyrene with oxidized MWCNTs with adsorbed vinyltriethoxysilane, vertically oriented
14	Polystyrene with oxidized MWCNTs with chemisorbed vinyltriethoxysilane
15	Polystyrene with oxidized MWCNTs with chemisorbed vinyltriethoxysilane, horizontally oriented
16	Polystyrene with oxidized MWCNTs with chemisorbed vinyltriethoxysilane, vertically oriented

(with different directions of the magnetic lines to the polymer plane) was applied in order to align the nanotubes within the polymer matrix. All samples were obtained in form of films by distributing the casting solution over a glass substrate.

The Magnetic field was provided by a flat permanent magnet with an induction of 0.039 T. The filling degree of the composites was 0.1 wt% for all samples. A list of the composite samples is given in Table 17.1.

The investigation of the electrical properties of the synthesised materials was carried out in the frequency range of 10^{-4}–10^{6} Hz using a Keithley Nanovoltmeter 2182A and a Novocontrol Alpha dielectric analyzer.

17.3 Results and Discussion

17.3.1 The Dielectric Permittivity of Composites with Pristine and Oxidized Nanotubes

Polystyrene is a dielectric, i.e. a compound with a low content of free charge carriers. However, the presence of conjugated bonds in the structure stipulates a certain conductivity. Filling of the polystyrene with nanotubes, which have conductive properties will improve the electrical properties of the resulting composite.

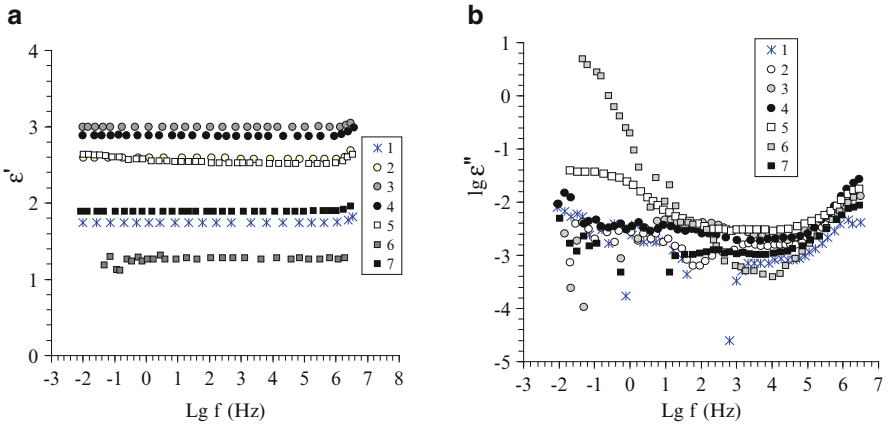

Fig. 17.1 Frequency dependences of the real (**a**) and the imaginary (**b**) parts of the dielectric permittivity for unfilled polymer (**1**) and composites **2**–**7** (Table 17.1)

The conductivity results in a displacement of electric charges under the influence of an applied voltage. The degree of the polarization is characterized by the value of the dielectric permittivity of the material [9]. Figure 17.1 shows the frequency dependence of the real part ε' and the imaginary part ε'' of the dielectric permittivity for composites filled with pristine and oxidized MWCNTs. Composites filled with nanotubes were found to have a higher value of ε' compared to a pure polystyrene (Fig. 17.1a), therefore the electrokinetic mobility (polarisation) filled composites is higher.

The increase of the real part of the dielectric permittivity for the filled polystyrene films is associated with an orientation of pseudocrystalline structures within the polymeric film [10]. Within the range of the frequencies investigated the dependence of ε' has a linear character, whereas the frequency dependence of ε'' has some extrema. For composites filled with pristine nanotubes maxima of resonance absorption are observed at $10^{-1.5}$, $10^{-0.3}$, $10^{0.5}$ and $10^{3.5}$ Hz; there is also a wide peak at $10^{6.3}$ Hz which is typical for all samples. With increasing frequency all peaks becomes broader as a consequence of an increase of the polarization relaxation times.

Maxima of the resonant absorption for the composite filled with oxidized nanotubes are observed at $10^{-0.5}$ and $10^{6.5}$ Hz only, they reflect a different mechanism of polarization within this sample.

The presence of many peaks in the frequency dependence of ε'' in a relatively narrow range of frequencies (Fig. 17.1a, curves 1 and 2) indicates a relaxation dispersion that leads to relaxation losses.

Since the value of the dielectric permittivity depends on the orientation of pseudocrystalline structures, an increase of ε' for materials obtained under the influence of an external magnetic field indicates an increase of the electrokinetic mobility of the structure [11] (Fig. 17.1, curves 3 and 4) and also an increase of the dielectric permeability due to the specific orientation of the pseudocrystalline

structures. It should be noted that a perpendicular orientation of the film to the magnetic lines of the applied field during the synthesis has no significant influence on the ε'' value. Thus the absorption resonance is low and the polarization mechanism is similar in the entire frequency range.

The direction of the magnetic lines of the field applied during the synthesis of composites 6 and 7 have more considerable impact on the dielectric permittivity of the materials as compared to samples 3 and 4. The real part of the dielectric permittivity decreases (Fig. 17.1a, curves 6 and 7), which indicates a decrease of electrokinetic mobility of the structure. A low value of ε' and a vertex value of ε'' (and thus the dielectric loss) were observed for composite **6** which was synthesized with an orientation of the film parallel to the lines of the applied field.

17.3.2 Composites Filled with Vinyltriethoxysilane-Modified Nanotubes

Figure 17.2 shows the frequency dependences of ε' and ε'' for composites filled with pristine and oxidized MWCNTs absorption-modified with vinyltriethoxysilane. The presence of the vinylsilane adsorbed in the surface layer of pristine or oxidized MWCNTs leads to a decrease of ε' in the final composite (Figs. 17.1 and 17.2).

The profiles of the frequency–dependent dielectric response of samples **8** and **10** are similar whereas the values of ε' differ considerably (Fig. 17.2). Therefore, the orientation of the magnetic field lines normal to the surface of the film promotes the formation of structures with a lower electrokinetic mobility but with an intensive resonance absorption; the mechanism of polarization and the relaxation times are similar to sample **8**. Thus, the distinction in the structure is determined by the

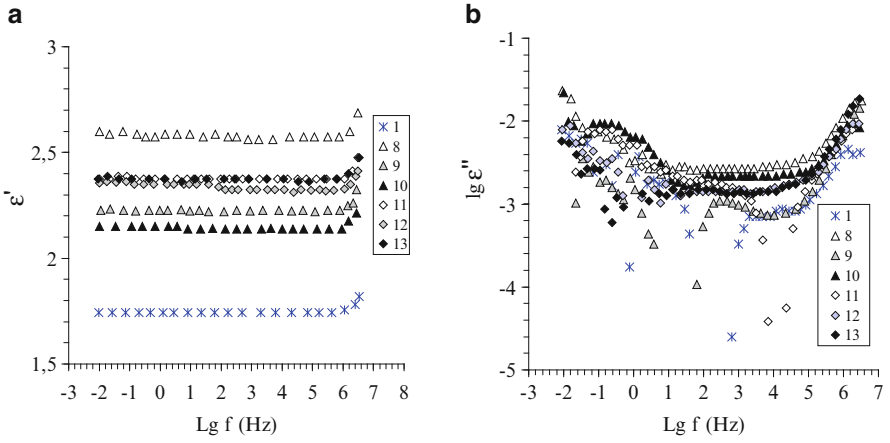

Fig. 17.2 Frequency dependences of the real (**a**) and imaginary (**b**) parts of the dielectric permittivity for the unfilled polymer (**1**) and composites **8**–**13** (Table 17.1)

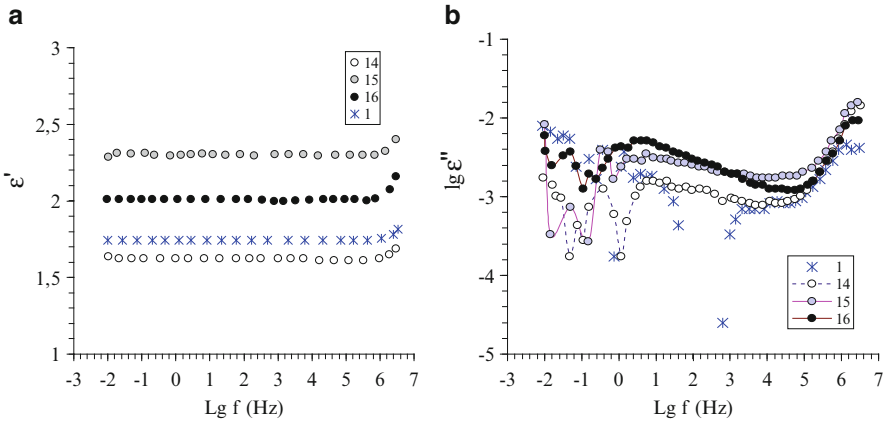

Fig. 17.3 Frequency dependence of the real (**a**) and imaginary (**b**) parts of the dielectric permittivity for the unfilled polymer (**1**) and composites **14–16** (Table 17.1)

difference of the distances between the elements engaged in the orientation–relaxation process. Composite **9** shows a different character of the frequency–dependent dielectric response. In the range of low frequencies the curve has an intensive resonance absorption peak, whereas in the range of high frequencies the curve is similar to the profile of the unfilled polymer. This indicates a different mechanism of polarization as compared to samples **8** and **10**.

The frequency–dependent dielectric response profile recorded for composite **12** (Fig. 17.2) has two extrema; the maximum in the high frequency range is broader and reflects the higher relaxation times. For composites filled with silane-functionalized oxidized nanotubes no significant impact of the magnetic field on the ε'-value was observed (Fig. 17.2a). Composites **12** and **13** possess a similar profile of the ε'' frequency dependence (Fig. 17.2b). However, the curve for sample **11** shows a shift of the resonance absorption peaks towards to higher frequencies; this shift implies a low degree of structure of the sample.

The real part of the dielectric permittivity for materials filled with nanotubes with chemisorbed vinyltriethoxysilane is lower than that of the unfilled polymer (Fig. 17.3a); this indicates a lower ability of bonds to polarization. However, under the influence of the magnetic field structures with more mobile bonds are formed, especially for a orientation of the magnetic lines parallel to the composite film.

Unlike other samples, the curves of the frequency dependence of the dielectric loss for samples **14–16** (Fig. 17.3b) comprise well-defined repeated maxima of the resonance absorption with approximately equal width and intensity. This indicates a highly ordered structure composed of the same type structural units. The mechanisms of polarization and relaxation times for these samples differ considerably from composites filled with nanotubes modified by absorption of organosilane. The lowest dielectric loss is observed for sample **15** which also has the highest ε'-value. Sample **16** is characterized by the higher dielectric loss than sample **15,** most likely due to amorphization of the structure.

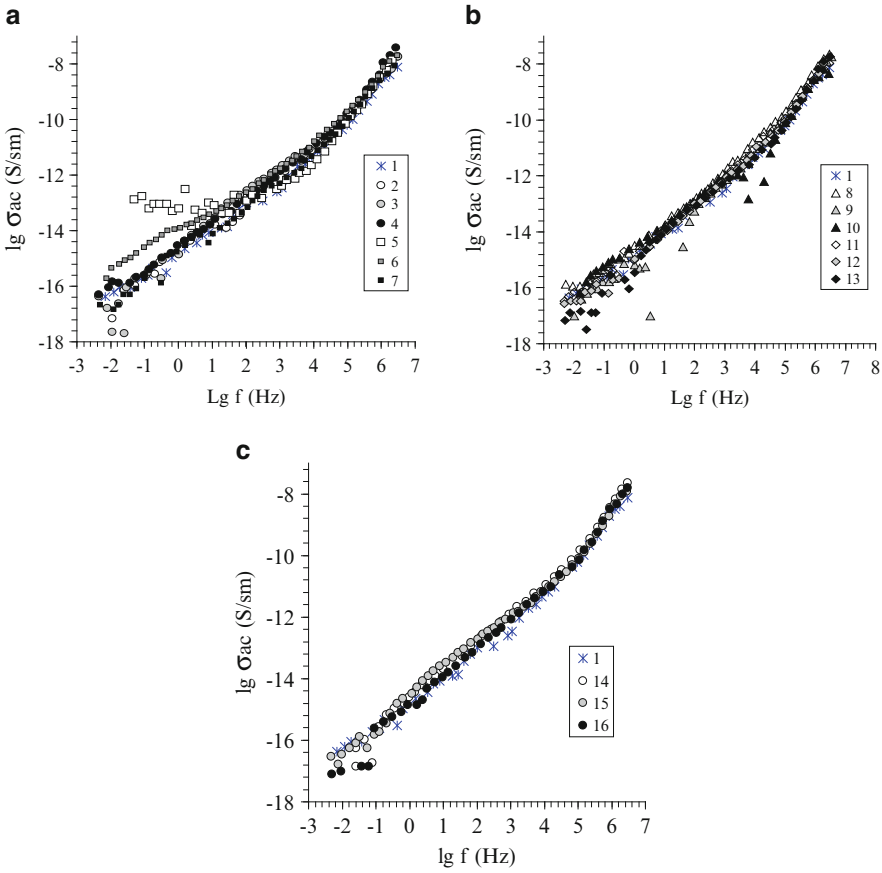

Fig. 17.4 Frequency dependences of the conductivity of polystyrene composites filled with pristine and oxidized nanotubes (**a**), nanotubes with adsorbed (**b**) and chemisorbed vinyltriethoxysilane (**c**) (Table 17.1)

17.3.3 Conductivity of Polystyrene Composites with Pristine and Functionalized Nanotubes

Figure 17.4 shows curves of the frequency–dependent conductivity of composites filled with pristine and modified nanotubes. Overall, the curves of the composites are similar that of the unfilled polymer. However, samples **5**, **6**, **9**, **10** and **13** differ. The conductivity of sample **5** does not change considerably in the low frequencies range; this can be explained by peculiarities of the polarization mechanism [12, 13], which is characteristic for this sample only. Composite **6** shows the similar frequency dependence, but its coefficient of dielectric loss in the low frequency range is significantly higher. For the composites **9**, **10** and **13** a strong decrease of the conductivity at frequencies for $10^{0.5}$, 10^{4} and 10 Hz was observed. Such a decrease

of the conductivity with a subsequent recovery to the common tendency can be associated with the propagation of relaxation and resonance processes within the conductive chains. Though at a filling degree of polystyrene with nanotubes of 0.1 wt% the percolation threshold is not reached, the results obtained in this work could provide a basis for further investigations of the electrophysical properties of the studied systems.

17.4 Conclusions

Polymeric composites based on polystyrene filled with pristine, oxidized and vinyltriethoxysilane-modified MWCNTs were synthesized. The frequency dependences of the real and imaginary parts of the dielectric permittivity were recorded for the synthesized composites and an unfilled polymer. The dependences of the electrophysical properties on the structure of composites were analyzed. The influence of morphological peculiarities of the filler on the macrostructure of the resulting materials and the mechanisms of polarization and relaxation in different frequency ranges were discussed.

References

1. Harris PJF (2009) Carbon nanotube science: synthesis, properties and applications. Cambridge University Press, New York
2. Xiao L, Chen Z, Feng C et al (2008) Nano Lett 8:4539
3. Chen W, Tao X, Xue P, Cheng X (2005) Appl Surf Sci 252:1404
4. Bolbukh YM, Gun'ko GS, Prikhod'ko GP, Tertykh VA (2009) J Nanostruct Polym Nanocomposit 5:14
5. Abdalla M, Dean D, Theodore M et al (2010) Polymer 51:1614
6. Steinert BW, Dean DR (2009) Polymer 50:898
7. Sementsov YI, Melezhik AV, Prikhod'ko GP et al (2007) Physics and chemistry of nanomaterials and supramolecular structures, vol 2. Naukova Dumka, Kyiv, p 116
8. Gunko GS, Bolbukh YM, Prikhod'ko GP, Tertykh VA (2009) Chem Phys Technol Surf 15:343
9. George JJ, Bhadra S, Bhowmick AK (2010) Polym Compos 2:218
10. Hazama Y, Ainoya N, Nakamura J, Natori A (2010) Phys Rev B 82:045204
11. Sen R, Zhao B, Perea D et al (2004) Nano Lett 4:459
12. Sun G, Chen G, Liu Z, Chen M (2010) Carbon 48:1434
13. Pradhan DK, Choudhary RNP, Samantaray BK (2008) Int J Electrochem Sci 3:597

Chapter 18
Synthesis, UV-VIS Spectroscopy and Conductivity of Silver Nanowires

Irena Kostova, Stefka Nachkova, Dan Tonchev, and Safa Kasap

Abstract In this work, we report on the synthesis of silver nanowires (AgNW) by a modified polyole process. Conductive thin films were prepared from synthesized nanowires; then their basic properties were characterized. The influence of the raw materials, solvents, washing and centrifugal separation of these synthesized AgNWs was studied. UV-VIS absorption/transmission spectra of clear solutions were measured, and the size of AgNWs was estimated from these measurements. We also studied the influence of light on synthesized AgNWs in solution, and performed optical microscopy studies to identify possible aggregation processes. Thin films of AgNWs were fabricated on different transparent flexible substrates by a spray-coating process and other coating techniques. The optical transparency and the sheet resistance of these films were also measured. The influence of some additives on the properties of these thin films was checked. Due to the high flexibility and electrical conductivity of AgNW thin films, these nanoproducts are excellent candidates for touch screen displays, solar cells conductive layers and other electronic devices.

Keywords Silver nanowires • Conductive thin films • Polyole synthesis process

I. Kostova (✉) • D. Tonchev
Departments of Chemical Technology, Analytical and Computer Chemistry, Plovdiv University "Paisii Hilendarski", Plovdiv 4000, Bulgaria

Department of Electrical and Computer Engineering, University of Saskatchewan, Saskatoon, SK S7N 5A9, Canada
e-mail: irena_k87@abv.bg

S. Nachkova
Departments of Chemical Technology, Analytical and Computer Chemistry, Plovdiv University "Paisii Hilendarski", Plovdiv 4000, Bulgaria

S. Kasap
Department of Electrical and Computer Engineering, University of Saskatchewan, Saskatoon, SK S7N 5A9, Canada

P. Petkov et al. (eds.), *Nanoscience Advances in CBRN Agents Detection, Information and Energy Security*, NATO Science for Peace and Security Series A: Chemistry and Biology, DOI 10.1007/978-94-017-9697-2_18

18.1 Introduction

Over the past several years, the synthesis of metal nanoparticles has been a subject of increasing interest from scientists due to their potential applications in various fields such as environmental protection, catalysis, optics and electronics [1]. These nanoparticles have found applications in a range of electronic products, such as touchscreen displays, organic and hybrid solar cells, and biosensors [2]. The metal nanoparticles can be synthesized by various methods, such as chemical reduction, electrochemically, gamma radiation, laser techniques, photochemical techniques, etc. Among these methods, the most popular is the chemical reduction of salts in the presence of a stabilizer. Thus, it is possible to synthesize nanoparticles with different shapes (spherical, cubic, wires, etc.) and various dimensions. Whilst there is a large variety of synthesis methods available, the most efficient and proven method for the synthesis and even production of silver nanowires is by means of ethylene glycol (EG) with polyvinylpyrrolidone (PVP), the so-called polyol process. This process is based on a chemical reduction; a variety of AgNWs structures can be prepared by similar mechanisms.

There are number of methods such as printing, spray-coating, drop-coating etc., by which it is possible to obtain different transparent, flexible and conductive thin film based on AgNWs.

The goal of this work is to find a convenient procedure for the synthesis of AgNWs, to characterize some of their properties and to obtain AgNW based conductive, transparent and flexible thin films.

18.2 Materials and Experimental Procedure

18.2.1 Materials and Synthesis

The reagents polyvinylpyrrolidone PVP (M = 55.000) 95.0 %, $AgNO_3$/CH_3COOAg (Alfa Aesar, 99.8 %), NaCl/$CuCl_2$ (99.8 %), ethylene glycol (PPH, Poland) were used to fabricate AgNWs. The modified polyole process was performed at a temperature 150–160 °C with constant mixing. PVP as a stabilizing agent was chosen for all synthesis procedures while ethylene glycol was always used as a reducing agent. We used various methods as one-step or two-step synthesis with different reagents. Depending on whether the one-step or two-step process was used, the fabricated products possess different optical properties according to the absorption spectra measured. Both processes have the same mechanism for the preparation of AgNWs. Initially, some of the silver ions in the solution coalesce in nuclei. These nuclei agglomerated and form seeds. By diffusion of atoms, these particles grow to a nanometer size. Then, these particles can agglomerate again to form nanowires and nanowire networks.

18.2.2 Washing Process

Samples were taken out of the cooled mixture by a pipette and placed in 2 ml tubes. Then, we added 2 ml of acetone into this mixture. The mixture was stirred and centrifuged at 2,000 rpm for 20 min. Subsequently, the clear top solution was decanted and the precipitate was washed 4 more times. After washing with acetone, the precipitate was treated in the same way with deionized water 4–5 times and centrifuged at 2,000 rpm for 20 min. During the treatment with the water, silver was deposited on the walls of the tube. The water was decanted after the first and final washing, subsequently all samples were used to measure their UV-VIS absorption spectra.

18.2.3 UV-VIS Absorption Spectra

A Boeco S24 Spectrophotometer was used to measure UV-VIS spectra. After dispersal of the precipitate, UV spectra of the remaining aqueous solutions were recorded again. The range of the spectrophotometer is between 200 and 1,000 nm. We obtained results similar to those shown in the work of Yingpu Bi et al. [3].

After the final washing, we studied the influence of light on the absorbance of the clear upper solution. It was divided into two portions. One sample was placed in dark and the other was exposed directly to sunlight for different times. UV-VIS spectra of these samples were recorded. A spectrum of deionized water was also recorded and used as a baseline for the all the spectra.

18.3 Result and Discussion

The preparation of longer silver nanowires depends on the conditions of the synthesis and the reagents used. The optimum temperature is 150–160 °C. It is especially important to ensure a good mixing during the synthesis to maintain a uniform distribution of the heat by constant stirring. It is also extremely important to monitor the rate of addition of the silver salt ($AgNO_3$/CH_3COOAg) and that of the accelerating agents (NaCl/$CuCl_2$). Transmission electron microscopy (TEM) images of the products are shown in Fig. 18.1. The diameter size of the nanoparticles is in a range 100–350 nm and a length is about 1 μm.

Washing the product after the synthesis is of particular importance, since the silver particles form complex aggregates with the polymer. Furthermore, PVP and ethylene glycol affect the electrical conductivity of the films. Ethylene glycol has a very good solubility in acetone, PVP in water. Therefore, these solvents are most commonly used in the washing processes. We have observed the behavior of the particles after each washing procedure with water and acetone under an optical microscope. In the one-stage process, we washed 15 times with acetone and 15 times with water, and we observed particle aggregation in some of the samples.

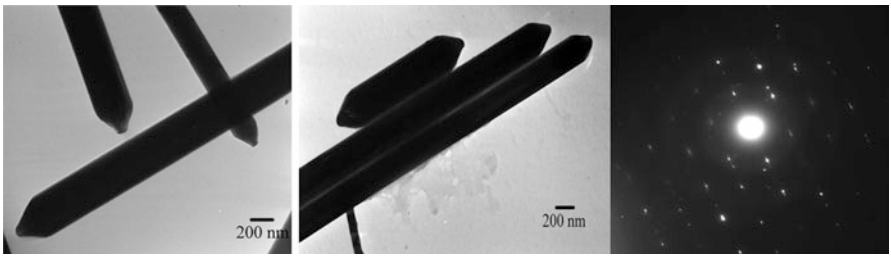

Fig. 18.1 TEM images of AgNWs

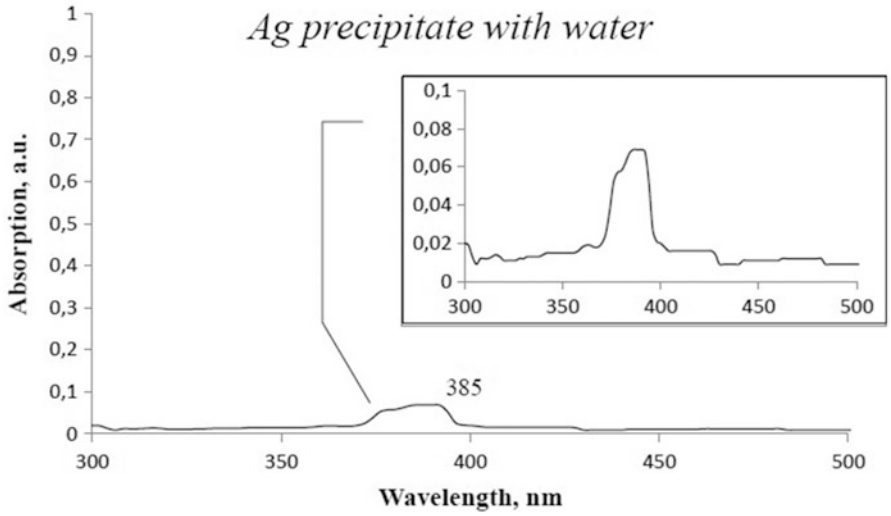

Fig. 18.2 UV-visible absorption spectra of Ag precipitate in water

We did not observe aggregation of particles from the two-step polyole process. We washed the products 4 times with acetone and 4 times with water.

Absorption spectra of the clear solution above the precipitate are shown in Fig. 18.2. The UV-VIS spectra indicate the presence of silver nanoparticles with a typical absorption maximum at 386 nm [3]. The same spectrum maximum was observed after the first wash but with a different intensity (Fig. 18.3). Looking at the UV-VIS spectra results it is clear that after every wash and centrifugation process, silver products are separated and removed. This means that silver particles have not fully precipitated. The results are shown in Figs. 18.2, 18.3 and 18.4.

The spectra of these clear samples show similar peaks with the absorption maximum in the range of 376–382 nm, but with different widths. According to the literature data, these peaks belong to silver nanoparticles in the form of wires [3]

We also recoded the UV-VIS spectrum of a dispersed sample after the first water wash as shown in Fig. 18.4.

The influence of light on a sample of a silver precipitate after the final wash is show in Fig. 18.5. The sample was divided into two portions. One portion was

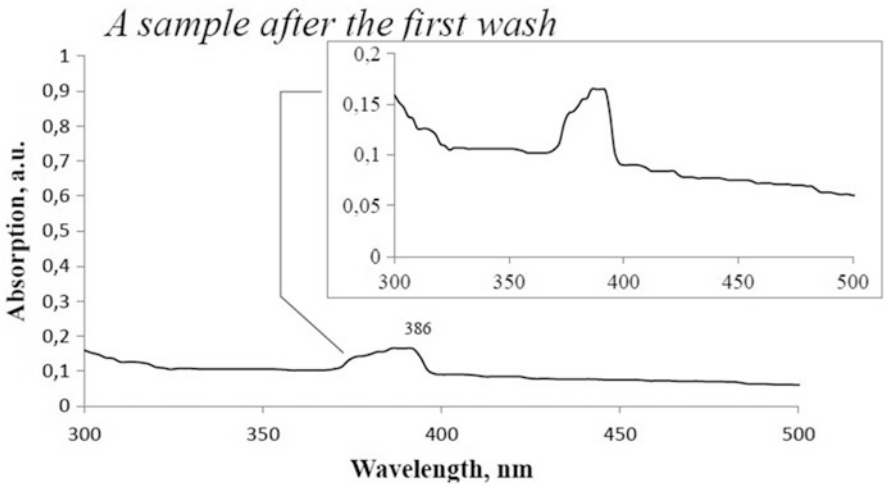

Fig. 18.3 UV-visible absorption spectra of a sample after the first water wash

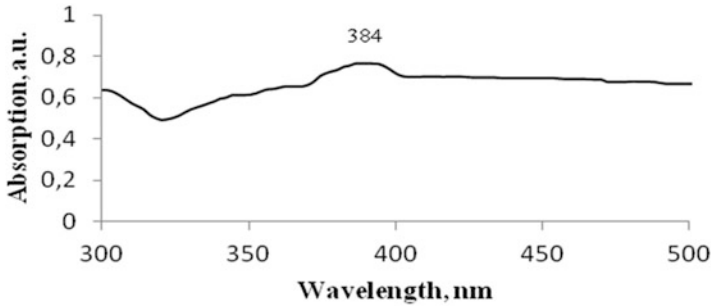

Fig. 18.4 UV-visible absorption spectra of a suspension after the first wash

kept in dark and the other was exposed to direct sunlight for different durations. Figure 18.5 shows the absorption spectra of these two samples as well as the spectrum of the deionized water. This study was performed 7 days after the synthesis.

Initially, the instrument was calibrated using deionized water. This spectrum serves as a baseline. Looking at Fig. 18.5, it is clear that the changes in the intensity of the absorption spectra are significant. Prolonged exposure of the samples to natural sunlight results in stronger absorption peaks. Peak shape and size of non-treated samples are different for those of treated samples.

It can be seen from the spectra that the most intense absorption peaks are for samples aged for 4 h in direct sunlight, and the spectra with the lowest intensity are those of samples aged for 2 days in the dark. Using the peak half-width method it is possible to estimate the average size or the thickness of Ag nanowires, which is about 20 nm.

It is clear that the AgNW size does not change much after different kinds of washing and treatment procedures.

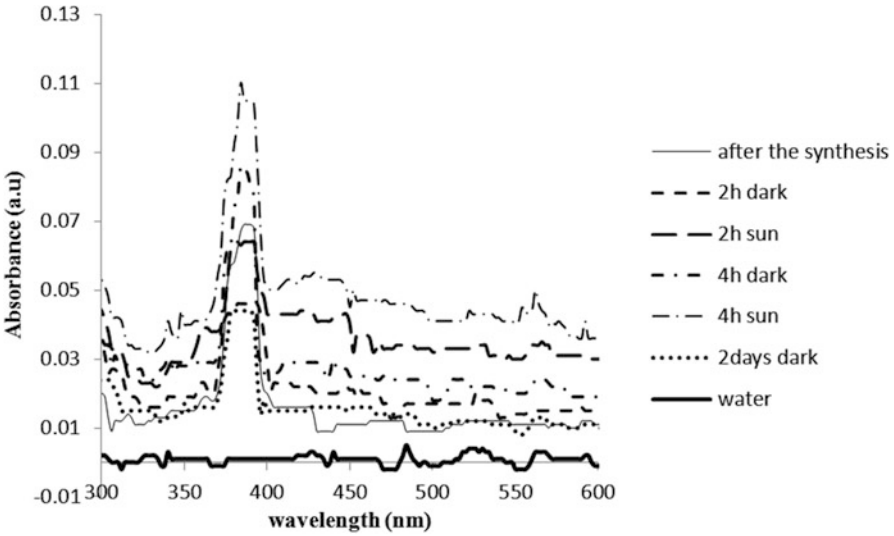

Fig. 18.5 Absorption of light treatment water sample content silver wires

18.3.1 Thin Films Fabrication

Different methods were used to fabricate films. Our intention was to fabricate thin, conductive, flexible and stable films. The following methods were used:

Preparation of polymer based thin films:

- The aqueous solutions were evaporated to form a dry residue at 100 °C in an oven. A acrylic polymer dispersion was made from the fine precipitate. Thin films were deposited on a substrate of polyethylene terephthalate (PET). We used a manual flexographic printing proofer (Anilox 11.8 BCM/180 lines) for roll printing and coating.
- After drying at room temperature, the electrical conductance of the layer was measured by a digital multimeter. Initially the layer was nonconductive, most probably because the Ag particles were fully enveloped by the polymer.
- The layers were studied under an optical microscope. There is a uniform distribution of particles on the surface of the substrate.
- The resulting films are transparent and flexible, but the conductivity was poor.

Preparation of layers from isopropyl alcohol dispersions:

- The aqueous solution was evaporated in an oven (100 °C) and a dry silver precipitate was deposited. The concentration of the fine precipitate in isopropyl alcohol dispersion was 16 mg/ml [4].
- The suspension was treated in an ultrasonic bath for 30 min at room temperature and used to coat a PET substrate by a spray-coating method. Films were dried at room temperature.

- According to literature data [4], the conductivity increases significantly by treating the layers with concentrated HCl vapor. The layer was treated for about 5 min with hydrochloric acid in the vapor phase; the conductivity of the film was subsequently measured.
- Before processing the layer by concentrated hydrochloric acid vapor, the resistance of the thin film is very high, on the order of several MΩ/sq, and the film was semitransparent.
- After the treatment, the film transparency was improved, the films possessed excellent conductive properties, with a resistance of the order of 10 Ω/sq.

18.3.2 Thin Films Characterization

As was mentioned above we used different techniques for the preparation of thin films from synthesized AgNWs. Depending on the purpose and potential use of these silver particles, we prepared films with different thickness and density. Films deposited on these substrates should be transparent, flexible and conductive. In some cases, depending on the application this is not necessary.

Some of methods described for the preparation of conductive films were used. It was found that the spray-coated silver suspension in isopropyl alcohol (the concentration of the Ag particles is 0.632 mg/L) exhibit the lowest resistance (highest conductivity). After coating and drying, the film is highly resistive ($R > 20$ MΩ/sq). After the treatment with concentrated HCl vapor for about 5–10 min, the layer exhibited excellent conductive properties ($R < 9.6$ Ω/sq). Hydrochloric acid does not only affect the conductivity of the films but also the absorption/transmission spectra. The transmittance is increased by 18 % after the treatment with hydrochloric acid as shown in Fig. 18.6. The transparence of the substrate was 99.7 % (absorbance 0.001 a.u.).

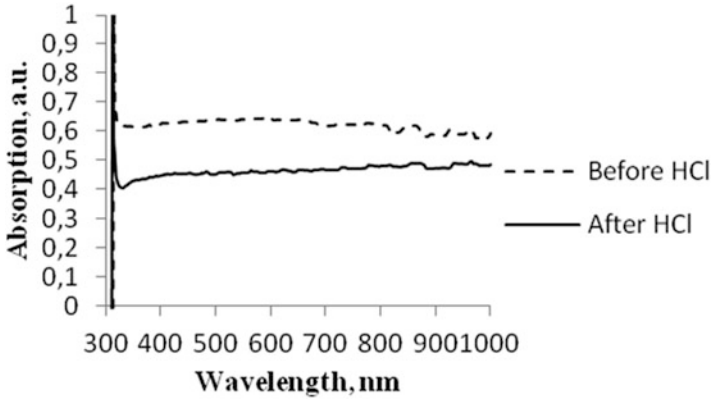

Fig. 18.6 Absorption spectra of the film before and after treatment with HCl

The latter effect is most probably due to the fact that HCl in vapor phase removes the resulting surface oxide layer and thereby improves the conductivity of the film.

18.4 Conclusion

- AgNPs suitable for various possible applications were successfully prepared by the reduction of Ag^+ ions *via* a modified polyole process;
- The optical UV-VIS absorption properties reveal information on the presence and size of synthesized silver nanoparticles, which also depend on the exposure time to sunlight.
- The particle size can be controlled by the processing time and the chemicals used.
- Thin films of AgNWs were obtained by spray-coating and flexographic methods. One of the main advantages of thin films is the ease of preparation, the accessibility and the costs.
- In addition, these thin films are semitransparent (45 %) and have a low electrical resistivity ($\approx 9.6\,\Omega$/sq).
- Generally, these results show that AgNPs possess good potential for practical applications. Further research is under way.

Acknowledgements The authors are grateful to Dr. Daniela Karashanova, Institute of Optical Materials and Technologies, Bulgarian Academy of Sciences for TEM analysis.

References

1. Pyatenko A, Yamaguchi M, Suzuki M (2007) J Phys Chem C 111:7910
2. Lee J, Sun F, Lee J (2013) J Exp Nanosci 8:130
3. Yingpu Bi, Hongyan Hu, Gongxuan Lu (2010) J Chem Commun 46:598
4. Cai-Hong Liu, Xun Yu (2011) Nanoscale Res Lett 6:75

Part VI
Materials: Nanoparticles

Chapter 19
Modification of Nanosilica Surfaces by Methyl Methacrylate Oligomers

Igor Telegeev, Evgenij Voronin, Evgenij Pakhlov, and Valentina Kalibabchuk

Abstract Composites based on silica and methyl metacrylate silane coupling agents are promising materials for sensor technologies. The present study deals with a new method of covering silica nanoparticles by methyl methacrylate oligomers in the pseudo-liquid state. The adsorption process of metacrylate-containing oligomers on the surface of nanosized silica was studied by means of IR-spectroscopy and thermal analysis. The study confirmed the full modification of the silica surface with oligomers. The composites obtained in this study exhibited a greatly reduced degree of shrinkage and better mechanical and physical properties. The composites explored here will serve as an important contribution to the current ongoing research efforts in designing materials in the nano-scale capable of sensing and detecting metal ions in solutions with high selectivity.

Keywords Nanosized silica • Surface modification • Methacrylate coatings

19.1 Introduction

The modification of the surfaces of inorganic particles by adsorption of macromolecules of oligomers is an important way to regulate the surface properties and to form a surface layer at the solid-matrix interfaces [1–10]. It is known [1, 8, 11, 12] that nanosilica particles interact with each other to form aggregates of different structures, so the study of the question of the degree of accessibility of the silica surface to interact with macromolecules such as methacrylate oligomers is important to understand the structure of the surface layer. From the different types of entities which that can be incorporated in silica nanoparticles, methacrylate oligomers have emerged as one of the most interesting, with applications in bioanalysis, optical sensors, and photoactive materials [13, 14].

I. Telegeev (✉) • E. Voronin • E. Pakhlov • V. Kalibabchuk
Chuiko Institute of Surface Chemistry, National Academy of Sciences of Ukraine, General Naumov Street 17, Kyiv 03164, Ukraine

Bogomolets National Medical University, T. Shevchenko 13, Kyiv 01601, Ukraine
e-mail: itelegeev@ukr.net

P. Petkov et al. (eds.), *Nanoscience Advances in CBRN Agents Detection, Information and Energy Security*, NATO Science for Peace and Security Series A: Chemistry and Biology, DOI 10.1007/978-94-017-9697-2_19

Liquid-phase methods of nanosilica surface modification by non-volatile methyl methacrylate oligomers are versatile and effective [10, 15]. Nanosilica can significantly change some of its initial properties such as its bulk density which increases several times; it also loses permanently its powdered state after liquid-phase modifications. It has also several other significant disadvantages which are mainly of technological and environmental nature [15–18]. These are in particular the need for solvents, which are often toxic or environmentally hazardous; thus the removal of these solvents is associated with difficulties in filtration processes. The drying of the filtrate and its grinding is essential, which is a heat- and energy-intensive process and requires additional costs. Accordingly, it creates a number of problems and limitations for further use and application in the production of large quantities of material.

There is a need to apply conditions which have only few disadvantages in terms of the technological process. Especially for dispersed silicas gas-phase modification methods are more suited [15], which are devoid of the drawbacks inherent to liquid-phase modification method. The basic requirement for the modifier that restricts an increasing use of gas-phase methods is the volatility which is not always sufficient. In addition, a volatile modifier can be effectively used only for chemical modification, as in this case durable surface compounds are formed. Adsorption modification by volatile substances is not applicable for practical purposes due to the low stability of surface sorption complexes formed.

In the Chuiko Institute of Surface Chemistry of the NAS of Ukraine a versatile method for efficient adsorption modification of silica surfaces by nanosized non-volatile soluble organic compounds and low molecular weight polymers was developed [15]. It allows to achieve a given degree of coverage of the silica surface modifier and almost completely retains its original dispersion [18].

The degree of coverage of silica surface modifier for the same content can be considered as one of the important criteria of modification [19]. To assess the effectiveness of the method we carried out a study of sorption modification of the nanosilica surface by methyl methacrylate oligomers.

19.2 Experimental

A-300 nanosilica (SiO_2 powder, average diameter 9.5 nm, with a surface area of 310 m^2/g) was used as received. The structures and names of the oligomers chosen as modifiers for the silica surface modification are shown in Table 19.1. Methyl methacrylate oligomers have been used as surface modifiers since they contain hydroxyl, amine and ester groups, which are capable of forming strong hydrogen bonds with silanol groups.

According to the design of the experiment, three independent variables were examined: the type of the oligomer, the concentration of the oligomer (0.35 and 0.7 mmol/g) and the treatment time (0.3, 0.6, 1, 2, 3 and 6 h). The nanosilica modification was performed in a reactor consisting of a flask and a high-intensity blender under intensive mixing [15]. When rotated at 300–500 min^{-1}, the nanosilica transforms into a pseudo-liquid state. An amount of 12 g nanosilica

Table 19.1 Some parameters of the modifiers

Chemical name	Structure	Molecular weight, [g/mol]
Oligo carbonate methacrylate (OCM-2)	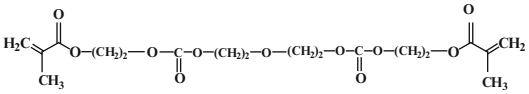	418
Triethyleneglycol dimethacrylate (TEGDMA)	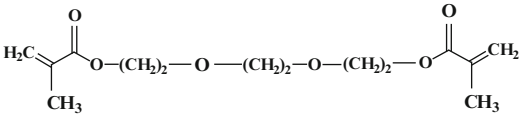	286
Bisphenol α glycidyl methacrylate (BIS-GMA)	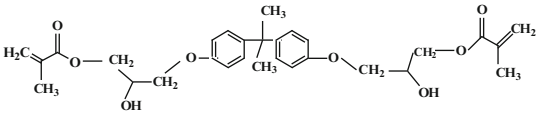	512
Ethoxylated bisphenol α dimethacrylate (BIS-EMA)	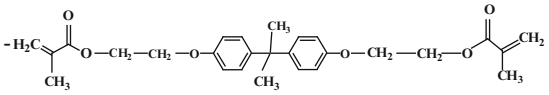	452
Urethane dimethacrylate (UDMA)	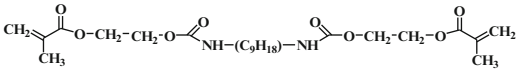	470

was stirred for 10 min. Then a specific amount of the oligomer (alcoholic solution ≈ 3.5 g of 30 wt%) was added to the mixture which was mixed for a specific time. According to IR spectral data a part of the silanol groups interacts with molecules of oligomers, giving the degree of filling of the surface, which depended on the content of the oligomer and was calculated.

To study the functionalization of the nanosilica surface with the methyl methacrylate oligomers, Fourier transform infrared (FTIR) spectroscopy was used (Thermo Nicolet, Nicolet Instrument Corporation). The nanosilica and the silica-covered substrates were scanned in the transmittance mode in the wavelength range from 1,200 to 4,000 cm^{-1} [20].

A thermal gravimetric analyzer (TGA) was used to measure the surface absorption of the nanosilica before and after surface treatment. The nanosilica powder was heated from room temperature to 1,000 °C with a ramping rate of 20 °C/min. The weight loss of the nanosilica powder was recorded as a function of temperature.

19.3 Results and Discussion

It was shown (Fig. 19.2) that nanosilica sorption surface modification in the fluidized state by methacrylate oligomers occurs fairly quick in 1 h. Nanosilica modified by this method is characterized by a given degree of surface coverage and almost completely maintains its original dispersion.

It was found that the entire nanosilica surface is available for adsorption interaction with oligomer macromolecules but the degree of filling depends on the amount of surface modifier which allows to adjust the properties of the composite material.

After adsorption modification complete a disappearance of isolated silanol groups (3,550 cm^{-1}) is observed in all cases, but other absorption bands (3,660–3,680 and 3,550 cm^{-1}) remain practically unchanged (Fig. 19.1). This indicates that the adsorbed molecules interact with the silica surface by formation of hydrogen bonds only with the free silanol groups (Fig. 19.2).

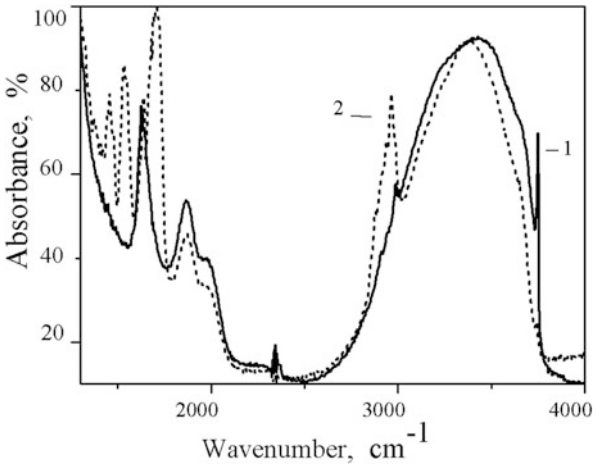

Fig. 19.1 FTIR spectra of the initial nanosilica (*1*) and after treatment with UDMA (*2*)

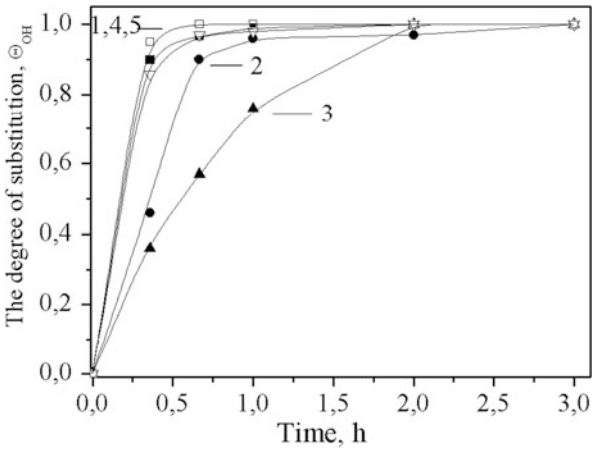

Fig. 19.2 The dependence of the degree of substitution of free silanol groups by UDMA (*1*), Bis-EMA (*2*), BIS-GMA (*3*), TEGDMA (*4*), OCM-2 (*5*) (0.7 mmol/g) as a function of the mixing time

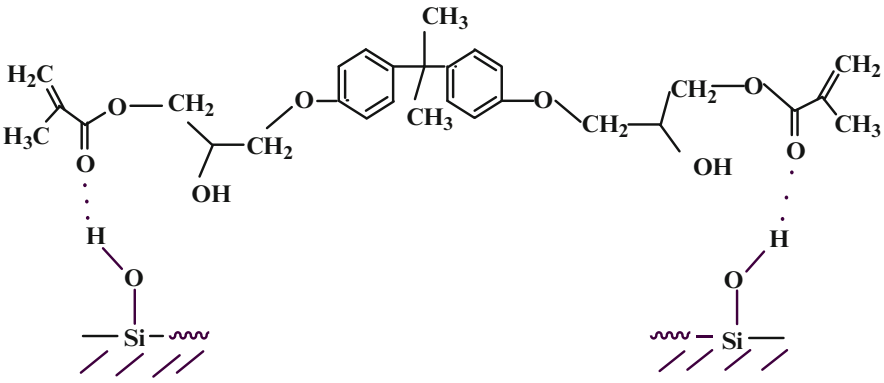

Fig. 19.3 Scheme of the interaction between BIS-GMA molecules and nanosilica surface silanol groups

Based on the fact that the carbonyl oxygen atoms are usually more prominent for the electron properties, and for reason of steric complications, it is assumed that the silanol groups form a hydrogen bond precisely with the carbonyl atoms. The number of silanol groups interacting with one oligomer molecule, in other words the number of active groups of molecules bonded to the surface, was calculated according to the data of the number of the sorbed oligomers. Thus, one molecule of BIS-GMA interacts with two silanol groups according to the scheme in Fig. 19.3.

The number of physically-sorbed water decreases as a result of the nanosilica surface modification by BIS-GMA. This indicates that the BIS-GMA molecules of as well as the other oligomers studied interact with surface hydroxyl groups directly without mediator molecules. Quantitative contents of BIS-GMA molecules on silica surface were determined by differential thermal gravimetry (DTG). According to the mass loss amount of modifier on the surface was determined and it is about 10 wt%. Curve 1 in Fig. 19.4 shows that thermo-destruction of the nanosilica modified by BIS-GMA begins at ~270 °C and reaches its maximum rate in the temperature range of 300–400 °C. The presence of exothermic effects (Fig. 19.4, curve 3) may indicate that oligomer oxidation occurs.

At the same degree of filling of the surface under the conditions of gas-phase surface modification, only a few silanol groups react with one molecule of oligomers. In our case the data obtained suggest the efficiency of the method. We have achieved almost the same results as when using liquid-phase modification methods, but there are advantages associated with the use of a gas-phase method.

The results allowed us to develop and optimize an effective method of sorption modification of nanosized silica by methyl methacrylate oligomers under gas dispersion conditions with vigorous mechanical stirring.

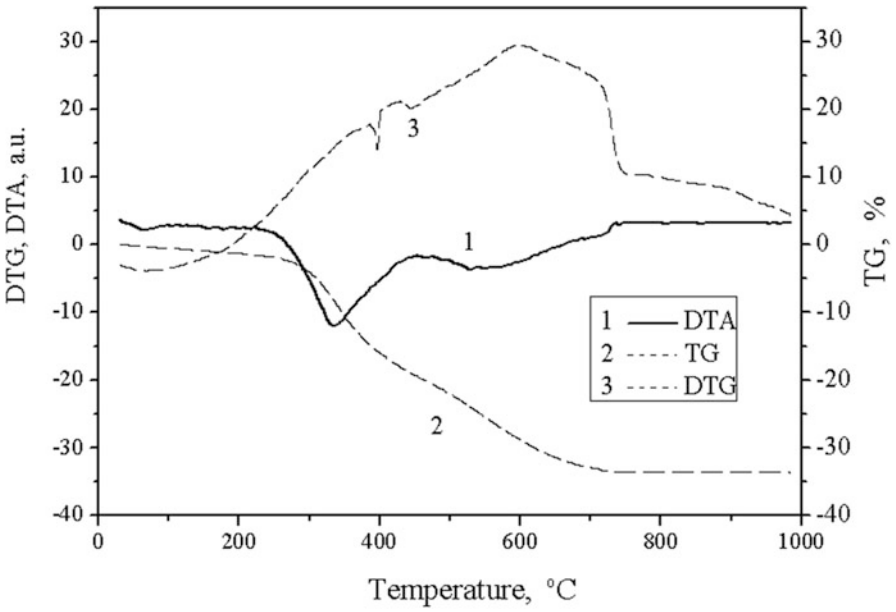

Fig. 19.4 TG/DTG/DTA curves of the nanosilica after treatment with BIS-GMA

References

1. Chuiko AA (2001) Surface chemistry of silica. UkrlNTEI, Kiev
2. Chuiko AA, Gorlov YI (1992) Surface chemistry of silica: surface structure, the active centers, mechanisms of sorption. Naukova Dumka, Kiev
3. Tertyh VA, Belyakova LA (1991) Chemical reactions involving silica surface, science. Dumka, Kiev
4. Ayler R (1982) Chemistry of silica: solubility, polymerization, colloid and surface properties. Mir, Moscow
5. Starokadomskii DL, Soloveva TN (1999) J Appl Spectrosc 1:119
6. Hair ML (1967) Infrared spectroscopy in surface chemistry. Marcell Dekker, New York
7. Voronin EF, Gun'ko VM, Guzenko NV (2004) J Colloid Interface Sci 279:326
8. Neimark IE (1982) Synthetic mineral adsorbents and catalyst carriers. Naukova Dumka, Kiev
9. Chuiko AA, Voronin EF, Tertykh VA (1983) Adsorption and adsorbents 11:22
10. Solomko VP (1980) Filled crystallizing polymers. Naukova Dumka, Kiev
11. Chuiko AA (2001) Chemistry, physics and technology of surfaces. UkrISTEI, Kiev
12. Tertyh VA, Belyakova LA (1988) Chemical reactions involving silica surface. Science Dumka, Kiev
13. Nozawa K, Gailhanou H, Raison L, Panizza P, Ushiki H, Sellier E, Delville JP, Delville MH (2005) Langmuir 21:1516
14. Zou H, Wu S, Shen J (2008) Chem Rev 108:3893
15. Voronin EF, Nosach LV, Gun'ko VM (2010) Surface 2(17):221
16. Avakumov E, Senna M, Kosova N (2001) Soft mechanochemical synthesis: a basis for new chemical technologies. Kluwer Academic Publishers, Boston

17. Avgul NN, Kiselev AV, Poshkus DP (1975) Adsorption of gases and vapors on homogeneous surfaces. Chemistry, Moscow
18. Nosach LV, Voronin EF (2006) Chem Phys Surf Technol 3:540
19. Bolbukh YM (2009) Chem Phys Surf Technol 15:55
20. Voronin EF, Gun'ko VM, Guzenko NV, Pakhlov EM, Nosach LV, Leboda R, Skubiszewska-Zieba J, Malisheva ML, Borysenko MV, Chuiko AA (2004) J Colloid Interface Sci 279:326

Chapter 20
Radioprotective Effect of CeO_2 and $GdEuVO_4$ Nanoparticles in "In Vivo" Experiments

E.M. Mamotyuk, V.K. Klochkov, G.V. Grygorova, S.L. Yefimova, and Yu.V. Malyukin

Abstract In experiments performed in vivo of the irradiation of rats, a strong radioprotective effect of nanoparticles based on orthovanadates of rare earth elements and cerium dioxide was found. The nanoparticles were injected per os by two different schemes - once and during 15 days. For the 15-days scheme of $GdEuVO_4$ nanoparticles injection the survival of animals irradiated with a dose of 6.0 Gy was 100 % during 30 days of observation. Injection of CeO_2 nanoparticles also effectively protects the bodies of rats from radiation. For an irradiation with the lethal dose of 7.0 Gy, the radioprotective effect of the nanoparticles is negligible.

Keywords Nanoparticles • Radioprotective effect • In vivo

20.1 Introduction

Exposure to radiation leads to destruction of tissues and cells of an organism predominantly by inducing free-radical processes. The primary effect of radiation of any kind on any biological object begins with the absorption of radiant energy, which is accompanied by the excitation of molecules and their ionization. During the ionization of water molecules (indirect action of radiation) in the presence of oxygen, active radicals are formed ($OH^{\bullet}$, $O_2^{\bullet -}$, etc.) as well as hydrated electrons, and molecules of hydrogen peroxide, which take part in the chain of chemical

Note: The work was conducted in accordance with international principles of the "European Convention for the Protection of Vertebrate Animals used for Experimental and other Scientific Purposes" (Strasbourg, 1986).

E.M. Mamotyuk
Grigoriev Institute for Medical Radiology-National Academy of Medical Science of Ukraine, 82 Pushkins'ka Street, Kharkiv 61024, Ukraine

V.K. Klochkov • G.V. Grygorova (✉) • S.L. Yefimova • Yu.V. Malyukin
Institute for Scintillation Materials NAS of Ukraine, 60 Lenin ave., Kharkiv 61001, Ukraine
e-mail: klochkov@isma.kharkov.ua; grigorova.ann@yandex.ua

P. Petkov et al. (eds.), *Nanoscience Advances in CBRN Agents Detection, Information and Energy Security*, NATO Science for Peace and Security Series A: Chemistry and Biology, DOI 10.1007/978-94-017-9697-2_20

reactions in the cells. During ionization of organic molecules (direct effect of radiation), also free radicals are formed, which in the chemical reactions taking place in the body disturb the metabolism, cause the appearance of compounds unusual for the body and disrupt the vital processes.

While cells release a level of protective molecules, such as glutathione and metallothionein, they are not capable of blocking all damage, thus resulting in the death of normal tissues; therefore, the development of strategies to protect normal tissues from radiation-induced damage has to be continued.

A radioprotective effect was found for a number of substances with different chemical structures. Among the most important ones from the viewpoint of possible practical use are cysteamine, serotonin, mexamine, amifostine and a variety of other organic compounds, the action of which is based both on a chemical modification of biologically sensitive target molecules and inactivation of oxidative radicals arising from the interaction of ionizing radiation with water and biomolecules.

Recent studies have shown that inorganic nanoparticles also exhibit radioprotective properties [1]. The role of nanoparticles as radioprotectants is a cutting-edge development in decades of scientific interest regarding the protection of normal cells and tissues.

In both in vitro and in vivo experiments it was shown that the cerium dioxide nanoparticles [2, 3], fullerenes and their derivatives [4, 5] protect cells and tissues from radiation injury. The chemistry of engineered nanoparticles supports a potential role as a biological free radical scavenger or antioxidant.

The work presented in this article addresses the effectiveness of CeO_2 and $GdEuVO_4$ nanoparticles in radioprotection in animal models during radiation exposure.

20.2 Experimental Procedure

The colloidal solutions based on orthovanadates $Gd_{0.9}Eu_{0.1}VO_4$ and cerium dioxide CeO_2 nanoparticles used in this work were obtained by methods previously described in [6, 7]. They were stabilized by sodium citrate (NaCit) with a molar ratio CeO_2/NaCit of 1:1. The solutions were stored in sealed ampules without changing their properties for more than 2 months at normal conditions.

The investigation was performed on 90 white male rats weighting 150–180 g. The X-ray irradiation of the animals was performed using a x-ray therapeutic unit model RUM 17 (USSR) in standard technical conditions.

The X-ray irradiation conditions were as follows: tube voltage 190 kV, current 10 mA, filters 0.5 mm Cu and 1.0 mm Al, area $20 \times 20\ cm^2$, absorbed doses 6.0 and 7.0 Gy, absorbed dose rate in air 0.57 Gy/min, $E_{ef} = 79.0$ keV.

0.5 ml of the solutions of nanoparticles with a concentration of 0.2 g/l were injected per os using the schemes:

- **Scheme 1**: injection of NPs during 5 days before irradiation, then irradiation with doses of 6.0 Gy and 7.0 Gy, followed by injection of solution for another 10 days.
- **Scheme 2**: single injection of NPs for 40 min before irradiation with a dose of 7.0 Gy. Control groups were irradiated without injection of nanoparticles.

20.3 Results and Discussion

In the experiments, colloidal solutions of nanoparticles with average sizes of 10 nm for CeO_2 and 8×20 nm for $GdEuVO_4$ were used (Fig. 20.1).

The main experimental results are summarized in Table 20.1.

The data show that at a dose of 6.0 Gy injection of nanoparticles by Scheme 1 reduces the 30 – dai mortality from 60 % to 10 % when using ceria; after injection of nanoparticles based on orthovanadates all animals have survived.

Radiation with a dose of 7.0 Gy is lethal, so in control 2 almost all animals died. However, after injection of nanoparticles according to schemes 1 and 2 a radioprotective effect of nanoparticles is observed, although it is quite negligible.

In addition to the analysis of the 30-dai survivability, different signs of acute radiation sickness were monitored, such as a ruffled fur (a common indicator for the state of the body), bloating, diarrhea, swelling of mouth and eyes. By all these characteristics a protective effect of the nanoparticles was observed in the case of per os injection of both types of nanoparticles and irradiation by 6.0 Gy. For an irradiation by 7.0 Gy the signs of acute radiation sickness did not differ from those of the controls.

Thus, in in vivo experiments it was found that per os injection of nanoparticles based on orthovanadates of rare earths and cerium dioxide protects the organism of rats following exposure to a lethal dose of radiation.

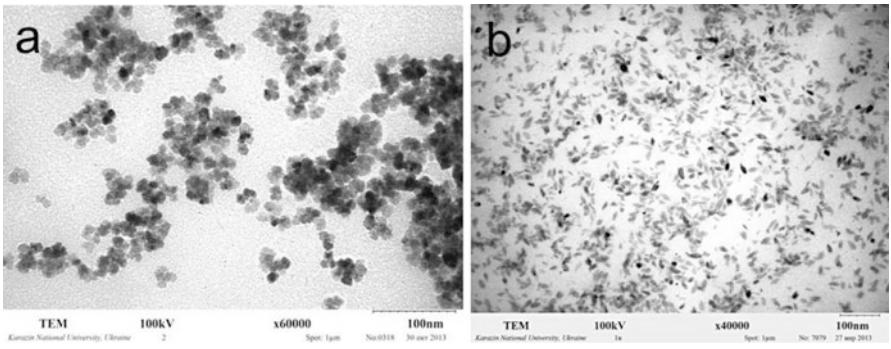

Fig. 20.1 TEM images of CeO_2 (**a**) and $GdEuVO_4$ (**b**) nanoparticles

Table 20.1 Mortality and lifetime of rats after 30 days after X-ray irradiation with 6.0 or 7.0 Gy

№ group	Type of nanoparticles	Dose of irradiation, Gy	Scheme	n	n_1	n_2	Animals died, %	Compared groups
1		6.0	Control 1	10	6	79	60	
2	CeO_2	6.0	1	10	1	11	10	1–2
3	$GdEuVO_4$	6.0	1	10	0	0	0	1–3
4		7.0	Control 2	20	19	161	95	
5	CeO_2	7.0	2	10	9	96	90	4–5
6	$GdEuVO_4$	7.0	2	10	6	47	60	4–6
7	CeO_2	7.0	1	10	8	59	80	4–7
8	$GdEuVO_4$	7.0	1	10	10	78	100	4–8

Note:
n – the total number of rats in the experiment
n_1 – number of dead rats
n_2 – the total number of days the dead rats survived
MLD – mean life duration

In general, the radioprotective effect of nanoparticles considered corresponds to, and even possibly exceeds the level of protection provided by conventionally used organic radioprotectors.

Probably, the radioprotective effect of nanoparticles is related to their antioxidant action. Moreover, unlike organic antioxidants, inorganic nanoparticles can provide "traps" for free radicals. Also, participating in the redox processes following neutralization of free radicals they can play the role of mediators of electron transfer without changing their physical and chemical properties. Thus, one inorganic nanoparticle is able to participate in an unlimited number of acts of capture and neutralization of reactive radicals.

One can not exclude the possibility of induction of protective functions of the organism itself after injection of nanoparticles. The mechanism of radioprotective action of considered types of nanoparticles requires further more in-depth research.

20.4 Conclusion

The effectiveness of CeO_2 and $GdEuVO_4$ nanoparticles in radioprotection in model animals during radiation exposure has been shown. Nanoparticles were injected per os by two different schemes – once and during 15 days. For the 15-days scheme of $GdEuVO_4$ nanoparticles injection during 30 days of observation the survival of animals irradiated with a dose of 6.0 Gy was 100 %; for ceria it was 90 % for ceria. It was revealed that 7.0 Gy radiation dose is lethal. These results can serve as a motivation to consider inorganic nanoparticles as the basis for new drugs possessing by radioprotective effect.

References

1. Menon A, Nair CKK, Dhanya KC (2012) Pushpagiri Med J 3:137
2. Tarnuzzer RW, Colon J, Patil S, Seal S (2005) Nano Lett 5:2573
3. Baker CH (2013) Transl Cancer Res 2:343
4. Vavrova J, Řezačova M, Pejchal J (2012) J Appl Biomed 10:1
5. Daroczi B, Kari G, McAleer MF, Wolf JC, Rodeck U, Dicker AP (2006) Clin Cancer Res 12:7086
6. Klochkov VK, Grigorova AV, Sedyh OO, Malyukin YV (2012) Colloids Surf A Physicochem Eng Asp 409:176
7. Klochkov VK, Malyshenko AI, Sedyh OO, Malyukin YV (2011) Funct Mater 1:111

Chapter 21
Synthesis of Highly Porous Micro- and Nanocrystalline Zeolites from Aluminosilicate By-Products

Denitza Zgureva and Silviya Boycheva

Abstract The present study is aimed to the preparation of synthetic zeolites of a defined Na-X type (Faujasite) from the fly ash (FA) generated by the incineration of Bulgarian lignite coals. FA zeolitization was carried out by three different methods: classical alkaline conversion, two-stage fusion-hydrothermal synthesis, and atmospheric aging, all with sodium hydroxide (NaOH) as an alkaline activator. The nature, morphology and chemistry of the zeolites were studied by X-ray diffraction, scanning electron microscopy (SEM) and energy-dispersive X-ray (EDX) analyses. The results from the classical alkaline conversion show the formation of an aluminosilicate hydrogel on the surface of the FA particles but a crystallization of any zeolitic phase does not take place. Zeolites with a dominant Na-X phase were obtained under by a two-stage synthesis under the following conditions: fusion at 550 °C, hydrothermal treatment at 90 °C for 2 h of duration, and NaOH/FA ratios of 2.0–2.4. Zeolite Na-X is also obtained by atmospheric aging for 1 year at a NaOH/FA ratio of 1.

Keywords Synthetic zeolites • Aluminosilicates • Fly ash recovery

21.1 Introduction

Mineral waste is one of the most spread solid by-products produced in enormous amounts all over the world, the so-called fly ash (FA), from coal combustion plants. It is normally reused in cement and concrete production, but recently, different advanced technologies are under development for its reduction by the component recovery. Due to the specific chemical composition and the amorphous-crystalline structure, FA is a suitable starting material for the synthesis of zeolites [1]. Zeolites are natural or synthetic crystalline aluminosilicates with a structural framework

D. Zgureva (✉) • S. Boycheva
Department of Thermal and Nuclear Power Engineering, Technical University of Sofia, Blvd. Kl. Ohridsky 8, 1000 Sofia, Bulgaria
e-mail: dzgureva@gmail.com; sboycheva@tu-sofia.bg

P. Petkov et al. (eds.), *Nanoscience Advances in CBRN Agents Detection, Information and Energy Security*, NATO Science for Peace and Security Series A: Chemistry and Biology, DOI 10.1007/978-94-017-9697-2_21

built-up of $SiO_{4/2}$ and $[AlO_{4/2}]^-$ tetrahedra linked each to other at the corners, sharing an oxygen bridge. Zeolites are characterized by a highly mesoporous structure and a large surface area which are favorable for surface phenomena and determine their applications as adsorbents, catalytic carriers, molecular sieves, etc. [2]. This investigation is a part of a broad experimental program on the conversion of lignite coal fly ash into synthetic zeolites and their applications in the flue gas cleaning systems.

21.2 Materials and Methods

21.2.1 Starting Material

FA generated from the combustion of local lignite coals in the largest thermal power plant in Bulgaria named TPP "Maritza-East 2", was subjected to zeolitization. The FA was preliminary studied with respect to its chemical and phase composition, and its thermal properties [3]. The FA used as a raw material for this study was found to contain 52.7 wt% SiO_2 and 23.4 wt% Al_2O_3; the amorphous phase was determined to 43 % vs. the crystalline one. The grain size distribution of the FA particles, determined by sieve separation, was found to be between 125 and 250 μm. The density of the FA is ~3.07 g/cm^3.

21.2.2 Classic Alkaline Conversion

This method is based on the combination of different ratios of activator and FA, with the temperature and the reaction time as parameters to obtain different zeolites types. For the purpose of this study a mixture of 5 g FA and 6 g NaOH was subjected to magnetic stirring in 100 ml distilled water for 12 h. The solution obtained was filled into an autoclave, and the synthesis was performed at 90 °C for different times (2, 3 and 4 h). After the hydrothermal activation, the solid part was separated by filtration, washed with distilled water and dried.

21.2.3 Two Stage Fusion-Hydrothermal Synthesis

The fusion stage prior to classical hydrothermal treatment is directed to obtain soluble sodium silicate and aluminate, which after dissolution under continuous stirring are converted to a hydrogel. Further, crystallization takes place in the gelous medium during the hydrothermal synthesis. Mixtures of NaOH and FA were prepared in different ratios: 1.6, 2.0, and 2.4. They were treated in two steps: fusion prior to hydrothermal synthesis. The first stage was performed at a

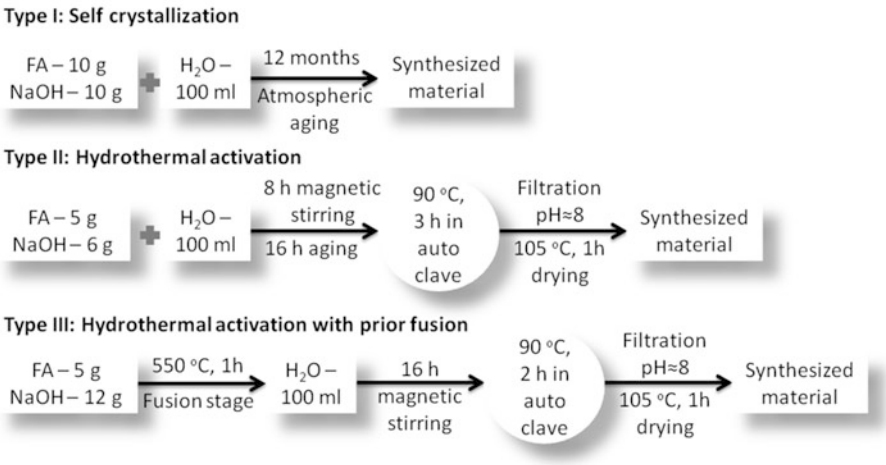

Fig. 21.1 Principle scheme of the three synthesis mechanisms realized

temperature of 550 °C for 1 h. Thereafter, the sintered alloys were crushed, mixed with distilled water and subjected to magnetic stirring for 16 h. The water suspensions obtained were filled into an autoclave; the hydrothermal synthesis stage was performed at 90 °C with a duration of 2 h. Then, the solid part was separated by filtration, thoroughly washed with distilled water and dried at 105 °C. In general, the process of zeolite synthesis, applying a fusion stage before the hydrothermal treatment, passes through the following reaction scheme:

$$\mathrm{NaOH} + \mathrm{xAl_2O_3} \cdot \mathrm{ySiO_2} \xrightarrow{\text{fusion}} \mathrm{Na_2SiO_3} + \mathrm{Na_2AlO_2} \xrightarrow{\text{dillution}} \mathrm{NaOH_{(aq)}} + \mathrm{Na_2Al(OH)_{4(aq)}} + \mathrm{Na_2SiO_{3(aq)}} \xrightarrow{\text{stirring}} \left[\mathrm{Na_x(AlO_2)_y(SiO_2)_z}\right]\mathrm{NaOH.H_2O_{(gel)}} \rightarrow \xrightarrow{90^\circ\mathrm{C}} \mathrm{Na_p}\left[\mathrm{(AlO_2)_n(SiO_2)_q}\right] \cdot \mathrm{hH_2O_{(zeol)}}\,\text{Atmospheric aging}$$

The atmospheric synthesis aimed to simulate a mechanism of formation of natural zeolites which is associated with alkaline activation of volcanic rocks. A mixture of 10 g FA, 10 g NaOH and 100 ml distilled water was prepared and filled into a tube. Part of the suspension was separated after 8, 10 and 12 months and dried at atmosphere conditions.

In Fig. 21.1 the principle schemes of the three different synthesis mechanisms performed in this research to obtain the zeolite Na-X are summarized.

21.3 Results and Discussions

XRD patterns and SEM images of the samples obtained by different approaches are presented in Figs. 21.2 and 21.3, respectively. The most of the reflections typical for zeolite Na-X are well expressed for the self-crystallized product. Some intensive

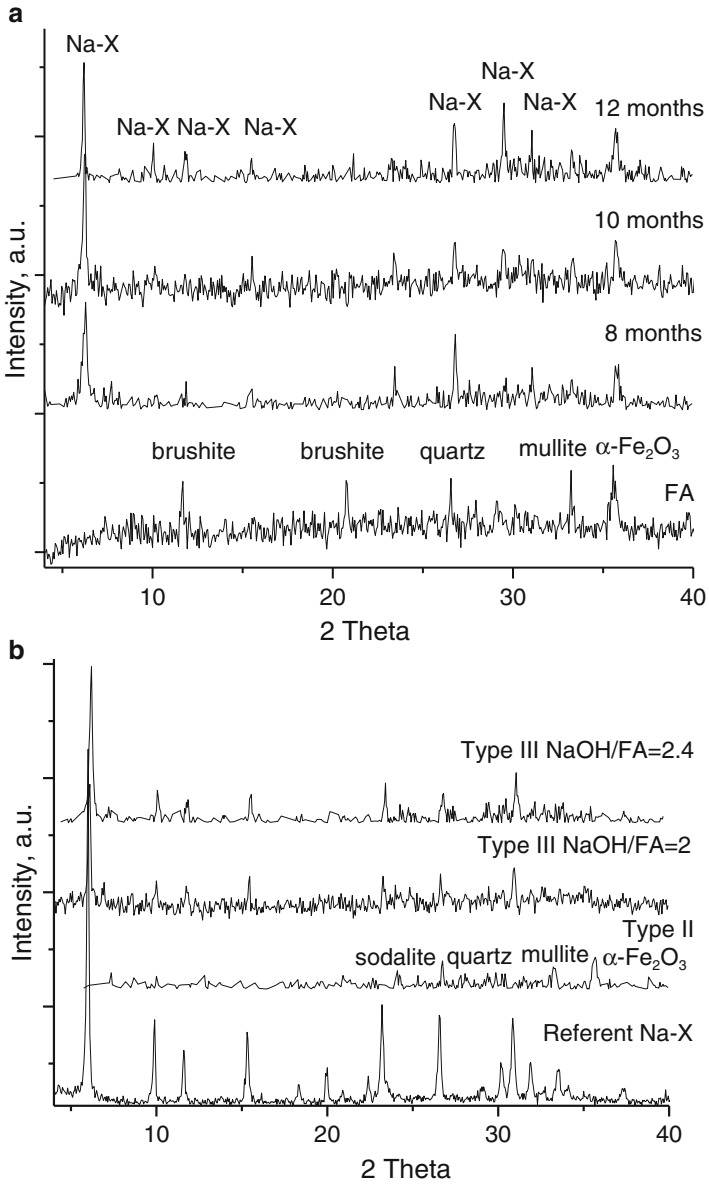

Fig. 21.2 XRD patterns of the synthesized samples (**a**) by atmospheric synthesis in comparison with the starting FA; (**b**) by hydrothermal and two-stage syntheses compared with the referent Na-X zeolite

peaks of different mineral components from the parent FA composition, mostly those of mullite ($2Al_2O_3SiO_2$) and magnetite (γ-Fe_3O_4) are preserved (Fig. 21.2a). Those two components need to be treated at higher temperature to achieve a transformation of their structure.

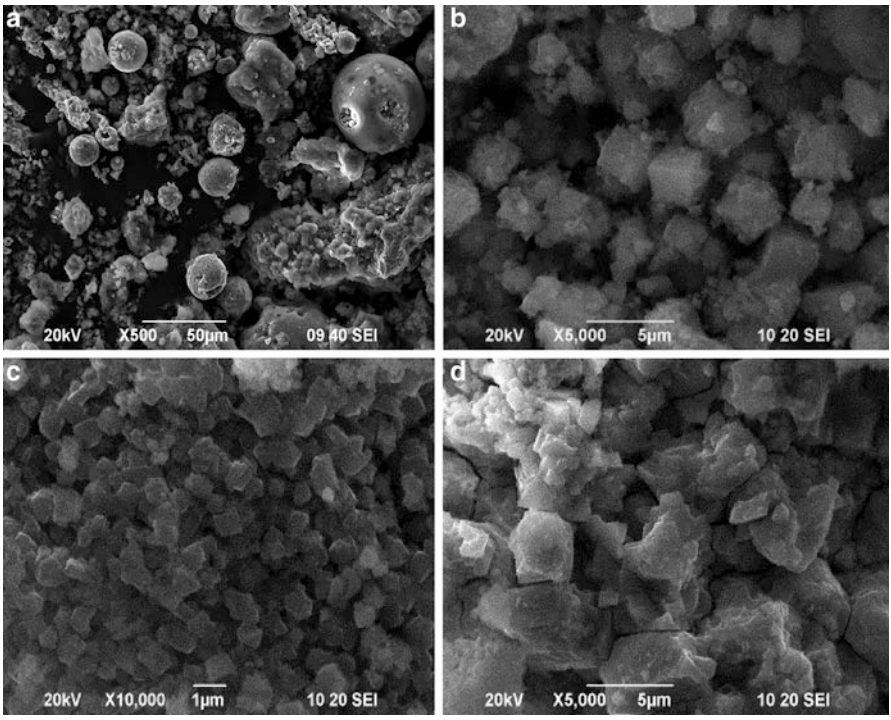

Fig. 21.3 SEM images of samples obtained by different reaction schemes

The influence of the duration of the atmospheric aging on the type of the synthesized materials was investigated by storing samples in a closed tube for 8, 10 and 12 months, respectively. It can be seen that with increasing self-crystallization time the characteristic peaks of the zeolite Na-X become more intensive. The intensity of the peaks belonging to the unreacted FA remains constant.

After the hydrothermal activation, the treated sample still contains parts of the raw material, as the reflections of mullite still exist in the XRD pattern (Fig. 21.2b, type II) and the FA particles remain unchanged (Fig. 21.3a). In addition, aluminosilicate hydrogel formation and its initial crystallisation over the FA particles can be observed in the SEM micrograph, confirmed by the appearance of a diffraction peak at $2\theta = 7.4$, typical for zeolite A.

Samples obtained by the two-stage syntheses at different NaOH/FA ratios of 1.6, 2.0, and 2.4 do not contain traces of the raw aluminosilicates (Fig. 21.2b, type III). The product obtained at the lowest NaOH/FA ratio of 1.6 possess cubic crystals of zeolite A (Fig. 21.3b). It can be seen also that the surface of the cubic crystals is covered by nanoscale particles probably belonging to some other zeolitic phase. Further, hexaoctahedral crystallites of Na-X appear at a higher NaOH/FA ratio of 2.0 (Fig. 21.3c), while some zeolite A phase is still preserved. Crystallites and reflections belonging only to Na-X zeolite are observed for a NaOH/FA ratio of 2.4 (Figs. 21.3d and 21.2, type III). The crystallite size changes with varying NaOH/FA

ratios from the nanoscale at 2.0 to microcrystallites at 2.4. A morphology analysis shows dimensions of 0.3–0.9 μm for the sample with the lower NaOH/FA ratio, and of 2.1–5.5 μm for the sample with the higher NaOH/FA.

21.4 Conclusions

The zeolitizaton of aluminosilicates by hydrothermal synthesis and atmospheric aging does not ensure complete alkaline conversion of the mullite from the raw FA. The hydrothermal process can be improved by increasing the duration and the concentration of the alkaline activator but this will result in a mixture of different zeolitic phases. The self-crystallization and the two-stage fusion-hydrothermal synthesis both result in a Na-X zeolitic material. The self-crystallization mechanism is the most energy efficient but results in a mixture of zeolitic phases and unreacted raw aluminosilicates. The two-stage synthesis is controllable to obtain different types of zeolites with defined morphology. With an increase of the NaOH/FA ratio, the crystallite size changes from nano- to microscales.

References

1. Ahmaruzzaman M (2010) Prog Energy Combust Sci 36:327
2. Querol X, Moreno N, Umana JC, Alastuey A, Hernandez E, Lopez-Soler A, Plana F (2002) Int J Coal Geol 50:413
3. Boycheva S, Zgureva D, Vassilev V (2013) Fuel 108:639

Part VII
Materials: Nanocomposites

Chapter 22
Organic-Inorganic Nanocomposites and Their Applications

Alexander V. Kukhta

Abstract The synthesis, the optical and electrophysical properties, and the morphology of thin films of nanocomposites based on electroactive polymers and inorganic nanofillers (metals, semiconductors, nanocarbons) are considered and analysed. Special attention is paid to polymer-graphene nanocomposites. Common and specific properties of such nanocomposites are discussed. Possible applications in the field of energy conversion and storage, light emitting devices, advanced sensors, EMI shielding and electronics elements are considered.

Keywords Electroactive polymer • Inorganic nanofiller • Conductivity • Morphology

22.1 Introduction

Electronic organic-inorganic hybrid materials consisting of two or more components of different nature attracted wide attention of scientists during the past decade. Materials of this type are widely known in nature (mollusc shells, radiolaria, etc.) and have even made been by people in ancient times (Egyptian inks, prehistoric frescos, etc.). There is a rich variety of possible combinations of organic-inorganic materials. Note that hybrid materials in which at least one of the components are nanosized are called nanocomposites. Conducting organics and polymers as organic component can be hybridized with metal or semiconductor nanoparticles as well as with nanocarbons. Commonly, polymers have advantages such as easy synthesis and processing, chemical and structural diversity, low weight, and flexibility. Especially attractive for electronic applications are conducting polymers such as polyaniline (PANI), polythiophenes, polypyrroles, polyphenylenevinylenes, etc. (Fig. 22.1). The addition of some amount of a nanofiller to a polymer results in combining the best properties of both partners,

A.V. Kukhta (✉)
Research Institute for Nuclear Problems, Belarusian State University, Babruiskaya Str. 11, 220030 Minsk, Belarus

Tomsk State University, Tomsk, Russia
e-mail: al.kukhta@gmail.com

P. Petkov et al. (eds.), *Nanoscience Advances in CBRN Agents Detection, Information and Energy Security*, NATO Science for Peace and Security Series A: Chemistry and Biology, DOI 10.1007/978-94-017-9697-2_22

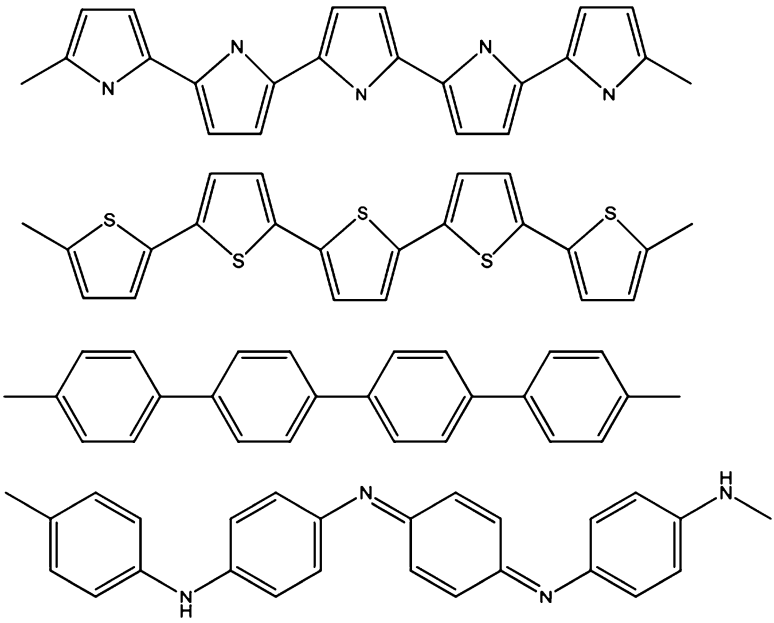

Fig. 22.1 Structures of conducting polymers (from *top* to *bottom*): polypyrrol, polythiophene, polyparaphenylene, polyaniline

and new properties often appear. Nanosized fillers results in an increased role of the interface between the components. It is easy to show that 100 nm particles contain some 10^7 atoms with 1 % of them at the surface, but 5 nm particles consist only a few thousands atoms with 40 % of them located at the surface. As a result, the properties of nanocomposite are determined by the properties of the polymer, the filler and the interface between them. Thus, the important advantage of nanoparticles as polymer additives is that compared to traditional additives the loading requirements are quite low. Microsized particles need much higher loadings; they also scatter light, thus reducing light transmittance and optical clarity.

On the other hand, nanostructured materials show unique properties depending on size and shape. Size-dependent properties such as quantum confinement in semiconductor particles, surface plasmon resonance in some metal particles and superparamagnetism in magnetic materials [1] are observed. Nanocomposites can be easily prepared by simple solution mixing, melting and in-situ polymerization or by nanofiller synthesis in a polymer. Particles coated with a polymer shell are considerably more stable against aggregation due to a large decrease of their surface energy in comparison to bare particles.

The electrical conductivity of nanocomposites depends on the conductivity of the constituents, the volume fraction of the filler and filler characteristics such as size, shape, surface area and morphology, the distribution and orientation of the filler as well as the interparticle filler spacing within the polymer matrix and the crystallinity of the matrix [2]. Many of the above factors depend on the processing

method and the conditions used to fabricate the composites. There is a percolation threshold defined as the minimum volume content of the filler, above which the filler particles form a continuous network, as described by percolation theory [3]. At this point the composite becomes electrically conductive. For spherical particles the interparticle distance increases at constant volume fraction with increasing diameter; it becomes more difficult to form a conductive pathway. For non-spherical particles (e.g. fibers, platelets), the critical concentration to induce bulk conductivity in the composite decreases significantly as the aspect ratio of the conductive filler increases. When the particles possess the same aspect ratio, theory predicts that rod-like particles percolate at one-half the volume fraction of disk-like particles [2]. The percolation threshold becomes higher if the particles are parallel aligned.

The presence of metal or semiconductor nanoparticles render even dielectric organic materials conductive with an electron type conductivity. Metal nanoparticles change the distribution of electric fields in polymers resulting in additional electron emission as in island films. The presence of organic shells on the metal nanoparticle surface can change its work function and, as a consequence, the conductivity of nanocomposite.

There are three main types of forces between particles in nanocomposites: van der Waals interactions (between two identical spherical particles), electrical double-layer interactions (between oppositely charged particles or moieties), and steric interactions [4].

The nanocomposites considered have opened the era of printed electronic circuits using the ink jet printing technology. Solution colloid based electrically conductive inks are available on the market, but they require to be sintered on the substrate at elevated temperatures or to be cured by UV radiation, as well as an catalytically active template in order to obtain the required electrical conductivity. A direct ink-jet printing of conductors without additional treatment would be very attractive. The proposed approach overcomes the inherent limitations of pure nanoparticle dispersions. Depending on the polymer and the nanofiller nature, nanocomposites have already been developed for manifold printable electronic applications such as conducting electrodes, transistors, memories, radio frequency identifiers, solar cells, light emitting devices, electrochromic devices, supercapacitors, electromagnetic interference (EMI) shielding, sensors, as well as in optics, biology and medicine, etc. [5].

In this paper, the conducting and in some cases the optical properties and the morphology of the most interesting electronic polymer nanocomposites in this wide area are briefly reviewed along with some applications in light emitting and photovoltaic devices, supercapacitors, sensors, etc.

22.2 Polymer-Metal Nanoparticles Nanocomposites

It is well known that metals are among the most conductive materials on earth due to their high free-electron density.

Metallic nanoparticles (NP) play an important role in a wide number of applications such as surface enhanced Raman scattering and luminescence display devices, catalysis, microelectronics, light emitting diodes, photovoltaic cells and also in medical or biological applications. Moreover, nanoparticles show changes of their electronical, optical and catalytic properties depending on the synthesis method. Many physical and chemical techniques of nanoparticles synthesis have been developed up to date. Pure nanoparticles readily aggregate. In order to prevent aggregation they are covered by organic surfactants, polymers, or inorganic shells [6].

The contact between metal particles and the polymer is crucial in molecular electronic devices because the charge transfer at the contact point plays an important role in their functionality. Conducting polymers containing either nitrogen or sulfur atoms in their repeating unit are attractive candidates for the preparation of metal/polymer nanocomposites.

The surface plasmon bands of gold (silver, copper) nanoparticles are prominent when they possess diameters greater than 5 nm. At relatively low diameters (less than 2 nm), surface plasmon absorption of gold nanoparticles disappears. Purified Au and Ag nanoparticles with diameters less than 2 nm become highly luminescing [1].

A micrograph of typical Ag nanoparticles and their size distribution is presented in Fig. 22.2. The random distribution of nanoparticles and their small diameter results in low light scattering, and the transmission of a nanocomposite film is close to that of the pure polymer (compare the absorption spectra in Fig. 22.3). The absorption spectrum of the nanocomposite film has a wide band in the region between 250 and 450 nm. It mainly stems from the absorption of the polymer. After introduction of nanoparticles the spectrum changes a little in the short wavelength region as compared to the spectrum of the pure polymer film due to

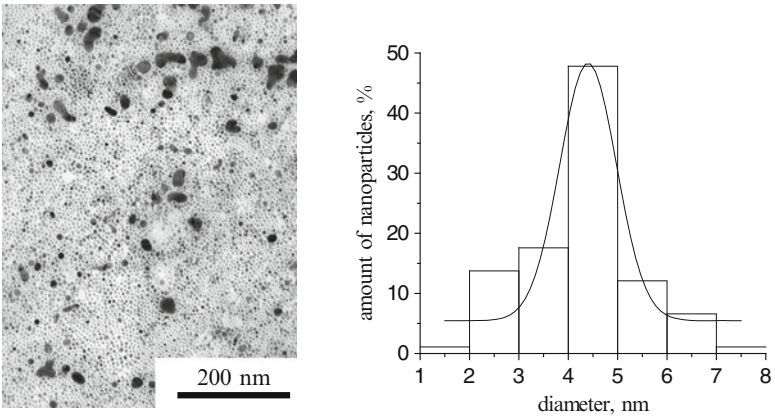

Fig. 22.2 Electron microscope micrograph of Ag nanoparticles (*left*) and their size distribution (*right*)

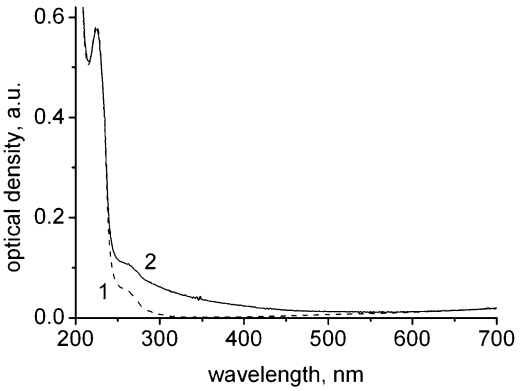

Fig. 22.3 Absorption spectra of thin films of PEDOT:PSS (*1*) and PEDOT:PSS + AuNP (*2*)

the low filler concentration. Nanocomposite thin film remains transparent in the whole visible region though an essential transparency decrease is observed in near UV region below 400 nm, up to 10 % at 300 nm. The transparency decrease in the region 400–700 nm does not exceed 3 %. No visible changes in transparency of nanocomposite films in vacuum and in air are observed.

Conducting AFM measurements did not reveal significant differences in the morphologies of thin films of pure poly(3,4-ethylenedioxythio-phene):poly (styrenesulphonate) (PEDOT:PSS) and the polymer containing nanoparticles. However, at low applied voltages, for both films there is no noticeable correlation between the morphology and the electric current distribution (Fig. 22.4), although a certain correlation appears as the voltage increases. Furthermore, the currents of PEDOT:PSS + Ag nanoparticles films are larger in magnitude and have a more pronounced structure than those of the pure polymer films. This means that the nanoparticles are located under the film surface in different depths and initiate an increase of the current. The electric field strength in this geometry is difficult to estimate. Based on the ratio of the voltage to the interelectrode distance, it exceeds 1 MV/cm. The sharp electrode further increases the field strength. Therefore, these measurements can be considered as measurements in a very strong electric field.

It has been found [7] for nanocomposites consisting of PEDOT:PSS and Au/Ag nanoparticles that the current-voltage characteristics of the nanocomposite films depend significantly on the electric field strength. The introduction of gold nanoparticles into PEDOT:PSS in weak electric fields leads to an increase in the bulk conductance by almost two orders of magnitude (due to donor–acceptor interactions) (Fig. 22.5), a 50 % decrease of the activation energy for conduction, and an increase in the sensitivity to adsorbed oxygen. The conductivity increases on introduction of nanoparticles in dielectric polymers can achieve seven orders [1] and more. It should be noted that oxygen adsorption on the surface and in the bulk of nanocomposite films in air always effect the value of the conductivity. It is not easy to measure the concentration of the adsorbed oxygen. However, it can be

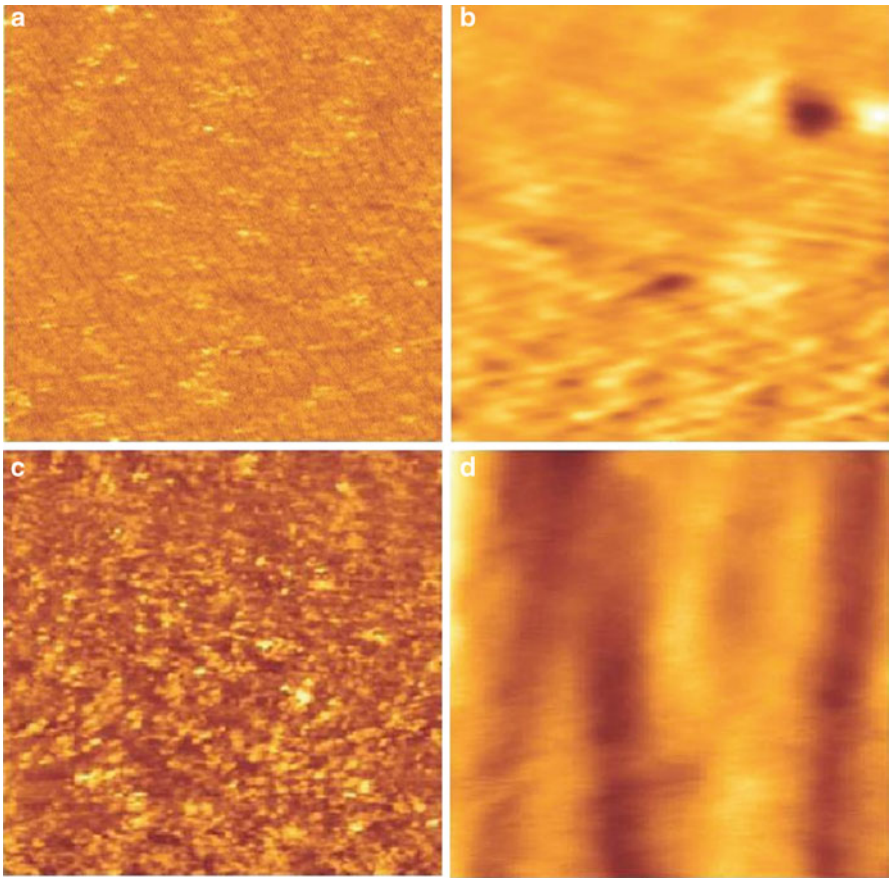

Fig. 22.4 (**a**, **c**) Electric current distributions and (**b**, **d**) topographies of (**a**, **b**) PEDOT:PSS and (**c**, **d**) PEDOT:PSS + AgNP films (1 × 1 μm) at a positive potential of 0.3 V across the sample

estimated using the cyclic thermodesorption method. The concentration of oxygen adsorbed in the sample will decrease if in every heating-cooling cycle temperature is increased. Using a number of such cycles and measuring the conductivity in vacuum and air during cooling one obtains a series of conductivity temperature dependences with different concentrations of adsorbed oxygen. Each curve corresponds to a fixed oxygen concentration.

The temperature dependences of the conductivity obtained by measuring in vacuum, in air or by cyclic thermodesorption method can be described by the formula $\sigma = \sigma_0 \exp(-E/kT)$, where E is the activation energy, and σ_0 is a pre-exponential factor. This formula describes hopping transport in many organic semiconductors. The relation between σ_0 and E can serve as a basis for a systematization of the measured temperature dependences of the electrical conductivity at

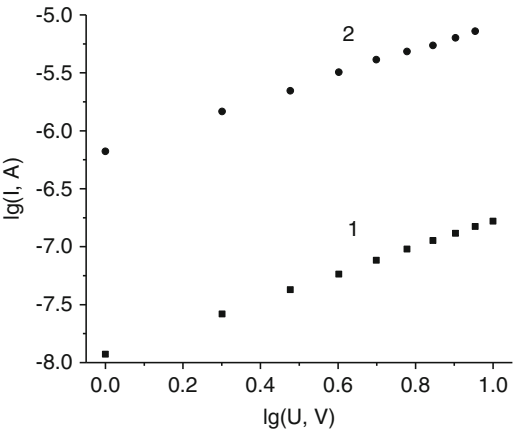

Fig. 22.5 Current-voltage characteristics of pure PEDOT:PSS (*1*) and PEDOT:PSS + AuNP (*2*) planar thin films on an interdigitated substrate

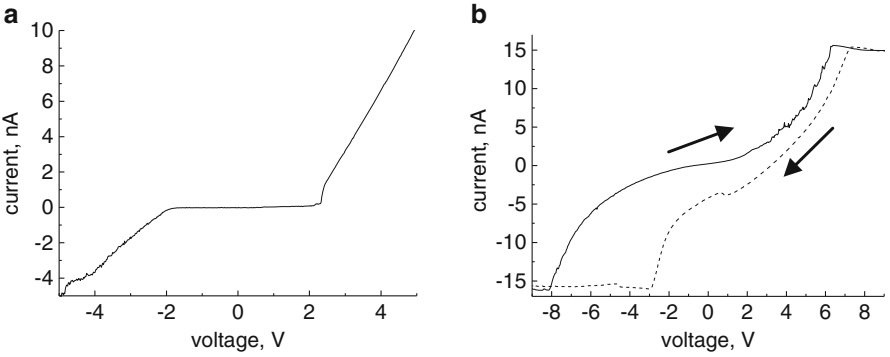

Fig. 22.6 Current-voltage characteristics measured with a conductive atomic force microscope for pure PEDOT:PSS (**a**) and PEDOT:PSS with Ag nanoparticles (**b**)

different oxygen concentrations, either confirming or rejecting the activation character of the conductivity. It also reflects the so-called compensation effect, showing a linear growth of $\ln(\sigma_0)$ with the activation energy.

The electrical conduction of PEDOT:PSS + AuNP films is provided by hopping charge transfer in the system of intrinsic localized states as well as in the system of impurity states of adsorbed oxygen. Gold nanoparticles promote electron transfer due to donor–acceptor interactions in the nanocomposite. In strong electric fields, the current–voltage characteristics exhibit a different behavior in forward and reverse scanning modes (Fig. 22.6) [7].

It has been found that the insertion of amine functionalized gold nanoparticles into PEDOT:PSS results in a strong increase of the conductivity. This increase was found to depend strongly on the surrounding medium. As compared to pure polymer films this increase is minor in vacuum, but very strong in air and oxygen.

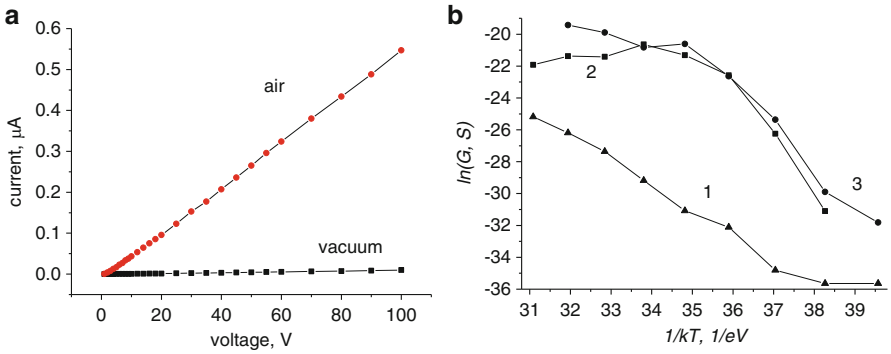

Fig. 22.7 (**a**) Current-voltage characteristic of a PEDOT:PSS + AuNP nanocomposite film in air and vacuum; (**b**) temperature dependences of the conductivity of pure polyepoxypropylcarbazole (PEPK) (*1*) and PEPK + Ag-AuNP nanocomposites (*2*,*3*) thick films with nanoparticle concentrations of 1.75×10^{-4} M; *3*: with aromatic thiol based shell

This property can be used for oxygen sensors. Current-voltage characteristics of pure polymer and nanocomposite thin films on interdigitated substrate are presented in Fig. 22.7 [8]. Figure 22.7b illustrates that the incorporation of metallic nanoparticles enhances the electrical conductivity of the films. The concentration of the nanoparticles is much less then the percolation threshold. It is well-known that aliphatic molecules are electrically insulating while aromatic molecules can conduct electricity. We can see that replacing organic aliphatic shell by a aromatic thiol (biphenyloxazole based) shells increases the conductivity Ag/Au-polyepoxypropylcarbazole (PEPK) nanocomposites (Fig. 22.7b).

The application of Ag nanoparticles to organic electroluminescence cells showed [9] that their insertion into single layered cells resulted in the improvement of all operation characteristics. The electroluminescence increase varied from about 50 % up to more than 100 % with the applied voltage as compared with undoped structures, the threshold of electroluminescence appearance is essentially lower. It should be noted that there is an optimal nanoparticle concentration due to luminescence quenching caused by the metal nanoparticles. The essential efficiency rises; its increase with applied voltage has also been observed. A numerical simulation of the processes in such a cell shows that a lower nanoparticle concentration (larger nanoparticle diameter) results in the decrease of the tunneling current due to an increase of the potential barrier; the field drops in many points on the cathode surface. This effect is more noticeable for low fields. Cu (for all concentrations) and Ni nanoparticles (for optimized concentrations) in the hole injection layer (PEDOT:PSS) also improved all characteristics of electroluminescent cells [10].

Nanocomposites based on nanoparticles made from magnetic metals are promising for various potential applications such as spin-polarized devices, carriers for drug delivery, magnetic recording media, high-frequency applications, magneto-optical storage, interference suppression, biomedical sensing, etc. [11].

22.3 Polymer-Semiconductor Nanoparticles Nanocomposites

Semiconductor nanoparticles (quantum dots, QD) are nanostructures composed of groups III−V or II−VI elements that exhibit interesting optical and electronic properties making them very attractive in applications such as biological labeling, solar cells, and light emitting devices. Many techniques for the synthesis of such nanoparticles have been developed. The most interesting nanoparticles are metal oxides, sulfides, selenides, and hydrides. To avoid aggregation these nanoparticles are covered by organic surfactants, polymers, or inorganic shells [6].

Special semiconductor nanoparticles with thermodynamically stable structures are called magic-sized nanoclusters, a term adopted from metal clusters having an exceptionally stable closed-shell structure. These magic-sized nanoclusters have a narrow emission bandwidth of 20−30 nm because they possess only one particle size [1] and show the highest luminescence quantum yield. Another type of semiconductor nanoparticles with unexpectedly high quantum yield (up to 80 %) is semiconductor nanoplatelets [12].

Quantum dots are highly luminescing with easy colour tuning by their dimensions [13]. Up to now a wide number of different semiconductor nanoparticles with high quantum yields and wide luminescence bands as in organic phosphors have been developed. The size and type of the nanoparticles determine the emission colour. There are a number of ways to increase the luminescence ability of semiconductor nanoparticles. First, modification of the nanoparticle surface by different organic and inorganic materials can not only prevent aggregation, but also luminescence quenching caused by surface defects, as well as charge and energy transfer from the nanoparticle to the environment. Typical materials for the creation of the surrounding shells for nanoparticles are amines, aliphatic thiols and other organic surfactants, inorganic substances (semiconductors, e.g. CdSe/ZnS, CdSe/CdS or metals with an electrolyte spacer), micelles, and dendrimers. In any case the band gap of the shell material has to be higher than that of the nanoparticle, and an alignment of the corresponding levels is required. Second, doping of semiconductor nanoparticles with d-element ions (Cu^{2+}, Mn^{2+}, Eu^{3+}, etc.) can be performed which is well-known also for the bulk materials. Third, the introduction of luminescing nanoparticles into conducting luminescent polymers results in a widening of the luminescence spectrum, a simpler deposition, and a higher stability. Even usual insulating polymers doped with luminescent semiconductor nanoparticles increase the brightness up to 40 %.

Usually, an effective interaction between nanoparticles shells and polymer molecules is observed. A luminescence enhancement can occur in the case of efficient energy transfer from the polymer to the nanoparticles when conditions of matching energy levels and the absence of steric barriers are fulfilled. In fact, even relatively long insulating nanoparticles ligand do not severely impede the transfer of excitations from the polymer to the nanoparticles, although shorter chains can improve the transfer efficiency. By controlling the average nanocrystal size, the band gap of quantum dots can be tailored continuously over an energy range wider

than possible in bulk semiconductors by changing the semiconductor alloy composition. In fact, bandgaps even smaller than those of the bulk semiconductor counterpart have been achieved in quantum dots-polymer composites, perhaps due to a bandgap narrowing that occurs as a result of high local electric fields between closely spaced quantum dots. Combining the unique optical properties of quantum dots with the electrical properties of conductive polymers results in quantum dot/polymer composites for alternative photonic devices. Generally the costs and the efficiency of these polymer-based devices can be significantly lower than their semiconductor counterparts, since economical high-volume manufacturing techniques can be employed for polymer films. Physical mixing of the CdSe/ZnS quantum dots with the blue-emitting electroluminescent polymer polyfluorene (PFO) cannot produce the required homogenous uniform dispersion for good energy transfer from PFO to the QDs; therefore, the development of integrated polymer/QD composite systems by molecular engineering is essential. Good results can be obtained with hybrid QD-oligomer nanocomposites, where the emitting oligomers are coordination bonded to the QD surfaces.

As a rule, polymer nanocomposites with luminescing quantum dots are also highly luminescing. Nanocomposites based on ZnO, GaN, HfO_2, ZrO_2, Al_2O_3, etc. show very good luminescences [14]. Semiconducting carbon nanoparticles were found to possess an efficient luminescence; they are attractive owing to their inertness [15].

The absorption and photoluminescence spectra of quantum dots allow them to act as wavelength conversion materials for light emitting diodes using the wavelength conversion properties of quantum dots for white lighting. One practical goal is to produce color-balanced white light with the highest possible energy efficiency and the lowest possible cost. One approach is to surround a blue light-emitting diode with a quantum dot polymer composite that converts some of the blue light to yellow light so that the human eye perceives the emission as white light. Although color mixing is possible with quantum dots, this approach is not energy-efficient enough to replace fluorescent lights.

For visible imaging, quantum dots have several potential advantages over organic dyes. First, traditional organic dyes have narrow absorption peaks which are very close to their photoluminescence peak. Therefore each dye requires its own expensive, carefully-tuned, sharp-cutoff filter to block the excitation background from the imaging camera. In contrast, quantum dots have a broad absorption tail over wavelengths shorter than the peak emission wavelength. Conjugation of QD with antibodies yields biomarkers that compete with traditional organic fluorescent tags in terms of biocompatibility, excitation and filtering simplicity, and photo-stability.

Transparent PMMA/Fe-oxide nanocomposites possess good magnetic properties and potentially interesting magneto-optic applications [16]. It was reported that very small magnetic nanoparticles have discrete spin quantum numbers whereas larger-sized particles exhibit a continuum of energy states. The stepped magnetic hysteresis curve derives from the quantization of spin states in the iron oxide particles due to their extremely small volume [1].

Many metal oxides nanoparticles (TiO_2, ZnO, SnO_2, ZrO_2) are widely used in cathodes of dye-sensitized solar cells [17] and supercapacitors.

22.4 Polymer-Graphene Nanocomposites

Many carbon nanoparticles have been developed up to date. Fullerenes, carbon nanoparticles, onion like particles, nanodiamonds, nanotubes, graphenes, nanofoams found wide scientific interests and applications owing to their chemical inertness, hardness, and good electrical and thermal conductivity. Among them graphene was one of most attractive carbon nanomaterial during the last decade. Graphene consists of a single-layer carbon sheet with a hexagonal packed π-electron system. It possesses many unique properties such as a high carrier mobility at room temperature (250,000 $cm^2V^{-1}s^{-1}$), a very high current carrying capacity (up to 10^9 A/cm^2), a large theoretical specific surface area (2,630 m^2g^{-1}), a good optical transparency (97.7 %), a high Young's modulus (1 TPa) and an excellent thermal conductivity (3,000–5,000 $Wm^{-1}K^{-1}$) [18, 19]. In practice, graphene networks consisting of graphene sheets fabricated by physical or chemical graphite exfoliation in solutions contain multiple boundaries and defects that dramatically decrease the properties of the resulting films. This is also one reason for the poor quality and stability of thin films made from graphene nanosheets. The absorption spectrum of graphene nanosheets (Fig. 22.8) represents a wide band with a maximum at 320 nm that is similar to that of graphene. It originates from π–π* transitions in aromatic sp^2 domains. A single layer graphene absorbs 2.3 % of the incident light [20]. Measurements [21] showed that an extreme difference (four to five orders of magnitude) of the inplane conductivity of a graphene sheet as compared to the transverse conductivity.

Though graphene is widely commercially available, in many cases one needs to use freshly prepared material without any surfactants. Mechanical graphite cleavage, chemical vacuum deposition and epitaxial growth (giving the most qualified large scale graphene), chemical graphite exfoliation, microwave and laser exfoliation are widely known. However, the most simple and scalable tool is sonication of graphite flakes in solutions [22].

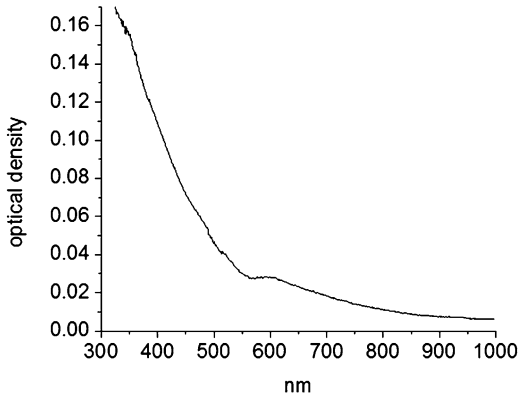

Fig. 22.8 Absorption spectrum of graphene nanosheets

The methods applied for the fabrication of graphene–polymer composites are solution mixing, melt blending, and in-situ polymerization. Solution mixing is one of the most commonly used methods for the preparation of polymer composites, since it is straightforward, requires no special instruments, and allows for large-scale production. The key issue to prepare advanced graphene-based nanocomposites is the engineering of the polymer-graphene interface. Pristine graphene is hydrophobic, not compatible with organic polymers and does not form homogeneous composites. The poor solubility of graphene in organic solvents, especially in the nonpolar ones, largely hinders its processability, being a bottleneck for the incorporation of graphene into most of the polymer matrices. That is why non-covalent or covalent functionalization of grapheme is used. It should also be noted that according to recent studies the hydrophobicity of graphene is actually due to airborne hydrocarbon contaminations. A clean graphite surface is in fact mildly hydrophilic with a water contact angle of 64° [23].

The $\pi-\pi$ interactions are the reason for restacking of the graphene sheets. Thus, they are one of the most important noncovalent interactions, in the sense that the negatively charged, diffusing electron clouds of the π systems exhibit an attractive interaction. This interaction is predominated by dispersion interactions when both π systems possess very similar electron densities. However, when one of the systems is electron-rich and the other electron-deficient, the resulting complexes are bound by induction interactions as is the case when the negative charge gets transferred from benzene to hexafluorobenzene [24]. The best interaction and solubility of graphene is observed in N-methylpyrrolidone and orthodichlorobenzene [25]. The solubility is also good in perfluorinated organic solvents (hexafluorobenzene and derivatives) and water-ethanol or water-isopropanol mixtures [26]. Many aromatic molecules (porphirin [27], tryptophan, congo red, tetracyanoquinodimethane, tetracyanoethylene, 1,5-naphthalenediamine, 9,10-dimethylanthracene, or tetrasodium 1,3,6,8-pyrenetetrasulfonic acid), ionic liquids, polymers (poly(N-vinylcarbazole), poly (styrene-co-butadiene-co-styrene), poly(2,5bis(3-sulfonato-propoxy)-1,4-ethynyl-phenylene-alt-1,4-ethynylphenylene)sodium salt) greatly improve the graphene solubility [22, 24]. Inorganic materials are also used for non-covalent functionalization.

Metallic and semiconducting nanoparticles are very attractive for this purpose in the last years. Graphite and graphene are often used as a substrate for the synthesis of free-standing metal nanoparticles due to their low chemical reactivity, small diffusion barriers for adsorbed species and high degree of structural order. Recent work suggests that graphene can promote the self-assembly of adsorbed metal atoms into nanoscale clusters with controllable size distributions potentially opening a new route to nanoparticle synthesis [24]. This methode of nanoparticle growth is attractive since being grown in situ the particles can be clean and densely packed without aggregating. The majority of the publications related to the preparation and applications of this new class of graphene based nanocomposites uses noble metals like gold, platinum, palladium and silver; however, there is also a growing interest in the use of other metals like iron, copper, tin and cobalt [24]. Figure 22.9 illustrates a stable graphene-copper nanoparticle composite. Note, that this nanocomposite can easily form stable, transparent and highly conducting 100 nm

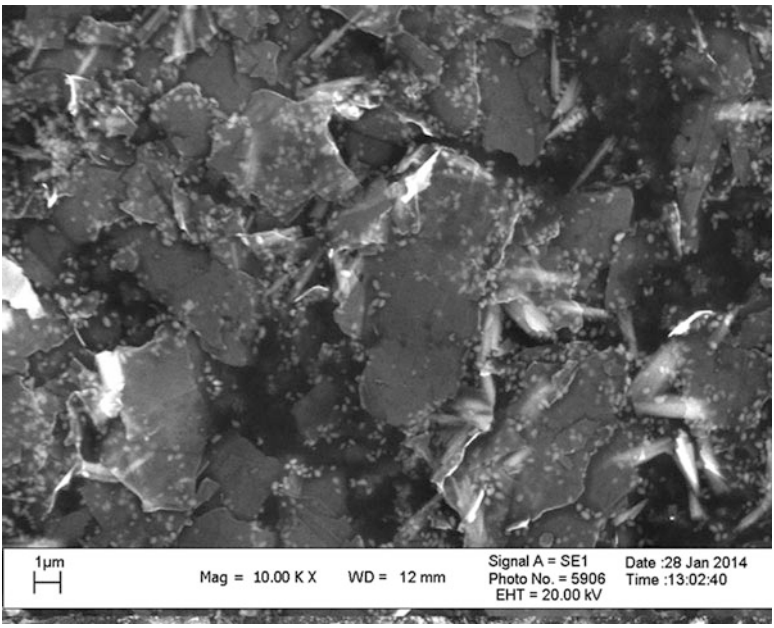

Fig. 22.9 Micrograph of graphene – Cu nanoparticles

thin films with a resistance of about 400 Ω/sq. Metal nanoparticles improve the stability of graphene films and their conductivity. The observation of superconductivity of tin nanoparticles activated graphene should be noted [28].

There is a great demand for the synthesis of graphene-semiconductor nanomaterial composites because of their promise in electronics, optics, and energy-based applications such as solar cells, Li-ion batteries, and supercapacitors. To date, various kinds of semiconductor nanomaterials have been synthesized and supported on graphene-based templates, which include TiO_2, ZnO, SnO_2, MnO_2, Co_3O_4, Fe_3O_4, Fe_2O_3, NiO, Cu_2O, RuO_2, CdS, and CdSe [24]. For luminescing CdS, CdSe, CdSe/ZnS quantum dots deposited on graphene, an efficient energy transfer occurs from the individual nanoparticles to the graphene surface. This energy transfer is indicated by a quenching of the fluorescence intensity of the CdSe/ZnS nanocrystals by a factor of 70. The fluorescence quenching of quantum dots from graphene oxide can be avoided by blocking the direct attachment of these species by an "insulating layer". As an example graphene oxide can be covered during its reduction step by a monolayer of a reductive agent such as the positively charged p-phenylene diamine, while CdSe nanoparticles were covered during their formation by negatively charged hexadecanoic chains as described in [24]. The composite is formed due to the electrostatic forces between the two components. The presence of the organic aliphatic molecules provides the composite with a high solubility in organic solvents such as toluene. Due to this insulating layer the composite showed a characteristic fluorescence spectrum after photoexitation of the quantum dots.

Quantum dots can absorb light and transfer it to graphene, but the efficiency of the transfer depends on how far the quantum dots and the graphene are separated from each other. The thickness of the organic molecule layer typically surrounding the quantum dots is crucial in attaining sufficiently high efficiencies of this light/energy transfer into the graphene. This transfer can be further optimized by engineering the interface between the two nanomaterials, especially by optimizing the thickness of the organic capping molecules [29].

To prepare more stable graphene inks and polymer nanocomposites, different types of covalent functionalizations are used [30]. Many types of organic surfactants, oxidation, bases and acids, bile salts have been developed up to date. However, while the dispersion of graphene in the polymer is greatly improved, the electrical conductivity often decreases in the case of covalent functionalization.

The conductivity of the studied polymer-graphene nanocomposites is higher than that of pure polymer, but it is still essentially lower than that of pure graphene. One of the mostly employed host polymers is PANI due to its high capacitive characteristic, low cost, and ease of synthesis by in-situ polymerization. Good results have been obtained with nafion-graphene nanocomposite (1,030 Ω/sq), but the transmittance was decreased to 50.5 % [31]. Recently, large-scale graphene-doped polymer films showed a low sheet resistance of 120 Ω/sq at ambient conditions with a transparency higher than 95 % [32].

To achieve better conductivities or lower costs, more than one kind of filler, particularly fillers with different aspect ratios, are used to prepare conducting nanocomposites. Figure 22.10 illustrates currents-voltage characteristics of polymer-metal nanoparticle-CNT (a) and polymer-metal nanoparticle-graphene (b) composites. It can be seen that the conductivity is drastically improved owing to the presence of additional contacts between carbon nanomaterial and polymer through the metal nanoparticles.

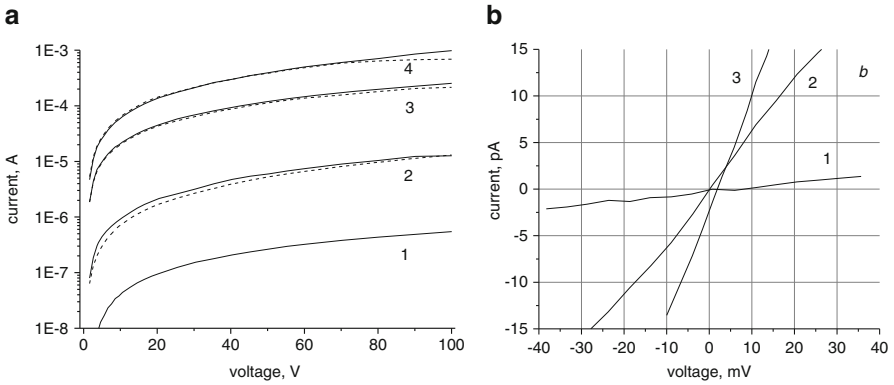

Fig. 22.10 Current-voltage characteristics of (**a**) polyfluorene (*1*) with MCNT (*2*), Ag nanoparticles (*3*) and MCNT + Ag nanoparticles (*4*) in air (*solid*) and vacuum (*dashed*); (**b**) PEDOT:PSS (*1*) with 0.05 % graphene (*2*) and 0.05 % graphene + CuNP (*3*) nanocomposite film

22.5 Applications

22.5.1 Supercapacitors

Supercapacitors (ultracapacitors or electrochemical capacitors) are energy storage devices that store energy as charge on the electrode surface or in a sub-surface layer, rather than in the bulk material as in batteries; therefore, they can provide high power densities (up to 10 kW kg^{-1}) due to their ability to release energy more easily from surface or sub-surface layer than from the bulk. Since charging-discharging occurs on the surface, which does not induce drastic structural changes of the electroactive materials, supercapacitors possess excellent cycling ability and a short charging time. Due to these unique features, supercapacitors are regarded as one of the most promising energy storage devices. In terms of their operation mechanism, there are two types of supercapacitors: electrochemical double layer capacitors (EDLCs) and pseudocapacitors. In EDLCs, the energy is stored electrostatically at the electrode–electrolyte interface in the double layer, while in pseudocapacitors charge storage occurs via fast redox reactions on the electrode surface. There are three major types of electrode materials for supercapacitors: carbon-based materials, metal oxides/hydroxides and conducting polymers. Each type of material has its own unique advantages and disadvantages. For example, carbon-based materials can provide high power densities and long life cycles but their small specific capacitance (mainly the double layer capacitance) limits their application for high energy density devices. Metal oxides/hydroxides possess a pseudocapacitance in addition to the double layer capacitance and have a wide charge/discharge potential range; however, they possess a relatively small surface area and a poor cycle life. Conducting polymers have the advantages of a high capacitance, a good conductivity, low costs and ease of fabrication but they have a relatively low mechanical stability and cycle life. Graphene derivatives and conducting polymers can be combined and used as a hybrid type of supercapacitor, i.e., a combination of EDLC and pseudo-capacitors. A promising way to allow an increased cell voltage and energy density is to develop asymmetric electrochemical capacitors, which comprise a battery-type Faradaic electrode and a capacitor-type electrode to combine the advantages of both energy storage devices. Graphene-based nanocomposites are expected to have a great future for applications in supercapacitors. The properties of nanocomposite electrodes depend not only upon the individual components used but also on the morphology and the interfacial characteristics. Nanorod-PANI-graphene composites exhibited a significantly improved performance with a maximum specific capacitance value of 879 F g^{-1} [33]. Graphene oxide/PANI composite achieved the maximum specific capacitance value of 1,136 F g^{-1} [33].

Graphene nanostructures are ideally suited as a carbon substrate for the use as anodes in Li-ion batteries. Such batteries are still considered as one of the promising storage systems due to their high absolute potential against the standard hydrogen cell (3.04 V) and their low atomic weight (6.94 g mol^{-1}), which leads to a large

energy density with theoretical values up to 400 $WhKg^{-1}$ [18]. Recently, conductive graphene/SnO_2 nanocomposites have been fabricated exhibiting an enhanced and stable specific capacitance compared to graphene. It was prepared from polyaniline/SnO_2 nanocomposites, with SnO_2 nanoparticles embedded in a netlike polyaniline network. This composite material is characterized by a 3 times higher energy storage density compared to pure SnO_2 and a specific capacitance decay of only 4.5 % after 500 cycles [29].

22.5.2 Photovoltaic Devices

Solar energy is a clean renewable energy resource, which can be directly converted into electricity by photovoltaic devices. There are two types of hybrid solar cells. One of them is based on the concept of bulk heterojunctions where a conducting polymer absorbs light, followed by charge transfer from this polymer to [6,6]-phenyl-C_{61}-butyric acid methyl ester and then by charge separation. Another type are dye-sensitized solar cells. It is composed of a porous layer of titanium dioxide nanoparticles covered with a molecular dye (ruthenium polypyridine) that absorbs sunlight. This structure is located between two electrodes and immersed in an electrolyte [34].

Graphene grafted to fullerenes resulted in a 2.5-fold increase of the power conversion efficiency with an enhanced short-circuit current density and an open-circuit voltage in bulk heterojunction solar cell [35]. It means that fullerene-graphene is an excellent electron accepting/charge transporting material for the construction of efficient polymer solar cells and for many other applications. Quite recently the positive influence of nanosized TiO_2, dispersed in polyvinylidene-fluoride on the long term stability of solar cells was demonstrated [29]. A unique capability of quantum dot-sensitized solar cells is a production quantum yield greater than one by impact ionization this capability produces higher conversion efficiencies than dye-sensitized solar cells [36].

A transparent window electrode is one of the key parts in solar cells. Presently, indium tin oxide (ITO) and fluorine tin oxide (FTO) are used with known problems (high price, brittleness, sensitivity to acidic and basic conditions). Graphene has also found its use in numerous related applications, e.g. as transparent electrodes, dye-sensitized and heterojunction solar cells. Graphene-doped conducting polymers such poly(3,4-ethyenedioxythiophene):poly styrenesulphonate (PEDOT:PSS) and poly(3-hexylthiophene) (P3HT) have shown better power conversion efficiencies than cells with PEDOT:PSS as counter electrode in dye-sensitized solar cells [35].

First hybrid organic-inorganic P3HT:CdSe nanowire heterojunction photodetectors were demonstrated on silicon substrates, exhibiting a greatly enhanced photocurrent, a fast response, and a recovery time shorter than 0.1 s [37].

22.5.3 Light-Emitting Diodes

A light emitting diode is a semiconductor diode which emits light under recombination of electrons and holes moving from opposite electrodes. Hybrid structures consisting of a conducting polymer and luminescent quantum dots offer tunable emission, easy processability from solutions and low materials cost. Inorganic nanofillers are used as additional [38] or emitting layers [39]. Brightness and efficiency of quantum dot based light-emitting structures are the same as those of phosphorescent polymer diodes [40]. Polymer-quantum dot hybrids are attractive also for white electroluminescent diodes [41]. Application of nanocomposites in transparent electrodes showed good results [33].

22.5.4 Sensors

Sensors are widely used in our daily life; their applications increase in electrochemical, biological and environment detection. Sensors have been widely used in many fields, such as industry (pollutant), research institutes (radiation measurements) and clinical diagnosis. Nanohybrids have thus been used to detect nerve agents, toxic gases, volatile organic compounds, glucose, dopamine, and DNA. Furthermore their application extends to pH, pressure and temperature sensors. A number of electrochemical techniques including cyclic voltammetry, differential pulse voltammetry and chronoamperometry were employed to study electrochemical sensors. In particular, electrochemical sensors offer selectivity and sensitivity with very low detection limits ranging from nanomolar to picomolar. Graphene/PANI nanocomposites have been employed for the determination of 4-aminophenol via the DPV technique, as well as hydrazine sensors [11].

22.5.5 Other Applications

The versatility of graphene polymer nanocomposites suggests their potential use in automotive, electronics, aerospace, and packaging applications. Various engineering applications such as antistatics and electromagnetic interference (EMI) shielding require a certain level of conductivity (10^1–10^7 Ω cm). The high value of shielding effectiveness due to absorption (41.6 dB which means >99.99 % microwave attenuation) has been obtained in a PANI-graphene oxide-Fe_2O_3 nanocomposite [42]. Transparent conducting films are also used in many electronic devices as in touch screens, flat panel displays, e-paper, etc. [19, 43]. A graphene-ink suitable for inkjet printing was prepared, achieving graphene TFTs with up to 95 $cm^2V^{-1}s^{-1}$ mobility and 80 % optical transmittance, paving the way to high mobility all-inkjet printed graphene-based optoelectronics. Hybrid inorganic/organic nanocomposites

composed of organic layers containing metal nanoparticles, semiconductor quantum dots, core-shell semiconductors, fullerenes, carbon nanotubes, graphene have great prospects for potential applications in nonvolatile memory devices [44].

22.6 Conclusions

In the twenty-first century hybrid organic–inorganic materials will play a major role in the development of advanced functional materials.

Research of such materials is being mostly supported by the growing interest of chemists, physicists, biologists and materials scientists to fully exploit this opportunity to create smart materials benefiting from the best of the three realms: inorganic, organic and biological.

References

1. Kim BH, Hackett MJ, Park J, Hyeon T (2014) Chem Mater 26:59
2. Kalaitzidou K, Fukushima H, Drzal LT (2010) Materials 3:1089
3. Stauffer D (1985) Introduction of percolation theory. Taylor and Francis, London
4. Rozenberg BA, Tenne R (2008) Prog Polym Sci 33:40
5. Sanchez C, Julian B, Belleville P, Popall M (2005) J Mater Chem 15:3559
6. Pomogailo AD, Kestelman VN (2005) Metallopolymer nanocomposites. Springer, New York
7. Kukhta AV, Pochtenny AE, Misevich AV, Kukhta IN, Semenova EM, Vorobyova SA, Sarantopoulou E (2014) Phys Solid State 56:827
8. Kukhta AV, Khanna PK (2013) In: Borisenko VE, Gaponenko SV, Gurin VS, Kam CH (eds) Physics, chemistry and applications of nanostructures. World Scientific, Singapore, p 242
9. Kukhta AV, Kolesnik EE, Ritchik DV, Lesnikovich AI, Nichik MN, Vorobyova SA (2005) In: Borisenko VE, Gaponenko SV, Gurin VS (eds) Physics, chemistry and application of nanostructures. World Scientific, Singapore, p 96
10. Oey CC, Djurisic AB, Kwong SY, Cheung CH, Chan WK, Nunzi JM, Chui PC (2005) Thin Solid Films 492:253
11. Park SJ, Kwon OS, Lee JE, Jang J, Yoon H (2014) Sensors 14:3604
12. Cherevkov SA, Baranov AV, Fedorov AV, Litvin AP, Artemyev MV, Prudnikau AV (2013) Proc SPIE 8807:88070A
13. Park HW, Kim D-H (2012) J Nanomater 2012:892506
14. Hanemann T, Szabó DV (2010) Materials 3:3468
15. Wang F, Pang S, Wang L, Li Q, Kreiter M, Liu C-y (2010) Chem Mater 22:4528
16. Li S, Qin J, Fornara A, Toprak M, Muhammed M, Kim DK (2009) Nanotechnology 20:185607
17. Zhang Q, Cao G (2011) Nano Today 6:91
18. Das TK, Prusty S (2013) Polym-Plast Technol Eng 52:319
19. Novoselov KS, Fal'ko VI, Colombo L, Gellert PR, Schwab MG, Kim K (2012) Nature 490:192
20. Mittal V (2014) Macromol Mater Eng. doi:10.1002/mame.201300394
21. Syurik YV, Ghislandi MG, Tkalya EE, Paterson G, McGrouther D, Ageev OA, Loos J (2012) Macromol Chem Phys 213:1251
22. Kim H, Abdala AA, Macosko CW (2010) Macromolecules 43:6515
23. Li Z, Wang Y, Kozbial A, Shenoy G, Zhou F, McGinley R, Ireland P, Morganstein B, Kunkel A, Surwade SP, Li L, Liu H (2013) Nat Mater 12:925

24. Georgakilas V, Otyepka M, Bourlinos AB, Chandra V, Kim N, Kemp KC, Hobza P, Zboril R, Kim KS (2012) Chem Rev 112:6156
25. Sahoo S, Hatui G, Bhattacharya P, Dhibar S, Das CK (2013) Graphene 2:42
26. Yi M, Shen Z, Ma S, Zhang X (2012) J Nanopart Res 14:1003
27. Malig J, Stephenson AWI, Wagner P, Wallace GG, Officer DL, Guldi DM (2012) Chem Commun 48:8745
28. Allain A, Han Z, Bouchiat V (2012) Nat Mater 11:590
29. Ajayi OA, Anderson NC, Cotlet M, Petrone N, Gu T, Wolcott A, Gesuele F, Hone J, Owen JS, Wong CW (2014) Appl Phys Lett 104:171101
30. Potts JR, Dreyer DR, Bielawski CW, Ruoff RS (2011) Polymer 52:5e25
31. Nguyen DD, Tai NH, Chueh YL, Chen SY, Chen YJ, Kuo WS, Chou TW, Hsu CS, Chen LJ (2011) Nanotechnology 22:295606
32. Ni G-X, Zheng Y, Bae S, Tan CY, Kahya O, Wu J, Hong BH, Yao K, Özyilmaz B (2012) ACS Nano 6:3935
33. Ramachandran R, Mani V, Chen S-M, Saraswathi R, Lou B-S (2013) Int J Electrochem Sci 8:11680
34. Yu D, Park K, Durstock M, Dai L (2011) Phys Chem Lett 2:1113
35. Wang X, Zhi L, Mullen K (2007) Nano Lett 8:323
36. Gorji NE (2013) J Electr Electron Eng Res 5:23
37. Wang X, Song W, Liu B, Chen G, Chen D, Zhou C, Shen G (2013) Adv Funct Mater 23:1202
38. Sessolo M, Bolink HJ (2011) Adv Mater 23:1829
39. Yang X, Divayana Y, Zhao D, Leck KS, Lu F, Tan ST, Abiyasa AP, Zhao Y, Demir HV, Sun XW (2012) Appl Phys Lett 101:233110
40. Lee K-H, Lee J-H, Kang H-D, Park B, Kwon Y, Ko H, Lee C, Lee J, Yang H (2014) ACS Nano 8:4893
41. Oner I, Stathatos E, Varlikli C (2011) Adv Opt Technol 2011:710628
42. Singh K, Ohlan A, Bakhshi AK, Dhawan SK (2010) Mater Chem Phys 119:201
43. Shin D, Bae S, Yan C, Kang J, Ryu J, Ahn J-H, Hong BH (2012) Carbon Lett 13:1
44. Kim TW, Yang Y, Li F, Kwan WL (2012) NPG Asia Mater 4:e18

Chapter 23
Microwave Electrical Properties of Nanocomposites

L.C. Costa

Abstract Several techniques have been proposed for the measurement of the complex dielectric permittivity at microwave frequencies. The cavity resonant method presents good accuracy, in particular for low loss materials, using the small perturbation theory. In this method, the resonance peak frequency and the quality factor of the cavity, with and without a sample, can be used to obtain the complex dielectric permittivity of the material. We measure the shift in the resonant frequency of the cavity Δf caused by the insertion of the sample, which can be related to the real part of the complex permittivity ε' and the change in the inverse of the quality factor of the cavity, $\Delta(1/Q)$, which gives the imaginary part, ε''. The relations are simple when we consider only the first order perturbation in the electric field caused by the sample. This technique is presented to study polymer nanocomposites that will be used in microwave oven doors, which purpose is to confine the energy to the cavity, where the microwave leakage must be strictly controlled.

Keywords Nanocomposites • Microwaves • Electrical properties

23.1 Introduction

Several methods can be used to measure the complex permittivity of materials $\varepsilon^* = \varepsilon' - i\varepsilon''$. In particular, the free space techniques [1], the cavity perturbation method [2] and the resonant techniques of Fabry-Perot [3] can be cited. Each of these methods presents advantages and disadvantages, depending on the type of material which is under investigation.

In 1947, Montgomery proposed the cavity perturbation technique [4] to study the complex permittivity of materials, and additional developments have been done by several researchers to improve it [5–8]. It provides a simple measurement procedure with high sensitivity, which can be used to calculate the complex dielectric permittivity or magnetic permeability [9, 10].

L.C. Costa (✉)
I3N and Physics Department, University of Aveiro, 3810-193 Aveiro, Portugal
e-mail: kady@ua.pt

P. Petkov et al. (eds.), *Nanoscience Advances in CBRN Agents Detection, Information and Energy Security*, NATO Science for Peace and Security Series A: Chemistry and Biology, DOI 10.1007/978-94-017-9697-2_23

The technique is based on the changes in the resonant frequency and quality factor of the cavity, due to the presence of a material inside the cavity. The resonant perturbation method was extensively used to study the microwave dielectric properties of various materials [11–13]. The transmission of the cavity depends on several factors, such as the volume, shape and location of the object that is introduced inside the cavity. For a cavity and a sample of known shape, it is possible to calculate the permittivity or the permeability of the material [14].

The values of the resonant frequency f and quality factor Q, before and after the insertion of the sample into the cavity, are used to calculate the properties of the material. The relationships derived from the perturbation theory of resonant cavities, were given by several authors [5, 15–18]. They are simple, when only the first order perturbation in the electric field caused by the sample [19] is considered. That is, if it is guaranteed the linearity between the measured perturbation and the volume of the inserted sample, an independent calculation of the real and imaginary parts of the permittivity can be made.

To avoid radiation leakage in microwave ovens a choke is used in the door. Filling of this choke with a material must be used to prevent the entrance of soil. Several possibilities were considered, but it must be guaranteed that the material results in very low losses, such as insulating polymers.

The electrical properties of these polymers can be altered by adding different conducting particles [20], like carbon [21–23], iron [24], nickel [25] or another conducting polymer [26–28]. The conductivity of the composite material can thus be controlled by properly choosing the components, their shape and their relative volume fractions. That is, small quantities of conducting particles can increase the dielectric constant, without exceeding the critical concentration of percolation [29] that is, avoiding high conductivity. If electrical losses become high, heating of the plastic will occur, resulting in melting or even carbonization.

23.2 Theory

The theoretical treatment of a cavity resonator consists of solving Maxwell equations considering the continuity of the boundary conditions of the cavity. The resonance frequencies appear as conditions in the solutions of the differential equation involved and are not significantly affected by the fact that the cavity walls have a finite conductivity. The small perturbation is guaranteed since linearity between the measured perturbation and the volume of the inserted sample exists [30].

The electromagnetic field in the cavity must satisfy the wave equation,

$$\nabla^2 \boldsymbol{\Phi} - \frac{\partial^2 \boldsymbol{\Phi}}{c^2 \partial t^2} = 0 \tag{23.1}$$

where Φ is the electric or magnetic field components of the wave and c the light velocity in the medium. For the electric field, and assuming that $E_z = 0$ since z is the propagation direction, we have the solution for (23.1) as

$$E_x = [A_{1x} \sin(k_1 x)]\,[A_{2x} \sin(k_2 y) + B_{2x} \cos(k_2 y)]\,[A_{3x} \sin(k_3 z)]\, e^{-i\omega t} \tag{23.2}$$

$$E_y = [A_{1y} \sin(k_1 x)]\,[A_{2y} \sin(k_2 y) + B_{2y} \cos(k_2 y)]\,[A_{3y} \sin(k_3 z)]\, e^{-i\omega t} \tag{23.3}$$

with E_x and E_y being the x and y electric field components, the A's and B's the amplitudes and $k_1 = m\pi/a_1$, $k_2 = n\pi/a_2$, $k_3 = p\pi/a_3$, where a_1, a_2, a_3, are the cavity dimensions in the x, y, z directions respectively and m, n, p are the number of the half wavelengths in each direction.

If $a_2 < a_1 < a_3$, the $TE_{1,0,1}$ mode has the lowest frequency and is the dominant mode. For a typical $TE_{1,0,p}$, Eqs. (23.2) and (23.3) can be reduced to

$$E_x = \left[A_{1x} \sin\left(\frac{\pi x}{a_1}\right)\right][B_{2x}]\left[A_{3x} \sin\left(\frac{p\pi z}{a_3}\right)\right] e^{-i\omega t} \tag{23.4}$$

$$E_y = \left[A_{1y} \sin\left(\frac{\pi x}{a_1}\right)\right]\ [B_{2y}]\ \left[A_{3y} \sin\left(\frac{p\pi z}{a_3}\right)\right] e^{-i\omega t} \tag{23.5}$$

with the resonant frequency $f = \omega/2\pi$ given by

$$f = \frac{c}{2\sqrt{\mu'\varepsilon'}}\sqrt{\left(\frac{m}{a_1}\right)^2 + \left(\frac{p}{a_3}\right)^2} \tag{23.6}$$

where μ' and ε' are the relative values of the permeability and dielectric constant, respectively.

When the field in the cavity is slightly changed by the insertion of the object, and that field is uniform over the volume, the shift in the resonant frequency of the cavity Δf can be related to the real part of the complex permittivity, while the change in the inverse of the quality factor of the cavity $\Delta(1/Q)$ can be related with the imaginary part ε''. The relations are simple when we consider only the first order perturbation in the electric field caused by the insertion of the sample. After some mathematic manipulations [19] we obtain

$$\frac{\Delta f}{f_0} = K(\varepsilon' - 1)\frac{v}{V} \tag{23.7}$$

$$\Delta\left(\frac{1}{Q}\right) = 2K\varepsilon''\frac{v}{V} \tag{23.8}$$

where K is a constant related to the depolarization factor, which depends on the geometric parameters, v and V are the volumes of the sample and the cavity respectively, and f_0 is the resonance frequency of the cavity before the introduction

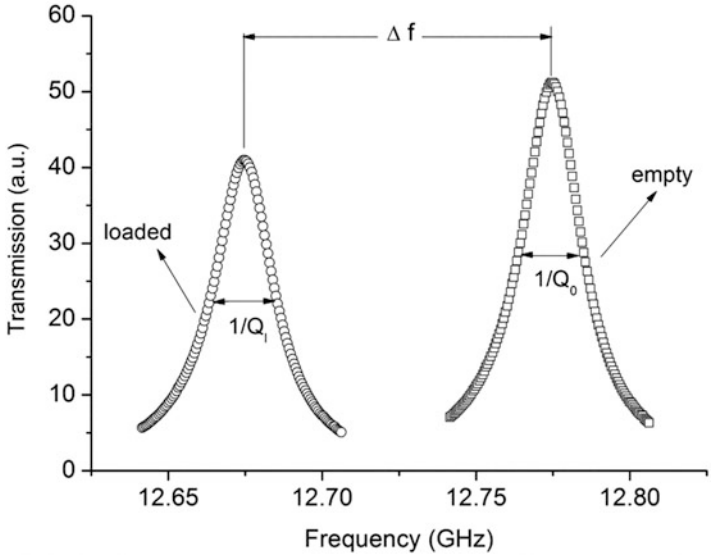

Fig. 23.1 Transmission of a resonant cavity, empty and loaded with a sample

of the sample. Using a sample of known dielectric constant, one can determine the constant K [30].

Figure 23.1 shows the transmission of a resonant cavity, empty and with a sample. The resonant frequency was shifted to lower frequencies and the quality factor decreased with the insertion of the sample.

For materials with high losses or high dielectric constant, the perturbation can be too high. The solution is to decrease the ratio v/V, that is, using very small samples or construct larger volume cavities.

23.3 Experimental

Figure 23.2 shows a resonant cavity, where the hole in its centre to introduce the sample holder with the material to be studied is visible.

This cavity was built from a standard rectangular metallic waveguide section coupled with external waveguides through small apertures in the opposite walls to operate with a resonant frequency of about 2.7 GHz. To couple the microwave to the cavity we used quarter-wavelength flange joints and small circular irises (10 mm in diameter). To measure the transmission of the cavity, we used an Agilent HP 8753D Network Analyser with an excitation power of 1 mW. To study the linearity of the cavity, and consequently to infer the possibility to use the small perturbation theory, we carried out measurements using glass micro-tubes filled with distilled water.

Fig. 23.2 Resonant cavity

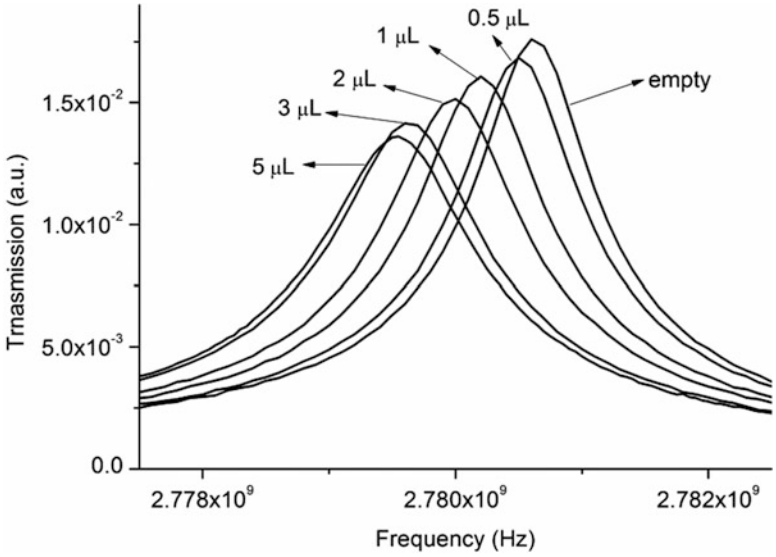

Fig. 23.3 Transmission of the empty cavity and with different volume micro-tubes with water

Figure 23.3 shows the transmission of the empty cavity and with micro-tubes of different volumes of water. It is clear that with the water volume increasing the resonant frequency changes to lower frequencies and the quality factor degrades as the curves becomes broader. We fitted the transmission data using a Lorentzian curve, and then we calculated $\Delta f/f_0$ and $\Delta(1/Q)$. The obtained values are presented in Fig. 23.4 as a function of the water volume. The errors were minimized by the standard partial derivative method.

Observing Fig. 23.4, we can infer that the shifts in the resonant frequency and in the inverse of the quality factor of the cavity remain in the linear regime, for measurements up to 3 μL of water.

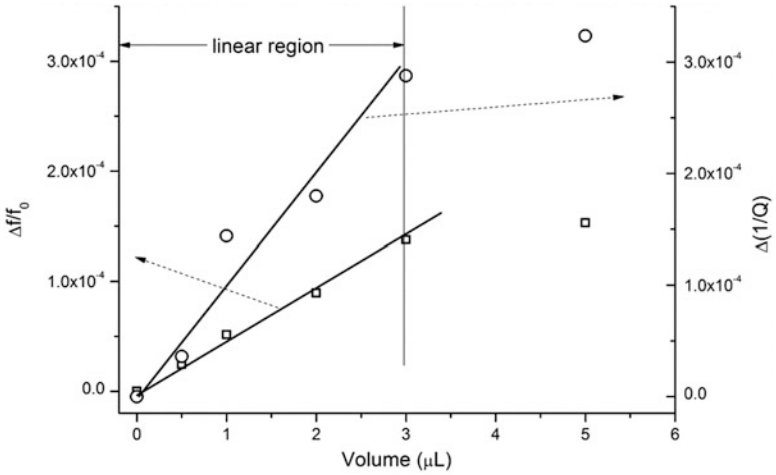

Fig. 23.4 Calculated $\Delta f/f_0$ and $\Delta(1/Q)$ for different quantities of water

This corresponds to different values of the shifts in the cavity parameters, but the conjugation of both conditions permits us to conclude that the cavity can be used up to variations of about 1.3×10^{-4}, in $\Delta f/f_0$. If the measurements overcome this limit, the sample volume should be reduced until the variations fall into the linear regime.

The samples used in this work were in the form of cylinders of 5 mm length and 1 mm diameter. To calculate the depolarizing factor K we used polytetrafluoroethylene (PTFE) samples with the same shape and size of the material samples. This polymer was used because it presents very low losses, on the order of 10^{-4}, which produces a very small perturbation in the electromagnetic field inside the cavity. Also, the complex permittivity shows less change over a wide range of temperatures and frequencies than any other solid materials [31].

23.4 Discussion

A very important part of microwave ovens is the door, the purpose of which is to provide access to the oven cavity and to confine the energy inside it. The radiation leakage must be minimized, with values internationally accepted by institutions of control. A very well-known method is to make a terminating surface with a quarter wavelength choke, which effectively prevents radiation from leaking externally through the gap between the door frame and the front panel of the microwave oven.

The filling of this choke with a material prevents the entrance of soil and reduces the dimensions of the choke cavity by the square root of the dielectric constant of the filler [32].

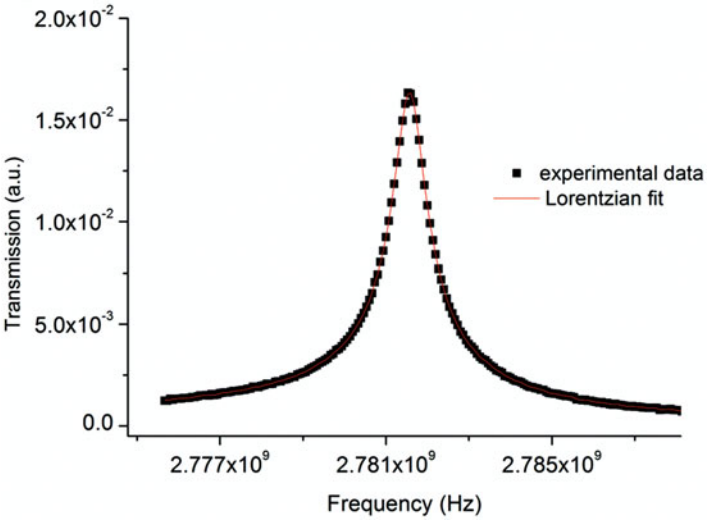

Fig. 23.5 Experimental data and Lorentzian fit for a cavity with a PBT sample

A very versatile family of polymers with interesting properties for this kind of applications includes polypropylene (PP), acrylonitrile butadiene styrene (ABS) and polybutylene terephthalate (PBT). They possess low thermal expansion coefficients, high dielectric strengths, very low dielectric losses, and they have good resistance to chemical attacks [33–35].

The absorbed power density of the material can be expressed by [36]

$$P = \frac{1}{2}\left[\left(\sigma + \omega\varepsilon''\right)E^2 + \omega\mu'' H^2\right] \tag{23.9}$$

where σ is the electrical conductivity, ε'' and μ'' the imaginary parts of the permittivity and permeability respectively. E and H are the absorbed electric and magnetic fields. In our case, the nonmagnetic material used in this work eliminates the need of using the second term in Eq. (23.9). We need a material with low losses, tg $\delta = \varepsilon''/\varepsilon'$.

In Fig. 23.5 we present the transmission of the 2.7 GHz cavity, when a PBT sample is inserted. The experimental data and the Lorentzian fit used to calculate the resonant frequency and the quality factor are shown. The obtained correlation factor was 0.989.

In Fig. 23.6 the measured transmission for the empty cavity and filled with PTFE and different polymers at a constant temperature $T = 300$ K are shown.

PBT is the most perturbing sample, which indicates the highest complex permittivity. Also, PP presents the lowest perturbation, which means, it has the lowest complex permittivity. This fact can be explained as PP is essentially a non-polar polymer, and consequently should not exhibit dielectric relaxation [37]; dielectric constant and loss factors are small at all frequencies.

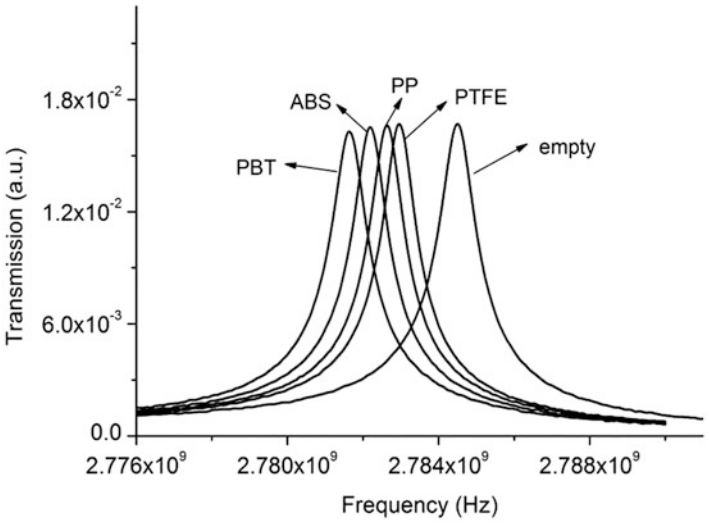

Fig. 23.6 Transmission of the empty cavity and with different samples

Table 23.1 Calculated complex permittivity for the different materials, at room temperature and frequency of 2.7 GHz

	ε'	tg δ (10^{-3})
PP	2.46	0.44
ABS	2.96	0.77
PBT	3.68	1.22

The calculus of the complex permittivity of the different polymers was done using the small perturbation theory, according to the expressions (23.7) and (23.8); the values are summarized in Table 23.1. It is clear that PBT has advantages as it possesses the highest dielectric constant, due to a small polarity, but without degrading the values of losses tg $\delta = \varepsilon''/\varepsilon'$. As expected, they are also the highest, but in the order of 10^{-3}, which is a guaranty that the material does not heat.

Then, the possibility to increase the dielectric constant of the material, while maintaining low losses was questioned. This combination has the advantage to reduce the quantity of material to fill the choke in the oven doors.

Small quantities of carbon black nanoparticles were then used as fillers, up to $x = 2$ % in volume, in the PBT polymer matrix. A three dimensional geometric model predicts a percolation volume fraction of about $x_c = 16$ % for spherically shaped conductive particles, but real systems can display critical percolation concentrations lower than that. For several carbon black composites this value is about $x_c = 12$ % [38], which means that the percolation threshold was not exceeded. This critical concentration depends on the shape of the inclusion, but also on the structure and morphology of the conducting particle, as well as on the material processing [39]. When the filler content is low, the mean distance between the conducting particles is large and the conductivity is controlled by the presence of

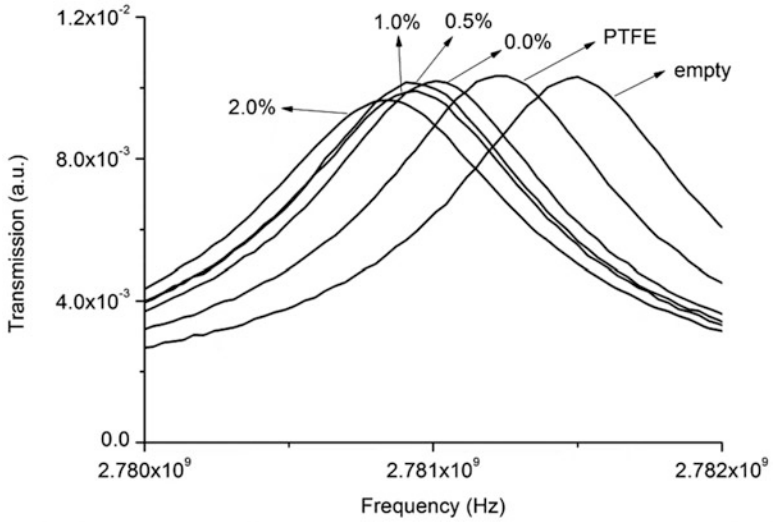

Fig. 23.7 Transmission of the cavity in different situations: empty cavity, PTFE and PBT composite samples with different concentrations of carbon black particles

Table 23.2 Calculated complex permittivity for the different composites at room temperature and frequency of 2.7 GHz

x (%)	ε'	tg δ (10^{-3})
0.0	3.68	1.22
0.5	3.86	2.33
1.0	3.98	3.33
1.5	4.30	5.44
2.0	4.41	7.12

the insulating matrix. This fact insures that the electrical conductivity is low, if we use nanocomposites with a low concentration of filler particles.

Figure 23.7 shows the transmission of the 2.7 GHz resonant cavity, for the empty cavity, a PTFE sample and PBT composite samples with different concentrations of carbon black particles. As expected, the most perturbing sample was referred to that with the highest concentration of conducting carbon black particles. Nevertheless, it is important to note that the quality factor degradation is low, which is a guarantee that the imaginary part of the complex permittivity is low. According to Eq. (23.9), the heating of the material will be negligible.

Using the small perturbation theory, we calculated the complex permittivity of the PBT/carbon black nanocomposites, the values of which are summarized in Table 23.2. Also, in these cases, we observed that the variations in the resonant frequencies and in the quality factors are within the limits to use the theory for the calculation of their values.

In order to interpret these data, some mixture laws can be used. In particular, the generalized Looyenga law is very useful for the interpretation of two phase

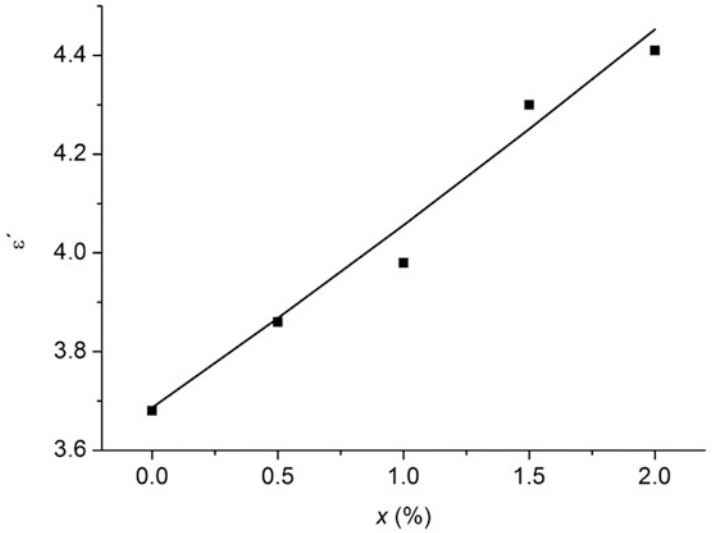

Fig. 23.8 Experimental data for ε' and the fit using the generalized Looyenga law with $t = 2.9$

composites [40]. If filler particles with a complex permittivity ε_f^* and a volume fraction φ_f are dispersed in a matrix material with complex permittivity ε_m^*, then according to that theory, the complex permittivity of the mixture can be calculated by

$$\varepsilon^{*1/t} = \phi_f \, \varepsilon_f^{*1/t} + \phi_m \, \varepsilon_m^{*1/t} \tag{23.10}$$

where $t = 3$ for spherical inclusions. In our case, we calculated $t = 2.9$; the spherical shape of the carbon black nanoparticles was confirmed by scanning electron microscopy (SEM).

Figure 23.8 shows the experimental data for the dielectric constant and the fit using the generalized Looyenga law, where a good agreement is observed.

Using the measured complex dielectric permittivity of the PBT matrix, $\varepsilon_m^* = 3.68 - i \ 4.49 * 10^{-3}$, and the calculated values for the nanocomposite, inverting the generalized Looyenga law, it was possible to calculate the complex permittivity of the filler $\varepsilon_f^* = 147.1 - i \ 78.7$, with a chi-squared χ^2 of about 0.09.

These values confirm the possibility to fit the experimental data using the generalized Looyenga law. It is also possible to use this law to calculate the volume of filler to be introduced in the matrix to obtain a particular value of the complex permittivity for use in electrical applications. The composite based on PBT with 2 % carbon black particles was then used to fill the choke of the microwave oven door.

Figure 23.9 shows the oven door, where the PBT composite is visible.

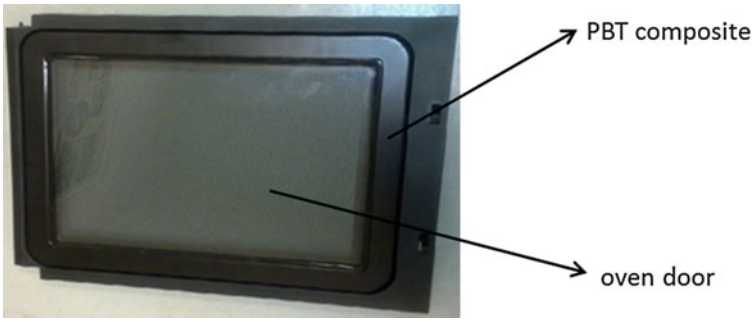

Fig. 23.9 Microwave oven door with the choke filled with the PBT nanocomposite

23.5 Conclusions

The cavity perturbation method is a very powerful tool to evaluate the dielectric permittivity of low loss materials. The dielectric function of two-phase materials can be accurately deduced using the generalized Looyenga model, in particular when the inclusion is conductive, and for low filler volume concentrations. In this case, the critical percolation concentration is not reached.

With this law, we can choose the adequate doping concentrations and then control the electrical properties, in order to obtain the desired behavior for a particular application.

A choke cavity in an oven door is used to prevent the leakage of energy of the oven. The choke can be filled with a polymer, preventing the entrance of soil and reducing the dimensions of the choke cavity by the square root of the dielectric constant of the filler. PBT is the preferred polymer, because it has a higher ε', that is, a higher capacity to absorb the microwave radiation, without increasing too much the conductivity, avoiding the heating of the material. To increase the performances of this polymer, we introduced small amounts of carbon black nanoparticles, forming a composite, nowadays used in industrial microwave oven doors.

Acknowledgements The author acknowledges Fundação para a Ciência e Tecnologia, Portugal, for the financial funding from the PEst-C/CTM/LA0025/2011 project, and to TEKA and Quiminova, which prepared the materials under study.

References

1. Meng B, Booske J, Cooper R (1995) IEEE Trans Microw Theory Tech 43:2633
2. Klein O, Donovan S, Dressel M, Griiner G (1993) Int J Infrared Millimeter Waves 14:2423
3. André P, Costa LC, Devesa S (2004) Microw Opt Technol Lett 43:106
4. Montgomery GA (1947) Techniques of microwave measurements. McGraw-Hill, New York

5. Altschuler HM (1963) Handbook of microwave measurements, vol 2, Brooklyn, Polytechnic Press, New York
6. Waldron RA (1960) Perturbation theory of resonant cavities. Proc IEEE 107:272
7. Waldron RA (1961) Ferrites: an introduction for microwaves engineers, Marconi series. D. Van Nostrand Comp Ltd, London
8. Subramanian V, Sobhanadri J (1994) Rev Sci Instrum 65:453
9. Zhu SC, Chen HY, Wen FP (1992) IEEE Trans Magn 28:3213
10. Verma A, Saxena AK, Dube DC (2003) J Magn Magn Mater 263:228
11. Chen L, Ong CK, Tan BTG (1996) Meas Sci Technol 7:1255
12. Costa LC, Devesa S, André P, Henry F (2005) Microw Opt Technol Lett 46:61
13. Costa LC, Correia A, Viegas A, Sousa J, Henry F (2005) Mater Sci Forum 480:161
14. Kraszewski AW, Nelson SO (1992) IEEE Trans Microw Theory Tech 40:151
15. Chen LF, Ong CK, Neo CP, Varadan VV, Varadan VK (2004) Microwave electronics: measurement and materials characterization. Wiley, San Francisco
16. Pozar DM (2004) Microwave engineering. Wiley, San Francisco
17. Fuller AJB (1987) Ferrites at microwave frequencies. P. Peregrinus on behalf of the Institution of Electrical Engineers, London
18. Mathew KT, Nair RU (1993) Microw Opt Technol Lett 6(2):104
19. Henry F (1982) Développement de la métrologie hyperfréquences et application à l'étude de l' hydratation et la diffusion de l'eau dans les matériaux macromoléculaires, Ph.D. thesis, Paris
20. Costa LC, Henry F (2012) Int J Microw Sci Technol 2012:628237
21. Brosseau C, Boulic F, Queffelec P, Bourbigot C, Le Meste Y, Loaec J, Beroual A (1997) J Appl Phys 81:882
22. Krupa I, Chodak I (2001) Eur Polym J 37:2159
23. Chen G, Wu D, Weng W, Bin H, Yan W (2001) Polym Int 50:980
24. Costa LC, Valente MA, Henry F, Ramanitra L (1998) J Chim Phys 95:1453
25. Khoroshilov AA, Koroleva I, Bolodin Y (2000) Russ J Appl Chem 73:1918
26. Costa LC, Henry F, André A (1996) Proceedings of Journées Polymères Conducteurs. Collonges la Rouge, France
27. Street G (1986) Handbook of conducting polymers. Dekker, New York
28. Roichman Y, Silverstein M, Siegmann A, Narkis M (1999) J Macromol Sci Phys 38:145
29. Valente MA, Costa LC, Mendiratta S, Henry F, Ramanitra L (1999) Solid State Commun 112:67
30. Rubinger CPL, Costa LC (2007) Microw Opt Technol Lett 49:1687
31. Teflon PTFE (1996) Properties handbook. DuPont Fluoroproducts, Washington
32. Copson DA (1975) Microwave heating. AVI Publishing Company, Connecticut
33. Johnson C, Hilton G (1988) Acrylonitrile-Butadiene-Styrenes, AMS international, engineered materials handbook, vol 2, AMS International, Ohio
34. Haynes WM (2014) CRC handbook of chemistry and physics. CRC Press, Cleveland
35. Vishn S (1984) Handbook of plastics testing technologies. Wiley Intersciences, New York
36. Henry F, Costa LC (2005) Microw Opt Technol Lett 45:335
37. McCrum N, Read B, Williams G (1991) Anelastic dielectric effects in polymer solids. Dover Pub. Inc., New York
38. McLachlan DS, Blaskiewic M, Newnham RE (1990) J Am Ceram Soc 73:2187
39. Balberg I, Anderson CH, Alexander S, Wagner N (1984) Phys Rev B 30:3933
40. Looyenga H (1965) Physica 31:401

Chapter 24
Pathways for the Production of Non-stoichiometric Titanium Oxides

Perica Paunović, Aleksandar Petrovski, Goran Načevski, Anita Grozdanov, Mirko Marinkovski, Beti Andonović, Petre Makreski, Orce Popovski, and Aleksandar Dimitrov

Abstract The subject of this study is the development of a bottom-up method for the preparation of nano-scaled Magneli phases. There are two steps involved; the first step is sol-gel preparation of $Ti(OH)_4$ using titanium tetraisopropoxide as organometallic precursor, and the second step is its thermal decomposition to TiO_2 or Magneli phases. Thermal treatment in an oxidative atmosphere (air) was performed at different temperatures to produce TiO_2 in order to determine the regions of stability of anatase and rutile. Next, thermal treatment in a reductive (10 % H_2 + 90 % N_2) atmosphere at temperature of rutile was performed to produce Magneli phases. Furthermore, a top-down approach was applied to produce non-stoichiometric titanium oxides by mechanical activation of commercial Magneli phases known as Ebonex. Examples of the application of top-down produced Magneli phases in electro- and photocatalysis are shown.

Keywords Sol-gel synthesis • Titania • Magneli phases • Nanoparticles • Electrocatalysis • Photocatalysis

24.1 Introduction

Titania is one of the most used materials in a wide range of technical and technological applications as a result of its low price, appropriate physical properties, chemical stability and of being an environmentally friendly material. Therefore, it

P. Paunović (✉) • A. Petrovski • G. Načevski • A. Grozdanov • M. Marinkovski
B. Andonović • A. Dimitrov
Faculty of Technology and Metallurgy, University "Ss Cyril and Methodius", Skopje, Republic of Macedonia
e-mail: pericap@tmf.ukim.edu.mk

P. Makreski
Institute of Chemistry, Faculty of Natural Sciences and Mathematics, University "Ss Cyril and Methodius", Skopje, Republic of Macedonia

O. Popovski
Military Academy "Mihailo Apostolski", Skopje, Republic of Macedonia

P. Petkov et al. (eds.), *Nanoscience Advances in CBRN Agents Detection, Information and Energy Security*, NATO Science for Peace and Security Series A: Chemistry and Biology, DOI 10.1007/978-94-017-9697-2_24

can be used as a pigment, in optical devices, sensors, sunblocking materials in cosmetics, binder in medicine, electro- and photocatalysis etc. [1–4].

The good properties of titania are induced by the variety of crystalline forms in which it exists. The natural prevalent crystalline forms of titania are rutile (tetragonal), anatase (tetragonal), brookite (orthorhombic) and TiO_2-B (monoclinic). The basic building units of titania consist of one Ti atom surrounded by six oxygen atoms in a TiO_6^{2-} octahedron. The crystalline structures differ from each other by distortions of the octahedrons and the way the octahedrons are connected in the octahedral chains. Thus, in rutile the octahedra are connected at the edges forming a tetragonal structure, whereas in anatase, the tetragonal structure is formed by connection of the octahedrons at the vertices. In brookite, the octahedra are connected by both edges and vertices forming an orthorhombic structure. The thermodynamically most stable crystalline form is rutile, while rutile and anatase play the main roles in the various applications.

Magneli phases are non-stoichiometric titanium oxides appearing in homologous order with the general formula Ti_nO_{2n-1}. The structure of the Magneli phases is based on the rutile building unit [5]. Hence, it can be considered that the first homologue of Magneli phases Ti_4O_7 is built up of three TiO_2 octahedra and one TiO octahedron, where the oxygen vacancies are created at the edges rather than vertices. Therefore, the Ti atoms are closer in the TiO layer than in other parts of the Ti_4O_7 unit cell [6].

They show similar physical and chemical properties as titania (Table 24.1), but due to the oxygen deficiency in the crystal lattice they have a high electrical conductivity in the same order of magnitude as carbon [5, 6]. The presence of lattice defects, possibly oxygen vacancies as a result of reductive rutile transformation, is an important factor to form visible light sensitive photocatalysts [7, 8]. The high electrical conductivity makes them appropriate for electrocatalytic purposes as catalyst support or electrode material [6, 9–11].

Table 24.1 Physical properties of titania and the first homologue Magneli phase Ti_4O_7

Chemical formula	Ti_4O_7	TiO_2
Appearance	Blue-black, odorless	White, odorless
Melting point (°C)	1,850	1,830–1,850
Boiling point (°C)	>3,000	2,500–3,000
Electrical conductivity ($S \cdot cm^{-1}$)	1,500	Semi-conductor
Bulk density ($g \cdot cm^{-3}$)	3.6–3.8	3.8–4.2
Porosity (%)	20	–
Flexural strength (MPa)	60–180	–
Hardness (Vickers)	230	–
Specific heat capacity ($J \cdot kg^{-1} \cdot K^{-1}$)	750	710
Thermal conductivity ($W \cdot m^{-1} \cdot K^{-1}$)	10–20	12

24.2 Synthesis of Nanostructured Magneli Phases

The nanostructured materials with their unique physical properties (mechanical, optical, highly developed surface area etc.) offer wider and more effective applications than the corresponding bulk materials. Namely, the transition from bulk to nanomaterials is followed by a remarkable change of the ratio of surface vs. interior atoms, where number of surface atoms or ions becomes a significant fraction of the total number of atoms or ions. As the surface energy plays a significant role in the thermal stability [12], this increase of the surface atoms is a reason for dramatic changes of the physical and chemical properties. Therefore, nanomaterials show highly superior properties over those of the corresponding bulk materials.

There are two main approaches for the formation of nanostructures and nanomaterials: top-down and bottom-up. An illustrative view of these pathways is shown in Fig. 24.1.

Top-down procedures involve mechanical reduction of the size of bulk particles. Attrition and milling are the most used top-down methods for the production of nanoparticles. The main disadvantage of the top-down approach is the creation of lots of defects in the crystalline structure during the mechanical reduction of particles. Also, the treated material can be contaminated by the corresponding parts of the equipment (balls, rollers, etc.).

The reduction of the size of particles is thermodynamically limited. Often, after some time of the mechanical treatment, the particle size begins to increase. Therefore, nano-sized particles cannot be reached, but submicron (more than 100 nm) ones instead. This can be explained by the fact that during the mechanical reduction of the particles, the increase of the surface area is followed by a considerable increase of the surface energy, making the treated material thermodynamically unstable. The mechanism by which the material can return to a thermodynamically steady state (reduction of the overall energy) is agglomeration of the grains.

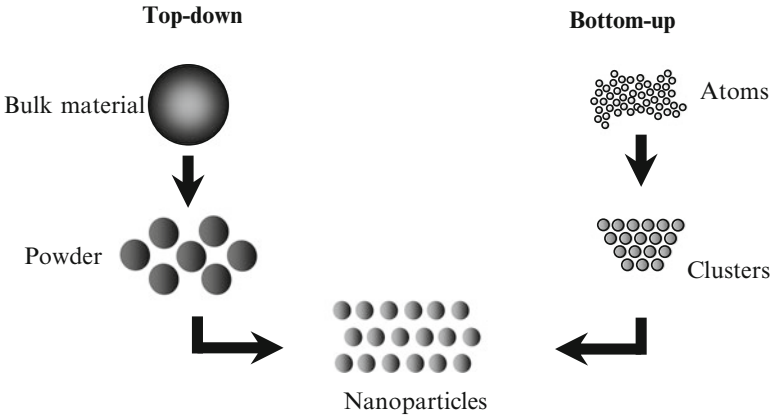

Fig. 24.1 Illustration of the pathways for the production of nanomaterials

Bottom-up approaches involve the formation of nanostructures atom-by-atom, molecule-by-molecule, ion-by-ion, or cluster-by-cluster depending on the applied synthesis method. Many bottom-up methods were developed for the synthesis of various nanostructures and nanomaterials, such as chemical vapor deposition, plasma vapor deposition, solvothermal synthesis, hydrothermal synthesis, microemulsion, sol-gel methods, electrochemical deposition, microwave radiation etc.

Compared with top-down approaches, bottom-up methods offer lower defect formation and more stable structures. Because the driving force for the formation of nanostructures is reduction of the free Gibbs energy, the produced material is in state close to thermodynamic equilibrium [12]. However, different synthesis processes occur under different kinetic conditions, therefore differences in composition, structure, morphology of the same material can be observed.

In the next section, top-down and bottom-up methods for production of nanoscaled non-stoichiometric titanium oxides will be given.

24.3 Top-Down Approach

In this section, the possibilities of top-down approaches for producing nano-scaled Magneli phases are shown. Mechanical milling/activation of commercial micro-scaled Magneli phases (trade name Ebonex®, Altraverda, UK) was used as a top-down procedure.

Mechanical milling/activation was performed in a Fritsch Planetary Mill (Pulverisisette 5) without binder. The dry ball milling was performed with a velocity of the balls of 200 rpm. The ball diameter was 1 cm, while the mass ratio of balls vs. treated material was 3:1. Several experiments of different duration were done −4, 8, 12, 16 and 20 h.

Determination of the particle size of the mechanically treated material was done using TEM analysis (Fig. 24.2). The grains shown in the corresponding TEM images were chosen as average ones after an comprehensive scan of the sample surface. The size of the support particles decreased from 1 μm in untreated samples to 200 nm in sample with Magneli phases treated for 20 h. The samples treated for 16 and 20 h show very close values of support particle size, 215 and 200 nm, suggesting that further mechanical treatment could cause agglomeration and enlargement of the particles. As was mentioned above, further treatment would exceed the critical value of the surface energy and the material would tend to reach the thermodynamically steady state through agglomeration of the particles.

The BET surface area achieved after 20 h mechanical treatment was 3.1 $m^2 \cdot g^{-1}$.

Magneli phases obtained by this method were used as catalyst support of electrodes aimed for water electrolysis and photocatalytical degradation of an aromatic hydrocarbon with two conjugated benzene rings (naphthalene).

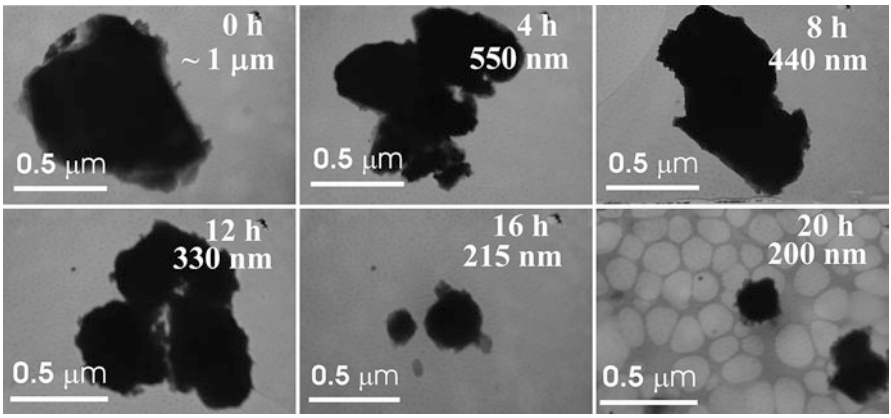

Fig. 24.2 TEM images of the mechanically treated Magneli phases

24.3.1 Application in Electrocatalysis

According to Jakšić's hypo-hyper d-theory for the improvement of the electrocatalytical activity of pure metals [13, 14], the mixture of a metal from the right side of the transition series (hyper d-component having more electrons in the outer shell and being a good individual catalysts) and a metal (or its compound) from the left side of transition series (hypo d-component having less electrons in the outer shell and being poor catalysts as individual metals) exhibits a pronounced synergetic effect. This is the basis for the preparation of non-platinum electrocatalysts with activities close to even better than that of pure platinum. Normally, for nano-scaled electrocatalysts the support material also plays a significant role; it is a highly conductive material which should provide good dispersion of the catalytic phase and prevent its agglomeration. The subject of our previous research activities were Co-based electrocatalysts deposited on a carbon support (traditional Vulcan XC-72 or multiwalled carbon nanotubes) containing nanostructured TiO_2 in the crystalline form of anatase [15–18]. Addition of TiO_2 to the support material contributes to an improvement of the intrinsic catalytic activity of metallic Co phases as result of hypo-hyper d-interaction between Co and TiO_2.

Due to their high electrical conductivity (Table 24.1), Magneli phases have a potential to be used as support material for electrocatalysts. In this case they have a bifunctional role: to provide an electron exchange with reacting ions through their high electrical conductivity and to improve the intrinsic catalytic activity of the metallic phase through hypo-hyper d-interaction, because non-stoichiometric Ti oxides are hypo d-component by their chemical nature. They should also provide a good dispersion of the catalytic phase, therefore the size of their particles should be small.

In this section, an application of the top-down prepared Magneli phases will be presented as catalyst support of Co based electrocatalysts aimed for hydrogen and

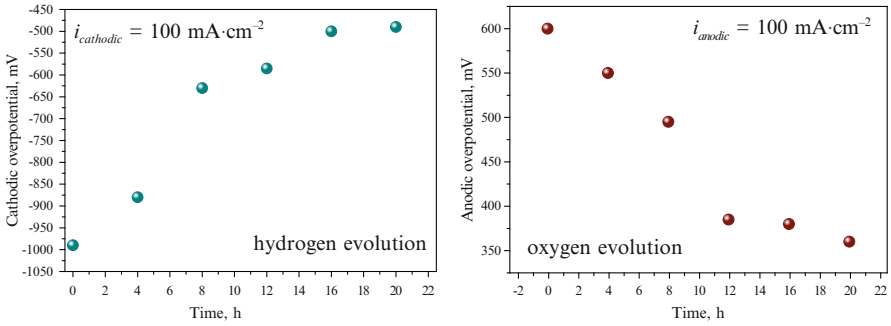

Fig. 24.3 Plots of the dependences of the overpotentials for hydrogen and oxygen evolution reaction at a current density of 100 mA·cm^{-2} on the duration of the mechanical treatment of the Magneli phases

oxygen evolution during water electrolysis in aqueous alkaline cells. The electrode material contains 10 wt% of the metallic phase (Co) while the rest is support material, i.e. Magneli phases. As precursor for the metallic Co phase Co-2,4-pentanedionate was used and deposited on Magneli phases prepared by mechanical activation for different time of treatment. The studied electrocatalytic material was prepared as gas-diffusion electrode and investigated in 3.5 M KOH. More experimental details are given elsewhere [19].

The electrocatalytic activity of the studied Co/Ebonex electrocatalysts for hydrogen evolution is shown in Fig. 24.3. It can easily be noticed that as the duration of the mechanical treatment of the Magneli phases rises, i.e. the size of the support particles deceases, the catalytic activities for hydrogen and oxygen evolution increase. It is clear that the catalytic activities for hydrogen evolution of Co electrocatalysts deposited on Magneli phases treated for 16 and 20 h are very close. Above it was shown that the size of Magneli phases treated for 16 and 20 h are also very close. In the case of oxygen evolution, the catalytic activity reaches its maximal value even for the catalyst deposited on Magneli phases treated for 12 h. Therefore, the duration of mechanical activation of Magneli phases aimed for oxygen evolution can be shorter.

Next, catalytic activity of the best behaving catalyst in this series (Co/Magneli phases treated for 20 h) is compared with the corresponding electrocatalysts deposited on different support materials in previous studies (Table 24.2). As indicator for the electrocatalytic activity for hydrogen evolution, the overpotential at q reference current density of 60 mA·cm^{-2} is taken.

Comparing Co/Magneli phase catalysts with corresponding Co catalysts deposited on Vulcan XC-72, a slightly better catalytic activity of the Co/Magneli phases can be noticed, expressed by a 15 mV lower overpotential for hydrogen evolution. Vulcan XC-72 has very high surface area (≈250 m^2·g^{-1}), considerably higher than the studied Magneli phases (3.1 m^2·g^{-1}), thus it is expected for catalysts deposited on Vulcan XC-72 to show better activity. But due to the nature of Magneli phases – titanium oxides which behave as hypo d-component which interacts with a metallic

Table 24.2 Comparison of the catalytic activity of Co/Magneli phase electrocatalysts with corresponding Co-based electrocatalysts deposited on different catalyst supports

Electrocatalyst	η_{60}, mV	Ref.
Co/Magneli phases	−365	[19]
Co/Vulcan XC-72	−380	[15]
Co/TiO_2/Vulcan XC-72	−280	[15]
Co/TiO_2/MWCNTs	−215	[16]

hyper d-phase (strong metal-support interaction, SMSI) – a synergetic effect of the intrinsic catalytic activity for hydrogen evolution is achieved. Co electrocatalysts deposited on grafted TiO_2 (anatase) on Vulcan XC-72 shows a higher catalytic activity for hydrogen evolution than Co/Magneli phases, expressed by a difference in the overpotential of 85 mV. This rise of the catalytic activity is a result of both the synergetic increase of the intrinsic activity through hypo-hyper d-interactions between Co and anatase and the highly developed surface area of Vulcan XC-72 (250 $m^2 \cdot g^{-1}$). Furthermore, a replacement of Vulcan XC-72 by activated multiwalled carbon nanotubes led to an additional rise of the catalytic activity, and the overpotential difference to the studied Co/Magneli phase electrocatalysts shifted to even 150 mV. This rise of the catalytic activity is a result of a very high real surface area of activated MWCNTs (twice higher than that of Vulcan XC-72 [20]) as well as the improved inter- and trans-particle porosity.

It should be mentioned that the electrocatalytic activity of the catalyst for oxygen evolution reactions is very satisfactory, compared to other similar electrocatalysts for oxygen evolution, as for example PtCo/Ebonex catalysts produced by boron-hydride reduction [21]. The good catalytic behaviour for oxygen evolution is connected with the formation of surface oxides and interaction between the metallic phase (Co) and the catalyst support (Magneli phases). The metal-support interaction was clarified above. The electrode surface is composed of oxide support and Co which is in an oxidized state at potentials close to the oxygen evolution region. In this case, Magneli phases behave not only as support material, but also as an active oxide electrode.

The inferior catalytic behaviour of the studied Co/Magneli phases electrocatalyst for hydrogen evolution is a result of the poorer surface characteristics of the Magneli phases compared to Vulcan XC-72 and MWCNTs. The lower surface area is due to the relatively large grains of the Magneli phases (~200 nm). The above results point out that such grains sizes and the corresponding catalytic activity of Co/Magneli phases electrocatalyst is the maximum achievement of the top-down approach for the preparation of nano-scaled Magneli phases. To produce smaller particles of Magneli phases which can be used for effective electrocatalysts for hydrogen evolution, bottom-up methods should be applied.

24.3.2 Application in Photocatalysis

Besides the industry, many usual human activities such as driving a car, mowing grass, burning firewood for heating etc. can be sources of organic pollutants emitted into the environment. Photocatalysis is a very promising method to solve many of the problems related to the increasing environmental pollution. Since the discovery of the photoactivity of titania (early-1970s) an intensive development has been made in the field of photochemistry. Recently, much attention has been focused on nano-sized photocatalytic materials [22]. Being highly active, stable, non-toxic and cheap, TiO_2 is one of the most used photocatalysts in many fields of environmental remediation [22–24].

Since by their nature Magneli phases are titanium oxides, they can be potentially used for photocatalytic purposes. In this section the applications of Magneli phases prepared by the top-down approach applied for the photocatalytic degradation of an aromatic hydrocarbon with two conjugated benzene rings (naphthalene) is discussed.

For the oxidation of naphthalene pure oxygen was used. The equipment for the photocatalytic degradation of naphthalene consisted of a Pyrex glass vacuum line (pressure of 10–15 Pa) as shown in Fig. 24.4. Within the line solid naphthalene ($C_{10}H_8$) is connected in a test tube with a valve, oxygen in a balloon and the photoreactor in which chemical vapor deposition occurs. The photocatalyst material was placed onto a glass carrier in the photoreactor. The mixture of oxygen and naphthalene was collected via the vacuum line in the Pyrex glass reactor before the UV irradiation. The excess gases were collected in renegade. At the end of the line, a vacuum pump was linked to achieve the required vacuum.

For the irradiation of the mixture of naphthalene, oxygen and photocatalyst, a mercury lamp was used (medium pressure, 100 W intensity). To allow in-situ FTIR spectroscopy measurements, the ends of the reactor were formed by KrS 5 (thallium bromide – thallium iodide) windows. The change of the gas phase composition during the photocatalytic experiments was observed by means of FTIR spectroscopy (Nicolet Impact 400).

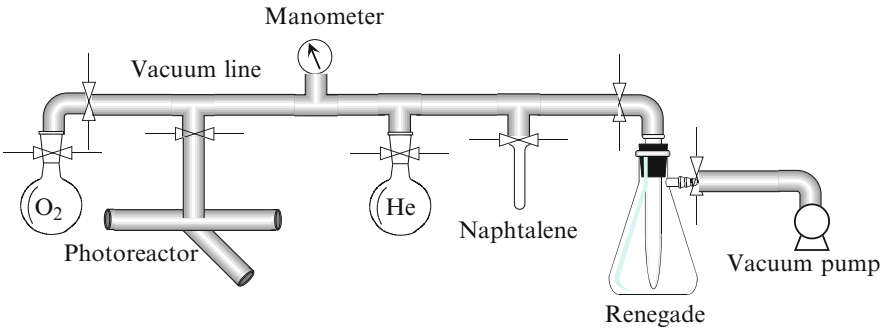

Fig. 24.4 Vacuum line for the photodegradation of naphthalene

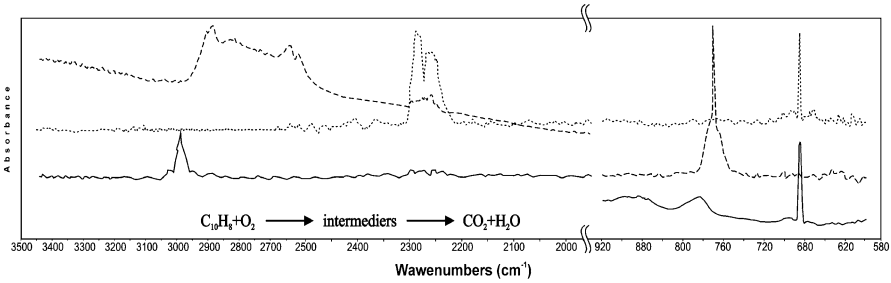

Fig. 24.5 FTIR spectra of naphthalene before irradiation (*solid line*), after 180 min irradiation in the presence of TiO_2 HOMBIKAT UV-100 (*dashed line*) and in presence of mechanically treated Magneli phases (*dotted line*)

The FTIR spectra of naphthalene before irradiation (1) and after 180 min irradiation in the presence of TiO_2 HOMBIKAT UV (2) or Magneli phases are shown in Fig. 24.5. The curve (1) shows that naphthalene has several characteristic peaks: a medium intensity peak at 3060.3 cm^{-1}, a peak of low intensity at 1263.4 cm^{-1}, a peak of very high intensity at 781.8 cm^{-1} (characteristic for naphthalene) and a peak of high intensity at 473.3 cm^{-1}.

FTIR spectra of degraded naphthalene after 3 h irradiation by an UV-lamp in the presence of Magneli phases is shown by curve (3). It can be seen that the peak at 3,066 cm^{-1} is totally disappeared which has the consequence of the degradation of the aromatic rings. In the region of 2,400–2,300 cm^{-1} a very pronounced peak exists as a result of surface CO_2 [25]. In the region from 1,800 to 1,380 cm^{-1} peaks characteristic for free water appear [26]. The peak at 781.8 cm^{-1} (characteristic for naphthalene) has disappeared (reduced more than 95 %), and consequently new a peak appears at 668 cm^{-1} which corresponds to free CO_2 [25]. For the degradation of naphthalene in the presence of TiO_2 HOMBIKAT UV (curve 2), the peak at 781.8 cm^{-1} is reduced by about 60 %. As in the previous case, a new peak characteristic for CO_2 at 668 cm^{-1} appears.

The FTIR analysis implies that the degradation of naphthalene in the presence of Magneli phases is over than 95 %, while in presence of HOMBIKAT UV it is less than 60 %.

In Table 24.3, the results of the activity of different titanium oxides for the photocatalytic degradation of naphthalene are summarized [27].

24.4 Bottom-Up Approaches

It was shown that by top-down approaches Magneli phases smaller than 200 nm (submicron scale) cannot be produced. Therefore, the path for the production of nano-scaled Magneli phases is using bottom-up approaches. Nano-scaled Magneli

Table 24.3 Degree of degradation of naphthalene by different photocatalysts based on titanium oxides [27]

Photocatalyst	Degree of degradation, %
Magneli phases	~95 %
TiO_2 anatase, sol-gel, ther. treated at 480 °C	85 %
Cr doped TiO_2	80 %
TiO_2 amorphous, sol-gel, ther. treated at 250 °C	70 %
HOMBICAT UV-100	55 %
Degussa P25	15

phases smaller than 100 nm can considerably improve the performances in electro- and photocatalysis shown above.

The bottom-up pathways for the production of Magneli phases presented in this section includes sol-gel production of nano-scaled $Ti(OH)_4$ and its further thermal treatment in a reductive atmosphere. Since Magneli phases possesses rutile building units, the first stage of the investigation is thermal treatment of $Ti(OH)_4$ in an oxidative atmosphere to determine the temperature region of stability of rutile. The next stage of the research is thermal treatment of $Ti(OH)_4$ in a reductive atmosphere at temperatures where rutile is stable.

$Ti(OH)_4$ was prepared by a sol-gel procedure using Ti tetraisopropoxide (TTIP) (Aldrich, 97 %) as a precursor. The synthesis was performed at ambient pressure, a temperature of 65 °C under stirring with 900 rpm.

The determination of the temperature region of rutile transformation was performed using thermogravimetric/differential thermal analysis (TGA/DTA). The studied material was heated in the temperature range from ambient temperature to 1,000 °C with a heating rate of 10 °C·min^{-1} in nitrogen atmosphere. In order to clarify the region of anatase and rutile stability, $Ti(OH)_4$ was thermally treated in an oxidative atmosphere at 250, 380, 550, 650 and 800 °C. To produce rutile with oxygen deficiency or non-stoichiometric titania (Magneli phases), the thermal treatment was performed in a reductive atmosphere (10 % H_2 + 90 % N_2) at 800 °C.

The produced titania-based samples were studied by means of Raman spectroscopy and transmission electron microscopy (TEM).

24.4.1 Production in Oxidative Atmosphere

More or less pronounced characteristic peaks of different processes and phase transformations in the range from ambient temperature to 1,000 °C can be seen in the DTA spectrum shown in Fig. 24.6. The endothermic peak at 95.6 °C corresponds to evaporation of physically adsorbed water in the studied samples as a result of the air contact. The next peak at 162.8 °C corresponds to the beginning of the decomposition of the residual organic precursor groups of Ti-tetraisopropoxide. At 220.8 °C, the decomposition of the organic residues is completed, and removal

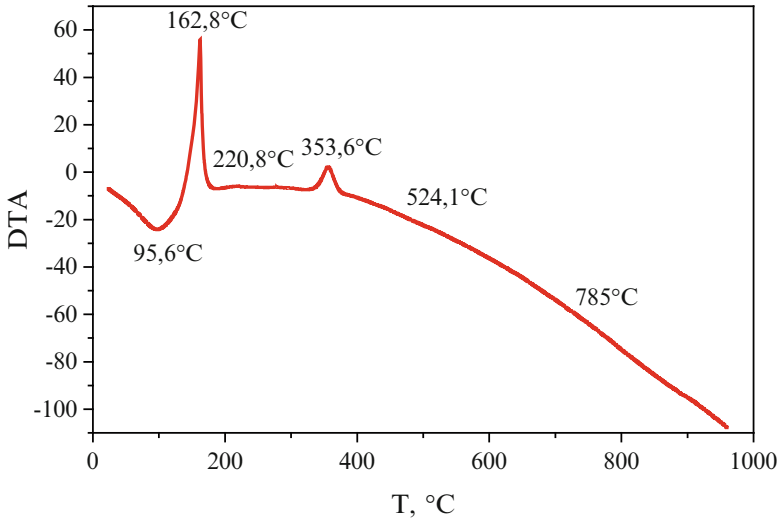

Fig. 24.6 DTA curve of thermal decomposition of $Ti(OH)_4$

of OH^- groups (dehydroxylation) starts, indicating that TiO_2 formation begins. The decomposition of OH^- groups is finished at 353.6 °C. Complete transformation to crystalline anatase occurs at 524,1 °C. The complete transformation of anatase to rutile occurs at 785 °C. These observations are in agreement with that of other authors [28, 29].

In order to determine the temperature of complete decomposition of anatase to rutile, thermal treatments of $Ti(OH)_4$ were performed at 250, 380, 550, 650 and 800 °C in an oxidative atmosphere. Further investigation of the produced samples was done by means of Raman spectroscopy. The shape and size of the rutile crystallites was observed by transmission electron microscope. Because the Magneli phases have a rutile crystalline structure with oxygen vacancies, the temperature region of existence of pure rutile is important. Transformation of rutile to Magneli phases should be performed in this temperature region in a reductive atmosphere.

Raman spectra of samples produced by thermal treatment in oxidative atmosphere are given in Fig. 24.7. In the spectra of samples treated at 250, 380, 550 and 650 °C, Raman vibration modes characteristic for the crystalline anatase structure can be recognized. The sloped and rugged spectrum of the sample treated at 250 °C points out its lower crystallinity compared to those treated at higher temperatures. This indicates the presence of amorphous TiO_2, thus, we can consider that this sample possesses a cryptocrystalline structure [30]. According to the Raman spectrum of the TiO_2 produced at 800 °C (or at 785 °C according to DTA analysis), it is obvious that the transformation from anatase to rutile is completed. Thus, this is the temperature at which Magneli phases can be produced, but in an reductive atmosphere.

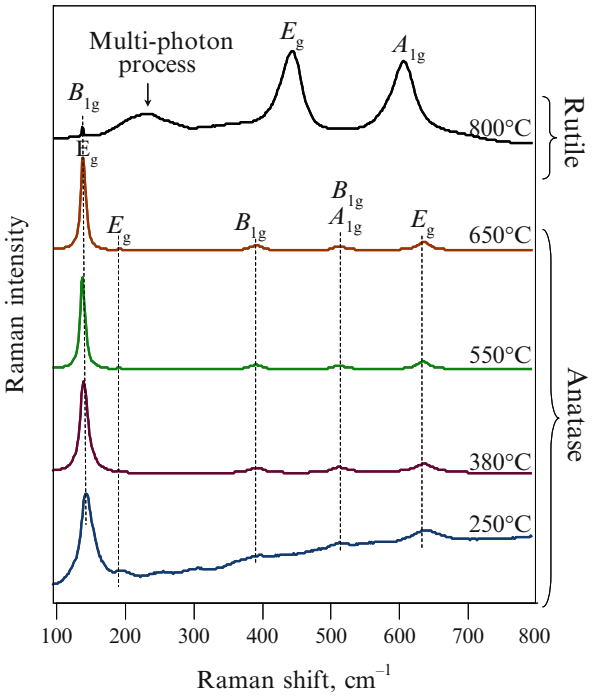

Fig. 24.7 Raman spectra of TiO_2 thermally treated in oxidative atmosphere

Shape and size of titania crystallites were observed by TEM analysis (Fig. 24.8). At lower temperatures (250, 380 and 550 °C) spherical forms of particles were observed with sizes of 6, 11 and 15–25 nm respectively. The formation of nanorods can be observed at 650 °C with diameters of 12 nm and lengths of 15–25 nm. At 800 °C, the rutile phase shows nanorods with diameters of about 20–25 nm and lengths of about 60–70 nm.

24.4.2 Production in Reductive Atmosphere

To produce non-stoichiometric titania, the thermal treatment was performed in a reductive atmosphere containing 10 % H_2 and 90 % N_2. A first indicator that the produced material is oxygen deficient is its color. This material is dark gray instead of clearly white rutile produced at the same temperature in an oxidative atmosphere. The presence of non-stoichiometric or oxygen deficient titania can be clearly seen in the Raman spectra shown in Fig. 24.9.

The spectra of pure rutile and Magneli phases show the same Raman vibration modes (B_{1g}, E_g, A_{ag} and multiphonon processes), but with shifted wavenumbers. The corresponding Raman modes of the samples produced in reductive atmosphere are between these values. As the time of the thermal treatment increases, the Raman

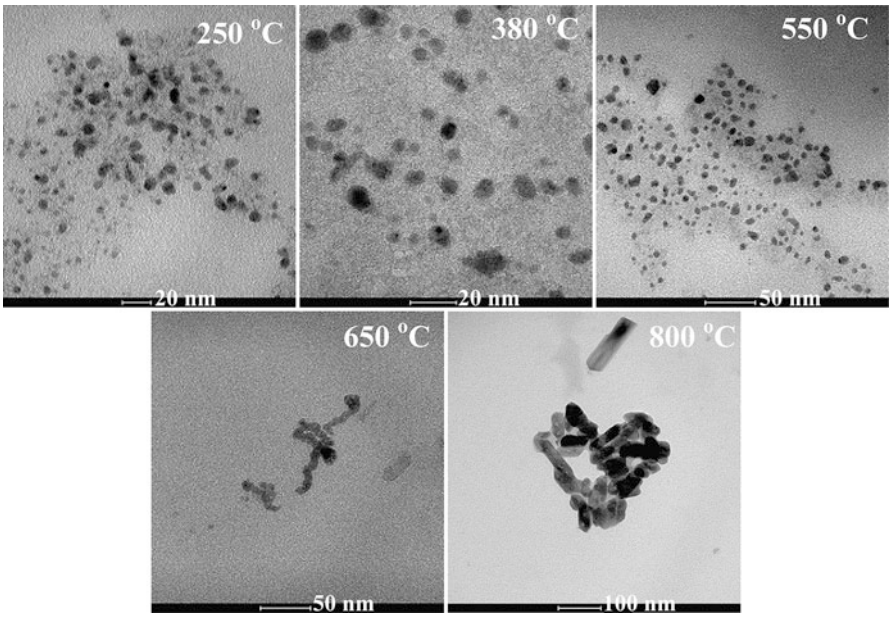

Fig. 24.8 TEM images of TiO_2 produced at different temperatures in an oxidative atmosphere

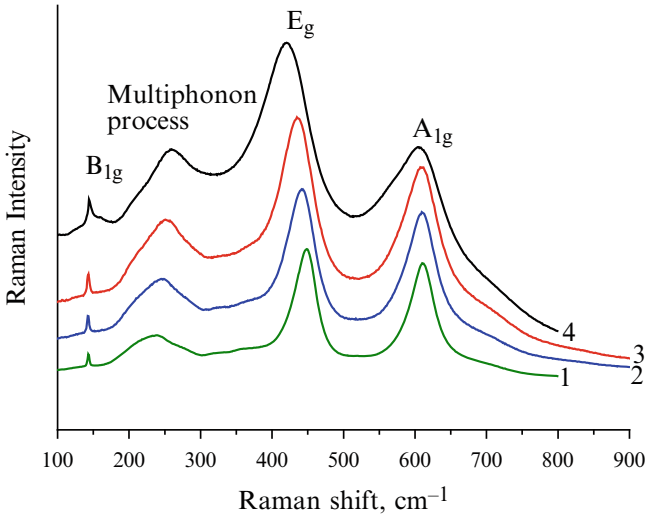

Fig. 24.9 Raman spectra of the titania samples thermally treated in a reductive atmosphere. *1*: Rutile, *2*: Sample treated for 2 h, *3*: Sample treated for 4 h and *4*: commercial Magneli phases

modes approach the corresponding values of the Magneli phases. The shift of Raman modes can be attributed to a confinement of the phonon within the crystallite as result of a decrease of the crystallite size and to non-stoichiometric defects

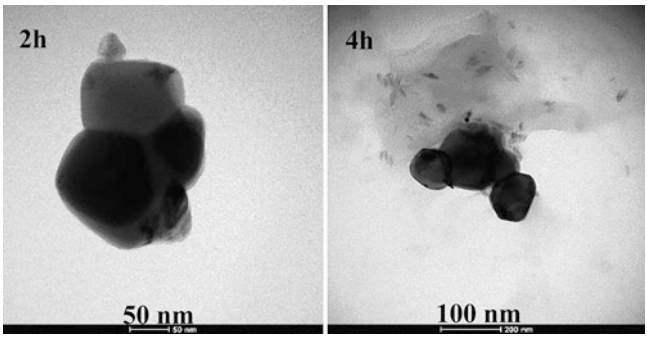

Fig. 24.10 TEM images of samples produced in reductive atmosphere

due to oxygen deficiency within the material [31, 32]. In this case, according to the TEM images (Fig. 24.10), the size of crystallites of the thermally treated samples is approximately equal (50–80 nm), hence the shift of the Raman modes is related to oxygen deficiency in the material. This is the reason why the values of the Raman modes of these samples approach the corresponding values of the Magneli phases.

24.5 Conclusion

According to the results presented above, we can draw several conclusions:

- Maximum achievement of top-down approaches for to reduce the size of micro-scaled particles of Magneli phases to 200 nm after 20 h mechanical treatment.
- Magneli phases prepared by top-down approaches have shown poor performances as catalyst support for electrocatalysts for hydrogen evolution reaction. However, this material has shown to be very effective as electrocatalyst for oxygen evolution reaction and as a photocatalyst for the degradation of naphthalene.
- The TiO_2 structure changes above 222 °C from cryptocrystalline to pure anatase (at 524.1 °C), while at 785 °C transformation from anatase to rutile was completed. Above 785 °C only the rutile phase exists.
- The size of TiO_2 crystallites increases by increase of the temperature in the following order: spherical nanoparticles of 6 nm at 250 °C, 11 nm at 380 °C, 15–25 nm at 550 °C, and nanorods of 50 to less than 100 nm in length and 12 nm in diameter at 800 °C.
- Thermal treatment at 800 °C in a reductive atmosphere for 2 and 4 h leads to partial transformation of rutile in non-stoichiometric oxides close to Magneli phases, but for complete transformation longer time or higher content of H_2 in the gas phase is needed.

Acknowledgments This paper has been supported by and carried out within the Project "Synthesis, characterization and application of nano-scaled nonstoichiometric titanium oxides – Magneli phases" of the Ministry of Education and Science of R. Macedonia (Agreement N^{o} 13-3576/2, 27.10.2010).

References

1. Diebold U (2003) Surf Sci Rep 48:53
2. Chen X, Mao S (2007) Chem Rev 107:2891
3. Carp O, Huisman CL, Reller A (2004) Prog Solid State Chem 32:33
4. Tauster SJ, Fung SC, Garten RL (1978) J Am Chem Soc 100:170
5. Walsh FC, Wills RGA (2010) Electrochim Acta 55:6342
6. Smith JR, Walsh FC, Clarke RL (1998) J Appl Electrochem 28:1021
7. Toyoda M, Yano T, Tryba B, Mozia S, Tsumura T, Inagaki M (2009) Appl Catal B Environ 88:160
8. Marinkovski M, Paunović P, Blaževska Gilev J, Načevski G (2012) Adv Nat Sci Theory Appl 1:215
9. Bejan D, Malcolm JD, Morrison L, Bunce NJ (2009) Electrochim Acta 54:5548
10. Dieckmann GR, Langer SH (1998) Electrochim Acta 44:437
11. Vračar LM, Gojković SL, Elezović NR, Radmilović VR, Jakšić MM, Krstajić NV (2006) J New Mater Electrochem Syst 9:99
12. Cao G (2004) Nanostructures and nanomaterials, synthesis, properties & applications. Imperial College Press, London
13. Jakšić MM (1987) Int J Hydrogen Energy 12:727
14. Jakšić MM (2000) Solid State Ionics 136–137:733
15. Paunović P, Popovski O, Dimitrov AT, Slavkov D, Lefterova E, Hadži Jordanov S (2007) Electrochim Acta 52:4640
16. Paunović P, Radev I, Dimitrov AT, Popovski O, Lefterova E, Slavcheva E, Hadži Jordanov S (2009) Int J Hydrogen Energy 34:2866
17. Paunović P, Dimitrov AT, Popovski O, Slavcheva E, Grozdanov A, Lefterova E, Petruševski D, Hadži Jordanov S (2009) Mater Res Bull 44:1816
18. Paunović P, Stoevska Gogovska D, Popovski O, Stoyanova A, Slavcheva E, Lefterova E, Iliev P, Dimitrov AT, Hadži Jordanov S (2011) Int J Hydrogen Energy 36:9405
19. Paunović P, Popovski O, Fidančevska E, Ranguelov B, Stoevska Gogovska D, Dimitrov AT, Hadži Jordanov S (2010) Int J Hydrogen Energy 35:10073
20. Paunović P, Dimitrov AT, Popovski O, Slavkov D, Hadži Jordanov S (2007) Maced J Chem Chem Eng 26:87
21. Burke LD, Murphy OJ (1980) J Electroanal Chem 109:373
22. Wilcoxon JP, Abrams BL (2008) In: Krug H (ed) Nanotechnology. Wiley-VCH, Weinheim, pp 51–124
23. Linsebigler AL, Lu G, Yates JT Jr (1995) Chem Rev 95:735
24. Hashimoto K, Irie H, Fujishima A (2005) Jpn J Appl Phys 44:8269
25. Jogi I, Kukli K, Aarik J, Aidla A, Lu J (2006) Mater Sci Semicond Process 9:1084
26. Navio JA, Colon G, Macias M, Real C, Litter MI (1999) Appl Catal A Gen 177:111
27. Marinkovski M (2009) Ph.D. thesis, Faculty of Technology and Metallurgy, University "Ss Cyril and Methodius", Skopje
28. So WW, Park SB, Kim KJ, Shin CH, Moon SJ (2001) J Mater Sci 36:4299
29. Holgado M, Cintas A, Ibisate M, Serna CJ, Lopez C, Meseguer F (2000) J Colloid Interface Sci 229:6
30. Xie Y, Yuan C (2004) Appl Surf Sci 221:17
31. Xu CY, Zhang PX, Yan L (2001) J Raman Spectrosc 32:862
32. Choi HC, Jung YM, Kim SB (2005) Vib Spectrosc 37:33

Chapter 25
Photocatalytic Activity of SnO_2-Doped SiO_2@TiO_2 Nanocomposites

B. Czech, M.A. Nazarkovsky, and V.M. Gun'ko

Abstract Bisphenol A (BPA) is worldwide used to produce plastics and/or epoxy-based foodstuff packages. But it is known that this compound is considered as a quite toxic contaminant due to (1) its similarity to the hormone estrogen and (2) its universal use in many industrial proceses. In our study the photodegradation of BPA stimulated by tin(IV) oxide-modified silica-titania nanocomposites was investigated. The reactions were characterized by the kinetic parameters (pseudo-first constant k_1 0.036–0.0896·10^{-2} min^{-1} for non-calcined and 0.0389–0.1144·10^{-2} min^{-1} for calcined photocatalysts), half-life time $t_{1/2}$ 7.74–19.23 and 6.66–17.83 min for non- and calcined ones, respectively, allowing to determine both the weight k_w and the specific surface area k_s of each sample. It will be shown that most SnO_2-doped silica-titania oxides are more active than commercially available TiO_2 (P-25, Degussa). The best results of BPA removal were obtained for 6 wt% addition of SnO_2 to both calcined and non-calcined photocatalysts.

Keywords Silica-titania • Bisphenol A • P25 • Tin dioxide

25.1 Introduction

The synthesis of effective TiO_2-based photocatalysts calls for novel techniques nowadays. This deals with the availability of various modern complex nanocomposites obtained in different forms [1–6]. Doping of titania has been shown to be one popular and routine approach to enhance its photocatalytic properties; the aspects of doping strategies have been studied for decades. SnO_2 is known as a wide band gap n-type semiconductor ($E_g = 3.60$ eV, $C_B = -0.07$ eV,

B. Czech
Faculty of Chemistry, Maria Curie-Skłodowska University, Maria Curie-Skłodowska sq. 3, 20-031 Lublin, Poland

M.A. Nazarkovsky (✉) • V.M. Gun'ko
Chuiko Institute of Surface Chemistry, National Academy of Sciences of Ukraine, 17 General Naumov Str., Kiev 03164, Ukraine
e-mail: nazarkovsky.michael@gmail.com

P. Petkov et al. (eds.), *Nanoscience Advances in CBRN Agents Detection, Information and Energy Security*, NATO Science for Peace and Security Series A: Chemistry and Biology, DOI 10.1007/978-94-017-9697-2_25

$V_B = +3.67$ eV) having weak photocatalytic properties and playing an important role in tuning TiO_2 structures [7–12]. The ionic radii of Sn^{4+} and Ti^{4+} are comparable: 0.69 and 0.61 Å, respectively. Thus, SnO_2 can easily form solid solutions in TiO_2 in accordance with the Vegard law [13, 14]. On the one hand, the enhancement of the photocatalytic activity of TiO_2 provided by SnO_2 is based on an effective charge separation in the TiO_2-SnO_2 heterostructures [12, 15, 16]. On the other hand, it is stated in [17] that TiO_2 is considered as a photosentisizer for SnO_2. Since the described SnO_2-doped TiO_2 systems are present as thin films or nanotubes, we synthesized a set of powder-like systems on nanosilica support (PS-300, $S_{BET} = 300$ m^2/g) with different concentrations of SnO_2. Such oxide systems are considered as ternary SiO_2-TiO_2-SnO_2 materials.

Nanosilica, as reported by various investigators [6, 18–21] enables a significant increase of the photocatalytic activity of TiO_2 due (1) to the combination of different surface Brønsted acidic sites:

$$\equiv \mathrm{Ti}(\mathrm{OH})\equiv \mathrm{Si} \longrightarrow \equiv \mathrm{Ti}(\mathrm{O}^-)\equiv \mathrm{Si} + \mathrm{H}^+ \tag{25.1}$$

$$\equiv \mathrm{Ti}(\mathrm{OH})\equiv \mathrm{Ti} \longrightarrow \equiv \mathrm{Ti}(\mathrm{O}^-)\equiv \mathrm{Ti} + \mathrm{H}^+ \tag{25.2}$$

$$\equiv \mathrm{TiOH} + \mathrm{H}^+ \rightarrow \equiv \mathrm{TiOH}_2^+ \tag{25.3}$$

$$\equiv \mathrm{SiOH} \rightarrow \equiv \mathrm{SiO}^- + \mathrm{H}^+ \tag{25.4}$$

and (2) the ability of charge separation as well. An important point is that the addition of a dopant to SiO_2-TiO_2 gives rise to complex changes in the textural and morphological properties of the nanocomposites produced. Furthermore, such changes are non-linear upon incremental addition of a dopant in frequent cases. Increasing or decreasing S_{BET} or total pore volume, the amount of the surface active sites is changed, too.

The structural and physicochemical properties of novel SnO_2-modified silica-titania materials were studied and discussed previously in [22, 23]. In the present work we aim to determine the influence of the SnO_2 concentration on the photocatalytic activity of TiO_2 deposited onto PS-300 under UV irradiation using bisphenol A – labeled as BPA – as a model anthropogenic contaminant. 0.01–44.65 μg/L BPA was detected in surface water and 0.37–491.54 μg/kg dry mass in biosolids [24]. Although BPA is removed during conventional waste water treatment (76–93 % ±6 %) [25], it possesses a tendency to accumulate in activated sludges [26]. The toxic effect of BPA has been debated for many years but it has been shown that this compound used as a part of plastic packages can be easily passed to drinks and food [27, 28]. Moreover BPA is employed as a model substrate for photocatalytic studies worldwide [29–32].

25.2 Experimental

The synthesis of SiO_2-TiO_2-SnO_2 oxides is described in detail in [22, 23]. Tin (IV) chloride was introduced into a glass reactor where silica and water were stirred. Thereupon $TiCl_4$ was added. The calculated concentration of TiO_2 was 15 wt% against SiO_2, that of C_{SnO2} was varied from 0.14 to 30 wt% with respect to TiO_2. The amount of each sample was halved. One half was subjected to thermal treatment at 600 °C, the other one was left non-calcined. XRD results indicated [23] that all calcined samples (SiO_2-TiO_2-SnO_2-c) contain crystalline anatase but non-calcined ones (SiO_2-TiO_2-SnO_2-nc) show its presence in a very narrow range of SnO_2 concentrations ($C_{SnO2} = 4$–6 wt%).

The photocatalytic activity of SiO_2-TiO_2-SnO_2 samples was studied during the photodegradation of bisphenol A (Sigma-Aldrich, Poland) in a photochemical batch reactor (Heraeus, System 2, 0.75 L) equipped with an UV low-pressure lamp TQ 150 ($\lambda = 254$ nm). A model solution prepared from BPA and a photocatalyst (10 mg/L and 0.5 g/L, respectively) were stirred at 500 rpm and kept in the dark during 30 min to attain an adsorption-desorption equilibrium before starting the photodestruction. The concentration of bisphenol A was evaluated by means of high-performance liquid chromatography (Waters, Alliance e2695, DAD, H_2O:$CH_3CN = 30$:70, flow rate = 0.5 mL/min) using a C18 Waters PAH column. Commercially available titania P25 (rutile/anatase = 80/20) produced by Degussa-Evonik was used as a reference.

The decrease of the BPA concentration c in the course of the treatment time t is described by means of pseudo first-order kinetics related to the equation:

$$r = -\frac{dc}{dt} = kc^n \tag{25.5}$$

where r, c and t represent the rate of degradation, the BPA concentration and the time respectively. Also k and n are the rate constant and reaction the order.

The initial concentration of BPA c_0 was kept fixed. The apparent pseudo first-order rate constant k_1 [min^{-1}] was calculated by fitting the experimental data to the relation:

$$-\ln\left(\frac{c}{c_0}\right) = k_1 \cdot t \tag{25.6}$$

The linear regressions obtained by plotting $-ln(c/c_0)$ vs. t were used in order to evaluate k_1. The other constants such as the apparent rate constants of the catalyst per mass units k_w and per surface area k_s were calculated from Eqs. 25.7 and 25.8 [33]:

$$k_w = \frac{k_1}{c_w \cdot V_r}\ , \tag{25.7}$$

$$k_s = \frac{k_1}{S_{BET} \cdot c_w \cdot V_r}\ , \tag{25.8}$$

where c_w is the concentration of the photocatalyst, S_{BET} the specific surface area of the photocatalyst [22] and V_r the reactor volume (0.75 L). Subsequently, the values of the half-life time $t_{1/2}$ were estimated from Eq. 25.9:

$$t_{1/2} = \frac{0.69314}{k_1} \tag{25.9}$$

25.3 Results and Discussion

Non-calcined samples demonstrate a considerable efficiency to destroy BPA. In all cases, adding SnO_2 provokes the increase of the pollutant destruction (Fig. 25.1). As far as the change of BPA concentration is concerned, it has drastically decreased (at least by 70 %) after 20 min of treatment.

The most pronounced results of diminution of the BPA concentration were obtained by the usage of the sample with $C_{SnO2} = 6$ wt%. We have every reason to believe that this fact relates to the textural features of the sample. As the analysis of the porosity has indicated [22], this nanocomposite is characterized by the greatest total pore volume to which the mesopores provide the main contribution.

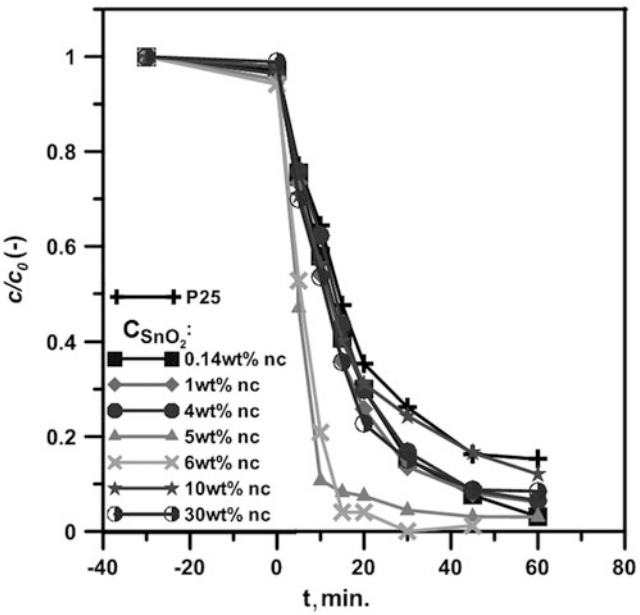

Fig. 25.1 The photocatalytic destruction of BPA (10 mg/L) using $SiO_2/TiO_2/SnO_2$-nc and P25 (0.5 g/L)

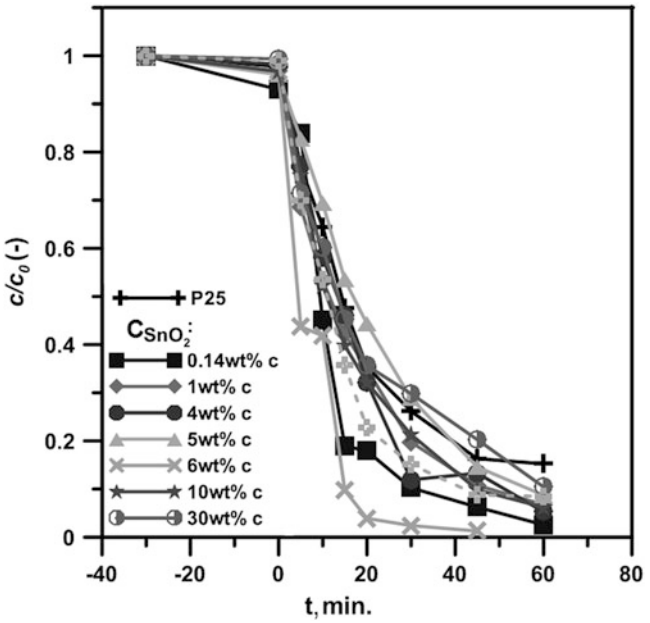

Fig. 25.2 The photocatalytic destruction of BPA (10 mg/L) using $SiO_2/TiO_2/SnO_2$-c and P25 (0.5 g/L)

As photodegradation of BPA occurs in the mesopores, i.e. in the voids between randomly packed oxide aggregates of SnO_2-modified SiO_2-TiO_2, their amount provides a greater availability of active surface sites than other samples. Besides, this suggestion correlates with the results obtained for annealed samples (Fig. 25.2): after the calcination at 600 °C the total pore volume of SiO_2-TiO_2-(6 wt%) SnO_2-c, however, has not decreased significantly [22]. Hence, the calcined sample at $C_{SnO2} = 6$ wt% is the most active.

Analyzing the kinetic curves of photodegradation of BPA in the presence of SnO_2-doped silica-titania calcined at 600 °C, we can conclude that they are mostly not so active, in contrast to non-calcined ones. These results are associated with the thermally stimulated reduction of Brønsted acidic sites shown previously in the course of surface charge density measurements [23].

The values of the coefficient of determination R^2 provide support of the accuracy of the experiment and first-order kinetics of the photodegradation (Fig. 25.3, Table 25.1). But the values of R^2 for $C_{SnO2} = 4$–6 wt% tend to decrease. This diminution may result from possible second-order kinetics of the photooxidation, i.e. the photodecomposition of BPA does not obey first-order kinetics; this process can by discussed in terms of two-step oxidation of BPA.

The values of k_1 of SiO_2-TiO_2-SnO_2-nc samples are higher compared to those of P25. It is self-evident that rate constants with due regard to the sample weight k_w change in the same way depending on C_{SnO2} because all the photocatalysts were exploited at the identical weights.

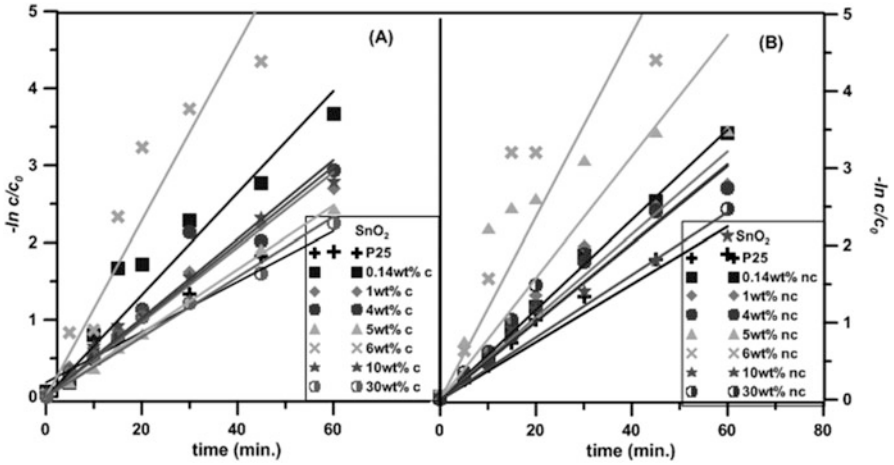

Fig. 25.3 Linear fitting of the kinetic curves of BPA (10 mg/L) photodecomposition using SiO_2/TiO_2/SnO_2-c (**a**) and SiO_2/TiO_2/SnO_2-nc photocatalysts (**b**)

A different situation arises with k_s. Since the samples have different values of the specific surface area exceeding that of P25 by almost a factor of 4, it comes as no surprise that the S_{BET}-corrected rate constants do not exceed k_s of P25. The most active nanocomposite with $C_{SnO2} = 6$ wt% have the highest k_1 and k_w values in comparison to all non-calcined and annealed oxide systems. However, the k_s value lower than that of P25. But the k_s value of calcined sample is only moderately larger than the value of non-heated sample (Tables 25.1 and 25.2).

The non-linear dependence of the photocatalytic activity on C_{SnO2} was found in various studies [9, 15]. It is important to keep in mind that BPA has been decomposed at least by 80 % during 60 min but not totally. The remaining by-products (phenol and quinones [34]) are resistant to further oxidation. Summing it up, we can conclude that the strategy to enhance the photocatalytic activity of SnO_2-modified TiO_2 deposited on PS-300 can be effected by simultaneous introduction of tin(IV) oxide and titania in the reactor or TiO_2 should be added before SnO_2. Different ways of the introduction of both oxides may be responsible for dissimilar crystalline and/or band gap structures of TiO_2 – tin(IV) oxides.

25.4 Conclusions

We have shown that SnO_2-modified SiO_2-TiO_2 nanocomposites are more active than the commercially produced P25 in the course of the photodecomposition of bisphenol A (BPA). The dependence of C/C_0 on the concentration of SnO_2 was established to be non-linear due to non-linear changes of the textural properties of SiO_2-TiO_2-SnO_2. The sample with $C_{SnO2} = 6$ wt% has been found to be the most

Table 25.1 First-order reaction rate constants k_1 per gram of catalyst k_w, per surface area of catalyst k_s and half-lifetime $t_{1/2}$ values of the photocatalytic oxidation reactions of BPA in the presence of $SiO_2/TiO_2/SnO_2$-nc samples and of P25

Photo-catalyst	k_1 (10^{-2} min^{-1})	R^2	k_W (10^{-2} $min^{-1} \cdot g^{-1}$)	S_{BET} $m^2 \cdot g^{-2}$	k_S (10^{-5} $min^{-1} \cdot m^{-2}$)	$t_{1/2}$ (min)
P25	0.0374	0.969181	0.0998	55	1.8146	18.52
C_{SnO2}, wt.%						
0.14	0.0583	0.99901	0.1555	245	0.6358	11.89
1	0.0536	0.977611	0.1430	272	0.5259	12.92
4	0.0453	0.878759	0.1208	279	0.4326	15.31
5	0.0702	0.770276	0.1872	273	0.6854	9.87
6	0.0896	0.688246	0.2389	271	0.8803	7.74
10	0.0360	0.860404	0.0961	210	0.4581	19.23
30	0.0505	0.958323	0.1347	216	0.6248	13.73

Table 25.2 First-order reaction rate constants k_1 per gram of catalyst k_w, per surface area of catalyst k_s and half-lifetime $t_{1/2}$ values of the photocatalytic oxidation reactions of BPA in the presence of $SiO_2/TiO_2/SnO_2$-c samples and of P25

Photo-catalyst	$k_1 \cdot (10^{-2}\ min^{-1})$	R^2	$k_W\ (10^{-2}\ min^{-1} \cdot g^{-1})$	$S_{BET}\ m^2 \cdot g^{-2}$	$k_S\ (10^{-5}\ min^{-1} \cdot m^{-2})$	$t_{1/2} \cdot (min)$
P25	0.0374	0.969181	0.0998	55	1.8146	18.52
C_{SnO2}, wt.%						
0.14	0.0661	0.973081	0.1763	250	0.7065	10.49
1	0.0485	0.991922	0.1294	262	0.4929	14.29
4	0.0511	0.976326	0.1363	247	0.5526	13.56
5	0.0413	0.999184	0.1102	263	0.4186	16.77
6	0.1144	0.957438	0.3050	281	1.0841	6.06
10	0.0497	0.992878	0.1326	234	0.5658	13.94
30	0.0389	0.984493	0.1037	229	0.4531	17.83

active among both non-calcined and thermally treated nanomaterials. The heating effect stimulates a moderate increase of the photocatalytic activity of this sample.

The most significant decrease of the BPA concentration has been observed for 20 min UV-irradiation in the presence of the photocatalysts. BPA was decomposed by 80 % in the course of 1 h, but its photodestruction was not total.

Acknowledgements The research leading to these results has received funding from the People Programme of the EU FP7 (FP7/2007–2013), Marie Curie International Research Staff Exchange Scheme (Project NANOBIOMAT, Grant No. 612484).

References

1. Wongpisutpaisan N, Vittayakorn N, Ruangphanit A, Pecharapa W (2013) Sains Malaysiana 42:175
2. Kuncewicz J, Zabek P, Stochel G, Stasicka Z, Macyk W (2011) Catal Today 161:78
3. Yao Z, Jia F, Jiang Y, Li C, Jiang Z, Bai X (2010) Appl Surf Sci 256:1793
4. Zaleska A (2008) Recent Patents Eng 2:157
5. Linsebigler A, Lu G, Yates J (1995) Chem Rev 95:735
6. Zhang H, Quan X, Chen S, Zhao H (2006) Environ Sci Technol 40:6104
7. Sayılkan H (2007) Appl Catal A Gen 319:230
8. Fresno F, Tudela D, Coronado JM, Fernandez-Garcıa M, Soria HABJ (2006) Phys Chem Chem Phys 8:2421
9. Hou L-R, Yuan C-Z, Peng Y (2007) J Hazard Mater 139:310
10. Lin C-F, Wu C-H, Onn Z-N (2008) J Hazard Mater 154:1033
11. Hattori A, Tokihisa Y, Tada H, Ito S (2000) J Electrochem Soc 147:2279
12. Zhou M, Yu J, Liu S, Zhai P, Jiang L (2008) J Hazard Mater 154:1141
13. Park M, Mitchell TE, Heuer AH (1975) J Am Ceram Soc 58:43
14. Cao Y, He T, Zhao L, Wang E, Yang W, Cao Y (2009) J Phys Chem C 113:18121
15. Vinodgopal K, Bedja I, Kamat PV (1996) Chem Mater 8:2180
16. Cao Y, Zhang X, Yang W, Du H, Bai Y, Li T, Yao J (2000) Chem Mater 12:3445
17. Robert D (2007) Catal Today 122:20
18. Pinho L, Mosquera MJ (2011) J Phys Chem C 115:22851
19. Kusakabe K, Ezaki M, Sakoguchi A, Oda K, Ikeda N (2012) Chem Eng J 180:245
20. Guo Y, Yang S, Zhou X, Lin C, Wang Y, Zhang W (2011) J Nanomater 2011:296953
21. Luo Y, Zou L, Hu E (2006) Environ Technol 27:359
22. Nazarkovsky MA, Gun'ko VM, Zarko VI, Skwarek E, Skubiszewska-Zięba J, Leboda R, Janusz W (2013) J Chem Technol Metall 48:373
23. Nazarkovsky MA, Goncharuk EV, Pakhlov EM, Oranska EI, Skwarek E, Skubiszewska-Zięba J, Leboda R, Janusz W, Gun'ko VM (2013) Prot Met Phys Chem Surf 49:541
24. Lee C-C, Jiang L-Y, Kuo Y-L, Hsieh C-Y, Chen CS, Tien C-J (2013) Chemosphere 91:904
25. Lee J, Lee BC, Ra JS, Cho J, Kim IS, Chang NI, Kim HK, Kim SD (2008) Chemosphere 71:1582
26. Asimakopoulos AG, Thomaidis NS, Koupparis MA (2012) Toxicol Lett 210:141
27. Staples CA, Dome PB, Klecka GM, Oblock ST, Harris LR (1998) Chemosphere 36:2149
28. Chen M-Y, Ike M, Fujita M (2002) Environ Toxicol 17:80
29. Fukahori S, Ichiura H, Kitaoka T, Tanaka H (2003) Environ Sci Technol 37:1048
30. Kaneco S, Rahman MA, Suzuki T, Katsumata H, Ohta K (2004) J Photochem Photobiol A Chem 163:419

31. Ohko Y, Ando I, Niwa C, Tatsuma T, Yamamura T, Nakashima T, Kubota Y, Fujishima A (2001) Environ Sci Technol 35:2365
32. Zhao L, Xiao X, Peng L, Gu FL, Zhang RQ (2014) RSC Adv 4:10343
33. Czech B, Rubinowska K (2013) Adsorption 19:619
34. Lu N, Lu Y, Liu F, Zhao K, Yuan X, Zhao Y, Li Y, Qin H, Zhu J (2013) Chemosphere 91:1266

Chapter 26
Phase Transformation of RGO/SiO_2 Nanocomposites Prepared by the Sol-Gel Technique

A. Shalaby, A. Staneva, L. Aleksandrov, R. Iordanova, and Y. Dimitriev

Abstract In a previous paper (Shalaby A, Yaneva V, Staneva A, Aleksandrov L, Iordanova R, Dimitriev Y, Nanoscience & nanotechnology – nanostructured materials application and innovation transfer (14), ISSN 1313-8995, 2014) we studied reduced graphene oxide (RGO)/SiO_2 composite material by adding a small amount of RGO to silica in order to avoid the aggregation process and to solve the problems connected with the exfoliation and distribution of the sheets inside the composites. But from a practical point we needed to study the effect of high amounts of RGO on the composites at different temperatures. The purpose of this investigation is to study the effect of RGO on phase transformations of the composites heated at 200, 400 and 800 °C. The sol-Gel method was used to obtain the RGO/SiO_2 composite by mixing high amounts of RGO with tetraethyl orthosilicate (TEOS). Data are presented for the transformation of the nanocomposites with increasing temperature in air atmosphere. RGO nanosheets were prepared by chemical exfoliation of purified natural graphite using the Hummers and Offeman method (Hummers WS, Offeman RE, J Am Chem Soc 80:1339, 1958) to obtain graphite oxide. Then the material was exfoliated to reduced graphene nanosheets by ultrasonication and reduction process using sodium borohydride ($NaBH_4$). Characterization of the material was performed by X-ray powder diffraction (XRD),

A. Shalaby (✉)
Science and Technology Center of Excellence (STCE), Km.3 Cairo-Belbeis Desert Rd., Cairo, Egypt

University of Chemical Technology and Metallurgy, 8 Kl. Ohridski blvd., 1756 Sofia, Bulgaria
e-mail: ashalaby@outlook.com

A. Staneva
University of Chemical Technology and Metallurgy, 8 Kl. Ohridski blvd., 1756 Sofia, Bulgaria

L. Aleksandrov • R. Iordanova
Institute of General and Inorganic Chemistry, Bulgarian Academy of Sciences, G. Bonchev str., bld. 11, 1113 Sofia, Bulgaria

Y. Dimitriev
Department of Materials Science, University of Chemical Technology and Metallurgy, 8 Kl. Ohridski blvd., 1756 Sofia, Bulgaria

P. Petkov et al. (eds.), *Nanoscience Advances in CBRN Agents Detection, Information and Energy Security*, NATO Science for Peace and Security Series A: Chemistry and Biology, DOI 10.1007/978-94-017-9697-2_26

infrared (IR) spectroscopy and scanning electron microscopy (SEM) analysis. In our previous studies we found that all samples with small amounts of RGO are amorphous up to 800 °C. By increasing the amount of RGO (20 %) crystal phases appear at 200, 400 and 800 °C. The carbon phases disappear above 400 °C and cristobalite is found at 800 °C. From the IR spectra it was established that the band related to Si-OH vibration is converted to a small shoulder at 400 °C, and the bands corresponding to vibrations of water molecules around 3,448 and 1,635 cm^{-1} were drastically reduced by increasing the temperature. The dominant band at 1,099.2 cm^{-1} (800 °C) is connected with the stretching vibration of Si-O bonds in SiO_4 tetrahedrons. SEM images of RGO/SiO_2 nanocomposites present randomly aggregated stacks of small sheets imbedded in an amorphous matrix.

Keywords Reduced graphene oxide • TEOS • Nanocomposite • Sol-gel

26.1 Introduction

Graphene is the first stable two-dimensional crystal composed of a single layer of sp^2 network of carbon atoms. It has extraordinary physicochemical properties such as high values of its Yong's modulus, fracture strength, thermal conductivity, specific surface area, and electrical conductivity [2, 3]. These features have made graphene and graphene derivatives ideal for diverse applications. Nevertheless, several of these applications are still not feasible because the large-scale production of unbroken pure graphene sheets remains challenging. Basically there are two different approaches to prepare graphene, exfoliation and growth on surfaces. The first approach which is more interesting includes micromechanical cleavage, dispersion of graphite, exfoliation of graphite oxide and substrate preparation. In the second approach, graphene layers can be grown directly on a substrate surface by epitaxial growth or by chemical vapor deposition [4]. One of the methods considered as an effective route to synthesize graphene sheets due to its simplicity, reliability, ability for large-scale production and exceptionally low costs is the isolation of graphene sheets from graphite by three steps. The first step is oxidation of graphite to graphite oxide [5, 6]. The second is sonication of graphite oxide to obtain exfoliated graphene oxide layers [7, 8]. The last one is reduction the colloidal dispersions of graphene oxide by chemical reducing agents, such as hydrazine [9], hydroquinone [10], or sodiumborohydride ($NaBH_4$) [11, 12]. The obtained sheets of reduced graphene oxide (RGO) generally contain some oxygen functional groups such as -OH or -COOH [13]. This reduced graphene oxide (RGO) is called in the literature chemically converted graphene, chemically modified graphene, or simply graphene [14].

In the past few years, significant efforts have been directed toward the preparation of graphene-based nanocomposites such as graphene/Bi_2O_3 [15], graphene/SnO_2 [16], graphene/gold [17], graphene/Silver [18], graphene/Mn_3O_4 [19], Ag_3VO_4/TiO_2/graphene [20], TiO_2/graphene [21, 22], ZnO/graphene [23, 24], graphene/cobalt [25], etc. The unique properties of these materials have been

demonstrated for a variety of catalysts, super capacitors and fuel cell batteries. It is indubitable that graphene-based nanocomposites are a new endeavor, indicating that future research efforts will be required. One of the future challenges is to maintain the excellent physical properties of graphene in the process of synthesizing nanocomposites [26]. Silica is a very appropriate compound for the preparation of composites due to its high chemical and thermal stability. The graphene fabricated on silica possesses interesting properties due to the local atomic configuration, and the binding sites of graphene with SiO_2. It has possible applications in the development of super capacitor devices, drug delivery, heavy metal removal, biosensors and electrochemical sensor [27–29]. There are a few literature data exploring methods for the synthesis of silica/graphene composites by using graphite oxide and TEOS as precursors with or without surfactants [30–32]. It is easier to prepare homogeneous composites by the sol-gel method with random distribution of RGO particles directly in the volume of the material. There are not enough data published studying the effect of RGO on the phase transformation of RGO/SiO_2 composites at increased temperatures. This was the motivation for us to start experiments with high amounts of RGO (20 %) to make the effect more clear. In our previous study [1] we performed some experiments with small amount of RGO (2.5, 5 %), but the effect was not strong enough to study the phase transformation of the composite since the silica remained amorphous up to 800 °C. The aim is to study phase transformations at different temperatures. Characterization was performed by X-ray analysis, IR-Spectra and SEM analysis.

26.2 Experimental

26.2.1 Preparation of RGO Sheets

In the first step, graphite oxide was prepared by chemical exfoliation of purified natural graphite powder (99.9 %, Alfa Aesar) using the Hummers and Offeman method [33]. Graphite oxide was exfoliated to reduced graphene nanosheets (RGO) by ultrasonication, followed by a reduction process using sodium borohydride (98 %, Alfa Aesar).

26.2.2 Preparation of RGO/Silica Composite

We selected the sol-gel technique to prepare the composite among different preparation methods according to the surface hydroxyl groups of the RGO sheets can act as nucleation sites for the hydrolysis step which facilitates chemical bonding with the surrounding materials. The common procedure for preparing graphene/silica composites is using aqueous graphite oxide dispersion with TEOS and reducing the mixture by chemical or hydrothermal methods in one-pot synthesis process [14, 30]

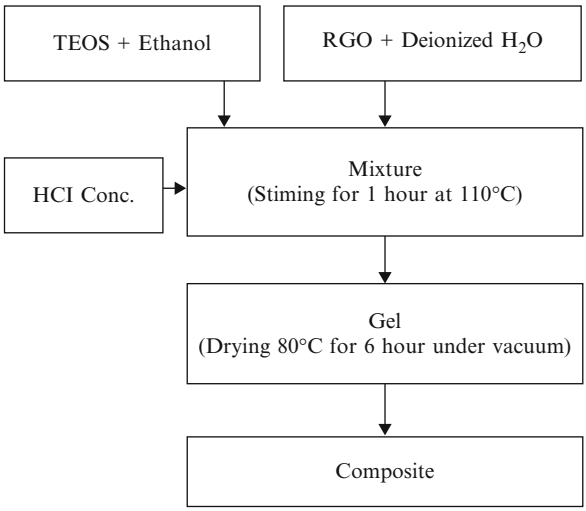

Fig. 26.1 Scheme of preparation

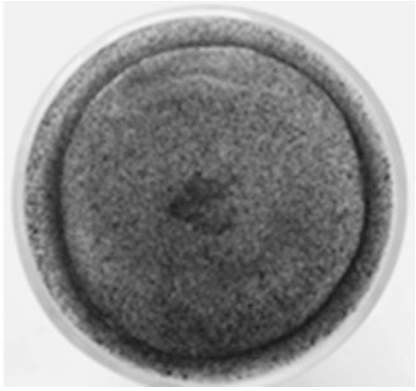

Fig. 26.2 RGO/SiO_2 gel

or by using surfactants [31]. While adding a mixture of high amounts of RGO (20 %) and deionized water directly to a solution of tetraethyl orthosilicate (TEOS, 98 %, Aldrich) dissolved in ethanol under stirring for 1 h at 110 °C to obtain a gel following the scheme shown in Fig. 26.1.

26.2.3 Methods of the Characterization

Figure 26.2 presents the RGO/SiO_2 composite gel which was heated to 110 °C. Visually it appears transparent with randomly distributed dark spots. The phase formation and structural transformation were detected by X-ray analysis (Bruker

D8 Advance, Cu Kα radiation). The microstructure and morphology of the crystalline products were studied by scanning electron microscopy (SEM, Jeol-357). The short range order of the nanocomposites were determined by a FTIR spectrophotometer (VARIAN series 600) with a wide wavelength range (79,000–50 cm^{-1}) and a spectral resolution better than 0.07 cm^{-1} at room temperature using a standard KBr pellet technique.

26.3 Results and Discussion

From the XRD analysis it was found that crystalline phases appeared at different temperature as shown in Fig. 26.3a. From room temperature to 200 °C the composites contain amorphous silica and RGO. Lignit is identified at 400 °C (Ref. Code 00-005-0625). All carbon phases disappeared above 400 °C, while at 800 °C cristobalite and amorphous silica co-exist together. If comparing these data with the graphite/SiO_2 composite shown in Fig. 26.3b we noticed that peaks of crystalline graphite at 200 and 400 °C while all carbon disappeared above 400 °C without enhanced the crystal phases of silica which still amorphous. This means that the exfoliated sheets of RGO work as catalyst to enhance the formation of cristobalite at low temperatures.

From the IR spectra shown in Fig. 26.4a, b it was established that between room temperature and 400 °C a transformation of silica gel to silica gel glass took place since the band at 950 cm^{-1} decreased to a small shoulder. This is connected with the replacement of Si-OH groups by Si-O-Si bridge bond. The bands corresponding

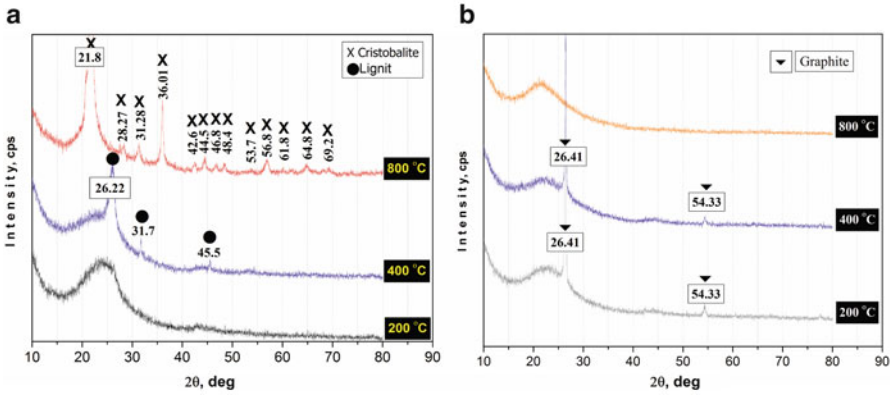

Fig. 26.3 X-ray diffraction patterns: (**a**) samples containing RGO; (**b**) samples containing graphite at different temperatures

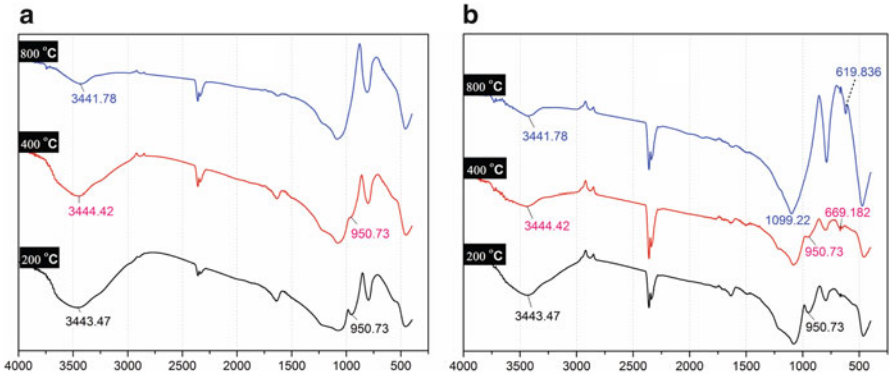

Fig. 26.4 IR spectra of the samples containing pure TEOS (**a**) and 20 % RGO (**b**) at different temperatures in the range 4,000–400 cm^{-1}

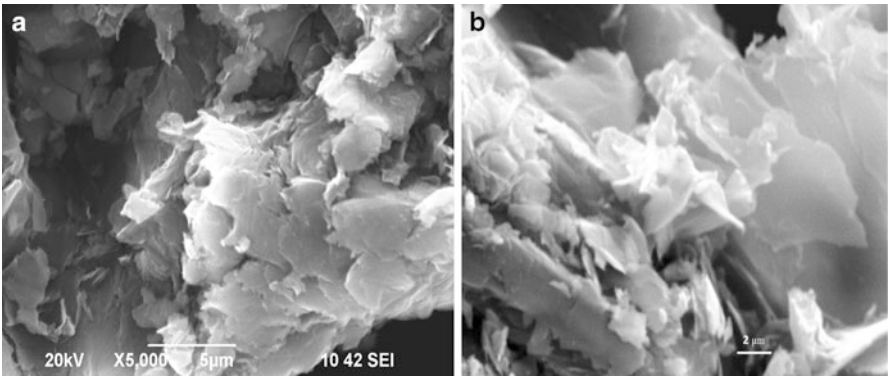

Fig. 26.5 SEM images of (**a**) the RGO/SiO_2 composite and (**b**) the pure RGO sheets. All samples were heated at 200 °C

to vibrations of water molecules around 3,444 and 1,635 cm^{-1} were drastically reduced by increasing the temperature. The dominant band at 1,099.2 cm^{-1} (800 °C) is connected with the stretching vibration of Si-O bonds in SiO_4 tetrahedrons. The small band near 620 cm^{-1} starts to appear above 400 °C which is typical for the formation of cristobalite as shown in Fig. 26.4b. As shown in Fig. 26.4a this band does not appear for pure TEOS. This means that the silica is still amorphous. These results confirm the XRD analysis.

From SEM images randomly distributed aggregates of stacked small sheets imbedded in the amorphous matrix are apparent (Fig. 26.5a). The pure RGO sheets appeared as exfoliated semitransparent layers as shown in Fig. 26.5b.

26.4 Conclusions

It was established that using the sol-gel technique by mixing RGO and TEOS it is possible to obtain composite materials. It was proven that high amounts of RGO (20 %) enhance the crystallization, and crystal phases like lignit are present at 400 °C while cristobalite appears at 800 °C. This means that the transformation of the composite materials should effects the properties of the final product. We believe that this information will be useful for further understanding of the complex nature of this composite, and it will be taken in to account for possible applications.

Acknowledgements Ahmed Shalaby thanks the Erasmus Mundus MEDASTAR (Mediterranean Area for Science Technology and Research) Program.

References

1. Shalaby A, Yaneva V, Staneva A, Aleksandrov L, Iordanova R, Dimitriev Y (2014) Nanoscience & nanotechnology – nanostructured materials application and innovation transfer 14:120
2. Novoselov KS, Geim AK, Morozov SV, Jiang D, Zhang Y, Dubonos SV, Grigorieva IV, Firsov AA (2004) Science 306:666
3. Geim K (2009) Science 324:1530
4. Krane N (2011) Selected topics in physics: physics of nanoscale carbon, Freie Universität Berlin
5. Meng LY, Park SJ (2012) Bull Kor Chem Soc 33:209
6. Shao G, Lu Y, Wu F, Yang C, Zeng F, Wu Q (2012) J Mater Sci 47:4400
7. Stankovich S, Dikin DA, Dommett GHB, Kohlhaas KM, Zimney EJ, Stach EA, Piner RD, Nguyen ST, Ruoff RS (2006) Nature 422:282
8. Zhu Y, Murali S, Cai W, Li X, Suk JW, Potts JR, Ruoff RS (2010) Adv Mater 22:3906
9. Stankovich S, Dikin DA, Piner RD, Kohlhaas KA, Kleinhammes A, Jia Y, Wu Y, Nguyen ST, Ruoff RS (2007) Carbon 45:1558
10. Wang G, Yang J, Park J, Gou X, Wang B, Liu H, Yao J (2008) J Phys Chem C 112:8192
11. Si Y, Samulski ET (2008) Nano Lett 8:1679
12. Shin H-J, Kim KK, Benayad A, Yoon S-M, Park HK, Jung I-S, Jin MH, Jeong H-K, Kim JM, Choi J-Y, Lee YH (2009) Adv Funct Mater 19:1987
13. Vallés C, Jiménez P, Muñoz E, Benito AM, Maser WK (2011) Nanotechnological basis for advanced sensors. Springer, Dordrecht, p 143
14. Machado BF, Serp P (2012) Catal Sci Technol 2:54
15. Nemade KR, Waghuley SA (2013) Solid State Sci 22:27
16. Li F, Song J, Yang H, Gan S, Zhang Q, Han D, Ivaska A, Li N (2009) Nanotechnology 20:455602
17. Biris R, Pruneanu S, Pogacean F, Lazar MD, Borodi G, Ardelean S, Dervishi E, Watanabe F, Biris AS (2013) Int J Nanomedicine 8:1429
18. Kumar SV, Huang NM, Lim HN, Zainy M, Harrison I, Chia CH (2013) Sensors Actuators B Chem 181:885
19. Wu Y, Liu S, Wang H, Wang X, Zhang X, Jin G (2013) Electrochim Acta 90:210
20. Wang J, Wang P, Cao Y, Chen J, Li W, Shao Y, Zheng Y, Li D (2013) Appl Catal B Environ 136–137:94
21. Zhang Y, Pan C (2011) J Mater Sci 46:2622

22. Guo J, Zhu S, Chen Z, Li Y, Yu Z, Liu Q, Li J, Feng C, Zhang D (2011) Ultrason Sonochem 18:1082
23. Chen X, He Y, Zhang Q, Li L, Hu D, Yin T (2010) J Mater Sci 45:953
24. Xu T, Zhang L, Cheng H, Zhu Y (2011) Appl Catal B Environ 101:382
25. Ji Z, Shen X, Song Y, Zhu G (2011) Mater Sci Eng B 176:711
26. Wang X, Chen S (2011) Graphene-based nanocomposites, physics and applications of graphene – experiments. In: Dr. Sergey Mikhailov (ed), ISBN: 978-953-307-217-3, InTech
27. Vallet-Regí M, Balas F, Arcos D (2007) Angew Chem Int Ed 46:7548
28. Dalagan JQ, Enriquez EP, Li LJ (2013) J Mater Sci 48:3415
29. Zhanhu G (2013) Patent application publication. US20130344237 A1, Lamar University, Beaumont TX, US, 26 Dec 2013
30. Zhou X, Shi T (2012) Appl Surf Sci 259:566
31. Guardia L, Suárez-García F, Paredes JI, Solís-Fernández P, Rozada R, Fernández-Merino MJ, Martínez-Alonso A, Tascón JMD (2012) Microporous Mesoporous Mater 160:18
32. Yang S, Feng X, Wang L, Tang K, Maier J, Müllen K (2010) Angew Chem Int Ed 49:4795
33. Hummers WS, Offeman RE (1958) J Am Chem Soc 80:1339

Chapter 27
Electrical Properties of Lithium Ferrite Nanoparticles Dispersed in a Styrene-Isoprene-Styrene Copolymer Matrix

S. Soreto Teixeira, M.P.F. Graça, M. Dionisio, M. Ilcíkova, J. Mosnacek, Z. Spitalsky, I. Krupa, and L.C. Costa

Abstract The main goal of this work was the preparation and study of a composite material by dispersing lithium ferrite particles in a polymeric matrix. The matrix selected was styrene-b-isoprene-b-styrene (SIS) copolymer. Lithium ferrite ($LiFe_5O_8$) is an attractive material for several potential technological applications, due to its physical properties $LiFe_5O_8$ crystallites were obtained by controlled heat-treatments of homogeneous Li_2O-Fe_2O_3 powders prepared by wet ball-milling method and using lithium and iron nitrates as raw materials. To achieve an effective dispersion of particles, we modified its surface. The structure of the composites, containing modified and unmodified ferrite particles, was studied by XRD and Raman spectroscopy. The dielectric properties were analyzed in the frequency range between 10^{-1} and 10^6 Hz, and as a function of the temperature between −73 and 127 °C. The frequency dependence of the ac conductivity is characterized by a low frequency region of constant conductivity followed by a frequency dependent conductivity. This behavior was interpreted using the Jonscher power law.

Keywords Nanocomposites • Lithium ferrites • Electrical properties

S.S. Teixeira (✉) • M.P.F. Graça • L.C. Costa
I3N and Physics Department, University of Aveiro, 3810-193 Aveiro, Portugal
e-mail: silvia.soreto@ua.pt

M. Dionisio
REQUIMTE, Departamento de Química, Faculdade de Ciências e Tecnologia, Universidade Nova de Lisboa, 2829-516 Caparica, Portugal

M. Ilcíkova • I. Krupa
Center for Advanced Materials, Qatar University, P.O. Box 2713, Doha, Qatar

Polymer Institute, Slovak Academy of Sciences, Dúbravská cesta 9, Bratislava, Slovakia

J. Mosnacek • Z. Spitalsky
Polymer Institute, Slovak Academy of Sciences, Dúbravská cesta 9, Bratislava, Slovakia

P. Petkov et al. (eds.), *Nanoscience Advances in CBRN Agents Detection, Information and Energy Security*, NATO Science for Peace and Security Series A: Chemistry and Biology, DOI 10.1007/978-94-017-9697-2_27

27.1 Introduction

Lithium ferrite is a hexaferrite due its hexagonal crystal structure and becomes a commercially and technologically important material due to its properties. Hexagonal ferrites had been discovered in the 1950s [1] and still attract a great interest nowadays. These ferrites are all ferrimagnetic materials with several applications such as magnetic recording, data storage, microwave electronic components, electromagnetic absorbers, magnetoelectric/multiferroic applications and hexaferrite fibres [2].

The main goal of this work was the study of the molecular dynamic of a composite containing lithium ferrite particles embedded in a thermoplastic elastomer matrix. The polymer matrix selected due to its good mechanical and electrical properties was a triblock copolymer with polystyrene end blocks and poly(styrene-isoprene) mid-block, SIS (or kraton as commercial name).

Before inserting lithium ferrite powders into the polymeric matrix, the surface of the particles was modified, first with silane and then with cholesteryl chloroformate, to ensure that the particles were well dispersed along the polymer chains.

Impedance spectroscopy is a powerful method that allows the study of the dynamics of polymers in a wide frequency range. Polymeric materials are very complex systems, when compared with low molecular weight compounds. Temperature has an important influence on the flexibility, and consequently this is reflected in the dielectric measurements. That technique allow us to understand the polarization mechanisms present in polymers, that is, the charge migration and that due to the orientation of permanent dipoles [3].

Conductivity and dielectric measurements at low frequency can give additional information on the charge transport mechanism which dc conductivity measurements alone doesn't provide [4]. The conductivity dispersion phenomenon can be analyzed using Jonscher's law [5]: $\sigma(\omega) = \sigma_{dc} + A\omega^n$, where σ_{dc} is the direct current conductivity, A is a constant, n is the power-law exponent in the range of $0 < n < 1$ and ω is the angular frequency. The exponent n is related to the frequency dependence of the dielectric losses.

27.2 Experimental

Lithium ferrite ($LiFe_5O_8$) powders were prepared by a solid state method. The raw materials used were iron (III) nitrate ($Fe(NO_3)_3{\cdot}9H_2O$) and lithium nitrate ($LiNO_3$). After weighting the $Fe(NO_3)_3{\cdot}9H_2O$ and $LiNO_3$ powders, and taking into account the stoichiometry of the lithium ferrite that presents a molar ratio between the lithium and iron ions of 1:5, the powders were homogenized in a planetary ball mill system (Fritsch – Pulverisette 7.0) at 250 rpm for 1 h. After this first mixture, 10 mL of ethanol were added and this wet mixture was milled for 3 h at 500 rpm. After this process, the vessel with the mixed powders was placed in a furnace at 80 °C for 24 h to promote the evaporation of the ethanol. After this milling process several

heat-treatments were done to obtain particles with high degree of purity; the highest temperature was 1,100 °C.

The composite formation is described in reference [6], and consists of several steps: modification of the lithium ferrite particles surface (first with 3-aminopropyl triethoxysilan and then with cholesteryl chloroformate) and final preparation to obtain the nanocomposites.

To prepare the composites, two different concentrations in weight were used, 1 and 8 % of modified and unmodified lithium ferrite particles. First, SIS was dissolved in toluene and the particles were added. The solution was mixed by using a high speed shear blade mixing device at 1,200 rpm for 2 h. Thereafter, the composite solution was cast into teflon chambers, where the solvent was evaporated at room temperature and atmospheric pressure. To completely remove the residual solvent, the composite was placed into an oven, and the temperature was increased to 80 °C in 10 °C steps per day. Then the pressure was decreased to 2 mbar by 100 mbar steps per day. Finally the temperature was increased to 100 °C for 30 min and the pressure kept at 2 mbar.

X-ray diffraction (XRD) patterns were obtained with an Siemens D5000 diffractometer (CuKα radiation, $\lambda = 1.54056$ Å) at 40 kV and 30 mA, with a curved graphite monochromator, an automatic divergence slit (irradiated length 20.00 mm), a progressive receiving slit (height 0.05 mm) and a flat plane sample holder in a Bragg-Brentano parafocusing optics configuration. Intensity data were collected by the step counting method (step 0.02° in 1 s) in the 2θ angle range of 10–60°.

Raman spectroscopy measurements were performed at room temperature in backscattering geometry, with a 532 nm laser line using a HR-800-UV Jobin Yvon Horiba spectrometer.

For the electrical measurements, the samples were inserted into two stainless steel electrodes (diameter 10 mm) of a parallel plate capacitor. The measurements were carried out using an Alpha-N broadband impedance analyzer (Novocontrol GmbH), in the frequency range from 10^{-1} up to 10^{6} Hz, with increasing temperature (10 °C steps) from −73 up to 127 °C. The sample cell (BDS 1200) was mounted in a cryostat (BDS 1100) and exposed to a heated gas stream evaporated from a liquid nitrogen dewar. The temperature control was performed within ±0.5 °C with the Quattro Cryosystem from Novocontrol.

27.3 Results and Discussion

$LiFe_5O_8$ particles were covalently modified with cholesteryl chloroformate to improve their interaction with the SIS polymer matrix. As was already proven, due to the chemical and sterical composition, the cholesteryl modification improves interactions with aliphatic polymer chains when used for the modification of fillers in polymer composites [7]. In this case this modification improves the interactions with the polyisoprene chains of the SIS copolymer [8].

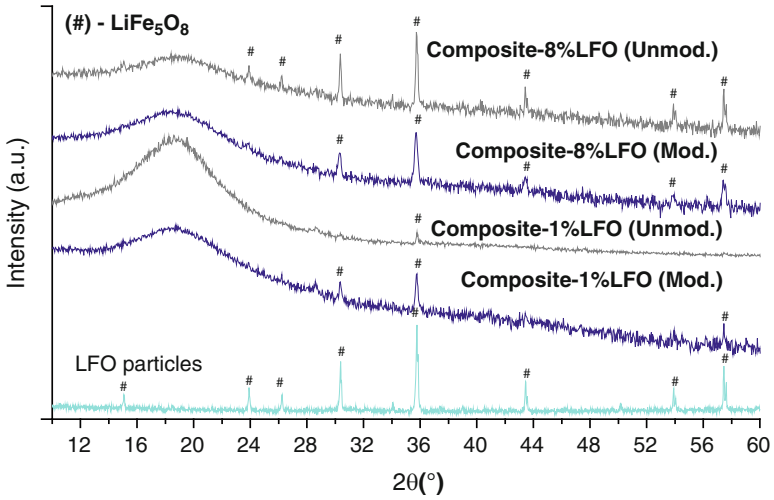

Fig. 27.1 XRD patterns of composite samples with 1 and 8 (% weight) unmodified and modified lithium ferrite particles

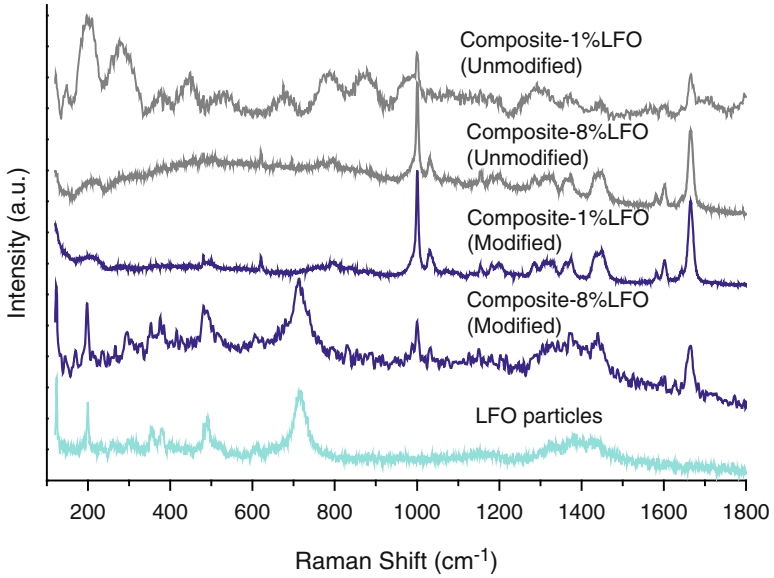

Fig. 27.2 Raman spectra of composite samples with 1 and 8 (% weight) unmodified and modified lithium ferrite particles

Figures 27.1 and 27.2 show the XRD patterns and Raman spectra of the lithium ferrite base powder and the composite samples.

The main diffraction XRD peaks of the lithium ferrite are visible in all of them, being more intensive in the unmodified type composites. These intensifications can

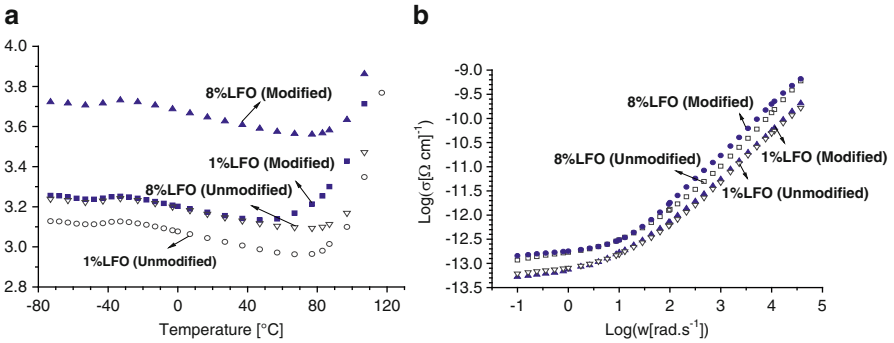

Fig. 27.3 (**a**) Real part of the permittivity versus temperature (1 kHz); (**b**) Conductivity versus angular frequency in logarithmic scales (T = 127 °C)

be related to the interactions between the LFO particles and the copolymer chains. The link between LFO particles and polymeric chains is less effective for composites having particles with unmodified surfaces resulting in lower intensity diffraction peaks than for composites containing modified surface particles. Obviously the amount of lithium ferrite particles, for both compositions, also contributes to an increase in the diffraction peaks intensities.

Raman spectroscopy is known as a potential technique to probe the structure of polymers [9], mainly those with carbon-carbon double bounds, which is here the case. The vibrational bands characteristics of $LiFe_5O_8$ particles (Fig. 27.2) are 198, 354, 380, 489, 608, 713, 1,154 and 1,373 cm^{-1}. These bands are still present in all the composites, but the composition with 8 % wt. of modified particles showed the most intensive bands. This means that, besides the amount of particles, also the surface modification of the ceramic powders in the polymeric matrix contributes to keep the LFO particles features. The bands at 1,000, 1,031, 1,154, 1,285, 1,438, 1,602 and 1,665 cm^{-1} are assigned to the copolymer polystyrene and polyisoprene phases. These bands have a lower intensity for the 8 % (modified) composite as to be expected. The bands centred at 1,584 and 1,603 cm^{-1} are assigned to the tangential stretch mode of carbon-carbon bonds in the benzene ring [9]. The characteristic vinyl group (C=C) leads to as a strong peak at 1,670 cm^{-1} which is also present in all composite samples, loosing intensity in the composite with 8 % wt. of modified particles. This evidence supports the conformational changes in the copolymer with the interactions between the LFO particles and the copolymer chains. The other band, centered at 1,000 cm^{-1}, is the most intensive in the composites and due to the C–C stretching [10], the nearby band centered at 1,031 cm^{-1} must be attributed to CH_3 groups.

Figure 27.3a shows the temperature dependence of the dielectric constant for composites containing different concentrations of modified and unmodified particles.

For both concentrations, 1 and 8 %, higher values of the dielectric constant, ε', are observed for the composites containing modified particles, achieving a maximum value of 3.65 at 1 kHz. For the composites with unmodified particles,

Table 27.1 Jonscher law parameters for all composites (T = 127 °C)

Composite	n	Δn	$-\log(\sigma_{dc}$ [Ωcm])	(σ_{dc} [Ωcm])
1 % wt LFO (unmodified)	0.91	0.02	−13.2	6.3×10^{-14}
8 % wt LFO (unmodified)	1.00	0.01	−12.8	1.6×10^{-13}
1 % wt LFO (modified)	0.91	0.01	−13.3	5.0×10^{-14}
8 % wt LFO (modified)	1.01	0.02	−12.9	1.3×10^{-13}

ε' increases with the rise of the concentration of $LiFe_5O_8$ particles. The difference between these two values is related to the influence of the polymeric network. The slight increase above ~−40 °C and the abrupt rise above ~50 °C, observed for all systems, are associated with the glass transition of the polymer constituents of the composites.

Analyzing the conductivity behavior by Jonscher law, at high temperatures (Fig. 27.3b for T = 127 °C), all samples have a power-law exponent close to 1. This means that we have an almost frequency-independent loss system. Also the composites with 8 % wt. of particles exhibit higher σ_{ac}.

Table 27.1 summarizes the calculated parameters of Jonscher's law, showing that at T = 127 °C the increment of LFO particles increases the dc conductivity. The same behavior is observed at all temperatures.

27.4 Conclusions

The surface modification and the amount of LFO particles contribute to an improvement of the dielectric constant and do not affect the good performance of the ceramic powders, as the modification contributes to maintain the LFO particles features. Jonscher law describes accurately the conductivity behavior, and the calculated parameters show that at high temperatures the composites presents almost frequency-independent behaviour. The increase of the particle concentration increases the electrical conductivity, but yield low enough values that allow their use in energy storage systems.

References

1. Went JJ, Rathenau GW, Gorter EW, Van Oosterhout GW (1952) Phys Rev 86:424
2. Pullar RC, Bdikin IK, Bhattacharya AK (2012) J Eur Ceram Soc 32:905
3. Macdonald JR (1992) Ann Biomed Eng 20:289
4. Williams G, McCrum N, Read B (1967) Anelastic and dielectric effects in polymeric solids. Wiley, New York
5. Jonscher AK (1978) J Mater Sci 13:553

6. Mrlík M, Ilčíková M, Pavlínek V, Mosnacek J, Peer P, Filip P (2013) J Colloid Interface Sci 396:146
7. Valentová H, Ilčíková M, Czaniková K, Spitalsky Z, Slouf M, Nebdal J, Osmatova M (2014) J Macromol Sci B 53:496
8. Ilčíková M, Mosnáček J, Mrlík M, Sedlacek T, Csomorova K, Czanikova K, Krupa I (2014) Polym Adv Technol 25:1293
9. Barraza HJ, Pompeo F, Rear EAO, Resasco DE (2002) Nano Lett 2:797
10. Arjunan V, Subramanian S, Mohan S (2001) Spectrochim Acta A 57:2547

Chapter 28
Magneto-Sensitive Biocompatible Adsorbents Based on Ferrites

L.P. Storozhuk, S.V. Khutornyi, and N.N. Iukhymenko

Abstract A magneto-sensitive adsorption complex as magnetic component/SiO_2/DNA was prepared and tested. We have developed and optimized a procedure for the synthesis of magnetically operating nanocomposites based on transition metal oxides (MFe_2O_4, $M = Fe^{2+}$, Ni^{2+}, and Co^{2+}) with a biocompatible coating. The relationship between structure, composition, and magnetic properties of the nanocomposites has been examined. We have studied adsorption interactions of DNA with the surface layer of the magnetically operating nanocomposites. The amount of DNA adsorption is 0.55–0.6 mg for 100 mg of the adsorbents. Our results demonstrate complete DNA desorption from the surface of the nanocomposites.

Keywords Magnetic adsorbents • Surface modification • Ferrites • Nanocomposite • Biological objects • DNA

28.1 Introduction

Biocompatible nanohybrid composites containing magnetic nanoparticles and nucleic acid molecules are of great interest for modern biomedicine. They are of great importance in the development of highly sensitive detection and quantitation systems identify DNA fragments and RNA molecules [1, 2]. This is connected with the unique magnetic properties of these nanoparticles providing ease of management and thigh detection efficiency of composites based on them. Nano-sized composites allow the identification of single molecules, which significantly increases the analysis sensitivity. The aim is to use nanoparticles based on ferrites to construct biomedical composites with a combination of excellent magnetic properties with higher resistance to oxidation and better biological inertness as to compared with metal nanoparticles. The relevance of studying the interaction of ferromagnetic nanoparticles and DNA molecules is dictated by the mechanisms

L.P. Storozhuk (✉) • S.V. Khutornyi • N.N. Iukhymenko
Chuiko Institute of Surface Chemistry, National Academy of Sciences of Ukraine,
17 General Naumov Str., Kyiv 03164, Ukraine
e-mail: storozhukl@mail.ru

P. Petkov et al. (eds.), *Nanoscience Advances in CBRN Agents Detection, Information and Energy Security*, NATO Science for Peace and Security Series A: Chemistry and Biology, DOI 10.1007/978-94-017-9697-2_28

underlying the effects of nanomaterials on biological systems, which are directly connected with the safety and quality of life of mankind as a whole.

Conclusions about the nature of emerging bonds are controversial. Obviously, the interaction between nucleic acids and magnetic nanoparticles can be implemented through several mechanisms involving different groups of the biomolecules. Adsorption of biomolecules groups on the surface of the particles can occur by formation of external (involving electrostatic interactions) or internal systems through direct coordination with individual metal atoms according to the Stern model [3–6].

This paper describes one approach to produce surface layers of a magneto-sensitive component/SiO_2 nanocomposite by sol-gel processing using a template for synthesis. Our main purpose was to create a porous biocompatible silica shell on Fe_3O_4, $NiFe_2O_4$, and $CoFe_2O_4$ particles [7] and, eventually, to obtain a mobile, magnetically controlled adsorbent in the form of magnetic component/SiO_2/DNA.

28.2 Experimental

Magnetic particles expected to have a low phase transition temperature (Curie–Neel point) were prepared through coprecipitation of metal salts in an alkaline medium in the form of metal oxides under hydrothermal synthesis conditions, followed by drying in a purpose-designed drying chamber [8–10]. As a result, we obtained ferrites with the following compositions: Fe_3O_4, $NiFe_2O_4$, and $CoFe_2O_4$.

To produced a porous structure in the surface layer of a composite, we used surfactants, which were removed by washing and heat treatment. The surface layer was obtained using tetraethyl orthosilicate (TEOS) as a precursor and sodium silicate. As a template, we used a nonionic block copolymer surfactant (poly (ethylene glycol)-b-poly(propylene glycol)-b-poly(ethylene glycol), $M_r = 8{,}400$ u) (P-123) and the ionogenic surfactants sodium dodecyl sulfate (SDS) and tetraethylbenzylammonium chloride (TEBA), which were added during TEOS hydrolysis under alkaline catalysis conditions with constant stirring [11, 12].

As a result of adsorption of DNA on the surface of the nanocomposites a magneto-sensitive complex (Fe_3O_4/SiO_2/DNA) was obtained.

DNA adsorption was carried out in distilled water. DNA of a fish (salmon) was used as a DNA sample. The amount of adsorbate on the surface of the nanocomposites was determined by measuring the DNA concentration in contact solutions before and after adsorption with spectrophotometer Lambda-35 (Perkin-Elmer USA). The concentrations were measured at $\lambda = 260$ nm using a calibration plot. Adsorption of DNA was carried out in TRIS buffer (pH = 8.5) with a high chaotropic salt concentration. Desorption of DNA was carried out in TE buffer or distilled water.

The properties of the original magnetite, nickel and cobalt ferrites, and the nanocomposites based thereon were investigated by combination of physical and chemical methods.

The specific surface area of the nanocomposites was determined by nitrogen adsorption measurements (BET method) with a Kelvin-1042 sorptometer (Costech International Instruments). The microstructures were examined by transmission electron microscopy with on a JEOL JSM-35 (Japan).

Using X-ray diffraction (XRD), we investigated the structure of the nanocomposites, identified magnetite, nickel ferrite, and cobalt ferrite, and determined the average crystallite size of these phases. XRD patterns were collected on a DRON-4-07 diffractometer (Fe-filtered CoK_α radiation, $\lambda = 0.179021$ nm, Bragg–Brentano reflection geometry). The SiO_2 layer in the nanocomposites was identified by Fourier transform IR spectroscopy in the range 600–4,000 cm^{-1} on a Thermo Nicolet Nexus spectrometer (USA).

The magnetic properties of magnetite and nanocomposite powders were studied using a vibrating sample magnetometer. The vibration frequency and the amplitude of the sample were set by an oscillator and a low-frequency amplifier. The measurements were made at 228 Hz and room temperature. The samples had the form of dry demagnetized powders [9].

28.3 Results and Discussion

Examination of the morphology of the powders by transmission electron microscopy (TEM) showed that the crystals in the nanocomposites were 20–60 nm in size. A significant percentage of the nanoparticles formed aggregates up to ~100 nm in size (Fig. 28.1).

XRD patterns of the Fe_3O_4/SiO_2 nanocomposite contain peaks at $2\theta = 21.2°$, 35.2°, 41.8°, 50.9°, 67.8°, and 74.8°, with interplanar spacings of 2.865, 2.546, 2.158, 1.792, 1.381, and 1.267 Å, corresponding to crystalline magnetite (JCPDS PDF 19-629 and 24-081). The peaks at $2\theta = 21.4°$, 35.3°, 41.7°, 43.5°, 50.7°, 63.5°,

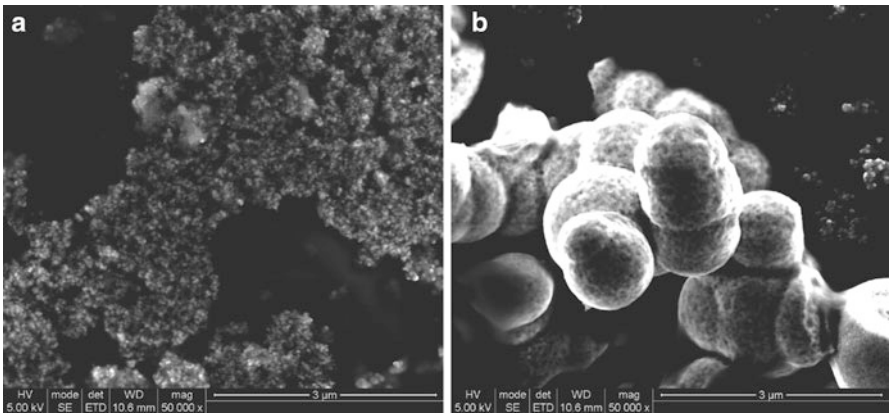

Fig. 28.1 Photomicrographs Fe_3O_4/SiO_2 nanocomposites synthesized without template (**a**), with SDS (**b**). The content of SiO_2 per 1 g Fe_3O_4: 0.15 g (**a**); 1.5 g (**b**)

Table 28.1 Magnetic characteristics of the samples

№	Samples	M [mg]	σ_s [μTl · m^3/kg]	H_c [kA/m]	M_r/M_s
1	Fe_3O_4/SiO_2 (P-123)	135	3.63 ± 0.01	6.56 ± 0.01	0.21 ± 0.01
2	Fe_3O_4/SiO_2 (SDS)	56	2.09	7.68	0.07
3	Fe_3O_4/SiO_2 (TEBA)	66	3.14	7.54	0.07
4	$NiFe_2O_4/SiO_2$ (P-123)	71	1.86	9.68	0.10
5	$NiFe_2O_4/SiO_2$ (SDS)	68	0.56	42.70	0.38
6	$NiFe_2O_4/SiO_2$ (TEBA)	46	0.82	31.31	0.34
7	$CoFe_2O_4/SiO_2$ (P-123)	68	1.76	19.21	0.21
8	$CoFe_2O_4/SiO_2$ (SDS)	64	0.90	27.04	0.29
9	$CoFe_2O_4/SiO_2$ (TEBA)	67	0.95	27.75	0.25
10	Fe_3O_4	96	5.42	4.30	0.19

Note: $\sigma_s = M_s/\rho$ is the specific saturation magnetization (where M_s is the saturation magnetization and ρ is mechanical density), H_c the coercive force, M_r/M_s the specific remanence, and m the sample mass

67.7°, and 74.7°, with interplanar spacings of 4.147, 2.539, 2.163, 2.077, 1.798, 1.463, 1.382, and 1.269 Å, in XRD patterns of the $NiFe_2O_4/SiO_2$ nanocomposite correspond to crystalline $NiFe_2O_4$ (JCPDS PDF 10-325). The peaks at $2\theta = 21.8°$, 35.6°, 42.0°, 51.1°, 63.9°, 68.2°, and 75.3°, with interplanar spacings of 4.072, 2.518, 2.148, 1.785, 1.455, 1.373, and 1.260 Å, in XRD patterns of the $CoFe_2O_4/SiO_2$ nanocomposite correspond to crystalline $CoFe_2O_4$ (JCPDS PDF 22-1086).

All nanocomposites possessed magnetic properties (Table 28.1). They had narrow hysteresis loops, typical of nanocrystalline materials.

For the obtained nanocomposites values of the mass concentration of magnetite were calculated based on the specific saturation magnetization of the samples and the starting material (sample number 10) Also, the volume concentration of magnetite in the samples and the thickness of the SiO_2 layer on the magnetite particles were calculated. The values of the latter were 6–11 nm for Fe_3O_4/SiO_2 composites (samples. 1–3), 14–28 nm for nickel ferrite (samples 4–6) and 14–21 nm cobalt ferrite (samples 7–9).

Let's consider the adsorption of DNA on the surface of Fe_3O_4/SiO_2 nanocomposites, which were obtained by using various magnetic cores with different pore sizes in the surface layer of the SiO_2, which is caused by the introduction of various surfactants in the synthesis process.

Figure 28.2 shows typical DNA adsorption curves for the magnetic core/SiO_2 nanocomposites (iron and nickel ferrites) prepared using SDS as a template. The adsorption isotherms for these composites (Fig. 28.2a, b) can be described by a BET equation typical for monomolecular adsorption on adsorbents with energetically active adsorption centers. For the highest DNA concentration of 0.05 mg/ml tested, the amount of adsorption was 2.91 and 1.74 mg/g (Fig. 28.2a, b). The nanocomposites synthesized with other templates showed weaker DNA adsorption.

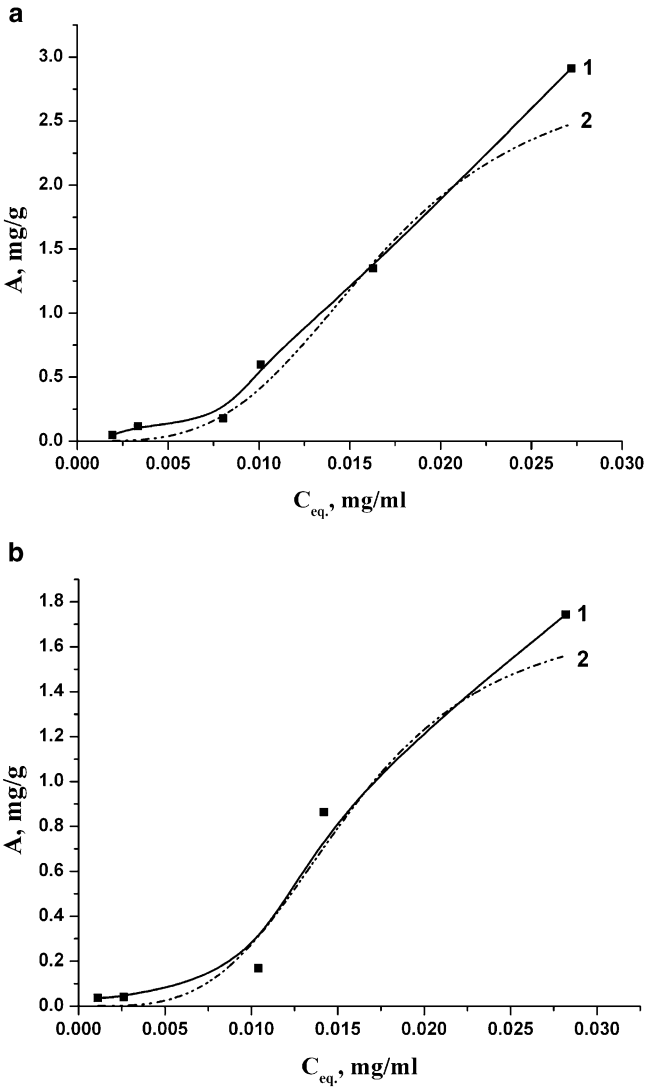

Fig. 28.2 Adsorption isotherms of DNA on the nanocomposites prepared with SDS: (*1*) experimental, (*2*) theoretical (Langmuir): (**a**) Fe_3O_4/SiO_2, (**b**) $NiFe_2O_4/SiO_2$

The data in Fig. 28.3 point to a complete DNA desorption to a TE-buffer (pH = 7.6) from the surface of the Fe_3O_4/SiO_2 and $NiFe_2O_4/SiO_2$ nanocomposites prepared with SDS.

It has been established that there is a complete desorption of DNA from the surface of Fe_3O_4/SiO_2 and $NiFe_2O_4/SiO_2$ nanocomposites obtained with SDS.

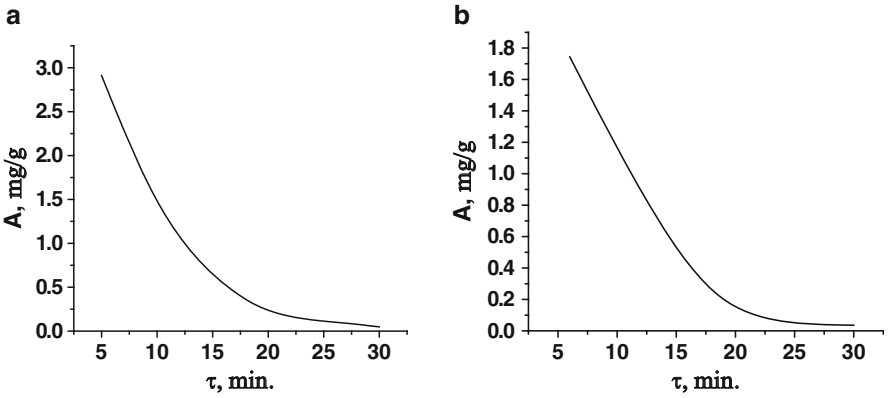

Fig. 28.3 Kinetics of DNA desorption from the surface of the nanocomposites prepared with SDS: (**a**) Fe_3O_4/SiO_2 (**b**) $NiFe_2O_4/SiO_2$

28.4 Conclusions

A synthesis procedure of magnetically operated nanocomposites based on transition metal oxides ($MeFe_2O_4$, $Me = Fe^{2+}$, Ni^{2+}, Co^{2+}) with a biocompatible coating $(SiO_2)_x$ has been designed and optimized.

It has been shown that for all samples are characterized by narrow hysteresis loops typical for nanocrystalline magnetic materials.

The adsorption of DNA on the surface layers of magnetically operating nanocomposites were investigated. It has been established that the adsorption of DNA is 0.55–0.6 mg per 100 mg of the adsorbent. There is further a complete desorption of DNA from the surface of nanocomposites Fe_3O_4/SiO_2 and $NiFe_2O_4/SiO_2$.

References

1. Gruttner C, Teller J, Sehutt W, Westphal F (2001) Preparation and characterization of magnetic nanospheres for In vivo application. In: Scientific and chemical applications of magnetic carriers. Plenum, New York, p 53
2. Wang G, Song E, Xie H et al (2005) Chem Commun 34:4276
3. Westall JC, Hohl H (1980) Adv Colloid Interface Sci 12:265
4. Davis JA, Kent DB (1990) Rev Mineral 23:177
5. Lьtzenkirchen J (2006) Surface complexation modelling. Elsevier, Amsterdam
6. Pershina AG, Serebrov YY, Sazonov AE (2010) Cell Mater 20:201
7. Brinker CJ, Scherer GW (1990) Sol–gel science: the physics and chemistry of sol–gel processing. Academic, New York, p 908
8. Upadhyay T, Upadhyay RV, Mehta RV et al (1997) Phys Rev B Condens Matter Mater Phys 55:5585
9. Zhao S, Lee D, Kang Y (2003) Mol Cryst Liq Cryst 407:33
10. Storozhuk LP, Khutornoi SV, Mudrak IM (2013) Inorg Mater 49:395
11. Li G, Li L, Smith RL, Inomata H (2001) J Mol Struct 560:87
12. Da Silva JB, Mohallem NDS (2001) J Magn Magn Mater 226:1393

Part VIII
Thin Films

Chapter 29
Structural, Optical and Electrical Properties of ZnO Thin Films Doped with Al, V and Nb, Deposited by r.f. Magnetron Sputtering

K. Lovchinov, M. Petrov, O. Angelov, H. Nichev, V. Mikli, and D. Dimova-Malinovska

Abstract Structural, optical and electrical properties of ZnO thin films doped with different elements (Al, Al + H, V, Nb), deposited by r.f. magnetron sputtering on glass substrates at different temperature T_s between 50 and 500 °C are studied. XRD spectra demonstrate a preferential (002) crystallographic orientation with the c-axis perpendicular to the substrate surface and grains sizes of about 19–29 nm. The value of band gap energy E_g is in the range of 3.49–3.58 eV for ZnO:Al, 3.51–3.58 eV for ZnO:Al:H, 3.44–3.47 eV for ZnO:V, and 3.28–3.44 eV for ZnO:Nb. The deposited ZnO films doped with Al, H, V and Nb have low resistivities of $1.6–2.2 \cdot 10^{-3}$ Ωcm. The transparency of the studied films is about 85–90 % in the visible region. The obtained transparent conductive ZnO thin films can be applied in solar cells and other optoelectronic devices as TCO.

Keywords ZnO • Magnetron sputtering • Transparent conducting oxide

29.1 Introduction

Transparent conductive oxides (TCO) with their variety of structural compositions are object of different scientific studies. The systematic investigation of the optical, structural, electrical and other properties of thin ZnO films in dependence on the deposition technology is nowadays topical in the development of new electronic thin film devices [1], magnetic memories [2], and transparent conductive oxides with applications in thin film solar cells [3]. ZnO doped with transition elements

K. Lovchinov (✉) • M. Petrov • O. Angelov • H. Nichev • D. Dimova-Malinovska
Central Laboratory of Solar Energy and New Energy Sources, Bulgarian Academy of Sciences, 72 Tzarigradsko Chaussee, 1784 Sofia, Bulgaria
e-mail: lov4@abv.bg

V. Mikli
Centre for Materials Research, Tallinn University of Technology, Ehitajate tee 5, 19086 Tallinn, Estonia

P. Petkov et al. (eds.), *Nanoscience Advances in CBRN Agents Detection, Information and Energy Security*, NATO Science for Peace and Security Series A: Chemistry and Biology, DOI 10.1007/978-94-017-9697-2_29

allows a variety of applications in gas sensors [4], spintronics [5], diluted magnetic semiconductors (DMS) [6] etc. The most frequently used ZnO growth techniques are metalorganic chemical vapour deposition MOCVD, pulsed laser deposition (PLD), magnetron sputtering and molecular beam epitaxy (MBE). R.f. magnetron sputtering is an attractive technique for the deposition of undoped and doped ZnO thin films with different concentration of doping metals [7, 8].

In this work, a study the influence of doping elements and of the substrate temperature, T_s, on the optical, structural and electrical properties of Al-, Al:H-, Nb- and V-doped ZnO thin films deposited by r.f. magnetron sputtering in Ar (or Ar + H_2 in the case of deposition of ZnO:Al:H) atmospheres is reported. The results are compared with data for undoped ZnO films.

29.2 Experimental

The ZnO:Al:H and ZnO:Al films are deposited by r.f. sputtering of a sintered ZnO + Al (ZnO 98 wt% + Al_2O_3 2 wt%) target (100 mm in diameter) in Ar (0.7 Pa) + H_2 (0.03 Pa) and Ar (0.7 Pa) atmospheres. Thin ZnO films doped with Nb and V were prepared by r.f. magnetron co-sputtering of a ZnO target (100 mm) with pieces of vanadium and niobium plates in the zone of maximal erosion of the surface in Ar atmosphere at a pressure of 0.5 Pa. Before the deposition the substrates are ultrasonically cleaned in $H_2O_2 + H_2SO_4$ (1:1) solution and de-ionized water. The deposition of ZnO films doped with Al, Al:H, Nb V were performed without heating (WH) of substrates or with heating between 50 and 500 °C. The r.f. sputtering power, P_s, was 150–180 W.

The thickness of the layers was 150–200 nm for ZnO:Al, ZnO:Al:H and 600–960 nm for ZnO:Nb and ZnO:V.

The film structure was studied by XRD and Raman spectrometry. XRD spectra were obtained using a Bruker D8 Advance spectrometer with Cu K_α radiation: $\lambda(\text{Cu } K_{\alpha1}) = 1.540560$ Å and $\lambda(\text{Cu } K_{\alpha2}) = 1.544426$ Å (half of the intensity of Cu $K_{\alpha1}$). The instrumental broadening in 2θ geometry was 0.04°. Raman spectra were recorded with a Horiba Jobin Yvon LabRam HR800 spectrometer using a 600 l/mm grating and a HeNe laser for excitation. The spectra were measured in back scattering geometry with a resolution of 1 cm^{-1}. Transmittance and reflectance spectra were measured by a spectrophotometer Shimadzu 3,100 in the ranges of 300–1,800 or 300–2,600 nm. The V and Al content in the films was determined by energy dispersive X-ray analysis (EDAX) using a Link AN10000 analysis system. SEM pictures were obtained by a Jeol JSM-840A with a $LaBa_6$ cathode. The resistivity of the films was measured by the four point probe method using a VEECO instrument.

29.3 Results and Discussion

29.3.1 ZnO Thin Films Doped with Al and Al:H

The Al concentration in ZnO thin films is between 1 and 2 at.% [8]. The transmittance and the product $(\alpha h\nu)^2$, where α is the absorption coefficient, are displayed in Figs. 29.1 and 29.2, respectively, as a function of the photon wavelength and the energy $h\nu$ for the thin ZnO:Al and ZnO:Al:H films obtained at different T_s. The spectra are corrected for the transmittance of the glass substrate.

The transmittance of ZnO:Al and ZnO:Al:H films deposited at different T_s (Figs. 29.1a and 29.2a, respectively) is higher than 90 % in the wavelength range between 550 and 1,200 nm.

The spectral dependence of the absorption coefficient α (Figs. 29.1b and 29.2b) was calculated from transmittance and reflectance spectra by the Eq. (29.1) [9]:

$$\alpha_\lambda = (1/d) \cdot \ln\left[(1 - R_\lambda)^2 / T_\lambda\right], \tag{29.1}$$

where R_λ is the reflectance, T_λ the transmittance, and d the film thickness, [nm].

The optical band gap of the films can be calculated for direct interband transitions at higher energies $h\nu > E_g$ according to the Tauc formula (29.2) [10]:

$$\alpha(h\nu) = B\left[\left(h\nu - E_g\right)^{1/2} / h\nu\right], \tag{29.2}$$

where B is a constant.

At photon energies $h\nu < E_g$ the spectral dependence of α is determined by the Urbach formula [11]:

$$\alpha(h\nu) = \alpha_0 \exp[(h\nu - E_1)/E_0], \tag{29.3}$$

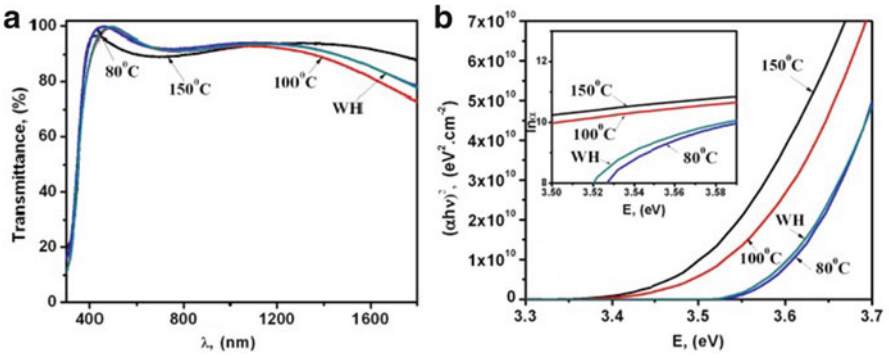

Fig. 29.1 Transmittance (**a**) and the dependence of $(\alpha h\nu)^2$ on the energy (**b**) for ZnO:Al thin films deposited at different T_s. The *inset* in (**b**) shows the dependence of ln α on the energy

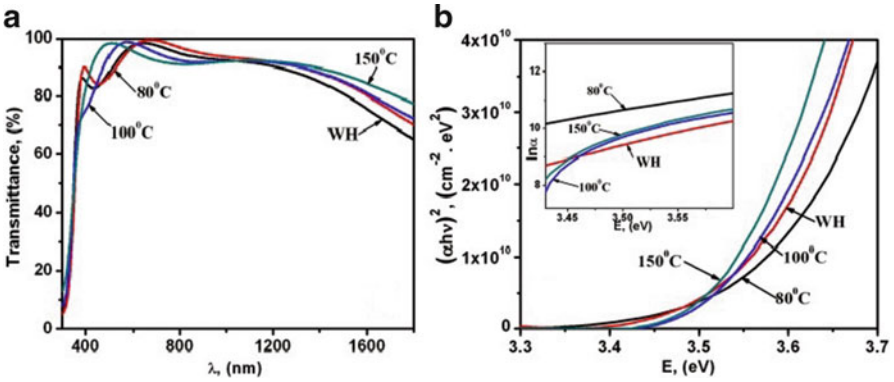

Fig. 29.2 Transmittance (**a**) and the dependence of $(\alpha h\nu)^2$ on the energy (**b**) for ZnO:Al:H thin films deposited at different T_s. The *inset* in (**b**) shows the dependence of ln α on the energy

where α_0 is the absorption coefficient at the edge E_1, E_0 the energy width of the Urbach tail, which is related to the structural disorder within the film. The Urbach energy region ($h\nu < E_g$) is due to the perturbation of the parabolic density of the states at the band edge.

The refractive index of the samples n was calculated from the transmittance spectra by the equation [12]:

$$\begin{aligned} \mathrm{n} &= \left[\mathrm{N} + \left(\mathrm{N}^2 - \mathrm{n_0}^2\right)^{1/2}\right]^{1/2}, \text{where N} \\ &= \left(1 + \mathrm{n_0}^2\right)/2 + 2\mathrm{n_0}[(\mathrm{T_{max}} - \mathrm{T_{min}})/(\mathrm{T_{max}}\mathrm{T_{min}})], \end{aligned} \tag{29.4}$$

where n_0 is the refractive index of the substrate and T_{max} and T_{min} are the maximum and minimum values of the transmittance for every λ_{max} and λ_{min}.

The calculated values of E_g, E_0, ρ, and n, for ZnO:Al and ZnO:Al:H thin films deposited at different T_s (without heating, 80, 100 and 150 °C) are presented in Tables 29.1 and 29.2, respectively.

A comparison between the data for ZnO:Al and ZnO:Al:H deposited at different T_s shows that in the both cases the values of the optical band gap, E_g, pass through a maximum with increasing T_s. The maximum of E_g is observed at $T_s = 80$ °C for ZnO:Al:H and $T_s = 100$ °C for ZnO:Al. A first-principles investigation based on density function theory gives strong evidence that hydrogen acts as a source of conductivity. It can be incorporated in high concentrations and behaves as a shallow donor [13]. It has to be noted that the experimental study of hydrogen in crystalline ZnO demonstrates that after annealing of ZnO crystals at 200 °C in a hydrogen atmosphere the conductivity increases due to in-diffusion of hydrogen with an activation energy of 0.91 eV [14]. The results obtained in the present work confirm the behavior of hydrogen as a donor impurity in ZnO thin films; the ZnO:A:H films have lower resistivity values compared to ZnO:Al films. The Urbach tail energy E_0, decreases with increasing T_s which can be related to the improvement of the

Table 29.1 The calculated values of optical band gap E_g, the Urbach tail energy width E_0, the resistivity, ρ, and the refractive index n, of ZnO:Al deposited with constant sputtering power P_s, in dependence on the substrate temperature T_s

Sample	T_s [°C]	P_s [W]	E_g [eV]	E_0 [meV]	ρ [mΩcm]	n
D407	WH	150	3.56	65	5.5	1.75
D402	80	150	3.57	63	4.4	1.76
D401	100	150	3.58	62	2.8	1.77
D400	150	150	3.49	59	7.8	1.84

Table 29.2 The calculated values of the optical band gap E_g, the Urbach tail energy width E_0, the resistivity ρ, and the index of refraction n, of ZnO:Al:H in dependence on the substrate temperature T_s

Sample	T_s [°C]	P_s [W]	E_g [eV]	E_0 [meV]	ρ [mΩcm]	n
D297	WH	150	3.54	134	2.1	1.94
D294	80	150	3.58	118	1.6	1.96
D311	100	150	3.53	105	2.9	1.85
D312	150	150	3.51	102	3.1	1.82

structural order in the films as reported in [8]. The refraction index of ZnO:Al:H films higher than for ZnO:Al films at all deposition temperatures. This result can be explained with an introduction of weak polarization in the ZnO lattice due to a slight increase in the length of the Zn-O bonds as a result of formation of O-H bonds in the ZnO lattice [13, 15].

29.3.2 ZnO Thin Film Doped with Nb

Transmittance spectra of the ZnO:Nb thin films are presented in Fig. 29.3. The spectra are corrected for the transmittance of the glass substrate. All spectra demonstrate transmittance values of about 90 % in the range from 550 to 1,200 nm. In the IR region beyond 1,200 nm the transmission decreases with decreasing of resistivity of the films due to the absorption of free carriers (plasma resonance).

The dependence of the absorption coefficient on the energy $h\nu$, for ZnO:Nb films is presented in Fig. 29.4. The value of the energy band gap E_g, the Urbach energy E_0, and the coefficient B^2 (Table 29.3) were calculated for direct inter-band electron transitions as described in [8, 17, 18]. The values obtained for the band gap are in the range 3.29–3.44 eV and typical for ZnO. The value of the band gap decreases with increasing of T_s as seen in Fig. 29.5. The blue shift observed for the films with lower resistivities is attributed to the Burstein–Moss effect [19].

The value of the resistivity ρ of ZnO:Nb films are in the range 2.2×10^{-3}–6.4×10^{2} Ωcm (Table 29.3) and are close to the data reported in [8]. ρ increases with increasing T_s, more significantly for $T_s > 350$ °C (Fig. 29.6). This is probably

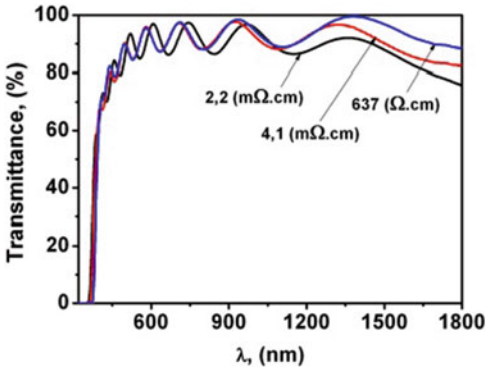

Fig. 29.3 Transmittance spectra of ZnO:Nb films with different resistivities

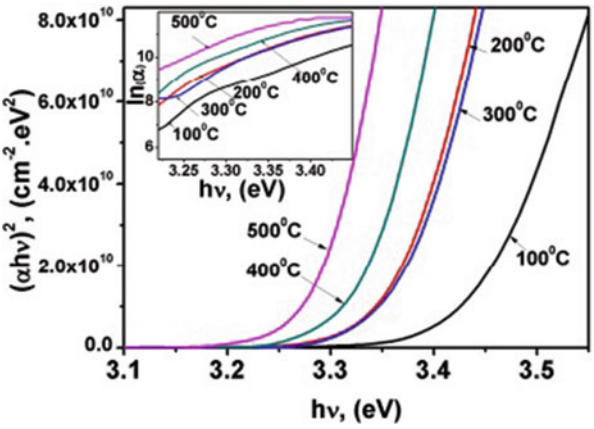

Fig. 29.4 Dependence of $(\alpha h\nu)^2$ on $h\nu$ for ZnO:Nb films deposited at different T_s. The *insert* shows the plot of $\ln\alpha$ on $h\nu$

Table 29.3 The values of the optical band gap E_g, Urbach tail E_0, the coefficient B (the value of B^2 is given), refractive index n, the thickness and the resistivity ρ of the ZnO:Nb deposited at different substrate temperature T_s

sample	T_s (°C)	Thickness (nm)	E_g (eV)	E_0 (meV)	B^2 (cm^2eV)	n	ρ (mΩcm)
D262 ZnO:Nb	50	860	3.42	77	8.4E11	1.99	2.2
D263 ZnO:Nb	100	950	3.44	76	7.79E11	1.97	2.5
D264 ZnO:Nb	150	760	3.43	77	9.84E11	2.00	3.95
D265 ZnO:Nb	200	710	3.37	72	1.15E12	1.96	4.1
D337 ZnO:Nb	250	810	3.37	71	1.14E12	1.95	4.2
D268 ZnO:Nb	300	750	3.38	69	1.22E12	1.99	4.9
D269 ZnO:Nb	350	850	3.38	69	1.25E12	1.99	3.5
D270 ZnO:Nb	400	750	3.34	67	1.32E12	1.95	13.5
D338 ZnO:Nb	450	860	3.32	62	1.44E12	1.94	15
D271 ZnO:Nb	500	770	3.29	59	1.52E12	1.93	6.37×10^5

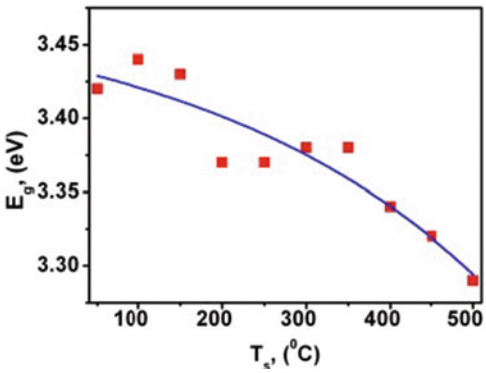

Fig. 29.5 Dependence of the optical band gap of ZnO:Nb films on T_s

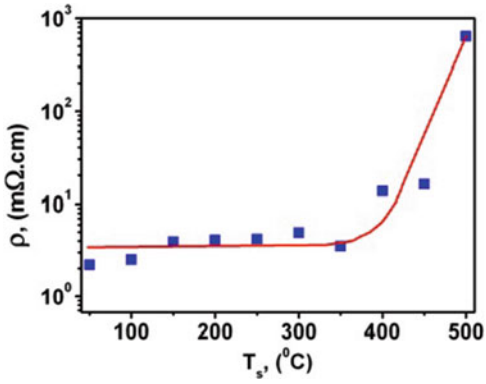

Fig. 29.6 Dependence of the resistivity of the ZnO: Nb films on the substrate temperature

due to the changes of the stoichiometry of the films deposited at higher temperature, as reported in [8].

The values of n were calculated for the range 500–1,200 nm and are given in Table 29.3. They were in the range 1.95–2.00 and decrease slightly with T_s above 400 °C. This can be related to the oxidation of interstitial Zn in the films or to a decreasing concentration of O vacancies at higher T_s, resulting in a decrease of the free carrier concentration. It is probable that the effect of any possible increase in the mobility μ with ρ is less pronounced than the changes in the stoichiometry of the films [16].

The changes of the coefficient B^2 and the Urbach energy with the substrate temperature are shown in Figs. 29.7 and 29.8, respectively. The values of the coefficient B^2 increase with increasing substrate temperature. The Urbach energy has an inverse dependence on T_s. The Urbach energy $(h\nu < E_g)$ is due to a perturbation of the parabolic density of the states at the band edge. An increase of the structural disorder results in an increase in Urbach energy. The coefficient B^2 and the Urbach energy are assumed as parameters for the conduction and valence band tail states, respectively [20, 21]. A decrease of B^2 and an increase in E_0 implies an increase of the width of the band tails. The observed dependences for ZnO:Nb

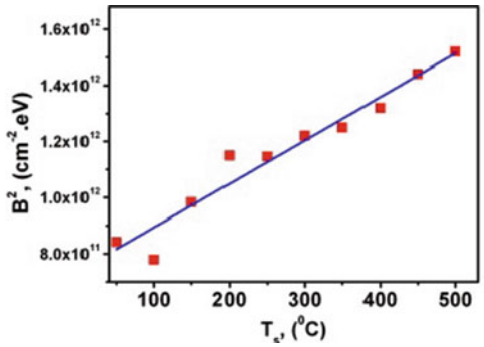

Fig. 29.7 Dependence of the coefficient B^2 on the substrate temperature for ZnO:Nb films

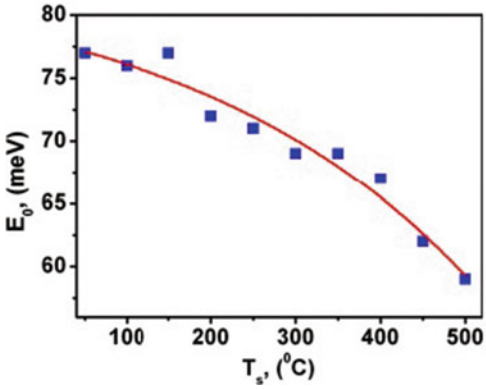

Fig. 29.8 Dependence of the Urbach energy E_0 on substrate temperature for ZnO:Nb films

demonstrate that the band tails width decreases with increasing substrate temperature, probably due to the better structural properties of the films deposited at higher T_s, as reported in [8, 18].

29.3.3 ZnO Thin Film Doped with V

The concentration of vanadium in the obtained ZnO:V thin films varies little with the substrate temperature, T_s, (Table 29.4). The presented values (0.86–0.89 at.%) are averaged after concentration measurements at four different points on the surface of the samples. In Table 29.4 the electrical and structural parameters of the films under investigation are presented as well. For comparison the data of undoped and Al doped ZnO films are given too.

XRD spectra are presented in Fig. 29.9. The diffraction patterns show that the deposited ZnO:V films are polycrystalline with reflections corresponding to the (002) plane of the wurtzite structure with the c-axis perpendicular to the substrate surface. The peak position for ZnO:V films is shifted to lower 2θ compared to

Table 29.4 The values of the optical band gap E_g, Urbach energy E_0, position of the (002) peak in the XRD spectra θ, the FWHM of 2θ Δ2θ, the average grains sizes D, the concentration of the dopants (Al or V) c, the values of the stress σ, refractive index n and the resistivity, ρ, of the films deposited at different T_s

Sample	T_s [°C]	E_g [eV]	E_0 [meV]	2θ [deg.]	Δ2θ [deg.]	D [nm]	c [at. %]	σ [GPa]	n	ρ [mΩcm]
ZnO[a]	150	3.33	63	34.30	0.52	16		−0.81	1.79	31
ZnO[a]	275	3.30	59	34.40	0.47	18		−0.18	1.80	20
ZnO[a]	500	3.27	60	34.40	0.33	25		−0.18	1.77	4,300
ZnO: Al[a]	150	3.36	120	34.20	0.62	14	1	−1.52	1.83	18
ZnO: Al[a]	275	3.41	100	34.15	0.61	13	2	−1.79	1.92	5.4
ZnO: Al[a]	500	3.33	91	34.27	0.62	13	1	−0.98	1.85	6.2
ZnO:V	150	3.44	91	34.18	0.39	21	0.86	−1.62	1.89	7
ZnO:V	275	3.47	98	34.14	0.33	25	0.88	−1.89	1.88	2
ZnO:V	350	3.47	86	34.19	0.35	24	0.89	−1.54	1.90	4
ZnO:V	500	3.44	83	34.19	0.29	29	0.87	−1.54	1.93	8

[a]Data from reference [8]

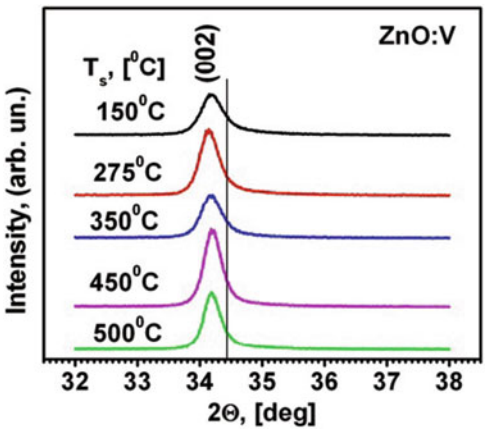

Fig. 29.9 XRD spectra of thin ZnO:V films at different T_s. The *black line* indicates the position of (002) peak in crystalline ZnO [23]

undoped ZnO films, and are close to that for Al-doped films. This shift to lower 2θ is evidence for the presence of tensile stress, probably due to the presence of the doping atoms. The (002) peak position slightly shifts to a lower 2θ value for the ZnO:V sample deposited at $T_s = 275$ °C. The stresses in ZnO:V films are higher than in undoped and Al doped-ZnO films. With increasing T_s, the full width at half maximum (FWHM) of the (002) peak and the value of the stress decreases, while the average grain sizes increases which demonstrates an improvement of the structure with T_s, as in the case of undoped and Al-doped ZnO films [8].

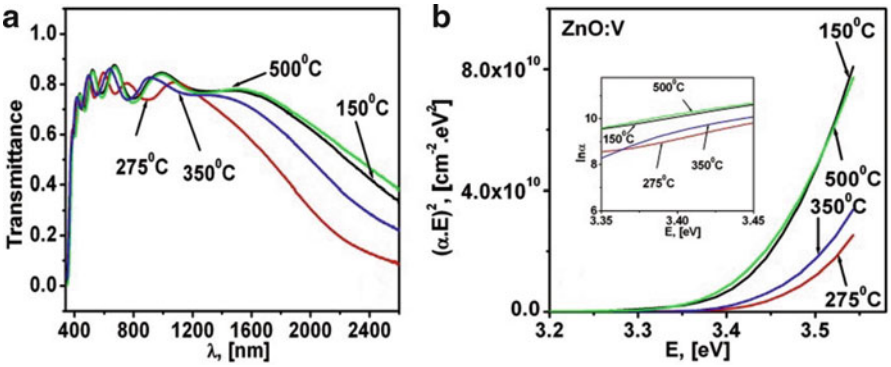

Fig. 29.10 Transmittance spectra (**a**) and $(\alpha E)^2$ versus energy E (**b**) for ZnO:V films deposited at different T_s. The *insert* in (**b**) shows the plot of lnα vs hν

Transmittance spectra of the ZnO:V films are presented in Fig. 29.10a. The spectra are corrected for the transmittance of the glass substrate. All spectra demonstrate transmittance values higher than 85 % in the range 500–1,200 nm, independent of T_s. In the IR region beyond 1,200 nm where absorption due to the free carrier concentration (plasma resonance) takes place, the transmission decreases. An absorption peak at about 850 nm appears for ZnO:V deposited at $T_s > 275$ °C; it is more clearly pronounced for samples with low resistivities. The peak is attributed to *d-d* absorption of V^{2+} ions in a tetragonal arrangement [5].

The values of the resistivity of V-doped ZnO films are lower than in the case of undoped and Al- or Nb-doped ZnO deposited at the same conditions; they are in the range of $2{\cdot}10^{-3}$–$8{\cdot}10^{-3}$ Ωcm. These values are in agreement with results reported in [22]. The average grain size is about 21–29 nm and increases with T_s.

The spectral dependences of α for samples deposited at different T_s are shown in Fig. 29.10b. The values of the optical band gap of V-doped ZnO films are in the range of 3.44–3.47 eV and typical for ZnO. However, they are higher than in the case of undoped and Al- or Nb-doped ZnO films. The optical energy gap increases with T_s increasing up to 275 °C, above which it decreases. It has to be noted, that this sample demonstrates the lowest value of the resistivity (see Tables 29.3 and 29.4). The observed rise of E_g of ZnO:V films as compared to undoped ZnO films could be due to an increase in the donor concentration, related to shallow V donors, as it is in the case of Al-doped ZnO films [24]. The Urbach energy decreases with T_s due to the improved structure in accordance with the XRD data. Layers doped with Al have the highest values of the Urbach energy, followed by V-doped layers; the smallest Urbach energies are found for layers doped with Nb. The differences of the values can be explained by the differences in the size of the various dopant ions (for Al^{3+} 0.20 Å, for Nb^{3+} 0.12 Å and for V^{2+} 0.14 Å) compared to that of Zn^{2+} (0.74 Å).

Raman spectra of ZnO:V films are presented in Fig. 29.11. The glass luminescence background was eliminated before drawing the plots. In the Raman spectra bands typical for ZnO are observed: 276 (B_2), 380 (A_1), 439 (E_2), and 580 cm^{-1} (LO).

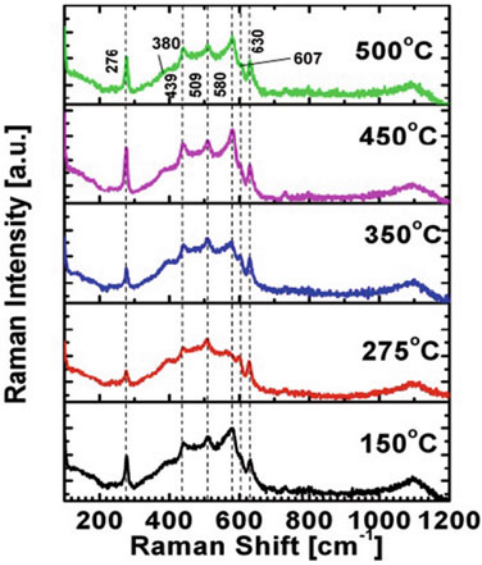

Fig. 29.11 Raman spectra of ZnO:V films deposited at different T_s

The band at 276 cm^{-1} (B_2) is related to the build-in electric field in the depletion region in the grains of the films [25]. Additional bands at 509, 607 and 630 cm^{-1} are present as well. These bands cannot be attributed to bulk phonon modes and are probably due to localized ones. The band at 509 cm^{-1} can be assigned to a phonon mode highly localized near the grain boundaries as it is in the case of Al doped ZnO films [25]. This mode was observed when the crystallite size was smaller than 30 nm as in the present case. The 607 and 630 cm^{-1} bands probably have a similar origin as the I_1 and I_2 modes in [26] and are related to dopant complexes or host defects.

29.4 Conclusions

The influence of the substrate temperature on the optical properties and the electrical resistivity of ZnO thin films, doped with Al, Al:H, Nb, or V are studied. In the range of 550–1,200 nm the transmission is higher than 90 % for ZnO:Al, ZnO:Al:H, and ZnO:Nb thin films and 85 % for ZnO:V. The XRD spectra proved a polycrystalline structure of the ZnO:V films with preferential peak reflections corresponding to the (002) crystallographic plane of the ZnO wurtzite structure with the c-axis perpendicular to the substrate surface. The values of the Urbach energy E_0 for ZnO:Al, ZnO:Al:H, ZnO:Nb and ZnO:V layers decrease with substrate temperature T_s; the coefficient B has a reverse dependence. This decrease of the Urbach energy and the increase of B can be related to an improvement of the crystal structure. Layers doped with Al possess the largest value of the

Urbach energy; the smallest values were found for layers doped with Nb. The differences can be explained by differences in the size of the various dopant ions (for Al^{3+} 0.20 Å, for Nb^{3+} 0.12 Å and for V^{2+} 0.14 Å) compared to that of Zn^{2+}. Comparison of the properties of ZnO:Al and ZnO:Al:H thin films shows that the optical band gaps does not depend on the hydrogen incorporation in the ZnO:Al:H films. However, the ZnO:Al:H films have a lower resistivity due to the incorporation of hydrogen during the deposition. The resistivity of the films decreases with T_s. The lowest resistivity was found for films deposited at low substrate temperature ($1.6–2.2 \cdot 10^{-3}$ Ωcm). For ZnO:Al layers the lowest values of resistance were found at 100 °C, for ZnO:Al:H at 80 °C, for ZnO:V at 275 °C and for ZnO:Nb at 50 °C. The values of the optical band gap of ZnO:Al, ZnO:Al:H, ZnO:Nb, and ZnO:V films are in the range of 3.28–3.58 eV and they passes through a maximum and decrease with further increase of T_s. The refractive index is in the range of 1.74–2.00 at about 500 nm. The layers with low resistivity and high transparence demonstrate potential for applications as a transparent conductive oxide in thin film solar cells and LEDs.

References

1. Li Y, Gong J, McCune M, He G, Deng Y (2010) Synth Met 160:499
2. Seshadri R (2005) Curr Opinion Solid State Mater Sci 9:1
3. Minami T (2005) Semicond Sci Technol 20:S35
4. Koshizaki N, Oyama T (2000) Sensors Actuators B 66:119
5. Saeki H, Tabata H, Kawai T (2001) Solid State Commun 120:439
6. Fukumura T, Jin Z, Ohtomo A, Koinuma H, Kawasaki M (2000) Appl Phys Lett 75:3366
7. Yin Z, Chen N, Yang F, Song S, Chai C, Zhong J, Qian H, Ibrahim K (2005) Solid State Commun 135:430
8. Dimova-Malinovska D, Angelov O, Nichev H, Kamenova M, Pivin JC (2007) J Optoelectron Adv Mater 9:2512
9. Pankove J (1971) Optical processes in semiconductors. Prentice-Hall, Inc., Englewood Cliffs
10. Dragoman D, Dragoman M (2002) Optical characterization of solids. Springer, Heidelberg
11. Girtan M, Folsher G (2003) Surf Coat Technol 172:242
12. Swanepoel R (1983) J Phys E Sci Instrum 16:1214
13. Van der Walle GC (2000) Phys Rev Lett 85:1012
14. Mollwo E (1954) Z Phys 138:478
15. Seraphin BO (1979) Solar energy conversion. Springer, Berlin/Heidelberg
16. Roth A, Williams D (1981) J Appl Phys 52:6685
17. Lovchinov K, Nichev H, Angelov O, Sendova-Vassileva M, Dimova-Malinovska D, Mikli V (2010) J Phys Conf Ser 253:012030
18. Dimova-Malinovska D, Nichev H, Angelov O (2009) Phys Status Solidi 5:3353
19. Burstein E (1954) Phys Rev 93:632
20. Mott N, Davis E (1979) Electronic processes in noncrystalline materials. Oxford, Clarendon, p 289
21. Saito N (1985) J Appl Phys 58:3504
22. Miyata T, Suzuki S, Ishii M, Minami T (2002) Thin Solid Films 411:76

23. Hickenell FS (1975) J Vac Sci Technol 12:879
24. Dimova-Malinovska D, Nichev H, Angelov O, Grigorov V, Kamenova M (2007) Superlattice Microst 42:123
25. Tzolov M, Tzenov N, Dimova-Malinovska D, Kalitzova M, Pizzuto C, Vitali G, Zollo G, Ivanov I (2000) Thin Solid Films 379:28
26. Ke X, Zou C, Li M, Liu C, Guo L, Fu D (2010) Jpn J Appl Phys 49:033001

Chapter 30
Breakdown Phenomena During the Growth of Anodic Films on Antimony

Ch. Girginov, E. Lilov, and E. Klein

Abstract Electrical breakdown during galvanostatic and isothermal growth of Sb_2O_3-films in aqueous solutions of sulfuric, boric, phosphoric and oxalic acid was analyzed. The breakdown voltage was registered at the onset of oscillations of the forming voltage. The oscillations in boric acid electrolytes were accompanied by acoustic emission. The number of events, the amplitude and the energy of the acoustic waves were registered. The values of these parameters did not differ essentially from the very beginning of the process. The effects of current density and nature and concentration of the forming electrolyte on the value of the breakdown voltage was studied. The results obtained do not contradict the concepts of dielectric breakdown of the anodic films under the impact of the electric field applied. Breakdown has been ascribed to the injection of electrons from the electrolyte into the bulk of the anodic oxide and their acceleration and multiplication to an avalanche.

Keywords Anodic antimony oxide • Oxalic acid • Breakdown phenomena • Breakdown voltage

30.1 Introduction

The anodic formation of oxide films is usually carried out at constant current density and temperature conditions. This regime ensures a good reproducibility of the film characteristics. A variety of electrolyte solutions have been used in growing anodic oxide films on antimony but the well known linear increase of the formation voltage U_f with time t or with charge density Q can be most easily achieved in aqueous solutions of acids. Such 'regular' kinetics with more or less extended linear

Ch. Girginov (✉) • E. Klein
University of Chemical Technology and Metallurgy, 8 St. Kl. Ohridski Blvd., 1756 Sofia, Bulgaria
e-mail: christian.girginov@gmail.com

E. Lilov
Department of Physics, University of Chemical Technology and Metallurgy, 8 Kl. Ohridski blvd., 1756 Sofia, Bulgaria

P. Petkov et al. (eds.), *Nanoscience Advances in CBRN Agents Detection, Information and Energy Security*, NATO Science for Peace and Security Series A: Chemistry and Biology, DOI 10.1007/978-94-017-9697-2_30

sections of the kinetic curves have been reported for anodization in electrolytes containing sulfuric acid [1–6], phosphoric acid [7, 8], boric acid [9] and oxalic acid [10–12]. Even in the abovementioned electrolytes, however, mainly depending on their concentration and on the current density used, the appearance of *S*-shaped curves, induction periods and maxima have been observed [3, 13–15].

Regardless of the shape of the kinetic curves, electrical breakdown will begin after U_f has reached a certain value denoted as the breakdown voltage U_B. At this voltage the film growth practically stops, various breakdowns follow each other, causing voltage oscillations, high-frequency fluctuations of the current, sparkling and sound effects. Prolonged breakdowns might provoke structural changes on the surface as well as in the bulk of the anodic film. Having in mind the presumed application of anodic antimony oxide as semiconducting and/or photo-conducting material [4], studies of the breakdown will be helpful not only in elucidating some theoretical aspects of the phenomenon but also in limiting the voltages of film formation, beyond which undesirable structural changes take place.

30.2 Analytical Review of Breakdown Investigations

30.2.1 Breakdowns in the System (+) Valve Metal/Oxide/Electrolyte

Under galvanostatic and isothermal conditions, the onset of breaking down in the system (+) valve metal/oxide/electrolyte is connected, by definition, to the time of reaching the breakdown voltage. As a matter of fact, the linear increase of the formation voltage with time ceases well below the value of U_B, even in the case of 'regular' kinetics; U_f slows gradually down. The use of different criteria for the onset of breakdowns and for the determination of U_B [16–22] creates some difficulties in comparing the results of different authors.

In the majority of studies, a weak dependence of U_B on the current density J used has been definitely established [23]. Further, it is generally agreed that U_B strongly depends on the nature and composition of the contact electrolyte (i.e. the electrolyte in which U_B is measured). Burger and Wu [24] have ascertained the following dependence of U_B on the resistivity ρ of the non-dissolving contact electrolyte

$$U_B = a_B + b_B \log\rho$$

Here, the constant a_B has been assumed to depend only on the nature of the anodized metal, and the constant b_B has been thought to be universal.

30.2.2 Breakdowns During the Formation of Sb_2O_3-Films

The growth of anodic oxide films on antimony has proven to be always accompanied by film dissolution as reported for anodization in different electrolyte solutions

of phosphoric acid [25, 26], sulfuric acid [27–29], hydrofluoric acid [30] and oxalic acid [10]. In spite of the use of film dissolving electrolytes, relatively thick anodic films have been formed, and the breakdown characteristics of the films have proven to be similar to those observed in non-dissolving solutions.

30.3 Determination of the Breakdown Voltage

The breakdown voltage during the anodization of antimony in different acidic electrolytes has been determined as the mean steady-state value of the oscillating or the flat section of the $U_f(t)$-curve. The determination of U_B is illustrated in Fig. 30.1 for anodization of Sb in two sulfuric acid solutions [31].

The anodic oxidation of antimony in certain electrolytes has proven to be accompanied [32] by an acoustic emission which can be distinctly registered, as illustrated in Fig. 30.2.

It is worth mentioning that the characteristics of the acoustic emission during breaking down do not differ essentially from those at the very beginning of anodization. The emergence of acoustic pulses in the circuit of galvanostatic anodization has not yet been clarified but it should be related with the current flow through the film.

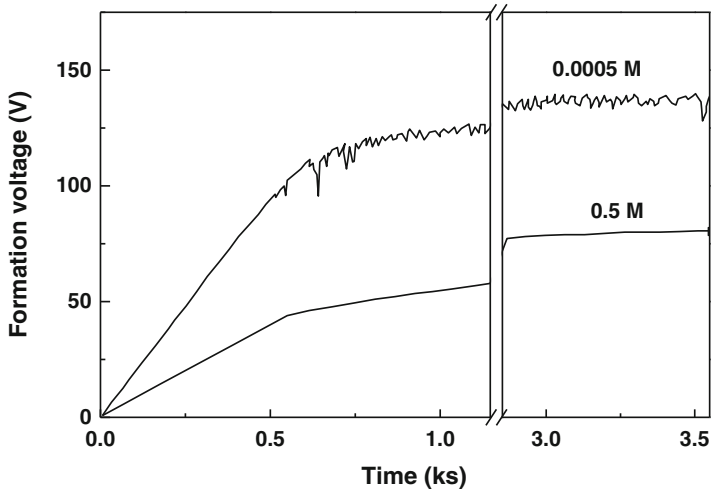

Fig. 30.1 Kinetic curves of anodization of antimony in 0.0005 M and 0.5 M aqueous solutions of sulfuric acid at 2.2 mA cm^{-2} and 20 °C. The values of the breakdown voltages are determined from the mean steady-state values of U_f at the *right side*

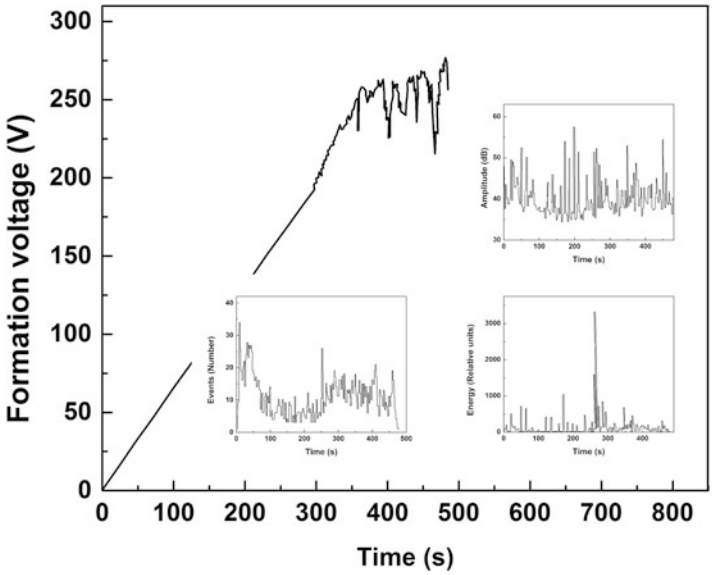

Fig. 30.2 Formation voltage vs. time dependence during anodization of antimony in a 3 % aqueous solution of boric acid (pH = 5.4) at 2.2 mA cm^{-2} and 20 °C. Inlet: amplitude, energy and number of events of the accompanying acoustic emission

30.4 Influence of the Current Density on the Breakdown Voltage

The weak current density dependence of U_B found for a number of valve metals [23] has been also confirmed [11] for the case of anodization of antimony. Values of U_B for anodization of Sb in 0.01 M oxalic acid at four current densities are shown in Fig. 30.3.

30.5 Influence of Nature and Composition of the Electrolyte on U_B

Numerical values for breakdown voltages in some acid, basic and salt solutions have been calculated by Ammar and Saad [3, 33]. Values of U_B can be calculated from the resistivity dependence of the breakdown voltage according to the empirical equation of Burger and Wu [24].

The only question remaining controversial is whether the constants a_B and b_B in the above equation depend on the electrolyte composition. To clarify this, the breakdown voltage of anodic antimony oxide has been studied in oxalic [11], sulphuric [31] and phosphoric [34] acid solutions of different concentrations

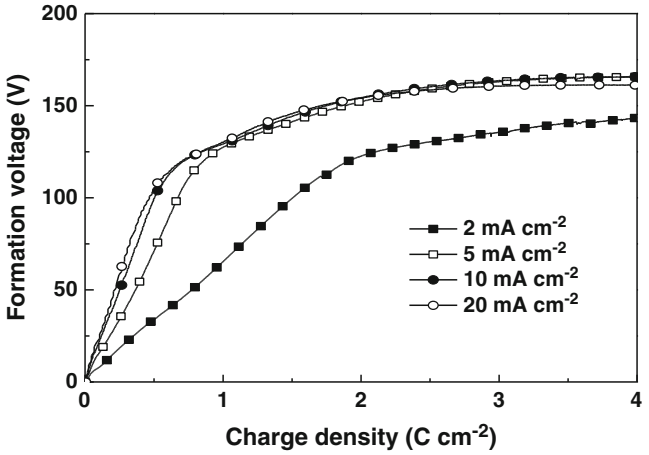

Fig. 30.3 Kinetic curves of anodic oxidation of antimony in 0.01 M $(COOH)_2$ at four different current densities up to the breakdown voltage

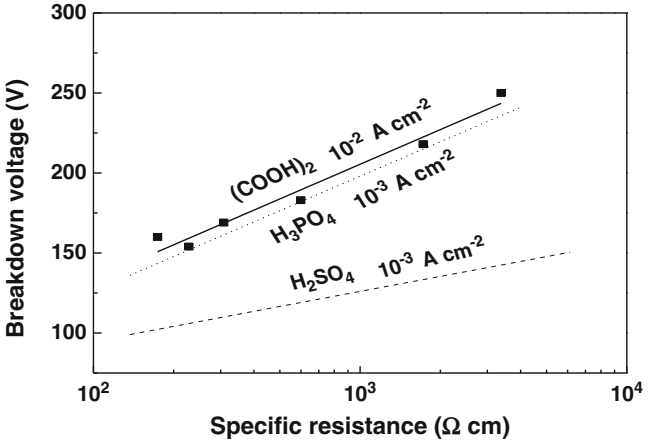

Fig. 30.4 Breakdown voltages as a function of the specific resistance of three different electrolytes under constant other conditions

(or resistivities, respectively) under otherwise constant conditions. The corresponding dependences are presented in Fig. 30.4.

In all three electrolytes, the typical voltage oscillations shown in Figs. 30.1 and 30.2 have been observed after reaching a certain value of U_f. The oscillations have been found to start at different values of U_f depending on type and concentration of the contact electrolyte. The values of the breakdown voltage determined as described above allowed the calculation of the constants in the Burger and Wu equation. The equation was found to describe the experimental data for anodization of antimony in acid solutions well. The calculated values of the constants a_B and b_B

Table 30.1 Values of the constants in Burger and Wu equation, Cd means current density

Electrolyte	pH range	Cd (Acm^{-2})	a_B (V)	b_B (V)
$(COOH)_2$ [11]		10^{-2}	-10.4 ± 1.8	72 ± 5
H_3PO_4 [34]		10^{-3}	-18.0 ± 2.3	72 ± 8
H_2SO_4 [31]		10^{-3}	58.5 ± 4.2	24 ± 3
Na_2CO_3 [35]	10.2–11.3	10^{-3}	-60.1 ± 5.2	108 ± 7
Na_2SO_4 [35]	5.4–6.1	10^{-3}	-5.2 ± 0.5	53 ± 4
NaCl [35]	5.5–6.2	10^{-3}	6.1 ± 0.4	31 ± 3

are presented in Table 30.1 in comparison with values of these constants for other electrolytes [35].

The values of the breakdown voltages of anodic antimony oxide in dissolving acid solutions have proven to obey the common regularities which are typical for valve metals. On the other hand, the constants a_B and b_B in the Burger and Wu equation [24] have been found to depend definitely on the nature of the forming (contact) electrolyte.

30.6 Mechanisms of Breaking Down

Different hypotheses about the mechanism of breaking down during anodization of valve metals have been proposed. Yahalom and Hoar have suggested [36] that thermally induced breakdowns are due to the accumulation of Joule heat during oxidation. According to Young [37–40], breakdowns are initiated from microfissures containing electrolyte within the oxide film. The concept of avalanche breakdowns through film flaws has been proposed by Odynets [41, 42]. The first quantitative theory of breaking down during anodization has been developed by Ikonopisov [43] on the base of a model of electron avalanche. Later on Kadary and *Klein* [44] have published a quantitative model of breakdowns through successive avalanches. The avalanche theories are generally based on the presence of an electron component J_e of the total current density J. According to these theories, the contact electrolyte not only delivers the oxygen ions for oxidation of the metal but also injects electrons into the conduction band of the oxide under the influence of the electric field. It is not clear, however, which electrolyte species deliver the electrons, how the reminders are balanced and why electrons in the conduction band can provoke avalanches.

Different models like Schottky emission or the Poole-Frenkel effect [45] have been proposed to explain the mechanism of electronic conductivity in anodic oxides. Only the Christov model [46] however explains the dependence of J_e on the nature and concentration of the contact electrolyte.

By adding the electronic current component, the total current flow during anodic polarization of valve metals is described by the expression:

$$J = J_i + J_{dis} + J_e$$

The ionic current J_i results from the field-assisted migration of metal and oxygen ions and realizes the anodic film growth. The dissolution current J_{dis} is related with an assumed electrochemical dissolution of the anodic film. In the case of anodic oxidation of metals in film dissolving electrolytes, it seems impossible to distinct between chemical and electrochemical dissolution. The electronic current J_e does not affect film growth or dissolution; the only impact of J_e is on the efficiency of the anodization. Recent studies [47] of anodic antimony oxide formation in oxalic acid electrolytes have shown that electronic conductivity had a negligible impact, if any, on the efficiency of film formation.

30.7 Conclusion

The breakdown characteristics of anodic oxide films formed on antimony in film-dissolving electrolytes have proven not to differ from those observed for the systems (+) valve metal/oxide/non-dissolving electrolyte. The dependence of the breakdown voltage on the resistivity of the contact electrolyte has been found to match the empirical equation of Burger and Wu. The constants in this equation were found strongly to depend on the nature of the electrolyte. This result is consistent with the known dependence of the electronic current on the nature and concentration of the electrolyte and supports the breakdown model based on the injection of electrons from the electrolyte into the film and their multiplication to electron avalanches. Nonetheless, the electron donor levels within the electrolyte as well as the formation of avalanches in the conduction band of the oxide still remain unclarified.

Acknowledgement The authors are grateful to the University of Chemical Technology and Metallurgy for the financial support through contract №11324 “Anodic oxide films on antimony formed in oxalic acid solutions”.

References

1. Laihonen S, Laitinen T, Sundholm G, Yli-Penti A (1990) Electrochim Acta 35:229
2. Metikoš-Huković M, Babić R, Brinić S (2006) J Power Sources 157:563
3. Ammar I, Saad A (1971) J Electroanal Chem 30:395
4. Metikoš-Huković M, Lovreček B (1980) Electrochim Acta 25:717
5. El-Basiouny M, Hefny M, Mogoda A (1984) Ann Chim 74:729
6. Pavlov D, Bojinov M, Laitinen T, Sundholm G (1991) Electrochim Acta 36:2087
7. Girginov A, Kanazirski I, Klein E (1991) C R Acad Bulg Sci 44:49
8. Bojinov M, Kanazirski I, Girginov A (1995) Electrochim Acta 40:873
9. Ikonopisov S, Kalfova V, Girginov A (1988) C R Acad Bulg Sci 41:89
10. Angelov I, Girginov C, Klein E (2011) Bulg Chem Commun 43:144
11. Lilov E, Girginov C, Klein E (2013) Bulg Chem Commun Special Ed A 45:94
12. Lilov E, Girginov C, Klein E (2012) Adv Nat Sci Theory Appl 1:115

13. Ikonopisov S, Girginov A, Tsochev V (1972) C R Acad Bulg Sci 25:653
14. Girginov A, Ikonopisov S (1974) Elektrokhimiya 10:638
15. El-Basiouny M, Hefny M, Mogoda A (1985) Corrosion 41:611
16. Davidov A (2002) Electrochim Acta 46:3777
17. Mamun A, Schennah R, Parga J, Mollah J, Hossain M, Cocke D (2001) Electrochim Acta 46:3343
18. Li Y, Young L (2001) J Electrochem Soc 148:B337
19. Jouve G (2000) Philos Mag 80:1507
20. Han S, Thompson G (1999) Han'guk Pyomyon Konghak Hoechi 32:341
21. Gudic S, Radosevic J, Kliskic M (1996) J Appl Electrochem 10:1027
22. Li Y, Shimada H, Sakairi M, Shigyo K, Takahashi H, Seo M (1997) J Electrochem Soc 144:866
23. Ikonopisov S, Girginov A, Machkova M (1979) Electrochim Acta 24:451
24. Burger F, Wu J (1971) J Electrochem Soc 118:2039
25. Linarez Perez O, Perez M, Teijelo M (2009) J Electroanal Chem 63:64
26. Hefny M, Badawy W, Mogoda A, El-Basiouny M (1985) Electrochim Acta 30:1017
27. Metikoc-Hukovic M, Babic R, Brinic S (2006) J Power Sources 157:563
28. Mogoda A (2001) Thin Solid Films 394:6
29. Mogoda A, El-Haleem A (2003) Thin Solid Films 441:173
30. Badawy W, Mogoda A, Ibrahim M (1988) Electrochim Acta 33:1367
31. Girginov A, Kalfova V, Kanazirski I, Ikonopisov S (1990) Elektrokhimiya 26:110
32. Girginov A, Lilov E, Ikonopisov S, Vodenicharov H, Lozev M (1990) C R Acad Bulg Sci 43:53
33. Ammar I, Saad A (1972) J Electroanal Chem 34:159
34. Girginov A, Lilov E, Vodenicharov H, Ikonopisov S (1989) C R Acad Bulg Sci 42:57
35. Girginov A, Lilov E, Ikonopisov S, Vodenicharov H (1989) C R Acad Bulg Sci 42:73
36. Yahalom J, Hoar T (1970) Electrochim Acta 15:877
37. Young L (1961) Anodic oxide films. Academic, London
38. Burger F, Young L (1962) Electrolytic capacitors. In: Progress in dielectrics, vol 5. Heywoods and Co., London, pp 1–36
39. Young L (1955) Trans Faraday Soc 51:1250
40. Young L (1959) Trans Faraday Soc 55:842
41. Odynets L, Platonov U, Prokopchuk E (1972) Elektronnaya tehnika 27:37
42. Orlov V, Odynets L, Ryungenen T (1973) Elektrokhimiya 9:818
43. Ikonopisov S (1977) Electrochim Acta 22:1077
44. Kadary V, Klein N (1980) J Electrochem Soc 127:139
45. Sze S (1981) Physics of semiconductor devices. Wiley, Hoboken
46. Christov S (1979) J Electroanal Chem 105:275
47. Girginov Ch, Lilov E, Klein E (in press) J Chem Technol Met

Chapter 31
Stress Measurements and Optical Studies of $(AsSe)_{100-x}Ag_x$ Films for Optical Sensor Applications

V. Ilcheva, E. Petkov, C. Popov, V. Boev, O. Koleva, P. Petkov, T. Petkova, and S.N. Yannopoulos

Abstract Thin $(AsSe)_{100-x}Ag_x$ (x = 0–25 mol.%) films have been deposited on glass substrates and silicon cantilevers by vacuum thermal evaporation from the corresponding bulk materials. The mechanical stability was investigated by measuring the stress of the films deposited on silicon cantilevers. The correlation between the stress and the composition has been investigated and will be discussed.

In order to investigate photoinduced changes in the refractive index, the films have been exposed to a He-Ne laser. The transmission spectra of the films have been measured before and after laser illumination; the refractive index has been derived by Swanepoel method. The photoinduced changes occurring in the films

V. Ilcheva (✉) • V. Boev • T. Petkova
Institute of Electrochemistry and Energy Systems, Bulgarian Academy of Sciences, Acad. G. Bonchev Bl.10, 1113 Sofia, Bulgaria
e-mail: vaniailcheva1976@gmail.com; vanya_ilcheva@yahoo.com

E. Petkov • C. Popov
Institute of Nanostructure Technologies and Analytics (INA), University of Kassel, Heinrich-Plett-Str. 40, 34132 Kassel, Germany

O. Koleva
Institute of Electrochemistry and Energy Systems, Bulgarian Academy of Sciences, Acad. G. Bonchev Bl.10, 1113 Sofia, Bulgaria

Foundation for Research and Technology Hellas FORTH/ICE-HT, Institute of Chemical Engineering and High Temperature Chemical Processes, P.O. Box 1414, GR-26 504 Patras, Greece

P. Petkov
Department of Physics, University of Chemical Technology and Metallurgy, 8 "Kl. Ohridski" blvd., 1756 Sofia, Bulgaria

S.N. Yannopoulos
Foundation for Research and Technology Hellas FORTH/ICE-HT, Institute of Chemical Engineering and High Temperature Chemical Processes, P.O. Box 1414, GR-26 504 Patras, Greece

P. Petkov et al. (eds.), *Nanoscience Advances in CBRN Agents Detection, Information and Energy Security*, NATO Science for Peace and Security Series A: Chemistry and Biology, DOI 10.1007/978-94-017-9697-2_31

after illumination lead to changes of the optical constants. These features make the investigated materials suitable for application in planar chalcogenide-based sensor devices.

Keywords Chalcogenide glasses • Thin films • Stress • Optical sensors

31.1 Introduction

Amorphous chalcogenides are subject of scientific interest due to their remarkable optical properties, enabling applications in optical biosensors [1]. The wide transmission window (1–20 μm), depending on the composition, the high refractive indices and the ability of chalcogenide materials to change their optical constants under the action of light allow them to be used as optical waveguides in optical sensors, working on the principle of evanescent waves. The sensing mechanism is based on the attenuation of the propagating light due to the interactions of the evanescent waves with the target molecules. Detection of the molecules takes place when light of a selected wavelength which corresponds to characteristic absorption bands of the target molecules, is transferred to a point where the propagating surface of the waveguide (and the accompanying evanescent wave) comes in contact with the optically detectable analyte.

The fabrication of planar chalcogenide-based sensor devices with high sensitivity over a wide spectral range requires films with good homogeneity, smooth surfaces (providing better photon-molecule interactions and higher sensitivity) and high mechanical stability, which basically depends on the presence of a residual stress. Moreover, the film composition has to be chosen for the creation of structures with a high refractive index contrast. This is why we focused our work on the investigation of the mechanical stability of As-Se-Ag thin films which allow to obtain refractive index modification by laser illumination and are suited for applications as active materials in planar optical waveguide sensors.

31.2 Experimental Details

Bulk $(AsSe)_{100-x}Ag_x$ glasses with $x = 0$, 5, 10, 15, 20 and 25 mol. % Ag, synthesized by the melt-quenching technique were used for thin film preparation by vacuum thermal evaporation (VTE).

The thermal evaporation process was carried out in a Leybold LB 370 vacuum set-up with a residual gas pressure of 1.33×10^{-4} Pa. A constant source – substrate distance of 0.12 m and evaporation temperatures in the range of 700–800 K were used in all experiments. During the deposition the substrates were kept at room temperature and rotated to obtain uniform layers.

The films were deposited on glass substrates for optical measurements and on silicon cantilevers for stress measurements. The cantilever substrates consisted of

seven strips with a thickness of 60 μm, widths between 0.7 and 2.0 mm and lengths between 2.0 and 8.0 mm. This configuration allows an accurate stress measurement in a wide range. The deflection of the cantilevers was determined from the curvature of the substrate measured by the depth of the focus of an optical microscope. The films were kept in dark under dry atmosphere for 8 months and measured again to study the relaxation of the film stress as described in [2].

The thickness was determined by the Fizeau interferometer technique [3] using a Zygo New View 5,000 interferometer.

The amorphous character of the obtained films was proved by the X-ray diffraction technique by using a Philips Analyzer APD-15 with Cu-Kα radiation; their structure and morphology were studied with a scanning electron microscope (SEM) Hitachi s-4000.

The optical properties of the $(AsSe)_{100-x}Ag_x$ films were investigated before and after 60 min irradiation with a He-Ne laser with an intensity of 5 mW/cm^2. Their optical transmission spectra were recorded in the wavelength range from 400 to 2,500 nm at room temperature using a double-beam computer-controlled JASCO spectrophotometer with an accuracy of ±0.5 nm. The refractive index of the as-deposited and illuminated films was estimated from the transmission spectra.

31.3 Results and Discussion

The as-prepared films are amorphous as shown by the XRD analysis. The patterns are typical for non-crystalline materials, with elevated broad halos and no sharp peaks present (Fig. 31.1). The SEM pictures reveal the smoothness and homogeneity of the film surface and interface (Fig. 31.2).

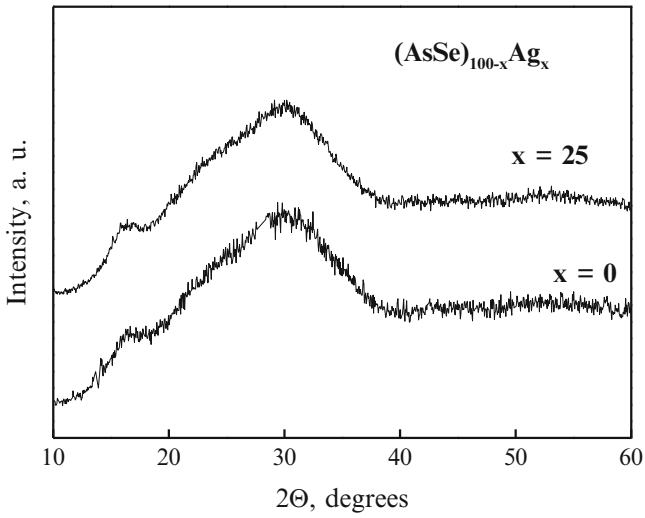

Fig. 31.1 X-Ray diffraction patterns of AsSe and $(AsSe)_{75}Ag_{25}$ thin films

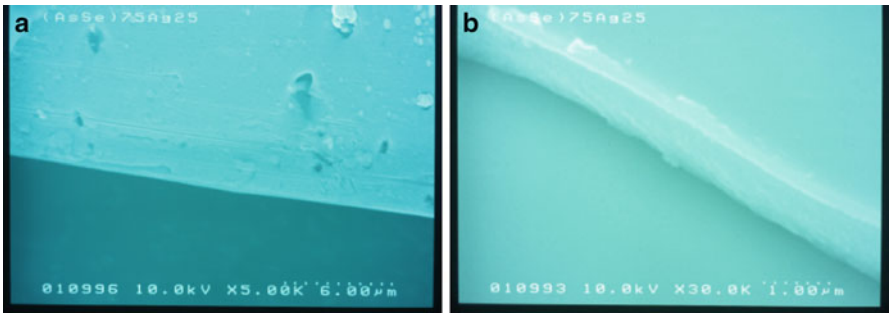

Fig. 31.2 SEM images of a $(AsSe)_{75}Ag_{25}$ film: (**a**) surface; (**b**) cross section

Table 31.1 Thickness of $(AsSe)_{100-x}Ag_x$ films

Composition	Thickness [nm]
AsSe	826
$(AsSe)_{95}Ag_5$	765
$(AsSe)_{90}Ag_{10}$	740
$(AsSe)_{85}Ag_{15}$	788
$(AsSe)_{80}Ag_{20}$	680
$(AsSe)_{75}Ag_{25}$	723

The thickness of the $(AsSe)_{100-x}Ag_x$ films determined interferometrically varies between 680 and 826 nm (Table 31.1).

The stress in the system thin film/substrate is the sum of the thermal stress, caused during the deposition process from the different thermal expansion coefficients of film and substrate, and the intrinsic stress, strongly dependent on the structure and the composition of the film. To reduce the thermal stress the substrates were kept at room temperature during the deposition process. Therefore we assume that the results obtained are only due to the intrinsic stress in the films. Consequently the film structure and composition are responsible for the sign and magnitude of the stress. The stress σ was determined by the deflection of the cantilever grids, and calculated with Stoney's equation [4]:

$$\sigma = \frac{E}{6(1-\nu)} \cdot \frac{D^2}{Rd}$$

where d is the film thickness, R the radius of the curvature of the substrate, and E, ν and D are the Young's modulus, Poisson's ratio and thickness of the substrate, respectively.

In our case, the thickness of the films (Table 31.1) is much smaller than that of the substrate (60 µm), which allowed applying an approximated Stoney equation for the stress determination:

$$\sigma = \frac{E}{3(1-\nu)} \cdot \frac{hD^2}{(l^2+h^2)d}$$

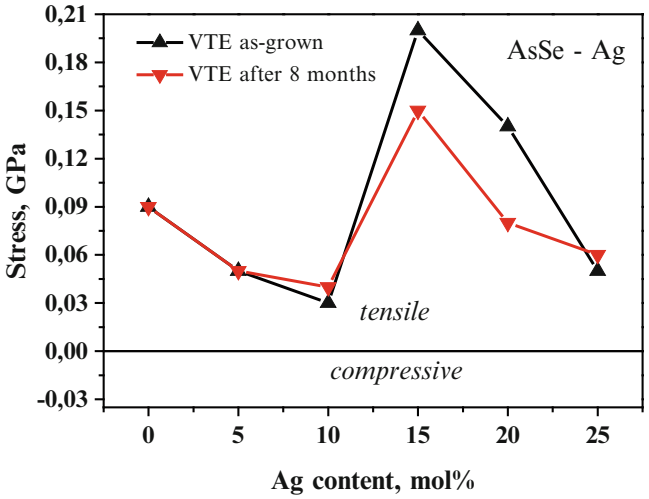

Fig. 31.3 Compositional dependence of the stress of $(AsSe)_{100-x}Ag_x$ thin films

where l is the length of the cantilever and h the maximum deflection of the cantilever tip. The measured stress of the thin films as a function of the silver content is presented in Fig. 31.3.

The measurements reveal a tensile stress irrespective of the composition of the films. When silver is introduced into the chalcogenide matrix, a maximum of the stress is observed at 15 mol % Ag. This is most probably related to the destruction of parts of the basic structural units ($AsSe_{3/2}$ pyramids) and the formation of new ones. This suggestion is confirmed by the results from the Raman spectroscopy of the bulk glasses.

The Raman spectra presented in Fig. 31.4 show that the addition of 15 mol.% Ag in the chalcogenide AsSe matrix decreases the intensity of the band at 237 cm^{-1}. This band is attributed to the stretching mode of $AsSe_{3/2}$ pyramids [5, 6]; its reduction indicates that structural changes have occurred in the films.

The transmission spectra of the as-deposited and illuminated AsSe-Ag thin films, recorded in the visible and IR spectral range (400–2,500 nm), show a shift of the absorption edge to shorter wavelengths after the addition of silver (Fig. 31.5).

The observed blue shift of the absorption edge is a result of the changes of the electronic structure of the material after silver addition, which probably leads to the formation of additional defect states, localized in the band gap.

The illumination of the films leads to a shift of the absorption edge to longer wavelengths, i.e. a photodarkening effect is observed (dashed lines in Fig. 31.5). The photoinduced effects in amorphous materials occur as a result of photoinduced structural changes, which depend basically on the wavelength of the light exposure, the intensity of the illumination light and the illumination time [7].

The refractive index of the films was estimated from the transmission spectra by the Swanepoel method [8]. The spectral dispersion of the refractive index

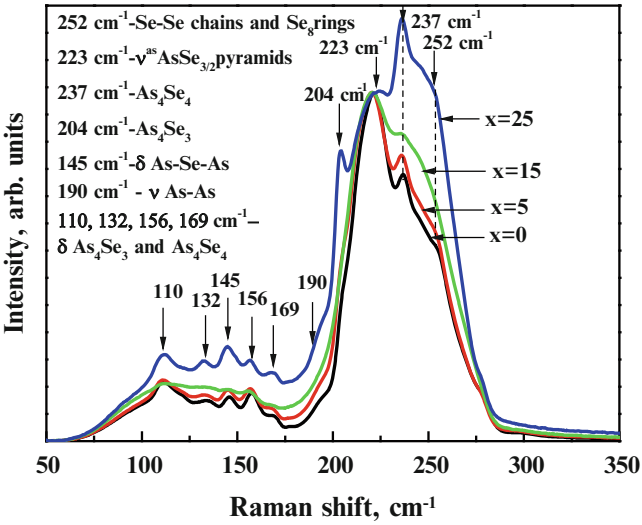

Fig. 31.4 Raman spectra of $(AsSe)_{100-x}Ag_x$ glasses

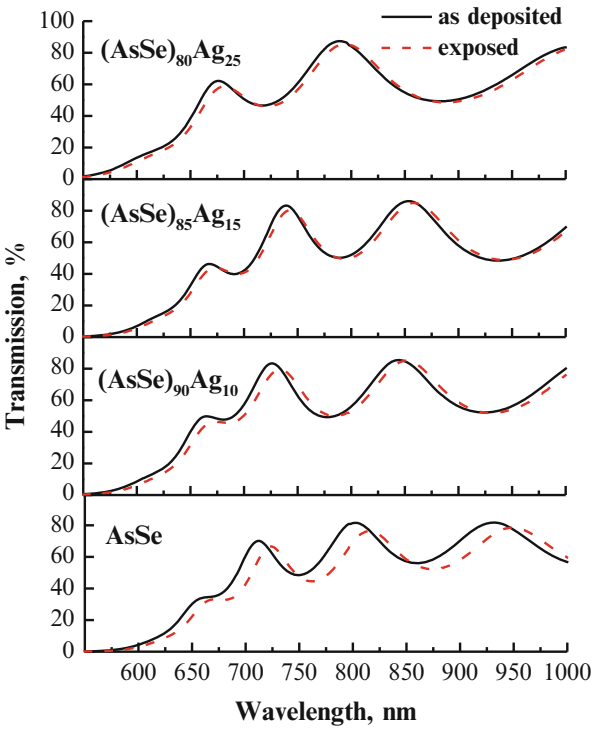

Fig. 31.5 Transmission spectra of as-deposited $(AsSe)_{100-x}Ag_x$ films and after 60 min exposure with He-Ne laser with an intensity of 5 mW/cm^2

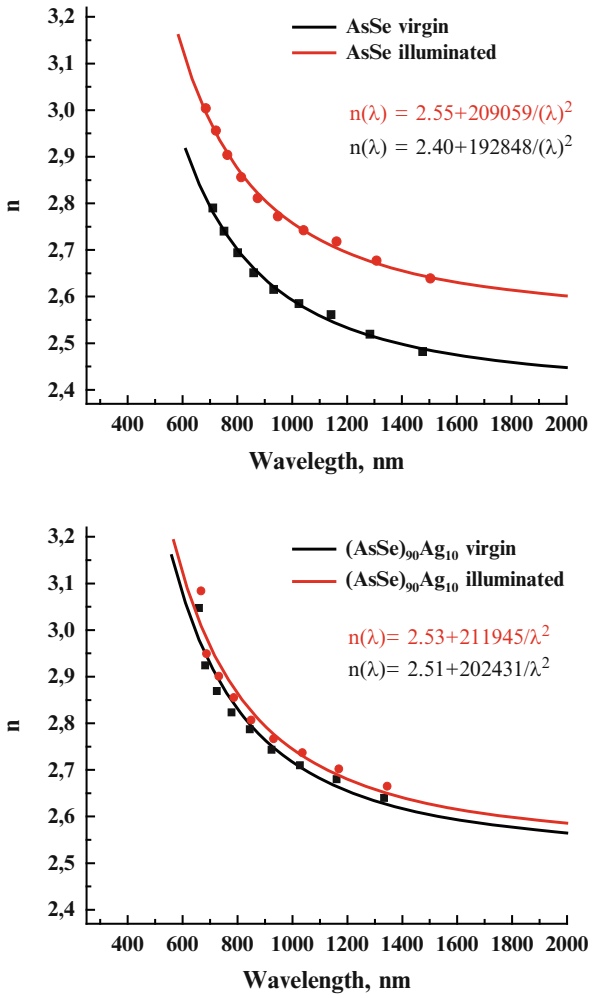

Fig. 31.6 Spectral dispersion of the refractive index n of as-deposited $(AsSe)_{100-x}Ag_x$ films and after He-Ne laser illumination

(Fig. 31.6) shows that the refractive index of the AsSe-Ag films increases after the addition of silver and also after their illumination.

31.4 Conclusions

The obtained thermally evaporated $(AsSe)_{100-x}Ag_x$ thin films are amorphous with smooth and homogeneous surfaces. The stress measurements show tensile stress with a maximum at 15 mol % Ag, when the number of the basic structural units ($AsSe_{3/2}$ pyramids) is reduced, and formation of silver enriched structural units

occurs. Stress relaxation, following the tendency of the as-deposited films, is observed with the time.

The optical transmission measurements reveal a shift of the absorption edge to shorter wavelengths after the addition of silver. A photodarkening effect after the exposure of the films by He-Ne laser illumination is observed.

The refractive index calculations, carried out by the Swanepoel method show a tendency of an increase of n after silver addition due to structural transformations in the films. The refractive index of the material changes also after the illumination.

The obtained results demonstrate that the amorphous thin As-Se-Ag films fulfill the requirements of homogeneity, uniformity, surface smoothness and minimal residual stress. The films undergo photoinduced changes after illumination, which result in changes of the optical constants. These features make the investigated materials suitable for application in planar chalcogenide-based sensor devices.

References

1. Anne M, Keirsse J, Nazabal V, Hyodo K, Inoue S, Boussard-Pledel C, Lhermite H, Charrier J, Yanakata K, Loreal O, Le Person J, Colas F, Compère C, Bureau B (2009) Sensors 9:7398
2. Popov C, Boycheva S, Petkov P, Nedeva Y, Monchev B, Parvanov S (2006) Thin Solid Films 496:718
3. Kongsakul J, Witit-anun N, Chaiyakun S, Kaewtrakulpong P (2005) Proceeding of the ECTI '05, Pataya Chonburi, p 450
4. Stoney G (1909) Proc R Soc Lond A 82:172
5. Iovu MS, Kamitsos EI, Varsamis CPE, Boolchand P, Popescu M (2005) Chalcogenide Lett 2:21
6. Kostadinova O, Chrissanthopoulos A, Petkova T, Petkov P, Yannopoulos SN (2011) J Solid State Chem 184:447
7. Liu Q, Zhao X, Gana F (2006) Chalcogenide Lett 3:15
8. Swanepoel R (1983) J Phys E Sci Instrum 16:1214

Chapter 32
Structure of Fe_3O_4(111) Films on Pt(111) and Ru(0001): The Role of Epitaxial Strain at the Iron Oxide/Metal Single Crystal Interface

M. Lewandowski, N. Michalak, Z. Miłosz, R. Ranecki, T. Luciński, and S. Jurga

Abstract Thin oxide films epitaxially grown on metal single crystal surfaces may exhibit structural properties that differ from the corresponding bulk oxide materials. The structure of the films is often rendered by their thickness, the structure and properties of the substrate and by the nature of the oxide/substrate interface. We prepared thin iron oxide films on Pt(111) and Ru(0001) and studied their structure using STM, LEED and XPS. The structure of FeO(111) – the iron oxide phase that forms at the interface with the metal single crystal – depends on the parameters of the support and is believed to further influence the structure of thicker iron oxide films, such as Fe_3O_4(111), that are being grown on top of it. In this article we discuss the role of one of the important parameters that may determine this structure – the epitaxial strain at the iron oxide/metal single crystal interface.

Keywords Iron oxides • Fe_3O_4 • Thin films • Structure • Epitaxial strain

M. Lewandowski (✉)
Institute of Molecular Physics, Polish Academy of Sciences, M. Smoluchowskiego 17, 60-179 Poznań, Poland

NanoBioMedical Centre, Adam Mickiewicz University, Umultowska 85, 61-614 Poznań, Poland
e-mail: lewandowski@amu.edu.pl

N. Michalak • Z. Miłosz • R. Ranecki • T. Luciński
Institute of Molecular Physics, Polish Academy of Sciences, M. Smoluchowskiego 17, 60-179 Poznań, Poland

S. Jurga
NanoBioMedical Centre, Adam Mickiewicz University, Umultowska 85, 61-614 Poznań, Poland

P. Petkov et al. (eds.), *Nanoscience Advances in CBRN Agents Detection, Information and Energy Security*, NATO Science for Peace and Security Series A: Chemistry and Biology, DOI 10.1007/978-94-017-9697-2_32

32.1 Introduction

Iron oxides, due to their unique electron and magnetic properties, are widely used materials in many chemistry and biology related fields, such as heterogeneous catalysis [1], drug delivery systems or magnetic imaging [2, 3]. The properties of iron oxide crystals often depend on their size and chemical surrounding. For example, ultrathin FeO(111) films epitaxially grown on Pt(111) exhibit superior catalytic activity in CO oxidation reaction in the millibar pressure range [4], which is related to the structural transformation of FeO(111) to FeO_x ($1 < x < 2$) phase, with a significant role of electron transfer from the FeO(111)/Pt(111) to the adsorbed oxygen [5].

Even though FeO(111) grows on Pt(111) epitaxially – forming a closed film – the structure of FeO(111)/Pt(111) is complex: due to ~10 % lattice mismatch between FeO(111) and Pt(111) (3.04 Å vs. 2.78 Å, respectively) the formation of a Moiré superstructure with 25 Å periodicity is observed [6]. Since FeO(111) is an interface layer for the further growth of thicker iron oxides – namely $Fe_3O_4(111)$ and $Fe_2O_3(0001)$ – on this support, its structure may influence the growth and structure of thicker iron oxide films.

Iron oxide thin films can be also grown on Ru(0001) [7]. Due to a larger than in the case of Pt(111) lattice mismatch between the oxide and the support (3.04 Å vs. 2.71 Å for FeO(111) and Ru(0001), respectively), the FeO(111)/Ru(0001) Moiré superstructure has smaller periodicity (21.6 Å). In contrast to FeO(111)/Pt (111), a significant lattice mismatch between the FeO(111) and Ru(0001) is not only reflected in a Moiré-type superstructure, but also in the presence of dislocations/domain boundaries, which could additionally influence the further growth of thicker iron oxide films. For Pt(111), it is well known from the literature that the Moiré structure of FeO(111) does not significantly influence the structure of $Fe_3O_4(111)$ that grows on top of it – the magnetite grows in a form of a continuous film and has bulk-like structural parameters [6]. For $Fe_3O_4(111)$ on Ru(0001), mainly $Fe_3O_4(111)$ islands [8] and structurally ill-defined/complex magnetite films [7] have been studied so far.

In this article we present a comparison of structural features of iron oxide thin films grown on Pt(111) and Ru(0001). The results indicate a significant role of epitaxial strain at the iron oxide/metal single crystal interface (which has an FeO (111)/Pt(111) and FeO(111)/Ru(0001) structure, respectively) on the structure of thicker iron oxide films (here $Fe_3O_4(111)$).

32.2 Experimental Details

The experiments were performed in an ultra-high vacuum (UHV) chamber (base pressure in the 10^{-10} mbar range; from *PREVAC*). Pt(111) and Ru(0001) single crystals (purity ≥ 99.99 %; *MaTeck*) were cleaned by repeated cycles of 0.3–1 kV Ar^+ (99.999 %; *Messer*) ion sputtering, annealing in O_2 (99.999 %; *Linde Gas*) and in UHV. The temperature was controlled with an optical pyrometer (*Minolta/Land*).

Iron oxide thin films were grown by repeated cycles of 1.5–3 monolayers iron (purity 99.999 %; *Alfa Aesar*) deposition and subsequent oxidation in 1×10^{-6} mbar molecular oxygen at 870–1,000 K. The cleanliness of the crystals and the formation of well-ordered iron oxide films were confirmed by scanning tunneling microscopy (STM; *RHK*), low energy electron diffraction (LEED; *SPECS*) and X-ray photoelectron spectroscopy (XPS; *PREVAC/VG Scienta*). The STM images were processed using WSxM [9] and Gwyddion (*gwyddion.net*) computer software. The XPS spectra were recorded at room temperature using a non-monochromatic AlKα (1,486 eV) X-ray radiation source and a semispherical electron energy analyzer. The exact binding energies were determined by shifting the spectra with respect to the bulk Pt and Ru peaks. The spectra were fitted using the CasaXPS software (*Casa Software Ltd*). A Voigt function (linear combination of Gauss and Lorentz functions) and a Shirley background subtraction were used for the fittings.

32.3 Results and Discussion

Figure 32.1 presents LEED patterns of clean Pt(111) and Ru(0001) single crystals, as well as patterns of FeO(111) and Fe_3O_4(111) films grown on these supports. FeO(111) films exhibit a characteristic satellite pattern originating from Moiré

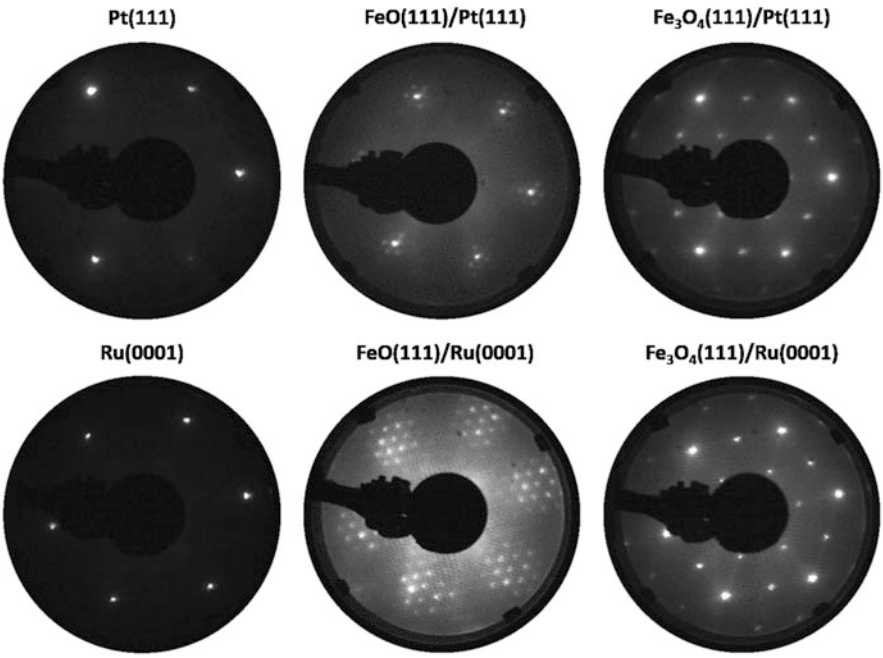

Fig. 32.1 LEED patterns of Pt(111) and Ru(0001) single crystals, as well as FeO(111) and Fe_3O_4(111) thin films grown on these supports (90 eV)

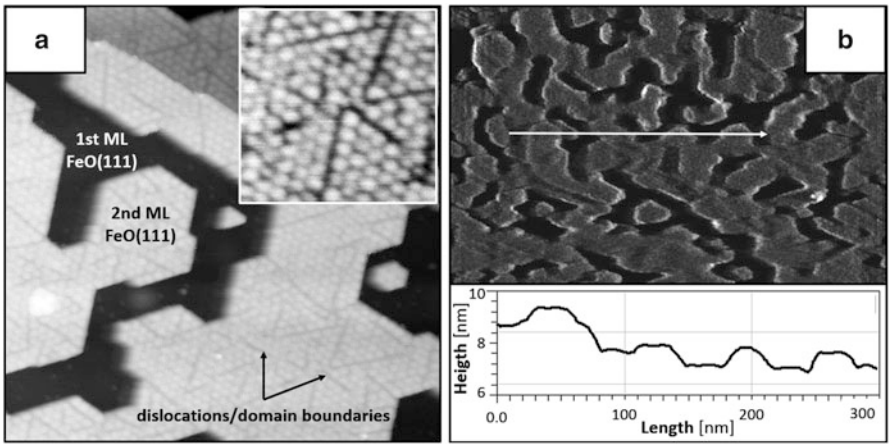

Fig. 32.2 STM images of (**a**) FeO(111)/Ru(0001) (topography, 100×100 nm^2, -0.7 V, 1.0 nA; inset: 25×25 nm^2 zoom) and (**b**) $Fe_3O_4(111)$/Ru(0001) (current, 500 nm $\times$ 380 nm, -3.0 V, 1.0 nA; inset: topography height profile) (**b**)

superstructures. $Fe_3O_4(111)$ films show (2×2) LEED patterns [6]. The patterns across the surface of all samples were uniform, indicating presence of single oxide phases for the FeO(111) and $Fe_3O_4(111)$ samples.

By analyzing the distances between the diffraction spots, we determined the surface lattice constants of the oxide films. For both FeO(111) samples, the lattice constant determined from LEED was close to the bulk value of 3.04 Å (slightly expanded), and for both $Fe_3O_4(111)$ samples the lattice constants were close to 5.94 Å, in agreement with the surface lattice constant of bulk magnetite grown in the (111) direction [6] (even though the films were only nanometer-thick).

STM image of FeO(111)/Ru(0001) is presented in Fig. 32.2a. It is known that FeO(111) grows on Ru(0001) in a double-layer form [8]. For this sample, the Ru (0001) substrate was covered with a non-complete FeO(111) double layer. A clear epitaxial relation could be observed, as the edges of the FeO(111) islands were running along the crystallographic directions of Ru(0001). The Moiré structure and the dislocations/domain boundaries were also clearly visible. These additional structural features most probably originate from epitaxial strain [10]. The non-uniform structure of FeO(111)/Ru(0001) may influence the growth of thicker iron oxide films. The surface topography of $Fe_3O_4(111)$/Ru(0001) samples prepared in our laboratory is presented in Fig. 32.2b (sum of forward and backward current images). As compared to closed films that form on Pt(111), we observed the formation of canyon-like structures on Ru(0001). The top surface of canyons/islands was atomically flat and the depth of the holes between them corresponded to a multiple of the size of Fe_3O_4 unit cell in the (111) direction (4.85 Å [6] – see the height profile under the STM image; the profile was taken from the sum of forward and backward topography images).

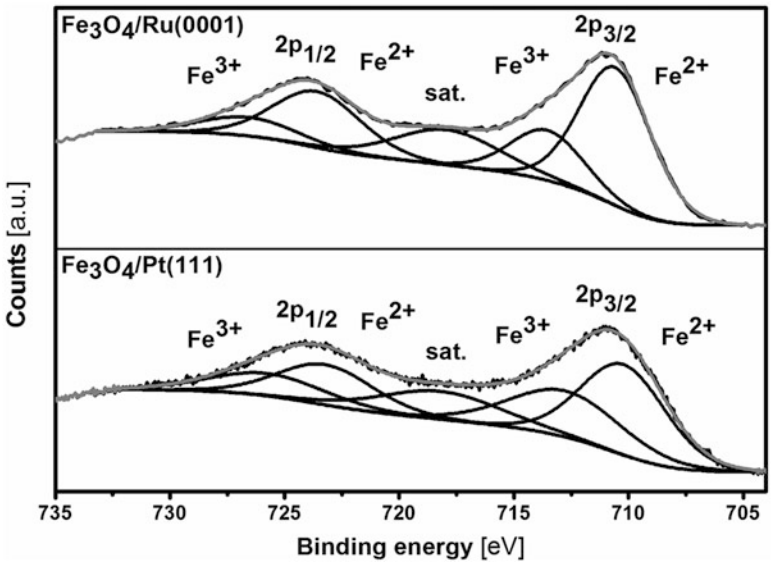

Fig. 32.3 XPS Fe2p spectra of Fe_3O_4(111)/Pt(111) and Fe_3O_4(111)/Ru(0001) (AlKα)

The fact that the films prepared by our group had different morphology than the films prepared by Ketteler et al. [7], could be due to slightly different preparation conditions, however, we got the same characteristic (2 × 2) LEED pattern.

Since a (2 × 2) LEED pattern could potentially also origin from γ-Fe_2O_3(0001) [11], we performed XPS studies trying to determine the phase of prepared iron oxides reflected in a Fe^{2+}:Fe^{3+} ratio. The XPS spectra recorded for Fe_3O_4(111)/Pt (111) and Fe_3O_4(111)/Ru(0001) samples are presented in Fig. 32.3. They confirm the presence of iron in Fe^{2+} and Fe^{3+} oxidation states for both samples, which is characteristic for magnetite. The magnetite film on Ru(0001) exhibited much more Fe^{2+} iron ions (73 % Fe^{2+} vs. 27 % Fe^{3+}), as compared to magnetite on Pt(111) (60 % vs. 40 %). This could be due to the formation of a thicker FeO(111) interface layer, as on Ru(0001) FeO(111) can be grown up to a thickness of 4 ML [7], while on Pt(111) only up to ~2.5 ML [6].

32.4 Conclusions

We prepared thin iron oxide films on Pt(111) and Ru(0001) and studied their structure using STM, LEED and XPS. The structure of FeO(111) depends on the parameters of the metal support and may further influence the structure of thicker iron oxide films, such as Fe_3O_4(111), that are being grown on top of it. We speculate that the canyon-like morphology of Fe_3O_4(111)/Ru(0001) origins from the complex structure of the FeO(111)/Ru(0001), which is in turn driven by epitaxial strain.

However, it has to be kept in mind that the structure of thicker iron oxide films on Pt (111) and Ru(0001) may not only be determined by the lattice mismatch/epitaxial strain at the interface, but also other effects, such as work function changes/charge transfer [12], surface energy/polarity effects [13] or diffusion of metal atoms into the crystal support [14, 15].

Acknowledgments This work was financially supported by the Polish Ministry of Science and Higher Education (Iuventus Plus programme, 2012–2015, grant No. IP2011 030071 – Ru(0001) part) and by the National Science Centre of Poland (SONATA programme, 2013–2016, grant No. 2012/05/D/ST3/02855 – Pt(111) part). S.J. acknowledges the support of the National Centre for Research and Development (PBS programme, 2012–2015, grant No. PBS1/A9/13/2012). M.L. would like to thank the Foundation for Polish Science for the START scholarship.

References

1. Lee EH (1974) Catal Rev Sci Eng 8:285
2. Sun C, Lee JSH, Zhang M (2008) Adv Drug Deliv Rev 60:1252
3. Chertok B, Moffat BA, David AE, Yu F, Bergemann C, Ross BD, Yang VC (2008) Biomaterials 29:487
4. Sun Y-N, Qin Z-H, Lewandowski M, Carrasco E, Sterrer M, Shaikhutdinov S, Freund H-J (2009) J Catal 266:359
5. Sun Y-N, Giordano L, Goniakowski J, Lewandowski M, Qin Z-H, Noguera C, Shaikhutdinov S, Pacchioni G, Freund H-J (2010) Angew Chem Int Ed 49:4418
6. Weiss W, Ranke W (2002) Prog Surf Sci 70:1
7. Ketteler K, Ranke W (2003) J Phys Chem B 107:4320
8. Monti M, Santos B, Mascaraque A, Rodríguez de la Fuente O, Niño MA, Menteş TO, Locatelli A, McCarty KF, Marco JF, de la Figuera J (2012) Phys Rev B 85:020404(R)-1
9. Horcas I, Fernandez R, Gomez-Rodriguez JM, Colchero J, Gomez-Herrero J, Baro AM (2007) Rev Sci Instrum 78:013705
10. Shen J, Johnston S, Shang S, Anderson T (2002) J Cryst Growth 240:6
11. Monti M, Santos B, Mascaraque A, Rodríguez de la Fuente O, Niño MA, Menteş TO, Locatelli A, McCarty KF, Marco JF, de la Figuera J (2012) J Phys Chem C 116:11539
12. Nilius N, Rienks EDL, Rust H-P, Freund H-J (2005) Phys Rev Lett 95:066101-1
13. Noguera C (2000) J Phys Condens Matter 12:R367
14. Duan Z, Wang G (2011) Phys Chem Chem Phys 13:20178
15. Cęgiel M, Bazarnik M, Biskupski P, Winiarz S, Gutek J, Boś A, Suto S, Mielcarek S, Wawro A, Czajka R (2008) Appl Surf Sci 254:6948

Chapter 33
Physical Properties of Bi_2Te_3 Nanolayers

R. Zeipl, M. Jelínek, M. Vlček, T. Kocourek, J. Vaniš, and J. Remsa

Abstract The properties of very thin Bi_2Te_3 (nano-) layers of different thickness prepared by pulsed laser deposition at different fluences are presented. Thermoelectric properties such as the thermal conductivity, the in-plain electrical conductivity, the Seebeck coefficient and also crystallinity, composition and morphology are presented. The surface properties were studied by atomic force microscopy.

Keywords Thermal conductivity • Thermoelectric materials • Thin layers • Pulsed laser deposition

33.1 Introduction

Thermoelectric structures in form of thin layers and multilayers are potential candidates for many thermoelectric applications and nano devices from solid-state coolers and generators, thermoelectric transducers, thermocouples to thermal sensors and detectors.

Bismuth and tellurium compounds, such as Bi_2Te_3, prepared in a form of very thin layers (nanolayers) have been well established candidates for many

R. Zeipl (✉)
Institute of Physics, Academy of Sciences of the Czech Republic, v.v.i., Na Slovance 2, 18221 Prague, Czech Republic
e-mail: zeipl.radek@gmail.com

M. Jelínek • T. Kocourek • J. Remsa
Institute of Physics, Academy of Sciences of the Czech Republic, v.v.i., Na Slovance 2, 18221 Prague, Czech Republic

Faculty of Biomedical Engineering, Czech Technical University, nám. Sitna 3105, 27201 Kladno, Czech Republic

M. Vlček
Institute of Macromolecular Chemistry, Academy of Sciences of the Czech Republic, v.v.i., Heyrovského nám. 2, 16206 Prague, Czech Republic

J. Vaniš
Institute of Photonics and Electronics, Academy of Sciences of the Czech Republic, v.v.i., Chaberská 57, 18251 Prague, Czech Republic

P. Petkov et al. (eds.), *Nanoscience Advances in CBRN Agents Detection, Information and Energy Security*, NATO Science for Peace and Security Series A: Chemistry and Biology, DOI 10.1007/978-94-017-9697-2_33

thermoelectric applications. Knowledge of the thermoelectric properties of such materials with lateral resolution of tens of nanometres is desirable.

We have already been working for some time on the development of a simple and reliable method to characterize the relative thermal conductivity of thin thermoelectric layers and multi-layered structures using a scanning thermal microscope working in constant current active DC and AC modes. For our experiments we need high quality thermoelectric layers and nanolayers with thermal conductivities in the range from about one-tenth to a few tens of $Wm^{-1}\,K^{-1}$ with a very smooth surface. An increased surface roughness might cause inaccuracy and create difficulties, such as artefacts, when using any scanning probe microscopy measurement technique, including thermal microscopy.

As a suitable thermoelectric material for our experiments we have chosen Bi_2Te_3 nano layers which were successfully prepared by several deposition methods including pulsed laser deposition (PLD) in the past [1–9].

Systematic studies to find the experimental conditions leading to polycrystalline stoichiometric thin films of Bi_2Te_3 by PLD were performed [3]; some were focused on the difficulties arising from the differences of vapour pressure between Te and Bi; it was reported that the type of substrate has no influence on film stoichiometry and crystallinity, but highly oriented growth can be achieved on mica due to van der Waals epitaxy [1]. Glass substrates and room temperature fabrication of n-type Bi_2Te_3 thin films using PLD was reported [4]; even operational thermoelectric devices (generating electric power) using c-axis oriented Bi_2Te_3 and $Bi_{0.3}Sb_{1.7}Te_3$ films on the same substrate were fabricated [5]. Systematic characterization of the film structures have demonstrated that a low laser pulse rate is the key to achieve epitaxial films [6]. Others focused more on studying the thermoelectric transport properties of Bi-Te thin films with different structures and morphologies [7]; a modified PLD process was used to enhance the nanostructure generation inside Bi_2Te_3 nanocrystals [8].

In this paper we present investigations on the influence of the main deposition conditions including the substrate temperature T_S and the fluence F on the quality of layer surface. X-ray diffraction (XRD) patterns, the composition obtained by energy dispersive X-ray analysis (EDX) and wavelength dispersive X-ray analysis (WDX), and the surface morphology revealed by atomic force microscopy (AFM) of the layers are presented.

33.2 Experimental

33.2.1 Layers Preparation

Two series of layers were prepared to study the influence of PLD deposition conditions on the resulting layer surface quality; the aim was to obtain the smoothest surface. The layer thickness was in range from 230 nm to 500 nm on

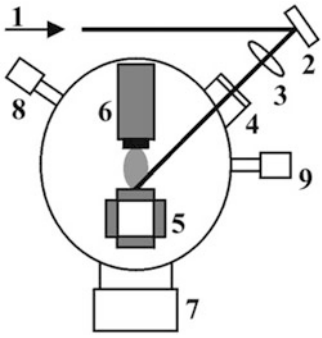

Fig. 33.1 The basic scheme of the PLD apparatus: (*1*) laser beam, (*2*) mirror, (*3*) focusing lens, (*4*) quartz window, (*5*) target holder, (*6*) substrate holder, (*7*) vacuum pump, (*8*, *9*) Pirani and Penning vacuum gauges, respectively

Si (100) substrates prepared from a Bi_2Te_3 target. The first series of layers was deposited at a substrate temperature $T_S = 360$ °C applying various laser fluence F (1, 2, 3, 4 and 5 Jcm^{-2}). The original choice of T_S was selected based on previously published experiments reporting smooth and crystalline Bi_2Te_3 layers [1, 2]. The second series layers were prepared at different T_S (200 °C, 250 °C, 300 °C and 400 °C), applying the same $F = 3$ Jcm^{-2}, which was chosen based on the results obtained from the first series.

The starting polycrystalline Bi_2Te_3 material was synthesized from elemental Bi and Te of 5 N purity in evacuated silica ampoules at 1,073 K for 48 h. After verification of the homogeneity of the compound by means of X-ray powder diffraction, the polycrystalline ingot was crushed using an agate mortar and sieved to obtain particle sizes below 100 μm. The targets for PLD deposition of 20 mm in diameter and 2 mm in height were prepared by the hot pressing method (temperature 500 °C, pressure ~60 MPa for 1 h). The density of the pressed targets reached about 96–98 % of the theoretical density.

The basic schema of the experimental apparatus for PLD is depicted in Fig. 33.1. Conceptually and experimentally, PLD is a very simple method. A high power pulsed excimer KrF laser (COMPexProTM 205 F, $\lambda = 248$ nm, $\tau = 20$ ns) (1) is used as an external energy source to vaporize material of the target (5) and to deposit a thin film. A set of optical components is utilized to focus the laser beam on the target surface (2, 3). After the laser pulse irradiation the temperature rises very rapidly (10^{11} Ks^{-1}) and the evaporation becomes non-equilibristic.

For our experiments the substrates were cleaned from mechanical dirt in an ultrasonic cleaner. Next the substrates were subsequently cleaned in ethyl alcohol, acetone and toluene. Cleaning in the vapour of boiling ethyl alcohol completed the process. A Si (100) wafer was cut to approximately 10×10 mm square shaped substrates. The substrates were finally annealed in an oven at a temperature of around 250 °C. Deposition took place in Ar atmosphere (13 Pa), the target to substrate distance was set to 40 mm, the base vacuum of the coating system was 5×10^{-3} Pa. In our case, we used a repetition rate of 10 Hz and a laser spot of 2×1 mm^2.

33.2.2 Characterization

Thickness and roughness of the layers were measured by an Alpha-step IQ mechanical profilometer (KLA TENCOR Co.). The uncertainty in the thickness estimation is about 10 % in the examined range of thicknesses which is partly due to the fact that the layer thickness in the centre of the sample is higher than at its rim.

The layer roughness and homogeneity were characterized by AFM (Solver NEXT NT-MDT) operating in the dynamic regime with HA_NC tips and in contact mode with CSG10 tips. The layers surface parameters were calculated from 50×50 μm area with software NOVA PX.

EDX and WDX analyses were realized with a X-ray microanalyser JXA-733 (JEOL) and was evaluated with the software from SAMxMonocrystalline Bi_2Te_3 was used as a standard.

33.3 Results and Discussion

EDX and WDX were performed on several layers prepared at $T_S = 360$ °C, $F = 5$ Jcm^{-2} to obtain information on the layer stoichiometry. An excess of Bi (Bi/Te ratio ~ 0.76) in comparison to the target Bi_2Te_3 stoichiometry (Bi/Te ratio ~ 0.67) was observed in all explored layers. The standard deviation was found to be ±1.5 %. Different deposition conditions or a different target would have to be selected to obtain the exact Bi_2Te_3 stoichiometry, which is, however, not necessary in our experiment. Our aim was to prepare thermoelectric layers with the smoothest surface possible. Thus, more valuable for us was the observation of a very granular surface covered with crystals of different dimensions.

The surface roughness of all layers was studied by AFM (scanned area 50×50 μm) and checked by a mechanical Alpha-step profilometer. The results of these measurements are summarized in Table 33.1.

Table 33.1 A comparison of surface roughness S_a (R_a) and its RMS value for each nanolayer measured byan Alpha-step mechanical profilometer and AFM

Deposition conditions		Thickness	Profilometer	AFM	
T_S [°C]	F [Jcm^{-2}]	[nm]	S_a (R_a) [nm]	S_a (R_a) [nm]	S_q (RMS) [nm]
360	5	271	1.62	8.76	11.23
360	4	309	1.86	9.81	12.71
360	3	329	1.61	7.72	10.13
360	2	311	1.77	9.46	12.95
360	1	494	10.47	Not measurable	
400	3	321	10.82	56.93	38.64
300	3	293	1.76	9.01	6.4
250	3	302	0.97	7.65	5.31
200	3	226	0.84	3.9	2.91

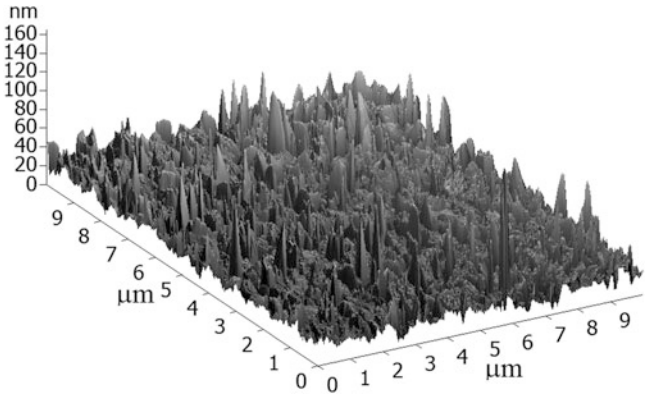

Fig. 33.2 AFM 3D surface visualization of the surface (detail area 10×10 um) of the layer prepared at $T_S = 300$ °C, $F = 3$ Jcm^{-2}, where crystals and droplets peaking over the surface are visible

Generally there are two types of objects observed on the layer surface. The first are regularly shaped crystals of Bi_2Te_3 or $Bi_{(2+N)}Te_{(3+M)}$ compounds, ranging in size from about 100 to 500 nm. These create a basic surface and were proved to be crystalline by XRD measurements. Usually the crystals peak less than 200 nm above the surface, as can be seen in the 3D surface visualization depicted in Fig. 33.2. The second are so-called PLD droplets. They are much more spread over the surface and much less frequent in comparison to the first type. The problem is that they are unfortunately much larger. Their height reaches 400 nm and their diameter is in the range of 200–300 nm.

The influence of the laser beam density on the surface roughness appears to be negligible, however the smoothest surface was observed applying $F = 3$ Jcm^{-2} (see Table 33.1).

The impact of the substrate temperature is more important (see Table 33.1). With increased T_S the layers become rougher. This was visible by eye for the layer prepared at $T_S = 400$ °C. This layer had a different colour (matt white) in comparison to the other layers which are usually silver and shiny. The same trend of dependencies was observed using AFM as well as a mechanical profilometer (see Table 33.1). The resulting values are different which is expected, due to the use of different methods which measure different kind of roughnesses.

In general the layers were homogeneous from a macro point of view (the AFM scans were performed on several different positions over the whole surface; the roughness and granularity remains the same).

The smoothest ($T_S = 200$ °C, 3 Jcm^{-2}) and the roughest ($T_S = 360$ °C, 4 Jcm^{-2}) layer surface is depicted in Fig. 33.3. It is important to emphasise that these deposition conditions might not be optimal for the thermoelectric properties point of view, as they may influence the layer stoichiometry.

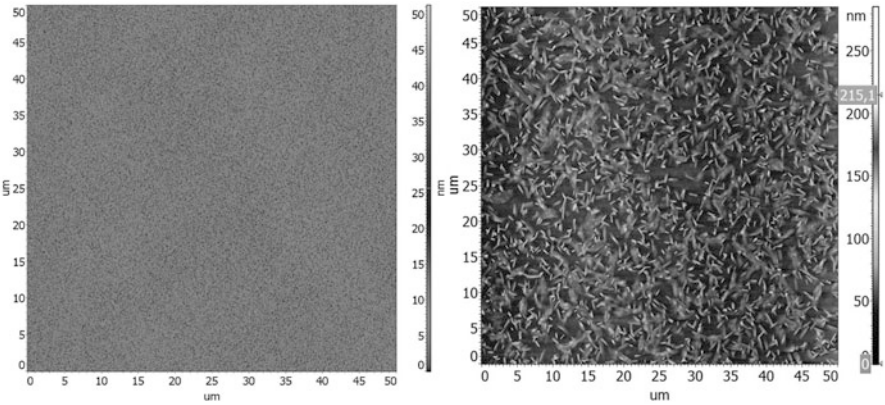

Fig. 33.3 AFM surface morphology of the smoothest (*left*) nanolayer prepared at $T_S = 200$ °C applying $F = 3$ Jcm^{-2} and of the roughest (*right*) layer prepared at $T_S = 360$ °C applying $F = 4$ Jcm^{-2}. The layer prepared at $T_S = 360$ °C applying $F = 1$ Jcm^{-2} was not measurable at all

33.4 Conclusions

The influence of the deposition conditions – the substrate temperature and the laser beam density – on the quality of the surface (homogeneity and roughness) was analysed for thermoelectric nanolayers prepared by PLD from a Bi_2Te_3 target. The smoothest layers were deposited at $T_S = 200$ °C while applying $F = 3$ Jcm^{-2}. Such deposition conditions may not be optimal from thermoelectric properties point of view, since the layer stoichiometry is influenced by the deposition conditions. The measurement of the thermoelectric properties has not been accomplished yet.

Acknowledgments This work was supported by the Grant Agency of the Czech Technical University in Prague, grants No. SGS14/168/OHK4/2T/17 and SGS13/220/OHK4/3T/14, and by Czech Grant Agency under P108/13-33056S.

References

1. Dauscher A, Thomy A, Scherrer M (1996) Thin Solid Films 280:61
2. Zeipl R, Karamazov S, Jelínek M, Lošťák P, Pavelka M, Winiarz Sz, Czajka R, Vaniš J, Šroubek F, Zelinka J, Walachová J (2003) Proceedings of the 22nd international conference on thermoelectrics, La Grande Motte, 17–21 August, p 342
3. Bailini A, Donati F, Zamboni M, Russo V, Passoni M, Casari CS, Li Bassi A, Bottani CE (2007) Appl Surf Sci 254:1249
4. Yu Z, Wang X, Du Y, Aminorroaya-Yamni S, Zhang C, Chuang K, Li S (2013) J Cryst Growth 362:247
5. Higomo S, Obara H, Yamamoto A, Ueno K, Iida T (2007) ICT 2007, 26th international conference on thermoelectrics, p 78. doi:10.1109/ICT.2007.4569428

6. Zhang SX, Yan L, Qi J, Zhuo M, Wang Y-Q, Prasankumar RP, Jia QX, Picraux ST (2012) Thin Solid Films 520:6459
7. Li Bassi A, Bailini A, Casari CS, Donati F, Mantegazza A, Passoni M, Russo V, Bottani CE (2009) J Appl Phys 105:124307
8. Lu Y, Knize RJ (2007) Appl Surf Sci 254:1211
9. Walachová J, Zeipl R, Zelinka J, Malina V (2005) Appl Phys Lett 87:081902

Chapter 34
Effect of the Ge Concentration on the Photoformation of Solid Electrolytes in Ag/As-S-Ge Thin Films

I. Stratan, M. Ciobanu, and D. Tsiulyanu

Abstract Solid electrolytes in the system Ag/As-S-Ge have been fabricated by Ag photodissolution into glassy thin As-S-Ge films of various composition. To realize the transition from a trigonal to a tetragonal structure of the network, the concentration of Ge was increased monotonically, along with a decreased As concentration. The process of Ag photodissolution into the films, followed by the formation of solid electrolytes was controlled by monitoring the changes that occur in the optical transmission of broadband light which is only weakly absorbed in Ag/As-S-Ge. The probing wavelength was $\lambda > 0.65$ μm ($h\nu < 1{,}9$ eV), the range in which the chalcogenide glasses (ChG) used are entirely transparent. It was shown that the kinetics profiles comprise of two consecutive linear steps, but the transition between these steps is not monotonic. The photodissolution rate and the amount of Ag incorporated in the first step were found (except of GeS_4) not to depend on the glass composition. This result provides evidence for a preferential and direct interaction of Ag with free sulfur at the interface. The rate of photodissolution in the second linear step exhibits a maximum for compounds with approximately 8 at. % Ge, being by two orders of magnitude higher than the rate for GeS_4. This maximum was qualitatively attributed to the fact that only a few, very specific Ag-photodoped glass compositions yield a homogeneous material.

Keywords Chalcogenides • Ag • Photodissolution • Solid electrolytes

34.1 Introduction

Photodissolution (PD) of metals (e.g. Ag) in chalcogenide glasses (ChG) has a considerable potential to be applied in high-resolution lithography [1] and Programmable Metallization Cell technologies [2, 3] due to the formation of solid ChG-Ag mixtures with a high ionic conductivity (superionic conductors) [4].

I. Stratan • M. Ciobanu (✉) • D. Tsiulyanu
Department of Physics, Technical University, bul. Dacia 41, MD-2060 Chisinau, Moldova
e-mail: ciobmarina@gmail.com

P. Petkov et al. (eds.), *Nanoscience Advances in CBRN Agents Detection, Information and Energy Security*, NATO Science for Peace and Security Series A: Chemistry and Biology, DOI 10.1007/978-94-017-9697-2_34

At the present time, only a few investigations are devoted to study the influence of the composition on the PD process, and these only for binary systems. Investigating the compositional dependences of the PD rate and the total amount of photodissolved Ag in glassy Ge_xS_{1-x} ($21 < x < 45$), Kawaguchi and Maruno [5] have shown a high PD rate of Ag in both S- and Ge-rich glasses, with the minimum for the composition GeS_2, known as the composition at which the threshold of the elastic and other properties is found [6, 7]. At the same time, the total amount of silver able to be adopted follows a vice-versa law: S- and Ge-rich glasses adopt a relatively low amount of Ag, but the maximum incorporation of Ag is found for GeS_2.

In the present work, we report how the addition of Ge to As – S-based chalcogenides, followed by a transition from a threefold coordinated As-based backbone to a fourfold coordinated Ge-based structure, influences the PD process and the formation of superionic films.

34.2 Experimental

The glassy alloys were prepared by melt-quenching of pure (99, 99 %) As, S and Ge in quartz ampoules evacuated to 5×10^{-5} Torr. The mixture was melted at 700–1,000 °C depending on the composition; thereafter the ampoules were quenched in air or on a copper refrigerator with running water.

Seven compositions have been synthesized, steadily increasing the concentration of Ge while decreasing that of As. They are shown in Table 34.1 together with values of the optical gaps E_g of the ChG materials [8]. The ChG thin films have been prepared by thermal "flash" evaporation of previously synthesized materials onto Pyrex glass substrates at room temperature. The evaporation was performed from a tantalum boat at a working pressure of 10^{-4} Pa. The thickness of the films was around 1 μm, the area of deposition about 1,5 cm^2. Silver films were deposited also by thermal evaporation in vacuum on top of the chalcogenide films, immediately (with breaking the vacuum) after their preparation. The thickness of the silver films (controlled by the equivalent quantity of evaporated Ag) was kept constant at about 50 nm.

Table 34.1 Composition, optical gap and rate of Ag photodissolution in As-S-Ge glasses in the second stage of the PD process

Nr.	Composition	E_g [eV]	Ge [at.%]	As [at.%]	ν [nm/s]
1	AsS_3	2.54	0	25	0.022
2	$As_{0.263}Ge_{0.053}S$	2.56	4.03	20	0.36
3	$As_{0.2}Ge_{0.1}S$	2.59	7.69	15.4	0.41
4	$As_{0.143}Ge_{0.143}S$	2.61	11.2	11.1	0.245
5	$As_{0.09}Ge_{0.182}S$	2.66	14.31	7.1	0.24
6	$As_{0.04}Ge_{0.217}S$	2.69	17.3	3.2	0.162
7	GeS_4	2.75	20	2	0.0034

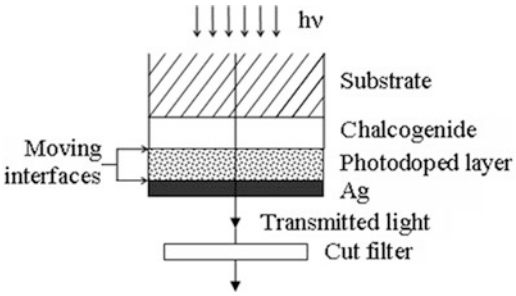

Fig. 34.1 Schematic cross-section through a sample during the photodissolution process

The PD of silver onto ChG was performed by illuminating the Ag film on top of the multilayer structure, using the light of a 100 W halogen lamp focused by a quartz lens onto the transparent side of the substrate (Fig. 34.1). The incident power was measured by vacuum thermo element VTh-8 (Carl Zeiss, Germany) and estimated at the sample surface to 250 mW/cm^2.

The process of Ag photodissolution into the films in question, followed by formation of solid electrolytes, has been studied by monitoring the changes of the transmission in the weakly absorbing spectral range of the Ag/As-S-Ge using broadband light with wavelengths $\lambda > 0.65$ μm ($h\nu < 1{,}9$ eV). For this purpose a cut filter (KC-15) with a transparency range of 650–3,000 nm was placed behind the sample, i.e. in front of the photomultiplier, which served as a light detector. A PC with a data acquisition board manufactured by National Instruments Inc. was used for processing. The measurements were carried out at room temperature.

Figure 34.1 shows schematically the multilayer structure of the sample. There are three well-defined boundaries: (1) substrate/undoped ChG; (2) undoped ChG/photodoped material (solid electrolyte); (3) photodoped material/Ag.

In the present work we traced the movement of the boundary between the photodoped material and the Ag layer by measuring the transmission of the ChG with PD of silver in progress.

The PD rate of Ag was estimated by measuring the recovery rate of the optical transmission of the two-layer structure ChG/Ag in the IR region [9], using the known dependence of the transmittance of the Ag film on its thickness [10].

34.3 Results and Discussion

Figure 34.2 shows the optical transmission of the two-layered structure ChG/Ag (broadband light $\lambda > 0.650$ μm) as a function of the exposure time as the PD proceeds at room temperature. The number of each curve corresponds to the samples listed in Table 34.1. The shaded area indicates the transmittance of pure chalcogenide film, i.e. without Ag layer. It can be seen that independent of the composition the transmission of the two-layer structures in the region of weak absorption recovers to that of pure ChG, i.e. before deposition of the Ag layer.

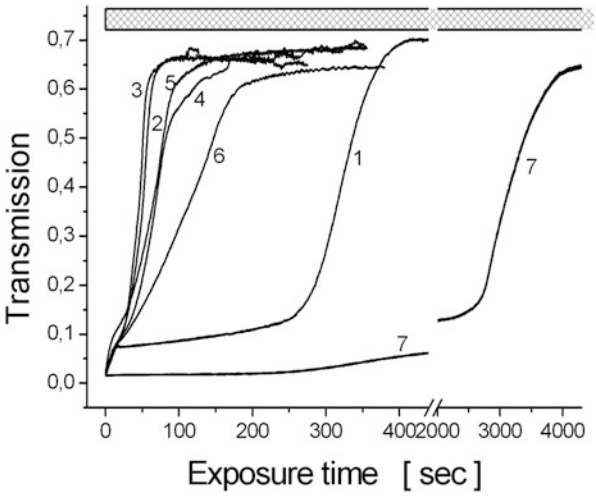

Fig. 34.2 Transmission of a broadband light $\lambda > 0.65$ μm of two-layered structures vs. exposure time

Obviously, this is due to a decrease of the effective thickness of the Ag layer. Except for GeS_4, an incubation period was not observed for the other compositions in this experiment. On the contrary, a very sharp rise of the transmittance was observed at early stages of the PD process. Note that a similar behavior, i.e. a high rate of Ag photodissolution, could be observed for glassy As_2S_3 only at enhanced temperatures (>75 °C) [9]. Further, this fast rise turns into a composition dependent shoulder, followed by a transition to the usual monotonic increasing of transmittance as the PD proceeds.

Figure 34.3 shows the thickness of the unreacted Ag layer (with error bars displayed) as a fuction of the exposure time for several compositions of ChG calculated with the method described above. For all compositions, except of GeS_4, three stages of PD kinetics can clearly be distinguished: (I) the first, very sharp step is nearly independent of the composition but the thickness of Ag layer linearly decreases with exposure time; (II) the second step is a linear shoulder with a slope (the PD rate) strongly influenced by the ChG composition; (III) the final step exhibits an weak sublinear dependence of the change of the thickness of the Ag layer on time, particularly observed for GeS_4.

Figure 34.4a shows the PD rate at the first linear step, for the glassy materials applied in the present investigation. As one can see from the figure, the PD rate of about 2.0 nm/s is several times higher than for As_2S_3 [9] under the same conditions and, more important, with the exception of GeS_4, the PD rate does not vary much with the glass composition. Obviously, this is due to the characteristics of multicomponent and/or nonstoichiometric chalcogenide glasses, originated from their compositional and structural complexity.

We assume that the availability of free sulfur in all examined glasses explains both the PD high rate of the first linear step and its weak dependence on the composition. The silver dissolution starts at the interface by chemical reactions between free sulfur and neutral Ag, which results in the formation of a sufficient

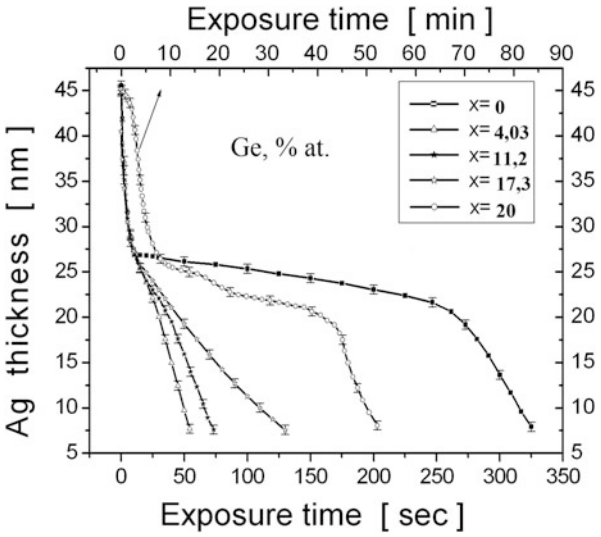

Fig. 34.3 Decrease of Ag film thickness versus exposure time for several compositions of the ChGs

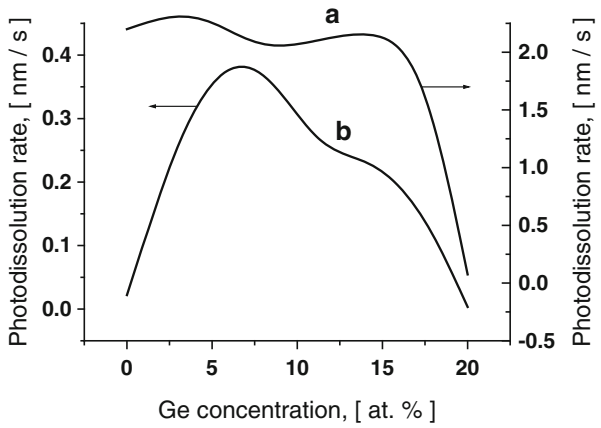

Fig. 34.4 The photodissolution rate during the first (**a**) and the second (**b**) linear steps versus the glass composition

amount of Ag_2S connected in the glass backbone. As a result, the percolation threshold is reached in the layer at the interface along with its transition to superionic conductivity [11]. Only small differences in the concentration of free sulfur in the compositions used results in the overlap of the kinetics curves in the first stage of PD, as well as in their identical width.

The second step of the PD kinetics (Fig. 34.3) also shows a linear dependence of the change of the Ag thickness with time (constant PD rate), but its slope strongly depends on the glass composition. The variation of the PD rate with composition, determined from the slope of the second step, is shown in Fig. 34.4b. As the Ge content is increased, the PD rate increases to a maximum at about 7.7 at.% Ge and then decreases. The maximum and minimum rates differ by a factor of 20 if the pure GeS_4 is not considered. We assume that the maximum of the photodissolution rate

for the composition $As_{0.2}Ge_{0.1}S$ is due to the change in the morphology of this glassy material i.e. its homogenization. A homogeneous backbone promotes the transport of both electrons and ions involved in the photoreaction because of the lack of phase boundaries and additional defects.

34.4 Conclusions

The kinetics profiles of Ag photodissolution in As-S-Ge glasses consist of two consecutive linear steps. The Ge concentration in the backbone does not influence the slope of the first very sharp step (rate ~ 2 nm/s) of the PD. This step is ascribed to direct interaction of Ag with free sulfur in the glassy material at the interface. The PD rate of the second linear step shows a maximum at about around 7.7 at.% Ge. It is assumed that this composition yield a homogeneous reaction product.

Acknowledgements This work is supported by SCSTD of the Academy of Sciences of Moldova, project 11.817.05.21A.

References

1. Tsiulyanu D (2004) In: Lucovsky G, Popescu M (eds) Non-crystalline for optoelectronics. INOE, Bucharest, p 297
2. Stratan I, Tsiulyanu D, Eisele I, Optoelectr J (2006) Adv Mater 8:2117
3. Mitkova M, Kozicki MN (2004) In: Lucovsky G, Popescu M (eds) Non-crystalline for optoelectronics. INOE, Bucharest, p 201
4. Plooccharski J, Przyluski J, Teodorezyk M (1987) J Non-Cryst Solids 93:303
5. Kawaguchi T, Maruno S (1992) J Appl Phys 71:2195
6. Tsiulyanu D, Dragich AD, Gumeniuk NA (1993) J Non-Cryst Solids 155:180
7. Tanaka K (1989) Phys Rev B 39:1270
8. Tsiulyanu D, Gumenyuk NA (1990) J Appl Spectrosc 52:625
9. Tsiulyanu D, Stratan I (2010) J Non-Cryst Solids 356:147
10. Sun X, Hong R, Hou H, Fan Z, Shao J (2007) Thin Solid Films 515:6962
11. Balan V, Piarristeguy A, Ramonda M, Pradel A, Ribes M (2006) J Optoelectron Adv Mater 8:2112

Chapter 35
Optical and Thermal Properties of the System $Bi_2(Se_{1-x}Te_x)_3$

A. Adam, E. Lilov, and P. Petkov

Abstract Samples from the $Bi_2(Se_{1-x}Te_x)_3$ system, where $x = 0$, 50 % and 100 mol.% have been studied with respect to their structure and properties. XRD analysis revealed a polycrystalline single phase structure of the materials. The crystallization temperature ($T_{c,p}$) and the melting temperature T_m of the samples have been determined from differential scanning calorimetric (DSC) and thermogravimetric (TGA) analyses. Thin films have been deposited from the respective bulk alloys by means of the vacuum thermal evaporation method. The thicknesses of the films, the optical constants and the optical band gap have been derived from transmission and reflection spectra.

Keywords Chalcogenide glasses • Thin films • Stress • Optical sensors

35.1 Introduction

The preparation and the physical properties of A_2B_3 (A = Bi, Sb; B = Se, Te) chalcogenide materials have been subject of investigations for more than half a century due to their interesting thermoelectric properties. The interest in these materials increased drastically in the last few years due to the discovery of 3D topological insulators [1].

Bi_2Te_3, Bi_2Se_3 and their solid solution crystals are narrow-band-gap semiconductors materials with an asymmetric band structure; they have a rhombohedral unit cell with the symmetric space group D53 (R3m) [2]. The optical band gap of Bi_2Te_3 and Bi_2Se_3 possesses values in the range from 0.13 to 1.4 eV and from 0.12

A. Adam (✉)
Physics Department, Faculty of Science, Sohag University, Sohag, Egypt

Department of Physics, University of Chemical Technology and Metallurgy, 8 Kl. Ohridski blvd., 1756 Sofia, Bulgaria
e-mail: adam_phy@yahoo.com

E. Lilov • P. Petkov
Department of Physics, University of Chemical Technology and Metallurgy, 8 Kl. Ohridski blvd., 1756 Sofia, Bulgaria

P. Petkov et al. (eds.), *Nanoscience Advances in CBRN Agents Detection, Information and Energy Security*, NATO Science for Peace and Security Series A: Chemistry and Biology, DOI 10.1007/978-94-017-9697-2_35

to 2.35 eV, respectively, as reported by various authors [3–5]. The materials show a layered structure formed by stacking of quintuple layers of mostly covalently bonded Te(1)–Bi–Te(2)–Bi–Te(1) with the neighboring layers connected by weak van der Waals bonds [6].

Many different techniques have been reported in the literatures for the deposition of Bi_2Te_3 and Bi_2Se_3 thin films such as: sputtering deposition [7], flash thermal evaporation [8], electrochemical deposition [9] and metal-organic chemical vapor deposition [10].

In the present paper we aim to study the structural and optical properties of bismuth telluride-bismuth selenide thin films deposited by vacuum evaporation from the bulk materials.

35.2 Experimental Details

35.2.1 Synthesis

Bi, Se and Te with 5 N purity were used to prepare $Bi_2(Se_{1-x}Te_x)_3$ bulk materials, where $x = 0$, 10 %, 50 % and 100 mol.%. The mixtures were transferred in a vacuum-sealed quartz ampoule and melted in a programmable furnace for 12 h at 900 °C. They were shaken several times to gain uniformity and homogeneity of the melt.

Bi-Se-Te crystalline thin films have been deposited onto cleaned glass substrates by vacuum thermal evaporation. The evaporation process was carried out from a tantalum crucible in a vacuum of 10^{-6} Torr. The substrates were rotated during the evaporation process to obtain uniform layers.

35.2.2 Characterization

The structural properties were studied by X-ray diffraction measurements (XRD) using a Philips instrument with a monocromatic Cu Kα radiation source (1.5406 Å). The scattering intensities were measured over the angular range of $10° \leq 2\theta \geq 60°$ with 0.04° steps and a counting time of 2 s per step.

Thermal analysis (STA) which consists of the simultaneous measurement of differential scanning calorimetry (DSC) and thermogravimetry (TGA) under the same conditions (atmosphere, heating rate, gases, sample preparation, etc.) was used to study the thermal behavior of the studied materials. The temperature precision of this equipment is ± 0.01 °C with an average standard error of about ± 0.5 °C. The samples were sealed and scanned at heating rates of 10 °C/min from room temperature to 800 °C. The values of the onset temperature of crystallization T_c, the peak temperature of crystallization T_{cp}, and the peak melting temperature T_m were determined from the thermal curves.

Transmission and reflection spectra of the films were measured in the wavelength range between 400 and 2,700 nm at normal incidence and ambient temperature using a double beam Jasco spectrophotometer UV–VIS-NIR (Model V-670).

35.3 Results and Discussion

The XRD patterns of Bi_2Se_3, $Bi_2Te_{1.5}Se_{1.5}$ and Bi_2Te_3 shown in Fig. 35.1 reveal the polycrystalline nature of the samples by a number of sharp diffraction peaks. The strongest and sharpest lines at $2\theta = 29.44°$ and 18.64° indicate the hexagonal phase corresponding to the (015) and (006) planes of the Bi_2Se_3, respectively. The main peak for Bi_2Te_3 observed at $2\theta = 27.719°$ corresponds to (015) as preferable orientation plane. The appearance of different peaks on the diffractogram is due to the different orientations of the crystallite structure in the corresponding sample. The shift of the main peak to $2\theta = 28.7°$ in $Bi_2Te_{1.5}Se_{1.5}$ sample suggests alloying of the material and formation of solid solution. Moreover, new peaks appear at 39.1° and 46.1° confirming the structure modification of the material.

The thermal properties of the samples investigated via DSC and TGA expose the onset temperature of crystallization T_c, the peak temperature of crystallization T_{cp} and the melting temperature T_m. The results show that thermal behavior is modified in the complex compound reflecting in higher values of the crystallization and the melting temperatures (Fig. 35.2 and Table 35.1).

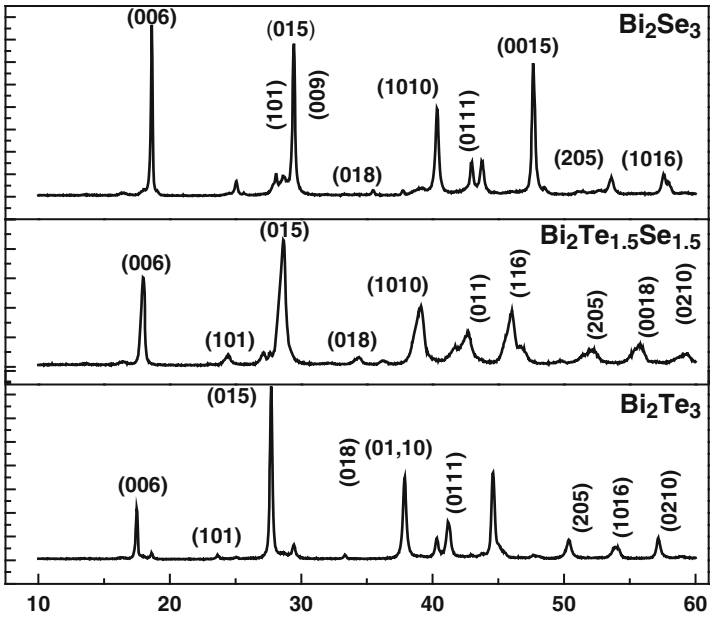

Fig. 35.1 The XRD diffraction patterns for the as-prepared Bi_2Se_3, $Bi_2Se_{1.5}Te_{1.5}$ and Bi_2Te_3 samples

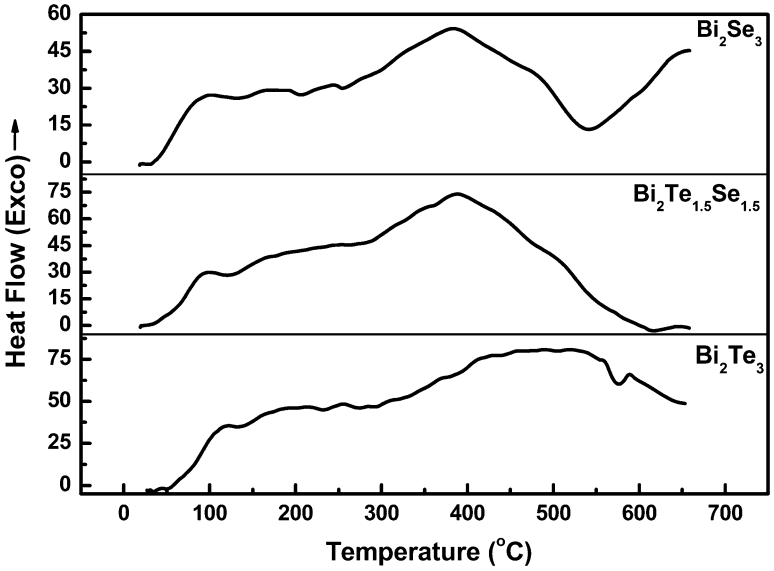

Fig. 35.2 DSC patterns of $B_{i2}Se_3$, Bi_2Te_3 and $Bi_2Te_{1.5}Se_{1.5}$

Table 35.1 The onset temperature of crystallization T_c, the peak temperature of crystallization T_{cp} and the melting temperature T_m of Bi_2Se_3, $Bi_2Te_{1.5}Se_{1.5}$ and Bi_2Te_3

Composition	T_c (°C)	T_{cp} (°C)	T_m (°C)
Bi_2Se_3	290	411	579.3
$Bi_{1.5}Te_{1.5}Se_{1.5}$	305	416	658.8
Bi_2Te_3	297	519.5	576.4

The transmission and the reflection spectra of the thin films were measured in the wavelength range from 400 to 2,700 nm. The optical band gap was calculated by means of Tauc's equation, a relation between the absorption coefficient α and the incident photon energy hν [11].

$$\alpha h\nu = B\,(h\nu - Eg)^n$$

where B is a constant related to the band tailing parameters and $n = 2$ for indirect allowed transitions.

From the plots of $(\alpha h\nu)^2$ versus hν the optical band gap has been determined by the extrapolation of the linear regions near the beginning of the absorption edge on the energy axis (Fig. 35.3). The values of the band gap energy obtained for the films are presented in Table 35.2. Most probably the higher optical band gap for the mixed composition is due to the formation of a new structure after partial substitution of selenium by tellurium. The selenium atoms are mostly 2-fold

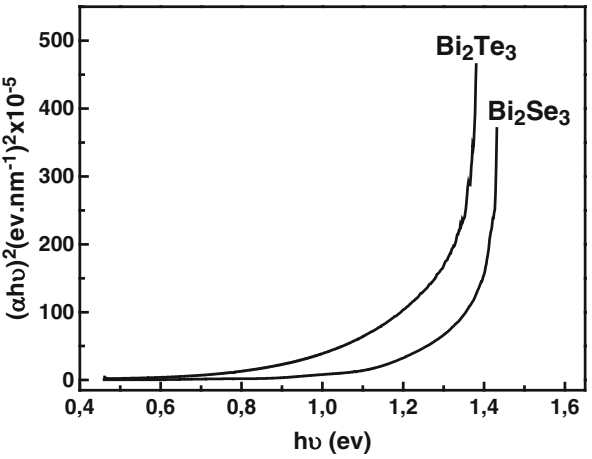

Fig. 35.3 Optical absorption vs. photon energy of Bi_2Se_3 and Bi_2Te_3

Table 35.2 Optical band gap of Bi_2Se_3, $Bi_2Te_{1.5}Se_{1.5}$ and Bi_2Te_3

Compound	Optical band gap (eV)
Bi_2Se_3	1.379
$Bi_2Te_{1.5}Se_{1.5}$	1.381
Bi_2Te_3	1.341

coordinated while the tellurium are 4-fold coordinated. The substitution facilitates the formation of "wrong" dangling bonds and the appearance of unsaturated bonds in the alloy.

35.4 Conclusions

Samples of Bi_2Se_3, $Bi_2Te_{1.5}Se_{1.5}$ and Bi_2Te_3 prepared by the melt quenching method possess a polycrystalline structure. The structure of the alloys is modified after the substitution of selenium atoms by tellurium in the solid solution formed. The substitution and the new structure formed define the different thermal behavior and the optical band gap variation of the mixed composition.

References

1. Zhang H, Liu C-X, Qi X-L, Dai X, Fang Z, Zhang S-C (2009) Nat Phys 5:438
2. Kulbachinski VA, Yu Kaminski A, Kindo K, Narumi Y, Sugak S (2002) Phys Status Solidi B 22:146
3. Dheepa J, Sathyamorthy R, Velumino S (2007) Mater Charact 58:782
4. Snbramanian S, Pathinathan D (2008) Mater Chem Phys 107:392

5. Soliman LI, Nassary MM, Shaban HT, Salwa AS (2010) Vacuum 85:358
6. Chen J, Zhou X, Uher C, Shi X, Jun J, Dong H, Li Y, Zhou Y, Wen Z, Chen L (2013) Acta Mater 61:1508
7. Kim DH, Byon E, Lee GH, Cho S (2006) Thin Solid Films 510:148
8. Goncalves LM, Couto C, Alpuim P, Rolo AG, Volklein F, Correia JH (2010) Thin Solid Films 518:2816
9. Li SH, Toprak MS, Soliman HMA, Zhou J, Muhammed M, Platzek D et al (2006) Chem Mater 18:3627
10. Boulouz A, Giani A, Pascal-Delannoy F, Boulouz M, Foucaran A, Boyer A (1998) J Cryst Growth 194:336
11. Tauc J (1979) Amorphous and liquid semiconductors. Plenum, New York

Part IX
Materials: Glasses and Polymers

Chapter 36
Samarium Doped Borophosphate Glasses and Glass-Ceramics for X-ray Radiation Sensing

D. Tonchev, I. Kostova, G. Okada, T. Pashova, G. Belev, G. Patronov, T. Eftimov, T. Wysokinski, D. Chapman, and S.O. Kasap

Abstract Samarium fluoride (SmF_3) and samarium oxide (Sm_2O_3) doped Zn- and Sr-borophosphate glasses with mixed oxide-fluoride matrix structures were prepared. The synthesized materials were studied by differential scanning calorimetry (DSC) and temperature-modulated DSC (TMDSC) to determine their glass transformation properties before and after various thermal treatments. X-ray diffraction (XRD) analysis was performed to characterize the structure, that is, whether the synthesized materials have a glass or polycrystalline structure, or is composed of a heterogeneous mixture. We observed that under certain conditions several post-treated materials are partially nanostructured, i.e. the formation of nanocrystals takes place within a glass matrix. The samarium doped materials were irradiated by different types of LEDs and laser light in the UV-NIR wavelength range to examine

D. Tonchev (✉) • I. Kostova
Department of Electrical and Computer Engineering, University of Saskatchewan, Saskatoon, SK S7N 5A9, Canada

Department of Chemical Technology and Department of Optics and Nuclear Physics, Plovdiv University "Paisii Hilendarski", Plovdiv 4000, Bulgaria
e-mail: dan.tonchev@usask.ca

G. Okada • S.O. Kasap
Department of Electrical and Computer Engineering, University of Saskatchewan, Saskatoon, SK S7N 5A9, Canada

T. Pashova • G. Patronov • T. Eftimov
Department of Chemical Technology and Department of Optics and Nuclear Physics, Plovdiv University "Paisii Hilendarski", Plovdiv 4000, Bulgaria

G. Belev
Department of Electrical and Computer Engineering, University of Saskatchewan, Saskatoon, SK S7N 5A9, Canada

Canadian Light Source (CLS), University of Saskatchewan, Saskatoon, SK S7N0X4, Canada

T. Wysokinski • D. Chapman
Canadian Light Source (CLS), University of Saskatchewan, Saskatoon, SK S7N0X4, Canada

P. Petkov et al. (eds.), *Nanoscience Advances in CBRN Agents Detection, Information and Energy Security*, NATO Science for Peace and Security Series A: Chemistry and Biology, DOI 10.1007/978-94-017-9697-2_36

the photoluminescence (PL) induced and also to study the changes in the PL signal before and after exposure to high-dose X-ray synchrotron irradiation due to a possible reduction of Sm^{3+} to Sm^{2+}. The different PL signatures of the two Sm-ions allow such materials to be used as x-ray dosimeters with optical readout. The X-ray induced luminescence (XL) spectra were also recorded. We discuss the experimental results in terms of established models for the behavior of rare-earths in glasses, crystalline solids and in nanocrystalline glass-ceramics.

Keywords Nano- and polycrystalline structures • Glass ceramics • Rare-earth doping • Scintillators • Thermal properties • DSC • TMDSC • Photoluminescence • X-ray luminescence

36.1 Introduction

Rare-earth (RE) doped crystalline and some glass-ceramics materials posses useful scintillating and storage properties and have received considerable attention due to their potential applications involving sensors, optical and X-ray detectors, waveguides, lasers etc. [1]. RE-doped crystals such as CsI, Cd_2O_2S etc. for digital X-ray imaging form a commercialized technology for digital X-ray imaging; however RE-doped glasses and glass ceramics make up a new, technology under development which has been shown to possess a great potential for high resolution x-ray imaging [2, 3]. In addition, this method has also the potential for measuring high dose radiation, e.g. radiation from a synchrotron light source since some rare-earth ions within the medium are reduced under irradiation, e.g. Sm^{3+} is converted to Sm^{2+} upon irradiation in certain glass hosts [4]. It was previously reported that in fluorite glass ceramics (GC) such as flurochlorozirconate (FCZ) based GCs, the active RE ions are embedded in nanocrystals, which are dispersed in the glass matrix. Heat treatment and annealing of the starting RE-doped FCZ glasses in various gaseous atmospheres are critically important to the formation and control of the nanocrystals [5–7]. The formation of nanocrystals, their structure and size, play an important role in the photoluminescence of rare-earth ions in FCZ-based GCs and some other glasses such as barium borophosphates [8].

In this work we report on the synthesis and characterization of samarium fluoride (SmF_3) and samarium oxide (Sm_2O_3) doped Zn- and Sr-borophosphate glasses with mixed oxide-fluoride glass matrix structures. We studied the synthesized materials by differential scanning calorimetry (DSC) and by temperature-modulated DSC (TMDSC) to determine their glass transformation and crystallization properties before and after thermal treatment (annealing) process. Additionally, X-ray diffraction (XRD) and scanning electron microscopy (SEM) analysis were used to characterize the structure, that is, whether the synthesized materials possess a glassy or polycrystalline structure or are a heterogeneous mixture; under certain conditions post-treated materials are nanostrucrured, i.e. the formation of nanocrystals takes place. The above RE-doped materials were irradiated by

different types of LEDs and laser light in the UV-VIS wavelength range to induce photoluminescence (PL) before and after exposure to X-ray synchrotron irradiation. We also recorded the X-ray induced luminescence (XL) spectra. The experimental results are c discussed in terms of established models for the behavior of rare-earths in glasses, crystalline solids and nanocrystalline glass-ceramics.

The main goal of synthesizing different materials with various compositions was to obtain homogenous and transparent glasses, and to look for compositional effects on the photoluminescence and x-ray luminescence properties. We eventually hoped to obtain X-ray sensing properties, for example, through the conversion of Sm^{3+} to Sm^{2+} ions after high energy irradiation. Their distinctly different properties provide a means to identify the converted amount of Sm^{2+} ions and hence the amount of incident radiation.

36.2 Experimental Procedure

The conventional melt-quenching technique in air was applied to form RE-doped glass, glass-ceramic and polycrystalline samples; subsequently these materials were thermally treated at different temperatures to obtain nanocrystalline structures if possible.

We used commercial grade high purity SmF_3 and Sm_2O_3 (both 99.99 %) as doping materials. The amounts of rare earth (RE) doping were varied in the range 0.05–1.3 mol. %. We used reagent grade stoichiometric amounts of ZnO (99.9 %), ZnF_2 (99 %) and $SrCO_3$ (99 %) with B_2O_3 (99.98 %) and P_2O_5 (98 %) to perform solid-state reactions and to obtain different Zn and Sr borophosphates as summarized in Table 36.1. (All chemicals were obtained from Alfa Aesar.)

Table 36.1 Compositions content

Components [mol%] composition	ZnO	ZnF_2	$SrCO_3$	SrF_2	P_2O_5	B_2O_3	Sm_2O_3	SmF_3
1	71.81	–	–	–	9.69	18	0.50	–
2	36.13	36.13	–	–	9.69	18	0.025	0.025
3	36.08	36.08	–	–	9.69	18	0.075	0.075
4	36.03	36.03	–	–	9.69	18	0.125	0.125
5	35.98	35.98	–	–	9.69	18	0.175	0.175
6	35.90	35.90	–	–	9.69	18	0.250	0.250
7	64.85	7.20	–	–	9.69	18	0.125	0.125
8	57.65	14.41	–	–	9.69	18	0.125	0.125
9	50.44	21.62	–	–	9.69	18	0.125	0.125
10	43.24	28.82	–	–	9.69	18	0.125	0.125
11	–	–	33.40	–	35.30	30	1.30	–
12	–	–		33.40	35.30	30	–	1.30
13	–	–	16.70	16.70	35.30	30	0.65	0.65

Differential scanning calorimetric (DSC) and temperature-modulated DSC (TMDSC) experiments were performed using a TA Instrument DSC Q100 with an attached fast air cooling system (FACS) with a heating rate of 2 K/min, modulation amplitude of ±1 K/min and modulation period of 60 s. Details regarding the thermal measurement procedures with TMDSC and DSC have been described elsewhere (e.g. [9]). The evaluation of DSC and TMDSC results was performed by TA Instruments Universal Analysis (UA) software.

The photoluminescence (PL) spectra of the synthesized glasses were measured by a fiber optic coupled CCD Aventes spectrometer AveSpec-2048 with gratings in the range 250–1,100 nm. Laser diodes (LD) and Light Emitting Diodes (LED) from the UV to the NIR range were used as excitation sources. 3D graphs were generated using a Matlab software.

In order to investigate the valence reduction of Sm ions by x-irradiation, as-prepared and heat-treated samples were exposed to radiation from a x-ray tube (43855D, Faxitron) set to 110 kV with a filament current of 3 mA. PL before and after X-ray irradiation was recorded by a spectrometer EPP2000. In order to test the conversion of Sm ion, the irraditation was performed for 60 min, which is equivalent to 3,000 Gy in air. X-ray luminescence (XL) was recorded under intense X-ray irradiations at the Biomedical Imaging and Therapy beamline (BMIT, 05B1-1) at the CLS. The dose rate was experimentally measured to be approximately 1.6 Gy s^{-1} at 250 mA of the storage ring current using an ionization chamber (96030, Keithley). The white x-ray beam was filtered by Cu filter with an effective thickness of 1.1 mm, which results in the spectrum with a peak energy ~50 keV.

36.3 Results and Discussion

Nearly all synthesized materials were visually homogenous and fully transparent glasses. Some samples containing Sr were found to be partially polycrystalline and opaque. It is important to measure the glass transition temperatures of the glass samples in order to estimate their stability and to schedule proper thermal treatment procedures. In order to obtain more accurate data of the for glass transformation properties we measured the glass transition temperatures (T_g) not only by conventional DSC (heat flow vs. temperature) but also by its temperature-modulated TMDSC (heat capacity vs. temperature). Figures 36.1 and 36.2 show that the observed trends in the dependence of T_g on the Sm-doping in Zn-borophosphate glasses are the same. The differences between DSC and TMDSC, and the advantages of TMDSC have been discussed previously [9]. The T_g values extracted for glasses from TMDSC measurements show very little dependence on aging and thermal history [10] in contrast to data from conventional DSC measurements; TMDSC thus provides a more reproducible means of characterizing the glass transition for a given frequency of modulation.

As apparent from Fig. 36.1, there is an initial decrease in T_g with increasing SmF_3 content. However, at about 0.175 mol% SmF_3 T_g increases with increasing

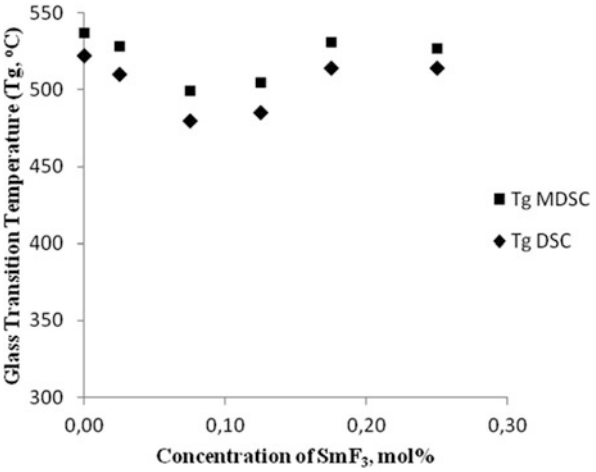

Fig. 36.1 Dependence of the glass transition temperature on the Samarium fluoride (SmF_3) doping of Zn-borophosphate glasses

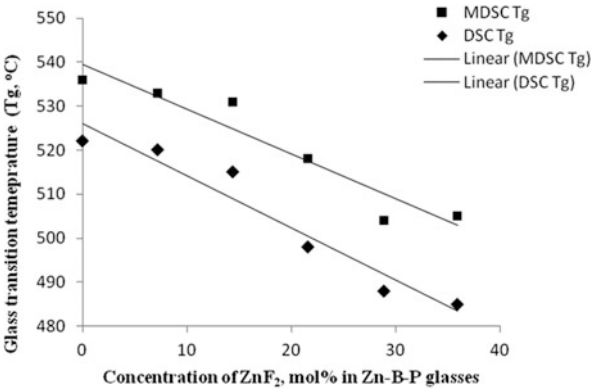

Fig. 36.2 Dependence of the glass transition temperature on the amount of ZnF_2 in Zn-borophosphate glasses

SmF_3 content; around 0.20 mol%, T_g is approximately the same than that of that of glasses only doped with Sm_2O_3 (no SmF_3). Possibly, samarium and fluorine ions have an opposite effect on the thermal properties of these glasses. Looking at the dependence of the glass transition temperatures on the amount of ZnF_2, as shown in Fig. 36.2, there is a clear and almost linear decrease in T_g.

Prior to any thermal annealing, samples with different compositions were tested with a number of different LEDs with emission wavelengths at 370, 395, 405, 410, 415, 425, 435, 450, 470, 490, 505, 515, 525, 535, 565, 572, 590, 605, 615, 632, 660 and 700 nm for their photoluminescence characteristics. The LED peak power and the illumination area were approximately the same; the results were normalized by the software used. The photoluminescence (PL) response results are shown in Fig. 36.3 as a function of the excitation wavelength.

Figure 36.3 represents a 3D graph of the PL emission intensity as a function of the excitation wavelength (all LEDs) and the emission wavelength for composition number 7 (Table 36.1). The 3D spectra of other compositions are similar; all show

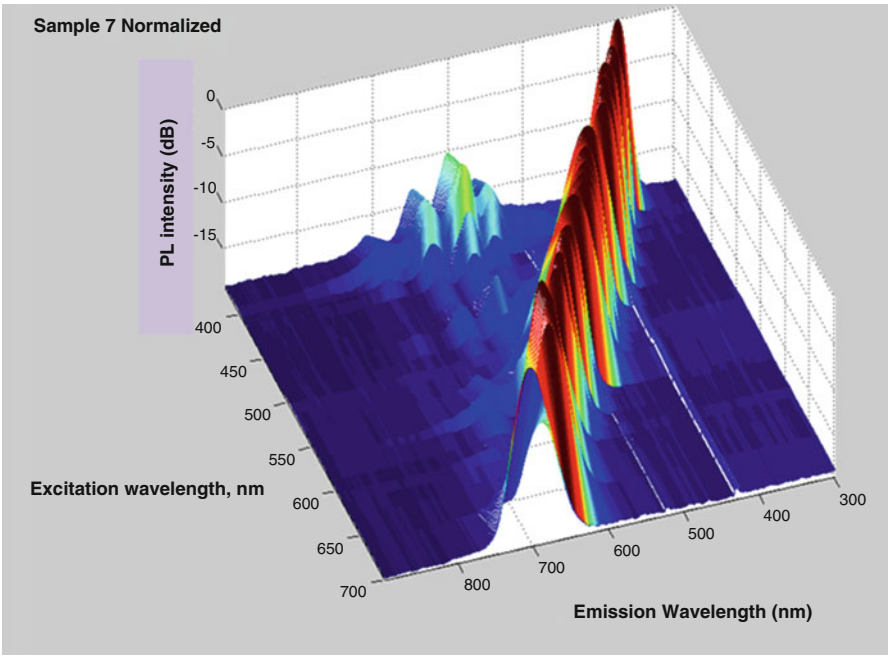

Fig. 36.3 Photoluminescence (PL) intensity vs excitation and emission wavelength of a Zn-borophosphate glass composition (# 7)

photoluminescence activities which are very strong in the UV and blue regions but less in the other visible spectral regions. Notice that the peak PL intensity varies significantly with the excitation wavelength. It also depends on the sample composition (not shown).

We investigated the effect of thermal treatments on the characteristics of the above glasses. Initially, below (450 °C) and also around the glass transition temperature (500, 520 and 530 °C) the annealing time was varied from 1 to 48 h. There were no any significant visible changes. The XRD signal of a treated sample (Fig. 36.4a) indicates the same amorphous state as for non treated sample. The samples remained transparent and homogeneous. The DSC and TMDSC results are almost the same and not shown here.

However, when the annealing temperature was increased to a value close to the crystallization temperatures of these glasses (650 °C and higher), the samples crystallized and became visually opaque. A phase separation of polycrystalline and amorphous fractions of treated materials was observed at elevated temperatures and after an annealing time of 1 h. Heat treated samples consist of crystalline particles embedded in a glassy matrix. This is the reason why most of the high-temperature treated and most of the Sr-containing samples show similar glass transition temperatures of around 500 °C similar to other fully glassy materials but with significantly reduced relaxation enthalpies, due to the reduction in the glassy phase.

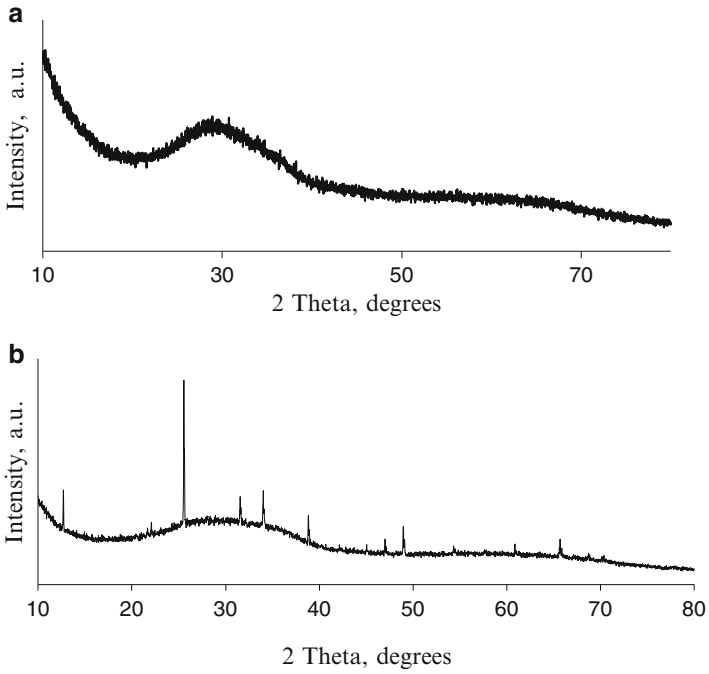

Fig. 36.4 (**a**) XRD of thermally treated (530 °C) Zn-borophospahe glass (composition1); (**b**) XRD (typical example) of partially crystallized Zn-borophosphate glass sample

We performed XRD analysis of some of the synthesized samples. All glasses show a fully amorphous state prior to any annealing. However, after annealing at temperatures around 650 °C and higher and the samples and also some Sr-based samples show partial crystallization with an XRD pattern similar to that presented in Fig. 36.4b for a partially crystallized Zn-borophosphate glass.

Some of the crystal structures of fully crystallized (polycrystalline) samples with oxide Zn-borophosphate compositions were identified as zinc borate phosphate $Zn_3(BO_3)(PO_4)$ and zinc borate α-$Zn_5B_4O_{11}$. This analysis was not yet done for crystallized oxyfluoride Zn-borophosphate structures and is a subject of a further investigation.

An SEM picture (Fig. 36.5) of the same 0.5 mol. % Sm_2O_3 sample (composition 1) shows that there is a mixture of polycrystalline features with dimensions larger than one micron and some nanocrystalline features. This result reveals that annealing temperatures close to T_g of about 500 °C are too low to induce nanocrystallization whereas 650 °C is sufficiently high to form polycrystalline samples.

The formation and sizes of larger nanocrystalline and polycrystalline structures can be seen in Fig. 36.5.

All samples were tested for high energy (X-ray) irradiation sensing in two different ways. The samples were kept in an X-ray chamber and exposed for 60 min (~3,000 Gy); there after PL spectra were measured to compare with the

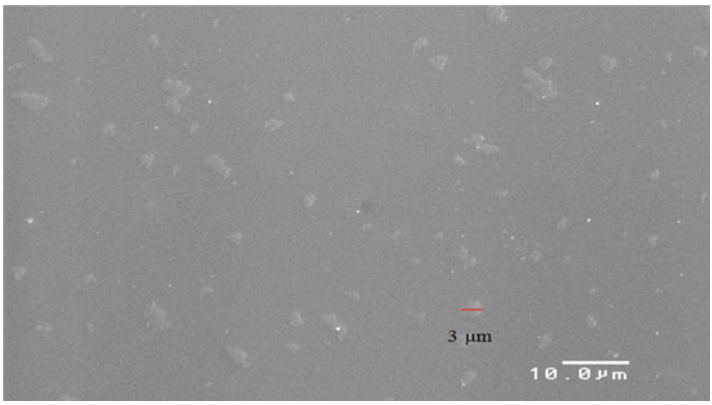

Fig. 36.5 SEM of partially crystallized Zn-borophosphate sample (composition 1)

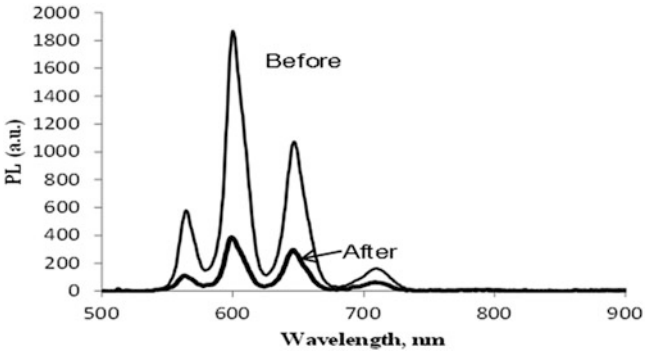

Fig. 36.6 Glass sample photoluminescence (excitation wavelength 405 nm) before and after X-ray irradiation for 60 min (composition 11)

PL of non-irradiated samples. In addition, samples were directly tested for X-ray luminescence (XL) at the CLS synchrotron facility.

Figure 36.6 shows the PL signal before and after X-ray irradiation of a glass sample (composition 11). There is a typical Sm^{3+} emission signal. However, no conversion from Sm^{3+} to Sm^{2+} is observed after X-ray irradiation for this sample. Most of the glass samples reveal a similar response. When the same samples are partially crystalized and then subjected to the same X-ray exposure, there is a clear indication for the conversion of some of Sm^{3+} to Sm^{2+} seen in PL spectrum as is shown in Fig. 36.7. Obviously, the crystalline portion of these materials allows the reduction of Sm^{3+} ions; however polycrystalline samples are fully opaque. X-ray imaging and dosimetry plates need to be transparent. The only way to combine the necessary transparency with the presence of crystalline structures is to induce the formation of crystals of nanometer size within the glass matrix, which is a subject of current studies.

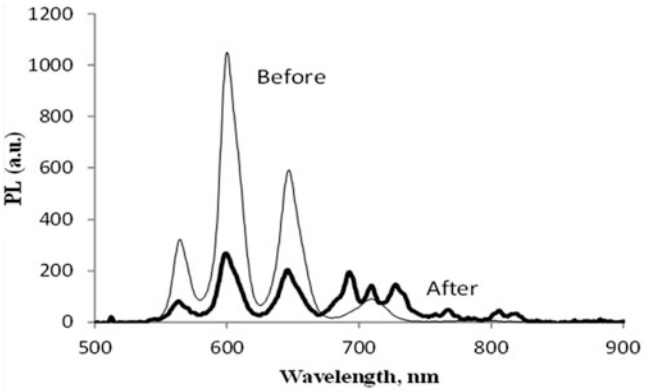

Fig. 36.7 Photoluminescence (excitation wavelength 405 nm) of a polycrystalline sample before and after X-ray irradiation for 60 min (composition 11)

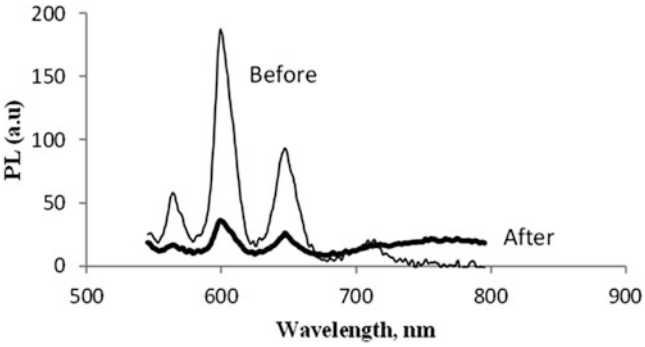

Fig. 36.8 Polycrystalline sample photoluminescence (excitation wavelength 535 nm) before and after X-ray irradiation for 60 min (composition 12)

The Sr-borophosphate with composition 11, which is $SrCO_3$ based and doped by Sm_2O_3, is different if compared to composition 12 by the fluorine component introduced in identical amounts; in the latter, SrF_2 replaces $SrCO_3$ and SmF_3 replaces Sm_2O_3, as dopant. A different shape (width) of the emission of Sm^{2+} around 700 nm converted from Sm^{3+}. When the PL is excited at 405 nm this conversion peak is week (not shown) but it is very clear when the PL is excited by 535 and 470 nm light (Figs. 36.8 and 36.9).

It was observed, that shown in Figs. 36.8 and 36.9 the excitation wavelength of 470 nm does not induce strong PL from Sm^{3+} but it induces very strong PL from Sm^{2+}. Another reason is that this wavelength is more efficient in the excitation of Sm^{2+} PL [11].

Glass samples of compositions 11, 12 and 13 were further exposed to synchrotron X-rays available at CLS (05B1-1 beam); the resulting X-ray induced luminescence (XL) spectra were measured for different times. The XL spectra obtained are

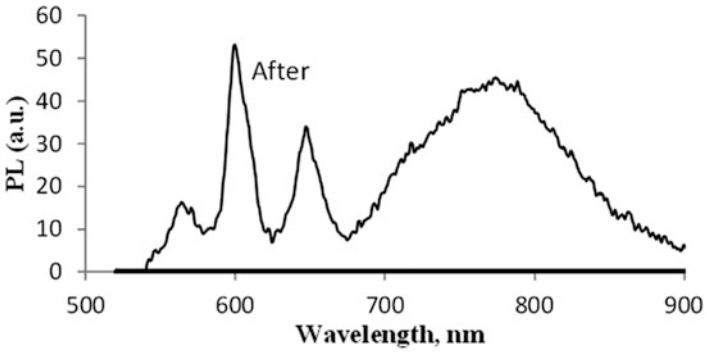

Fig. 36.9 Polycrystalline sample photoluminescence (excitation wavelength 470 nm) after X-ray irradiation for 60 min (composition 12)

shown in Fig. 36.10. The XL intensities of the samples were compared by their integrated signals. For all the samples the XL intensities decrease with the irradiation time. We think that this is due to creation of defect centers by the X-ray irradiation, which results in a darkening of glass matrix. Among our samples tested, Sample 12 seems to show less X-ray-induced darkening. Some additional research is needed to find a composition with less x-ray induced discoloration, which are more suitable for radiation sensing applications like a dosimeter for the microbeam radiation therapy (MRT) described previously [4] or for other types of high energy high dose ionizing radiation sensing as well.

36.4 Conclusions

Homogeneous, transparent, non-hygroscopic and stable samarium doped Zn-borophosphate and Sr-borophosphate glasses with mixed oxide-fluoride glass matrix structures were synthesized and studied. The following results were obtained:

1. The thermal analysis by DSC and MDSC reveals T_g values around 500 °C which do not depend on the annealing temperature and time but on the fluorine content (ZnF_2, SrF_2 and SmF_3);
2. All Sm-doped glasses exhibit a typical Sm^{3+} photoluminescence, which depends on the excitation wavelength;
3. When annealed around 650 °C, the glasses crystallized with a mixed nanocrystalline /polycrystalline structure, as shown by SEM and XRD;
4. Polycrystalline and glass-ceramic samples are shown to convert Sm^{3+} to Sm^{2+} after X-ray irradiation better than glass samples of the same composition;

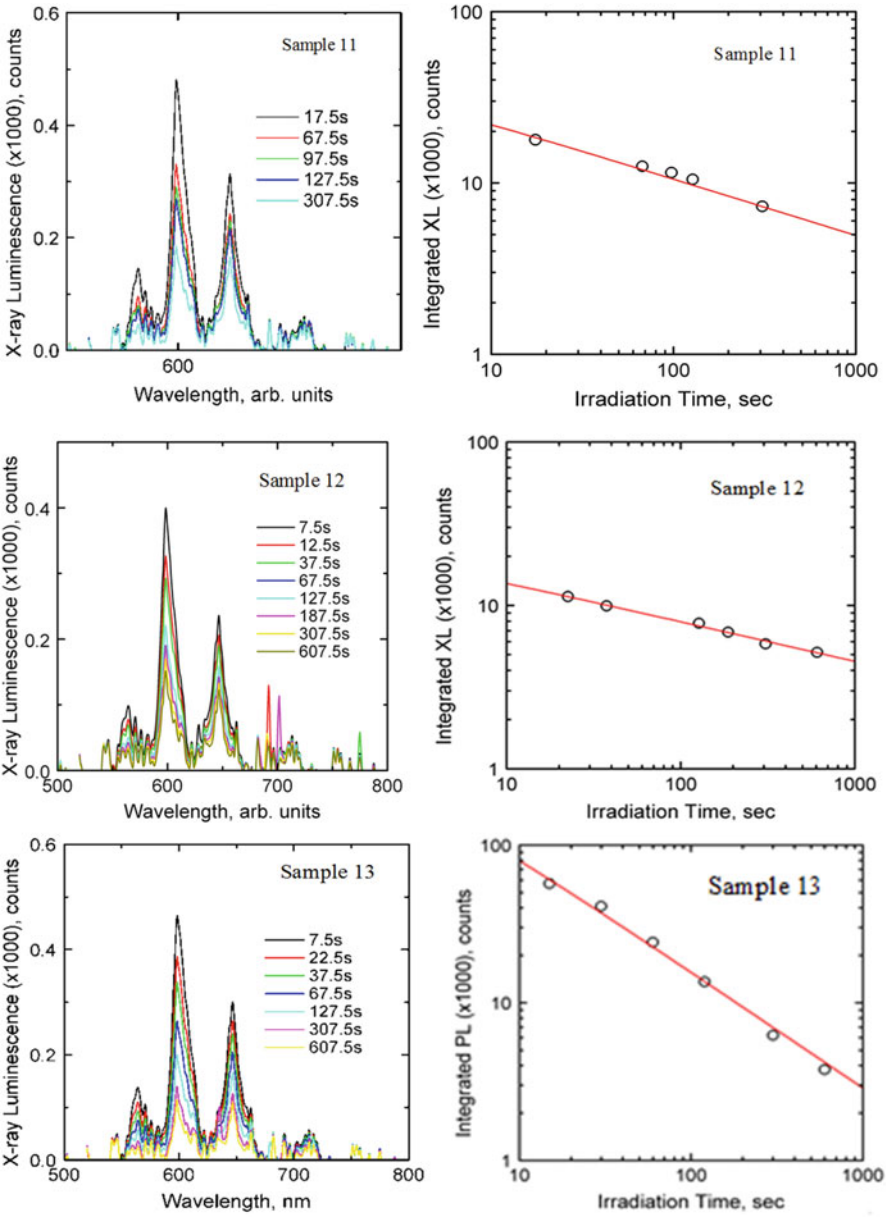

Fig. 36.10 X-ray luminescence of compositions 11, 12 and 13 recorded at BMIT (CLS) synchrotron beam line facility and the corresponding photo darkening effect

5. It was shown that conversion peaks (Sm^{3+} to Sm^{2+}) are different for oxide and oxifluoride compositions;
6. X-ray luminescence was induced by a synchrotron light source with a photodarkening effect that depends on the composition.

References

1. EdgarA (2006) Luminescent materials. In: Kasap S, Capper P (eds) Springer handbook of electronic and photonic materials, vol 40. Springer, p 983
2. Edgar A, Williams GVM, Sgara PKD, Secu M, Schweizer S, Spaeth JM, Hu X, Newman PJ, MacFarlan DR (2003) J Non-Cryst Solids 326&327:489
3. Riesen H, Kaczmarek W (2007) J Inorg Chem 46:7235
4. Belev G et al (2011) Phys Status Solidi C 8:2822
5. Koughia C et al (2011) J Non-Cryst Solids 357:2272
6. Tonchev D, Belev G et al (2011) In: Reithmaier JP, Paunovic P, Kulisch W, Popov C, Petkov P (eds) Nanotechnological basis for advanced sensors, NATO Science for Peace and Security series-B: physics and biophysics. Springer, Dordrecht, p 241
7. Tonchev D, Belev G (2009) In: Reithmaier JP, Petkov P, Kulisch W, Popov C (eds) Nanostructured materials for advanced technology applications, NATO Science for Peace and Security series-B: physics and biophysics. Springer, Dordrecht, p 377
8. Tonchev D et al (2012) J Univ Chem Technol Metall 4:439
9. Kasap SO, Tonchev D (2001) J Mater Res 16:2399
10. Tonchev D, Kasap SO (2002) Mater Sci Eng A 328(1–2):62
11. Okada G et al (2014) J Am Ceram Soc 97:2147

Chapter 37
Synthesis of Nano- and Submicron-Sized Crystals for the Preparation of Oxide Glass-Ceramics with Advanced Magnetic and Dielectric Properties

R. Harizanova, A. Mazhdrakova, L. Vladislavova, C. Bocker, G. Avdeev, M. Abrashev, I. Gugov, and C. Rüssel

Abstract In the present study we explore the possibility to obtain nano- to submicron-sized crystals in an oxide glass-matrix which can serve as a part of the construction of various types of sensors. Two sets of compositions are developed: one in the systems $Na_2O/Al_2O_3/B_2O_3/SiO_2/(V_2O_5)/Fe_2O_3$ and $Na_2O/MnO/SiO_2/Fe_2O_3$ with very high concentrations of Fe_2O_3 ($\geq$ 10 mol%) where the crystallization of magnetite Fe_3O_4 and solid solutions of the type $(Fe, Mn)^{II}O{\cdot}(Fe, Mn)^{III}{}_2O_3$ is established and another in the systems $Na_2O/Al_2O_3/BaO/TiO_2/B_2O_3/SiO_2$ and $Na_2O/Al_2O_3/BaO/TiO_2/B_2O_3/SiO_2/Fe_2O_3$. Here no or only small amounts of iron oxide ($\leq$5.8 mol %) are used and the crystallization of cubic $BaTiO_3$ crystals is achieved. The phase composition is investigated by X-ray diffraction and for selected glass-ceramic samples also by Raman spectroscopy. The microstructure of all synthesized materials is studied by SEM.

Keywords Oxide glasses • Crystallisation • Nano- and submicronparticles • Phase composition • Microstructure

R. Harizanova (✉) • A. Mazhdrakova • L. Vladislavova • I. Gugov
University of Chemical Technology and Metallurgy, 8 Kl. Ohridski Blvd, 1756 Sofia, Bulgaria
e-mail: ruza_harizanova@yahoo.com

C. Bocker • C. Rüssel
Otto-Schott-Institut, Jena University, Fraunhoferstr. 6, 07743 Jena, Germany

G. Avdeev
Institute for Physical Chemistry, Bulgarian Academy of Sciences, Acad. G. Bonchev Str. Bl. 11, 1113 Sofia, Bulgaria

M. Abrashev
Faculty of Physics, Sofia University, 5 James Bourchier Str., 1164 Sofia, Bulgaria

P. Petkov et al. (eds.), *Nanoscience Advances in CBRN Agents Detection, Information and Energy Security*, NATO Science for Peace and Security Series A: Chemistry and Biology, DOI 10.1007/978-94-017-9697-2_37

37.1 Introduction

The synthesis of nano- and submicron-sized crystals with advanced magnetic and electrical properties as potential candidates for use as parts of biosensors and sensors for environmental monitoring is a topic widely investigated in the past few years [1–6]. The preparation of glass-ceramic materials with magnetite Fe_3O_4, solid solutions of the type $(Fe, Mn)^{II}O{\cdot}(Fe, Mn)^{III}{}_2O_3$ and $BaTiO_3$ is of great interest to many authors. The amorphous matrix offers chemical as well as mechanical support and protection of the obtained crystals, thus preventing them from clustering or degradation during transportation, storage or operation of the devices in which they find application [7–9]. The synthesis of oxide glasses containing large amounts of polyvalent 3d-metals ions and alkaline earth metals has been investigated for a long time due to the interesting electrical and magnetic properties of the obtained products [7, 8]. The melts of the corresponding compositions possess a pronounced tendency towards crystallization but at the same time offer the possibility to receive glass-ceramic materials with very large volume fractions of the precipitated crystalline phase.

Subject of the present study is the synthesis and investigation of the phase composition and the microstructure of glass-ceramic materials with two types of properties: magnetic and dielectric. For the synthesis of materials with magnetic properties four compositions are used aiming at the precipitation of transition metal-containing magnetic nanocrystals (Table 37.1, compounds **A** – **D**). The synthesis of glass-ceramics with dielectric properties is studied for two compositions (Table 37.1, **E** and **F**), the first of which could also combine electrical and magnetic properties into a multiferroic property [6, 10].

37.2 Experimental

37.2.1 Preparation of the Glasses

Reagent grade raw materials (Na_2CO_3, $MnCO_3$, SiO_2, Fe_2O_3 or $FeC_2O_4{\cdot}2H_2O$, NH_4VO_3, $BaCO_3$, $B(OH)_3$, $Al(OH)_3$ and TiO_2) were used for the preparation of the glasses. The batches (100 g) for the preparation of the magnetic type materials were

Table 37.1 Compositions used in the work (in mol%)

Compound	Composition
A	$12Na_2O/12Al_2O_3/14B_2O_3/37SiO_2/25Fe_2O_{3-x}$,
B	$13.75Na_2O/13.75Al_2O_3/\ 15.96B_2O_3/42.22SiO_2/14.32Fe_2O_{3-x}$
C	$13.75Na_2O/13.75Al_2O_3/15.97B_2O_3/36.55SiO_2/5.68V_2O_5/14.3Fe_2O_{3-x}$
D	$13.6Na_2O/8.5MnO/62.9SiO_2/15Fe_2O_{3-x}$
E	$20.1Na_2O/\ 3Al_2O_3/23.1BaO/23TiO_2/7.6B_2O_3/17.4SiO_2/5.8Fe_2O_3$
F	$20.1Na_2O/\ 3Al_2O_3/23.1BaO/23TiO_2/9.8B_2O_3/21SiO_2$

homogenized and melted in SiO_2-crucibles using a $MoSi_2$-furnace and melting temperatures in the range from 1,400 to 1,450°C (for 1.5 h). Then some melts were quenched on a Cu block, while others were annealed for 10 min at 480 °C. Some amount of the melts was drawn to fibers when possible. The batches for the dielectric materials were 60 g; they were homogenized and melted in Pt-crucibles using a SiC and $MoSi_2$-furnace and a melting temperature of 1,250°C for the system with Fe and 1,400 °C for that without Fe (always kept for 1 h in air). Some of the melts were quenched on a Cu-block, others were transferred after the quenching to a pre-heated graphite mould. The glasses cast into the graphite mould were transferred to a muffle furnace and kept at 450°C for 10 min. Then, the furnace was switched off and the samples were allowed to cool to room temperature. All glassy samples were heat treated at temperatures above T_g for different times.

37.2.2 Characterization Methods

The phase compositions were analyzed by X-ray diffraction (XRD) on powdered samples, using $Cu_{K\alpha}$-radiation with 2θ-values in the range from 10 to 60°, or $Fe_{K\alpha}$-with 2θ-values in the range from 10 to 90°. The glass-transition temperatures were determined by differential thermal analysis (DTA) using a heating rate of 10 K/min and Al_2O_3 as reference material. The microstructure was investigated by scanning electron microscopy (SEM) using a backscattered electron (BSE) and a secondary electron (SE) detector. Additional information about the phase composition and the allotropic modifications present was gathered by means of Raman spectroscopy at room temperature and as function of temperature.

37.3 Results and Discussion

37.3.1 Magnetic Glass-Ceramics

The compositions **A** – **D** listed in Table 37.1 were reduced by using $Fe_2CO_4{\cdot}2H_2O$ instead of Fe_2O_3 as raw material, thus higher concentration of Fe^{2+} ions should be supplied. Three of the compositions (**A** – **C**) show precipitation of nano-sized magnetite Fe_3O_4 (JCPDS 86–1352) or maghemite (JCPDS 89–5892) particles, as seen in the X-ray diffraction patterns in Figs. 37.1 and 37.2. For the vanadium-containing sample **C** also some amount of hematite Fe_2O_3 (JCPDS 89–0599) was detected by XRD. The shorter the melting time and the lower the melting temperature, the higher are the hematite peaks. Since the x-ray diffraction data alone was insufficient to decide between magnetite and maghemite in both compositions in Fig. 37.1, further Raman spectroscopy analysis was performed. As a result, shown in Fig. 37.3, in both samples mainly magnetite is present.

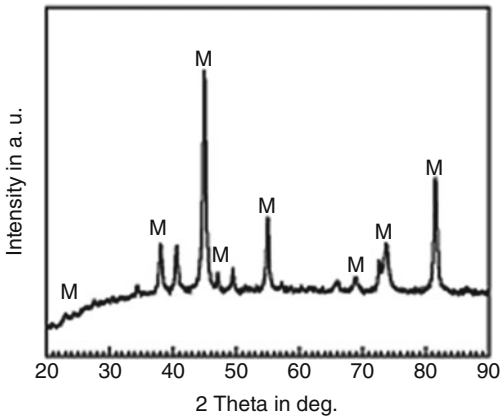

Fig. 37.1 XRD-pattern of a reduced sample with composition **A** showing the formation of magnetite Fe_3O_4 (M); unassigned peaks are attributed to different magnetite modifications

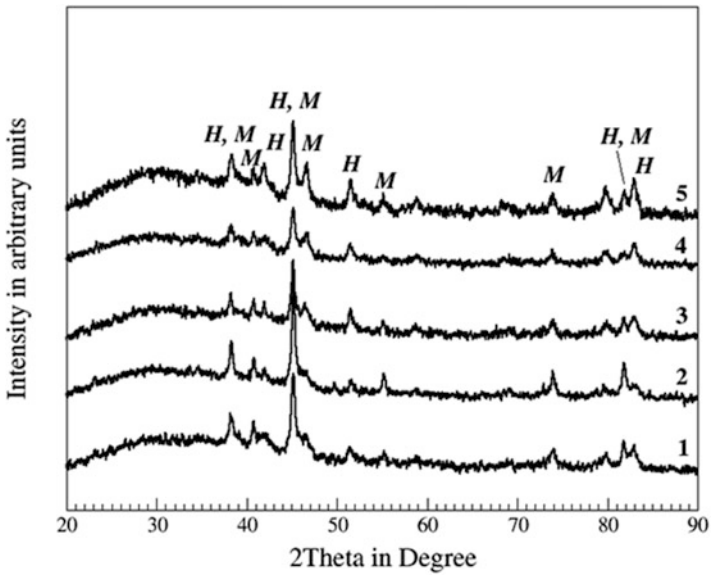

Fig. 37.2 XRD patterns of V_2O_5-containing samples melted at 1,400 °C for (*1*) 30 min, (*2*) 1 h, (*3*) 1.5 h, (*4*) 2 h and (*5*) 2.5 h prove the formation of both magnetite (M) and hematite (H)

The small amount of maghemite was attributed to an artifact due to the oxidation of magnetite by local heating of the sample caused by the laser beam. This behavior was already observed by other authors investigating Fe-based phases by Raman spectroscopy [11]. For composition **D** glass was formed after pouring of the melt. This glass was further subjected to thermal treatment at different temperatures above the glass-transition temperature; solid solutions of $MnFe_2O_4$ (JCPDS 88–1965) and Fe_3O_4 (JCPDS 87–2334), i.e. a mixed spinel of

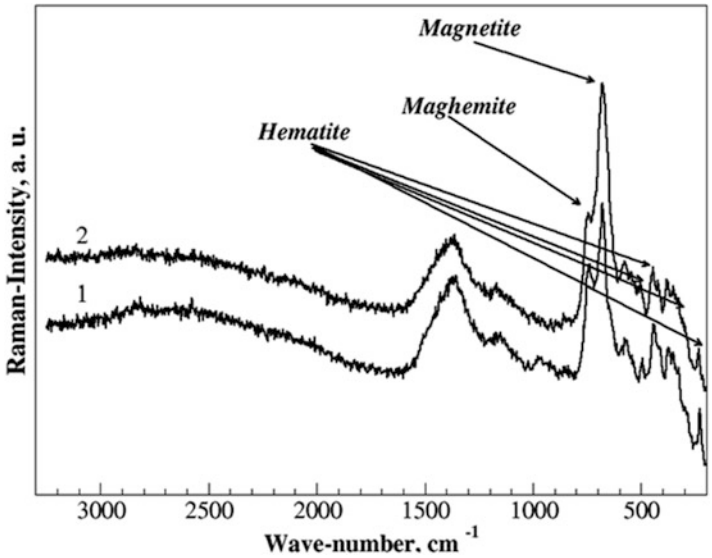

Fig. 37.3 Raman spectra of samples with composition **C** (*1*) and **B** (*2*)

the type $(Mn, Fe)^{II}O{\cdot}(Mn, Fe)^{III}{}_2O_4$ was obtained as shown in Fig. 37.4. The broadening of the peaks in Fig. 37.4 is a hint for precipitation of nanocrystals in the corresponding samples.

The SEM images of the compositions without manganese utilized for the preparation of magnetic glass-ceramics reveal that they were separated into two phases: droplets enriched in Fe and a matrix in which all other elements from the glass composition are mainly concentrated, as shown in Figs. 37.5 and 37.6, and is already known for similar sodium aluminoborosilicate glasses [12, 13]. In the SEM micrograph of the vanadium-containing glass-ceramics it can be seen that the droplets are not homogeneous but have their own structure. Actually, from our earlier work it is known that each droplet consists of separate cubic magnetite crystals with an average size of about 40 nm [12]. The average size of the droplets ranges from 100 to 1,000 nm and is comparable to that in the vanadium-containing samples. However, the formation of Fe_2O_3 in the V_2O_5-containing samples is undesirable since hematite has the tendency to form dendrites during growth. Additionally it is neither ferro- nor ferrimagnetic at room temperature. The latter makes the utilization impractical for the preparation of devices using magnetic particles.

The investigation of the microstructure of the glass-ceramics formed in the samples with the composition **D** shows precipitated globular crystals which have average size of some tens of nm (Fig. 37.7). Here self-constrained growth of the magnetic particles is observed; for this reason the average size of the formed crystals is hardly changing for samples heat-treated for different times at the same temperature. This fact leads to superparamagnetic properties as reported in [14].

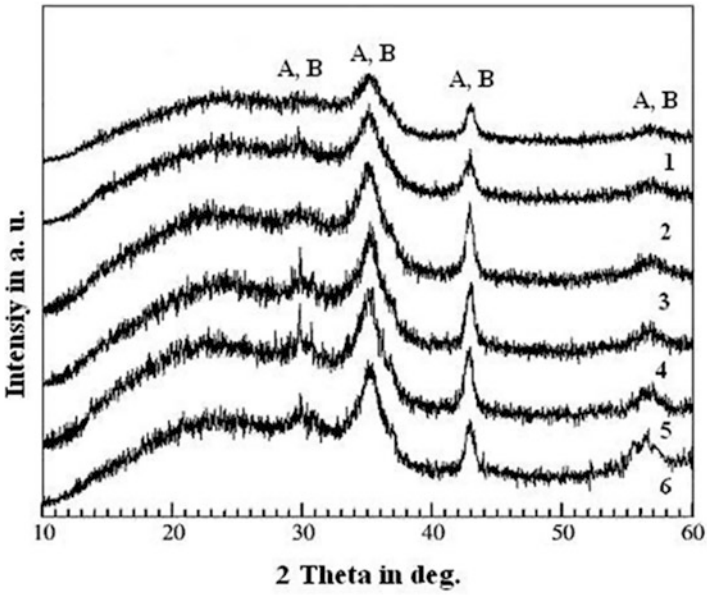

Fig. 37.4 XRD-patterns of reduced samples with the composition **D**, annealed at 600 °C for (*1*) 3 h, (*2*) 7 h, (*3*) 10 h, (*4*) 16 h, (*5*) 19 h, (*6*) 24 h show the formation of mixed crystals of $MnFe_2O_4$ (A) and Fe_3O_4 (B)

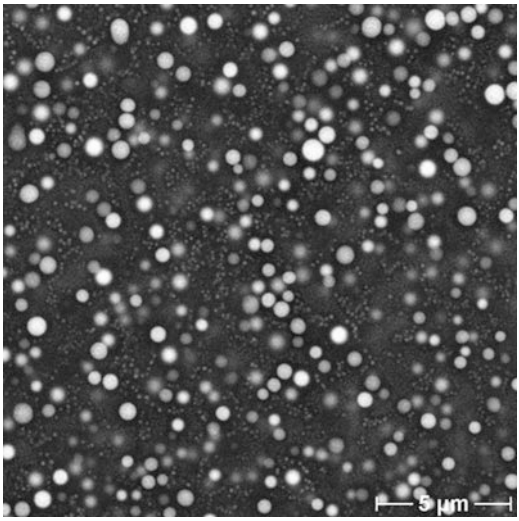

Fig. 37.5 SEM micrograph of a sample with composition **A** melted 2.5 h at 1,400 °C

The two types of particles formed – the submicron magnetite particles and the nanosized (Fe, Mn)-based ones – are potential candidates for the preparation of sensor devices for bio-medical applications and environmental monitoring [2, 3] as well as for purifying waste waters from poisonous metals such as In, Cr, Pb, As, Cu [15].

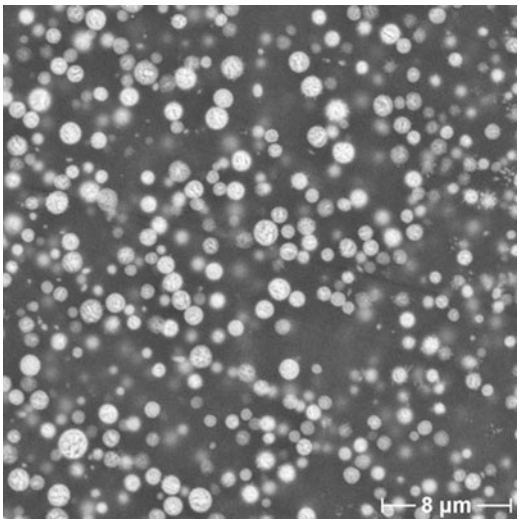

Fig. 37.6 SEM micrograph of a sample with composition **C** melted 2 h at 1,350 °C

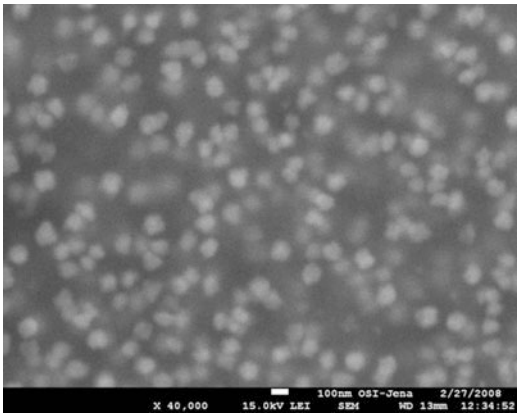

Fig. 37.7 SEM of a polished C-covered surface of sample with the composition **D**, annealed at 650 °C for 3 h: growth of spherical nanosized crystals

37.3.2 Dielectric Glass-Ceramics

The second set of samples (**E** and **F**) was intended to allow the crystallization of a $BaTiO_3$-phase which has outstanding dielectric properties and will enable the preparation of glass-ceramic materials with very high dielectric constants. Thus, depending on the crystallizing allotropic form of barium titanate, the obtained materials can be suitable for applications in electronics, i.e. for the preparation of multilayered capacitors, microwave devices and piezoelectric transducers [16–18].

The quenching of the melts from the two compositions resulted in amorphous products. To achieve higher mechanical stability and to release the mechanical stresses in the glasses they were transferred to a graphite mould and annealed below the glass-transition temperature. The stabilized glasses obtained were subjected to

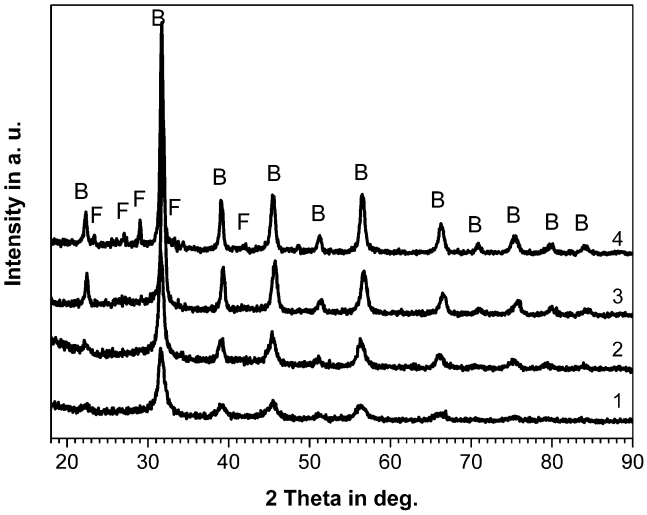

Fig. 37.8 XRD-patterns of samples with compositions **E** (*1*): 30 min/550 °C, (*2*): 5 h/550 °C and **F** (*3*): 30 min/650 °C, (*4*): 5 h/650 °C, B: $BaTiO_3$ and F: $Ba_2Ti_2SiO_8$

thermal treatment at different temperatures near the crystallization temperature as determined by DTA. The results for both compositions are precipitation and, for longer annealing times, growth of $BaTiO_3$ crystals as seen in the XRD-patterns in Fig. 37.8. Since the peaks for composition **E** are slightly broadened and the typical splitting of the $2\,\theta = 45.3°$ peak characteristic for the tetragonal modification of barium titanate [16, 17] could not be recognized, additional phase analysis was performed by means of Raman spectroscopy. Raman spectra of the untreated glass and samples isothermally annealed at 550 °C for different times are shown in Fig. 37.9. The absorption bands typical for the cubic modification of $BaTiO_3$ are observed in the Raman spectra of the annealed samples, independent of the annealing time [18]. Since the peaks of the XRD-patterns for composition **F** is Fig. 37.8 are not broadened, it can be seen here that the peak at 45.3° is not split. So, for the composition without iron oxide the formation of larger crystals is expected and only cubic $BaTiO_3$ should be present. Thus, no additional methods to identify the modification of the obtained barium titanate are needed. The longer annealing times in the Fe-containing composition lead to the formation of single crystalline phases, while for the composition without Fe longer annealing times at constant temperature results in the occurrence of a second phase (fresnoite, $Ba_2Si_2TiO_8$, JCPDS 98-20-1844) as evident in Fig. 37.8.

Information about the microstructure and the morphology of the crystals was obtained by means of SEM. Micrographs of annealed samples from the two compositions are shown in Figs. 37.10 and 37.11. In Fig. 37.10, a microstructure typical for $BaTiO_3$-containing glass-ceramics from the system with Fe_2O_3 is evident. Here the formation and growth of bright globular crystals is seen which tend to aggregate and grow together for longer annealing times. From the material contrast in the image, it can be concluded that the bright appearing crystals are enriched in the heavier elements of the glass composition, i.e. Ba and Ti.

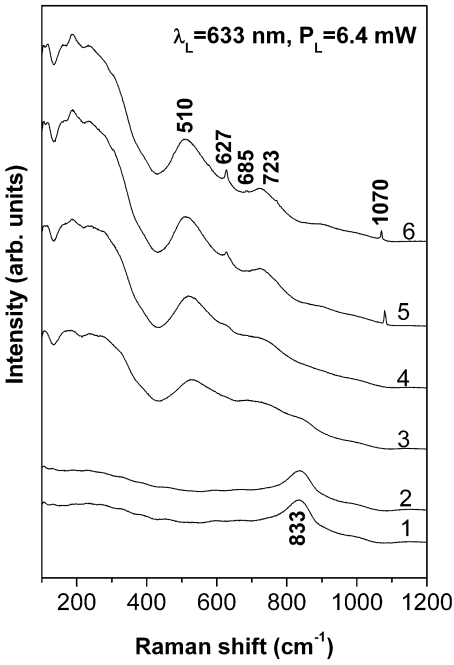

Fig. 37.9 Raman spectra of samples with composition **E**: glass (*1*) and annealed samples at 550 °C: (*2*) 5 min, (*3*) 15 min, (*4*) 1 h, (*5*) 3 h and (*6*) 7 h: peaks of cubic $BaTiO_3$ are indicated

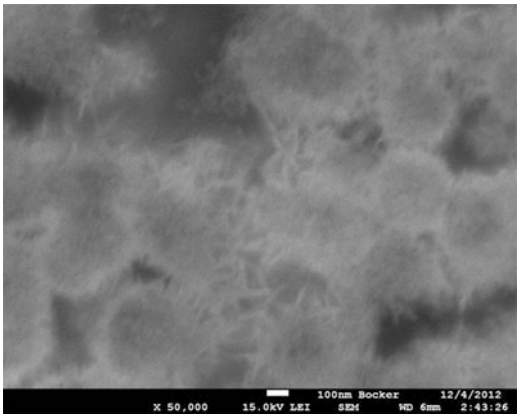

Fig. 37.10 SEM micrograph of a sample with the composition **E** annealed 2 h at 550 °C

The spherical shape of the crystals and the tendency to agglomerate suggests that in this composition phase separation occurs; in the phase-separated regions barium titanate crystallizes. In contrast to the SEM image in Fig. 37.10, the micrograph of the iron-free composition from Fig. 37.11 shows globular crystals with a different morphology. Here the crystals grow in a dendrite-like manner radially from the centre of the spherical crystals. At some stage of the growth for both iron-containing and iron-free samples, the crystals start touching each other and forming larger aggregates. This process can be explained by Ostwald ripening leading to larger crystals.

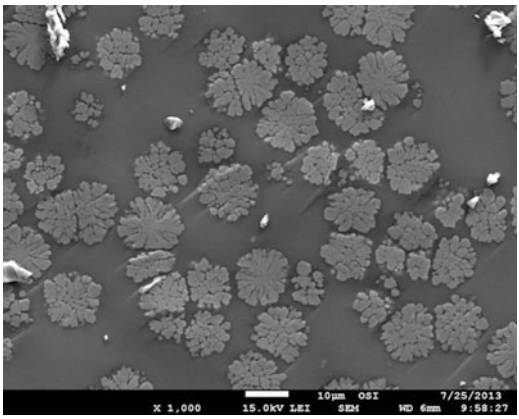

Fig. 37.11 SEM micrograph of a sample with the composition **F** annealed 2 h at 600 °C [19]

37.4 Conclusions

The synthesis of submicron sized magnetite crystals was achieved in phase-separated sodium-aluminoborosilicate glasses containing high concentrations of the 3d-transition metals Fe and/or V, while in sodium-silicate glasses with high concentrations of Fe and Mn no phase separation, but the precipitation of mixed (Fe, Mn)-spinel nanocrystals was observed. In a second set of compositions with high concentrations of alkaline and alkaline-earth metals with or without Fe, the precipitation of $BaTiO_3$ crystals with sizes from some hundred nm to some micrometers was possible. Raman spectroscopy was successfully applied as a precise method for phase identification of the exact magnetic phase in the magnetic glass-ceramics and for the identification of the allotropic $BaTiO_3$ modifications in the dielectric glass-ceramics. In all sodium-aluminoborosilicate glasses with iron, phase separation is observed which leads to growth of globular crystals of either Fe_3O_4 or $BaTiO_3$ in the amorphous matrix.

References

1. Odenbach S (2004) J Phys Condens Matter 16:1135
2. Sakai Y et al (1995) J Ferment Bioeng 80:300
3. Aytur T et al (1995) J Immunol Methods 314:21
4. Zhou GY et al (2004) Smart Mater Struct 13:309
5. Zhang ZJ et al (1998) J Am Chem Soc 120:1800
6. Zvezdin AK et al (2007) Bull Russ Acad Sci Phys 71:1561
7. Woltz S, Hiergeist R, Görnert P, Rüssel C (2006) J Magn Magn Mater 298:7
8. Guo-Ping D et al (2006) J Alloys Compd 492:L79
9. Vijatović MM et al (2008) Sci Sinter 40:235. doi:10.2298/SOS0803235V
10. Maiti RP et al (2009) J Non-Cryst Solids 355:2254
11. Bersani D et al (1999) J Raman Spectrosc 30:355

12. Harizanova R et al (2010) J Mater Sci 45:1350
13. Vogel W (1985) Glass chemistry, 2nd edn. Springer, Berlin/New York
14. Harizanova R et al (2013) Bulg Chem Commun 45:84
15. Zhang F et al (2014) J Mater Sci 49:3478
16. Libor Z et al (2011) J Mater Sci 46:5385
17. Capsal JF et al (2010) J Non-Cryst Solids 356:629
18. Joshi U et al (2006) J Phys Chem B 110:12249
19. Harizanova R et al (2014) Adv Nat Sci Theory Appl 3:21

Chapter 38
Nano-indentation Study and Photo-Induced Effects in Amorphous $As_2Se_3:Sn_X$ Chalcogenides

Diana Harea, Evghenii Harea, Eduard Colomeico, and Mihail Iovu

Abstract The mechanical characteristics of amorphous As_2Se_3:Sn prepared by thermal evaporation in vacuum on glass substrates heated to $T_{substr} = 100$ °C are investigated. It was established that the hardness H of amorphous thin films is generally higher than the hardness of bulk samples of the same chemical composition. The combination of depth sensing indentation and band-gap illumination has been used to study the photoplastic effect in chalcogenide glasses and thin films. The prominent photoplastisity of thin films has been revealed through hardness deviations during nanoindentations under light illumination from those observed for the materials in the darkness. Some optical properties, the modification of optical parameters (optical band gap E_g, absorption coefficient α, refractive index n) under light irradiation and heat treatment of the amorphous $As_2Se_3:Sn_x$ thin films, and the relaxation of the photodarkening effect under light exposure were also investigated.

Keywords Chalcogenide glasses • Hardness • Photoplasticity • Photostructural transformations • Light-induced phenomena • Young's modulus

38.1 Introduction

Amorphous materials represent a class of advanced materials exhibiting attractive combinations of properties such as high strength/hardness and excellent wear/corrosion resistance [1–4]. These distinguished properties are primarily due to the disordered atomic arrangement in the amorphous materials resulting in the absence of grain boundaries and defects in the microstructure. While the non-equilibrium nature of amorphous materials offers outstanding properties, it also presents significant challenges in the processing of such materials.

D. Harea (✉) • E. Harea • E. Colomeico • M. Iovu
Institute of Applied Physics, Academy of Sciences of Moldova, Str. Academiei 5, MD-2028 Chisinau, R. Moldova
e-mail: dyanaharea@yahoo.com

P. Petkov et al. (eds.), *Nanoscience Advances in CBRN Agents Detection, Information and Energy Security*, NATO Science for Peace and Security Series A: Chemistry and Biology, DOI 10.1007/978-94-017-9697-2_38

The elements of group six of the periodic table, are known as the chalcogens. The interest in chalcogenide As-Se films is engendered by their low optical losses, wide transparency range in the mid-IR, and good mechanical and physicochemical properties. Amorphous ChG films have served as a base of many applications in photonics and optoelectronics, especially as inorganic photo-resists for sub-micron technology, optical diffractive elements, sensors and photonic crystals [5–7].

The effect of light-induced photo-structural transformations is characteristic for many amorphous chalcogenides films [8, 9]. Of special interest is doping of chalcogenide glasses (ChG) with metal impurities, which alter the optical, photoelectrical and transport properties of the host material [10–12]. At the same time it was shown that doping of ChG by tin impurities assist in stabilizing the glassy matrix with respect to light exposure and thermal treatment [13, 14]. It was shown that the addition of tin impurities to amorphous As_2Se_3 films can provide a pronounced effect on the electrical and transport properties as well as on optical and photo-induced phenomena [10–12, 14–17].

In this paper the experimental results on some mechanical and optical, properties and photo-induced characteristics of thermally evaporated amorphous As_2Se_3:Sn_x ($x = 0$–10 at.%) thin films (thickness $d \sim 2.0$ μm). Transmission spectra were used to calculate the absorption coefficient α, the optical band gap E_g as well as the dependence of the refractive index on the composition, and its modification Δn under light irradiation and heat treatment. Considerable information on the behavior of materials under irradiations can be obtained using the nanoindentation technique based on continuous recording of the nanoindentation process and the determination of the hardness and the Young's modulus from the measured "load-indenter displacement" curve. The photoplastical effect was discovered about 60 years ago. The first work was dedicated to crystalline semiconductors [18]. The photoplastical effect is manifested by hardening of illuminated materials [19], as well as by their softening [20–24], and depends on a number of factors such as radiation power, temperature and wavelength. Studies of the spectral dependence of the photoplasticity showed the maximum effect for illumination with a wavelength close to the band gap $h\nu \geq E_g$ [21]. The nature of the photoplastical effect is not definitively understood yet. The effect was attributed to thermal expansion of the film due to absorption of exciting light as well as recombination of the photoexcited non-equilibrium electrons and holes. Investigations of the photoplastical effect are usually performed under in-situ illumination during indentation [25, 26] as well as by indentation after illumination [27].

38.2 Experimental

The As_2Se_3:Sn_x glasses ($x = 0$ to 10.0 at.%) were synthesized from the starting elements of 6 N (As, Se, Sn) purity by a conventional melt quenching method. The starting components As_2Se_3 and Sn were mixed in quartz ampoules and then evacuated to a pressure of $p \sim 10^{-5}$ Torr, sealed and heated to $T = 900$ °C with a

rate of 1 °C/min. The quartz tubes were held at this temperature for 48 h for homogenization and then slowly quenched in the heating furnace. The amorphous As_2Se_3:Sn_x films were obtained by thermal flash evaporation in vacuum ($p = 5 \cdot 10^{-5}$ Torr) of the initially synthesized material onto glass substrates held at $T_{substr} = 100$–120 °C. The thickness of the amorphous films was in the range of $d \sim 1$–3.0 μm. The investigation of the mechanical properties of As_2Se_3:Sn_x bulk and amorphous thin film samples was performed with a PMT-3 device using a Berkovich indenter. For the measurement of the optical transmission spectra, a UV/VIS ($\lambda = 300$–800 nm), a Specord NIR 61 ($\lambda = 800$–$3{,}500$ nm, Carl Zeiss Jena). To initiate photostructural transformations in the thin film samples, a continuous He-Ne laser with a wavelength $\lambda = 633$ nm was used as a light source. For data acquisition the experimental set-up included a digital built-in PC-card PCI-1713A connected with the registration module [28].

38.3 Results and Discussions

The photoplastical investigation was performed using the nanohardness tester NHT CSM. The hardness was calculated from the load-displacement curves by the methods of Oliver and Pharr. In-situ illumination of the samples was performed with a green laser ($\lambda = 532$ nm) with a power of $P = 50$ mW/cm^2. To change the direction of the incident laser beam an optical glass prism was used (Fig. 38.1). The maximum indentation load was 5 mN, which results in a maximal penetration depth not exceeding 15 % of the film thickness. The hardness was calculated using the expression:

$$H_B = (1570 * P)/l^2, \tag{38.1}$$

where P is the applied load, and L the height of the remaining imprints [29].

Figure 38.2 shows the variation of the glass transition temperature T_g(x) and the non-reversing heat $\Delta H_{nr}(x)$ for the bulk As_2Se_3:Sn_x glasses. For low Sn concentrations, T_g of the base glass increases with x, suggesting that the base glass becomes more connected. However, as x approaches 5 %, T_g show a threshold behavior [14].

It has previously been shown that Sn is tetrahedrally coordinated to 4 Se nearest neighbors in a local $Sn(Se_{1/2})_4$ structure [14]. Apparently, the introduction of Sn to the As_2Se_3 base glass promotes the growth of $Sn(Se_{1/2})_4$ units; as a consequence the base glass becomes As-rich. The latter leads to the formation of $As_2(Se_{1/2})_4$ and As_4Se_4 structural units. It has been established that the hardness H of amorphous As_2Se_3:Sn_x thin films is generally higher than the hardness of bulk samples of the same chemical composition (Fig. 38.3).

The experimental results of the investigation of the hardness for bulk and amorphous thin As_2Se_3:Sn_x films are presented in Fig. 38.3; they are in good agreement with experimental results obtained earlier by Borisova [30]. The hardness values of bulk samples depend of the Sn concentration in the As_2Se_3:Sn_x

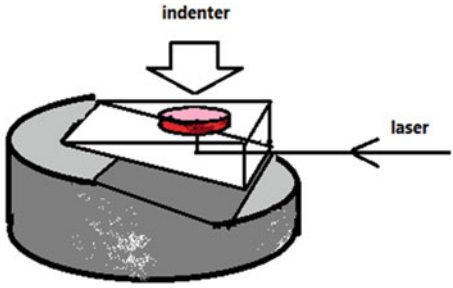

Fig. 38.1 Experimental set-up for the investigation of the photoplastical effect in chalcogenide glasses

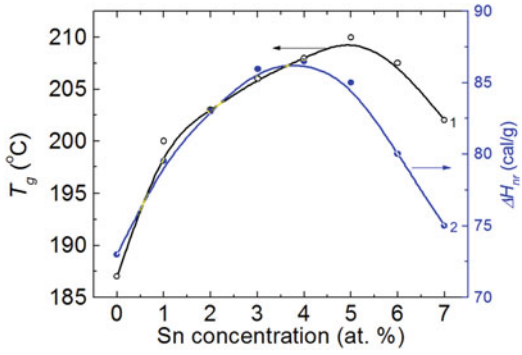

Fig. 38.2 Variations of $T_g(x)$ (1) and $\Delta H_{nr}(x)$ for As_2Se_3:Sn_x glasses. The *smooth lines* are computer fittings

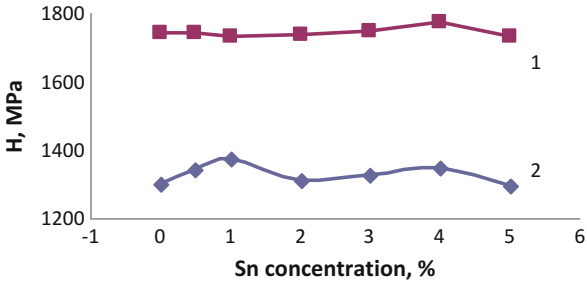

Fig. 38.3 The hardness of $(As_2Se_3)_{1-x}$:Sn thin films (*1*) and bulk samples (*2*)

glasses and vary between 1,297 and 1,376 MPa. The hardness of the amorphous thin films possesses a non-monotonous dependence on the Sn concentration. A sharp increasing of the hardness is observed when the impurity concentration exceeds the value of 3–4 % Sn. The hardness H of $(As_2Se_3)_{1-x}$:Sn_x films varies between $H = 1{,}732$–$1{,}780$ MPa. For both bulk samples and thin films the hardness is lower according to the data presented in Ref. [31]. This fact may be connected with some technological specifics in the preparation of the ChG.

In our experiments the photomechanical properties of As_2Se_3:Sn_x was investigated with a NHT-SCM nanohardness tester. The essential difference of the hardness values of films obtained using a micro hardness tester and a nanohardness tester is most probably due to the different methods of toperation. A microhardness

Table 38.1 The hardness vs. Sn concentration for amorphous As_2Se_3:Sn_x thin films

Nr.	Film composition	H (MPa) as-deposited films	H (MPa) illuminated films	H (MPa) bulk samples
1	As_2Se_3	1,780	1,768	1,300
2	$As_2Se_3:Sn_{0.5}$	1,762	1,783	1,341
3	$As_2Se_3:Sn_{1.0}$	1,734	1,614	1,376
4	$As_2Se_3:Sn_{2.0}$	1,735	1,628	1,311
5	$As_2Se_3:Sn_{3.0}$	1,745	1,656	1,327
6	$As_2Se_3:Sn_{4.0}$	1,774	1,660	1,347
7	$As_2Se_3:Sn_{5.0}$	1,732	1,607	1,297

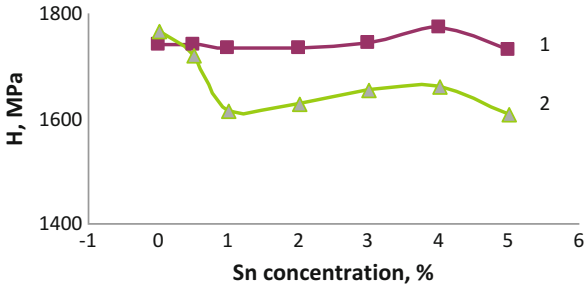

Fig. 38.4 The hardness of ss-deposited (*1*) and illuminated (*2*) $(As_2Se_3)_{1-x}$:Sn_x thin films

tester calculates the hardness values from the projected area of relaxed imprints. The nanohardness testers operate in the dynamic mode of data collection, and calculate the hardness values using projected imprint area when the indenter is unloaded, but is not totally removed from the material. During in-situ illumination of the films, a decrease of the hardness was observed (Table 38.1 and Fig. 38.4). The photo-plastic effect becomes more pronounced when the Sn concentration increases. Under illumination the nanohardness of amorphous As_2Se_3:Sn_x thin films decreases. This effect is more pronounced for Sn concentrations greater than 1.0 at.%. A decrease of nanohardness under illumination was also observed for as-deposited and annealed amorphous $As_{40}Se_{60}$ thin films [24].

A microscopic model of this phenomenon is based on the assumption of a athermal decrease of the viscosity of the films during irradiation, which is close to the viscosity of vitreous semiconductors near their glass transition temperature T_g [23]. It was suggested that the photoviscous effect, i.e. the athermal decrease of the viscosity of non-crystalline chalcogenides upon illumination is the key for considerable photoinduced effects in different amorphous chalcogenide films [25].

Figure 38.5 presents the changes of the surface morphology of the as-deposited amorphous As_2Se_3:$Sn_{0.1}$ thin film under an indentation load after (a) and before light illumination (b).

In order to investigate the modification of the optical parameters (optical band gap E_g, absorption coefficient α, refractive index n) by light irradiation, the transmission spectra $T = f(\lambda)$ of amorphous As_2Se_3:Sn_x thin films with different amounts of Sn were measured. Increasing the Sn concentration increases the absorption

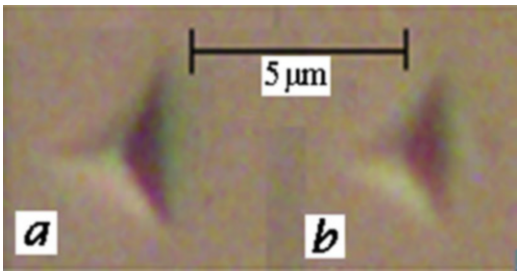

Fig. 38.5 The surface morphology of as-deposited amorphous $As_2Se_3:Sn_{0.1}$ thin film after indentation after light illumination (**a**) and before light illumination (**b**) mW/cm^2

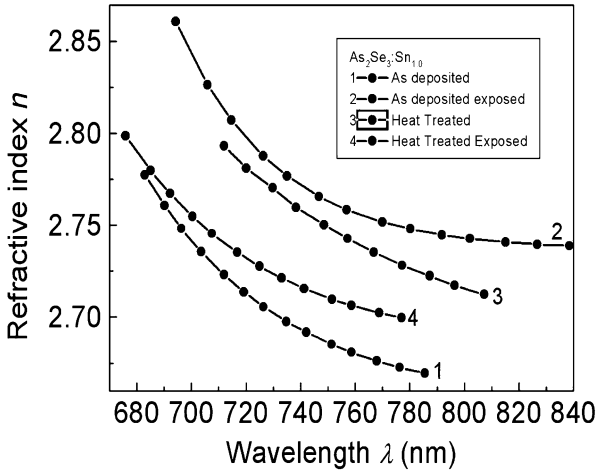

Fig. 38.6 Dispersion curves of the refractive index $n = f(\lambda)$ for the amorphous $As_2Se_3:Sn_{1.0}$ thin films: as-deposited (curve 1), as-deposited upon light exposure (curve 2), as–deposited upon heat treatment (curve 3), and as- deposited upon heat treatment and light exposed (curve 4)

coefficient and decreases the optical band gap [32]. At the same time the Sn concentration in amorphous $As_2Se_3:Sn_x$ thin films and light illumination increase the refractive index n.

Figure 38.6 represents dispersion curves of the refractive index $n = f(\lambda)$ for amorphous $As_2Se_3:Sn_{1.0}$ thin films. From Fig. 38.6 one can observe that the maximum modification of the refractive index Δn take place for fresh as- deposited amorphous films upon light exposure ($\Delta n = 0.078$, curves 1 and 2). For annealed amorphous thin films the modification of the refractive index Δn under light exposure is smaller ($\Delta n = 0.016$, curves 1 and 4). These observations may be explained by the fact, that for the annealed amorphous films the structure of the films became more stable.

The plot $(n^2 - 1)^{-1}$ vs $(h\nu)^2$ (Fig. 38.7) allows the determination of the oscillator parameters by fitting a straight line to the experimental points. For as-deposited amorphous $As_2Se_3:Sn_{1.0}$ thin films, by extrapolating the fitting line towards $(h\nu)^2 = 0$, one can obtain the static refractive index $n(0) = 2.321$ and the static dielectric constant $\varepsilon_s = n^2(0) = 5.386$. For as-deposited thin films these values are higher after the light exposure $n(0) = 2.338$ and $\varepsilon_s = n^2(0) = 5.464$, respectively.

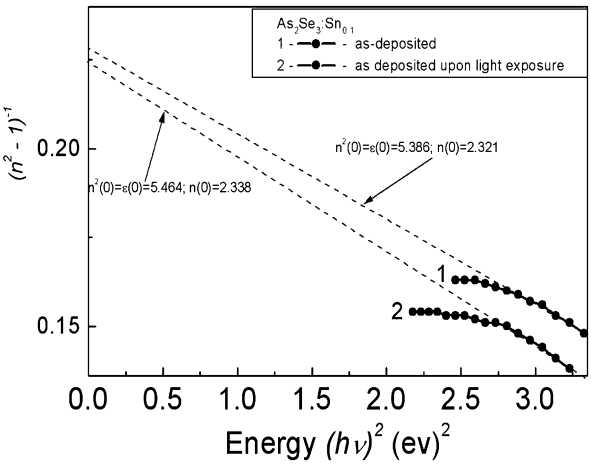

Fig. 38.7 The dependence $(n^2-1)^{-1}=f((h\nu)^2)$ for as-deposited amorphous As_2Se_3:$Sn_{1.0}$ thin films (*1*) and as-deposited films after light exposure (*2*)

The dispersion of the refractive index is related to the electronic absorption spectrum through the Wemple equation based on the single electronic oscillator model [33]:

$$\left(n^2-1\right)=\frac{E_dE_0}{E_0}-(h\nu)^2, \tag{38.2}$$

where E_0 is the average electronic energy gap, and E_d the dielectric oscillator strength.

Large values of the refractive index n are obtained for small E_0 and large E_d and lead to a large dispersion in the chalcogenide material. From (38.2) one obtains

$$\left(n^2-1\right)^{-1}=\frac{E_0}{E_d}-\left(\frac{1}{E_0E_d}\right)(h\nu)^2 \tag{38.3}$$

Using the plot $(n^2-1)^{-1}$ vs $(h\nu)^2$, for amorphous As_2Se_3:$Sn_{1.0}$ thin films E_0 and E_d were calculated to values of $E_0=3.094$ eV and $E_d=13.571$ eV for as-deposited films, and $E_0=2.906$ eV and $E_d=12.972$ eV for as-deposited films after light exposure, respectively. The value of $E_0=3.094$ eV is higher than the value of the optical band gap $E_g=1.82$ eV calculated from a Tauc plot. For the amorphous $As_{12.6}Ge_{23.8}S_{63.6}$ the relationship between the values of E_0 and E_g was established to be $E_0\approx 2\times E_g$ [34].

38.4 Summary

In this paper the effect of Sn addition on the nano-hardness and related thermo-mechanical properties of glassy As_2Se_3:Sn_x bulk samples and thin films were investigated. It was found that the nano-hardness of As_2Se_3:Sn_x changes

significantly after the incorporation of Sn as a chemical modifier. The interrelation between the mechanical properties of As_2Se_3:Sn_x bulk glasses and thin films has been determined. It was established that the hardness of amorphous thin films is generally higher than the hardness of bulk samples of the same chemical composition. From transmission spectra, the degree of modification of the optical constants under light exposure and heat treatment was determined. It was established that light exposure increase the refractive index. The oscillator parameters E_0 and E_d also were estimated by fitting a straight line to the data.

Acknowledgments The work is supported by the Project no. 11.817.05.03A (IAPh ASM).

References

1. Inoue A, Shen B, Nishiyama N (2008) In: Miller M, Liaw P (eds) Bulk metallic glasses. Springer, New York, p 1
2. Inoue A, Shen B, Takeuchi A (2008) Mater Trans 47:1275
3. Inoue A (2001) Mater Sci Eng A 304–306:1
4. Johnson WL (1999) MRS Bull 24:42
5. Aggarwal ID, Sanghera JS (2002) J Optoelectron Adv Mater 11(3):665
6. Andriesh AM, Iovu MS (2004) In: Lucovsky G, Popescu M (eds) Non-crystalline materials for optoelectronics, vol 1, Optoelectronic materials and devices. INOE Publishing House, Bucharest, p 155
7. Freeman D, Madden S, Luther-Davies B (2005) Opt Express 13(8):3079
8. Gerbreders A, Teteris J (2007) J Optoelectron Adv Mater 9(10):3164
9. Reinfelde M, Teteris J (2011) J Optoelectron Adv Mater 13(11–12):1531
10. Iovu MS, Shutov SD, Toth L (1996) Phys Status Solidi B 195:149
11. Iovu MS, Syrbu NN, Shutov SD, Vasiliev IA, Rebeja S, Colomeico E, Popescu M, Sava F (1999) Phys Status Solidi A 175(2):623
12. Iovu MS, Shutov SD, Arkhipov VI, Adriaenssens GJ (2002) J Non-Cryst Solids 299&302:1008
13. Iovu MS, Shutov SD, Popescu M (2002) J Non-Cryst Solids 299&302:924
14. Boolchand P, Georgiev DG, Iovu MS (2005) Chalcogenide Lett 2(4):27
15. Iovu MS, Harea DV, Cojocaru IA, Colomeico EP, Prisacari A, Ciorba VG (2007) J Optoelectron Adv Mater 9(10):3138
16. Kumar P, Thangaraj R (2006) J Non-Cryst Solids 352:2288
17. Kumar P, Bindra KS, Suri N, Thangaraj R (2006) J Phys D Appl Phys 39:642
18. Kuczynski GC, Hochman RF (1957) Phys Rev 108:946
19. Yamane M, Mackenzie JD (1974) J Non-Cryst Solids 15(2):153
20. Gerasimov AB, Chiradze GD, Kutivadze G (2001) Semiconductors 35(1):72
21. Carlsson L, Svensson C (1970) J Appl Phys 41(4):1652
22. Trunov ML, Bilanish VS (2003) J Optoelectron Adv Mater 5(5):1085
23. Trunov ML, Bilanish VS, Dub SN (2007) J Non-Cryst Solids 353:1904
24. Trunov ML (2008) J Phys D Appl Phys 41:074011 (9 pp)
25. Yannopoulos SN, Trunov ML (2009) Phys Status Solidi B 246(8):1773
26. Trunov ML, Lytvyn PM, Nagy PM, Dyachynska OM (2010) Appl Phys Lett 96:111908
27. Asahara Y, Izumitani T (1974) J Non-Cryst Solids 15(2):343–346

28. Iovu MS, Harea DV, Colomeico EP, Cojocaru IA (2008) J Optoelectron Adv Mater 10(12):3469–3476
29. Boyarskaya YS (1986) Physics processes of micro indentation. Shtiintsa, Chisinau
30. Borisova ZU (1972) Physics of vitreous semiconductors. Chimia, St. Petersburg (in Russian)
31. Borisova ZU (1983) Chalcogenide semiconducting glasses. Chimia, St. Petersburg (in Russian)
32. Iaseniuc OV, Harea DV, Iovu MS, Colomeico EP, Harea EE, Cojocaru IA, Shepel DF, Meshalkin A (2012) Proc SPIE 8411:84110L
33. Ruan Y, Jarvis AR, Rode AV, Madden S, Baarry L-D (2005) Opt Commun 252:39
34. Stronski AV, Vlcek M, Tolmachov ID, Pribylova H (2009) J Optoelectron Adv Mater 11:1581

Chapter 39
$BaTiO_3$-Based Glass-Ceramics: Microstructure and Phase Composition

L. Vladislavova, R. Harizanova, C. Bocker, G. Avdeev, G. Tsutsumanova, I. Gugov, and C. Rüssel

Abstract $BaTiO_3$ is a well-known dielectric material with numerous allotropic modifications and interesting electrical and mechanical properties. Two modifications of barium titanate are usually of practical interest – the cubic and tetragonal one. Due to their high dielectric constants they both find application as parts of capacitors, different sensors or transducers. The present work reports on the synthesis of oxide glasses with high concentrations of alkali and alkaline earth metals and varying ratios of sodium to aluminium oxide in which further the crystallization of $BaTiO_3$ is envisaged. The glasses obtained were subsequently subjected to annealing above the glass-transition temperature which results in the precipitation of barium titanate with very high volume fractions. The identification of the phase composition was performed by X-ray diffraction which suggests the formation of cubic $BaTiO_3$. The investigation of the microstructure by scanning electron microscopy revealed the presence of phase separation and further growth of barium titanate globular crystals in the unmixed regions.

Keywords Oxide glass • Barium titanate • Crystallization • Microstructure

39.1 Introduction

The preparation of oxide glasses containing alkaline earth and 3d-metal oxides with high concentrations has been intensively investigated in the past few years due to the electrical and magnetic properties of the resulting synthesis products and the

L. Vladislavova • R. Harizanova (✉) • I. Gugov
University of Chemical Technology and Metallurgy, 8 Kl. Ohridski Blvd, 1756 Sofia, Bulgaria
e-mail: ruza_harizanova@yahoo.com

C. Bocker • C. Rüssel
Otto-Schott-Institut, Jena University, Fraunhoferstr. 6, 07743 Jena, Germany

G. Avdeev
Institute for Physical Chemistry, Bulgarian Academy of Sciences, Acad. G. Bonchev Str. Bl. 11, 1113 Sofia, Bulgaria

G. Tsutsumanova
Faculty of Physics, Sofia University, 5 James Bourchier Str., 1164 Sofia, Bulgaria

P. Petkov et al. (eds.), *Nanoscience Advances in CBRN Agents Detection, Information and Energy Security*, NATO Science for Peace and Security Series A: Chemistry and Biology, DOI 10.1007/978-94-017-9697-2_39

possibility to combine them in a single material [1–6]. The high crystallization tendency of the resulting compositions offers the possibility to obtain glassy materials in which furthermore crystallization of phases containing the modifying ions with large volume fraction of the crystals formed can be achieved. Thus, after applying appropriate time-temperature heat-treatment regimes to the glasses obtained, the crystallization of one dielectric and one magnetic phase, i.e. multiferroic crystals, can be achieved [1]. The resulting glass-ceramic materials will find application for the preparation of powerful capacitors, as parts of different sensor devices and as resistance elements with a positive thermal coefficient [1–9].

Subject of the present investigation is the synthesis of glasses in the system $Na_2O/BaO/TiO_2/B_2O_3/SiO_2/Al_2O_3/Fe_2O_3$ with high barium and titanium concentrations and with less than 30 mol% glass-forming oxides. By varying the ratio $[Na_2O]/[Al_2O_3]$ and applying appropriate time-temperature programs to the glasses obtained, the precipitation of $BaTiO_3$ and possibly, $BaTiO_3$-Fe_3O_4 was aimed. As a further step of the investigation, the phase composition and the microstructure of the resulting glass-ceramics were studied.

39.2 Experimental

39.2.1 Preparation of the Glasses

Reagent grade raw materials Na_2CO_3, $BaCO_3$, SiO_2, $B(OH)_3$, $Al(OH)_3$, Fe_2O_3 and TiO_2 were used for the preparation of the batches and melting of the glasses. The batches (60 g) were melted in Pt-crucibles using a $MoSi_2$-furnace and a melting temperature of 1,250°C (always kept for 1 h in air). The melts were either quenched on a Cu-block or cast onto a metal plate and thereafter transferred to a pre-heated graphite mould and annealed in a muffle furnace for 10 min at 450 °C in order to release the mechanical stresses. Then, the furnace was switched off and the samples were allowed to cool to room temperature. In order to precipitate ferroelectric $BaTiO_3$ or multiferroic $BaTiO_3$-Fe_3O_4, the glasses were heat treated at different temperatures above T_g, according to the T_g and T_c-values determined from differential thermal analysis (DTA) measurements.

39.2.2 Characterization Methods

The characteristic temperatures of the glasses were determined on powdered samples by DTA using a heating rate of 10 K/min and Al_2O_3 as reference material. The phases were analyzed by X-ray diffraction (XRD) using $Cu_{K\alpha}$-radiation and 2θ-values in the range from 10 to 90°. The microstructure was investigated by scanning electron microscopy (SEM: JEOL 6510LV and LYRA/TESCAN), using

backscattered electron (BSE) and secondary electron (SE) detectors. The samples for SEM were coated with carbon to avoid charging.

39.3 Results and Discussion

Glasses were formed in all 3 sets of compositions in the investigated system $(23.1-x)Na_2O/23.1BaO/23TiO_2/7.6B_2O_3/17.4SiO_2/5.8Fe_2O_3/xAl_2O_3$, $x = 0$, 3 and 7 mol%. Only slight surface crystallization was observed. The glass-transition and crystallization temperatures were determined by DTA and the glasses were annealed according to the DTA results. In Fig. 39.1 a comparison of the XRD-patterns of 3 annealed samples is shown: without Al_2O_3 (4 h at 550 °C), with 3 mol% Al_2O_3 (3 h at 550 °C) and with 7 mol% Al_2O_3 (3 h at 610 °C). It is seen that in all samples cubic $BaTiO_3$ (JCPDS 98-003-1885) crystallizes as already reported by other authors [5, 8, 9]. Since the typical splitting of the peak at 2 theta = 45.3° is not observed, we conclude that the only modification of barium titanate crystallized in our samples is the cubic one [7–9]. In the annealed sample with 7 mol% Al_2O_3 also the formation of a second crystalline phase, i.e. $NaAlSiO_4$ (JCPDS 19-1176) is observed. In the XRD-pattern its strongest reflexes are marked by arrows. The peaks corresponding to $BaTiO_3$ are broadened. This is a hint that the crystals formed have sizes of some ten to some hundred nm. Similar results have also been reported for barium titanate crystals obtained by different chemical routes [9]. In Fig. 39.2, the crystal growth in case of isothermal annealing at 560 °C of samples with 3 mol% Al_2O_3 is shown. It can be seen that even for the shortest annealing period (5 min) crystallization of $BaTiO_3$ has taken place. When the annealing time is increased from 5 min to 100 h, the size of the barium titanate crystals will also increase and the volume fraction of the crystalline phase becomes larger as revealed in Fig. 39.2.

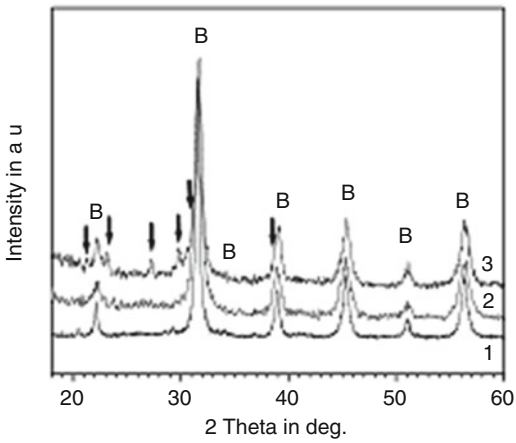

Fig. 39.1 XRD patterns of samples: (*1*) with 0 mol% Al_2O_3 annealed for 4 h at 550 °C, (*2*) 3 mol% Al_2O_3 annealed for 3 h at 550 °C and (*3*) 7 mol% Al_2O_3 annealed for 3 h at 610 °C – crystallization of $BaTiO_3$ (B) and a second (Na, Al)-silicate phase (*arrows*)

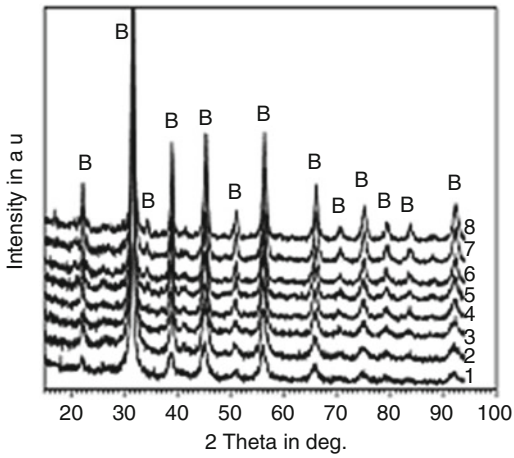

Fig. 39.2 XRD patterns of annealed samples with 3 mol% Al_2O_3: 5 min (*1*), 15 min (*2*), 1 h (*3*), 5 h (*4*), 10 h (*5*), 24 h (*6*), 48 h (*7*) and 100 h (*8*) at 560 °C – crystallization of $BaTiO_3$

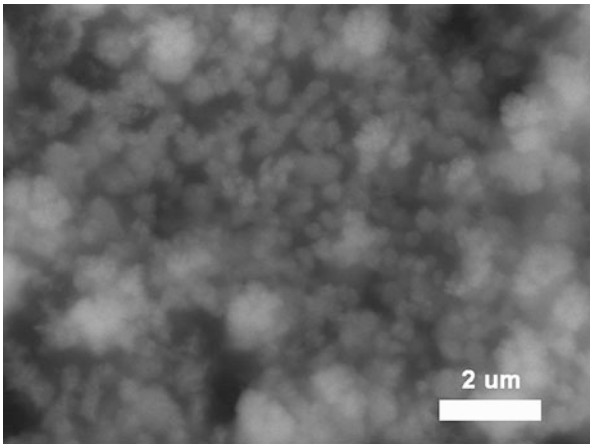

Fig. 39.3 SEM (BSE) micrograph of a sample with 3 mol% Al_2O_3 – annealed 1 h at 550 °C

The results from X-ray diffraction are supported by the SEM images of the fracture cross-sections of the glass-ceramics obtained. In Fig. 39.3, a SEM (BSE) micrograph of the fractured surface of the sample with 3 mol% alumina annealed for 1 h at 550 °C is shown. It is observed that spherical crystals which appear bright in the BSE image are formed. From this material contrast it is supposed that the crystals contain the heavier elements of the glass composition, i.e. $BaTiO_3$ is formed which is in agreement with the results from the X-ray diffraction. Additionally, the spherical particles tend to grow together and form interpenetrating aggregates – something already observed for a composition with 0 mol% alumina [2]. This suggests that in the samples phase separation occurs. Phase separation phenomena are typical for sodium aluminoborosilicate glasses [10, 11] and here

again, as already described in [10], a separation of the material into two phases takes place, one of them is enriched in Ba and Ti from which later the $BaTiO_3$ crystals are crystallized. The second one, i.e. the matrix is enriched in all other glass constituents. The average crystallite size of the formations in Fig. 39.3 is about 350 nm. In comparison to the SEM micrograph of the sample with 7 mol% alumina annealed for 1 h at 610 °C (near T_c) it is obvious that the increase in the alumina concentration leads to a decrease of the crystallite size. However, in Fig. 39.4 again interconnected bright structures are seen which also supports our idea about the existence of phase separation. The same microstructure is observed for the sample with 0 mol% alumina annealed for 24 h at 600 °C as shown in Fig. 39.5. Here also globular crystals are growing together, thus forming interconnected aggregates. For samples with 3 mol% alumina, attempts to perform energy dispersive X-ray

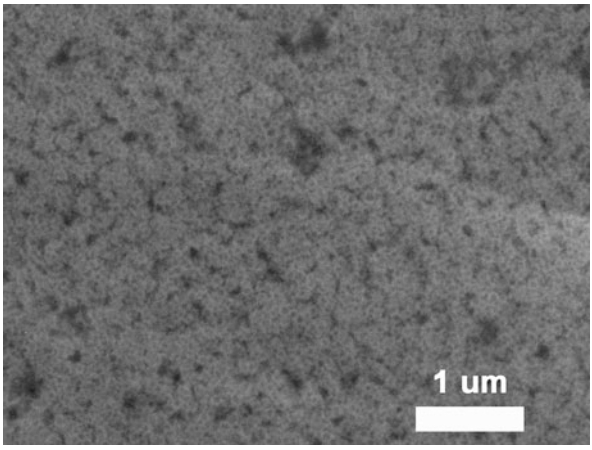

Fig. 39.4 SEM micrograph of a sample with 7 mol% Al_2O_3 – annealed 1 h at 610 °C

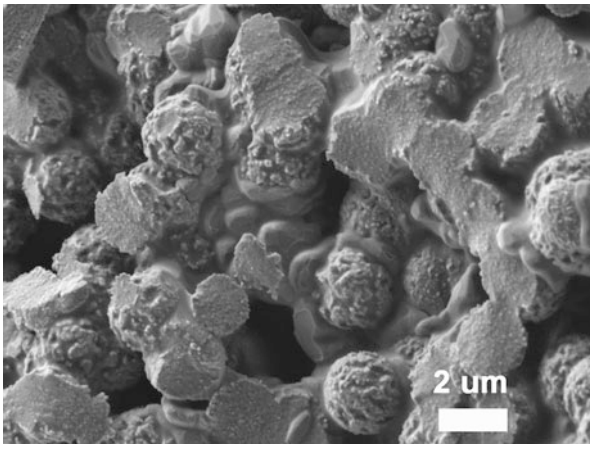

Fig. 39.5 SEM micrograph of a sample with 0 mol% Al_2O_3 – annealed 24 h at 600 °C

analysis (EDX) in the SEM on the bright crystals show that they are mainly enriched in Ba and Ti. The presence of Fe as a substitute of either Ti^{4+} or Ba^{2+} could not be excluded [12] but up to now no evidence exists from X-ray diffraction or EDX analysis in our study which supports this hypothesis.

39.4 Conclusions

The synthesis of bulk glasses is possible for all three sodium to aluminium oxide ratios. Annealing of the glasses near the corresponding crystallization temperatures results in the crystallization of $BaTiO_3$ for all time-temperature regimes applied. The increase of the alumina concentration to 7 mol% leads to the occurrence of a second sodium-aluminium silicate phase. Always globular interconnected barium titanate crystals are formed which implies the conclusion that phase separation occurs in all three compositions. There is no evidence from the available data that Fe takes part in the composition of the crystals formed.

References

1. Maiti RP, Basu S, Bhattacharya S (2009) J Non-Cryst Solids 355:2254
2. Vladislavova L, Harizanova R, Vasilev S, Gugov I (2012) Adv Nat Sci Theory Appl 1:89
3. Guo-Ping Du et al (2010) J Alloys Compd 492:L79
4. Jackson TJ, Jones IP (2009) J Mater Sci 44:5288
5. Libor Z et al (2011) J Mater Sci 46:5385
6. Zvezdin AK, Logginov AS, Meshkov GA, Pyatakov AP (2007) Bull Russ Acad Sci Phys 71:1561
7. Smith MB, Page K, Siegrist T, Redmond PL, Walter EC, Seshadri R, Brus LE, Steigerwald ML (2008) J Am Chem Soc 130:6955
8. Vijayalakshmi R, Rajendran V (2010) J Nanomater Biostruct Dig 5:511
9. Capsal JF et al (2010) J Non-Cryst Solids 356:629
10. Harizanova R, Völksch G, Rüssel C (2010) J Mater Sci 45:1350
11. Vogel W (1985) Glass chemistry, 2nd edn. Springer, Berlin/New York
12. Battisha IK, Hamad ABA, Mahani RM (2009) Physica B 404:2274

Part X
Applications: Sensors and Detectors

Chapter 40
Nanocrystalline Tellurium Films: Fabrication and Gas Sensing Properties

Dumitru Tsiulyanu and Adelina Moraru

Abstract A brief review of achievements in the fabrication of nanostructured tellurium thin films for applications in sensor technology is reported, paying particular attention to physical growth of nanocrystalline films in vacuum. The structure, growth and properties of Te films are determined by fabrication parameters such as the microstructure of the substrate, the growth rate or post-deposition UV irradiation. As shown by SEM, AFM and XRD, the rate most strongly influences the microstructure of the films and their gas sensing properties. An increase of the rate results in the transformation of the microcrystalline structure of the film to a nanostructured one, or even to an amorphous state. The gas sensing mechanism is explained in terms of a model that involves hole accumulation at the Te nanocrystallites surfaces due to interactions of dangling bonds and a lone-pair electron of the chalcogen. This model can explain, for instance, the "strong" chemisorption of nitrogen dioxide, which results in an increase of the work function $\Delta\Phi > 0$ and the electrical conductivity $\Delta\rho > 0$ as a consequence of the additional charging of the surface and band bending. In ultrathin (<40 nm) amorphous tellurium thin films, a damping of the sensitivity induced by high gas (NO_2) concentration was observed for the first time. The sensitivity of an ultrathin Te film decreases near linearly with increasing concentration between 150 and 500 ppb nitrogen dioxide which needs to be taken into consideration by the sensor technology.

Keywords Nanotechnology • Tellurium films • Gas sensors

40.1 Introduction

Tellurium is a high functional semiconductor material with wide applications in microelectronics and optoelectronics [1], but its application in nanotechnology is still in progress. In the past decade it became evident that tellurium nanostructures such as nanocrystals, nanotubes, nanoribbons and nanowires are potential blocks

D. Tsiulyanu (✉) • A. Moraru
Department of Physics, Technical University, bd. Dacia 41, 2060 Chisinau, Moldova
e-mail: tsiudima@gmail.com

P. Petkov et al. (eds.), *Nanoscience Advances in CBRN Agents Detection, Information and Energy Security*, NATO Science for Peace and Security Series A: Chemistry and Biology, DOI 10.1007/978-94-017-9697-2_40

for building new effective electronic devices, including physical and chemical sensors. This is the reason why the main efforts were conducted in the development of new methods of the growth of nanoblocks and their aligning to construct thin films or others device architectures. Wang et al. [2] developed a facile route to prepare two-dimensional (2D) nanostructured thin films, which consists of Te nanoflakes, via thermal decomposition of tellurium diethyldithiocarbamato (TDEC) films. The methods of tellurium nanotube growth include: vacuum deposition on silicon substrates with silver/gold nanoparticles as nucleation centers [3], synthesis by galvanic displacement [4], direct vapor phase process [5], synthesis through a microwave reflux method [6], filling of double-wall carbon nanotubes (DWCNTs) with trigonal tellurium [7] etc. Considerable effort has been devoted to produce various Te nanowires and nanoribbons.

Nanowires with diameters around 25 nm were synthesized via a hydrothermal reaction using Na_2TeO_3 and $Na_2S_2O_3$ as starting materials [8], but Te nanoribbons were aligned using a lithographically patterned nanowire electrodeposition technique [9]. In spite of the variety of methods available to produce nanodimensional blocks of tellurium, until lately gas sensing performances have not been demonstrated, due to difficulties to construct devices with aligned one- or two-dimensional nanoelements. In this context, the thermal vacuum deposition [10] or related technologies such as thermal evaporation in an inert atmosphere [11], direct vapor phase processes [5] or physical vapor deposition [12] are the most used techniques for sensor fabrication. In this work we applied the thermal vacuum evaporation method for the fabrication of nanocrystalline Te films and established the interdependence between the technological fabrication parameters, the growth process, the phase/state structure, the morphology and the gas sensor properties of the films.

40.2 Fabrication of Nanostructured Tellurium Thin Films

One of the advantages of Te films over compound semiconductors is the avoidance of the stoichiometry problem. This advantage allows to use a large variety of methods of preparation, which can be divided in two large groups: physical and chemical (electrochemical) methods. Chemical methods have emerged in the last decade and, despite imperfections, attract more and more attention due to its simplicity and low costs. Let us consider some of them.

The method proposed by Shun Wang and coworkers [2] consists in thermal decomposition of tellurium dietyldithiocarbomato (TDEC) film resulting the growth of Te nanoflakes. The fabrication follows three stages:

(a) Preparation of a precursor solution via dissolving the TDEC in chloroform.
(b) Preparation of a TDEC thin film by dipping a glass substrate into the precursor solution at −10 °C.
(c) Preparation of nanostructured Te films via pyrolyzing TDEC thin films at constant temperature (350–450 °C) for 30 min in the presence of flowing nitrogen.

By pyrolyzation, decomposition of the TDEC occurs and 2D nanofilms composed of uniform nanoflakes can be obtained.

A simple method for synthesis of Te nanowires through a chemical reaction in an aqueous solution was proposed by Liang and Qian [8]. The method consists in hydrothermal treatment of a mixture of Na_2TeO_3, poly(vinyl pyrrolidone) and $Na_2S_2O_3$ dissolved in distilled water at 160 °C. During the hydrothermal reaction, Na_2TeO_3 is reduced by $Na_2S_2O_3$ to form Te clusters; at the same time, $Na_2S_2O_3$ becomes oxidized to $Na_2S_2O_4$. Because the synthesized trigonal tellurium has a highly anisotropic crystal structure, the formation of nanowires with diameters in the range 20–35 nm occurs.

Tellurium nanotubes are of particular interests for a chemical sensor technology as the area of contact with the species to be detected is essentially enlarged. Rheem and coworkers [4] proposed a method to synthesize Te nanotubes with controlled diameter and wall thickness by galvanic displacement of sacrificial cobalt nanowires. The synthesis consists of following stages:

(a) Synthesis of sacrificial cobalt nanowires (diameters of 70, 120 and 220 nm) by a template-directed electrodeposition from a 1 M $CoCl_2$ + 1 M $CaCl_2$ electrolyte using polycarbonate membranes as scaffolds.
(b) Releasing of cobalt nanowires by dissolving the template in 1-methyl-2-pryrrolidinone.
(c) Proper synthesis of Te nanotubes by galvanically displacing the sacrificial cobalt nanowires in *an* electrolyte (0.01 M $HTeO_2^+$ +1 M HNO_3). The synthesized nanotubes diameters are slightly larger than that of the sacrificial cobalt nanowire, but the wall thicknesses are in the range from 15 to 30 nm.

Traditional physical methods are still very attractive for the fabrication of tellurium thin films due to the possibilities to control the technological process and the easy construction of devices with aligned nanoblocks. Recently, Chiun and Huang [5] have synthesized Te nanotubes by a catalyst-free direct vapor phase process in an evacuated quartz tube heated in a furnace with three heating zones. The silicon substrates were placed in the last zone, so the nanotubes are grown in form of thin films. Experiments with different temperatures in the zones of the furnace have shown that Te nanotubes gradually evolve from nanoparticles to nanoflakes, to two-faced nanoscreens, to four-faced nanogrooves, to intermediary nanotubes, and finally to perfect hexagonal nanotubes.

Taking into account that so far thermal vacuum evaporation is the most used technology for sensor fabrication, we have applied it for the fabrication of nanocrystalline Te films. We have established that the structure, growth process and properties of Te films are strongly determined by the fabrication parameters such as the microstructure and temperature of the substrate and especially the growth rate. Tellurium (purity 99.999 %) based thin films have been prepared using different rates (1–30 nm/s) onto glass, sintered alumina, SiO_2, or electrochemically nanostructured Al_2O_3 substrates. The evaporation was performed from a tantalum boat at a working pressure of $\approx 10^{-4}$ Pa without heating or cooling the substrate. The growth rates of the films varied from 1 to 40 nm/s. The area of deposition was about

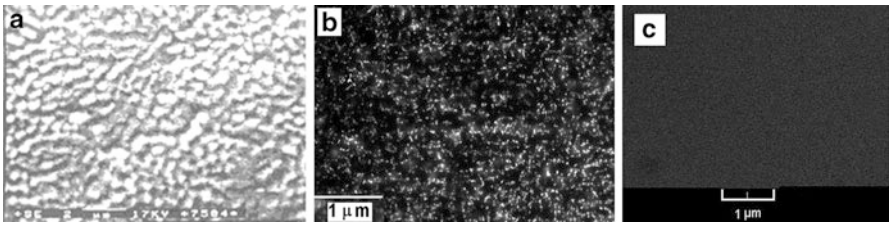

Fig. 40.1 SEM images of tellurium thin films grown on Pyrex glass substrates with deposition rates of (**a**) 1 nm/s, (**b**) 10 nm/s, and (**c**) 30 nm/s

70 mm^2. Rectangular samples of different thicknesses were prepared by variation of the evaporation time, while the distance between the evaporation boat and the substrate has been kept constant at 20 cm. The thicknesses and the shape of the films have been measured after their preparation using an atomic force microscope (SIS SCAN Control/C). The surface morphology of the films was investigated, using either a VEGA TESCAN TS 5130 MM or a TESLA BS 340 scanning electron microscope (SEM). X-ray analyses using a DRON –YM1 diffractometer with FeK α radiation was applied for structural investigations of the grown films. The rotation velocity of the scintillation counter was 2 (or 4) degrees/min. Experiments with different substrates have shown that the films grown with high deposition rates on glass and nanostructured Al_2O_3 substrates are continuous and smooth, but those grown on sintered alumina consists of interconnected islands. Therefore, we have concentrated our attention to films grown with different rates on glass Pyrex substrates. Figure 40.1a–c show the surface morphology of tellurium thin films grown on glassy substrates with different rates.

As can be seen the grown slowly film (1 nm/s) consists of a dense layer with crystal sizes of about 0.5–1.0 μm, which are oriented along the substrate. An increase of the deposition rate to 10 nm/s (Fig. 40.1b) results in the transformation of the microcrystals to nanocrystals. The layer remains dense but the aligned crystallites possess nanosize dimensions. When the growth is performed with a higher rate of ~ 30 nm/s (Fig. 40.1c) the film consists of a continuous amorphous layer.

The X-ray diffraction (XRD) pattern of these samples shown in Fig. 40.2a–c is in agreement with the above observations. The pattern of the microcrystalline films grown with a rate of 1 nm/s (Fig. 40.2a) shows them to be highly crystalline and to consist of the hexagonal phase of Te. The peaks positions match the standard values: the first, highest peak is due to reflections from (100) crystal planes, the second peak is observed due to reflections from (101) crystal planes and the third due to reflections from (110) crystal planes. It can be observed that the (100) peak appears to be unusual strong, compared with the standard pattern of trigonal tellurium. This suggests that the predominant growth orientation of the microcrystals is along the substrate. Figure 40.2b shows typical XRD pattern of a Te film

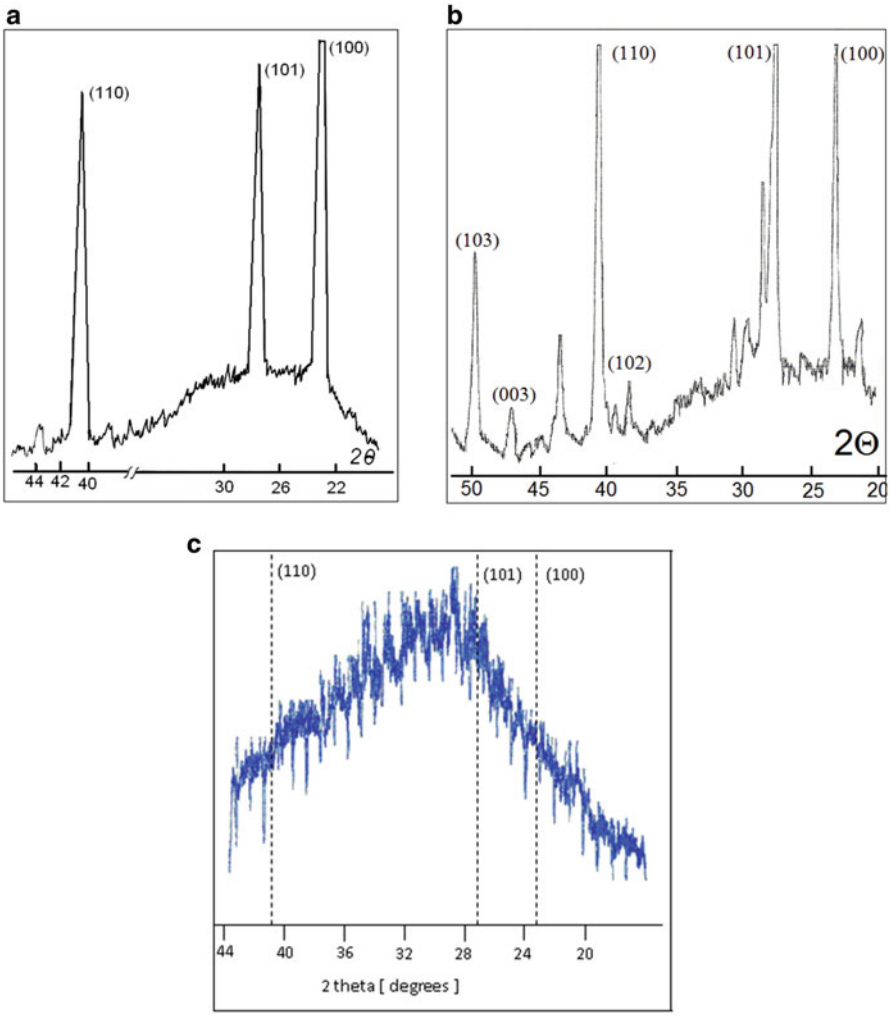

Fig. 40.2 XRD patterns of tellurium thin films grown on Pyrex glass substrates with deposition rates of (**a**) 1 nm/s, (**b**) 10 nm/s, and (**c**) 30 nm/s

prepared with a deposition rate of 10 nm/s; it shows that the crystallites sizes are in the nanometer range. It is clear that all X-ray reflections can be readily indexed to the hexagonal phase of tellurium (ASTM 4 -554). The intensities of the main reflection peaks is approximately the same, which indicates that there is no preferential grow orientation. Figure 40.2c shows the XRD pattern of tellurium film grown with a high deposition rate of ~ 30 nm/s. The reflection peaks corresponding to hexagonal Te (shown by the dotted lines) are not present, indicating the predominantly amorphous nature of the film.

40.3 Gas Sensing Characterization

To characterize the gas sensing properties of both nanocrystalline and amorphous Te films two kind of gas sensitive devices have been developed and realized: They are based either on a reversible variation of the resistivity or the work function under the influence of the tested gas. The first type is usually called resistive (or conductive), the second one is called work function operating gas sensor.

40.3.1 Conductive Sensors

The sensitivity of a conductive sensor is usually defined as the relative resistance variation expressed in percent, while the response and recovery times are the times required to reach 90 % of the steady-state value of the signal. To measure the electrical resistance, two electrodes were deposited onto the film surface by thermal evaporation of gold. Copper wires were then attached to the electrodes by silver paste. In some experiments, two indium dots were pressed on top of the film surface to serve as electrical contacts for the gas-sensing element. The distance between electrodes was ~ 5 mm so that the sensing area consists of about 30 mm^2.

Testing with gases with different concentrations was performed by using the experimental setup described in our previous publications (for instance [10]). A membrane pump provides a flow of the carrier gas (ambient air) which is split into two independent streams. Both lines lead to a thermostat, where they are connected to U-shaped glass tubes in which the carrier gas is saturated by the gas of interest at constant temperature. The saturation takes place in one of the U-shaped glass tubes, where a calibrated permeation tube with the gas is placed (Vici Metronics, USA). The second line is used either for dilution or as the reference. Both lines are fed through a diluting/switching system to the waste or the test cell, respectively. The devices were placed into a test cell (10 ml volume); the gases were injected parallel to the film surface with a flow rate of 100 ml/min, maintained by mass flow controllers (MFC, Wigha, Germany). A computer with a data acquisition board manufactured by National Instruments Inc. was used for processing.

Current transient characteristics were recorded while exposing samples grown with different rates, either as-grown or post-deposition treated by UV irradiation, to different gas concentrations. The applied voltage was usually kept at 5 V while the delay time between the measurements was varied between 0.1 and 3.0 s.

Figure 40.3 illustrates typical transient characteristics (in the described experimental setup) of as-grown nanocrystalline samples to a rectangular NO_2 pulse with 1.0 ppm concentration at room temperature. Comprehensive studies of such characteristics allow to completely characterize the sensor parameters: sensitivity, response and recovery times, the dynamic range (the range of concentrations, which can be detected), reversibility, selectivity (cross sensitivity) and stability.

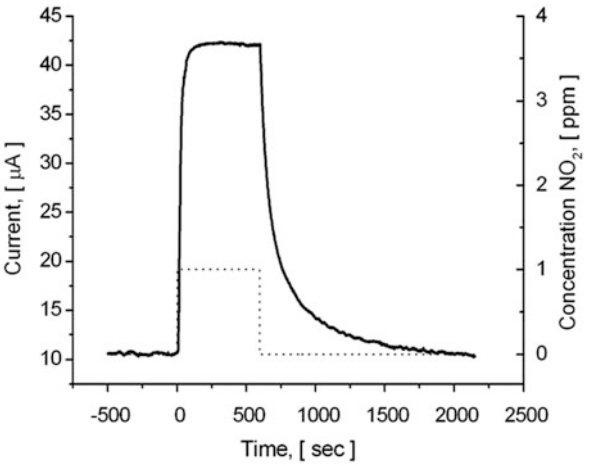

Fig. 40.3 Transient characteristics of the gas-induced current in a nanocrystalline Te film towards NO_2 applied at room temperature, according to the profile shown as *dotted line* at the bottom. The film was grown on a Pyrex glass substrate with a deposition rate of 10 nm/s

We concentrated our attention to effects of the dimensionality of the crystallites on response time and sensibility of the film towards the gas by choosing NO_2 as a model gas. Figure 40.4a–c show the dynamic response of Te thin films grown on glassy substrates with different rates which results in different phases/states: microcrystalline, nanocrystalline or amorphous.

It can be seen that transition from a microcrystallane structure to a nanocrystalline one and further to amorphous state of the films results in a noticeable diminishing of response the time. The diagram in Fig. 40.5a illustrates this observation. Amorphous thin films exhibit the shortest response time of only 10 s which is 60 times shorter than of microcrystalline films. The nanocrystalline film shows an intermediate response time of about 40 s.

On the other hand, the microcrystalline films exhibit the largest sensitivity. The diagram in Fig. 40.5b depicts the sensitivity of Te thin films to nitrogen dioxide versus their growth rate. Again the nanocrystalline films exhibit an intermediate value of about 30 %, which is in between the sensitivities of microcrystalline and amorphous films. To enhance the sensing parameters of nanocrystalline Te films we have used either post-deposition UV treatments or their thinning.

40.4 Effect of UV Irradiation

The sensitivity of Te film to ammonia (and other gases) arises from an induced reduction of tellurium oxides (TeO_2 and TeO_3) to Te metal on the top surface of the crystallites [13] and, obviously, depends on the existence and parameters of this oxide layer. On the other hand, it is long known [14, 15] that UV treatment of tellurium films results in their surface oxidization. Confirmed by X-ray photoelectron spectroscopy (XPS) [14], UV treatment of tellurium thin films oxidizes the

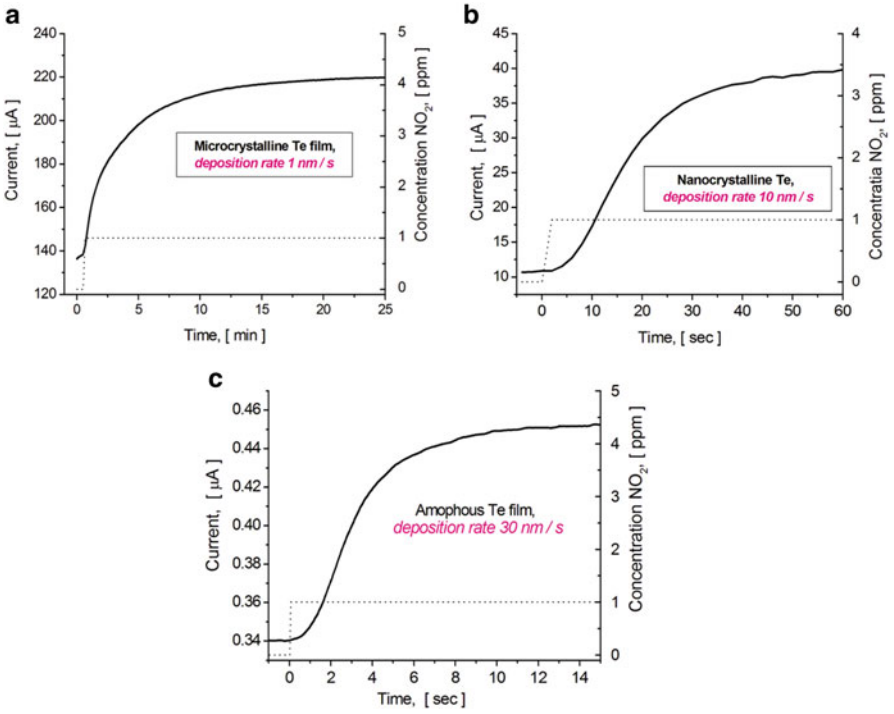

Fig. 40.4 Dynamic response at room temperature of tellurium thin films grown by different rates on glass substrates

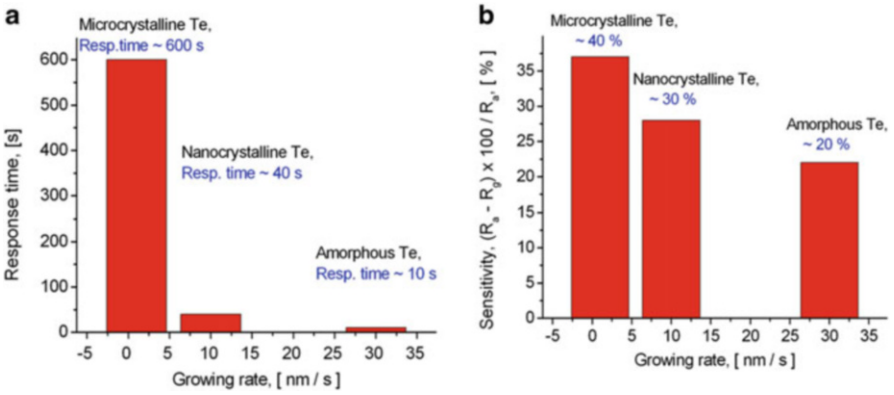

Fig. 40.5 Response time (**a**) and sensitivity of tellurium thin films to 1 ppm of NO_2 at room temperature (**b**) versus grown rate

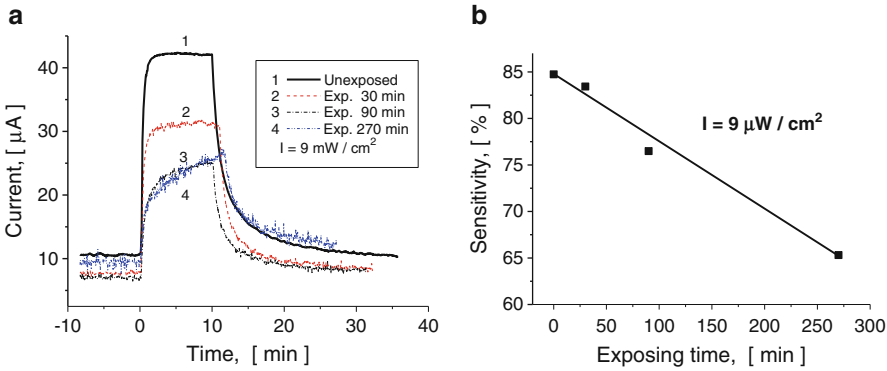

Fig. 40.6 Current transient characteristics of nanocrystalline Te films treated with different durations with a constant intensity of UV irradiation in the presence of 1 ppm NO_2

surface layer to TeO_2 down to a depth of about 25 nm which can contribute to photoconduction and other properties of the film.

We have performed UV irradiation of nanocrystalline tellurium films (grown with a rate of around 7 nm/s) at room temperature in an air atmosphere by exposing the films to the light of a 100 W mercury vapor lamp with a quartz window. The light intensities were calibrated using a vacuum thermoelement VTh-8 (Carl Zeiss, Jena, Germany). Two kinds of experiments have been carried out maintaining either the exposure time or the intensity of irradiation light constant. Figure 40.6a shows the transient characteristics of gas-induced currents in nanocrystalline Te films towards 1 ppm NO_2 applied at room temperature to an untreated sample and one UV treated with a constant intensity of ~ 9 mW/cm^2 for different exposure durations.

It is seen that an increase of the exposure time results in a linear decreasing of the gas sensitivity (Fig. 40.6b) of the sensors as well as in a increase of the response time but diminishes its recovery time. On the other hand, a considerable improvement of the gas-sensing parameters of the films can be obtained by treatment with high intensities of UV irradiation using short exposure times. This is illustrated in Fig. 40.7a, b.

Figure 40.7a shows the sensitivity of nanocrystalline Te films to 1 ppm NO_2 vs the intensity of UV irradiation applied in a post-growth treatment with a constant (30 min) exposure time. It can be seen that the treatment with UV intensities up to approximately 5 mW/cm^2 essentially (~ 20 %) enhances the sensor sensitivity, but at higher intensities a saturation is reached. Simultaneously, as shown in Fig. 40.7b, both response and recovery times decrease nonlinearly, also reaching saturation at high intensities of the UV irradiation used for treatment. It is remarkable that the response time decreases faster by nearly one order of magnitude in the range of UV intensities applied.

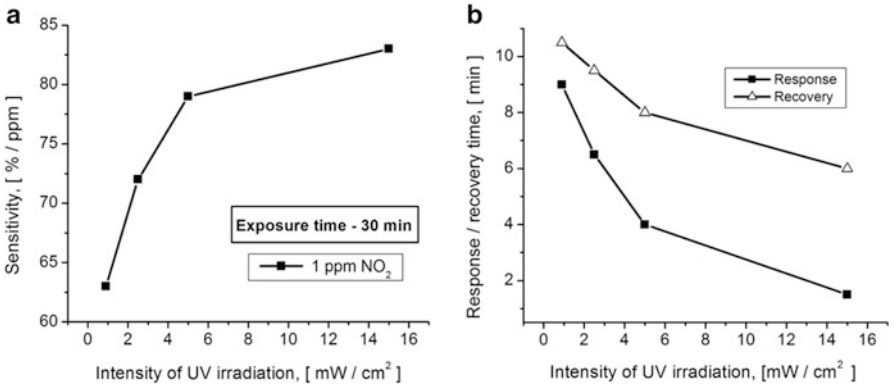

Fig. 40.7 Gas sensitivity (**a**) and response/recovery times (**b**) vs intensity of the UV irradiation used for a post-growth treatment for 30 min

40.5 Effect of Film Thickness. Concentration Induced Damping of the Sensitivity

Earlier, we have demonstrated [16] that the gas sensitivity of tellurium thin films depends on their thickness and can be enhanced essentially by reducing the thickness. A decrease of the Te film thickness from 120 nm to approximately 40 nm results in an increase of the sensitivity to NO_2 by more than 10 times. A current flow through two parallel channels explains such a behavior [17]. In a compact layer, the current flows through two parallel channels, one of them being the surface channel, which is affected by the gas reaction and the other, is the gas-unaffected bulk. Decreasing the layer thickness leads to an enhancement of the influence of the surface resistance and reduces that of the gas-unaffected bulk parallel resistance. In this context it appeared to be interesting making experiments with compact ultrathin layers (less than 40 nm). On the other hand, an increase of the deposition rate is associated with a shortening of the lifetime of atoms migrating on the substrate surface, a decrease of the degree of crystallite order and an increase of the compactness of the film [18]. That is the reason why we have studied [19] the gas (NO_2) sensing properties of ultrathin compact tellurium films grown with a high evaporation rate (around 30 nm/s). As the thickness could not be controlled during the growth, AFM was used to assess (by post deposition scratching) the thickness and homogeneity of the films.

Figure 40.8 shows AFM images of as-prepared thin (a) ~ 110 nm and ultrathin (b) ~30 nm Te films. It is seen that exception of separate jumps (which can be caused by measurement process) the surfaces of these films are smooth. The average roughness of 5 μm × 5 μm areas is about 2–3 nm.

SEM observations shown in Fig. 40.9a, b confirm that the films are smooth and without any traces of crystallites. X-ray diffraction data shown in Fig. 40.9c, d for these samples are in agreement with the above observations. The peaks

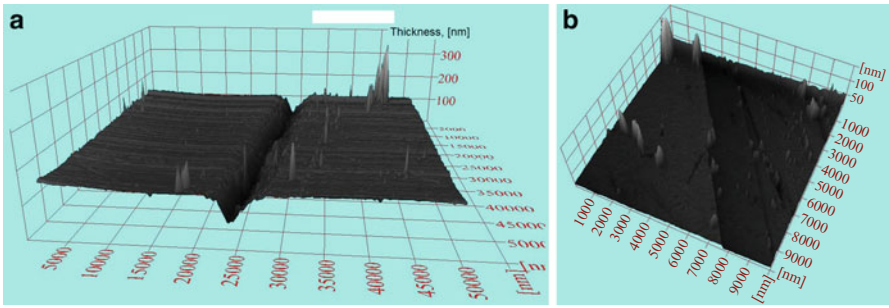

Fig. 40.8 AFM images of as-prepared (**a**) thin (110 nm) and (**b**) ultrathin (30 nm) Te films

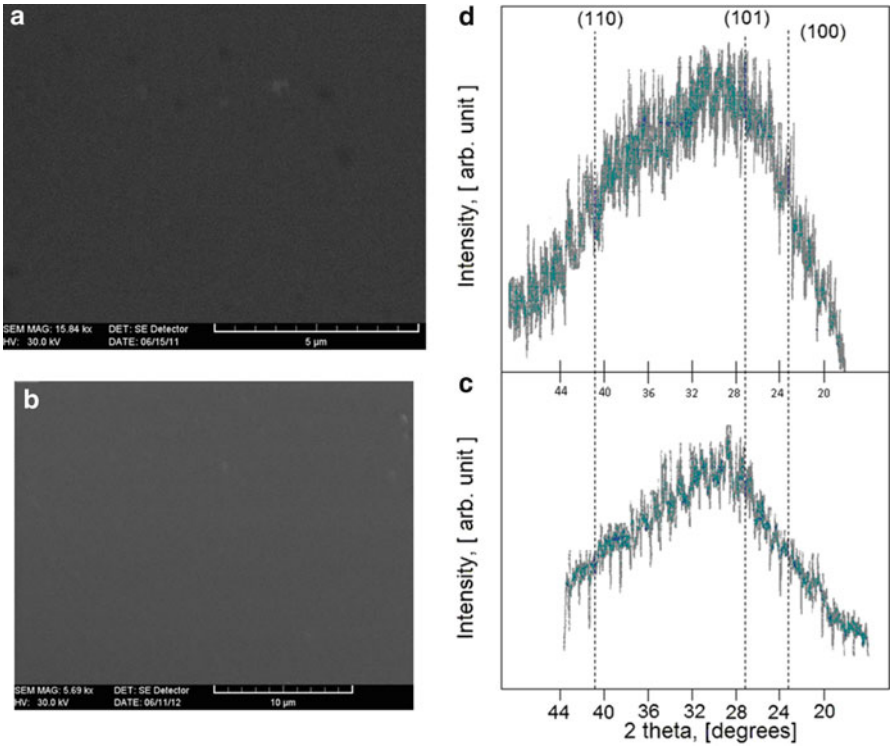

Fig. 40.9 SEM micrographs (**a**, **b**) and XRD diffraction pattern (**c**, **d**) of thin (110 nm) and ultrathin (30 nm) tellurium films, respectively

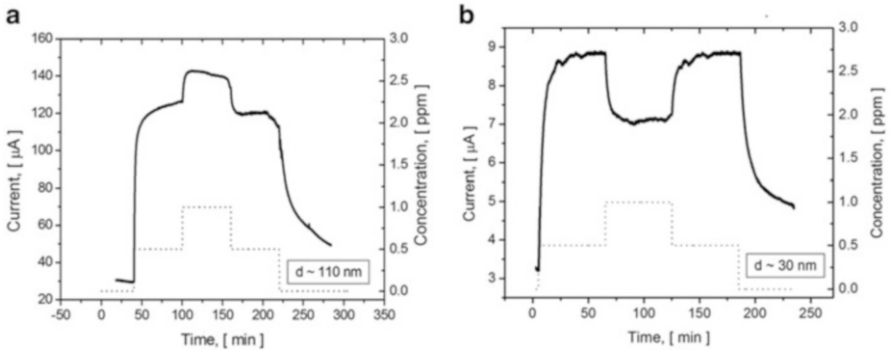

Fig. 40.10 Transient characteristics of gas-induced current by exposure of Te films to various concentrations of NO_2 according to the profile shown as *dotted lines* at the bottom. The film thicknesses were (**a**) 110 nm and (**b**) 30 nm

corresponding to hexagonal Te (shown by dotted lines) were not found, indicating the amorphous state of the films.

Current transient characteristics for these films are depicted in Fig. 40.10a, b. Squared pulses of NO_2 vapor were applied. The dotted line gives the switching schedule. Figure 40.10a shows the current flow through a thin (~110 nm) tellurium film under repeated switching the NO_2 gas mixture at constant bias voltage, room temperature (25 °C) and a relative humidity of 32 %. Humidification of the carrier gas was accomplished using a saturated solution of $CaCl_2$ in water, while a platinum resistive temperature detector PT-100 close to the sensor served as a temperature controller. It can be seen that the current follows the schedule showing the usual behavior: an increase of the concentration from 0.5 to 1.0 ppm NO_2 results in an increasing of the current. The recovery time is longer than the response time, which is only a few seconds. There is also a noticeable baseline drift.

Figure 40.10b illustrates the transient characteristics of the gas-induced current in an ultrathin (~30 nm) film on exposure to various concentrations of NO_2 according to the profile shown by the dotted lines at the bottom. In this film transition from 0.5 to 1.0 ppm NO_2 surprisingly results in a decrease of the current, i.e. a damping of the sensitivity induced by the high NO_2 concentration takes place.

Figure 40.11 depicts the sensitivity versus gas concentration in the range 0.15–0.5 ppm NO_2 (limited by our experimental set-up). It can be seen that in these limits of NO_2 concentrations the sensitivity of the sensor is near linearly damped with increasing gas concentration.

The concentration-induced damping of the sensitivity, i.e. the decrease of the conductivity may be due to a nitrogen dioxide catalytic gate created since the film surface may be NO_2 covered in excess [20]. The initial reactions for different concentrations of nitrogen dioxide take therefore place on different types of surfaces. Moreover, it seems that during the transient the switching phenomenon predicted by Lundström [20] occurs (Fig. 40.10b), where one type of coverage is rapidly transformed to another.

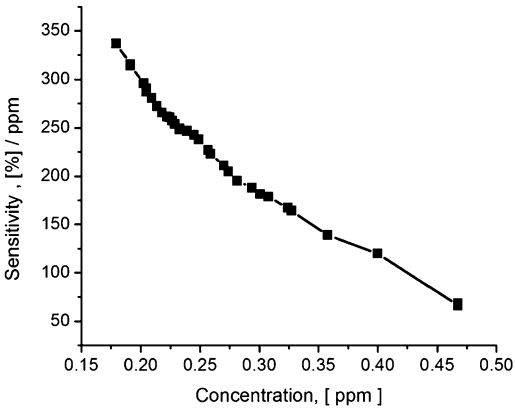

Fig. 40.11 Sensitivity of an ultrathin Te sensor vs. NO_2 gas concentration

From our experiments it follows that the other factors determining the damping effect are the thickness of the film and its phase/structural state (or compactness). SEM and XRD spectra show the tellurium films, physically grown in the present work by high rate thermal deposition in vacuum on glass substrates, to be amorphous. This is obviously due to the increase the of pressure of the tellurium vapor in the substrate area, which lowers the lifetime of atoms migrating on the substrate surface before being trapped in a suitable position with a minimal surface energy. The density of tellurium films strongly increases with the deposition rate; for deposition rates larger than 8,6 nm/s the density does not depend on the film thickness [18]. As in the present work the Te films were prepared with much higher rates (~ 30 nm/s) they definitely should be regarded as compact layers. In such a layer, the current flows through two parallel channels [17]: (a) the surface channel, which is strongly affected by the gas reaction, and (b) the bulk channel, in which the gas reaction is controlled by diffusion processes. Electrically this means two parallel resistors R_s (surface) and R_b (bulk) differently affected by the pollutant gas in question, although the microscopic mechanism of the gas interaction may be the same. Obviously, the bulk channel can be removed by reducing the film thickness to the nanoscale (<30 nm). In such a case, the reaction sites of the film are fully involved in the sensing response even at very low concentrations of nitrogen dioxide. An excess of NO_2 results in the formation of a catalytic gate that damps the sensitivity.

40.5.1 Work Function Operating Gas Sensors

The work function operating gas sensitive devises exhibit a good stability as the sensitive layer is not electrically treated; that is, in contrast to conductive sensors, electromigration cannot take place. The ability of a sensitive layer to be used in a work function operating devise can be tested with the Kelvin probe method, which is based on detection of the ac current induced in a dc voltage supplied circuit by a mechanical change of the capacitance value of a capacitor. The capacitor plates

consist of two materials; one is a reference material and other the material for which the work function has to be evaluated during the adsorption process. The current in such a circuit is given as:

$$I(t) = \frac{dQ}{dt} = \frac{d}{dt}\left[(V_0 - \Delta\Phi)\right] C = (V_0 - \Delta\Phi)\frac{dC}{dt} \tag{40.1}$$

were $\Delta\Phi$ is the work function difference between the two materials.

The Kelvin probe equipment usually consists of a gold grid reference electrode, oscillating by a piezoelectric transducer normal to the sample surface. In the present work, a commercial Kelvin probe (Besocke GmbH, Julich, Germany) was used for the work function measurements. Its gold grid reference electrode oscillates at a frequency of about 170 Hz. By use of this technique, the relative change of the work function $\Delta\Phi$ of the tellurium films was measured in the presence of a carrier gas (ambient air with different degree of humidification) and during exposure to a vapor with different concentration of pollutants:

$$\Delta\Phi = \Phi_{vapour} - \Phi_{air} \tag{40.2}$$

where Φ_{air} and Φ_{vapour} are the work functions of the sensitive film measured in air and in the presence of the vapor of interest, respectively.

40.6 Effect of NO_2 and Water Vapor. Cross Sensitivity to Other Gases

Figure 40.12 shows the work function variation $\Delta\Phi$ on exposing a Te thin film to different concentrations of nitrogen dioxide. The measurements were performed with repeated on/off switching of the NO_2 gas mixture. The dotted line gives the switching schedule.

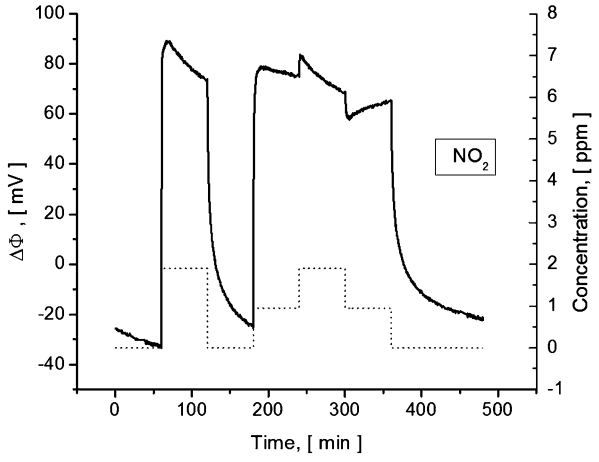

Fig. 40.12 Work function variation of a tellurium layer exposed to NO_2 according to the profiles shown at the *bottom*

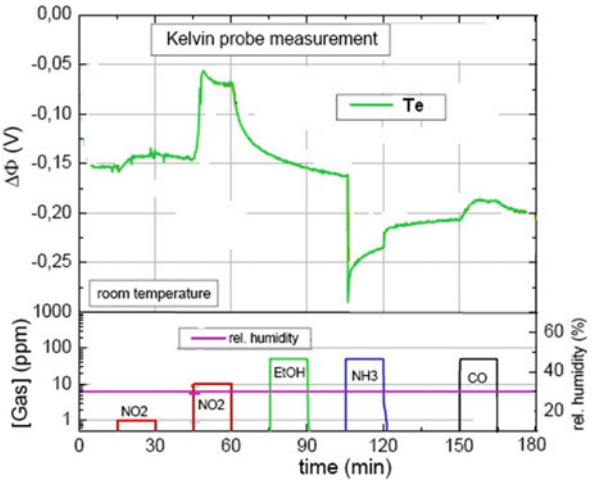

Fig. 40.13 Response of a Te film towards different gaseous pulses. The species and their concentrations are indicated in the picture

It can be observed that the NO_2 vapor results in an increase of the work function of the tellurium film, but after switching off the pollutant gas, the $\Delta\Phi$ curves return to their initial position. A NO_2 gas concentrations of 1.9 ppm lead to an increase of the work function by about 120 mV.

Such a remarkable response makes tellurium films attractive to be used as basic functional elements in gas sensitive field-effect transistors (GSFET) for the detection low concentrations of nitrogen dioxide, which is a highly toxic gas released by combustion, plants, automobiles etc. However, this application requires a low cross sensitivity to other possible harmful or toxic gases from the environment as well as to humidity. That is why we have investigated the work function variation exposing Te films to sequence of pulses of different gases (NO_2, CO, NH_3, C_2H_5OH, H_2S et al.). Figure 40.13 depicts the results of the work function response to a number of the species mentioned. It can be seen that the Te films manifest a strong cross sensitivity to ammonia and humidity but low cross sensitivity to CO and ethanol. The effect of water vapor was investigated in this work more detailed.

Figure 40.14 shows the temporal evolution of the work function as the surface of a Te layer is exposed to air with different relative humidities. An increase in the humidity of the carrier gas (air) leads to a nonmonotonic increase of the work function variation ($\Delta\Phi > 0$). Saturation occurs for applied relative humidities higher than 45 %. The work function change $\Delta\Phi$ is very high, reaching approximately 200 mV. The response and the recovery time τ_{90} are only a few minutes.

40.7 Mechanism of Gas Induced Work Function Variation

The contact potential difference (CPD) measured in the present work vs. a vibrating gold grid reference electrode is

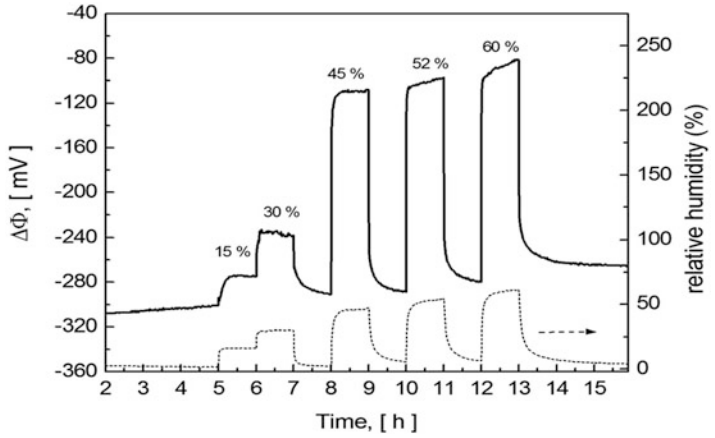

Fig. 40.14 Work function variation for a sequence of pulses of humid air (15, 30, 45, 52, and 60 % RH) for an operating temperature of 23 °C

$$\mathrm{CPD} = (\Phi - \Phi_{Au})/e \tag{40.3}$$

where Φ is the work function of the sample, Φ_{Au} the work function of the gold grid reference electrode, and e is the elemental charge. On the other hand, the work function value in a semiconductor material is the sum of several terms:

$$\Phi = \mu + \phi_0 + \varphi \tag{40.4}$$

where μ is a bulk chemical potential, ϕ_0 is the surface dipole potential and φ is the (eventual) band bending. Considering gold as an inert reference material, the work function variation $\Delta\Phi$ due to gas adsorption can be caused by variation of ϕ_0 or/and φ of the Te film, which depends on the nature and number of adsorbed particles, whiles μ is independent on adsorption, being determined by the nature and state (nature and concentration of impurities, temperature, etc.) of the semiconductor, that is,

$$\Delta\Phi = \Delta\phi_0 + \Delta\varphi \tag{40.5}$$

Consequently, it is necessary to additionally investigate the presence of either ϕ_0 or /and φ contributions in to the work function variations caused by gas adsorption.

The investigation of influence of nitrogen dioxide or/and water vapor adsorption on the electrical conductivity can help to determine the possible contributions of band bending or of a surface dipole potential to changes of $\Delta\Phi$, which cause CPD variation. Above (Fig. 40.3) it was shown that the current flow through a tellurium film exposed to NO_2 increases when the gas is applied and depends on its concentration. Thus, the adsorption of NO_2 results in an increase of both the work function

difference ($\Delta\Phi > 0$) and the electrical conductivity ($\Delta\rho > 0$) of the films under discussion.

As far as the influence of water vapor is concerned, the film behavior is particular. Earlier, we have shown [10] that the humidity decreases the electrical conductivity of the film. A relative humidity of 58 % in air at 23 °C diminishes the conductance of the film by ~ 15 % in approximately 45 min. Thus, the effect of water vapor on the electrical conductivity appears to be opposite to that of nitrogen dioxide: the adsorption of water vapor leads also to an increase in the work function change ($\Delta\Phi > 0$) but diminishes the electrical conductivity of the film ($\Delta\rho < 0$). Note, that the humidity response of the sensor heated to 70 °C becomes negligible [10].

Such a behavior can be understood by considering the peculiarities of tellurium, which belongs to so-called lone-pair (LP) semiconductor materials [21]. The main feature of lone-pair semiconductors is that the upper part of the valence band is formed by p-state lone-pair electrons. If the network of a LP glassy or crystalline semiconductor contains defects, such as unsaturated chemical bonds (dangling bonds), an interaction between these defects and lone-pair electrons takes place. The dangling bonds interact with a neighboring lone-pair, bond to it and distort its environment (Fig. 40.15a). This interaction results in the formation of lattice defects and release about 10^{13}–10^{15} holes/cm^3, which causes p-type conductivity.

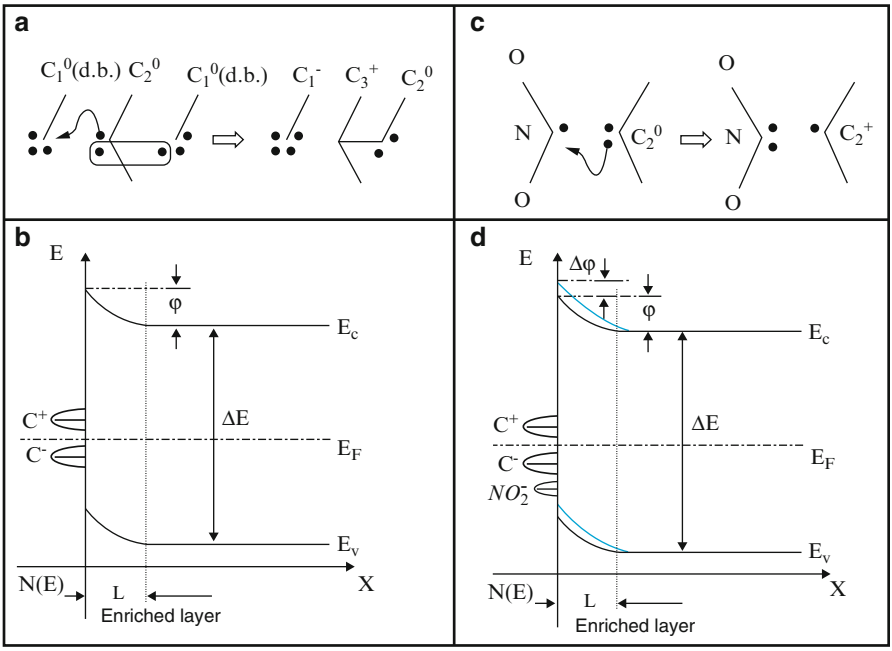

Fig. 40.15 Model of the dangling bonds – lone pair electrons interactions and the surface state bands at the tellurium surface, before (**a**, **b**) and after (**c**, **d**) adsorption of acceptor-like gas molecules (NO_2)

Since the maximum concentration of dangling bonds is situated on the surface, a hole enriched (accumulation) region is formed there; as a consequence the, the bands bend up (Fig. 40.15b). This region includes also the grain boundaries. In this respect, the gas sensing is due to variation of hole density or/and their mobility in the accumulation region (surface and grain boundary) in the presence of gaseous media.

When a tellurium film is exposed to a gaseous environment adsorption of gas molecules takes place, which can create either donor or acceptor levels. As far as the adsorption of nitrogen dioxide is concerned, its molecule possesses an odd electron [22]; that is, after covalently bonding of the nitrogen to the oxygen, one of the atoms remains with a single unpaired electron. Being adsorbed on the surface of the Te (grain) surface, the NO_2 molecule acts as a dangling bond (Fig. 40.15c) which can accept a LP electron to form an electron pair via the reaction:

$$NO_2 + e^- \rightarrow NO_2^- + h \tag{40.6}$$

Thus, the capture of a LP electron, i.e., the transition of an electron from the upper part of the valence band to a NO_2 acceptor level is accompanied by the release of an additional hole at the surface. As a result, both the band bending (φ) and electrical conductivity ρ increase (Fig. 40.15d), which gives rise to an increase of the work function ($\Delta\Phi > 0$) and the dc current, which is indeed observed in experiments. It is obvious that chemisorption of others gases implies other surface reactions, which can lead either to an increase or a decrease of the majority carrier density in the grain boundary region and hence to an increase or a decrease of the work function and conductivity of the film. In fact, the response of tellurium films to ammonia was shown [13] to result in a reduction of tellurium oxide atoms present on the surface and the intergrain regions, which also act as acceptors. Note that in this experiment the influence of the dipole component of the work function, which can arise from the existence of an electrical double layer at the surface, does not manifest itself evidently. Therefore, the potential drop across such a possible double charged layer is omitted in Fig. 40.15d.

On the other hand, an electrical double layer can be easily created and controlled by the adsorption of dipole molecules such as water. The water increases the work function change ($\Delta\Phi > 0$) but diminishes the electrical conductivity of the film ($\Delta\rho < 0$) which can be related to the peculiarities of water molecules. It is well-known that a water molecule is an unusual molecule. Being threefold coordinated, it exhibits a high dipole moment ($15 \cdot 10^{-30} C \cdot m$). As a H_2O molecule approaches the surface of a positively charged tellurium film, it rotates and orientates its dipole moment perpendicular to this surface with a negative pole inward.

At the same time, the free lattice hole becomes more and more localized at the point of the surface that water molecule approaches, and a very weak bond due to electrostatic polarization forces is formed. Localization of these free holes diminishes the electrical conductivity of the film; that is, the opposite as in the case of NO_2 can be observed. Figure 40.16a, b schematically illustrate how a decrease of the conductivity and an increase of the work function are produced

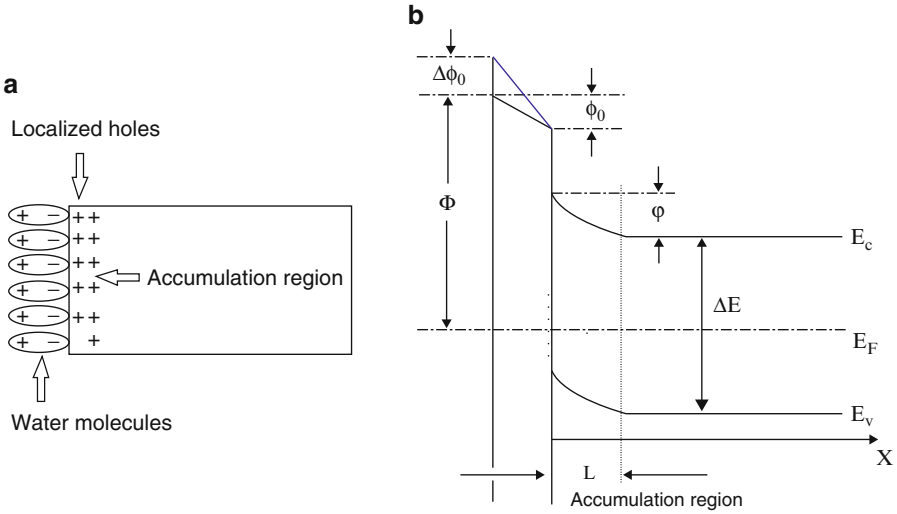

Fig. 40.16 Formation of an electric double layer by water physisorption (**a**) and its effect on the work function (**b**)

by surface hole localization resulting from the preferential alignment of the water dipoles.

40.8 Conclusions

Due to its special chemistry and physical properties, nanostructured tellurium becomes one of the most attractive functional materials in advanced sensor technology. They are very suitable for the development of both conductive and work function room temperature operating gas sensitive devices, with short response/recovery times and a good sensitivity in the ppm and sub-ppm concentration range.

The phase/structural state and the thickness of the Te films control the adsorption/desorption processes and the basic parameters of gas sensitive devices. In ultra thin tellurium films a concentration increase of gaseous analyte damps the sensitivity, which should be taken into consideration in the development of gas sensors.

The NO_2 sensing mechanism involves "strong" chemisorption, which results in increasing of both work function (band bending) as well as the electrical conductivity of the films.

The effect of water vapour is due to simple physical adsorption of dipole molecules, accompanied by an increase of the potential drop across the electric dipole layer, which results in an increase of the work function as well, but the electrical conductivity of the film decreases, due to hole localization at the surface.

References

1. Tsiulyanu D (2011) Tellurium thin films in sensor technology. In: Reithmaier JP et al (eds) Nanotechnological basis for advanced sensors. Springer, Dordrecht, p 363
2. Wang S, Wen H, Guan W, Zhang L, Ma D, Huang S, Wang J (2010) Thin Solid Films 518:4215
3. Kumar V, Sen S, Sharma M, Muthe KP, Jagannath, Gaur NK, Gupta SK (2009) J Nanosci Nanotechnol 9:5278
4. Rheem Y, Chang CH, Hangarter CM, Park D-Y, Lee K-H, Jeong Y-S, Myung NV (2010) Electrochim Acta 55:2472
5. Yung Chiun Her, Sing Lin Huang (2013) Nanotechnology 24:215603
6. Guan L, Wang S, Gu W, Zhuang J, Jin H, Zhang W, Zhang T, Wang J (2014) Sensors Actuators B 196:321
7. Belandria E, Millot M, Broto J-M, Flahaut E, Rodriguez F, Valiente R, Gonzalez J (2010) Carbon 48:2566
8. Liang F, Qian H (2009) Mater Chem Phys 113:523
9. Jung H, Kim C, Myung NV (2014) Eng Mater 605:290
10. Tsiulyanu D, Stratan I, Tsiulyanu A, Liess H-D, Eisele I (2007) Sensors Actuators B 121:406
11. Siciliano T, Filippo E, Genga A, Micocci G, Tepore M, Siciliano M, Tepore A (2009) Sensors Actuators B 142:185
12. Sen S, Bhatta UM, Kumar V, Muthe KP, Bhattacharya S, Gupta SK, Yakhmi JV (2008) Cryst Growth Des 8:238
13. Sen S, Muthe KP, Joshi N, Gadkari SC, Gupta SK, Roy JM, Deshpande SK, Yakmi JV (2004) Sensors Actuators B 98:154
14. Sunada J, Oishi K, Kasai A, Kitahara T (1982) Jpn J Appl Phys 21:1781
15. Oishi K, Okamoto K, Sunada J (1987) Thin Solid Films 148:29
16. Tsiulyanu D, Tsiulyanu A, Liess H-D, Eisele I (2005) Thin Solid Films 485:252
17. Simon I, Barsan N, Bauer M, Weimer U (2001) Sensors Actuators B 73:1
18. Janda M, Kubovy A (1976) Phys Status Solidi A 35:391
19. Tsiulyanu D, Mocreac O (2013) Sensors Actuators B 177:1128
20. Lundström I (1996) Sensors Actuators B 35–36:11
21. Popescu M, Andriesh A, Chiumach V, Iovu M, Shutov S, Tsiulyanu D (1996) The physics of chalcogenide glasses. Editura Scientifica, Bucharest
22. Greyson J (1990) Carbon, nitrogen and sulfur pollutants and their determination in air and water. Marcel Dekker, New York

Chapter 41
Technology for a Highly Sensitive Sensor System Based on Competing Modes in Semiconductor Lasers

S. Blom, J. Shreshta, N. Storch, J. Sonksen, and H. Hillmer

Abstract A semiconductor laser-based optical sensor concept is presented which allows the implementation of highly sensitive measurement systems to monitor trace gases. The sensors are based on a highly sensitive detection principle that uses mode degeneracy in dual mode lasers to enhance the sensitivity of the sensor system. Fiber based macroscopic set-ups to prove the concept are presented including first measurements with liquids showing a direct sensor response for propofol. The influence of the mode intensity ratio on relative intensity noise (RIN) is shown which enables RIN as a suitable readout method.

Keywords Sensor • Tunable laser • Intracavity Laser Absorption Spectroscopy (ICLAS) • Mode competition • Relative Intensity Noise (RIN)

41.1 Introduction

To maintain constant high quality in modern industrial applications requires precise knowledge of any physical parameter involved in a fabrication process. Also in many medical applications it is necessary to detect trace gases to ensure the health of patients. As a non contaminative system to detect trace gases in many application fields, optical spectroscopy has shown great potential.

Many techniques specially tailored for high sensitivity have been invented, i.e. opto thermal spectroscopy [1], multi-reflection cells [2, 3], cavity ring down

S. Blom (✉) • J. Shreshta • N. Storch • H. Hillmer
Institute of Nanostructure Technologies and Analytics (INA), Center for Interdisciplinary Nanostructure Science and Technology (CINSaT), University of Kassel, Heinrich-Plett-Str. 40, 34132 Kassel, Germany
e-mail: blom@ina.uni-kassel.de

J. Sonksen
B. Braun Melsungen AG, Schwarzenberger Weg 21, 34212 Melsungen, Germany

P. Petkov et al. (eds.), *Nanoscience Advances in CBRN Agents Detection, Information and Energy Security*, NATO Science for Peace and Security Series A: Chemistry and Biology, DOI 10.1007/978-94-017-9697-2_41

spectroscopy [4] and intra cavity laser absorption spectroscopy (ICLAS) [5]. The ICLAS principle is the most sensitive approach from these methods due to the exploitation of multi mode competition. The exploitation of a multimode laser leads to the necessity of costly and highly complex readout methods. The use of a single mode laser for ICLAS allows a cheap and fast readout but limits the sensitivity due to the missing mode competition.

A suitable solution for a cost effective and highly sensitive device is an ICLAS setup that operates with two modes. Such a setup would also benefit from the mode competition [6]. The high cost and complexity of an optical readout is significantly reduced by using an electrical readout by means of relative intensity noise (RIN) [7]. The main idea [8] is to have a laser setup that operates with two modes in degeneracy by using two independent operation currents to influence the tuning mechanisms (e.g. plasma effect and thermal tuning).

The sensing process is separated in two steps: (i) without a fluid or gas in the system the two modes are tuned over a spectral range of a few nm while keeping both modes in degeneracy. This step gives the precise relation of the two independent operation currents to keep the mode degeneracy for each reached spectral position. In step (ii) the liquid or gas is added to the system and the currents are varied again in the same way. By this a characteristic deviation from the mode degeneracy is recorded which is based on the characteristic of the absorption fingerprint of the fluid or gas. The optical absorption of a liquid or gas is changing the gain profile of the system by spectral hole burning. The information about the special absorption and the concentration of the fluid or gas inside the system is included in the side mode suppression ratio (SMSR).

41.2 Results

A first fiber based setup (see Fig. 41.1) was implemented to proof the concept of the idea. The system consists of a fixed 50/50 optical fiber coupler, a semiconductor optical amplifier (SOA), loop mirror, optical spectrum analyzer (OSA) and two tuneable Fiber Bragg gratings (FBG). These components are grouped to form a laser resonator with two Fabry-Pérot cavities sharing a common active medium.

This initial setup had some major disadvantages by means of low SMSR, low output power and no tuneability of the two lasing modes. To overcome these problems the FBG's were arranged in a serial configuration, and tunable optical fiber couplers were added to the setup (see Fig. 41.2).

This setup can be described as a laser (loop mirror – FBG 1) with an additional external cavity (FBG 2). The two variable couplers enable a mode degeneracy at all possible wavelength by adding broadband losses to the associated cavity. In a last improvement step a collimation range has been implemented in the setup (see Fig. 41.3) to enable the introduction of a test substance in the resonator and optical isolators to inhibit back reflections.

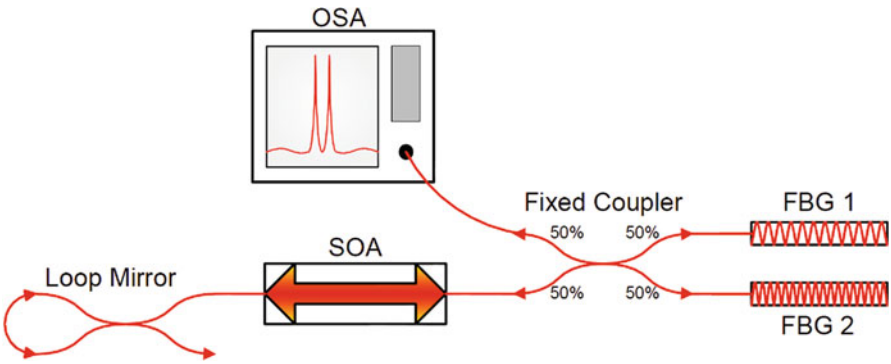

Fig. 41.1 First fiber based setup. Two FBG's in parallel with a 50/50 optical fiber coupler

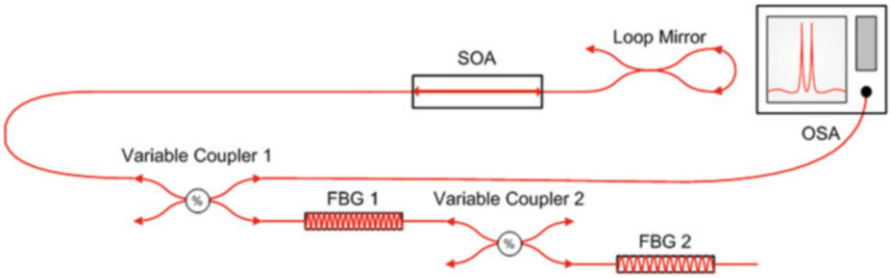

Fig. 41.2 Improved setup with two FBG's in series and two variable optical couplers to control the mode intensity ratio by adding broadband losses to the according cavity

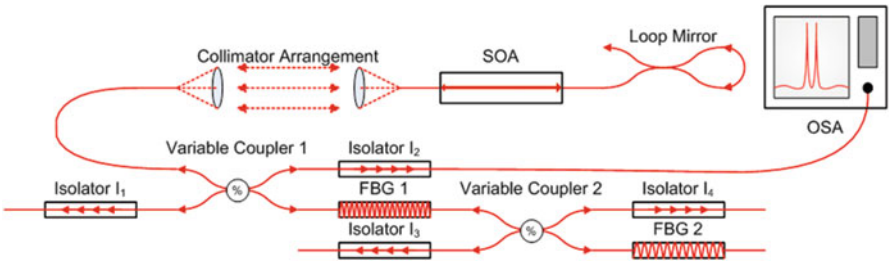

Fig. 41.3 Setup for proof of concept with an implemented collimation range to introduce absorber in the cavity and isolators to prevent back reflections

The FBG's are placed on metal blocks that can be heated to change the Bragg wavelength. By this mechanism the system can emit a two mode spectrum within the operation range of the FBG's between 1,541 and 1,545 nm with a SMSR of 55 dB and a FWHM <0,06 nm [9]. The impact of the changes is illustrated in Fig. 41.4 were (b) shows the spectral output of the setup in Fig. 41.3 compared to

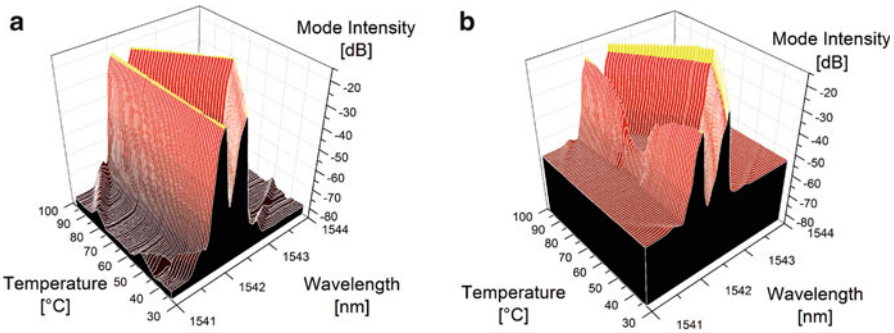

Fig. 41.4 Output spectrum showing the tuning capability of the setup with (**a**) usage of variable optical coupler to keep mode intensity equal and (**b**) without tuning the variable optical couplers to maintain mode degeneracy

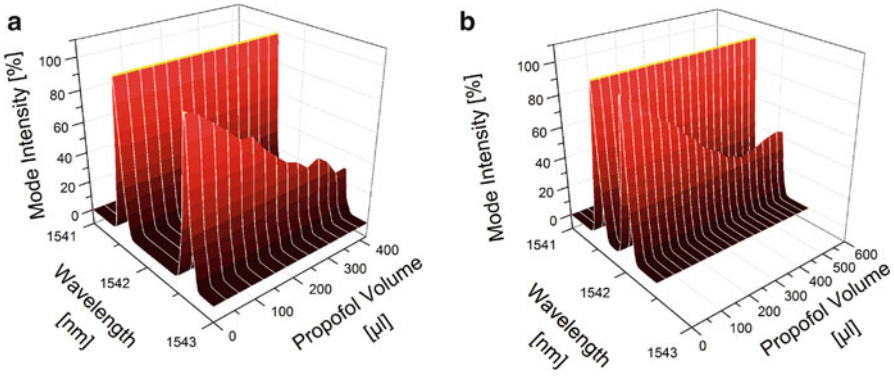

Fig. 41.5 Normalized output spectra of the setup with absorption from propofol with dichloromethane (DCM) as solvent as solvent for two different mode spacing's (**a**) 1 nm and (**b**) 0.5 nm

(a) the spectral output of the setup in Fig. 41.2 without using the variable couplers to maintain mode degeneracy.

After a holder for liquid cells was implemented in the setup measurements with propofol were performed in different solvents at different mode spacings to evaluate the impact of the mode separation on the detection. Figure 41.5 shows normalized output spectra of the laser system for different propofol concentrations with (a) 1 nm mode spacing and (b) 0.5 nm mode spacing.

Both measurements start at mode degeneracy without propofol. Adding propofol results in a decrease of the outer mode (corresponding to FBG 2). The sensor system responds directly to the targeted test substance.

To use RIN as sensor readout the intensity ratio between the two modes needs to be related to the RIN spectra. Figure 41.6 illustrates the measured RIN spectra at

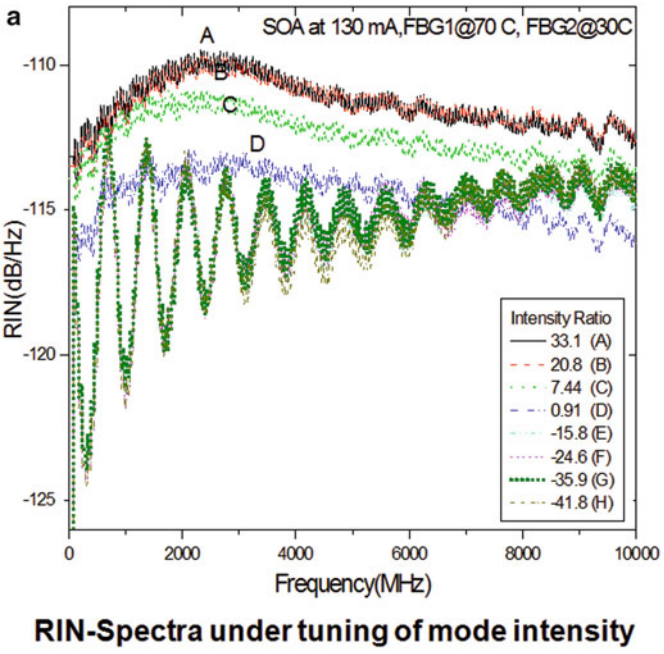

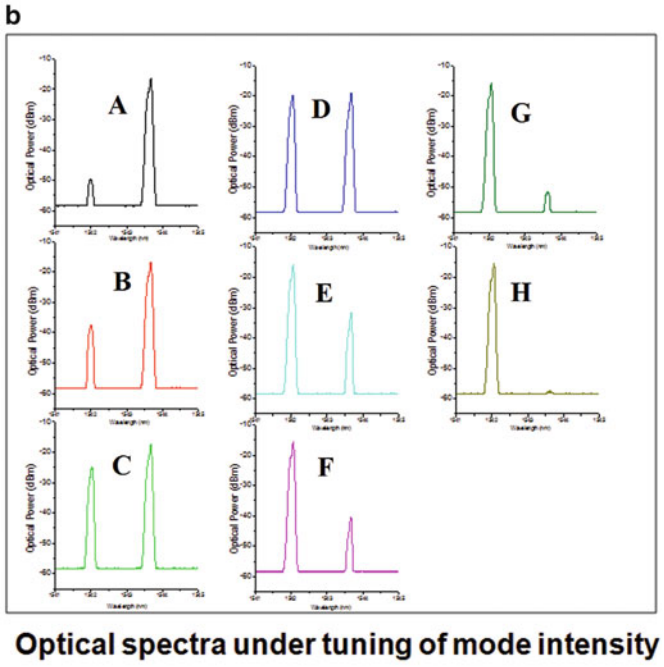

Fig. 41.6 (**a**) RIN spectra of the setup for different mode intensity ratios. (**b**) The corresponding optical output spectra

different mode intensity ratios for the setup shown in Fig. 41.3. Changing the mode intensity ratio from degeneracy (see Fig. 41.6: D) results in a direct change of the RIN spectra. Further measurements have shown that the mode spacing has no influence on the average RIN. This means that the sensor can operate at the smallest possible mode spacing to achieve the highest sensitivity without influencing the usability of RIN for the read out of the intensity ratio.

41.3 Conclusions

The influence of the modes intensity ration on RIN has been shown making RIN a suitable and cost efficient tool for the read out. The system reacts directly on Propofol in the resonating cavity. The sensor response depends up on the mode spacing which indicates the influence of mode competition. These results show that the concept of using a two mode laser with RIN as readout is valid.

Acknowledgments The financial support by the European Union (EU), the Federal Ministry of Education and Research (BMBF) and B. Braun Melsungen AG is gratefully acknowledged.

References

1. Platz T, Demtröder W (1998) Chem Phys Lett 294:397
2. White JU (1942) J Opt Soc Am 32:285
3. Ballard J, Strong K, Remedios JJ, Page M, Johnston WB (1994) J Quant Spectrosc Radiat Transf 52:677
4. O'Keefe A, Deacon DAG (1988) Rev Sci Instrum 59:2544
5. Baev VM, Latz T, Toschek PE (1999) Appl Phys B Lasers Opt 69:171
6. Lacot E, Stoeckel F, Romanini D, Kachanov A (1998) Phys Rev A 57:4019
7. Krause H, Sonksen J, Baumann J, Troppenz U, Rehbein W, Viereck V, Hillmer H (2008) SPIE photonics Europe 6997, May 2008, p 22
8. Hillmer H (2008) Sensor device and process for determining a physical value. German Patent: DE102004037519 B4, European Patent: EP1771720 B1, US Patent: US8120775 B2
9. Sonksen J (2010) Sensor process and device for determining a physical value: DE10 2004 037 519 B4. A proof of concept. Suedwestdeutscher Verlag fuer, Hochschulschriften. ISBN 3838118596

Chapter 42
Development of Nanocomposite Alpha-Detectors Based on Silica Matrices and Organic Scintillators

V.V. Seminko, A.A. Masalov, O.G. Viagin, I.I. Bespalova, L.I. Voloshina, O.V. Zelenskaya, V.A. Tarasov, and Yu. V. Malyukin

Abstract New materials based on highly-porous SiO_2 matrices with incorporated molecules of organic scintillators (POPOP, PPO) were fabricated. The composite scintillators are characterized by decay times in the nanosecond range, a high transparency in the visible region (about 70 %) and an intensive photoluminescence. At excitation by 5.46 MeV alpha particles the light yield of SiO_2 (POPOP, PPO) was equal to 4,400–5,100 photon/MeV, the resolution was 27–32 %.

Keywords Scintillators • Nanocomposites • Silica

42.1 Introduction

Recent developments of the scintillation technique have shown a number of principal limitations of bulk crystals as detectors for ionizing radiation [1–5]. So, one of the most important challenges of modern high-energy physics is to find an alternative to the extremely expensive production of bulk scintillators and to obtain commercially available and low resource demanding materials with a high effectiveness for the detection of ionizing radiation. To overcome the restrictions of bulk scintillators nanodispersed materials (nanocrystals, thin films, nanocomposites) can be used [2–5]. As the low resource demand of the methods to fabricate such materials, the simplicity to produce such systems allows to consider these systems as a perspective material for soft X-rays and charged particles registration.

For the most practical applications of scintillating nanocrystals, an assembly to bulk detectors is required. This assembling can be achieved by sintering of

V.V. Seminko (✉) • A.A. Masalov • O.G. Viagin • I.I. Bespalova • L.I. Voloshina
O.V. Zelenskaya • V.A. Tarasov • Yu.V. Malyukin
Institute for Scintillation Materials, STC 'Institute for Single Crystals' NAS of Ukraine,
60 Lenin Ave., 61001 Kharkov, Ukraine
e-mail: seminko@isma.kharkov.ua

P. Petkov et al. (eds.), *Nanoscience Advances in CBRN Agents Detection, Information and Energy Security*, NATO Science for Peace and Security Series A: Chemistry and Biology, DOI 10.1007/978-94-017-9697-2_42

nanopowders to high-dense ceramics, but also by incorporation of nanocrystals into various porous matrices.

The interest for porous inorganic compounds obtained by sol-gel method has sufficiently grown recently. The high pore concentrations obtained in such materials allows the incorporation of different scintillating and luminescent additives [6, 7]. Sol-gel matrices also possess a wide range of transparency, high mechanical durability and chemical stability. As was shown in [8], the photostability of organic luminophors in silica matrices is higher than that in solutions and polymer matrices.

In our work we have used silica matrices as a base for the creation of nanocomposite scintillation materials. As scintillation additives, well-known organic scintillators widely used for creation of alpha detectors, namely POPOP (1,4-bis(5-phenyloxazol-2-yl) benzene) and PPO (2,5-diphenyloxazole) were used.

42.2 Experimental

The SiO_2 matrices were synthesized according to the following method [9]. To 3.15 ml of methanol (CH_3OH) 3.75 ml of tetramethoxysilane (TMOS) were added, the resulting mixture was stirred for 5 min. Then 4.5 ml of distilled water were added to the mixture which was again stirred. To increase the rate of hydrolysis, 0.525 ml of hydrochloric acid were added. The mixture obtained was poured to Petri dishes of 35 × 10 mm and sealed. The process of gel formation took 24 h, followed by drying at 45 °C during for 5 days. Annealing of the dried samples took place at 250 °C, 500 °C and 750 °C with 60 min exposure at each temperature. The samples obtained were transparent colorless disks with a diameter of 20 mm and a thickness of 1 mm (Fig. 42.1a).

According to XRD (Fig. 42.1b) and AFM (Fig. 42.1c) the silica matrices had an amorphous structure and consisted of sintered spherical nanoparticles with average sizes of 35 nm. Density and porosity of the silica matrices determined by

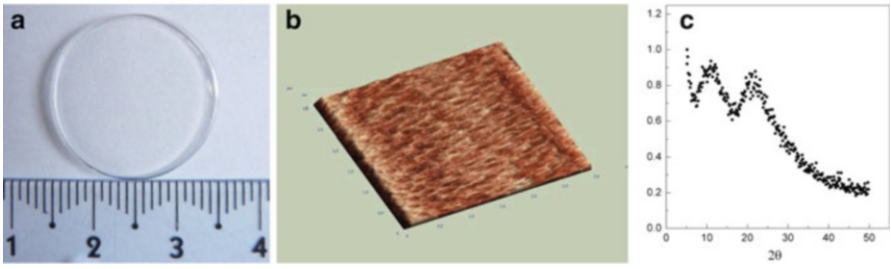

Fig. 42.1 (**a**) SiO_2 matrix, (**b**) XRD of the SiO_2 matrix (**c**) AFM image of surface of SiO_2 matrix

the method of hydrostatic weighing were 1.40 g/cm^3 and 54 vol.%, respectively. The average value of the microhardness was 170 kg/mm^2, which is practically two times higher than the values reported by different authors [10, 11].

The incorporation of organic scintillators was performed by impregnation of the silica matrices. Two series of PPO and POPOP solutions in toluene with concentrations of 0.1 mass.%, 1 mass.% and 10 mass.% were prepared. The matrices were placed in solutions for 2 h, 24 h and 48 h, then they were dried at 50 °C until the mass was constant. Experimentally it was shown that the most intensive luminescence is observed for matrices with about 4 mass.% of the activator.

Optical transmission spectra were measured by means of a spectrophotometer SPECORD 200 (Analytik Jena, Germany). Luminescence spectra were registered by a spectrofluorimeter based on a grating monochromator. Luminescence was excited by a He-Cd laser (325 nm). Decay curves were measured by means of a picosecond spectrofluorimeter FluoTime 200 (PicoQuant, Germany), as excitation source semiconductor laser with wavelength of 330 nm was used.

Pulse height spectra were measured by means of standard spectrometric path, consisting of preamplifier, linear amplifier and multi-channel pulse-height analyzer. As a photodetector R1307 (Hamamatsu, Japan) photomultiplier tube (PMT) was used. scintillations were excited by alpha-particles with energy of 5.46 MeV (^{238}Pu source).

42.3 Results

In Fig. 42.2 optical transmission spectra (a), luminescence spectra (b), and luminescence decay curves (c) of obtained composite scintillators are shown.

The pure SiO_2 matrix is transparent from 250 to 700 nm, while the transmission at 450 nm is about 85 %. For SiO_2:PPO and SiO_2:POPOP, the edge of fundamental absorption shifts to 370 nm and 420 nm, respectively; and the transmission at 450 nm is about 75 %. The luminescence spectra of SiO_2 matrices consist of wide intensive bands with peaks at 415 nm for SiO_2:PPO and at 485 nm for SiO_2: POPOP (Fig. 42.2b). The luminescence spectra of the organic scintillators in SiO_2 matrix are red-shifted as compared with spectra of the same scintillators in toluene (~30–35 nm). Such a shift was previously observed for composite materials and is connected with a change of microenvironment of molecules in the pores [12, 13]. The decay of the photoluminescence lies in the nanosecond range; the decay curves are well fitted by the sum of two exponents (Fig. 42.2c, Table 42.1).

In Fig. 42.3 pulse height spectra on excitation of the nanocomposites by alpha-particles (5.46 MeV) are shown. Both spectra are symmetrical and have a typical gaussian form. The symmetry of spectra indicates a low dependence of the pulse height on the position of scintillation, so the activator is distributed uniformly within the volume of the silica matrix. The pulse height resolution R was about 27 % for SiO_2:PPO and 32 % for SiO_2: POPOP (Table 42.1).

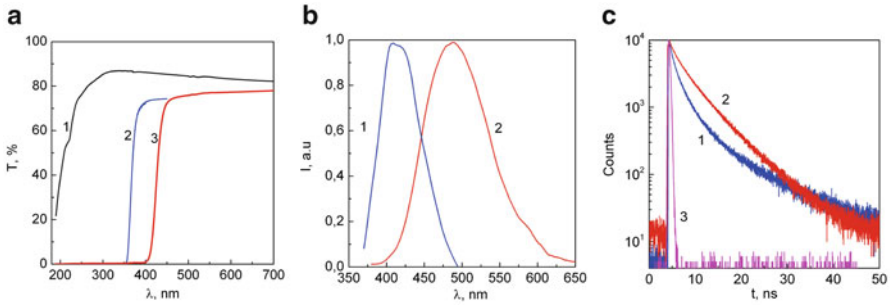

Fig. 42.2 (**a**) Transmission spectra: *1* – SiO_2 pure, *2* – SiO_2:PPO, *3* – SiO_2:POPOP, (**b**) Luminescence spectra ($\lambda_{exc} = 325$ nm): *1* – SiO_2:PPO, *2* – SiO_2:POPOP, (**c**) Decay curves ($\lambda_{exc} = 330$ nm): *1* – SiO_2:PPO, *2* – SiO_2:POPOP

Table 42.1 Characteristics of obtained composite scintillators: edge of fundamental absorption (λ_{FA}), maximum of luminescence spectrum (λ_{em}), decay times (τ_1; τ_2), energy resolution (R) and absolute light yield (N_{ph})

Sample	λ_{FA} [nm]	λ_{em} [nm]	τ_1; τ_2 [ns]	R [%]	N_{ph} [photon/MeV]
SiO_2: PPO	370	415	2.1; 8.2	31.6	4,400
SiO_2: POPOP	420	485	2.2; 6.1	27.3	5,100

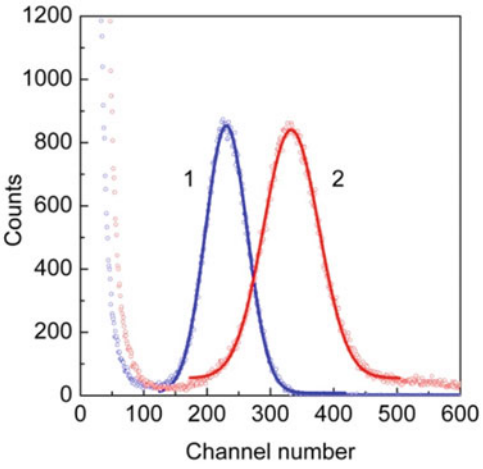

Fig. 42.3 Pulse height spectra of composite scintillators at excitation by alpha particles ($E_\alpha = 5.46$ MeV). Experimental data are shown by *dots*, the gaussian fitting by *solid lines*. *1* – SiO_2:PPO, *2* – SiO_2:POPOP

One of the main characteristics of a scintillator is the absolute light yield (the number of photons emitted per 1 MeV). The absolute light yield of the composites obtained was determined by calculating the number of scintillation photons from number of photoelectrons collected on the anode of the PMT [14]. the light collection coefficient in scintillators was determined by means of mathematical Monte Carlo simulations [15], taking into account the optical properties of the

composites (refraction and reflection coefficients) and also the experimental conditions (absence of a reflector, no optical contact of the sample with the PMT, penetration depth of alpha particles) and was determined to be equal to 0.14 for both samples. Thus, the values of the absolute light yield are equal to 4,400 photons/MeV for SiO_2:PPO and 5,100 photons/MeV for SiO_2:POPOP (Table 42.1).

42.4 Conclusions

Composite samples obtained by incorporation of PPO and POPOP to porous SiO_2 matrices possess a high intensity of photoluminescence, a relatively high transparency in the visible region and a decay in the range of nanoseconds. However, the light yield of the samples is rather low. Probably, this is connected with the presence of non-radiative relaxation channels of high energy excitations in the matrices. A determination of the nature of quenching in such composites would allow to optimize the synthesis technology and to improve the scintillation parameters. Also the field of application of the composites obtained can be extended by incorporation of ions with high thermal neutron cross-sections (such as Gd, B, Li, Cd) that will make possible its application as neutron detectors.

References

1. Shionoya S, Yen WH, Yamamoto H (2006) Phosphor handbook. CRC Press, Boca Raton
2. McKigney E, Del Sesto R, Jacobsohn L et al (2007) Nucl Inst Methods Phys Res A 579:15
3. Wang CL, Goub L, Zaleski JM, Friesel DL (2010) Nucl Inst Methods Phys Res A 622:186
4. Letant SE, Wang T-F (2006) Nano Lett 6:2877
5. Thomas J, Ellison E (2001) Adv Colloid Interf Sci 89–90:195
6. Nikl M, Solovieva N, Apperson K et al (2005) Appl Phys Lett 86:101914
7. Parvathy Rao A, Venkateswara Rao A (2003) Sci Technol Adv Mater 4:121
8. Benedict JB, Wallace PM, Reid PJ et al (2003) Adv Mater 15:1068
9. Blank TA, Ganina II, Malyukin YV, Eksperiandova LP (2009) Funct Mater 16:517
10. Lam KS, Zhu X-L, Lo D (1999) Appl Phys B 68:1151
11. Rahn MD, King TA (1995) Appl Opt 34:8260
12. Bezkrovnaya ON, Pritula IM, Maslov VV et al (2010) Funct Mater 17:433
13. Kuznetsova RT, Savenkova NS, Mayer GV et al (2007) J Appl Spectrosc 74:485
14. Grinyov BV, Ryzhikov VD, Sidletskiy OT et al (2010) IEEE Trans Nucl Sci 57:1236
15. Tarasov VA, Kilimchuk IV, Vyday YT (2010) Funct Mater 17:100

Part XI
Applications: Health, Water Treatment and Environment

Chapter 43
Nanoparticles Containing a Copper Chelator: A Possible Instrument for Radiation Protection

V.V. Vasilieva, M. Alyakov, and M.D. Apostolova

Abstract Nanotechnology is considered as an emerging technology with great potential in a wide range of applications. In addition to various industrial uses, several innovations are foreseen in biotechnology, medicine and medical technology. The application of nanotechnology to medicine also provides an innovative approach that can enhance the effectiveness of radiotherapies or radioprotection. The aim of the present study was to investigate the radioprotective effect of neocuproine-nanodiamond nanoparticles on gamma irradiated human hepatocellular carcinoma cells. We revealed a significant increase in the radioprotection efficacy against gamma irradiation of HepG2 cells pre-exposed to nanodiamonds or nanodiamonds-neocuproine nanoparticles. The results showed that the protective effect of nanoparticles is connected with decreasing free radicals released during the irradiation and with cytokinesis-blocked micronucleous formation, does protecting cells from cyto- and genotoxic effect of gamma irradiation.

Keywords Nanodiamonds • Neocuproine • Radioprotection • ***In vitro***

43.1 Introduction

Nanotechnology is considered as an emerging technology with great potential in a wide range of applications. In addition to various industrial uses, several innovations are foreseen in biotechnology, medicine and medical technology. Manufactured

V.V. Vasilieva
Medical and Biological Research Laboratory, "Roumen Tsanev" Institute of Molecular Biology – Bulgarian Academy of Sciences, Sofia, Bulgaria

Department of Radiation Protection, Military Medical Academy, Sofia, Bulgaria

M. Alyakov
Department of Radiation Protection, Military Medical Academy, Sofia, Bulgaria

M.D. Apostolova (✉)
Medical and Biological Research Laboratory, "Roumen Tsanev" Institute of Molecular Biology – Bulgarian Academy of Sciences, Sofia, Bulgaria
e-mail: margo@obzor.bio21.bas.bg

P. Petkov et al. (eds.), *Nanoscience Advances in CBRN Agents Detection, Information and Energy Security*, NATO Science for Peace and Security Series A: Chemistry and Biology, DOI 10.1007/978-94-017-9697-2_43

nanoparticles can have physicochemical characteristics and coatings that give them unique electrical, thermal, mechanical, biochemical, and imaging properties. The application of nanotechnology to medicine also provides an innovative approach that can enhance the effectiveness of radiotherapy [1] or radioprotection [2, 3]. Targeted and non-targeted tissues and cells are, in general, damaged along an indirect pathway during radiation treatment and exposure as a result of the production of free radicals [4]. Radiation also interacts with other atoms or molecules in the cell (particularly water) to produce different reactive oxygen species (ROS) that are able to diffuse over distances sufficient to interact with, and cause damage to, critical targets – enzymes, proteins, peptides, lipids, membranes and DNA [5].

The free radicals formed during water radiolysis include *O-O*, H*, O*, and HO*. They are highly reactive, very short-living species, which may kill or seriously damage any cells and lead to serious long-term injury such as cancer [5]. In addition, some free radicals can interact with each other to form oxidizing species such as H_2O_2 or other peroxides that may also cause tissue damage. It is generally assumed that DNA damage, mediated by hydroxyl radicals (HO*) that are formed by radiolytic cleavage of water, is responsible for cell death caused by ionizing radiation.

Superoxides exert their toxicity through their ability to reduce metal ions *in vivo*, for example Cu(II) to Cu(I) and to form OH* radicals which combine to form toxic H_2O_2. Copper (I) and copper (II) are also highly reactive microelements and cofactor of many enzymes, transcription factors, and intracellular mediators which can react with various cell signal pathways [6]. When the levels of Cu are slightly above the normal physiological amounts, it can be toxic. Because of Cu reduction properties expressed *in vivo*, copper ions maybe the cause of most oxidative damage, resulting in the generation of ROS by the action of various factors, including ionizing radiation (IR) [7].

Metal chelators were also found to alter metal catalyzed oxidation. Copper or iron atoms that are close to DNA can interact with highly diffusible, but weak free radicals H_2O_2 in metal-catalyzed Fenton/Haber–Weiss type reactions to produce OH*-/O2*-mediated DNA damage, strand breaks and DNA mutations [8]. On the other hand, chelating agents may protect DNA from hydroxyl radicals and prevent damage of enzymes which are responsible for the enzymatic DNA repair system [8].

Neocuproine (NeoC) is a membrane permeable Cu(I) specific chelator. It is frequently used as a protective agent against oxidative stress caused by Cu [9]. This chelator suppress thermally induced H_2O_2 production. The influence of NeoC on the H_2O_2 production upon heating indicates that copper ions are predominant electrondonors leading to superoxide anion formation from singlet oxygen [10]. It has also been shown that in lymphocytes NeoC can inhibit DNA degradation, indicating that a copper redox cycle and reactive oxygen generation are two major determinants involved in DNA damage caused by gamma radiation [11].

In an effort to combat the harmful effects of radiation, various nanoparticles and/or free-radical scavengers have been tested for their ability to protect normal cells and tissues [12]. Composites containing nanodiamonds (NDs) can enhance mechanical properties, provide improved bonding of certain biological materials, and protect subjects from ultraviolet (UV) radiation [13]. NDs can also reduce and prevent the formation of free radicals. It was established that oral administrations of

NDs in suspension to rats before x-ray exposure or gamma irradiation reduce radiation sickness and manifestations of the gastrointestinal syndrome, and significantly decrease the mortality, thus possessing a possible radio-protective effect [14].

In this study we have explored the ability of ND and NDNeoC nanoparticles to protect DNA from the damages caused by gamma irradiation.

43.2 Experimental

43.2.1 Production and Modifications of Nanodiamonds

NDs were produce, purified and characterized according Ivanova et al. [15]. Neocuproine hydrochloride hydrate and all chemicals used were obtained from Sigma.

The synthesis of NDNeoC was achieved as follows: NDs with average sizes of 3–7 nm produced by the detonation method [15] were used in the chemical synthesis illustrated in Fig. 43.1. At first, NeoC was functionalized at the 5-position via bromination. It was carried out with bromine in the presence of fuming H_2SO_4 (min 20 % SO_3). Replacement of the bromine with a 4-aminophenil linking group was successfully achieved via Suzuki coupling with

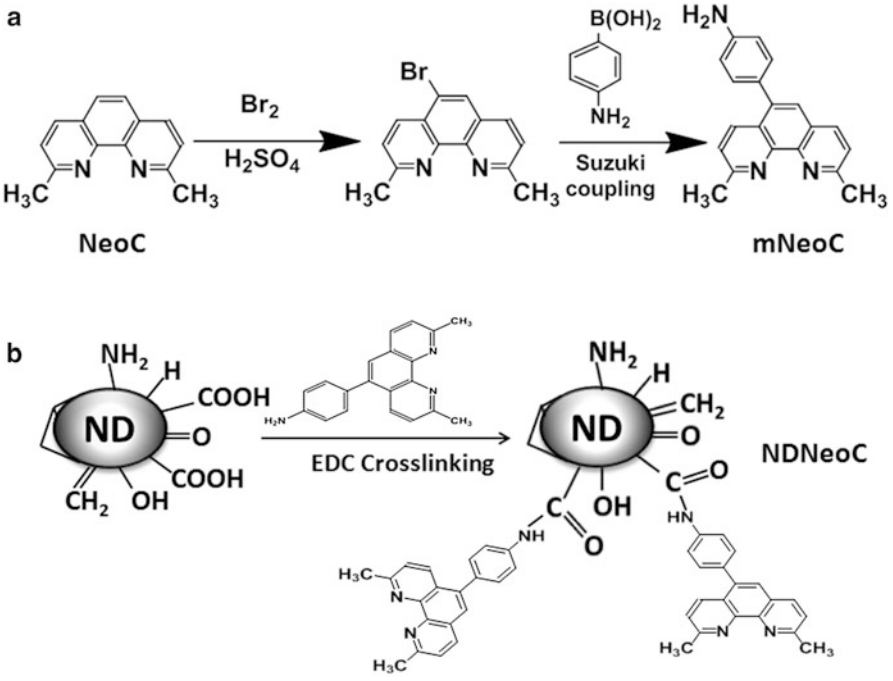

Fig. 43.1 Synthesis scheme for modified neocuproine (mNeoC, **a**) and nanodiamond-neocuprone (NDNeoC, **b**)

4-aminophenylboronic acid (Fig. 43.1a). The modified NeoC (mNeoC) was then chemically immobilized onto the surface of ND particles using a zero-length crosslinker 1-(3-dimethylaminopropyl)-3-ethylcarbodiimide hydrochloride (EDC, Scheme 1). In details: 0.5 g of mNeoC dissolved in 20 ml of 2-(N-morpholino) ethanesulfonic acid (MES) buffer (pH 6.5) was mixed with 0.15 g of ND dispersed in 30 ml of MES buffer and sonicated for three cycles of 5 min with a cell disruptor (W-375, Ultrasonics Inc., USA). The dispersed solution was than mixed with 0.35 g of N-hydroxysuccinimide (NHS) followed by the addition of 0.30 g of EDC (Fig. 43.1b). Following the adjustment of the pH to 6.5 by 1.0 M NaOH, the solution was agitated at 4 °C for 30 min. The reaction mixture was agitated at 4 °C for another 12 h; then the produced NDNeoC was centrifuged and rinsed repeatedly with deionized nanopure water until the supernatant approaches a neutral pH.

43.2.2 Fourier Transform Infrared Spectroscopy

The functional groups of the sample surface, before and after the different modifications, were registered by Fourier transform infrared spectroscopy (FTIR). The spectra were obtained with a micro FTIR spectrometer (TENSOR 37, Bruker).

43.2.3 Dynamic Light Scattering

For all nanoparticles studied dynamic light scattering (DLS) was used to evaluate the dispersion quality. The particle size distribution was determined at 657 nm and 90° with a Dynamic Laser Scatter Bi-90 plus equipped with a correlator and an avalanche photo detector (Brookhaven Instruments Corporation, USA). Data were analyzed using the BIC Particle sizing Software version 5.23. Samples were measured at 37 °C in 4 ml disposable polystyrene cuvettes following different dilutions in a cell culture medium. For calculations of the hydrodynamic size, a refractive index of 2.41 for NDs and standard properties for H_2O and the solvents were used. The measurements were performed in triplicate (one run consists of three cycles of 3 min).

43.2.4 Cell Culture and Treatment

The human hepatoma HepG2 cell line (ATCC, HB-8065) was cultured in DMEM (Dilbecco's Modified Eagle Medium, Applichem, Germany) supplemented with 10 % (v/v) fetal bovine serum (FBS, Lonza, Switzerland), penicillin (100 µg/ml), streptomycin (100 µg/ml) and 4 mM L-glutamine (Lonza, Switzerland) at 37 °C in a

humidified atmosphere of 5 % CO_2 and 95 % air. The cells were routinely checked for mycoplasma contamination, by DAPI staining (Roche Diagnostics, Mannheim, Germany) and found free of it.

The cells (1×10^5 cells/ml) were treated with different concentrations of NDs, NeoC or NDNeoC in the complete cell culture medium 3 h prior to exposure to irradiation.

43.2.5 Irradiation

A portable research irradiator GOU-3 M with ^{137}Cs was used as a source of irradiation at a dose rate of 0.03 Gy/s. After the cells were treated with NDs, NeoC or NDNeoC, they were irradiated with 0, 1, 3, 5, 7 or 9 Gy. The cell viability was determined by a 3-(4,5-dimethylthiazol-2-yl)-2,5-diphenyltetrazolium bromide (MTT) colorimetric assay [16]. The MTT-formazan product was dissolved in isopropanol and the absorption at 550/630 nm was measured on an ELISA plate reader (Bio-Tek Instruments Inc., USA). The cytotoxic effect of the compounds was expressed as percentage of viable cells with respect to the controls.

43.2.6 Colony Formation Assay

Immediately after the cell treatment or irradiation, the nonadherent cells were removed, and the attached ones were seeded on 12-well plates with a density of 400 cells/cm^2. Colony-forming units (CFU), defined as a central core of round cells with a minimum of 50 sprouting cells at the periphery, were counted on day 9 after staining with 0.5 % crystal violet.

The plating efficiency (PE) of the cell population was calculated by dividing the number of colonies formed by the number of cells plated. The ratio of the PE for the irradiated cells to the PE for control cells showed the fraction of cells that have survived (SF) [17].

43.2.7 Micronucleus Assay

A micronucleus assay was performed following the OECD 487 protocol with the application of Cytochelasin B (CytoB). The 5 μg/ml CytoB (Sigma) was added 6 h after irradiation to block cells at cytokinesis. Following 48 h incubation period, cells and supernatant were collected by centrifugation (800 rpm for 5 min) and fixed with a solution containing methanol:acetic acid (3:1 v/v) with 1 % formaldehyde. All procedures for cells preparation were in accordance to [18]. At the last step, the cells were gently re-suspended, dropped onto wet clean glass slides and dried at room

temperature. The slides were embedded in UltraCruz mounting media containing DAPI (SantaCruz Biotechnology, USA). The slides were pictured with an Axiovert 200 M (Zeiss). Nuclei in close proximity with similar staining intensity, staining pattern (distribution of eu- and hetero-chromatin), and of approximately the same size were considered as originating from one cell and therefore scored. For scoring, the modified criteria presented by [19] and the IAEA manual [20] were used.

43.2.8 Intracellular ROS Detection and Flow Cytometry

The HepG2 cells exposed to different concentrations of NDs, NeoC or NDNeoC and the one irradiated were washed twice with 37 °C pre-warmed phosphate buffer, trypsinized with trypsin/EDTA solution (Lonza) for 10 min, re-suspended in DMEM at approximately 10^6 cells/ml and centrifuged at 800 × g for 10 min. Pelleted cells were re-suspended in corresponding cell culture media (500 µl) and transferred into Eppendorf tubes. Each sample was incubated with 10 µM H_2DCF-DA solution (10 mM H_2DCF-DA-Stock Solution, Invitrogen) for 30 min in the dark. Following centrifugation at 800 × g for 10 min the pellets were collected and re-suspended in 0.5 ml ice cold phosphate buffer prior to analysis.

The samples were measured with a FACS Calibur flow cytometer (Becton Dickinson, USA) equipped with the Cellquest software. The cell doublets were removed by gating the left area of FL2-W/FL2-A plot for analyses. The green fluorescence of DCF was monitored using a 525 nm long pass filter. For statistical significance, 10,000 HepG2 cells were recorded. Non-stained cells also served as autofluorescence control.

43.2.9 Statistical Analysis

The data were evaluated by analysis of variance (ANOVA) followed by Tukey's post-hock test. A F-test followed by an one-way Kruskal-Wallis test (unequal variances) was applied to the data obtained from micronucleus test. Differences in the results at the level of $p < 0.05$ were considered statistically significant. The statistical analysis was carried out using the PASW 18.0 statistical software package (IBM) for Windows.

43.3 Results and Discussion

In recent years, the complexity of some of the nanomaterials prepared has necessitated the development of a variety of chemical-coupling procedures for their modification. These procedures are also very useful in terms of efficiency

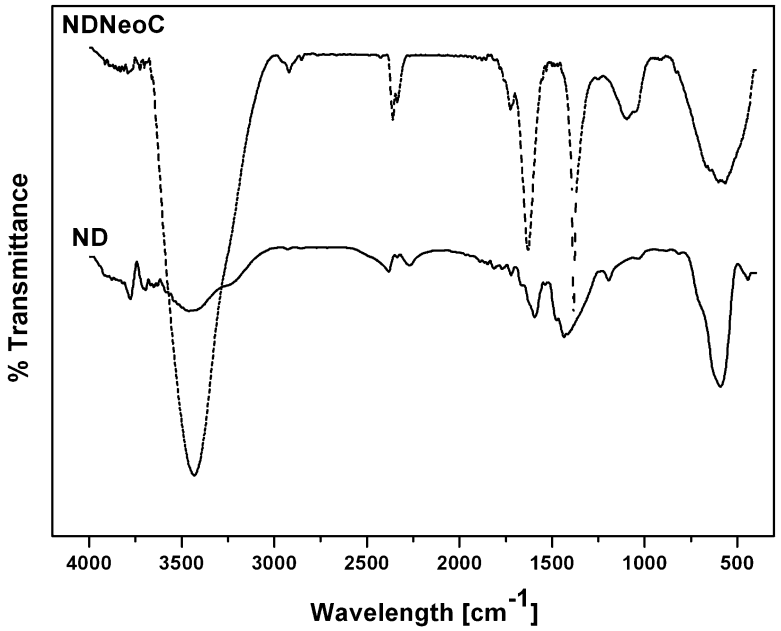

Fig. 43.2 IR Spectra of ND and NDNeoC

leading to high yields and easily purified materials. In this paper we described a simple method for modification of ND surfaces with NeoC, which can be used as a radioprotector.

To confirm the introduction of NeoC onto the ND surface FTIR was performed. A transformation of functional surface groups of ND during the synthesis of NDNeoC was observed in the FTIR spectra as shown in Fig. 43.2. The absorption peaks at 2,923 and 2,855 cm^{-1} in the ND spectrum correspond to asymmetric and symmetric C–H stretching vibrations, respectively. The absorption peaks at 3,259 and 3,436 cm^{-1} corresponds to the O–H stretching vibration, while that at 1,118 cm^{-1} correspond to the O–H deformation vibration. It is also obvious that NDs are rich in carboxyl surface groups as evident from the carbonyl stretching vibration (1,721–1,730 cm^{-1}) in Fig. 43.2. These surface groups were conjugated with amines on mNeoC with the aid of EDC. After introducing mNeoC onto the NDs, the obtained derivative (NDNeoC) is characterized by the appearance of a strong signal at 1,608 cm^{-1} characteristic of aromatic C = C vibrations, a strong signal at 1,386 cm^{-1} characteristic of C-H bending, a signal at 1,688 cm^{-1} characteristic of amid C = O stretching, and a very broad signal N-H (amide) at 3,100–3,600 cm^{-1} overlapping the O-H and C-H (stretching) signals in the same area. The presence of all these bands is indicative for a covalent incorporation of NeoC onto the NDs.

Since we aimed to test the radioprotective effect of NDs and NDNeoC in ***in vitro*** studies by using a cell culture, it was very important to characterize the behavior of

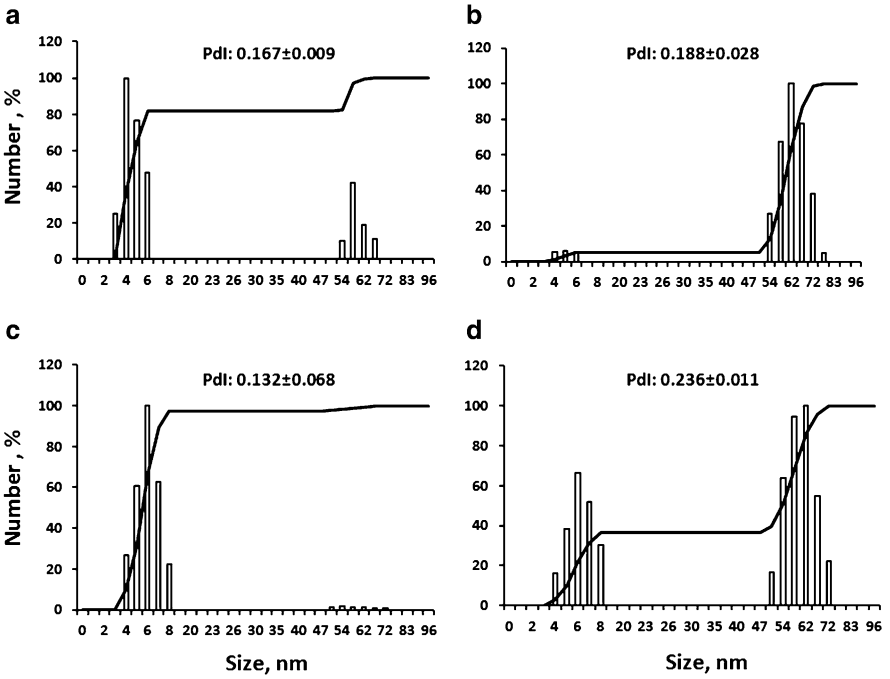

Fig. 43.3 Hydrodynamic size-distributions in dispersions obtained with ND (**a**, **b**) and NDNeoC (**c**, **d**) in complete cell cultured medium at 37 °C (n = 6). (**a**) and (**c**) represent the data obtained at 3 h, (**b**) and (**d**) show the results at 6 h after the preparation of the dispersions. PdI: polydispersivity index

the nanoparticles in solution before further investigations. The characterization of the nanoparticles (size, distribution, state of dispersion) was evaluated by DLS in the cell culture medium used (DMEM with FBS) at 37 °C. It was observed that the dispersion of the nanomaterials in the cell culture medium leads to a distribution around a primary particle size (Fig. 43.3) with less than 5 % agglomeration within the first 3 h following the preparation. Further incubation of these nanomaterials in the cell culture medium (Fig. 43.3b, d) considerably increased the presence of agglomerates. As seen in Fig. 43.3, ND and NDNeoC particles exhibited a similar pattern by agglomerating to nearly the same size when dispersed in the medium. The PdI values for each sample varied slightly within these 3 h and did not increase significantly. Since the agglomeration raises concern when considering size- and dose-dependent treatment of ***in vitro*** experiments, we decided to use only treatments with ND or NDNeoC nanoparticles not longer than 3 h to avoid the effect of agglomeration.

The next step in our investigation was to test the possible radioprotective effect of both nanoparticles. For this reason, parallel cell viability assays on HepG2 pre-treated with NDs or NDNeoC for 3 h in combination with gamma irradiation were conducted. MTT assays showed that treatment with NDs or NDNeoC for 3 h

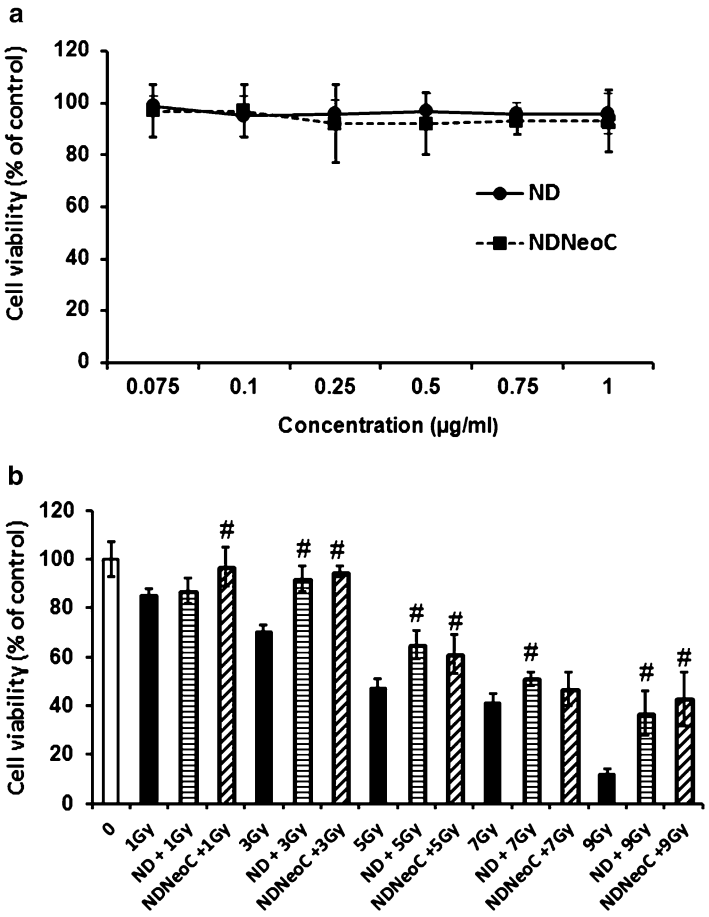

Fig. 43.4 Viability of HepG2 cells shown as percentage of the control following different treatments. (**a**) 3 h after treatment with nanodiamonds (ND) or nanodiamond-neocuproine nanoparticles (NDNeoC). The bars in (**b**) represent the cell viability at 24 h following 3 h pretreatment with 250 ng/ml NDs or NDNeoC and the indicated radiation. Each data set is the mean value of three independent experiments with the standard deviation shown. #: $p < 0.05$ compared to the control

did not have a toxic effect compared to the untreated control cells (Fig. 43.4a). Since there is no cytotoxic effect of the nanoparticles studied within the concentration range used, for all further investigations we selected the concentration of 250 ng/ml ND and NDNeoC. There was also no effect on the cell viability following treatment with NeoC for 3 h in the concentration range of 0.075–1 µM (data not shown).

Gamma irradiation of HepG2 cells treated with doses from 1 to 9 Gy lead to a significant dose-dependent decrease of the cell viability, with LD50 = 4.17 Gy (Fig. 43.4b) at 24 h and LD50 = 0.8 Gy at 72 h. The pretreatment of HepG2 cells

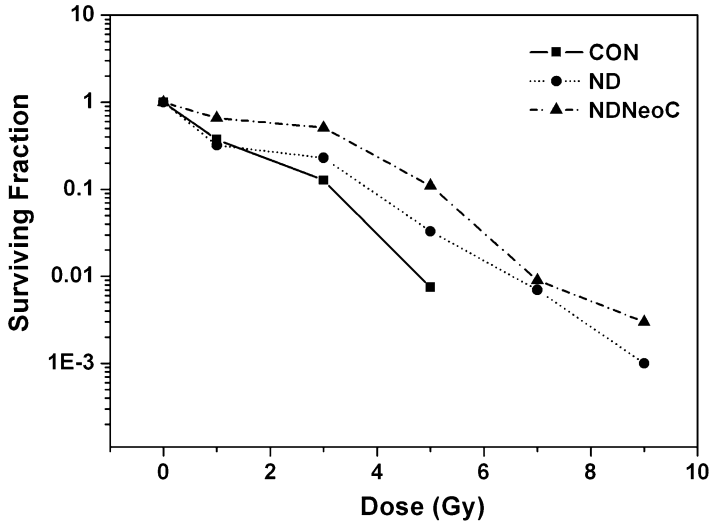

Fig. 43.5 Survival curves of HepG2 cells 9 days after treatment. HepG2 cells were pretreated or not with 250 ng/ml NDs or NDNeoC nanoparticles for 3 h, irradiated with the indicated doses, and seeded at 400 cells/cm^2 in complete culture medium to form colonies. The colonies were then fixed, stained and counted. The surviving fraction was calculated as indicated in the experimental section

for 3 h with 250 ng/ml ND or NDNeoC has a significant protective effect on cell survival 24 h after the irradiation (Fig. 43.4b).

To look for long lasting cytotoxic effects on HepG2 cells following irradiation we performed a colonogenic assay. Cell survival factors up to 9 days following irradiation were calculated using this assay. The technique used enabled any effect caused by the presence of the nanoparticles and/or the irradiation to be observed and quantified. The results show that HepG2 cells show a response varying with the treatment dose (Fig. 43.5). It is evident that 250 ng/ml ND and NDNeoC exhibit a protective effect to HepG2 cells when irradiated up to 5 Gy (Fig. 43.5). A higher surviving fraction was observed in the presence of both nanoparticles relative to the control sample for all doses. The radiosensitivity of HepG2 cells increases without the presence of NDs or NDNeoC with a corresponding increase in the damage.

The observed cell damage was probably due to free radical formation. Several studies have provided strong evidence for a link between irradiation with gamma rays and subsequent generation of oxidative stress and cyto- and geno-toxicity. Oxidative stress plays an important role in many types of cellular injury caused by gamma irradiation, which resulted in DNA damage and apoptotic cell death. ROS are chemical species which are produced by cellular oxygen metabolism, which occurs via mitochondrial respirations [21–24]. To know the effect of NDs and NDNeoC particle pretreatment on the oxidative stress produced following gamma irradiation, we measured ROS generation using the H_2DCF-DA assay, where the intracellular peroxide-dependent oxidation of DCFH-DA forms fluorescent DCF.

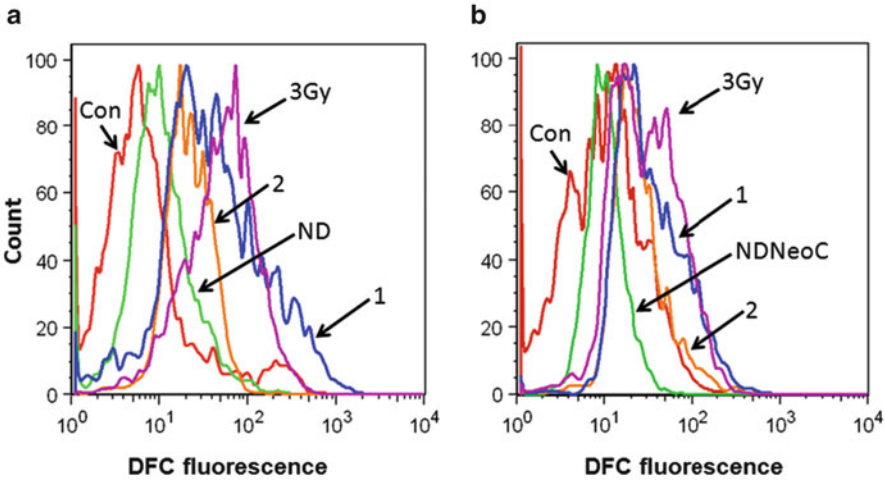

Fig. 43.6 Flow cytometry analysis of intracellular reactive oxygen species. (**a**) HepG2 cells pretreated with 250 ng/ml and 500 ng/ml ND (*1* and *2*) and irradiated with 3 Gy. (**b**) HepG2 cells pretreated with 250 ng/ml and 500 ng/ml NDNeoC (*1* and *2*) and irradiated with 3 Gy. **Con**: Control, untreated cells; **3Gy**: Cells irradiated with 3 Gy only; **DCF**: dichlorofluorescein

The level of ROS generation was markedly increased within 1 h in HepG2 cells treated with 3 Gy (Fig. 43.6). These results confirmed that ROS induced by gamma rays is a significant factor for cell injuries. As shown in Fig. 43.6, the ROS levels generated in response to pretreatment of HepG2 with NDs and NDNeoC were significantly smaller than the irradiated one. Thus the cytotoxic effects induced by irradiation were effectively reduced by NDs and NDNeoC at two different concentrations (Fig. 43.6), suggesting that the intrinsic mechanisms of gamma rays and cytotoxicity are associated with oxidative damage-dependent pathways. These mechanisms are also altered by NDs and NDNeoC probably by neutralization of the free radicals formed.

To examine the genotoxicity protection from gamma irradiation following pre-treatment of HepG2 cells with ND and NDNeoC, we analyzed the micronucleus formation. Figure 43.7a shows that there was no significant difference within the number of micronuclei formed in binucleated cells following treatment with NDs, NeoC or NDNeoC for 3 h compared to the control untreated cells. Gamma irradiation of HepG2 cells with 3 Gy resulted in an significant increase (15 times) in micronucleated binucleated cells formed in comparison with the controls (Fig. 43.7a). Pretreatment with the compounds studied showed a marked decrease in the micronuclei formation – 24 % for NeoC, 50 % for NDs, and 59 % for NDNeoC. The results showed that pretreatment with the compounds studied contributes to a decreased level of genotoxic DNA damage, expressed by the number of micronuclei in irradiated cells (number of MN/1,000 binucleated cell). We did not observe any effect of ND, NeoC, and NDNeoC on the proliferation index (data not shown). The frequency of mononuclear cells containing at least one micronucleus

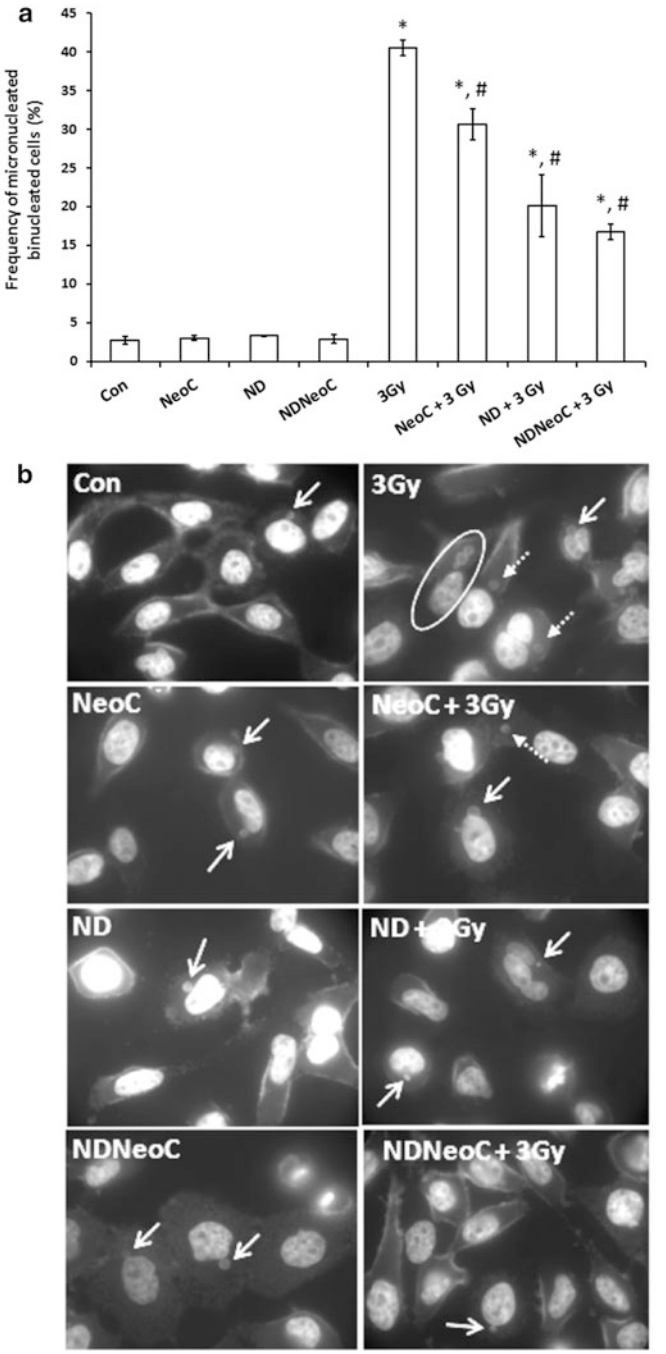

Fig. 43.7 Micronucleus induction in HepG2 cells. (**a**) The frequency of micronucleated HepG2 cells is expressed per 1,000 binucleated cells. The cells were treated with 250 ng/ml nanodiamonds (ND) and nanodiamonds-neocuproine (NDNeoC) nanoparticles or 1 μM neocuproine (NeoC) for 3 h followed by irradiation with 3 Gy. Each data set mean value of three independent experiments with SD shown. *$p < 0.001$ compare to the control untreated cells; # $p < 0.05$ compare to the cells irradiated with 3 Gy. (**b**) Localization of micronuclei in HepG2 cells. The cells were treated as indicated in (**a**) and the formations of micronuclei (MN) were counted 48 h later. The pictures show cells with intact nuclear membrane and MN. *Solid arrows*: MN laying over a nucleoplasmic bridge; *dashed arrows*: intact micronuclei; *circle*: Binucleated cell with 3 MN. Magnification 630×

was not statistically increased after nanoparicles treatment (Fig. 43.7b). The results showed that the pretreatment with the compounds studied contributes to a decreased level of genotoxic DNA damage.

43.4 Conclusions

The present study showed that pretreatment of HepG2 cells with NDs or NCNeoC reduce the formation of ROS and indicates its ability to protect from radiation induced damages. These nanoparticles effectively protect DNA against ionizing radiation probably affecting the system of replication machinery. The protection of DNA damages shown by ND and NDNeoC is also possibly due to the scavenging of radiation-derived primary as well as secondary reactive oxygen species.

Our data provide the first experimental evidence that NDNeoC nanoparticles can effectively block the cyto- and genotoxic effect of gamma irradiation in cell cultures. Extended investigations will be needed to further characterize the mechanisms underlying the protection activity of NDNeoC.

References

1. Deep K, Venugopal A, Shrikant A (2013) Transl Cancer Res 2:330
2. Baker CH (2014) JSM Nanotechnol Nanomed 2:1019
3. Jimmie C, Nelson H, Ferguson A, Kupelian P, Seal S, Jenkins W, Baker C (2010) Nanomed Nanotechnol Biol Med 6:698
4. Rzigalinski BA, Meehan K, Davis RM, Xu Y, Miles WC, Cohen CA (2006) Nanomedicine 1:399
5. Kaplan HS (1960) Bull N Y Acad Med 36:649
6. Rahman K (2007) Clin Interv Aging 2:219
7. Lobo V, Patil A, Phatak A, Chandra N (2010) Pharmacogn Rev 4:118
8. Henle ES, Linn SJ (1997) Biol Chem 272:19095
9. Sung-Ho C, Jen-Kun L, Shing-Hwa L, Yu-Chih L, Shoei-Yn LS (2008) Toxicol Sci 102:138
10. Bruskov V, Malakhova L, Masalimov Z, Chernikov A (2002) Nucleic Acids Res 30:1354
11. Nazeem S, Asfar SA, Sarmad H, Satheesh K (2008) Austral – Asian J Cancer 7:65
12. Hunter RJ, Preedy VR (2011) Nanomedicine in health and disease. Science Publishers, Enfield
13. Chien-Min S (2011) Compositions and methods for providing ultraviolet radiation protection. Patent: US 20110286943A1
14. Mamotyuk JM, Gusakova VA, Uzlenkova NJ, Revenkova SY, Nenyukova OV, Yivashchenko VN, Tsiganok RY, Borodyin VG (2009) Ukrayins'kij Radyiologyichnij Zhurnal 17:65
15. Ivanova L, Popov C, Kolev I, Shivachev B, Karadjov J, Tarassov M, Kulisch W, Reithmaier JP, Apostolova MD (2011) Diam Relat Mater 20:165
16. Mosmann TJ (1983) Immunol Methods 65:55
17. Lehnert S (2007) Biomolecular action of ionizing radiation. Taylor & Francis Group, New York
18. Pejchal J, Vasilieva V, Hristozova M, Vilasová Z, Vávrová J, Alyakov M, Tichý A, Zárybnická L, Šinkorová Z, Tambor V, Kubelková K, Dresler J (2011) Mil Med Sci Lett 80:28

19. Fenech M, Chang WP, Kirsch-Volders M, Holland N, Bonassi S, Zeierf E (2003) Mutat Res 534:65
20. IAEA (2001) Cytogenetic analysis for radiation dose assessment: a manual, Technical reports series. IAEA, Vienna
21. Franco-Molina MA, Mendoza-Gamboa E, Sierra-Rivera CA, Gómez-Flores RA, Zapata-Benavides P, Castillo-Tello P, Alcocer-González JM, Miranda-Hernández DF, Tamez-Guerra RS, Rodríguez-Padilla C (2010) J Exp Clin Canc Res. doi:10.1186/1756-9966-29-148
22. Kim S, Ryu DY (2013) J Appl Toxicol 33:78
23. Franco JL, Posser T, Dunkley PR, Dickson PW, Mattos JJ, Martins R, Bainy AC, Marques MR, Dafre AL, Farina M (2009) Free Radic Biol Med 47:449
24. Martindale JL, Holbrook NJ (2002) J Cell Physiol 192:1

Chapter 44
Determination of the Distribution of Inhaled Drugs in Human Airways by Raman Spectroscopy

A. Kerekes, M. Veres, L. Himics, S. Tóth, A. Czitrovszky, A. Nagy, D. Oszetzky, Sz. Kugler, and M. Koós

Abstract A novel Raman spectroscopic method has been developed to study the distribution of inhaled drugs and other airborn substances in human airway replicas. A drug from a metered dose inhaler was introduced into a realistic human respiratory tract prepared by 3D printing from computer tomographic data recorded on humans, and the deposited material was collected on silicon substrates fixed to the hollow airway's walls. The analysis of the covered area was performed by mapping the characteristic Raman peak intensity of the drug over the substrate surface; the amount was determined by integration of the total intensity measured at different points. The Raman mapping method was verified by comparison with optical microscopic images of the same surface area.

Keywords Inhaled drug distribution • Raman mapping • Realistic human airway models

44.1 Introduction

Investigation of the deposition of aerosol drugs and other materials in the human respiratory system constitutes an intensively studied area of aerosol and medical sciences nowadays. It is particularly of great importance in the fields of development and approval of inhaled drugs, where the delivery of the required dose to the targeted area and a possible overdose has to be controlled precisely. In addition to the properties of the inhaled particles, the characteristics of the inhalation itself also effect how and in which tracts of the respiratory system the deposition of a given drug will take place. Therefore the knowledge of the aerodynamic parameters of an

A. Kerekes • M. Veres (✉) • L. Himics • S. Tóth • A. Czitrovszky • A. Nagy • D. Oszetzky
Sz. Kugler • M. Koós
Wigner Research Centre for Physics, Hungarian Academy of Sciences, P.O.B. 49,
H-1525 Budapest, Hungary
e-mail: veres.miklos@wigner.mta.hu

P. Petkov et al. (eds.), *Nanoscience Advances in CBRN Agents Detection, Information and Energy Security*, NATO Science for Peace and Security Series A: Chemistry and Biology, DOI 10.1007/978-94-017-9697-2_44

aerosol drug alone is not sufficient to determine how it will be deposited in the airways. A more comprehensive approach is required that takes into account the physiological factors and breathing conditions of the patient, too.

Obviously, *in vivo* determination of inhaled drugs in human lung is not a trivial task. The methods used so far include gamma scintigraphy involving the introduction of radioisotopes [1], photon emission computer tomography [2] or positron emission tomography [3] of radiolabeled particles on humans, as well as magnetic resonance imaging [4] and fluorescence imaging [5] on animals. Because of the use of markers these methods influence the drug deposition process itself to some extent.

Recently we have developed a new experimental setup for the investigation of the inhalation of aerosol drugs. It consists of an actuator for metered dose inhalers that can be used to time the initiation of the drug delivery; a sealed chamber where the hollow airways can be placed and which is connected to a pulmonary waveform generator. The latter is able to reproduce different breathing patterns, including simulated ones and others created by recording the breathing of healthy people and patients having different respiratory diseases (asthma, COPD etc.) for example. The airways are produced by 3D printing of real human respiratory tracts constructed from computer tomographic data recorded on different patients. This system allows synchronization of the delay of the actuation of the metered dose inhaler compared to the inhalation phase produced by the waveform generator. It can be used to study the delivery and deposition of inhalation drugs (and other materials) into realistic human airways and other models and to determine the effect of different factors (like the relative timing of the drug introduction to the breath, the presence of obstructions in the airways, physiological differences etc.) on the effectiveness of the drug delivery.

After an inhalation experiment is made, one of the main tasks is to determine the amount of the drug deposited in different tracts of the hollow airway. Since one dose from a metered dose inhaler contains only milligrams of active material, and just a part of it is spread over a relatively large internal surface of the artificial lung, this can be achieved only by using a highly sensitive method which is easy to use, has the require spatial resolution and is preferably substance-specific (it can distinguish different components of a combined medication). The addition of marker molecules to the drug is not to be preferred, since it could affect the aerodynamic properties of the aerosol. Among other techniques micro-Raman mapping was found to be best suitable for this purpose.

44.2 Experimental Details

Different drugs were tested with the method; the one the Raman mapping results of which presented here is a metered dose inhaler delivering 100 mg of salbutamol per actuation. Other medications were based on beclometasone dipropionate and formoterol fumarate dehydrate, as well as ciclesonide.

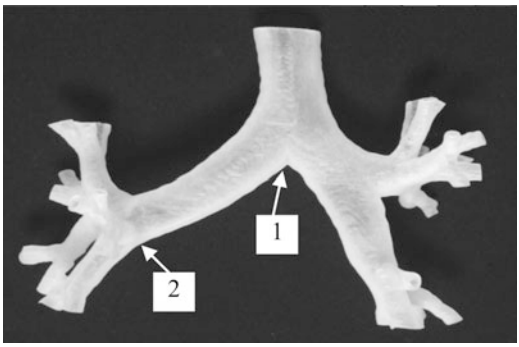

Fig. 44.1 Realistic hollow airway prepared by 3D printing from computer tomographic data. The two numbers indicate the places where the silicon substrates were placed

The drug deposited inside the hollow airway was collected by attaching 1 mm × 2 mm size silicon wafers to the inner surface of the airway wall with double-sided tape. After the inhalation experiments the substrates were collected and used for Raman mapping measurements. A typical 3D printed realistic respiratory tract is shown on Fig. 44.1.

Raman measurements were performed on a Renishaw 1,000 Raman spectrometer attached to a Leica DM/LM microscope. Preliminary measurements were carried out using different excitation energies (488, 532 and 785 nm), in order to determine the optimal measurement conditions for a given medication.

Mapping Raman spectra were recorded over a 30 × 30 or 40 × 40 micron area with 2 micron lateral resolution. Raman maps were created for the intensity of a Raman band specific for the drug. In addition, optical microscopic images of the mapped area were also recorded for comparison.

44.3 Results and Discussion

44.3.1 Determination of Optimal Raman Measurement Conditions

Small sample amounts require highly sensitive Raman measurement conditions. This usually means finding laser wavelength(s) exciting resonant Raman scattering, which occurs when the energy of the incident photons is equal or close to the energy of an electronic transition of the sample and results an increase of the Raman scattering cross-section by 3–5 orders of magnitude [6]. Another factor to be taken into account is the photoluminescence (PL) that could be excited by the incident light and that could be so intense that it will overlap the Raman lines. Figure 44.2a compares the Raman spectra of salbutamol recorded with three different excitation wavelengths. It can be seen that the spectrum recorded with 785 nm excitation has a very poor signal to noise ratio and a relatively intense PL background. The 532 nm excited spectrum is much better, with clearly detectable characteristic peaks and a low PL background, while the use of a 488 nm laser results in a higher PL

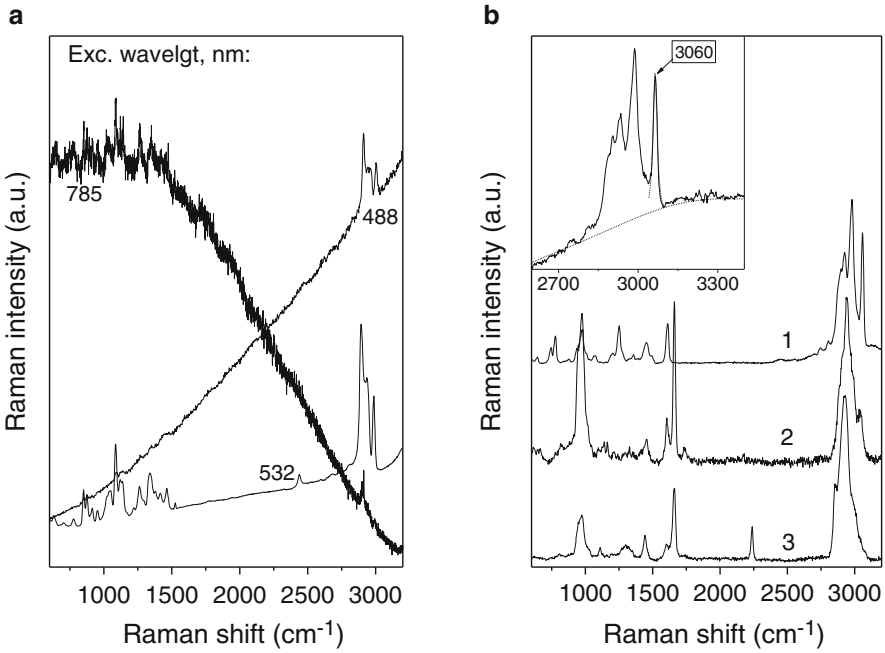

Fig. 44.2 (**a**) Raman spectra of a salbutamol containing inhalation drug recorded with different excitation energies. (**b**) Comparison of the 488 nm excited Raman spectra of inhalation drugs containing (*1*) salbutamol, (*2*) beclometasone dipropionate and formoterol fumarate dehydrate and (*3*) ciclesonide

background, but still good peaks around 3,000 cm^{-1}. Accordingly, in case of this medication the use of 532 nm excitation is preferred, but 488 nm is still acceptable.

Figure 44.2b demonstrates the selectivity of the method by comparison of the Raman spectrum of three different drugs. It can be seen that there are specific peaks in the spectrum of each sample which can be used to identify it (this is important for map creation using the peak intensity). For example, the band at 3,060 cm^{-1} can be used for sample 1, the one at 1,660 cm^{-1} for sample 2 and the peak at 2,240 cm^{-1} for sample 3. By selecting the appropriate peaks mapping Raman spectroscopy allows determination of the spatial distribution of each constituents of a combined medication.

Precise mapping of the Raman peak intensity requires the subtraction of the PL baseline and fitting of the required part of the resulted spectrum with an appropriate peak function, as shown in the inset of Fig. 44.2b for sample 1.

44.3.2 Mapping Raman Measurements of Deposited Aerosol Drug

Raman intensity maps were created for two silicon substrates placed at different points of the hollow airway, corresponding to the thracea and lob bronchus (marked

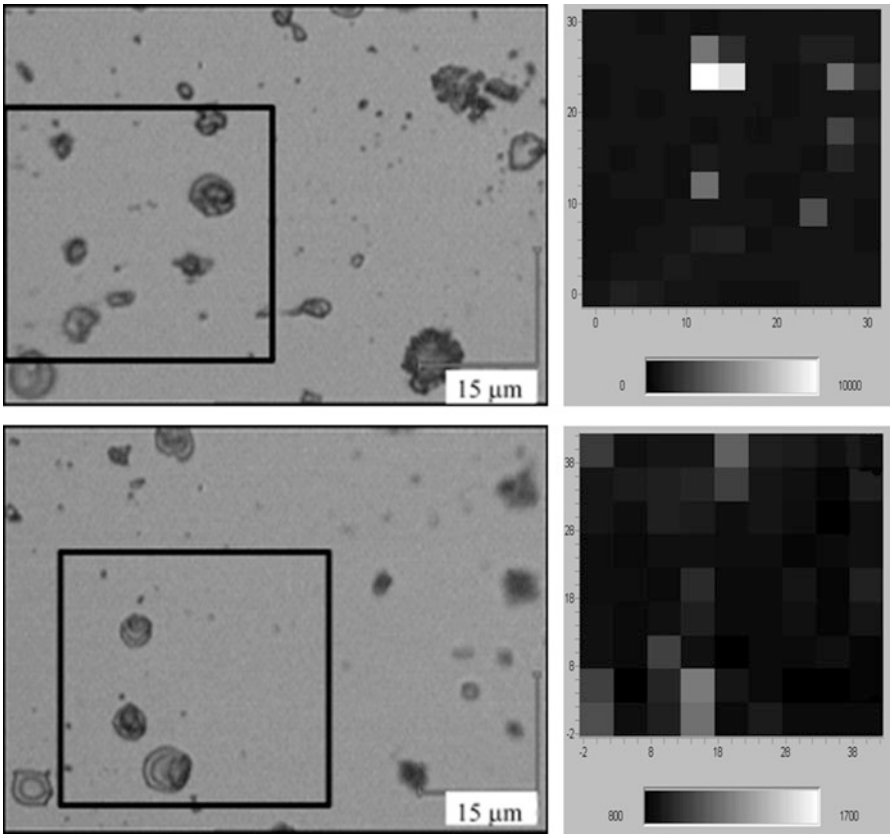

Fig. 44.3 Optical microscopic images (*left*) and Raman peak intensity maps (*right*) of silicon substrates used to collect aerosol drug deposited on the wall of an artificial lung in points 1 (*upper row*) and 2 (*lower row*) in Fig. 44.1. The *black squares* indicate the areas of the Raman mapping

as points 1 and 2 in Fig. 44.1). The maps are shown on Fig. 44.3, together with optical microscopic images of the parts of the substrates where the maps were recorded.

Optical microscopic images clearly show the deposited drug on the silicon surface. It can be seen that the coverage is non-uniform; stains of different size and shape are found on the substrate surface. As expected, the coverage of the substrate placed in the thraceal region is higher than that of the other. The patterns observable on the Raman intensity maps march those of stains in the optical microscopic images indicating the possibility of determination of the distribution of the deposited material on the substrates using Raman spectroscopy.

Although Raman intensity maps provide information on the distribution of the medication, the total amount of material deposited per unit area has also to be determined. In order to test if Raman spectrosopy is suitable for this purpose, the

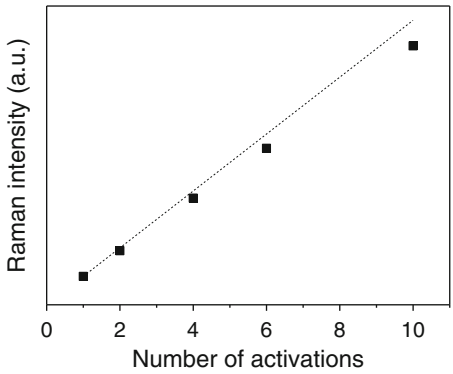

Fig. 44.4 Dependence of the salbutamol Raman peak intensity on the dose. The *dashed line* indicates the theoretical relationship

relationship between the Raman peak intensity and the number of activations of the metered dose inhaler was determined (Fig. 44.4) and was found to be nearly linear. Our ongoing experiments are aimed to find the correlation between the Raman peak intensity and the mass of the deposited material, the last step to provide precise information on the deposition of inhaled drugs in realistic hollow airway samples.

44.4 Conclusions

A novel Raman spectroscopic method has been developed that can be used to study the deposition of aerosol drugs and other airborn substances in realistic human airway replicas. Silicon substrates attached to the internal surface of 3D printed hollow airway walls were used to collect the deposited drug and their surface was analyzed by mapping Raman spectroscopy. Intensity maps of characteristic Raman peak of the medication were found to be in good agreement with optical microscopic images of the scanned areas.

Acknowledgement This work was supported by the Hungarian National Research Agency under grants KTIA_ AIK_12-1-2012-0019 and TéT_10-1-2011-0725.

References

1. Newman SP (1993) Crit Rev Ther Drug Carrier Syst 10:65
2. Snell NJC, Ganderton D (1999) Respir Med 93:123
3. Gardner SF, Green JA, Bednarczyk EM, Farnett L, Miraldi F (1992) Am J Hosp Pharm 49:1499
4. Thompson RB, Finlay WH (2012) J Aerosol Med Pulm Drug Deliv 25:55
5. Yi D, Wiedmann TS, Naqwi A, Price AP, Panoskaltsis-Mortari A (2012) Exp Lung Res 38:325
6. Efremov E, Ariese F, Gooijer C (2008) Anal Chim Acta 606:119

Chapter 45
Synthetic Micro- and Nanocrystalline Zeolites for Environmental Protection Systems

Silviya Boycheva, Denitza Zgureva, Borislav Barbov, and Yuri Kalvachev

Abstract Coal combustion ash with a 2.25 ratio of SiO_2/Al_2O_3 was used to synthesize an X-type zeolite by alkaline fusion followed by hydrothermal treatment. The reaction products were investigated for phase identification by X-ray diffraction analysis. The surface morphology and the elemental composition were determined by scanning electron microscopy with an energy-dispersive X-ray analyzer. The vibrations of the structural units in the zeolite framework were revealed by IR spectroscopy. Zeolite X obtained from pure initial materials was used as a reference sample for comparison. The results confirmed the conversion of coal ash into a zeolite possessing a dominant Na-X phase of micro- or nanocrsystalline morphology depending on the synthesis conditions. The coal ash Na-X zeolite was studied for adsorption of carbon dioxide under static conditions.

Keywords Synthetic zeolites • Environmental protection systems

45.1 Introduction

Due to their highly developed microporous structure with a defined pore size synthetic and natural zeolites have been successfully applied as gas dryers, adsorbents of polar gaseous molecules and molecular sieves in gas cleaning systems [1]. Zeolites are also adsorptive materials and ion-exchangers for effective removal of pollutants from contaminated waters, enabled by the presence of replaceable cations in their structural network [2]. The development of nanocrystalline zeolites has been a new trend in materials sciences because of their unique surface reactivity

S. Boycheva (✉) • D. Zgureva
Department of Thermal and Nuclear Power Engineering, Technical University of Sofia, Blvd. Kl. Ohridsky 8, 1000 Sofia, Bulgaria
e-mail: sboycheva@tu-sofia.bg; kalvachev@clmc.bas.bg

B. Barbov • Y. Kalvachev
Bulgarian Academy of Sciences, Institute of Mineralogy and Crystallography, Acad. G. Bonchev Str., Bl.107, 1113 Sofia, Bulgari

P. Petkov et al. (eds.), *Nanoscience Advances in CBRN Agents Detection, Information and Energy Security*, NATO Science for Peace and Security Series A: Chemistry and Biology, DOI 10.1007/978-94-017-9697-2_45

and ability to functionalization which make them advanced materials for catalytic and photocatalitic reduction processes [3]. Zeolite synthesis is usually performed by hydrothermal crystallization of silica gel, alkaline activators and aluminium salts at elevated temperatures in strong alkaline media. Recently, low-cost sorbents have been produced by conversion of mineral aluminosilicate wastes that can replace successfully their natural analogues in the systems for environment protection. Coal ash is mainly composed of silica and alumina oxides obtained by thermal decomposition of fuel mineral constituents. The chemical composition of this abundant resource makes it suitable for processing of synthetic zeolites [4]. The fusion of the alkaline–ash mixture facilitates the formation of soluble Na-aluminate and silicate, what enhances the zeolite formation and leads to a full utilization of the raw material [5]. X-type zeolite, which is an analog on the natural faujasite, is characterized by an extremely developed surface and a structure with large size pores. Therefore it is extensively used for gas adsorption. Fusion followed by hydrothermal treatment has been reported to be the most reliable method to selectively obtain the Na-X type zeolite from coal ash of different compositions [1].

The present study reports on the conversion of coal combustion aluminosilicate by-products into synthetic zeolites of the Na-X type and on initial studies of their potential to act as adsorbents for carbon dioxide.

45.2 Materials and Methods

Ash residues, containing 52.66 wt% SiO_2 and 23.37 wt% Al_2O_3, were subjected to a double stage fusion-hydrothermal conversion. Coal ash and NaOH mixtures with different ratios were sintered at 550 °C; after dilution in water under continuous stirring, the reaction mixture was charged into an autoclave for hydrothermal reaction. The product morphology was observed by scanning electron microscopy (SEM) with a JEOL JSM6390 microscope coupled with an energy-dispersive X-ray (EDX) analyser (Oxford Instruments). Phase identification was performed by X-ray diffraction (XRD) with a Brucker D2 Phaser diffractometer with CuK_{α}-radiation and a Ni filter. Na-X zeolite was exposed for carbon dioxide adsorption under static conditions. The experiment was performed in an autoclave at 0.1 MPa. The framework structure of the synthesized materials and the possibility of CO_2 adsorption were studied by Fourier Transform Infrared Spectroscopy (FT-IR) with a Brucker Tensor 37. The referent zeolite X was synthesized by hydrothermal treatment of pure starting materials with a stoichiometric ratio.

45.3 Results and Discussions

The conditions under which the coal ash zeolitization experiments were performed are listed in Table 45.1.

Table 45.1 Experimental conditions of coal ash zeolitization

Sample	NaOH/coal ash ratio	Fusion [°C]	Hydrothermal synthesis	
			Temperature [°C]	Duration [h]
12	2.0	550	90	2
13	2.4	550	90	2
18	2.0	550	90	4

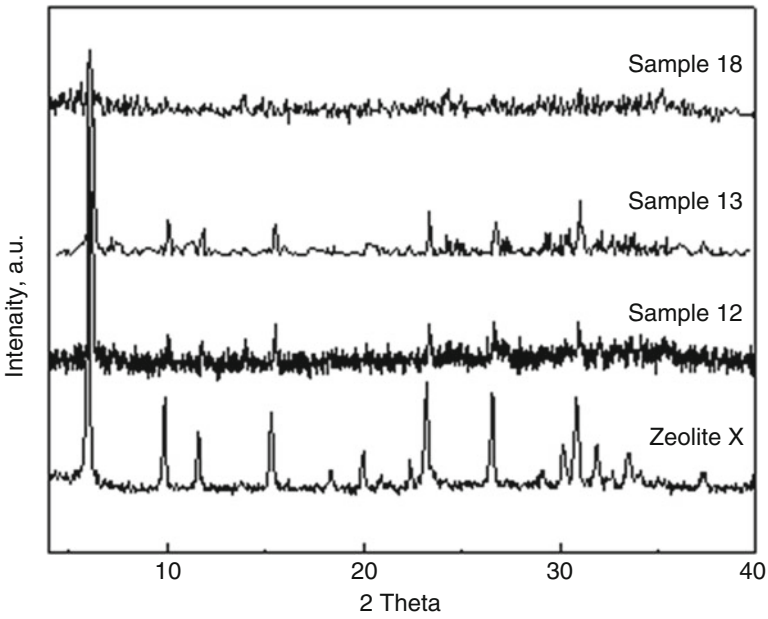

Fig. 45.1 XRD pattern of the reference and synthesized zeolites

XRD patterns of the synthesized samples and the reference zeolite X are plotted in Fig. 45.1.

It is evident that the coal ash zeolites are X type, as the characteristic diffraction reflexes are present in the patterns of all samples. Sample 18 is characterized by low crystallinity, while samples 12 and 13 are dominantly crystalline, but their peaks are less intensive in comparison to those of the referent zeolite. The coal ash zeolites consist of octahedral crystals typical for zeolite X, as revealed by SEM analysis (Fig. 45.2).

The reference zeolite X and sample 13 consists of particles with micrometer sizes, while nano-sized crystallites are predominant for the structure of samples 12 and 18. The elemental composition of coal ash zeolites, studied by integral EDX analyses, is presented in Table 45.2.

It can be seen, that the content of Si and Al in the coal ash zeolites is very similar to that of the reference composition of zeolite X, while it has a deficit of Na^{+}-ions. In general, there are three stages in alkaline hydrothermal conversion of coal ash into zeolites: (1) dissolution of Si^{4+} and Al^{3+} ions from the raw aluminosilicates into

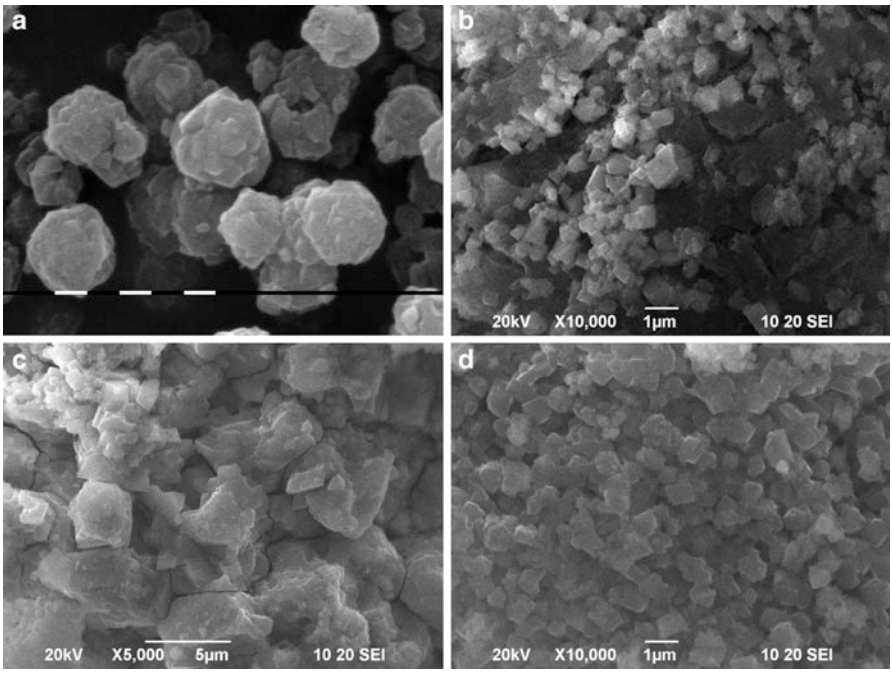

Fig. 45.2 SEM micrographs of the reference sample (**a**) and coal ash zeolite samples 12 (**b**), 13 (**c**) and 18 (**d**)

Table 45.2 Elemental composition of zeolite samples (in wt. %)

Sample	O	Na	Mg	Al	Si	Fe	Ca
12	42.06	12.61	1.03	11.57	16.43	11.08	5.22
13	41.91	13.02	0.67	12.81	17.37	9.623	3.653
18	46.39	12.01	0.94	10.67	13.77	11.47	4.348
X	37.67	34.33	–	11.57	16.43	–	–

the alkaline solution; (2) condensation of the aluminosilicate hydrogel; (3) crystallization of the zeolite phase from the aluminosilicate gel. The OH^- ions contribute to the dissolution stage, while Na^+ ions play a role in the zeolite crystallization. Na^+ ions are stabilizers of zeolite structure as they compensate the negative charges of $AlO_{4/2}$-tetrahedra. It could be expected that cations from the raw ash acting as charge compensators in coal ash zeolites also contribute to keep their overall framework neutral. Hence, coal ash zeolites could not be obtained in a defined ionic form corresponding to the alkaline activator due to drawback ions present in the starting composition. A typical IR spectrum of a coal ash zeolite is presented in Fig. 45.3. The IR spectra of zeolites possess common features as their framework is composed of TO_4 tetrahedra (T = Si/Al). However, each zeolite type is characterized by its own specifics. The framework type and the basic structural units of

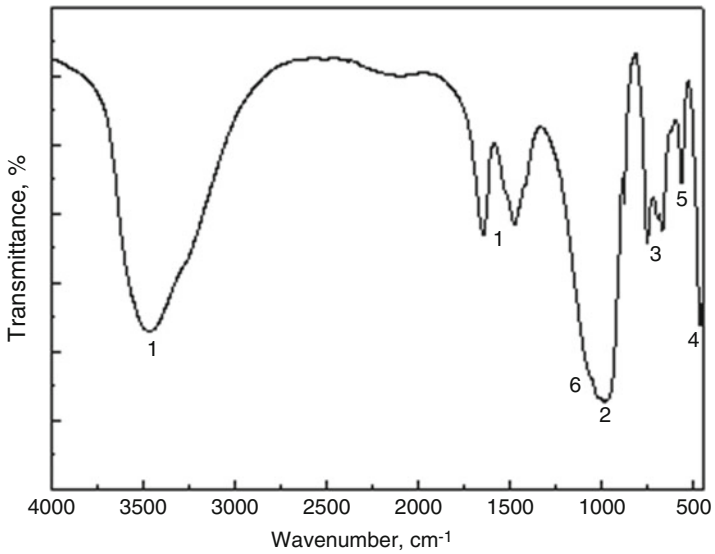

Fig. 45.3 FT-IR spectrum of the synthesized coal ash zeolite

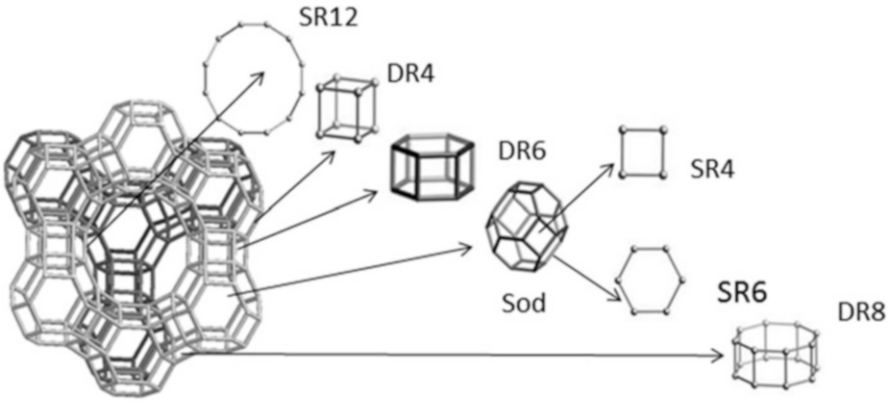

Fig. 45.4 Schematic presentation and structural units of zeolite X. *SOD* sodalite cage, *SR*-single- and *DR*-double rings composed of the indicated number of atoms

zeolite X are presented in Fig. 45.4, while the vibration modes and their assignments are summarized in Table 45.3.

The framework of zeolite X is built of sodalite cages connected by double six rings (DR6). The characteristic internal and external sodalite cages vibrations, which are typical for zeolite X, are shown in the experimental spectrum of the coal ash zeolite (Fig. 45.3).

Table 45.3 IR modes for zeolite X and their assignments

No.	IR vibrations	Wavenumber, cm^{-1}
1	Water region, H-O-H	3,467, 1,643
	Internal tetrahedral vibrations	
2	Asymmetric stretching mode in $TO_{4/2}$ tetrahedra	1,048, 977
3	Symmetric stretching mode in $TO_{4/2}$ tetrahedra	744,666
4	T-O bending mode in $TO_{4/2}$ tetrahedra	460
	External linkages vibrations	
5	Double rings (DR6)	560
6	Asymmetric T-O stretching mode	1,070

Recently, the greenhouse effect has provoked greater attention to carbon dioxide capture and storage technologies (CCS) and their compatibility with thermal power plants (TPPs) [6]. Three approaches for carbon dioxide (CO_2) removal during energy generation have been outlined: pre-combustion capture, oxy-fuel combustion and post-combustion capture. The last technologies are the most compatible to the existing TPPs; theirs cost- and energy-efficiency depends mainly on the capturing mechanism. A variety of methods exists for the post-combustion capture, such as chemical or physical sorption as well as membrane or cryogenic separation. Adsorption on solids as a CO_2 capture technology has a number of advantages compared to others, due to the reusable adsorbents, simple reactors, low capital investments, and adsorption/desorption enhancement by pressure and temperature variation.

The highest adsorption potential toward CO_2 has been reported for zeolite 13X which is a commercial artificial faujasite prototype [7]. In this context, the synthesized coal ash Na-X zeolites have been investigated with respect to their adsorption ability toward carbon dioxide. Tests were performed under static conditions in a stainless steel autoclave filled with CO_2 through a gas transportation line to reach pressure of 0.1 MPa. The required pressure was adjusted using a booster pump and a channel for inert gas (N_2). The experimental set-up is presented in Fig. 45.5. A powder zeolite sample was packed in a gas permeable bag, dried at 105 °C and exposed immediately to a CO_2 atmosphere for 2 h.

The adsorption of CO_2 onto the zeolite was confirmed by IR spectroscopy. The IR spectra of samples exposed to CO_2 are plotted in Fig. 45.6. The IR active modes of physically adsorbed CO_2 which are O-C-O bending and C-O asymmetric stretching, are found at 667 and 2,350 cm^{-1}, respectively. The IR vibration of free CO_2 can be observed clearly in the spectrum of the zeolite after CO_2 capture. This result is indicative for physical surface adsorption of CO_2 onto the zeolite tested. It has been reported that chemisorptions of CO_2 onto zeolites yield carbonate species, whose signals appear as a pair of bands at 1,711 and 1,365 cm^{-1}, assigned to the bicoordinated CO_2 (type I) with both a T atom and a cation (Fig. 45.7).

The bicoordinated species can be converted into a true carbonate structure (type II) characterized by bands at 1,488 and 1,431 cm^{-1}. The chemisorption characteristic lines fall into the vibration regions of the zeolite groups. Such a chemisorption

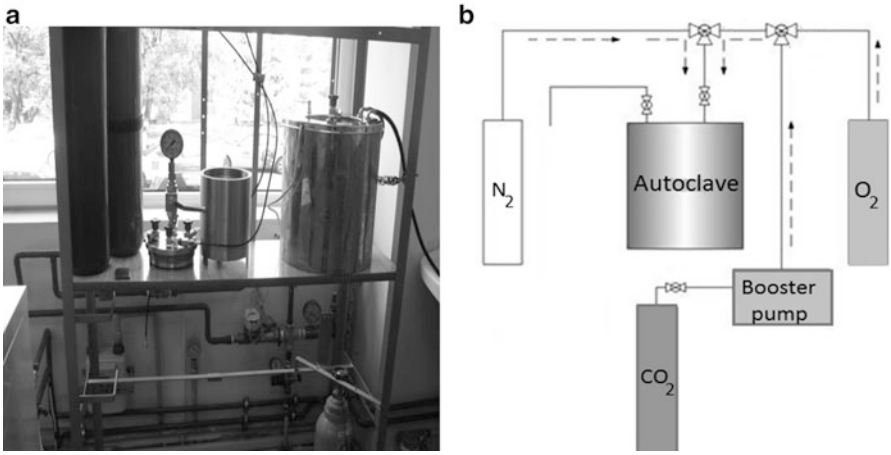

Fig. 45.5 Picture (**a**) and a schematic diagram (**b**) of the adsorption test set-up

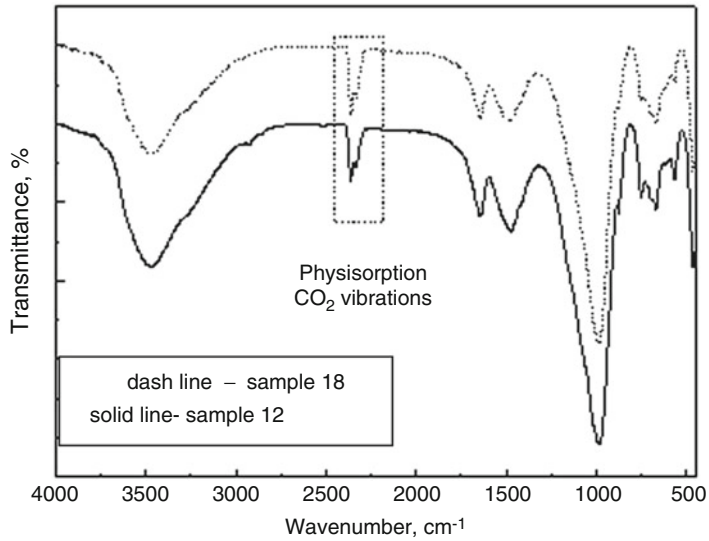

Fig. 45.6 FT-IR spectra of coal ash zeolites after exposition to CO_2

Fig. 45.7 Species yielded from the chemisorptions of CO_2 onto zeolite X [8]

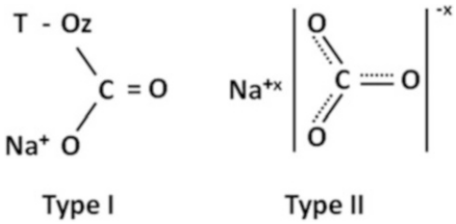

mechanism can not be confirmed by IR spectroscopy in the case of weak appearance.

Thus, it could be supposed that CO_2 physisorption is the dominant adsorption process at a pressure of 0.1 MPa.

45.4 Conclusions

Coal ash was converted into zeolite X by a double stage fusion-hydrothermal synthesis, which is confirmed by structural and morphological studies. Coal ash zeolites can be obtained as micro- or nanocrystalline materials by varying the synthesis conditions. These zeolites are CO_2 adsorptive materials which will be further studied under dynamic conditions and at higher pressures to elucidate their morphology. The utilization of coal ash after its zeolitization for carbon capture is an environment-friendly method for zero emissions and end of pipe technologies in energy generation plants.

References

1. Majchrzak-Kuceba I, Nowak W (2005) Thermochim Acta 437:67
2. Moreno N, Auerol X, Ayora C, Pereira CF, Janssen-Jurkovicova M (2001) Environ Sci Technol 35:3526
3. Larsen SC (2007) J Phys Chem C 111:18464
4. Querol X, Moreno N, Umana JC, Alastuey A, Hernandez E, Lopez-Soler A, Plana F (2002) Int J Coal Geol 50:413
5. Purnomo C, Salim C, Hinode H (2012) Microporous Mesoporous Mater 162:6
6. Davidson R (2010) Woodhead Publ Ser Energy 1:183
7. Ruen-ngam D, Rungsuk D, Apriratikul R, Pavasant P (2009) J Air Waste Manag Assoc 59:1140
8. Auerbach S, Carrado K, Dutta P (2003) Handbook of zeolite science and technology. Marcel Dekker, Inc., New York

Chapter 46
Nano- and Microsized Phases in the WO_3-ZnO-Nd_2O_3-Al_2O_3 System for Applications in Environmental Monitoring

M. Ataalla, M. Milanova, M. Hassan, Ahmed S. Afify, J.M. Tulliani, and Y. Dimitriev

Abstract WO_3 and WO_3-based materials in the form of thin films, either as bulk or as nanostructures, have been widely used for the detection of a variety of gases, such as NO_2, H_2, NH_3 and Cl_2. The purpose of this study was to prepare materials from the WO_3-ZnO-Nd_2O_3-Al_2O_3 system containing high amount of WO_3 for applications in environmental monitoring by applying the melt quenching method. Homogenized batches of the starting oxides were melted for 20 min at 1,240 °C in platinum crucibles in air atmosphere. The melts were quenched by pouring and pressing between two copper plates (cooling rates 10^1–10^2 K/s). Glassy-crystalline samples containing the monophase $AlW_{12}O_{37.5}$ was produced by quenching a melt with the composition of $80WO_3 \cdot 10Nd_2O_3 \cdot 10Al_2O_3$. Glassy-crystalline sample containing nanosized $W_{18}O_{49}$ (~60 nm) was obtained after cooling of a melt with the composition 76WO3·9.5ZnO·9.5Nd_2O_3-5Al_2O_3. A mixture of WO_3 and $AlW_{12}O_{37.5}$ in the amorphous matrix was prepared by crystallization of a quenched sample with the composition $75WO_3 \cdot 10Nd_2O_3 \cdot 5ZnO \cdot 10Al_2O_3$. Samples were prepared by the screen printing technique as gas sensor s; thereafter dc resistance measurements were performed in the presence of relative humidity and ammonia. It was established that the glassy-crystalline sample containing the monophase $AlW_{12}O_{37.5}$ exhibits a significant sensitivity towards ammonia and relative humidity, while other phases show a good sensitivity only towards relative humidity.

M. Ataalla (✉) • Y. Dimitriev
Department of Materials Science, University of Chemical Technology and Metallurgy, 8 Kl. Ohridski blvd., 1756 Sofia, Bulgaria
e-mail: sobhy.88@hotmail.com

M. Milanova
Institute of General and Inorganic Chemistry, Bulgarian Academy of Sciences, 1113 Sofia, Bulgaria

M. Hassan • A.S. Afify • J.M. Tulliani
Department of Applied Science and Technology, Politecnico di Torino, 10129 Torino, Italy

P. Petkov et al. (eds.), *Nanoscience Advances in CBRN Agents Detection, Information and Energy Security*, NATO Science for Peace and Security Series A: Chemistry and Biology, DOI 10.1007/978-94-017-9697-2_46

Keywords Crystallization • Gas sensors • Melt quenching • Nanosized materials • Screen-printing technique

46.1 Introduction

WO_3 and ZnO are well-known transition metal-oxide materials that show a promising gas-sensing performance due to their catalytic properties. WO_3 and WO_3-based materials in the form of thin films, either as bulk or nanostructures, have been widely used for detecting of variety of gasses, such as NO_2, CO, H_2, SO_2, H_2, H_2S, NH_3 and Cl_2 [1–6]. The gas sensing properties of WO_3 was investigated in many studies by preparing it as a pure material [7–11] or by doping it with other oxides such as ZnO, SnO_2 and Co_3O_4 [2, 12, 13] or with other metals such as Au and Pd [4, 14]. The ammonia sensing properties of $W_{18}O_{49}$ nanowires synthesized by a low temperature solvothermal technique have been investigated by Zhao et al. [15]. Ammonia is both caustic and hazardous to humans especially when its concentration exceeds the TLV (toxicity and threshold limit) value of 25 ppm [6]. Many techniques such as electrospinning [7], solvothermal methods [14], modified thermal evaporation [8], precipitation [9], flame spray pyrolysis [2] and sol-gel methods [11, 12] have been used for the preparation of WO_3 and WO_3-based gas sensing materials. The sensing properties of ZnO have been investigated by many researches [1, 2, 16, 17]. ZnO thin films gas sensor showed a high sensitivity towards methanol, ethanol, propyl alcohol and methane [1, 18, 19]. Many metal ions such as Al, In, Cu, Fe, Sn and Ru have been used as dopants in ZnO gas sensors in order to improve their gas sensing properties [1, 2]. Recently it has been found that the combination of ZnO and WO_3 with an appropriate ratio is a useful approach to enhance the gas-sensing performance. The preparation technique can considerably affect the physical, chemical and gas sensing properties of mixed oxide sensors. Developments of a new preparative routes and as well as compositional variations are two perspective approaches for the design of new highly-sensitive and selective gas sensor materials.

The purpose of this study is to investigate the possibility to prepare materials from a multi-component WO_3-ZnO-Nd_2O_3-Al_2O_3 system for application in environmental monitoring such as gas sensors for ammonia and the relative humidity. New techniques as melt quenching and crystallization from glasses will be applied for the preparation of different phases.

46.2 Experimental

Batches with the nominal compositions (A) $76WO_3{\cdot}9.5ZnO{\cdot}9.5Nd_2O_3{\cdot}5Al_2O_3$, (B) $80WO_3{\cdot}10Nd_2O_3\ {\cdot}10Al_2O_3$, and (C) $75WO_3{\cdot}5ZnO.10Nd_2O_3{\cdot}10Al_2O_3$ were prepared using reagent grade WO_3, Al_2O_3, Nd_2O_3 and ZnO as starting compounds.

Table 46.1 Investigated compositions in the system WO_3-ZnO-Nd_2O_3-Al_2O_3

Nominal composition	Phases before heat treatment	Sample symbol	Phases after heat treatment	Sample symbol
$76WO_3 \cdot 9.5ZnO9 \cdot 5Nd_2O_3 \cdot 5Al_2O_3$	$W_{18}O_{49}$ crystals + amorphous matrix	A	–	–
$80WO_3 \cdot 10Nd_2O_3 \cdot 10Al_2O_3$	$AlW_{12}O_{37.5}$ crystals + amorphous matrix	B	$AlW_{12}O_{37.5}$ crystals + amorphous matrix	D
$75WO_3 \cdot 10Nd_2O_3 \cdot 5ZnO. 10Al_2O_3$	Amorphous matrix	C	WO_3 $AlW_{12}O_{37.5}$ crystals + amorphous matrix	E

The homogenized batches were melted for 20 min. at 1,240 °C in platinum crucibles in air. The melts were quenched by pouring and pressing them between two copper plates (cooling rates 10^1–10^2 K/s). The glass sample (B) and (C) were subjected to heat treatment at 530 °C and 550 °C after estimation crystallization temperature by (DTA) Differential thermal analysis (STA PT1600 TG-DTA/DSC) (Table 46.1). The phase formation of the samples was established by X-ray analysis with a Bruker D8 Advance diffractometer, using Cu Kα radiation in the range $10° < 2\Theta < 80°$. The microstructure and morphology of the crystalline products were studied by scanning electron microscopy (SEM) (Jeol-357).

Three sensors were prepared by using a screen printing technique [20, 21] as follows: firstly interdigitated gold electrodes (ESLEUROPE 8835) were screen-printed onto planar α-Al_2O_3 substrates (Coors Tek, USA, ADS-96 R, 96 % alumina, 0.85 cm × 5 cm) by using a rubber squeegee and a 270 mesh steel screen. After drying overnight, these substrates were heated at 520 °C for 18 min with a 2 °C/min heating ramp to optimize the electrical conductivity of the electrodes, according to the recommendations of the ink manufacturer. The second step of the sensor preparation included the preparation of the so-called first ink, containing 2 g of the sensing material mixed with a suitable amount of ethyleneglycolmonobutyalether (Emflow, Emca Remex, USA) in which poly-(vinyl butyral-co-vinyl alcohol-co-vinyl acetate) (PVB, Aldrich, USA) acts as a binder to produce the ink. The first ink was manually screen printed through a 270 mesh steel screen onto the gold electrodes. The thick-films formed were porous with thicknesses of about 30–40 μm and areas of about 1 cm^2.

In order to improve the adhesion to the electrode, WO_3 was applied to the samples prepared by sol-gel technique. Tungsten oxide was synthesized as follows: 0.294 g of WCl_6 was dissolved in 4 ml ethanol, then stirred for 30 min; subsequently 1.5 mL monoethanolamine (MEA) was added under stirring for 24 h (pH around 7). Then 2.25 ml EMFLOW was slowly added to the solution.

All humidity and ammonia (NH_3) tests of the sensors were carried out by using a laboratory apparatus consisting of a thermo stated chamber operating at 25 °C, in which the relative humidity (RH) could be varied between 0 and 96 %, the NH_3

concentration between 0 and about 75 ppm [22]. The apparatus was calibrated to ensure a constant air flow during the electrical measurements; relative humidity was varied in steps of 3 min each. An external alternating voltage (V = 3.6 V at 1 kHz) was applied to each tested sensor, acting as a variable resistance of the electrical circuit described above. The sensor response SR, expressed in %, is defined as the relative variation of the starting resistance compared with the resistance measured in the gas atmosphere:

$$SR\ (\%) = 100\ \times \frac{|R_0 - R_g|}{R_0} \tag{46.1}$$

Here R_0 is the original resistance in the presence of air flow and Rg is the resistance after gas exposure until equilibrium, i.e. at saturation of the active surfaces.

46.3 Results and Discussions

As seen from the XRD data shown in Fig. 46.1 for compositions containing high amounts of WO_3 glassy and glassy-crystalline materials obtained by applying the melt quenching technique. The glassy-crystalline sample containing $W_{18}O_{49}$ as crystalline phase (Sample A) was obtained after cooling melt with the nominal composition 76WO3·9.5ZnO·9.5Nd_2O_3·5Al_2O_3. The average size of the $W_{18}O_{49}$ crystals calculated from the broadening of the diffraction lines using Scherrer's equation is about 60 nm. $AlW_{12}O_{37.5}$ (Sample B) was detected in the diffraction pattern of the glassy-crystalline sample obtained by quenching melt with the nominal composition 80WO_3.10Nd_2O_3.10Al_2O_3. The quenched sample C (75WO_3·10Nd_2O_3·5ZnO.10Al_2O_3) was fully X-ray amorphous. Figure 46.2 shows DTA curves of the samples up to 800 °C with a heating rate of 10 °C/min. The crystallization time was 6 h at temperatures of 530 °C (Sample B) and 550 °C (Sample C) in air. Figure 46.3 shows XRD patterns of samples D and E. After heat treatment a mixture of WO_3 and $AlW_{12}O_{37.5}$ appeared in the amorphous matrix (Sample E).

According to SEM images (Figs. 46.4 and 46.5) the crystal aggregates are dispersed randomly in the amorphous matrix with dimensions between 0.5 and 1 μm.

Figure 46.6 presents the response of the humidity sensors at room temperature as a function of RH for all samples investigated. It can be seen that the sensors based on the samples A and E react to water vapour over 50 % RH, while the response of sample D started already started at 10 % RH thus showing the best sensitivity for relative humidity. The sensors based on glassy-crystalline the sample containing monophase $AlW_{12}O_{37.5}$ (sample D) was the only one able to detect ammonia with a good response (Fig. 46.7).

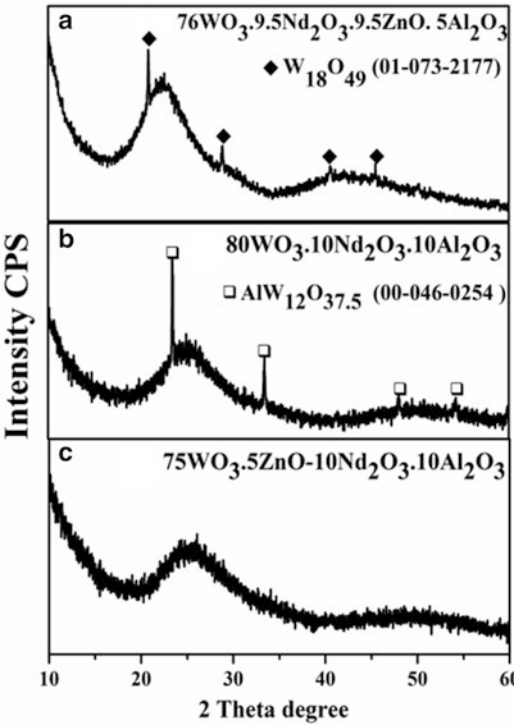

Fig. 46.1 XRD patterns of glassy and glassy-crystalline samples A, B, and C

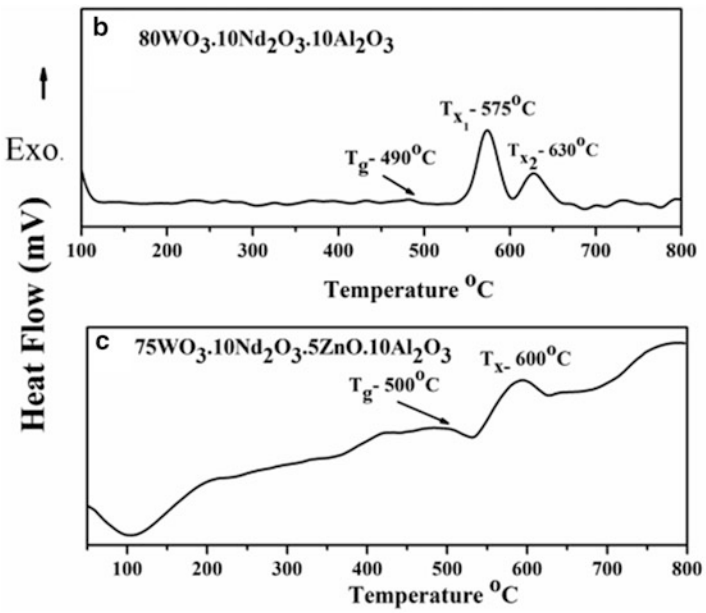

Fig. 46.2 DTA curves for samples B and C

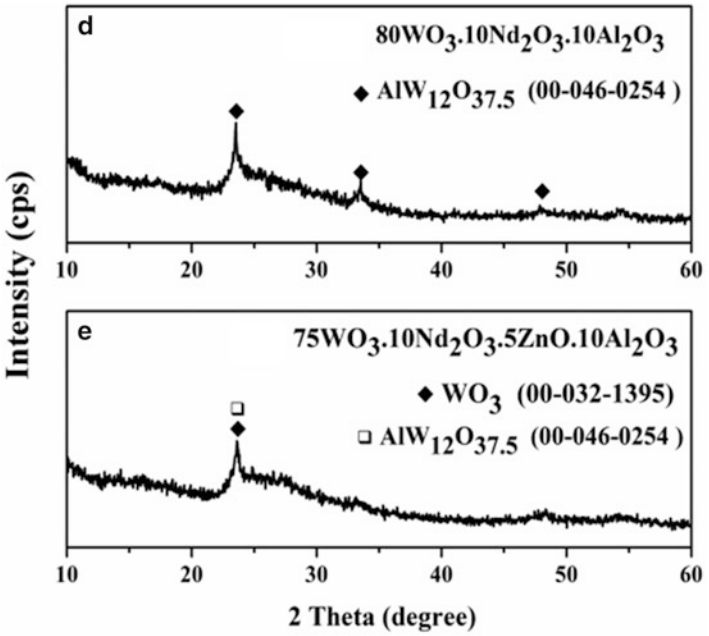

Fig. 46.3 XRD patterns of glassy-crystalline samples after heat treatment D and E

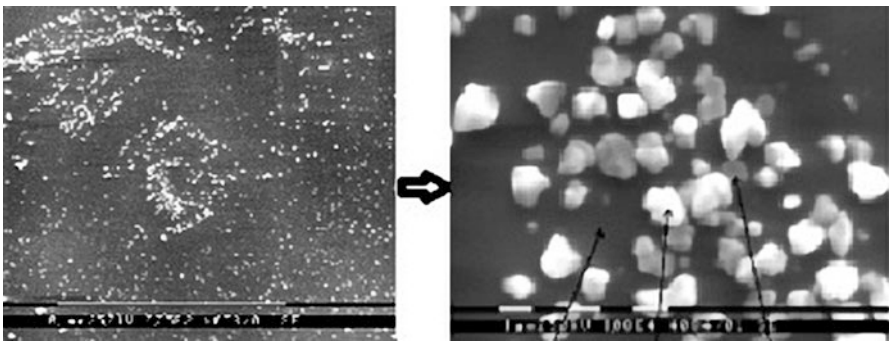

Fig. 46.4 SEM images of sample D with low and high magnifications

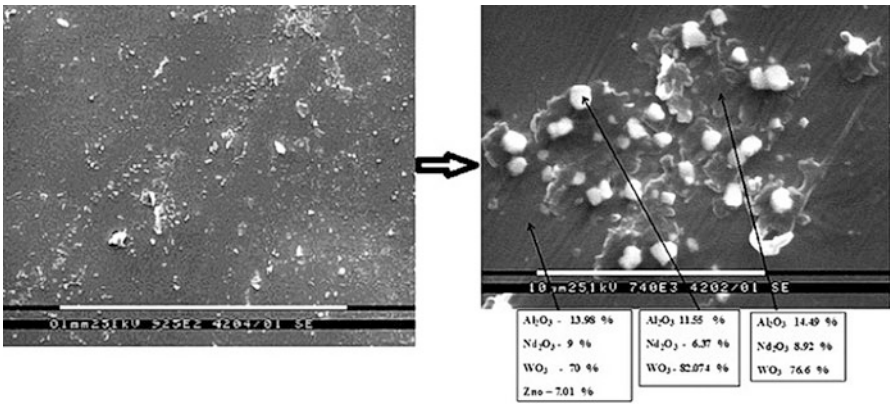

Fig. 46.5 SEM images of sample E with low and high magnifications

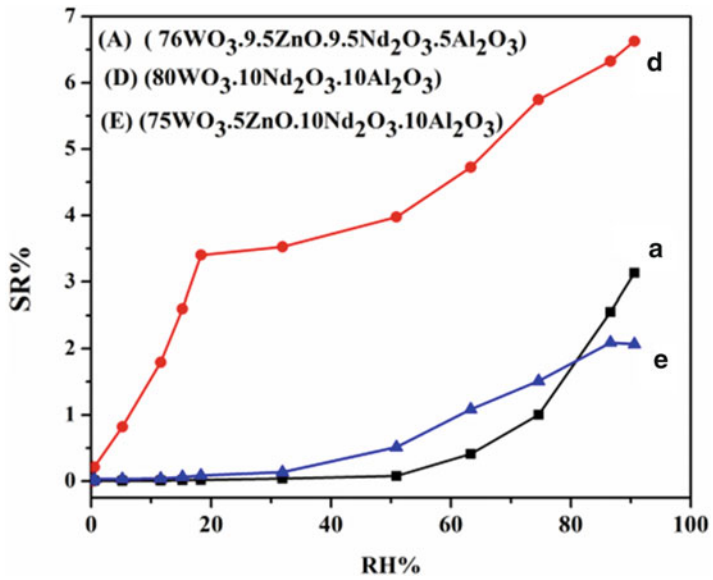

Fig. 46.6 Sensor response for samples A, D and E as a function of relative humidity

46.4 Conclusions

A new method was used for the preparation of active phases such as WO_3, $W_{18}O_{49}$ and $AlW_{12}O_{37.5}$ embedded as small crystal aggregates in an amorphous matrix. The preliminary results showed that the materials may be used as ammonia and relative humidity sensors. The advantages of this method are low costs and faster preparation compared to other methods.

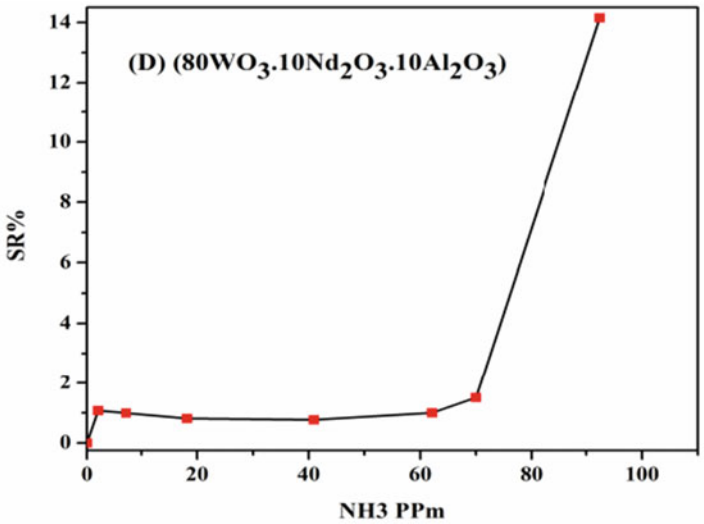

Fig. 46.7 Sensor response of sample D to ammonia

The problem which has to be solved in the future is the selection of an appropriate heat treatment scheme to control the amount of active phases and the distribution of particles in the volume of the materials.

References

1. Kanan SM, El-Kadri OM, Abu-Yousef IA, Kanan MC (2009) J Sens 9:8158
2. Siriwong C, Wetchakun K, Wisitsoraat A, Phanichphant S (2009) IEEE Sens Conf. p 118
3. Hieu NV, Quang VV, Hoa ND, Kim D (2011) J Curr Appl Phys 11:657
4. Reghu A, Deniz D, Stennett R, Bernhardt G, Frankel D, Lad R, Vetelino J (2012) Proceedings of the 14th international meeting on chemical sensors – IMCS, p 457
5. RAO MC (2013) J Non-Oxide Glasses 5:1
6. Wetchakun K, Samerjai T, Tamaekong N, Liewhiran C, Siriwong C, Kruefu V, Wisitsoraat A, Tuantranont A, Phanichphant S (2011) J Sens Actuator B Chem 160:580
7. Leng J, XU X, Lv N, Fan H, Zhang T (2011) J Colloid Interface Sci 356:54
8. Ponzoni A, Comini E, Ferroni M, Sberveglieri G (2005) J Thin Solid Films 490:81
9. Sriyudthsak M, Supothina S (2006) J Sens Actuator B Chem 113:265
10. Bender F, Kim C, Mlsna T, Vetelino JF (2001) J Sens Actuator B Chem 77:281
11. Ryu HW, Park KH (2003) J Korean Phys Soc 42:727
12. Kim SJ, Cho PS, Lee JH, Kang CY, Kim JS, Yoon SJ (2008) J Ceram Int 34:827
13. Akamatsu T, Itoh T, Izu N, Shin W (2013) J Sens 13:12467
14. Liu B, Cai D, Liu Y, Wang D, Wang L, Wang Y (2014) J Sens Actuator B Chem 193:28
15. Zhao YM, Zhu YQ (2009) J Sens Actuator B Chem 137:27
16. Özgür Ü, Alivov YI, Liu C, Teke A, Reshchikov MA, Doğan S, Avrutin V, Cho S-J, Morkoç H (2005) Appl Phys Lett 98:041301

17. Tulliani JM, Cavalieri A, Musso S, Sardella E, Geobaldo F (2010) J Sens Actuator B Chem 152:144
18. Nunes P, Fortunato E, Lopes A, Martins R (2001) J Int Inorg Mater 3:1129
19. Cheng XI, Zhao H, Huo LK, Gao S, Zhao JG (2004) J Sens Actuator B Chem 102:248
20. Franzosi G, Tulliani JM (1999) J Ceram 4:273
21. Savage J (1976) In: Holmes PJ, Loasby RG (eds) Handbook of thick film technology. Electrochemical Publications, Scotland, pp 105–106
22. Tulliani JM, Bonvile P (2005) J Ceram Int 31:507

Chapter 47
Nanoecological Threats of Nanofood and Nanoparticles

Ganna Kharlamova, Oleksii Kharlamov, and Marina Bondarenko

Abstract After the recent discovery and synthesis of nanodimensional nanochemical objects (nanostructures, nanophases and nanoparticles) and their extensive application, in particular in food, water, different sensors, suncreams, cosmetics and nanotextiles, new nanotoxicological threats have essentially appeared. Nanodimensional objects are capable to penetrate into internal organs of living organism by all possible routes (gastrointestinal, respiratory, dermal, auditory and ocular) and to destroy or change their functional features. The evolution has not created yet any natural protection mechanisms against nanoobjects. Nanoparticles are capable to easily overcome biological barriers of human organisms, to change their physiological and biochemical properties, and to cause various pathologies.

Keywords Nanomaterials • Nanoparticles • Nanoobjects • Nanothreats • Nanofood

47.1 Introduction

At the end of the last century two important developments in biochemistry and nanochemistry were invented which had essentially changed the structure and quality of modern food industry. In the years 1981–1982 the first living transgenic essences (mouse and Drosophila fly) and genetically modified (GM) agricultural crops were created, and somewhat later a new state of matter, namely nanodimensional objects (NDO) and materials was developed, in particular as components (additives) of diversified food stuff. The main feature of agricultural GM cultures is that they have an increased productivity and stability to droughts,

G. Kharlamova (✉)
National Taras Shevchenko University of Kyiv, 64 Volodymyrsska Str., 03001 Kyiv, Ukraine
e-mail: akharlamova@ukr.net

O. Kharlamov • M. Bondarenko
Frantsevich Institute for Problems of Materials Science of NASU, Krzhyzhanovsky St. 3, 03142 Kyiv, Ukraine

P. Petkov et al. (eds.), *Nanoscience Advances in CBRN Agents Detection, Information and Energy Security*, NATO Science for Peace and Security Series A: Chemistry and Biology, DOI 10.1007/978-94-017-9697-2_47

herbicides, insects and viruses. It is important to note that NDOs are widely used for various external decorations and additives in food stuff and food packaging. The creation of the first genetically modified organisms (GMO) (microorganisms, plants and animals), the development and subsequent large scale manufacture of nanodimensional objects have, as a matter of fact, opened new era of preparation of artificial food modified by GMO and NDO, as already millions inhabitants of the planet perish from a lack of organic food perish.

The main feature of this new state of matter (nanomatter) as closed spheroidal molecules and nanostructures, nanodimensional anisotropic 1D and 2D structures and of isotropic 3D nanoparticles is that the properties of the new substances depend not only on structure and composition (as it is characteristic for already known substances), but also on the size and morphology of nanoparticles and nanostructures. First of all, it is necessary to understand that chemical and toxicological behavior of these new objects essentially differs from that of known substances. However such nanosized particles and structures, the toxic properties of which have only begun to be studied, are distributed everywhere: in air, water, various creams and clothes. These nanoobjects can easily penetrate into human organism through skin, nose and mouth, in particular with food products.

One of the objectives of this publication is to present experimental results about the harmful influence of nanochemical nanoobjects and to discuss in more detail possible nanoecological threats related with large scale manufacture and use in particular in nanofood and various creams.

47.2 Routes of Penetration of Nanodimensional Objects into Human Organisms

After their recent (1985) the development of NDOs already find wide applications in various manufactures: more than 1,000 products in the market are made on the basis of nanomaterials and nanotechnologies [1]. Therefore it is extremely important to know the influence of nanoobjects as carriers of new unknown properties on human organisms. An extremely aggressive and unpredictable behavior of NDO was marked earlier [2, 3] and may be stipulated by:

- The dependence of the properties of nanoparticle on size and morphology;
- A small size comparable with the size of some molecules;
- A high surface area and the presence of huge amounts of free valences on them resulting in an extremely high reactivity comparable to that of radicals;
- The difficulty of detection and removal of nanoparticles from the environment with the help of traditional filtration method;
- The possibility to penetrate easily into human organisms, interact very quickly with their different components and catalyze the formation of unusual toxic substances.

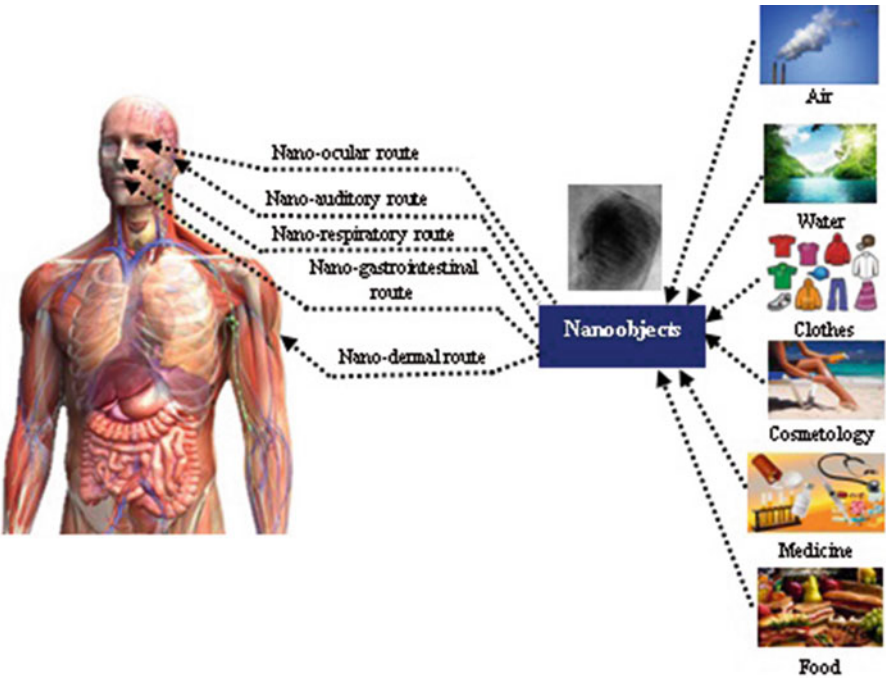

Fig. 47.1 Five routes of penetration of nanoobjects into the human body

The penetration of nanoparticles into the biosphere may cause many problems which are similar to the influence of genetically modified products. The evolution has not created yet natural mechanisms of protection from these carriers of new properties, which are produced and applied already in large amounts for different sensors, suncreams, cosmetics, nanotextiles, and foods. Nanoparticles are capable to easily overcome biological barriers of the human organism, to change their physiological and biochemical mechanisms and to cause various pathologies.

The penetration of nanoobjects into human organism (Fig. 47.1) can take place by all possible routes [2–4], i.e. gastrointestinal, respiratory, dermal, auditory and ocular routes.

Nanoparticles get in the gastrointestinal tract (GT) by water, food stuff (Fig. 47.2), cosmetics, medicines and means of the delivery of medicaments. So, cytotoxic copper nanoparticles (copper NPs), after penetration in lymph, stomach, liver, spleen or the kidneys of mice, cause defects of these bodies [5]. Besides copper NPs, getting through gastrointestinal tract, cause tremors and hunchbacks of mice.

Zhang et al. [6] investigated the toxic influence of gold nanoparticles (nanogold or AuNPs) covered by polyethylene glycol on organs of mice depending on the size of the AuNPs: 5, 10, 30 and 60 nm. They established that under natural conditions (*in vivo*) within 28 days and a concentration of 4,000 μg/kg AuNPs with sizes of 5 and 10 nm collect in the liver while particles of 30 nm size collect in the spleen. By means of transmission electron microscopy it was shown that nanogold with sizes of 5, 10, 30 and 60 nm are located in the blood and the bone marrow cells while nanogold with sizes of 5 and 60 nm mainly aggregate in blood cells. 10 nm

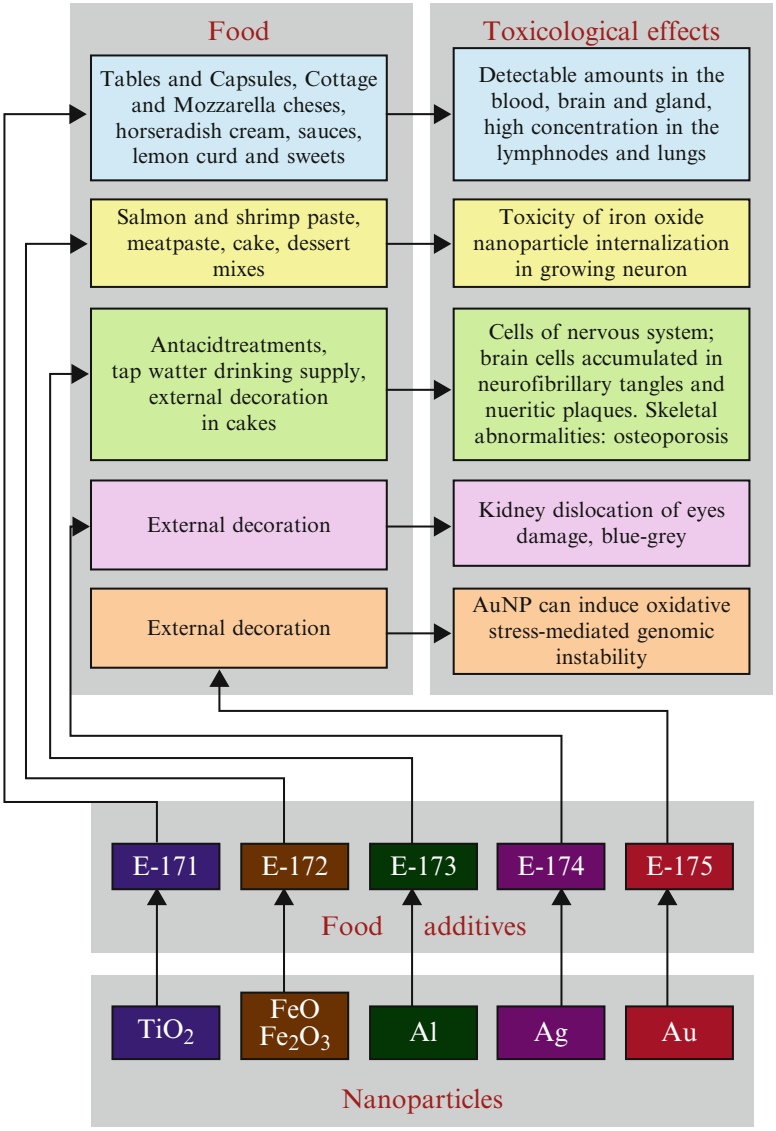

Fig. 47.2 The use of nanoparticles as food additive

AuNPs cause an increase of white blood cells while AuNPs with sizes of 5 nm and 30 nm cause the reduction of leukocytes and erythrocytes.

Silver nanoparticles (nanosilver) have a strong antibacterial activity and are widely used today in the textile industry, food packagings, household devices and bioapplications. However it is necessary always to remember that nanosilver is extremely toxic to the liver of rats [2, 3].

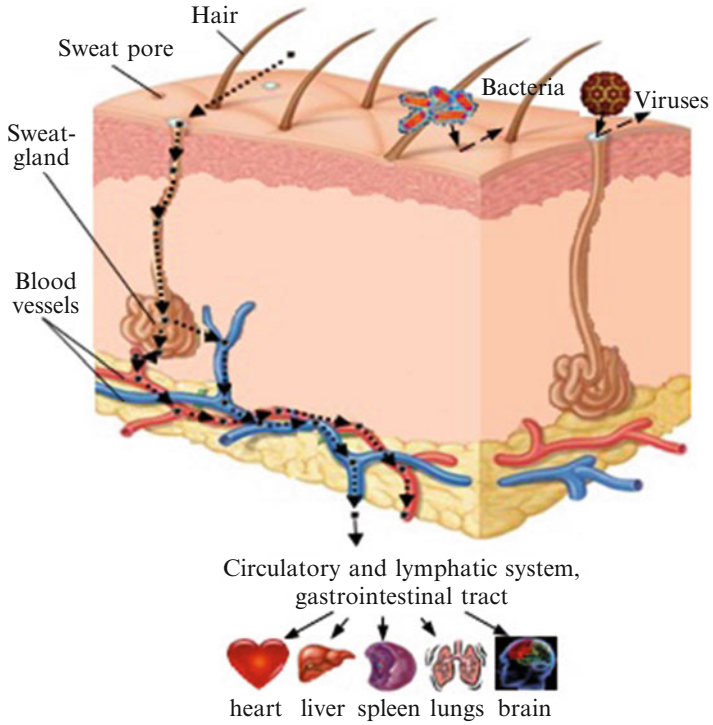

Fig. 47.3 Peculiarities of the penetration of nanosized objects through a skin and their impact on different organs

Nanoparticles penetrating in organism through respiratory ways not only destroy the breath organs but also easily penetrate through alveolar cells into blood circulation organs and get with the bloodstream in other organs [7]. Moreover, discrete NPs from the nasal area (of experimental animals) penetrate into the brain through the olfactory nerve [8]. According to [9], inhaled MnO_2 NPs (30 nm) in the olfactory nerve of experimental rats are penetrated during 7 days of texposure.

In contrast to normal-scale titanium oxide (TiO_2) particles, TiO_2 nanoparticles (TiO_2NPs), frequently used in cosmetic means, easily penetrate through the pores of the skin (Fig. 47.3) into various organs of animals [10]. It was established [10] that in all groups of mice exposed to the influence of TiO_2 NPs, serious damages of the skin are observed. Considerably higher concentrations of ZnO nanoparticles were found in a skin treated by suncream [10] in a study with a diffusion cell with human epidermal membranes.

Iron and iron oxide nanoparticles penetrated through a skin caused swelling of the stratum corneum [10]. Fullerene nanoparticles superficially functionalized with peptide penetrate the epidermis and dermis of a pig skin already after 8-h exposition. For longer exposition (24 h) the penetration of such functionalized fullerenes through the skin has considerably increased. Nanoparticles containing cadmium and selenium with a nucleus of cadmium sulfite penetrate through the pores of pig

skin and in neonatal human epidermal kerationcytes and cause inflammatory reaction [11]. It is considered [10] that NP can cause toxic reactions in a viable skin layer. In industrial enterprises up to 82 % of the workers show damages of the epidermal barrier [12] which essentially rise the probability of penetration of nanoparticles in human organisms.

There are researches showing that nanoparticles are capable to penetrate into living organism through the acoustical pass (Fig. 47.1). So, according to investigations [13], iron oxide NP with a polymeric covering of polylactic/glycolic acid (PLGA) penetrates through the eardrum of chinchillas into the internal ear and in the tissue of the snails located there. By electron microscopy it was shown [14] that superparamagnetic nanoparticles (SPION) easily penetrate through a membrane in the eardrum of anesthetized guinea pigs.

Investigations of the ocular route (Fig. 47.1) of penetration of NP in human organisms are innumerous today [15]. Aniruddha et al. [16] studied an opportunity of the use of nanoparticles as a mean of delivery of a medicine into the eye. The penetration of luminescent nanoparticles (Fluospheres TM, 20 nm) containing sodium fluorescein, through the subconjunctival administrations of male rats (Sprague-Dawley) was completed in 15 min. In [17] is shown that DNA NPs penetrate into the mouse retina.

Jani et al. [18] reported that nanoparticles of encapsulating albumin after introduction in the intact cornea of mice were found in the corneal keratocyte cytoplasm.

The toxicity of molecules and nanostructures of carbon [19–21] and heterocarbon [22–25] is basically caused by their ability to induce active forms of oxygen (oxygen ions, free radicals and different kinds of peroxides), which cause apoptosis and necrosis of the cells of lungs [10] and kidneys [11] (Fig. 47.4).

47.3 Conclusions

The threats connected to manufacture and application NDO in food, cosmetics, packages, clothes, goods, medicine can be compared by the influence with the weapon of a mass defeat of the slowed down action. NDO containing GMO in food are especially dangerous: they destroy the organism, naturally, only that majority of the people, which uses them, whereas the manufacturers of these products should not only observe but to study their harmful possible impact.

It is necessary especially to note the role of the blood system as a transit route of penetration of nanoparticles in any internal human organs. Nanoparticles in organisms reach by the bloodstream any internal organ of the man and cause his health of an irreparable damage.

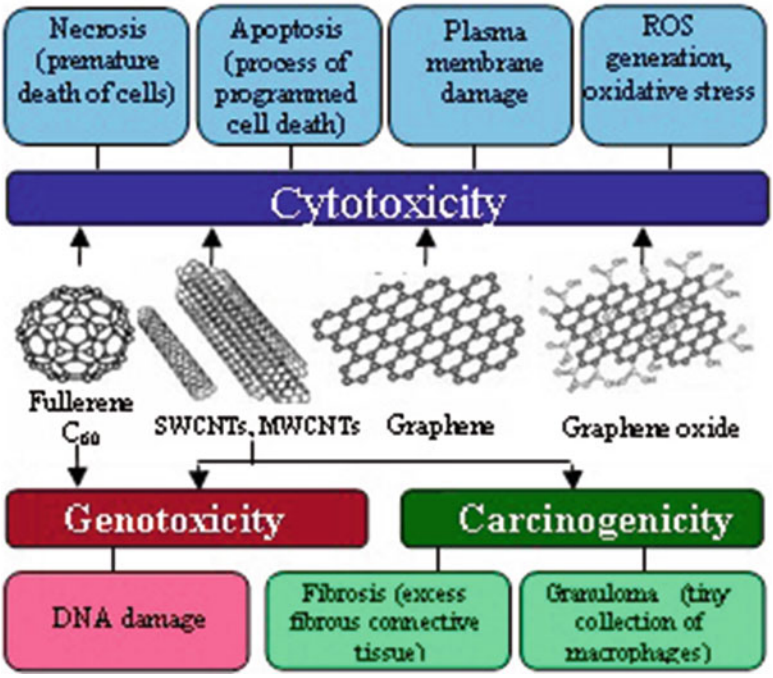

Fig. 47.4 Some unusual toxic peculiarities of carbon nanostructures

References

1. Lin M (2013) Toxic nanoparticles might be entering human food supply. University of Missouri-Columbia. Science Daily, 22 August 2013. www.sciencedaily.com/releases/2013/08/130822194530.htm
2. Kharlamov A, Skripnichenko A, Gubareny N et al (2011) In: Mikhalovsky S, Khajibaev A (eds) Biodefence, NATO science for peace and security series A: Chemistry and Biology, Part 1. Springer, Dordrecht, p 23
3. Kharlamov A, Bondarenko M, Skripnichenko A, Kharlamova G (2013) In: Voica DR, Duyan A (eds) Trends and developments in contemporary terrorism, vol 103. IOS Press, Amsterdam, p 33
4. Yah CS, Simate GS, Iyuke SE (2012) Pak J Pharm Sci 25:477
5. Chen Z, Huan M, Gengmei X et al (2006) Toxicol Lett 163:109
6. Zhang XD, Wu D, Shen X et al (2011) Int J Nanomedicine 6:2071
7. Das M, Patil S, Bhargava N et al (2007) Biomaterials 28:1918
8. Flesken AN, Toshkov INJ, Katherine MT et al (2007) Toxicol Pathol 35:804
9. Oberdorster G, Oberdorster E, Oberdorster J (2005) Environ Health Perspect 113:823
10. Korinth G, Drexler H (2013) In: Deutsche Forschungsgemeinschaft (DFG) (ed) Nanomaterials, Chapt. 1.4. WILEY-VCH Verlag, Weinheim, p 37
11. Zhang WL, Yu WW, Vicki LC, Monteiro-Riviere NA (2008) Toxicol Appl Pharmacol 228:200
12. Korinth G, Weiss T, Penkert S et al (2007) Occup Environ Med 64:366
13. Xianxi G, Ronald J, Jianzhong L, Balough B, Hoffer ME (2007) In: Chinchilla Cochlea (ed) The 13th annual midwinter research meeting of the Association for Research in Otolaryngology, Denver, Colorado, pp 10–15

14. Barnes AL, Wassel RA, Mondale F et al (2007) Biomagn Res Technol 5:1. doi:10.1186/1477-044X-5-1
15. Herrero-Vanrell R, Refojo MF (2001) Adv Drug Deliv Rev 52:5
16. Aniruddha CA, Surya PA, Uday BK (2008) Drug Deliv Technol 3:2
17. Farjo F, Skaggs J, Quiambao AB et al (2006) PLoS One 1:e38
18. Jani PU, Halbert GW, Langridge J, Florence AT (1990) J Pharm Pharmacol 42:821
19. Kharlamov AI, Bondarenko ME, Kirillova NV (2012) Russ J Appl Chem 85:233
20. Kharlamov AI, Kharlamova GA, Bondarenko ME (2013) Russ J Appl Chem 86:1174
21. Kharlamov O, Kharlamova G, Bondarenko M, Fomenko V (2013) In: Vaseashta A, Khudaverdyan S (eds) Advanced sensors for safety and security, NATO science for peace and security series B: Physics and Biophysics. Springer Science + Business Media, Dordrecht, p 329
22. Kharlamov AI, Kharlamova GA, Bondarenko ME (2013) Russ J Appl Chem 86:167
23. Kharlamova G, Kharlamov O, Bondarenko M (2013) In: Vaseashta A, Khudaverdyan S (eds) Advanced sensors for safety and security, NATO science for peace and security series B: Physics and Biophysics. Springer Science + Business Media, Dordrecht, p 339
24. Kharlamov AI, Kharlamova GA, Bondarenko ME (2013) Russ J Appl Chem 86:1493
25. Kharlamov A, Bondarenko M, Kharlamova G et al (2013) Univ J Mater Sci 1:78

Chapter 48
Artificial Neural Network Modeling of Cd(II) Ions Adsorption on Nano-porous Inorganic Sorbents

Stefan Kuvendziev, Mirko Marinkovski, Kiril Lisichkov, and Perica Paunović

Abstract A three-layer artificial neural network (ANN) model was developed to predict the efficiency of Cd(II) ion removal from aqueous solutions by nano-porous zeolite, based on 105 experimental sets obtained in an experimental kinetic study. The effects of operational parameters such as the initial concentration of Cd(II) ions in the aqueous solution, the mass of the nano-porous adsorbent and the contact time were studied to optimize the conditions for maximum removal of Cd(II) ions. On the basis of the results of this kinetic test, optimal operating conditions were determined to a contact time of 1,700 min and an initial concentration of Cd(II) ions in aqueous solution of 200 mg/dm^3 for a constant mass of the adsorbent of 3 g. The second set of experiments resulted in an optimal contact time of 1,600 min and an adsorbent mass of 3 g for an initial concentration of Cd(II) ion of 50 mg/dm^3. After supervisory backpropagation (BP) training, the ANN model was able to predict the adsorption efficiency. The ANN model consisted of a hidden layer with 4 neurons and a tangent sigmoid transfer function (*tansig*) and an output layer with a linear transfer function (*purelin*). The Levenberg–Marquardt algorithm (LMA) was found to provide a minimum mean squared error (MSE) of 0.0695 compared to other BP algorithms. The linear regression between the network outputs and the corresponding targets was proven to be satisfactory with a correlation coefficient of 0.936 for the three model variables used in this study.

Keywords Cd(II) ions • Adsorption • Granular activated carbon • Artificial neural network

S. Kuvendziev (✉) • M. Marinkovski • K. Lisichkov • P. Paunović
Faculty of Technology and Metallurgy, University "Ss Cyril and Methodius", Skopje, Republic of Macedonia
e-mail: stefan@tmf.ukim.edu.mk

P. Petkov et al. (eds.), *Nanoscience Advances in CBRN Agents Detection, Information and Energy Security*, NATO Science for Peace and Security Series A: Chemistry and Biology, DOI 10.1007/978-94-017-9697-2_48

48.1 Introduction

Fresh water supply is a necessity for the modern world and nowadays becomes a concerning issue for many countries [1]. Excessive levels of heavy metals may be harmful to human health and therefore the US Environmental Protection Agency established a maximal permitted concentration of cadmium of 0.005 mg/L [2, 3].

Several processing techniques are available to reduce the concentrations of heavy metals in wastewater, including precipitation, ion exchange, membrane separation, adsorption, electrochemical deposition, ozonation etc. [4–8].

Several low cost adsorbents, including nano-porous natural zeolites, have been investigated to study the adsorption performance for the removal of heavy metals such as Cadmium from aqueous solutions [9–13].

In fixed bed systems, the adsorbate is continuously in contact with a given quantity of fresh adsorbent, thus providing the required concentration gradients between adsorbent and adsorbate for adsorption. The performance of packed beds is described through the concept of the breakthrough point [14, 15].

The fixed bed is the most frequently used operation for ion exchange, and adsorption is the predominant way of conducting such sorption separations [15].

Although direct addition of adsorbent to wastewater to remove heavy metals is quiet efficient, separation of the adsorbent from wastewater for repeated use is very time- and resource-consuming [12].

Currently, artificial neural networks (ANNs) have been widely used to solve environmental problems including cleaning of water resources modeling and management problems. Therefore, this study implemented ANNs to determine the most significant water quality variables that contribute to the water pollution [16].

48.2 Materials and Methods

48.2.1 Preparation of the Adsorbate

The adsorbate used within the experimental analysis is hydrated cadmium sulphate salt ($CdSO_4 \cdot 7H_2O$) with different initial concentrations of cadmium ions in the aqueous solution.

48.2.2 Adsorbents Characteristics

Natural zeolite (NZ) was used as adsorbent in the dynamic experiments in the frames of this work. Natural zeolite (90 % clinoptilolite) was supplied by "Nemetali", Vranjska Banja, Serbia. Prior to the performances of the experiments the NZ was dried at 330 °C for 48 h. The chemical composition of natural zeolite is given in Table 48.1.

Table 48.1 Chemical composition of natural zeolite (NZ)

Ingredients	SiO_2	Al_2O_3	Fe_2O_3	TiO_2	CaO	MgO	Na_2O	K_2O	Ignition loss
NZ (mass %)	64.88	12.99	2.00	0.37	3.26	1.07	0.95	0.89	13.59

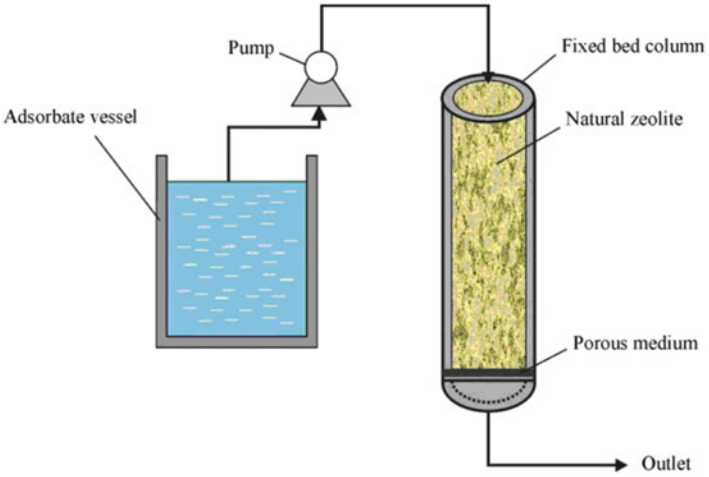

Fig. 48.1 Fixed bed column adsorption system

48.2.3 Working Conditions

For the purpose of dynamics experiments, the initial concentrations of cadmium in aqueous solution were set to 50, 100, 150, 200 and 250 mg/dm^3. The flow rate of adsorbate in the fixed bed column was set to 10, 15 and 20 cm^3/min, and the bed height of the adsorbent to 8, 16 and 23 cm of nano-porous natural zeolite (NZ). All dynamic experiments were conducted under continuous conditions. The prepared solution was passed through the fixed bed column (Fig. 48.1).

The concentration of cadmium ions at the output of the fixed bed column was measured using an AERL 3520 Atomic Absorption Spectrophotometer.

48.2.4 Definition of the Artificial Neural Network (ANN) Model

In this study, the MATLAB software Neural Network Toolbox V6.0 was used to predict the concentration of cadmium in the effluent. To develop the ANN model 4×196 experimental sets were used. The input parameters were the contact time, the initial concentration of Cd(II) ions, the adsorbate flow rate and the adsorbent

bed height. The effluent concentration of Cd(II) ions was studied as an output (target) parameter (Fig. 48.1). 136, 30 and 30 samples were used for the training, validation and test subsets, respectively.

48.3 Results and Discussion

48.3.1 Selection of the Feed Forward Backpropagation (BP) Algorithm

Considering the type of conducted experiments, a feed forward back-propagation (BP) model of the ANN network was determined as the most appropriate model for neural network fitting. The Levenberg-Marquart algorithm produced the highest correlation coefficient $R^2 = 0.99888$ (mean squared error MSE = 0.0033). This algorithm was used in the further analysis (Table 48.2).

48.3.2 Optimization of the ANN Structure

The optimal architecture of the ANN model and its parameter variations were determined based on the minimum value of the MSE of the training and prediction sets. Table 48.3 and subsequently Fig. 48.2 illustrate the dependence of the MSE from the number of neurons in the hidden layer.

Figure 48.2 shows that the MSE of the network possesses three local minimums. Generally, the overall minimum was found for 10 hidden neurons (MSE 0.0033).

Finally, the optimized ANN, with a flowchart of the BP algorithm presented on Fig. 48.3, consisted of a three-layer ANN.

Table 48.2 Comparison of FF BP algorithms with 10 neurons in the hidden layer

BP algorithms	Function	MSE	R^2	BLE
Resilient backpropagation	trainrp	0.252	0.94566	y = 0.92x + 11
Polak-Ribiere conjugate gradient BP	traincgp	0.187	0.96685	y = 0.93x + 5.5
Powell-Beale conjugate gradient BP	traincgb	0.0245	0.9967	y = 0.99x + 1.3
Levenberg-Marquardt BP	trainlm	0.0033	0.99888	y = 1x−0.038
Scaled conjugate gradient BP	trainscg	0.498	0.88187	y = 0.82x + 11
Bayesian regularization BP	trainbr	0.617	0.98966	y = 0.98x + 0.16
Gradient descent with adaptive learning rate BP	traingda	8.076	0.42097	y = 66x + 26

Table 48.3 Dependence of the mean squared error (MSE) on the number of neurons

No. of neurons	7	8	9	10	11	12	13
MSE	10.014	0.022	10.623	0.0033	11.803	3.752	20.994

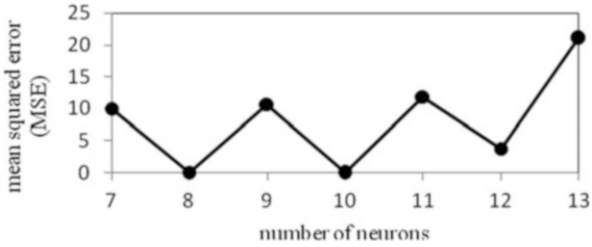

Fig. 48.2 Dependence of the MSE on the number of neurons in the hidden layer for the LMA (Levenberg-Marquart algorithm)

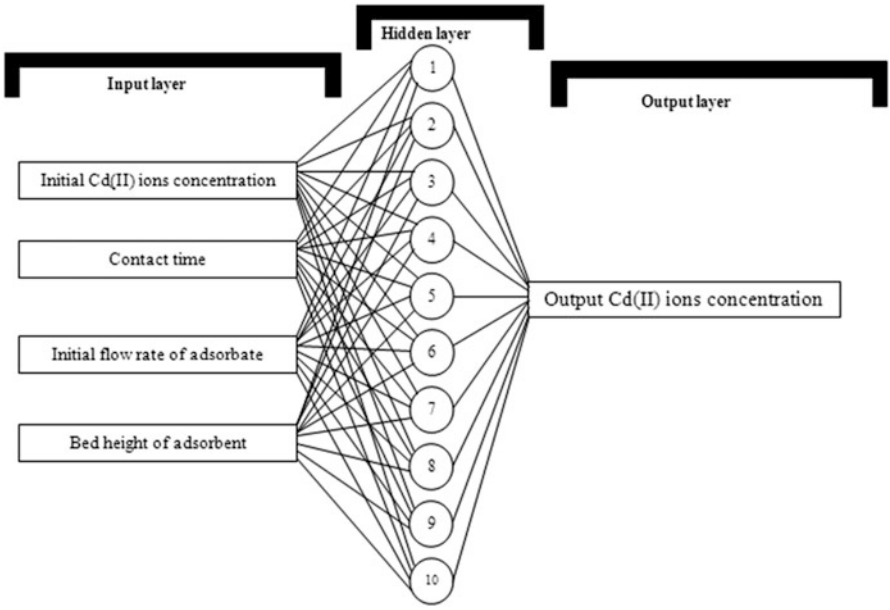

Fig. 48.3 Optimal ANN structure combined with a flowchart of the BP algorithm for the prediction of the adsorption dynamics

48.3.3 Sensitivity Analysis

Figure 48.4a presents the mean squared error of the training, validation and test subsets of data for the chosen ANN model. The best obtained value relates to the optimal number of hidden neurons (MSE = 0.0033).

Figure 48.4b presents the correlation between the output values predicted by the ANN model and the experimentally obtained output concentrations of Cd (II) ions.

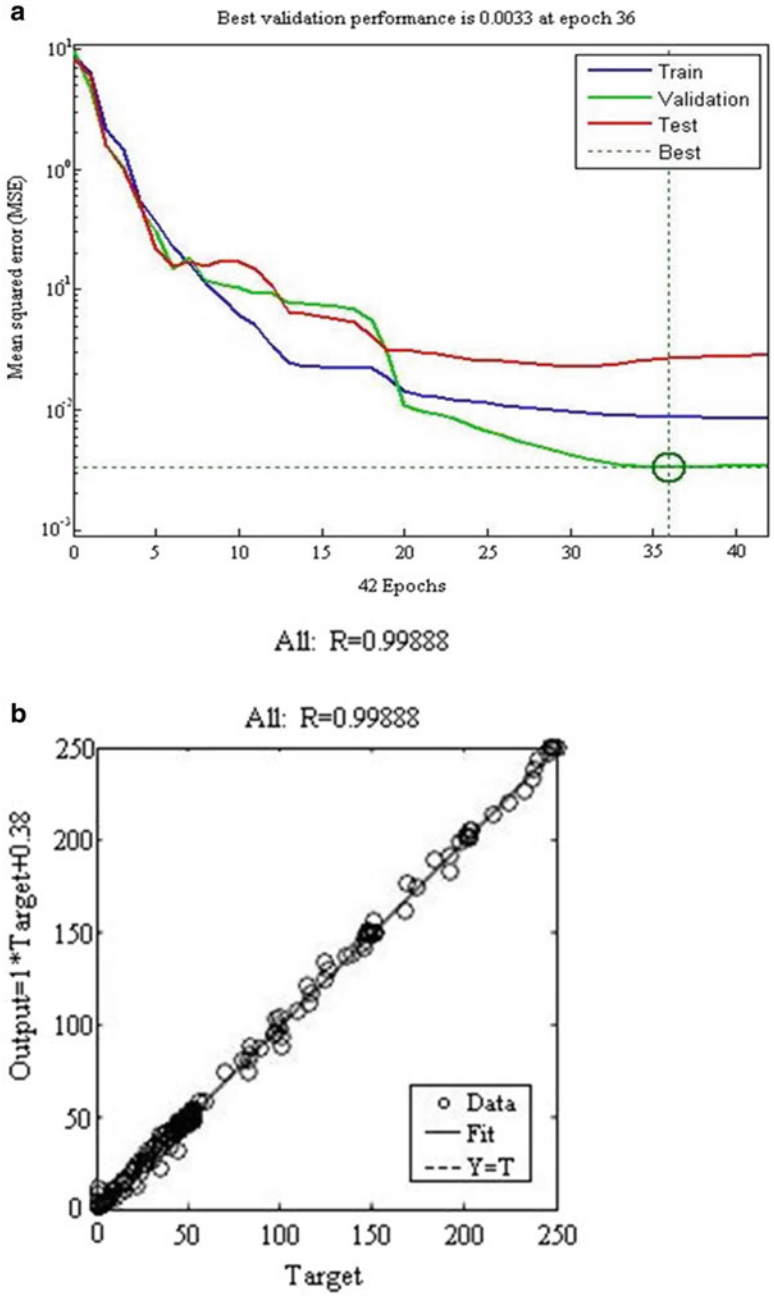

Fig. 48.4 (**a**) Training, validation and test mean squared errors (MSE) for the Levenber-Marquart algorithm (LMA); (**b**) Regression of training, validation, test and total correlation of target and output values

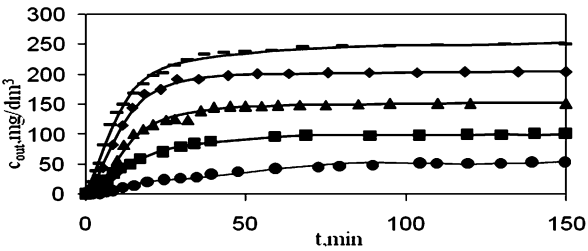

Fig. 48.5 Fitting between experimental data of the initial Cd(II) concentration and ANN data for a flow rate F = 10 cm^3/min and a zeolite bed height of L = 23 cm

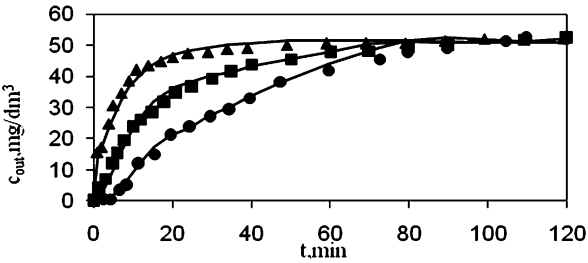

Fig. 48.6 Fitting between experimental data of the adsorbate flow rate and ANN data for a bed height of L = 23 cm and an initial Cd(II) ion concentration C_0 = 50 mg/dm^3

48.3.4 Effect of the Initial Concentration of Pb(II) Ions on the Output Pb(II) Ion Concentration

From Fig. 48.5 it can be concluded that the increase of the initial concentration of Cd(II) ions in the aqueous solution has a significant effect on the removal of Cd(II) ions. By increasing the initial Cd(II) ion concentration the breakthrough point is achieved faster.

48.3.5 Effect of the Adsorate Flow Rate on the Output Pb(II) Ion Concentration

From Fig. 48.6 it can be concluded that the increase of the adsorbate flow rate in a fixed bed column has a less significant effect on the removal of Cd(II) ions. By increasing the rate the breakthrough point is achieved in a reduced contact time.

48.3.6 Effect of the Bed Height of the Zeolite Adsorbent on the Output Pb(II) Ion Concentration

From Fig. 48.7 it can be concluded that the increase of the bed height of natural zeolite in a fixed bed column has a significant effect on the removal of Cd(II) ions. By increasing the bed height of the adsorbent the breakthrough point is achieved for a prolonged contact time, which means longer utilization of the adsorbent.

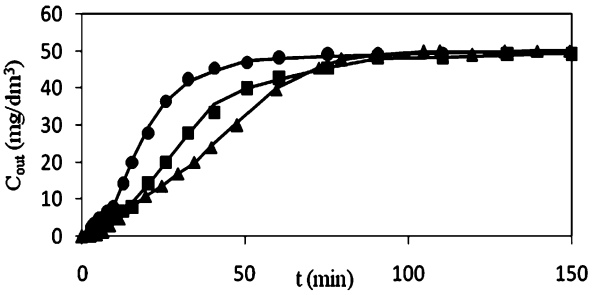

Fig. 48.7 Fitting between the experimental data of the bed height of the adsorbent and ANN data for a flow rate F = 10 cm^3/min and an initial Cd(II) ion concentration $C_0 = 50$ mg/dm^3

48.4 Conclusions

The effect of various operating parameters on the adsorption of Cd(II) ions onto a nano-porous adsorbent (natural zeolite NZ) was investigated and optimized. The increase of the adsorbent bed height of the analyzed fixed bed system from 8 to 23 cm at a constant adsorbate flow rate (10 cm^3/min) resulted in an increase of the total purification time from 45 to 50 min. At an initial Cd(II) ion concentration of 50 mg/dm^3 the breakthrough point is detected after 45–50 min. For an initial Cd(II) ion concentration of 250 mg/dm^3 the breakthrough point of the fixed bed column is achieved after 90 min of operation.

A three layer ANN was proposed to predict the efficiency of Cd(II) ions removal. The benchmark comparisons conducted with 10 hidden neurons and the LM learning algorithm provided the lowest MSE values compared to other BP algorithms. The proposed ANN model showed a precise and effective prediction of the experimental data with a satisfactory correlation coefficient of 0.99888.

References

1. Tiwari DK, Behari J, Sen P (2008) World Appl Sci J 3:417
2. Etorki AM, El-Rais M, Mahabbis MT, Moussa NM (2014) Am J Anal Chem 5:225
3. Wang C, Ren X, Li W, Hou Z, Ke C, Geng Q (2013) Pol J Environ Stud 22:6
4. Thakur LS, Parmar M (2013) IJCPS 2:6
5. Xiong C, Yao C (2013) Iran J Chem Chem Eng 32:2
6. Kouakou U, Ello AS, Yapo JA, Trokourey A (2013) J Environ Chem Ecotoxicol 5:6
7. Bernard E, Jimoh A (2013) Int J Eng Appl Sci 4:2
8. Mandal NK (2014) Int J Sci Res (IJSR) 3:1
9. Suganthi N (2012) Coromandal J Sci 1:1
10. Budak TB (2013) Asian J Chem 25:8
11. Igwe JC (2007) Electron J Biotechnol 10:4
12. Johnson TA, Jain N, Joshi HC, Prasad S (2008) J Sci Ind Res 67:647
13. Foroughi-dahr M, Abolghasemi H, Esmaili M, Shojamoradi A, Fatoorehchi H (2013) J Pet Sci Technol 3:2
14. Vassilis IJ (2010) J Eng Stud Res 16:3
15. Lee IH, Kuan YC, Chern JM (2008) J Hazard Mater 152:241
16. Chetouani Y (2007) Int J Comput Sci Appl 4:3

Part XII
Applications: Energy and Quantum Information Technology

Chapter 49
Nanostructured Diamond Electrodes for Energy Conversion Applications

S. Pehlivanova, Ch. Petkov, C. Popov, P. Petkov, V. Boev, and T. Petkova

Abstract The subject of our work is the investigation of boron doped nanocrystalline diamond (NCD) layers functionalized with photosensitive molecules of manganese phthalocyanine. The functionalized NCD sample was used as a working electrode in a three electrode cell and electrochemically studied. The two methods applied were stationary volt-ampere (VA) measurements and cyclic voltammetry (CV) in dark and under illumination. The VA and CV measurements showed that the electrode has a wide potential range and a high photosensitivity. The results obtained are promising for future application of functionalized diamond electrodes in light conversion systems.

Keywords Diamond electrode • Photoelectrochemistry

49.1 Introduction

Diamond thin films have been proven to be excellent materials for electrochemical applications since the performance of diamond electrodes can be much superior to that of alternative materials, such as glassy carbon and graphite. Boron doped

S. Pehlivanova (✉)
Department of Physics, University of Chemical Technology and Metallurgy, 8 Kl. Ohridski blvd., 1756 Sofia, Bulgaria

Institute of Electrochemistry and Energy Systems, BAS, Acad. G. Bonchev bl.10, 1113 Sofia, Bulgaria
e-mail: silviya.pehlivanova@gmail.com

Ch. Petkov • C. Popov
Institute of Nanostructure Technologies and Analytics, University of Kassel, Heinrich-Plett-Str. 40, 34132 Kassel, Germany

P. Petkov
Department of Physics, University of Chemical Technology and Metallurgy, 8 Kl. Ohridski blvd., 1756 Sofia, Bulgaria

V. Boev • T. Petkova
Institute of Electrochemistry and Energy Systems, BAS, Acad. G. Bonchev bl.10, 1113 Sofia, Bulgaria

P. Petkov et al. (eds.), *Nanoscience Advances in CBRN Agents Detection, Information and Energy Security*, NATO Science for Peace and Security Series A: Chemistry and Biology, DOI 10.1007/978-94-017-9697-2_49

diamond (BDD) electrodes possess many outstanding properties, including a wide electrochemical potential window in aqueous solutions (ca. 3 V), low and stable background currents, electrochemical stability, and corrosion resistance in aggressive media [1, 2].

For electrochemical applications, the diamond thin films must possess a significant conductivity, and the majority of work in this area has been carried out using very heavily doped boron diamond layers, which display almost metal-like properties.

The increasing energy demand and the environmental pollutions have led to a need for clean renewable energy. The photosynthesis is a well-known process for many years, and scientists are trying to mimic it, because of its possible application for energy harvesting. For electrocatalysis in reactive environments, such as those taking place in solar energy conversion processes, it is important to attach electrochemically active molecules to the surface of inert electrodes. Electrochemical polymerization of metal phthalocyanine (MePc) complexes onto electrodes is one of the most effective means of developing active surfaces for electrocatalytic purposes.

The metal phthalocyanines have attracted significant attention due to their diverse electronic, optical and structural properties, which make them very good candidates for photosensitizers, photoconducting agents and photovoltaic cells. Due to their extraordinary thermal stability, MePcs can capture or harvest more sun light than many conjugated polymers [2].

In the present work we studied NCD electrodes functionalized with manganese phthalocyanine (MnPc). The structure and the optical properties of the MnPc solution in dichloromethane were analyzed and the functionalized electrodes were electrochemically tested. We demonstrate differences in the electrochemical properties due to electrode illumination; the results indicate that the NCD films may be a preferred choice for a number of photoelectrochemical applications.

49.2 Experimental Details

49.2.1 Synthesis of Nanocrystalline Diamond (NCD) Films

Nanocrystalline diamond films were grown on silicon substrates using the chemical vapor deposition (CVD) technique from a mixture of methane and hydrogen. Typical CVD diamond synthesis includes activation of a gas mixture, gas phase reactions and a subsequent transfer of the diamond forming gas species onto the substrate surface [3]. To obtain conducting material boron was introduced in the reactions chamber during the growth process. NCD surfaces are chemically inert and have a hydrogen termination after the deposition. The surface can be modified by plasma- or photo-chemical processes in order to achieve a desired surface termination. In this work the samples were subjected to oxygen plasma modification (2.45 GHz) in an oxygen asher (TePla 200-G) for 5 min at 200 W discharge power and 0.67 mbar working pressure [4].

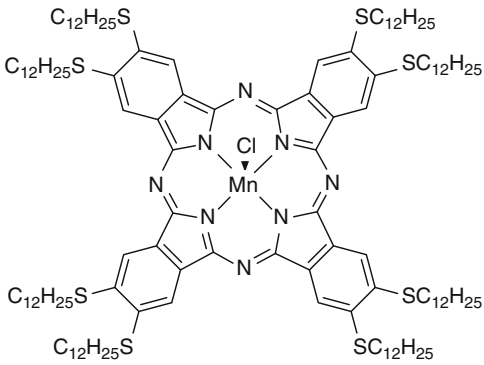

Fig. 49.1 Structure of the manganese (III) phthalocyaninato complex

49.2.2 Characterization of Manganese (III) Phthalocyanines

The manganese (III) phthalocyaninato complex ($C_{128}H_{208}ClMnN_8S_8$), MnPc, synthesized in the group of Prof. Siemeling, Institute of Chemistry, University of Kassel, Germany has a molecular structure with a square-planar configuration with a central metal atom of manganese, as shown in Fig. 49.1

The MnPc powder was dissolved in CH_2Cl_2 to a concentration of 1 μM. The structure of the MnPc in the solution was characterized by FT-IR spectrometry (VARIAN 660-IR). The spectra were recorded in the spectral region of 500–5,000 cm^{-1}.

The optical behavior of the MnPc solution was studied by UV-VIS spectroscopy using a Cary 100 instrument in the double beam mode. The samples were scanned in the region of 200–900 nm with a scan rate of 600 nm/min; CH_2Cl_2 was used as a reference solution.

The NCD films were kept in the MnPc solution for 12 h for attachment of the photosensitive molecules, afterwards electrodes were prepared from the functionalized NCD films.

49.2.3 Electrochemical Tests of the Diamond Electrode

The BDD layers deposited on silicon substrates were assembled as electrodes by covering the substrate backs and attaching a Pt wire.

The electrochemical tests were carried out in a three-electrode cell with a buffered electrolyte (a water-based salt solution containing sodium phosphate, sodium chloride and, in some cases, potassium chloride and potassium phosphate with pH 7.4). The working active surface area of the electrode was ~0.5 cm^2. Platinum served as a counter electrode, a reversible hydrogen electrode (RHE) was chosen as a reference.

The electrochemical behavior of the BDD electrodes were studied in dark and under illumination with a light-emitting diode (LED) with a wavelength of ~720 nm:

1. By measuring the change of the electrochemical potential with the time in dark and after short illumination (volt-ampere characteristics) and
2. By cyclic voltammetry at different experimental conditions.

The electrochemical variations due to light illumination were recorded with an experimental set-up consisting of a light chopper and a computerized UT 60 A measuring system.

The cyclic voltammetry experiments were carried out in a Faraday cell with a rate of 100 mV/s at room temperature.

49.3 Results and Discussion

The IR spectrum of manganese phthalocyanine (Fig. 49.2) displays a high number of bands which originate from the relatively large and complex molecule. Most of the peaks of phthalocyanine are located in the middle IR region since peaks associated with the central metal atom are not visible in this spectral range. The IR spectra, however, should reflect the changes in the configuration of phthalocyanine macrocycles due to the introduction of a template metal.

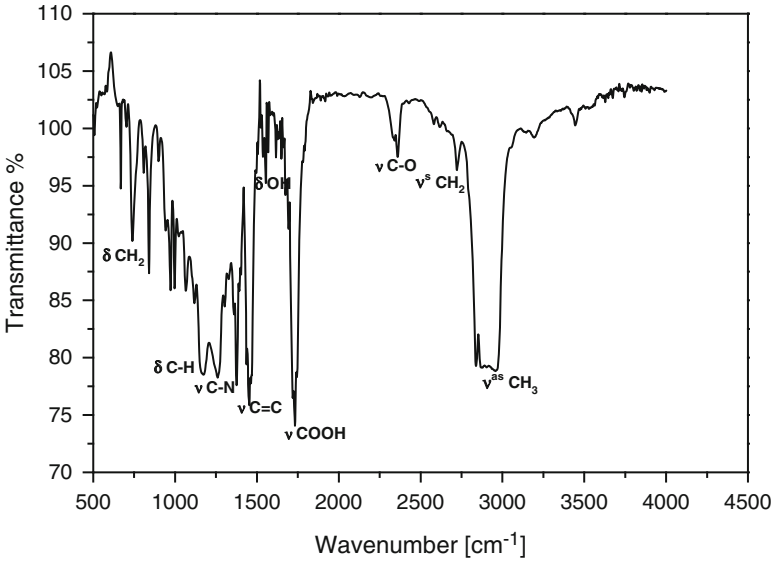

Fig. 49.2 IR spectrum of ($C_{128}H_{208}ClMnN_8S_8$) in the region of 500–4,000 cm^{-1}

The sharp band at about 1,700 cm^{-1} is due to stretching deformations of the aromatic rings consisting of carbon-carbon bonds. Deformation vibrations associated with carbon-hydrogen interactions stemming from the Pc rings and out-of-plane bending of the carbon-hydrogen bonds in the ring system are detected at 740 and 1,170 cm^{-1}. The broad bands of valence vibrations related to the same bonds are situated in the region 2,700–2,950 cm^{-1}. The valence vibrations observed at 1,450 and 1,360 cm^{-1} are due to C = C and C-N bonds typical for Pc rings. Some carbon-oxygen bonds around 2,500 cm^{-1} are also observed as well as complex C-O-OH vibrations at 1,750 cm^{-1} [5].

Figure 49.3 shows the absorption spectra of MnPc dissolved in CH_2Cl_2 in the spectral region of 300–900 nm. The UV–VIS spectra of MePcs strongly depend on the central metal atom; the absorption spectra can be shifted to the IR or UV region by changing the central metal atom in the phtalocyanine molecule. The MnPc complex shows strong absorption regions in the UV region at about 346 nm (B band) and in the visible region at 719 nm (Q band), respectively (Fig. 49.3). In the region from 450 to 600 nm the solution transmits the light to a large extent. The intense absorption peak at 719 nm and the shoulder with a lower intensity at 684 nm are very typical for phthalocyanines containing S and O, or S, O and N cyclic substituents [6].

The electrochemical studies under illumination were performed with a LED emitting at a wavelength of about 720 nm close to the absorption maximum of the MnPc under study. The surface properties of the BDD electrodes are important for the electrochemical reactions occuring at the interface between the electrolyte and the electrode surface. The functionalized BDD electrodes measured in dark

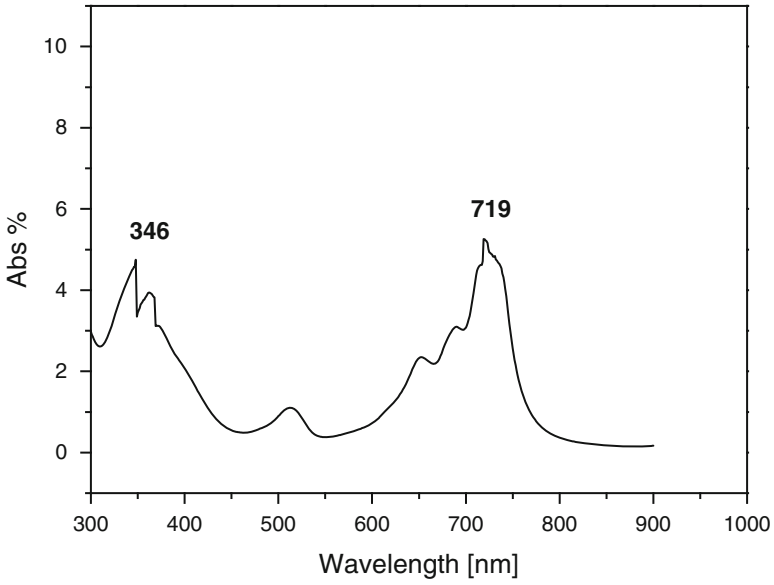

Fig. 49.3 UV-VIS spectrum of MnPc dissolved in CH_2Cl_2

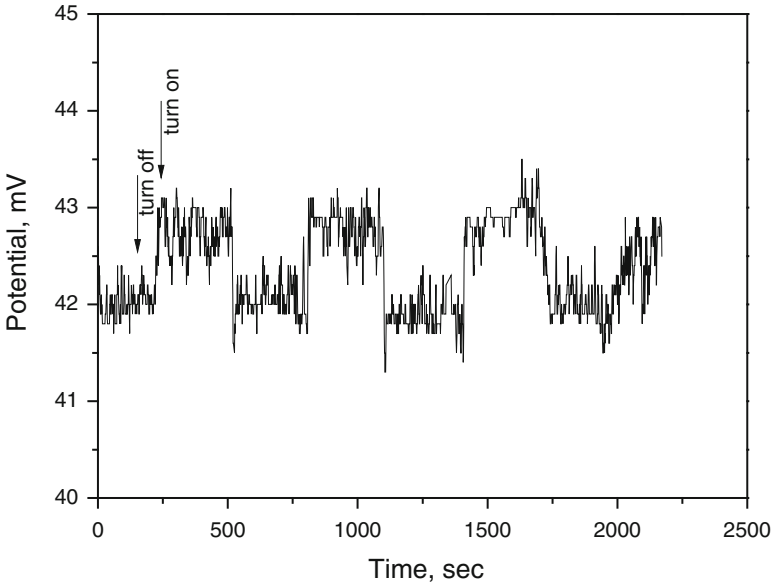

Fig. 49.4 Photo measurements of the BDD electrode functionalized with MnPc

and under illumination show a potential difference of several mV due to the photocurrent generated at the interface (Fig. 49.4). These measurements prove that the phthalocyanine molecules were successfully attached on the diamond electrode surface.

The diamond electrode was electrochemically studied also with cyclic voltammetry in the region between hydrogen and oxygen evolution with a scan rate of 100 mV/s in dark (1), under illumination (2) and after illumination (3) (Fig. 49.5). The four main peaks observed in curve 1 are labeled as I, II, III, IV. These peaks are due both to oxidation and reduction processes. The peak I is observed at about −50 mV and it is most probably related to the reduction from Mn^{3+} to Mn^{2+} of the central atom of the MnPc complex. The next peak is associated with a further reduction of the atom to Mn^{1+} (peak II). The phthalocyanine reduction is observed at about −650 mV associated with valence transition from Pc^{2-} to Pc^{3-} (peak III). The reverse reaction of the phthalocyanine oxidation is clearly seen at about −500 mV where most probably the phthalocyanine part of the complex changes the valence from Pc^{3-} to Pc^{2-} (peak IV).

The illumination with a LED modifies the curve (curve 2) increasing the intensity of the peaks. The light removes an electron from the phthalocyanine (the photosensitive part of the complex) and catalyzes the process. As a result an increase of the current is registered. After the illumination the current decreases (a relaxation of the system is observed).

The peak positions are slightly shifted in negative direction after the illumination. This may be attributed to modification and reconstruction of the phthalocyanine structure after the illumination [7].

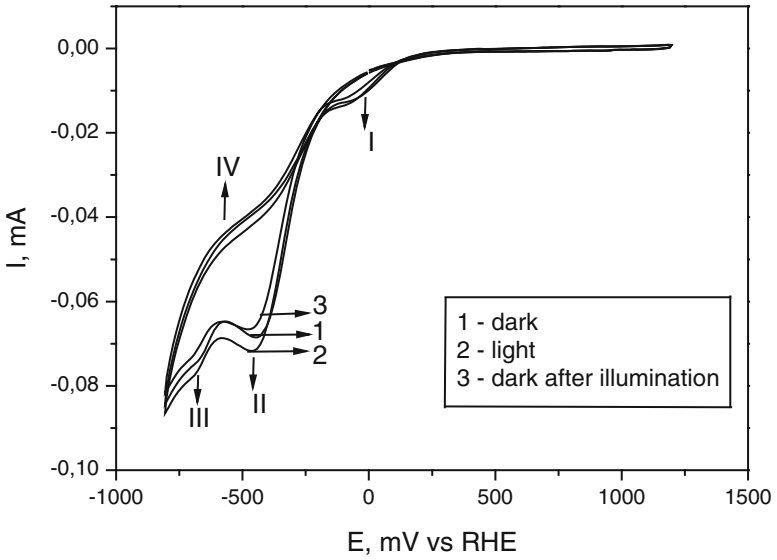

Fig. 49.5 Cyclic voltammograms of BDD electrodes functionalized with MnPc

49.4 Conclusions

Thin boron doped NCD films were deposited on silicon substrates using the CVD technique, and photosensitive MnPc molecules were successfully immobilized on the diamond surface.

The IR spectra of the MnPc showed stretching deformations of the aromatic rings consisting of carbon-carbon bonds, deformation vibrations associated with carbon-hydrogen interactions stemming from the Pc rings and vibrations due to C = C and C-N bonds typical for the Pc rings.

The complex exhibits a strong absorption at 719 nm in the UV-VIS spectra.

The electrochemical measurements revealed that the light catalyzes the process of oxidation and reduction. The process is associated with electron transfers between the central manganese atom and the phthalocyanine complex resulting in an increase of the current.

The experiments suggest that the NCD films functionalized with MnPc are suitable as catalyst for electrochemical reactions.

References

1. Salazar-Banda G, Einaga Y, Martinez-Huitle C (2012) Int J Electrochemistry 2012:1
2. Yuen AP, Jovanovic SM, Hor A, Klenkler RA, Devenyi GA, Loutfy RO, Preston JS (2012) Sol Energy 86:1683
3. Srikanth VVSS, Kumar PS, Kumar VB (2012) Int J Electrochemistry 2012:1

4. Petkov C, Glebe U, Petkov E, Pasquarelli A, Pietzka C, Veres M, Himics L, Merz R, Kulisch W, Siemeling U, Reithmaier JP, Popov C (2013) Phys Status Solidi A 210:2048
5. Singh S, Tripathi SK, Saini GSS (2008) Mater Chem Phys 112:793
6. Şaşmaz S, Kahveci B, Kantar GK, Hacıalioğlu E (2014) El-Cezerî J Sci Eng 1:1
7. Obiraia J, Rodriguesb NP, Bediouib F, Nyokong T (2003) J Porphyrins Phthalocyanines 7:508

Chapter 50
Structural Study of Perovskite Materials for SOFCs Applications

O. Koleva, S. Simeonov, S. Kozhukharov, and M. Machkova

Abstract Solid oxide fuel cells (SOFCs) are a forward-looking approach for highly efficient, environmentally friendly power generation. Economically competitive SOFC systems appear suited for commercialization, but widespread market penetration requires continuous innovation of materials and fabrication processes to enhance system lifetime and reduce costs. A very effective way for enhancing the cell efficiency is to the improve properties of the cathode by achieving conductivity through oxygen ions while at the same time the material maintains the electronic one. As it is known, revealing the microstructure of a material opens the door for improving its macroscopic properties and consequently its practical use. The perovskite family, including Ruddlesden-Popper phases, successfully fulfills many of the requirements for SOFC cathode materials application. Therefore, in the present work two different perovskite compositions, i.e., $La_{1.7}Sr_{0.3}CuO_4$, and $Nd_{1.6}Sr_{0.4}NiO_4$ have been object of structural studies by X-ray diffraction and IR spectroscopy. An adequate conclusion for each of the spectra is presented.

Keywords SOFC • Cathodes • Perovskite-type materials • IR spectroscopy • Structural study

50.1 Introduction

Solid oxide fuel cells (SOFCs) are a forward-looking approach for highly efficient, environmentally friendly power generation. A SOFC is a high-temperature (800–900 °C) device that converts the chemical energy of fuels (such as hydrogen,

O. Koleva (✉)
Department of Silicate Technology, Laboratory for Advanced Materials Research, University of Chemical Technology and Metallurgy – Sofia, 8 "Kl. Ohridski" Blvd., 1756 Sofia, Bulgaria

Section of Solid State Electrolytes, Institute of Electrochemistry and Energy Systems (IEES), Bulgarian Academy of Sciences, Bl.10 Acad. G. Bonchev Str., 1113 Sofia, Bulgaria
e-mail: ofeliya.kostadinova@gmail.com

S. Simeonov • S. Kozhukharov • M. Machkova
Department of Silicate Technology, Laboratory for Advanced Materials Research, University of Chemical Technology and Metallurgy – Sofia, 8 "Kl. Ohridski" Blvd., 1756 Sofia, Bulgaria

P. Petkov et al. (eds.), *Nanoscience Advances in CBRN Agents Detection, Information and Energy Security*, NATO Science for Peace and Security Series A: Chemistry and Biology, DOI 10.1007/978-94-017-9697-2_50

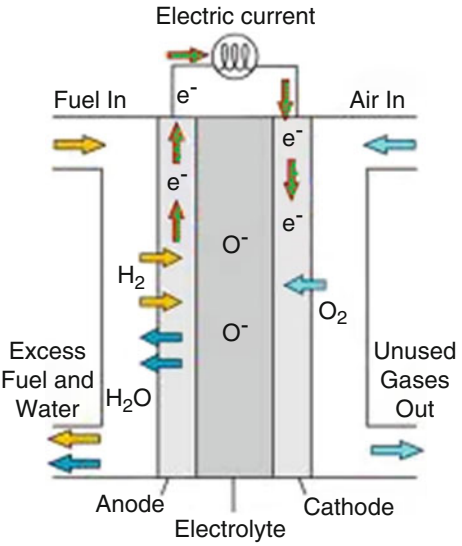

Fig 50.1 Basic scheme of a SOFC

natural gas or other hydrocarbons) directly into electricity through electrochemical oxidation of the fuel with an oxidant, typically oxygen from air. Figure 50.1 shows the basic scheme and work principle of a SOFC. The conversion of chemical into electrical energy is achieved by separating the chemical reaction into two electrochemical reactions (50.1 and 50.2) taking place inside the porous electrodes. At the negative electrode (anode) the hydrogen and carbon monooxide are oxidized with oxygen ions from the electrolyte to form water and carbon dioxide, respectively. The resulting electrons are transported through an external circuit to the positive electrode (cathode) where they are used to reduce oxygen to oxygen ions which are subsequently transported through the electrolyte to the negative electrode.

$$\text{Cathode reaction} : \tfrac{1}{2}\,O_2 - 2e^- \rightarrow O^{2-} \tag{50.1}$$

$$\text{Anode reaction} : H_2 + O^{2-} \rightarrow H_2O + 2e^- \tag{50.2}$$

Economically competitive SOFC systems appear poised for commercialization, but widespread market penetration requires continuous innovation of materials and fabrication processes to enhance system lifetime and reduce cost [1].

An effective approach to cost reduction is the lowering of the operating temperature without inferring performance losses [1]. This can be achieved either by using of thin electrolytes or electrolytes with high ionic conduction (Ce-based doped electrolyte) [2–4]. In these cases it is necessary to develop cathode materials which are adapted to the low-temperature electrolyte and which, at the same time, possess a high conductivity and low cathodic polarization at intermediate temperatures to diminish energy losses from the ohmic resistivity [5]. It was found that decreasing the electrolytic membrane width leads to a decrease in

electrolytic resistivity. This had been attained in SOFCs with planar geometry by using an additional porous anode, on which firstly an uniform thin film (10 μm) from the electrolyte material and thereafter a porous cathode material with a thickness around 50 μm are deposited. For such a type of configuration a very high energy density at temperatures from 700 to 800 °C were achieved.

On the other hand, a very effective way to improve the cell efficiency is to change the properties of the cathode by achieving oxygen ion conductivity while at the same time the material maintains the electronic one. In such a way the process is influenced into two directions: it is shifted outside to triple-phase boundaries (TPB) and it is performed on the surface. A TPB is a point where air, electrolyte and cathode electrode meet each other. It is believed that the cathode properties can be improved by increasing the number of triple phase boundaries.

From a general viewpoint, mixed electronic and ionic conducting oxides (MEIC) can be formulated as $(A, A')_n(M, M')_mO_{x \pm \delta}$, where A and A′ are either rare-earth or alkaline earth cations of large size and M and M′ are 3d elements, respectively. Depending on the n/m ratio, various structural types can be formed, for instance perovskite or derived compounds of the Ruddlesden-Popper type ($A_2MO_{4+\delta}$, where A = La, Nd, Pr, Sr, and M = Ni, Cu, Co). Varying the nature of the A and A′ cations and the A/A′ ratio, as well as the nature of M and M′, results, firstly, in mixed valences of the M, M′ cations, which confers usually a p-type electronic conductivity, and secondly either to a sub- or an over-stoichiometry of oxygen, which can induce ionic conductivity. The perovskite family which form the so-called Ruddlesden-Popper phases successfully fulfill above mentioned requirements for SOFCs cathode materials [6]. The main feature of most members of this family is that they exhibit some oxygen over stoichiometry associated with the mixed valence of the transition metal M-cations. Their structure (K_2NiF_4-type) is made up of sheets of (MO_6) elongated corner-sharing octahedra, interleaved by A_2O_2 layers with a NaCl-type structure in which additional oxygen atoms O_i can be inserted (Fig. 50.2). The amount of inserted oxygen atoms (δ) may reach values

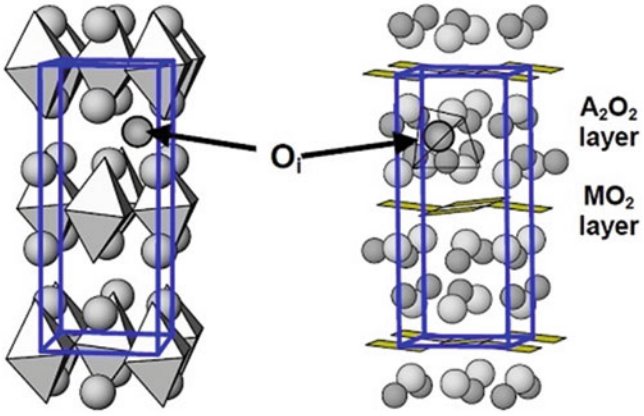

Fig. 50.2 Structure of $A_2MO_{4+\delta}$ compounds showing the location of interstitial oxygen atoms [6]

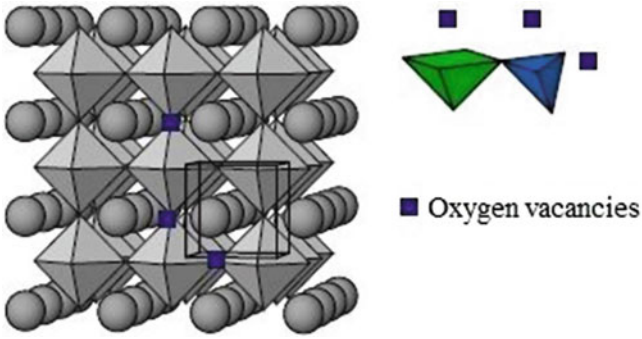

Fig. 50.3 Structure of $AMO_{3-\delta}$ perovskite showing the location of the oxygen vacancies [6]

as high as 0.22 for $Nd_2NiO_{4+\delta}$ or even 0.25 for electrochemically oxidized $La_2NiO_{4+\delta}$ [6]. They are located in tetrahedral sites $(O_IA)_4$, as shown in Fig. 50.3. Compared to the perovskite compounds, the oxygen transport in these materials is supposed to be quite different with respect to the non-stoichiometric type that involves interstitial oxygen atoms instead of oxygen vacancies. Basic properties of these materials have been studied [7, 8] using the $^{18}O/^{16}O$ isotope exchange/depth profile (IEDP) method. It has been proven that this family of compounds exhibit indeed larger oxygen bulk diffusion (D^*) and surface exchange (k) coefficients in comparison to the classical perovskite compounds.

Nevertheless, they exhibit some shortcomings which should be pointed out. The first one is the fact that they react with the zirconium-based electrolyte and form unwanted isolating phases. The others are related to the high costs of lanthanum oxide and the fact that the oxygen conductivity is limited to less than 10 % of the whole conductivity.

Taking into account the above discussion it becomes clear that it is necessary to develop new materials and compositions which could overcome these [9]. Therefore, in this study we synthesized and characterized structurally new compositions of advanced perovskite-like materials which are directly used as SOFC cathodes. For structural investigation we employed IR spectroscopy, a technique which is very powerful and can provide important information on the distinct structural units that built a material. As it is known, revealing the microstructure opens the door for improving the macroscopic properties and consequently the practical use of a material.

50.2 Experimental

In the present work the investigated compositions are $La_{1.7}Sr_{0.3}CuO_4$ and $Nd_{1.6}Sr_{0.4}NiO_4$, respectively. The samples origin is CerPoTech AS Company, Norway. The synthesis followed a standard solid state reaction procedure,

i.e. thermal treating process at 1,250 °C. In order to reveal the existing phases in the samples, we performed XRD analysis by a Bruker D8-Advance using Cu K_α radiation in the 2θ range from 10 to 80°. The measurement took place at ambient temperature with 0.020° steps and a step time of 17.5 s. IR spectra were measured with a FT-IR spectrometer model VARIAN 660-IR FT-IR. Test samples were prepared in KBr tablets and measured at ambient temperature in the spectral range between 4,000 and 400 cm^{-1}.

50.3 Results and Discussion

Although the method is very useful, the IR spectroscopy bears some limitations. For instance, one of the reasons for the difficulties in studying the IR-active phonons is the large in-plane polarizability due to the presence of free carriers. This causes masking of the phonon-related structure and allows only the c-axis vibrations to be observed [10, 11]. For this reason, most of IR-active phonon studies of similar systems were focused on the frequency region from 50 to 520 cm^{-1} [12–15]. Few publications have been found about IR study in the frequency region between 600 and 700 cm^{-1} [11, 16, 17].

50.3.1 Structural Behavior of $La_{1.7}Sr_{0.3}CuO_4$ System

50.3.1.1 X-ray Diffraction Investigation

X-ray diffraction analysis of the $La_{1.7}Sr_{0.3}CuO_4$ system, presented in Fig. 50.4 displays diffraction maxima for only one compound, i.e. $La_{1.7}Sr_{0.3}CuO_4$. This result suggests that the sample is well-synthesized and homogenous.

50.3.1.2 Infrared Study

The IR spectrum of $La_{1.7}Sr_{0.3}CuO_4$ composition is presented in Fig. 50.5. At lower frequencies the spectrum contains two modes located at 503 and 668 cm^{-1}, respectively. Due to above mentioned limitations of the method, their assignment is not straightforward. While studying a sample from the same system but with different compositions, i.e. $La_{2-x}Sr_xCuO_4$, $0 \leq x \leq 0.125$ %, Napoletano et al. [16] discussed the two most pronounced peaks in their spectra, located at 684 cm^{-1} and 514 cm^{-1}, respectively. Taking into account the stability of the peak intensity, the authors attributed the latter band in the undoped La_2CuO_4 to the La–O asymmetric stretching mode. This assignment is also supported by its slight shift to lower frequencies with increasing Sr concentration. Actually, Sr doping causes the apical

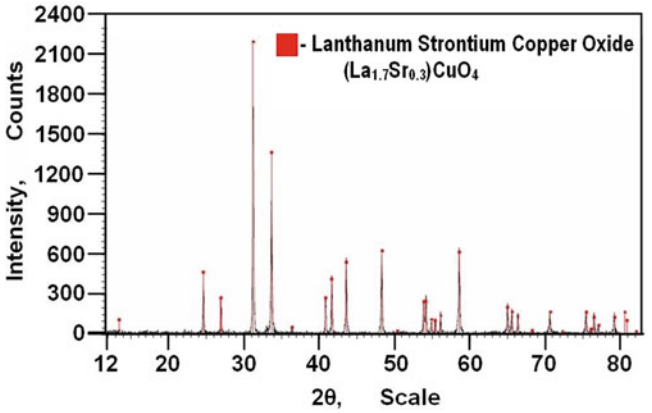

Fig. 50.4 XRD diffraction pattern of a $La_{1.7}Sr_{0.3}CuO_4$ compound

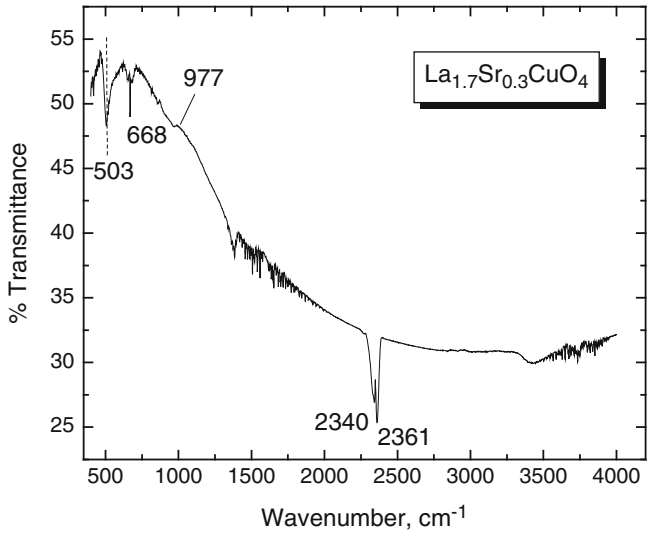

Fig. 50.5 The infrared spectrum of a $La_{1.7}Sr_{0.3}CuO_4$ sample

La(Sr)-O bond length to increase significantly resulting in a gradual shift down of the corresponding stretching modes.

Having in mind that all these findings are valid for a maximum Sr content $x = 0.125$ %, it seems quite logical to assume that an increase of the Sr concentration to $x = 0.3$ % as in our case would lead to larger down-shift, reaching

eventually 503 cm^{-1}. Therefore, taking into account both, the different Sr concentrations and the band shifting in comparison to the one found in the work of Napoletano et al. [18], we attributed the mode located at 503 cm^{-1} in our spectrum as a contribution from La–O asymmetric stretching vibrations. Assignments of the next higher frequency band found at 668 cm^{-1} are contradictory. As it was already mentioned, in the work of Napoletano et al. [16] the authors discuss a peak located at 684 cm^{-1}. In order to interpret it, they followed the idea that the random substitution of La ions by alkali earth ions results in increased apical O–Cu bond lengths and slightly decreased in-plane O–Cu bond lengths.

As it is known, the higher frequency bands should certainly be assigned to vibrational modes primarily involving the stretching of shorter and stronger bonds. In the present case such bonds are the basal Cu–O ones with a length of 1.90 Å and perhaps La–O bonds with a length of 2.35 Å. Stretching modes of the longer apical Cu–O bonds (length 2.5 Å) are expected at lower frequencies. Following this concept, as a conclusion, the authors suppose that the band situated at 684 cm^{-1} is due to the superposition of two asymmetric stretching modes of CuO_4 "squares". They ascribe the steady reduction of this peak by doping from $0 \leq x \leq 0.125$ %, to the increased symmetry of the unit cell when the latter changes from orthorhombic to tetragonal. This alteration results in losing the splitting of the asymmetric Cu–O stretching effect. A similar phenomenon has been observed also in other works [11, 17]. In the work of Pu et al. [11], where the authors studied $La_{1.85+x}Sr_{0.15-x}Cu_{1-x}Li_xO_y$, they observed the disappearance of the 683 cm^{-1} absorption band. Although that they observed the same effect as in the work of Napoletano et al. [16], they give a different explanation. They proposed [11] the idea that the free carriers can cause IR active phonon in-plane polarization and mask phonon-related structures in the spectra. These so-called screening effects have also been reported in other works [15, 18]. Thus, the authors ascribe the disappearance of the IR vibrational mode at 696 cm^{-1} in their spectra to screening effects of charge carriers. With Li content increasing further, Li doping at Cu sites replaces Cu^{2+} spins and destroys the Cu^{2+} spin correlation. This effect inspires the charge carriers to change from a delocalized state to a localized state. Then this frequency peak appears again but at a higher frequency of ~705 cm^{-1} when the dopant concentration exceeds $x \geq 0.2$. The authors attributed the newly appearance of the band to the monotonous decrease of the lattice parameter *a* which is in good agreement with the gradual hardening of the Cu–O(1) stretching modes in the $La_2Cu_{1-x}Li_xO_y$ system. Thus, the IR mode at 683 cm^{-1} shifts to 703 cm^{-1}.

It is known that the Cu–O stretching modes are closely related to the Cu–O bond length. The shift of the IR modes can be interpreted based on the changes of the lattice parameters *a* and *c* [11]. Hence, an increase of the distance between planar O and Cu^{2+} will result in downward shifting of the Cu–O(1) stretching modes to lower frequencies [17]. We suppose that disappearance of the 684 cm^{-1} band in the work of Napoletano et al. [18] might be due to the screening effect that was described by other authors [11, 15, 18]. Since the Sr content in their study does not exceeds 0.125 %, the band does not appear again. In our study, adding a quantity of more than 0.125 % [19] stimulates two effects. The first one is related

to the appearance of a mode, which is due to planar Cu-O again. The second effect concerns the shifting of the same mode to lower frequencies. The latter has been caused by an increase of the planar O and Cu^{2+} distance.

Turning our attention to higher frequencies, we observe a band located at 977 cm^{-1}. This mode most probably is due to vibrations of water molecules. In the spectral range between 2,340 and 2,365 cm^{-1} two vibrational modes appear. They are related to vibrations of CO_2 molecules. In the very high frequency region, a slight peak appears at 3,415 cm^{-1}. Most probably, this peak is a contribution of O-H stretching vibration of H_2O molecules [20]. Both, water molecules and CO_2, are contribution from absorption effect from the air.

50.3.2 Structural Behavior of $Nd_{1.6}Sr_{0.4}NiO_4$ System

50.3.2.1 X-ray Diffraction Investigation

A X-ray diffraction analysis of the $La_{1.7}Sr_{0.3}CuO_4$ system is shown in Fig. 50.6. The diffractograms displays diffraction maxima for two compounds, i.e. $Nd_{1.6}Sr_{0.4}NiO_4$ and small amount of Al. Aluminum appears as an impurity. Nevertheless, the sample is crystalline, without any detectable vitreous phase and homogeneous.

50.3.2.2 Infrared Study

Since this compound is innovative, only few publications have been found during our detailed searching. An IR spectrum of the investigated composition $Nd_{1.6}Sr_{0.4}NiO_4$ is presented in Fig. 50.7. Two indicative bands situated at 510 and 710 cm^{-1} are

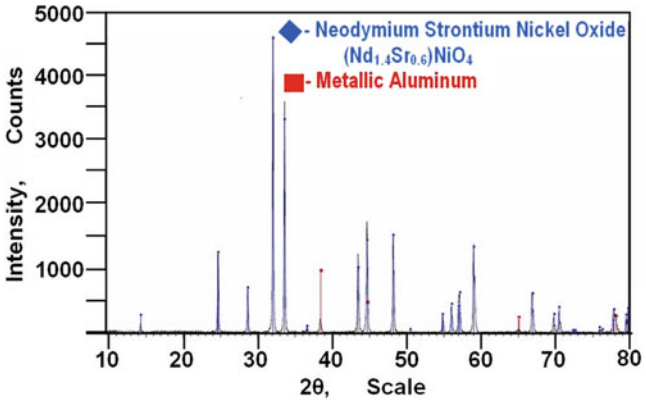

Fig. 50.6 XRD analysis of the $Nd_{1.6}Sr_{0.4}NiO_4$ system

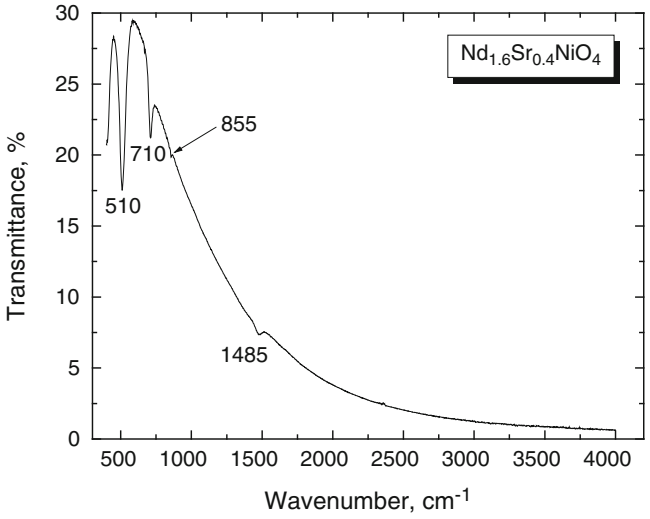

Fig. 50.7 The infrared spectrum of a $Nd_{1.6}Sr_{0.4}NiO_4$ powder sample

examined. According to Ref. [21], these two modes are characteristic for Ni-O stretching vibrations.

In addition, two more weak bands positioned at 855 and 1,485 cm $^{-1}$ are observed. According to Zhu et al. [22] both peaks are contributions from $SrCO_3$ vibrations. More exactly, they originate from both inorganic carbonate C-O stretch at 1,510–1,410 cm^{-1} and C-O out-of-plane bending in the wavenumber range from 880 to 860 cm^{-1}. Following the discussion carried out above, these small absorption bands may be due to CO_2 molecule vibrations. These structural units are typical for inorganic carbonates and are probably formed after the synthesis of the material due to CO_2 absorption from the air. No contributions from H_2O molecules, i.e. O-H stretching vibrations were registered.

50.4 Conclusions

Two different perovskite-type compositions, i. e. $La_{1.7}Sr_{0.3}CuO_4$ and $Nd_{1.6}Sr_{0.4}NiO_4$ were structurally investigated by X-ray diffraction and IR spectroscopy. On the base of X-ray diffraction analysis both samples seem well-synthesized and homogenous which is the first preliminary condition for the next studies and usage. Interpretation of the lanthanum-cuprate IR spectrum is not straightforward which has a two-fold origin: (i) higher La-content and appearance of the so-called screening effect which is typical for this system. Nevertheless, two characteristic bands were detected for this system and were attributed to La-O asymmetric stretching vibrations and to asymmetric Cu-O vibrations in CuO_4 squares,

respectively. The interpretation of IR spectrum of $Nd_{1.6}Sr_{0.4}NiO_4$ powder sample is simpler. Few vibrational modes were observed. Among them, two were found indicative and attributed to Ni-O stretching vibrations. Moreover, inorganic carbonate C-O vibrations from $SrCO_3$ were also observed. In brief, judging from this preliminary structural investigation, $La_{1.7}Sr_{0.3}CuO_4$ and $Nd_{1.6}Sr_{0.4}NiO_4$ are appropriate for cathode materials in SOFCs, which is in agreement with our preliminary results [23].

Acknowledgments The authors kindly acknowledge the financial support from the Bulgarian National Science Fund – project No. TK-X-1711

References

1. Barbucci A, Piccardo P, Carpanese MP, Viviani M (2006) In: Stoynov Z, Vladikova D (eds) Portable and emergency energy sources. Prof. Marin Drinov Publishing House, Sofia, p 329
2. Steele BCH (2000) Solid State Ionics 134:3
3. Will J, Mitterdorfer A, Kleinlogel C, Perednis D, Gauckler LJ (2000) Solid State Ionics 131:79
4. Mogensen M, Sammes NM, Tompsett GA (2000) Solid State Ionics 129:63
5. Fuel Cell Today (2007) Technology article solid oxide fuel cells. http://www.fuelcelltoday.com/media/pdf/surveys/2007-SOFC-Survey.pdf
6. Grenier JC, Bassat JM, Lalanne C, Mauvy F (2009) In: Vladikova D, Stoynov Z (eds) Proceedings international workshop "Advances and Innovations in SOFCs", Katarino, Bulgaria, 13–16 September 2009, p 21
7. De Souza RA, Kilner JA, Walker JF (2000) Mater Lett 43:43
8. Boehm E, Bassat JM, Steil MC, Dordor P, Mauvy F, Grenier JC (2003) Solid State Sci 5:973
9. Patent No US 20070207373: Solid oxide fuel cell cathode material (2007)
10. Genzel L, Wittlin A, Bauer M, Cardona M, Schronherr E, Simon A (1989) Phys Rev B 40:2170
11. Pu Q, Xu G, Zhang Z, Ding Z (2002) Physica C 370:269
12. Henn R, Kircher J, Cardona M (1996) Physica C 269:99
13. Henn R, Wittlin A, Cardona M, Uchida S (1997) Phys Rev B 56:6295
14. Humliček J, Litvinchuk AP, Kress W, Lederle B, Thomsen C, Cardona M, Habermeier HU, Trofimov IE, König W (1993) Physica C 206:345
15. Schutzmann J, Tajima S, Miyamoto S, Sato Y, Hauff R (1995) Phys Rev B 52:13665
16. Napoletano M, Amores JMG, Magnone E, Busca G, Ferretti M (1999) Physica C 319:229
17. Xu G, Pu Q, Zhang Z, Ding Z (2002) Physica C 370:101
18. Heyen ET, Kliche G, Kress W, König W, Cardona M, Rampf E, Prade J, Schröder U, Kulkarni AD, de Wette FW, Pinol S, Paul DM, Moran E, Alario-Franco MA (1990) Solid State Commun 74:1299
19. Wang SH, Song Q, Clayman BP (1990) Phys Rev Lett 64:1067
20. Kadinov G, Institute of Catalysis, Bulgarian Academy of Sciences, Laboratory of New catalytic and Nano-sized Catalysts, Private communications
21. Si-Wen L, Yu-Fang R (1995) Mater Res Bull 30:1505
22. Zhu J, Dehai X, Jing L, Xiangguang Y, Yue W (2005) J Mol Catal A Chem 234:99
23. Kozhukharov S, Machkova M, Kozhukharov V, Simeonov S (2013) Bulg Chem Commun 45(2):207

Chapter 51
Deposition of Perylene Diimide Derivatives for Dye-Sensitized Solar Cells

N. Georgiev, H. Nichev, M. Petrov, K. Lovchinov, D. Dimova-Malinovska, and V. Bojinov

Abstract The aim of this work is to examine the photosensitivity of dye-sensitized materials. Three types of organic dye sensitizers, i.e. perylene diimide (PDI) derivatives with different terminal groups were synthesized. The synthesized PDI derivates were deposited by dipping on a glass/ITO substrate covered with arrays of ZnO nanorods (NR) grown by an electrochemical process. An Ag grid contact was deposited on the PDI films on the stack glass/ITO/ZnONR/PDI; then I-V characteristics of the structures were measured in dark and under illumination with a halogen lamp. The photosensitivity of the different dye-sensitized materials is discussed.

Keywords Photoconductivity • Perylene diimide derivatives • ZnO nanorod arrays

51.1 Introduction

The main efforts in the photovoltaic (PV) technology are focused on increasing the efficiency and decreasing the price of the solar cells and modules. Solar cells on perylene diimide derivatives (PDI) have attracted the interest of researchers as an alternative to the high cost Si solar cells. The synthesis and the study of the characteristics of these materials are of high importance for the fabrication of solar cells. The increased interest in solar cells based on organic materials is due to their advantages: a potential low cost thin film PV technology, low toxicity, technological merits in producing photoconductive compositions, and the possibility of deposition of large area substrates.

N. Georgiev • V. Bojinov
Department of Organic Synthesis and Fuels, University of Chemical Technology and Metallurgy, Bul. "Sv. Kliment Ohridski" 8, 1756 Sofia, Bulgaria

H. Nichev (✉) • M. Petrov • K. Lovchinov • D. Dimova-Malinovska
Central Laboratory of Solar Energy and New Energy Sources, Bulgarian Academy of Sciences, 72 Tzarigradsko Chaussee, 1784 Sofia, Bulgaria
e-mail: nitschew@yahoo.de

P. Petkov et al. (eds.), *Nanoscience Advances in CBRN Agents Detection, Information and Energy Security*, NATO Science for Peace and Security Series A: Chemistry and Biology, DOI 10.1007/978-94-017-9697-2_51

For the last 10 years increasing efforts have been devoted to the development of organic sensitizers, and reasonable photo-conversion efficiencies have been reached with some push-pull type organic chromophores. The representatives of these materials are perylene diimide derivatives owing to the unique outstanding chemical, thermal and especially photochemical stability.

The reduction of the dimensions of materials to a nanometer scale gives rise to several advantages in terms of device applications. Nanomaterials such as nanowires and nanorods have unique advantages that make them useful in photovoltaic devices [1]. Nanostructured materials can be produced by non-vacuum technologies on large area substrates. All these advantages offer the possibility to increase the efficiency of solar cells and modules and to reduce their costs. Layers of nanostructured arrays can be deposited with very large surface area per unit volume and offer a possibility to improve light trapping properties of solar cell due to the rough interface with increased effective areas between the films.

The photovoltaic devices based on inorganic semiconductor such as ZnO with vertically oriented nanowire and nanorod structure [2] have been applied as anti-reflecting coating (ARC) in Si heterojunction solar cells [3] and used as substrates for a-Si:H thin film solar cells [4] with improved efficiency. ZnO nanorod arrays have been integrated in organic photo-active materials, as well [2, 5, 6].

In this work we report on the preparation of three types of PDI layers on ZnO nanorod arrays grown by electrochemical process on glass/ITO substrates via dip-ping in a solution. An Ag grid contact was deposited on the structure glass/ITO/ZnO NR/PDI, and I-V characteristics of the structures were measured in dark and under illumination with a halogen lamp for assessment of their photosensitivity.

51.2 Experimental

The three types of perylene diimide derivatives (PDI) were synthesized on the base of the perylene diimide derivatives (1 in Fig. 51.1). P.a. grade N, N-dimethylethylenediamine, ethylenediamine, methyl acrylate and perylene-3,4,9,10-tetracarboxylic (Aldrich) were used without purification. All solvents (Aldrich, Fisher Chemical) used for the process of synthesis were pure or of spectroscopy grade.

The properties of the synthesized PDIs were evaluated by FTIR, UV-VIS and fluorescence spectroscopy. FTIR spectra of were recorded with a Varian Scimitar 1000 spectrometer. UV-VIS absorption spectra were recorded with a spectrophotometer Hewlett Packard 8452A. Fluorescence spectra were taken with a Scinco FS-2 spectrofluorimeter at room temperature (25 °C). The relative fluorescence quantum yield Φ_F was determined using Coumarin 6 (Aldrich, $\Phi_F = 0.78$ in ethanol [7]) as a standard. The I-V characteristics of the structures

glass/ITO/ZnO NR/PDI/Ag grid were measured using a Keithley 2400 Source Meter in dark and under illumination by a halogen lamp in order to study their photosensitivity.

51.3 Results and Discussion

51.3.1 Synthesis of PDI 2 and PDI 3

The dyes PDI 2 and PDI 3 were synthesized using by the consecutive refluxing a suspension of 2 g (5 mmol) perylene-3,4,9,10-tetracarboxy anhydride (1 in Fig. 51.1) and N,N-dimethylethylenediamine or ethylethylenediamine in water/propanol. 2.1 ml of the primary amine N,N-dimethylethylenediamine was added to obtain PDI 2 or 2 ml ethylenediamine to obtain PDI 3. Additionally, a mixture of 50 ml water and 50 ml n-propanol was added.

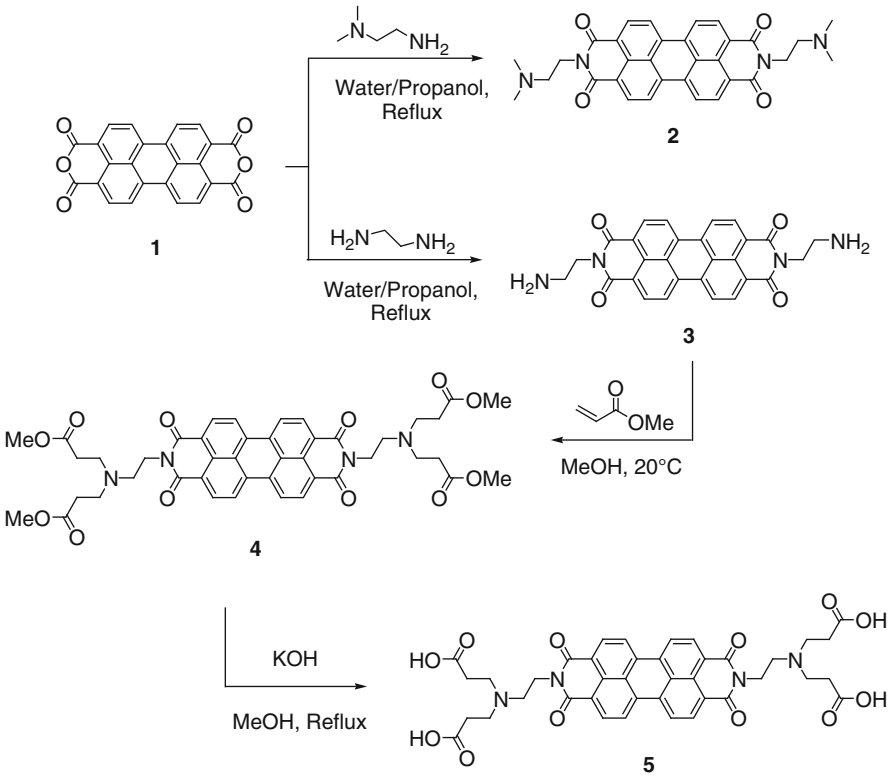

Fig. 51.1 Scheme of the procedure of the synthesis of PDIs

The resulting mixture was heated at 90 °C under reflux for 4 h. After cooling to room temperature the precipitate was collected by filtration, washed with water and dried. Then the obtained solid powder was treated with 100 ml of 5 % aqueous solution of sodium hydroxide to give the pure compounds after filtration, washing with water and drying. The results of analyses show:

- PDI 2: Yield = 2.4 g (91 %). IR (KBr) cm^{-1}: 2,962 and 2,770 (νCH); 1,694 (ν_{as}N-C=O); 1,658(ν_sN-C=O). Elemental analysis: Calculated for $C_{32}H_{28}N_4O_4$ (MW 532,6): C 72.16, H 5.30, N 10.52 %; measured: C 71.89, H 5.22, N 10.85 %.
- PDI 3: Yield = 2.2 g (94 %). IR (KBr) cm^{-1}: 3,352 (νNH2); 1,696 (ν_{as}N-C=O); 1,659 (ν_sN-C=O). Elemental analysis: Calculated for $C_{28}H_{20}N_4O_4$ (MW 476,5): C 70.58, H 4.23, N 11.76 %; measured: C 70.83, H 4.17, N 11.47 %.

51.3.2 Synthesis of Perylene-3,4,9,10-Tetracarboxylic Diimide (PDI 4)

The synthesis of the novel perylene tetracarboxydiimide PDI 4 is shown in Fig. 51.1. The dye PDI 4 was synthesized via a divergent strategy, involving initial Michael-addition of the aminofunctional core PDI 3 with methyl acrylate. The structure and purities of the prepared products were confirmed by conventional techniques (elemental analysis, UV-VIS, fluorescence and FTIR spectroscopy).

A mixture of methyl acrylate (2.7 ml, 32 mmol) and 1.5 g of PDR 3 (3.2 mmol) in 30 ml methanol was stirred for 4 days at room temperature, then the precipitate was collected by filtration, washed with water and dried. Then the crude solid was extracted with boiling chloroform to give, after vacuum evaporation of the solvent and silica-gel chromatography in CH_2Cl_2, pure PDI 4 as dark-red crystals (melting point 206–209 °C). The results of the analyses were:

- PDI 4: Yield = 0.74 g (28 %). IR (KBr) cm^{-1}: 1,730 (n$COOCH_3$); 1,688 (ν_{as}N-C=O); 1,660 (ν_sN-C=O). Elemental analysis: Calculated for $C_{44}H_{44}N_4O_{12}$ (MW 820.9): C 64.38, H 5.40, N 6.83 %; measured: C 63.19, H 4.99, N 6.70 %.

51.3.3 Synthesis of Perylene-3,4,9,10-Tetracarboxylic Diimide (PDI 5)

PDI 5 was obtained by conversion of PDI 4 by hydrolysis. A suspension of PDI 4 (0.5 g, 0.6 mmol) in EtOH (15 mL) was added to NaOH (0.25 g, 6.3 mmol) and dissolved in hot EtOH (20 mL). The mixture was heated to reflux for 12 h. The precipitated crude product was filtered off after cooling, washed with water

and dried. Silica gel chromatography yielded 0.24 g of PDI 5. The results of analyses were:

- PDI 5: – Yield = −0.24 g (53 %). IR (KBr) cm^{-1}: 3,052 (nOH); 1,669 and 1,681 (νN-C=O). Elemental analysis: Calculated for $C_{40}H_{36}N_4O_{12}$ (MW 764.7): C 62.82, H 4.74, N 7.33 %; measured C 62.52, H 4.49, N 7.44 %

The IR spectra of the prepared perylene diimides PDI 2 to PDI 5 show two absorption bands in the range 1,650–1,690 cm^{-1} resulting from the presence of the imide ring. No absorption bands above 1,750–1,800 cm^{-1} corresponding to anhydride carbonyl group absorptions were observed. This is evidence that the starting perylene anhydride (1) was completely converted to the perylene diimides PDI 2–5.

The dyes under investigation are based on the same chromophoric system, thus their absorption spectra are identical. In dimethyl formamid (DMF) solution the examined PDIs demonstrate UV-vis absorption spectra typical for perylene tetracarboxydiimide [8] with three pronounced peaks at 460, 490 and 526 nm which corresponds to the 2–0, 1–0 and 0–0 electron transitions, as the highest intensity was observed for the lowest energy band.

The synthesized PDIs are based on the "fluorophore-spacer-receptor" model, where the perylene diimides core is the fluorophore and the tertiary amines are the receptors. For these particular cases it was predicted that a photoinduced electron transfer (PET) from the receptor to the excited state of the fluorophore would quench fluorescence emission of the PDI unit [9]. This is why the dyes PDI 2, 4 and 5 show extremely low fluorescence with quantum yields in range between 0.005 and 0.008. We chose the PET based PDIs as dye sensitizers since the PET process stabilizes the excited dye state and favours the charge separation.

The correct design of the binding groups plays a critical role to prevent aggregation of the chromophores and to tune the properties of the dye layer. It is well known that carbonyl derivatives are suitable linkers for different metal oxides [10]. That is why the dyes PDI 4 and PDI 5 are ester and carboxylic acid terminated, respectively. Compound PDI 2 which lacks a linker group was introduced in the present study in order to receive a more complete comparative picture for the influence of the dye terminal groups.

51.3.4 Deposition of ZnO Nanorods Arrays

ZnO layers were deposited by mean of an electrochemical process in an aequeous solution of $ZnCl_2$ and KCl using a electrochemical three-electrode cell with a saturated calomel electrode (SCE) as reference electrode [11]. The electrolyte contents $ZnCl_2$ (5×10^{-4} M) and KCl (1 M) with pH ~ 5. The deposition temperature was 80 °C. The deposition was carried out controlling the potential by a high power potentiostat system WENKING HP 96. Since the potential of Zn in the electrolyte is −1.05 V vs. SCE, the deposition process of ZnO was carried out at −1.0 V vs. SCE to prevent deposition of metallic Zn. Good quality ZnO films

were obtained at a redox potential within the range between +0.30 and +0.40 V vs. SCE. At a redox potential higher than +0.4 V zinc peroxide (ZnO_2) was formed on the samples with a poor adhesion to the substrate. A spectrally pure graphite plate was used as an anode. The electrolyte was agitated by a magnetic stirrer. ITO on glass was used as conductive substrate for the growth of ZnONR [12]. The growth time was 20 min. The deposition of thin ZnO films at a redox potential lower than +0.4 V can be explained as a product of the interaction of OH^- and Zn^{2+} on the surface of the electrode [13].

$$Zn^{2+} + 2OH^- \rightarrow Zn(OH)_2 \rightarrow ZnO + H_2O$$

After deposition of the ZnO layers on the glass/ITO substrates they were cleaned with acetone. For coating with the PDIs the cleaned substrates was immersed into a dye solution in DMF (dye concentration 1×10^{-5} mol/L), kept for 24 h and then dried in air.

51.3.5 I-V Measurements

An Ag grid contact was deposited on the structure glass/ITO/ZnO NR/PDI (Fig. 51.2). The Ag contact was deposited on the ITO layer. The photocurrent was measured between the Ag metal electrode on the ITO and the front Ag grid electrode in dark and under illumination by light from a halogen lamp (−900 W) on the side of the Ag grid. The positive potential was applied to Ag electrode deposited on ITO.

The I-V characteristics in dark and under illumination are presented in Fig. 51.3. The I-V characteristics of the structures with PDI 2 and 4 demonstrate a rectifying effect. The structures with the three different PDI under investigation demonstrate photosensitivity. The structure with PDI 4 possesses the highest photosensitivity. In this case the dye is Probably deposited as monolayer on the surface of the ZnO NR which results in a decrease of the recombination of the carriers genarated by the light.

The synthesized dye PDI 2 demonstrates a lower photosensitivity probably because it possesses no anchor groups which could help to bind the PDI on the

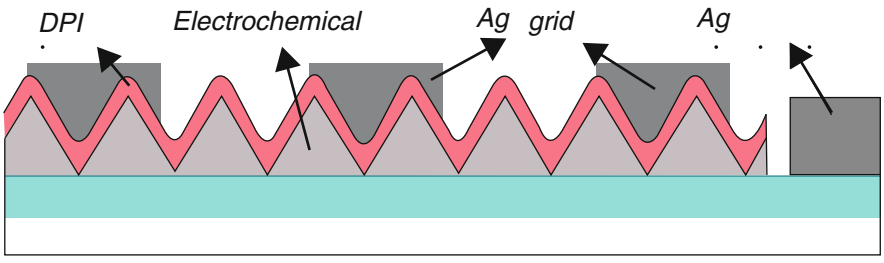

Fig. 51.2 Scheme of the structures with ZnO NR arrays and PDI derivatives for I-V measurement

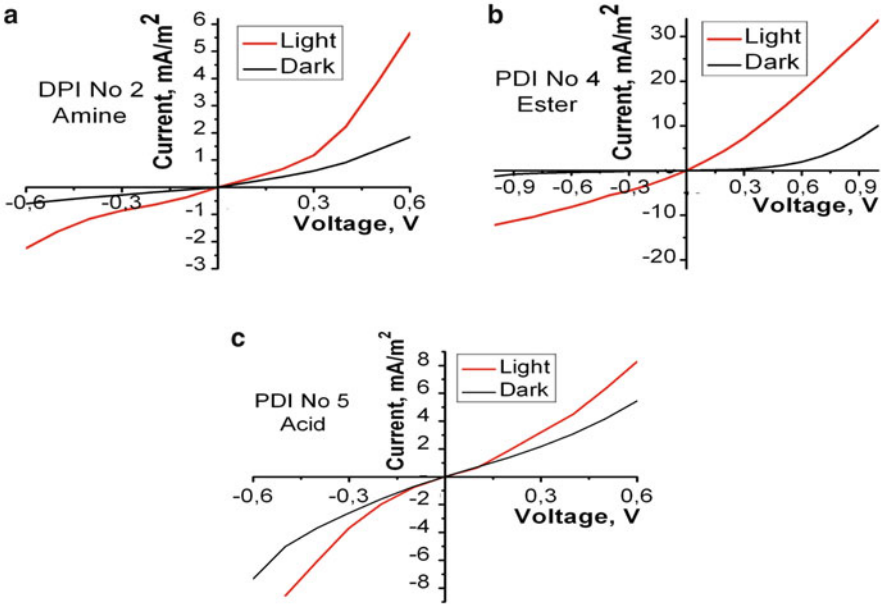

Fig. 51.3 I-V a characteristics of the structures glass/ITO/ZnO NR/PDI/Ag grid in *dark* and under illumination for PDI 2 (**a**), PDI 4 (**b**) and PDI 5 (**c**)

rough nanostructured ZnO surface. The samples with PDI 5 shows a very weak photosensitivy. Due to the poor solubility the synthesized dye forms very easily aggregates, which prevent formation of a homogeneous continuous PDI film; thus it is necessary to apply high voltages to obtain a photo-current.

51.4 Conclusions

In this work it was shown that perylene diimide derivatives with different terminal groups can be synthesized using perylene-3,4,9,10-tetracarboxy anhydride by adding different primary amines. The synthesized PDI derivatives were deposited on the surface of ZnO nanorod arrays grown by an electrochemical method on conductive glass/ITO substrate. The photosensitivity of the structure ITO/ZnO NR/PDI/Ag grid was studied. The PDI 4 (ester terminated) demonstrated the highest photosensitivity probably as a result of the formation of a monolayer which impedes carrier recombination.

Acknowledgement The work has been supported by the Bulgarian Scientific Fund – project N DDVU 02/97 (20.12.2010)

References

1. Duan X, Huang Y, Cui Y, Wang J, Lieber M (2001) Nature 409:66
2. Huang S, Chou Y, Lin F (2010) Sol Energy Mater Sol Cells 94:182
3. Petrov M, Lovchinov K, Ganchev M, Dimova-Malinovska D, Leendertz C (2013) Proceedings of the scientific studies, vol 38. University of Plovdiv, p 4. ISSN 0861-0029
4. Zhang D, Petrov M, Dörenkämper M, Bakkea K, Soppe W, Malinovska D, Schropp R (2014) *29 EUPVSEC*, Amsterdam, submitted
5. Takanezawa K, Tajiama K, Hashimoto K (2008) Appl Phys Lett 93:063308-1-3
6. Ravirajan P, Peiro A, Nazeeruddin M, Gratzel M, Bradley D, Durrant J, Nelson J (2006) J Phys Chem B 110:753509
7. Reynolds G, Drexhage K (1975) Opt Commun 13:222
8. Pasaogullari N, Icil H, Demuth M, Dragoman M (2006) Dyes Pigments 69:118
9. Daffy L, de Silva A, Gunaratne H, Huber C, Lynch P, Werner T, Wolfbeis O (1998) Chem Eur J 4:91810
10. Galoppini E (2004) Coord Chem Rev 248:1283
11. Dimova-Malinovska D, Lovchinov K, Ganchev M, Angelov O, Graff JS, Ulyashin A (2013) Phys Status Solidi A 210:737
12. Petrov M, Lovchinov K, Nichev H, Karashanova D, Dompva-Malinovska D (2015) Proceedings of the NATO ASI nanoscience advances in CBRN agents detection, information and energy security, 141st edn. Springer, Dordrecht
13. Lide D, Frederikse H (1996) Handbook of chemistry and physics, 77th edn. CRC Press, Boca Raton

Chapter 52
Micromirror Arrays for Smart Personal Environments

A. Tatzel, B. Einwögerer, I. Bergmair, N. Worapattrakul, B. Khudhair, V. Viereck, and H. Hillmer

Abstract Energy saving potentials of micromirror arrays in active windows for smart personal environments (SPE) are studied. Such systems enable large area daylight guiding in buildings by application of electrostatically actuated micromirror arrays inside the noble gas or vacuum spacer between the panes of insulation glazings. The working principle in winter and summer scenarii is described. An alternative fabrication process for micromirror arrays, called transfer printing, is presented. For the first time we succeeded in fabricating micromirror arrays applying this novel transfer print.

Keywords Active windows • Smart personal environments • Micromirror • Micromirror arrays • Energy saving • Transfer printing

52.1 Introduction

Advances in micro-electromechanical system (MEMS) technology lead to increasingly more powerful MEMS-based sensors and actuators. It is accompanied by a reduction in size and average cost of these devices. The broad availability of low-cost sensors and actuators allows the creation of new network systems operating in the background and improving daily life without being noticed by the user. Such systems work autonomously based on data collected by sensors, programs or learned rules, and change the environment by actuators. These systems are referred to as smart systems [1, 2]. By tailoring the system performance to individual preferences or medical needs, these systems can be personalized.

A. Tatzel (✉) • N. Worapattrakul • B. Khudhair • V. Viereck • H. Hillmer
Institute of Nanostructure Technologies and Analytics (INA), Center for Interdisciplinary Nanostructure Science and Technology (CINSat), University of Kassel, Heinrich-Plett-Str. 40, 34132 Kassel, Germany
e-mail: tatzel@ina.uni-kassel.de

B. Einwögerer • I. Bergmair
Functional Surfaces and Nanostructures, PROFACTOR GmbH, Im Stadtgut A2, 4407 Steyr-Gleink, Austria

P. Petkov et al. (eds.), *Nanoscience Advances in CBRN Agents Detection, Information and Energy Security*, NATO Science for Peace and Security Series A: Chemistry and Biology, DOI 10.1007/978-94-017-9697-2_52

Therefore, such a system is called smart personal environment (SPE). The SPE described in this paper, the active window, enables large area guiding of daylight in buildings by use of a MEMS technology, namely electrostatically actuated micromirror arrays [3]. They are placed in between the interspace of two window panes to protect them from external influences. The functional principle of the micromirror arrays and the active window is described below.

52.2 Active Windows

An active window is a SPE that uses electrostatically actuated micromirror arrays allows large-area daylight guiding in buildings. Such a micromirror array comprises several hundred thousand mirrors that can be actuated simultaneously. It is the smallest light-guiding unit of an activewindow which itself consists of several independently actuable micromirror arrays. This segmentation allows for very flexible light-steering that excels any conventional daylight-guiding system on the market. Enabling the system to tailor the ambience of the room to specific situations in an unprecedented way, the micromirror array segments of the active window provide various possibilities to block or guide light. These diverse possibilities require a SPE to utilize the full potential of such a active window. An example of such a SPE is depicted in Fig. 52.1. Sensors for temperature, light intensity, sun position, health-care and motion detection deliver the data to the networked control unit that manages the active window.

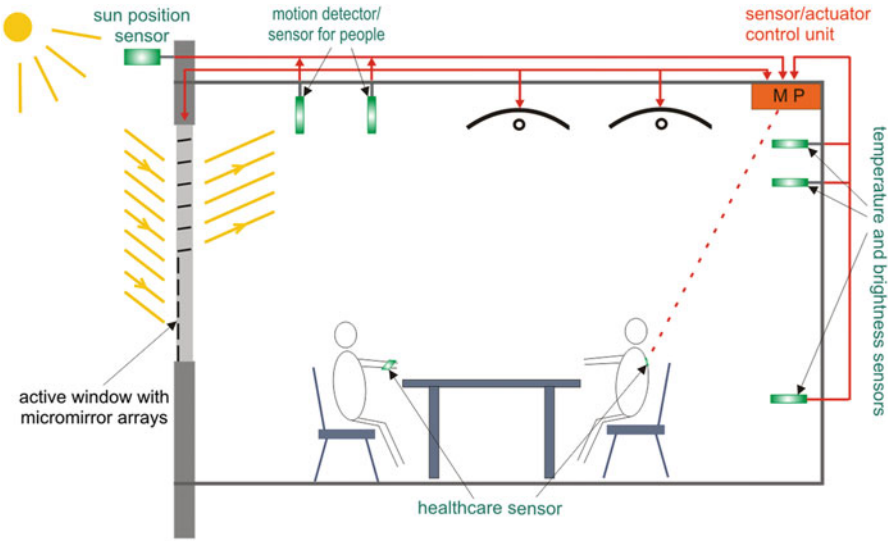

Fig. 52.1 Example of a SPE: The active windows are managed by a networked control unit processing the data collected by the sensors

Active windows improve the energy efficiency of buildings in several ways: Heat control (protection/input) thereby reducing the load on air-conditionings, support of heating units and reduction of the need of artificial light. In order to illustrate this, two scenarii are considered in the following.

52.2.1 Summer Scenario

The sunlight is blocked by the major part of the active window, thus keeping the room cool while the input of natural light can be maintained by opening some arrays in the upper part of the active window guiding light to the ceiling. The use of artificial light can be reduced resulting in additional energy saving and an improvement of the room atmosphere. In addition it has been proven that the presence of natural light has a positive influence on human physiology.

52.2.2 Winter Scenario

Light incidence is maximized to use the sunlight as a heating source while some micromirror arrays can be closed which avoids glaring people inside the room. Keeping the amount of natural light high in winter is also desirable for the aforementioned reasons. In addition the SPE can improve the room climate by monitoring the presence of people and their activities. An empty room can be exclusively optimized under energy saving aspects until a person enters. Then the human demands stand in the foreground of the automatic control.

A further aspect in favor of such a system is a high life-time, since nowadays windows are expected to last at least 30 years. This is achieved by placing the micromirror arrays in the space between the regular insulation or vacuum panes. The micromirrors themselves are long-term stable due to the well-known advantage of miniaturization: downscaling causes a change in the influence of fundamental forces [4]. Furthermore thin film technology requires very little resources in terms of required material. That makes the active window saving resources in comparison to e.g. macroscopic lamella systems. Active windows consume very little energy due to the electrostatic actuation principle of the micromirrors [5, 6]. A life cycle assessment of the micromirror arrays in comparison with an optimized conventional slat blind system has shown that the micromirror arrays require less primary energy [7].

52.3 Fabrication Method

The crucial point in designing a MEMS-based daylight guiding system that can compete with conventional systems on the market is to find a low-cost fabrication process. This challenge does not only involve the use of low-cost materials but also a

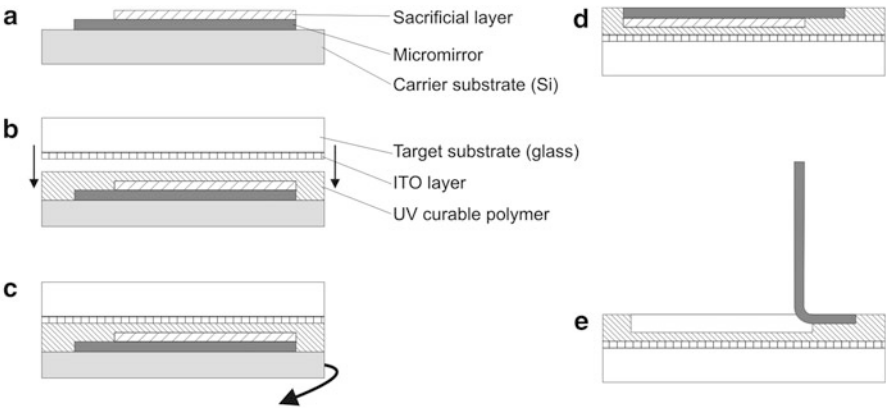

Fig. 52.2 Transfer print process for micromirror arrays: Deposition of a layer stack containing micromirrors and a sacrificial layer onto a Si-substrate (**a**), application of an UV-curable material (glue) and joining with the ITO glass (**b**), hardening of glue and removal of carrier substrate (**c**), transfer of the printed structure (**d**), release of the micromirror by removal of sacrificial layer (**e**)

reduction of the process steps and controllable processes compatible with standard production lines available in industry. Another big issue is the fact that the windows have not to be produced in a cleanroom environment which is necessary for the micromirror array fabrication. By separating micromirror and window production, introduction of the system to the market will be facilitated. To this end we propose a novel fabrication method for micromirror arrays called transfer printing.

This method involves transferring a layer stack from a carrier substrate to a target substrate. In the first step the layer stack is produced on the carrier. The carrier with the layer stack on it is then 'glued' to the glass. After hardening of the glue the carrier is removed leaving the layer stack on the target substrate [8].

The transfer printing process for the micromirror arrays is shown in Fig. 52.2. In the first step an aluminum layer is deposited on the carrier substrate. In the following a photolithography step creates the etch mask. Then wet etching is carried out; mirrors and electrical interconnections are formed. The sacrificial layer is deposited by spin coating and structured by photolithography (a). Then a diluted ultraviolet (UV) curable hybrid polymer (Ormocomp) is applied as 'glue' by spin-coating. Finally the whole layer stack is transferred to the target substrate, an ITO glass (b). After hardening the resist the carrier substrate is pulled off (c) and the layer stack remains on the ITO glass (d). This is possible due to the different adhesion properties of the materials. By removing the sacrificial layer the mirrors can be released (e).

52.4 Results

We were able to produce a micromirror layer stack and transfer it from a silicon wafer to ITO glass by using Ormocomp as a transfer medium. To ensure a successful transfer print of the whole layer stack the adhesion properties of the

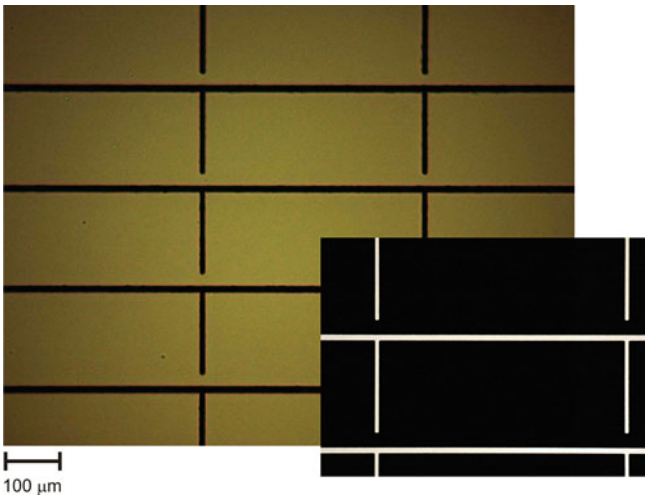

Fig. 52.3 Bright-field (*left*) and transmission (*right*) photomicrographs of transfer printed micromirror structures before release. The rectangles are the moveable mirror parts connected by conducting lines from left to right. The separations between the mirrors were created by wet etching causing minor transmission

utilized materials had to be adjusted. This has been achieved by applying an anti-sticking FDTS (1H,1H,2H,2H-Perfluorodecyltrichlorosilane) layer in order to reduce the adhesion between the silicon wafer and the mirror layer. Figure 52.3 shows the first result of transfer printed micromirror structures.

52.5 Outlook

The transfer print method is a very promising process to separate the production of the micromirrors from that of the windows. In future more investigations on the applicability on large areas (i.e. window size and larger) are required. This will involve further process optimizations and application of large-area processes (e. g. spray coating).

Acknowledgments The authors acknowledge funding by the European Union's 7th Framework Programme for research, technological development and demonstration under grant agreement no. 314578 MEM4WIN (www.mem4win.org).

References

1. Cook DJ, Das SK (2007) Pervasive Mob Comput 3:53
2. Nakashima H (Hrsg), Aghajan H (Hrsg), Augusto JC (eds) (2010) Handbook of ambient intelligence and smart environments, Springer US, Boston, p 1

3. Hillmer H, Schmid J, Stadler I Micromirror array. EP 1700152 B1; US 7,677,742 B2
4. Hillmer H, Daleiden J, Prott C, Römer F, Irmer S, Rangelov V, Tarraf A, Schüler S, Strassner M (2002) Appl Phys B Lasers Opt 75:3
5. Jäkel A, Li Q, Viereck V, Hillmer H (2011) In: Voß A (ed) Nanotechnology and energy. Pan Stanford Publishing, Singapore
6. Hillmer H et al (2014) Proceedings of the GlassCon 2014, Philadelphia, USA 7–10 July 2014
7. Viereck V et al (2011) Proceedings of the Solar World Congress 2011
8. Bergmair I et al (2011) Nanotechnology 22:325301

Chapter 53
Synthesis and Characterization of Novel Oxides as Active Material in Lithium Ion Batteries

D. Nicheva, T. Stankulov, D. Blyskova-Koshnicharova, E. Lefterova, O. Koleva, A. Momchilov, and T. Petkova

Abstract The aim of the present work is the synthesis and characterization of novel oxide materials in view of their potential use as active material in lithium ion batteries. Bulk materials from $(TiO_2)_x(V_2O_5)_y(P_2O_5)_{100-x-y}$ system, where $x = 5$, 10, 15 and $y = 60$, 70, were prepared by means of the melt quenching method. The materials were characterized by physical chemical and electrochemical methods, i.e. X-ray diffraction, infrared spectroscopy and cyclic voltammetry measurements. The electrochemical properties were investigated against metallic lithium as active materials in a half-cell system.

Keywords Phosphate glasses • Lithium ion batteries

53.1 Introduction

The limited amount of fossil fuels and growing environmental problem associated with their production and combustion leads to an continuously increasing need for renewable energy sources and storage methods. Lithium batteries (LIBs) are the systems of choice, offering high energy densities, flexible, lightweight design and longer lifespan than comparable battery technologies [1]. Besides high-power high-energy-density applications and, in addition vehicular transport, LIBs are also actively being considered for power tools, back-up power supply units, and off-peak energy storage (load leveling) from the electric grid for civil, but also for military supplies. For all these uses, LIBs need to satisfy four important criteria [2]:

D. Nicheva (✉) • T. Stankulov • D. Blyskova-Koshnicharova • E. Lefterova • O. Koleva
A. Momchilov • T. Petkova
Institute of Electrochemistry and Energy Systems Acad. E. Budevski,
Bulgarian Academy of Sciences, Bl.10 Acad. G. Bonchev Str., 1113 Sofia, Bulgaria
e-mail: denitza_vladimirova@abv.bg

P. Petkov et al. (eds.), *Nanoscience Advances in CBRN Agents Detection, Information and Energy Security*, NATO Science for Peace and Security Series A: Chemistry and Biology, DOI 10.1007/978-94-017-9697-2_53

(1) cost reduction, (2) improvement of the energy density from ~120 to ~250 Wh/kg, (3) safety-in-operation and (4) improvements of low- as well as high-temperature operation.

One way to achieve higher capacities is to use an electrode material in which the metal ion can change its oxidation state by two or more units. In this study we present the results of our investigation of the TiO_2-V_2O_5-P_2O_5 system in view of electrochemical application.

53.2 Experimental Details

Bulk materials from the $(TiO_2)_x(V_2O_5)_y(P_2O_5)_{100-x-y}$ system, where $x = 5, 10, 15$ % and $y = 60, 70$ %, were prepared by means of the melt quenching method from TiO_2 and V_2O_5 powders and liquid orthophosphoric acid H_3PO_4 as precursors. The initial materials were mixed for better homogenization, placed in a quartz crucible and melted in a high temperature furnace in air. The synthesis was carried out as follows: the temperature was increased stepwise to 1,200 °C, the melt was kept for 1.5 h at 1,200 °C and quenched between copper plates.

XRD analyses were performed by using a X-ray diffractometer model Philips APD-15. The data were collected at ambient temperature with a constant step of 0.02 deg·s^{-1} from angles $2\theta = 20 - 60°$ at the wavelength $\lambda = 1.54178$ Å using a CuKα tube. The structure of the materials was studied by means of an FTIR spectrometer model VARIAN 660-IR.

The electrodes were prepared by spreading them (one-side) on an Al foil. Electrodes consisting of 50 % (w/o) active materials and 50 wt% conductive binder (TAB2, teflonized acetylene black) were dried at 120 °C in a vacuum oven for 12 h and then pressed to enhance the contact between the active materials and the conductive carbons. Galvanostatic tests were carried out in a three-electrode half cell (the prototype of the 2032 button cell), using a metallic Li foil as both counter and reference electrode. The electrolyte used was 1 M $LiPF_6$ dissolved in a mixture of ethylene carbonate (EC) and dimethyl carbonate (DMC) (1:1 in vol.). The cells were assembled in a glove box under highly pure dry argon atmosphere. Cyclic voltammograms (CVs) were measured with an Autolab PSTAT 10 with a scan rate of 0.05 mV/s in the potential range from 1.5 to 3.5 V. Constant current (CC) tests were performed with the aid of an Arbin Instruments BT 2000. The capacities C of materials were based on the experimentally obtained data from the CV tests of the materials.

53.3 Results and Discussion

53.3.1 X-ray Diffraction Analysis

The XRD analyses used to prove the nature of the samples show that $(TiO_2)_5(V_2O_5)_{70}(P_2O_5)_{25}$ and $(TiO_2)_{15}(V_2O_5)_{70}(P_2O_5)_{15}$ compounds are amorphous (Fig. 53.1a). The diffractogram of $(TiO_2)_{10}(V_2O_5)_{60}(P_2O_5)_{30}$ (Fig. 53.1b) displays

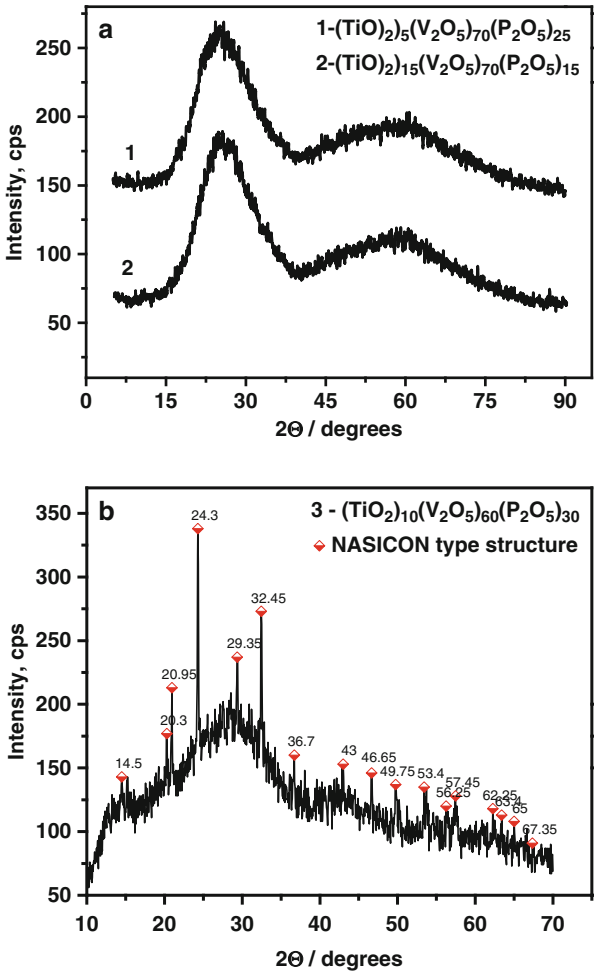

Fig. 53.1 XRD diffractograms of (**a**): $(TiO_2)_5(V_2O_5)_{70}(P_2O_5)_{25}$ (*1*), $(TiO_2)_{15}(V_2O_5)_{70}(P_2O_5)_{15}$ (*2*) and (**b**): $(TiO_2)_{10}(V_2O_5)_{60}(P_2O_5)_{30}$ (*3*)

amorphous an halo and weak peaks indicating crystalline phases distributed in the amorphous oxide matrix. The peaks positions are very similar to those of $Ti_4P_6O_{23}$, $NaTi_2(PO_4)_3$ and $NaVTi(PO_4)_3$. These peaks validate the presence a NASICON type structure (Na super ionic conductor) in the samples of this study [3, 4].

53.3.2 Infrared Study

Infrared spectra of $(TiO_2)_x(V_2O_5)_y(P_2O_5)_{100-x-y}$ glassy system are presented in Fig. 53.2. The band at 1,005 cm^{-1} can be attributed both to VO_5-groups and to isolated PO_4^{3-} (Q^0) phosphate groups observed for $(TiO_2)_5(V_2O_5)_{70}(P_2O_5)_{25}$ and $(TiO_2)_{15}(V_2O_5)_{70}(P_2O_5)_{15}$ glasses. The band splits into two peaks located

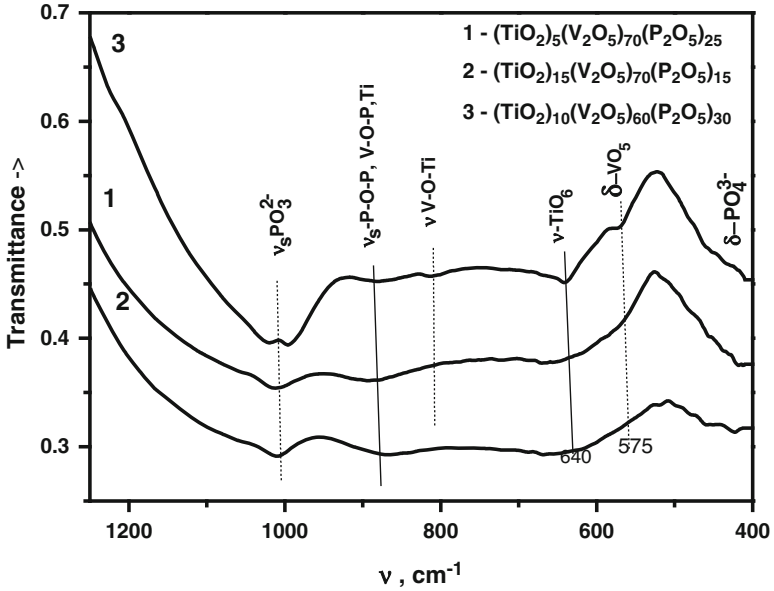

Fig. 53.2 Infrared spectra of $(TiO_2)_x(V_2O_5)_y(P_2O_5)_{100-x-y}$ glassy sample

at 990 and 1,020 cm^{-1} with increasing TiO_2 and P_2O_5 content probably due to the appearance of VO_4 groups that occupy octahedral positions in the NASICON structure.

The wide absorption band between 600 and 670 cm^{-1} originates from TiO_6 octahedra, while absorption below 600 cm^{-1} is due to bending vibrations of VO_5-groups and to the network vibrations.

Three other bands located at 640, 575 and 811 cm^{-1} are indicated. We can very likely assign the 640 cm^{-1} band to TiO_6 groups as part of the NASICON structure, the 811 cm^{-1} mode might be attributed to mixed V-O-Ti bonds.

The structure of phosphate glasses might be considered as a polymeric network composed of tetrahedral $[PO_4]$ groups. The structure is usually determined by Q^n molecules, where n stands for the number of bridged oxygen atoms in a tetrahedron. Depending on the [O]/[P] ratio phosphor-containing amorphous materials can be composed of: (a) a network of Q^3 tetrahedra (in glassy P_2O_5) with asymmetric stretching vibrations of the P=O bond at ~1,270 cm^{-1}, (b) polymeric metaphosphate chains of Q^2 tetrahedra $(PO_2)^-$ with asymmetric bond vibrations at ~1,280 cm^{-1} and symmetric stretching vibrations at 1,100 cm^{-1}, (c) "inverted" glasses, based on Q^1 with a structural unit of $(PO_3)^{2-}$ groups with stretching vibrations at ~1,050 cm^{-1}, and (d) orthophosphate Q^0 with the main structural group of $(PO_4)^{3-}$ tetrahedra the stretching of which is located at 1,000 cm^{-1}. Addition of TiO_2 to the phosphate glasses enhances the glass forming ability, chemical stability and compactness of the structure. TiO_2 as glass modifyer contributes to the appearance of non-bridged oxygen atoms in the glass and

depolymerization of the phosphate network after distortion of the P-O-P bridge structure. The IR spectra of glassy and crystalline V_2O_5 are comparable with difference in the peak sharpness. They consist of deformed trigonal bi-pyramids of VO_5 groups with one vanadium ion in the center of the polyhedron and one shorter V=O (vanadyl) bond.

The results of the IR study show that the material is composed of TiO_6 octahedron connected to six PO_4 tetrahedra building a NASICON structure. They form 3D interconnected channels with two types of empty positions occupied to some extent by VO_5 groups. The existence of VO_5 groups and isolated PO_4^{3-} (Q^0) structural units, as well as TiO_6-octahedra was proven for all materials. When the TiO_2 and P_2O_5 content increases, new structural unit of VO_4 groups are formed.

53.3.3 Electrochemical Investigations

The CV-curves of the electrodes under study are presented in Fig. 53.3. The peak appearing at potentials of about 2.5 V in the CV curve can be assigned to some structural reorganisation in the compounds. The effect has been ascribed to different factors, including structural effects after reduction of V^{5+} to V^{4+} and lithium incorporation into the structure (electrochemical lithiation). We assume that probably lithium ions occupy the empty positions in the NASICON structure or/and form new bonds.

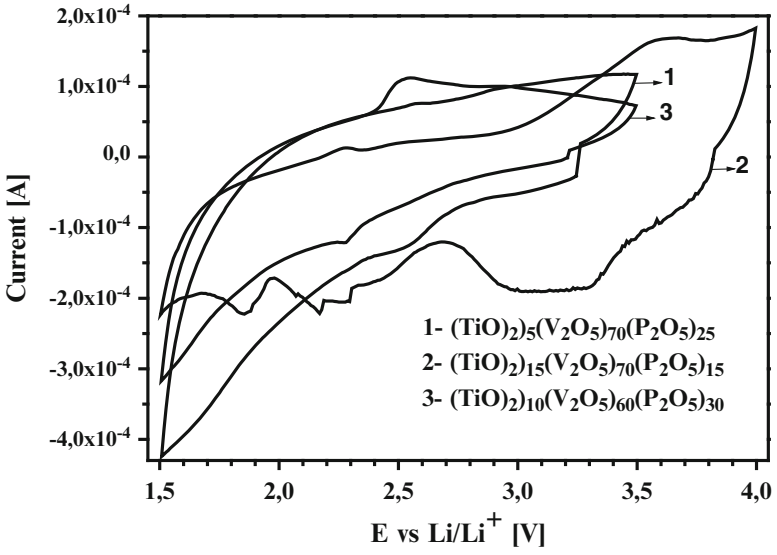

Fig. 53.3 Cyclic voltammogram curves of the materials with a scan rate of 0.05 mV/s

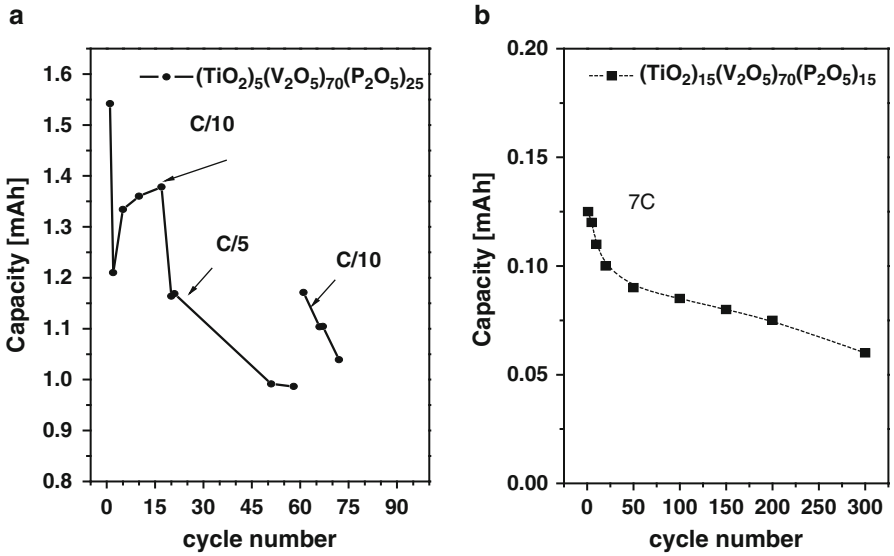

Fig. 53.4 Discharge capacity vs. cycle number of (**a**) $(TiO_2)_5(V_2O_5)_{70}(P_2O_5)_{25}$ and (**b**) $(TiO_2)_{15}(V_2O_5)_{70}(P_2O_5)_{15}$ for various C-rates

The electrochemical lithiation of $(TiO_2)_5(V_2O_5)_{70}(P_2O_5)_{25}$ shows 38 % increase during the first CV cycle; the increase is higher after the second (79 %) and the third cycle (93 %).

The discharge capacity of the $(TiO_2)_5(V_2O_5)_{70}(P_2O_5)_{25}$ was tested at various current rates (Fig. 53.4a). The material shows a stable capacity after 15 cycles with a C/10-rate (the C-rate is a standard charge-discharge regime for electrochemical power sources, where the current is expressed by means of the electrode capacity). The capacity increases by 23 %, analogous to that observed in the CV test, and decreases by 16 % during the further study with a current of C/5 rate.

The CV results of the $(TiO_2)_{15}(V_2O_5)_{70}(P_2O_5)_{15}$ compound (Fig. 53.3) shows electrochemical activity of the material above 4.0 V. To this end CC cycling tests were carried out with a high current of 7C (Fig. 53.4b). The results reveal a capacity of 12.5 % obtained from CV test. The material lost 28 % of the capacity after 50 cycles, 11 % during the next 100–200 cycles, and 20 % during the cycles 200–300.

53.4 Conclusions

Bulk materials from $(TiO_2)_x(V_2O_5)_y(P_2O_5)_{100-x-y}$ system, where $x = 5$, 10, 15 and $y = 60$, 70 were synthesized and characterized. It was found that $(TiO_2)_5(V_2O_5)_{70}(P_2O_5)_{25}$ and $(TiO_2)_{15}(V_2O_5)_{70}(P_2O_5)_{15}$ are amorphous, while $(TiO_2)_{10}(V_2O_5)_{60}(P_2O_5)_{30}$ consists of an amorphous matrix with nanocrystals of the NASICON type. IR investigation showed the presence of VO_5 groups and

isolated PO_4^{3-} (Q^0) structural units, as well as TiO_6-octahedra in all materials. When the TiO_2 and P_2O_5 content increases, new structural units of VO_4 groups are formed. The electrochemical properties were investigated against metallic lithium as active materials in a half-cell system. The results show that the studied oxides possess rechargeable Li intercalation due to the presence of V_2O_5. The $(TiO_2)_{15}(V_2O_5)_{70}(P_2O_5)_{15}$ compound has an electrochemical activity at 4 V, i.e. the material is suitable for application as active element in high voltage lithium-ion batteries.

References

1. Van Schalkwijk W, Scrosati B (eds) (2002) Advances in lithium-ion batteries. Springer, Berlin
2. Reddy MV, Subba Rao GV, Chowdari BV (2013) Chem Rev 113:5364
3. Agaskar PA, Grasselli RK, Butterey DJ, White B (1997) In: Oyama ST, Gaffney AM, Lyons JE, Grasselli RK (eds) Third World Congress on Oxidation Catalysis. Elsevier, Amsterdam, p 219
4. Dimitrov V, Dimitriev Y (2009) Structural analysis. UCTM, Sofia

Chapter 54
Quantum Information Technology Based on Diamond: A Step Towards Secure Information Transfer

Cyril Popov, Emil Petkov, Christo Petkov, Florian Schnabel, Johann Peter Reithmaier, Boris Naydenov, and Fedor Jelezko

Abstract The new field of quantum information technology uses qubits (quantum bits) instead of classical bits to carry out certain computation operations or for secure transfer of information (quantum cryptography). There are a number of physical systems that can act as qubits including a wide range of materials and technologies, e.g. ions in traps, local defect states in crystal lattices, superconducting junctions, etc. All these material systems offer different challenges and opportunities for the creation of qubit-based quantum devices. The search for defect states in solids with a capability to store and manipulate quantum information represents a exciting area of research. One of the most promising (and maybe the best studied) defects are the so-called nitrogen-vacancy (NV) centers in diamond, which are perspective candidates for a number of applications, including quantum computation and cryptography. A NV center represents a nitrogen atom in the diamond crystalline lattice adjacent to a vacancy, i.e. a site with a missing carbon atom. The attractiveness of this system stems from the long-lived quantum coherence, which can be initialized, acted upon, and measured using readily available techniques. A particularly exciting feature of these defects is the persistence of long coherence times even at room temperature. Single NV centers can be patterned on demand, and much like atomic defects surrounded by a stable environment (the crystalline lattice), they have highly reproducible properties. In order to exploit the outstanding properties of NV centers by increasing both the photon emission yield and the collection efficiency of the emitted photons, they should be embedded in an optical cavity, e.g. in all-diamond devices like nanopillars, photonic crystals, microrings, etc.

Keywords Quantum cryptography • NV centers • Diamond nanostructures

C. Popov (✉) • E. Petkov • C. Petkov • F. Schnabel • J.P. Reithmaier
Institute of Nanostructure Technologies and Analytics, University of Kassel, Kassel, Germany
e-mail: popov@ina.uni-kassel.de

B. Naydenov • F. Jelezko
Institute of Quantum Optics, University of Ulm, Ulm, Germany

P. Petkov et al. (eds.), *Nanoscience Advances in CBRN Agents Detection, Information and Energy Security*, NATO Science for Peace and Security Series A: Chemistry and Biology, DOI 10.1007/978-94-017-9697-2_54

54.1 Cryptography – From Substitution Ciphers to Flying Qubits

Cryptography (from Greek κρυπτοσ, "hidden, secret", and γραφειν, "writing") is the practice of techniques for secure communication in the presence of third parties. Being almost as old as the written language itself, the earliest examples of encryption, i.e. the conversion of a readable plain text into an apparently meaningless ciphered one, dated thousands of years ago. One example is the so-called *Caesar cipher* used by Julius Caesar to communicate with his generals which represents an alphabetic substitution cipher, in which each letter is replaced by another one that follows a given number of places after it in the alphabet. The code (the number of shifting places) for reading of the encrypted messages was shared only with the intended recipients. Prior to modern times, the cryptography was based in general mainly on substitutions and permutations.

The modern cryptography, starting after the end of World War II, is predominantly based on mathematical theory and computer science. Historically it included several stages, e.g. the application of symmetric-key cryptosystems using the same key for encryption and decryption of the messages or of asymmetric ones with a public key for encryption and a private ("secret") one for decryption. The designed cryptographic algorithms were becoming more and more complex and considered as computationally secure, i.e. they are secure due to the limited computational power. Since the mid-1980s a new era of cryptography started, that of quantum cryptography.

Quantum cryptography implies quantum mechanical effects to perform cryptographic tasks or to break cryptographic keys. The most developed application of quantum cryptography is the quantum key distribution (QKD), the process of using quantum communication to establish a shared key between two parties. Any attempt for reading or copying the quantum key from third parties will change (disturbed) it and will be noticed by the communicating parties. The quantum communication uses quantum bits (the so-called "qubits") in place of the classical bits. Qubits represent a two-state quantum system, where each state is described by a wave function. In a coupled two-potential well system the ground state $|0>$ is symmetric, the higher energy state $|1>$ is asymmetric. Such two-level systems can be represented by spin states of electrons, nuclear spins in molecules, electronic states in quantum dots, electron-photon states in resonators, atoms or ions in magnetic fields (in traps), the charge states in nanostructured superconductors, etc. The material platforms for qubits include nanostructures of III-V and IV-IV semiconductors (quantum dots, nanowires), ions in traps, local defect states in crystal structures (for details see Ref. [1]). Each of them have to address a number of challenges related e.g. to the coherence time and the ability for coupling, which are objects of intensive research.

The current contribution is dedicated to one of the most studied defect states, namely the nitrogen-vacancy (NV) centers in diamond. Single NV centers can be prepared on demand and exhibit very reproducible properties, like long coherence times even at room temperature. The quantum coherence can be initialized, changed and read out with already available techniques.

54.2 Diamond and Its NV Centers

Diamond possesses various unique properties such as an extreme hardness, a low friction coefficient, chemical inertness, a high electrical resistance, an excellent thermal conductivity and good biocompatibility [2]. Upon doping it becomes a large band-gap semiconductor with extremely high breakdown voltages and high carrier mobilities. It is transparent over a wide wavelength range from UV to far IR and can withstand high electromagnetic radiation power fluxes from X-ray or laser sources. These outstanding properties make diamond of potential interest for a wide spectrum of applications including wear resistive and transparent protective coatings for optical components, heat spreaders, novel semiconductor devices, etc. This holds for all forms of diamond: monocrystalline (natural or artificial) and poly- (PCD), nano- (NCD) and ultrananocrystalline (UNCD) films. In the last decade diamond has emerged also as a unique platform for novel applications, e.g. in quantum information technology (QIT) or in magnetometry on a nanoscale, using one of the most common luminescent defects in its lattice, namely the nitrogen–vacancy (NV) color centers.

Pure diamond is composed only of carbon atoms in sp^3-hybridization arranged in a face-centered cubic crystal lattice. However, diamond can include some impurities, the most important of them being nitrogen and boron since they can occupy positions in the diamond lattice replacing the carbon atoms. This is the reason why the diamond type classification is based on the presence or absence of these elements. There are four major types of diamond: type Ia (with aggregated N impurities), type Ib (with isolated N impurities), type IIa (without N or B impurities) and type IIb (with B impurities) [3]. The same classification holds for synthetic diamonds prepared by the so-called high-pressure high-temperature (HPHT) method. It is based on the conversion of graphite in the presence of metal catalysts (Ni, Fe, Co) at pressures of several GPa (i.e. several ten thousands atmospheres) and temperatures usually on the order of 1,500 °C. Further, diamond in the form of films can be prepared by chemical vapor deposition (CVD) which is performed under low-pressure and moderate-temperature conditions. Generally hydrocarbons, e.g. mixtures of methane (CH_4) and hydrogen (H_2), are used as precursors, which are introduced at low pressures (1–30 kPa) into a reactor, and activated by hot filaments, microwave plasmas, arc discharges or laser beams, leading to the deposition of diamond films on substrates heated to temperatures of 500–1,000 °C. Depending on the deposition conditions (gas phase composition, substrate temperature, etc.) and the pre-treatment process (necessary to enhance the nucleation of diamond on non-diamond substrates), diamond films with different crystallite sizes (PCD, NCD and UNCD films) can be obtained [4].

The diamond coatings discussed in this chapter, namely NCD films, as well as single diamond nanocrystallites were grown by hot-filament CVD (HFCVD) from gas mixtures containing 1 % CH_4 in H_2. A set-up using seven parallel tungsten filaments of 0.3 mm was employed which is capable to coat 3-inch silicon wafers homogeneously; a scheme of the HFCVD set-up is given in Fig. 54.1. The substrate

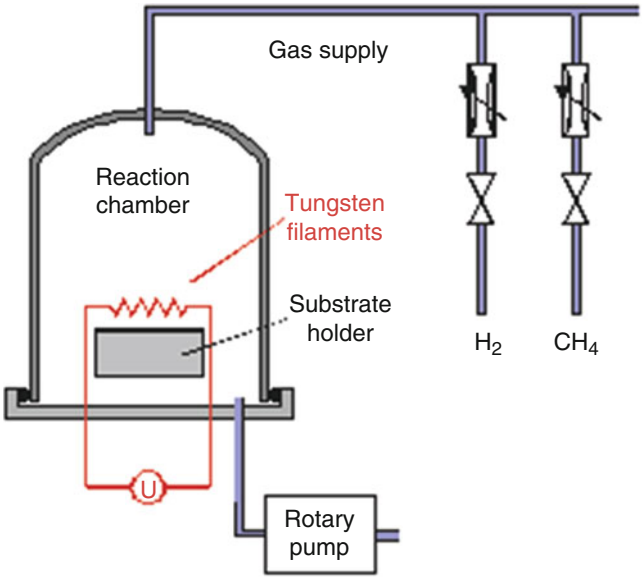

Fig. 54.1 Scheme of the HFCVD set-up

temperature was kept at 870–900 °C, the working pressure was 2.5 kPa, the filament temperature >2,000 °C and the deposition time 180 min for the NCD films and 15 or 30 min for the diamond nanocrystallites. The films deposited under the above conditions were typically 900–1,000 nm thick. Monocrystalline Si wafers were used as substrates after ultrasonic pretreatment in a suspension containing diamond powders with different grain sizes (ultra-disperse diamond powder with a grain size of 3–5 nm and nanodiamond powder with an average grain size of 250 nm) in order to control the nucleation density: a high nucleation density ($>10^{10}$ cm^{-2}) was achieved for the NCD layers when a mixture of both diamond fractions mentioned above was used in the pretreatment suspension, and a low one (ca. 10^8 cm^{-2}) for the individual diamond nanocrystallites applying only the nanodiamond powder. The usual duration of the pretreatment was 1 h, followed by ultrasonic cleaning in acetone and isopropanol.

The quality of the nanocrystalline diamond films prepared by HFCVD were investigated by atomic force microscopy (AFM), scanning electron microscopy (SEM), X-ray diffraction (XRD) and Raman spectroscopy. The AFM images (Fig. 54.2) reveal that the topography is clearly dominated by facetted diamond crystallites. Owing to the low film thickness and the high nucleation density, the crystallite size is on the order of a few hundred nm, the rms roughness in the range of 20–26 nm. The top-view and cross-section SEM micrographs (Fig. 54.3) reveal well-defined facetted crystals grown upwards from the nucleation sites on the silicon surface.

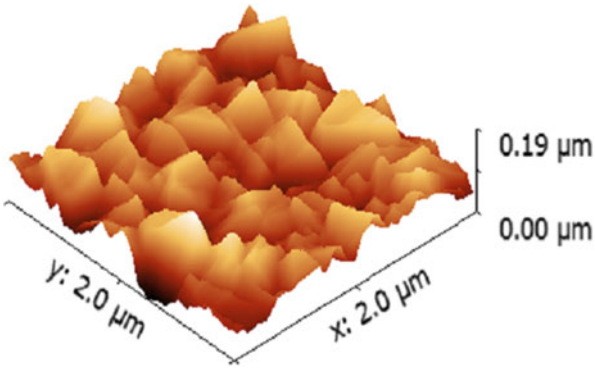

Fig. 54.2 Typical AFM image of NCD film

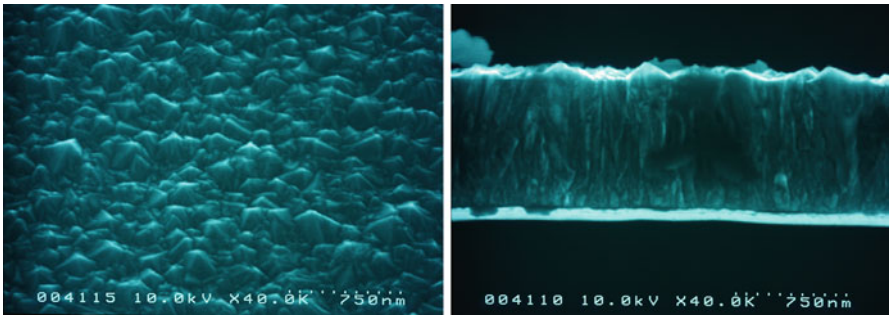

Fig. 54.3 SEM micrographs of the NCD films: top-view (*left*) and cross-section (*right*)

The XRD spectrum exhibits the (111) and (220) diffractions peaks of diamond at $2\theta = 44.0°$ and 75.4°, respectively, in correspondence with JCPDS card 6-675 (Fig. 54.4) revealing that the films are free of stress. The intensity ration I_{220}/I_{111} is much lower than 0.25 (according to the JCPDS card) meaning that the films are dominated by a {111} texture which is in accordance with the pyramidal facets visible in the SEM images in Fig. 54.3. Finally, the Raman spectrum of the films, taken with excitation wavelength of 488 nm, shows the characteristic diamond peak at 1,332 cm^{-1} together with a broad peak around 1,550 cm^{-1} originating from a non-diamond sp^2-bonded phase in the grain boundary material (Fig. 54.5).

Since the Raman sensitivity for sp^2-carbon is roughly 50 times higher than that of diamond [5], it can be concluded that although containing some sp^2-bonded carbon material, the deposited films consist predominantly of diamond. Comparing the results from Figs. 54.3, 54.4, and 54.5 with the definition of diamond films [6], it is evident that the films deposited under the above mentioned conditions are polycrystalline diamond films, in our case NCD films due to the relatively high nucleation density and the reduced lateral size of the crystallites.

The creation of NV centers in diamond can be accomplished by ion implantation either starting from nitrogen-rich native Ib type diamond implanting for example

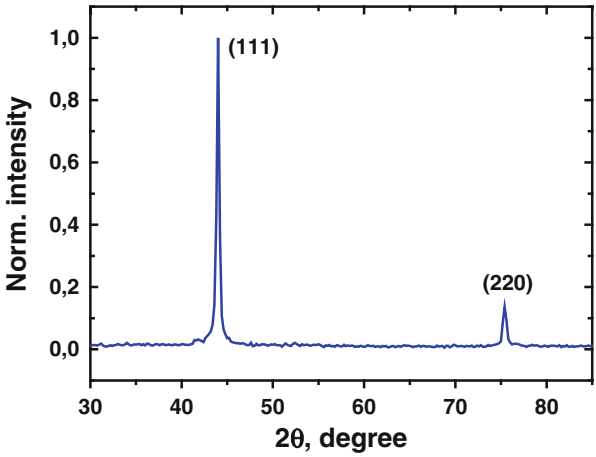

Fig. 54.4 Typical XRD pattern of NCD film

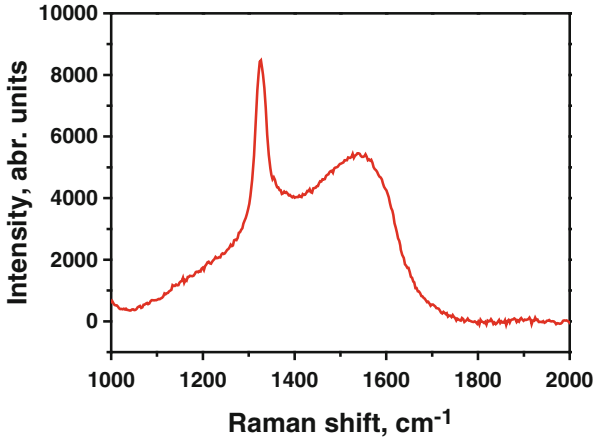

Fig. 54.5 Raman spectrum of NCD film

gallium, carbon or helium to generate vacancies, or from nitrogen-poor IIa type diamond implanting nitrogen ions, which additionally create vacancies along their tracks. In both cases, subsequent annealing above 600 °C is required to enhance the migrations of the vacancies towards the substitutional N sites in the diamond lattice and hence the formation of NV centers. However, NV centers can be incorporated in the diamond lattice during the growth relying on the background nitrogen pressure in the deposition chamber (exploited in our investigations) or by introduction of nitrogen for a short time during the growth (delta-doping). The nitrogen incorporation within the diamond films during their growth was studied by time-of-flight secondary ion mass spectrometry (ToF-SIMS) which showed an equal distribution through the whole depth (Fig. 54.6).

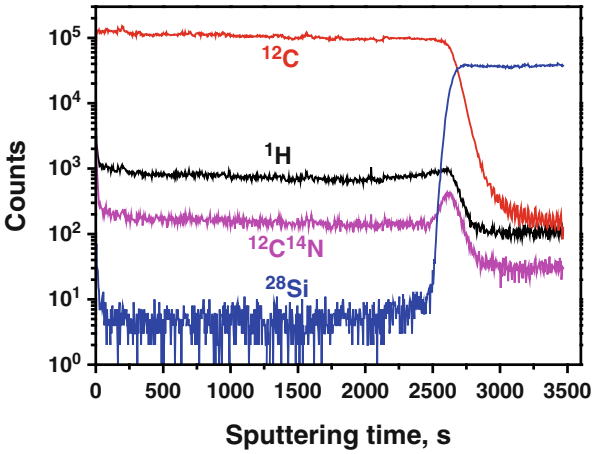

Fig. 54.6 SIMS depth profiles of registered species in NCD

54.3 Properties of NV Centers

There are several hundred known optical defect centers in diamond [7], but most of them have not been yet observed as single sites. One notable exception is the NV center in diamond, the crystal structure of which is shown in Fig. 54.7(a). This defect has attracted the attention of many research groups during the last decade, due to its unique properties. The energy level diagram of the NV is shown in Fig. 54.7(b).

It consists of a triple ground and excited states, which are connect by an optical transition. The center can be excited non-resonantly with a green laser (usually at 532 nm) and a broad red shifted emission is observed [8] (see Fig. 54.8(a)). The fluorescence is so intense that single NV centers can be observed even at room temperature. The most interesting feature of this color center is that its fluorescence depends on the electron spin state m_s of the ground state. If the center is in the state $m_s = 0$, the laser will excite it and then fluorescence will be emitted. However, if the NV center is in the $m_s = 1$ (or $m_s = -1$) state, then there is a certain probability of decay via the singlet states $^1A_1$ and ^1E. From the latter, the population decays only to the $m_s = 0$ state.

Thus we can perform electron spin resonance (ESR) with single spins, in this case the so-called optically detected magnetic resonance (ODMR) [9]. As the ODMR transition can be shifted by applying a static magnetic field (see Fig. 54.8 right), the NV center can be used as an atomic sized magnetometer [10, 11]. Its sensitivity is limited by the coherence time, but the latter is very long for this solid state quantum system [12].

The NV center is a single quantum emitter [13], which makes it a candidate for a single photon source for QKD and quantum communication applications. The first commercial device is already available [14]. Although this quantum

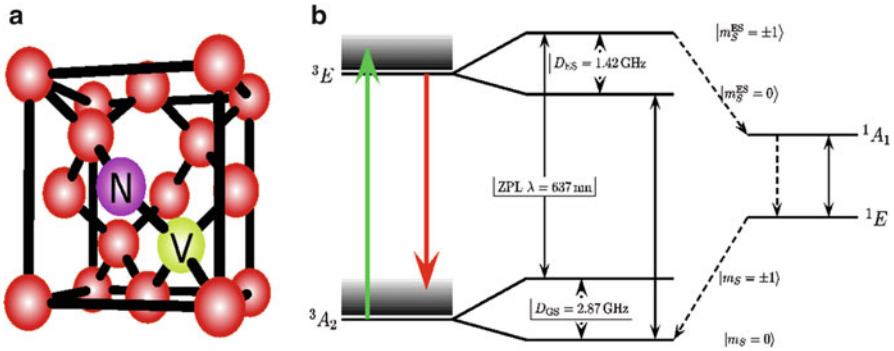

Fig. 54.7 (**a**) Crystal structure of the NV center in diamond. (**b**) Energy level scheme of the NV center

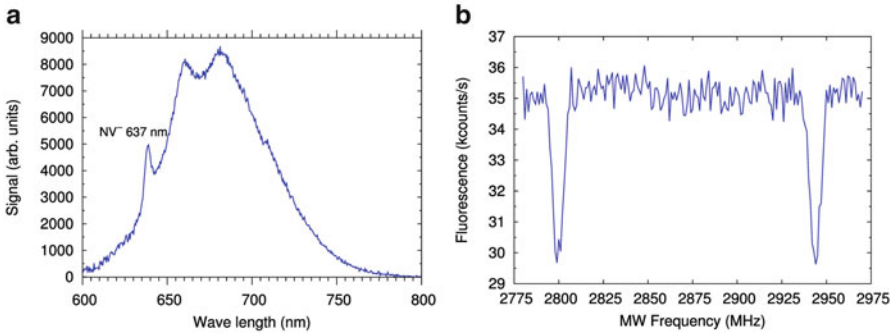

Fig. 54.8 (**a**) Fluorescence spectrum of a single negatively charged NV center in diamond. (**b**) ODMR spectrum of a single NV center. The splitting between the two resonance lines is proportional to the applied constant magnetic field

system seems to be very promising, there are still some experimental limitations part of which have already been solved during the last decade. Firstly, the emission of the NV is only about 4 % in the zero phonon line (ZPL), so most of the emitted photons cannot be used for QIT applications. The solution to this problem is to use photonic devices (see the next section), which can increase the emission in a desired part of the spectrum. The second disadvantage of the NV centers is that the optical resonance varies from center to center, so it will be difficult to entangle two NVs (which is required for QIT protocols) as indistinguishable photons are required. The latter problem has been solved by tuning the NV resonance by applying external electric fields and using the Stark shift [15]. Combing these two methods two photon interference [16] and entanglement between two remote NVs has been demonstrated [17].

54.4 All-Diamond Photonic Devices

In order to exploit the outstanding properties of the NV centers by increasing the emission yield of photons and the collection efficiency of the emitted photons, the NV centers should be embedded in an optical cavity, like nanopillars [18], photonic crystals [19], microrings [20], etc. The materials of choice for the fabrication of the cavities are quartz, III-V semiconductors, but also diamond (the so-called all-diamond devices). In the latter cases either N implantation is implemented before or after the structuring for the formation of the NV centers or they were incorporated during diamond growth, like in our case. The fabricated 1-D and 2-D structures possess the extreme mechanical, thermal, optical and electrical properties of diamond; they also have the advantage of a great surface-volume ratio, which is of importance for the quantum information technology [18], but also for other novel high-tech applications, e.g. in nanobiotechnology.

Most of the diamond nanostructures are fabricated using different "top-down" techniques including lithography and dry etching. Several studies have been reported on the dry etching of diamond, including ion-beam etching (IBE) [21, 22] and reactive ion etching (RIE) [23, 24]; disadvantage of these methods are the low etch rates. Much higher etch rates of up to ca. 200 nm/min have been achieved by electron cyclotron resonance plasma (ECR) [25] and inductively coupled plasma (ICP) etching [26]. In our work we have implemented electron beam lithography (EBL) and ICP-RIE for the fabrication of diamond nanopillars and two-dimensional photonic crystals. Diamond nanopillars with different diameters (from 1 μm down to 50 nm) were etched from nanocrystalline diamond films (thickness on the order of 700–900 nm) using two different hard masks, either SiO_2 or gold.

The fabrication process with a SiO_2 mask included the following steps (as shown in Fig. 54.9): (a) deposition of a 250 nm SiO_2 layer as a hard mask, (b) deposition of the resist; (c) electron beam lithography definition of the nanopillars in the resist; (d) reactive ion etching (RIE) of the SiO_2 mask with CHF_3 (3 sccm) and Ar (5 sccm) at a RF power of 230 W and working pressure of 19 mTorr. When a hard Au mask was used the process included: (a) deposition of the resist; (b) electron beam lithography definition of the nanopillars in the resist; (c) evaporation of 5 nm Ti (adhesive layer) and 200 nm Au; (d) lift-off process with N-Methyl-2-pyrrolidone.

After the mask definition, irrespective of the material, ICP-RIE of the diamond nanopillars with oxygen followed. The experimental conditions for this final step were optimized with respect to the RF power applied to the substrate holder to generate a bias voltage (varied between 50 and 300 W), the ICP power (from 500 to 2,000 W), the O_2 flow (between 10 and 40 sccm) and the working pressure (from 5 to 15 mTorr). The etching rate was monitored *in situ* by an interferometer.

The dependence of the etching rate on the parameters has been also investigated. The etching rate basically depends on the ICP and RF powers. Higher powers lead to faster material removal, but on the other hand too high values cause mask degradation and worsening of the quality of the pillar walls. The etching rate is proportional to the oxygen flow, i.e. the oxygen concentration, as a result of kinetic

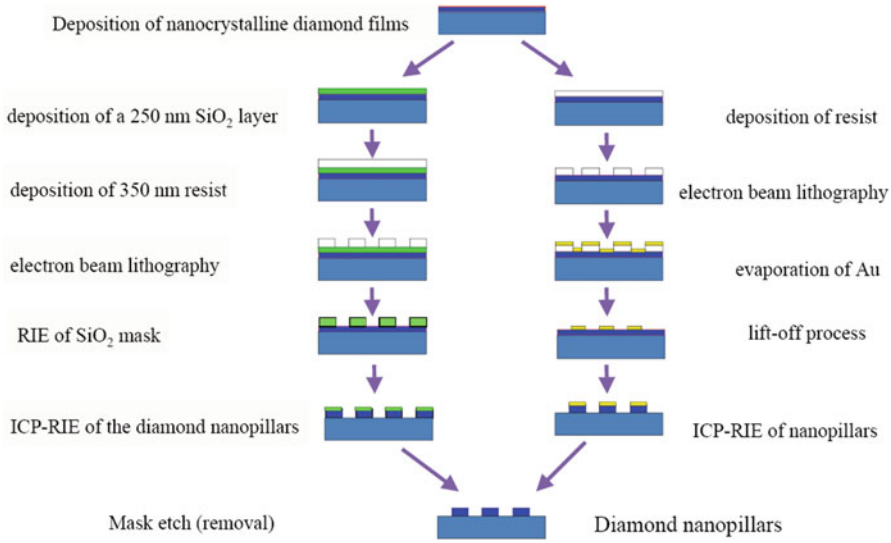

Fig. 54.9 Technological steps for fabrication of diamond nanopillars applying SiO_2 and Au hard masks

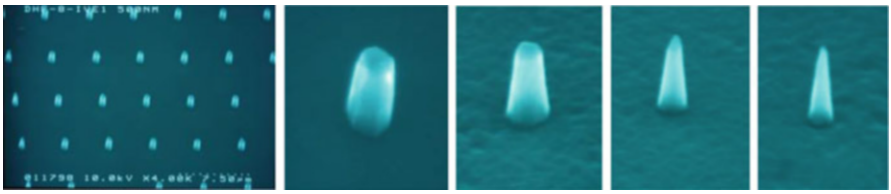

Fig. 54.10 Array of diamond nanopilars and single nanopillars with a diameter of 500, 200, 100 and 50 nm

effects. The etching rate is reverse proportional to the working pressure, because at higher pressures the mean free path of ions is reduced due to collisions, and they loose partially their energy. The next factor on which the etching rate depends is the mask material. The rate for the optimal etching recipe (with respect to the quality of the nanopillars) was 73 nm/min using SiO_2 masks and 112 nm/min for gold masks. In general, the highest etching rate achieved was 200 nm/min, but in this case the quality of the pillar walls was low. The larger pillars fabricated with a Au mask and the optimized etching conditions showed a good quality with smooth and vertical walls, but with decreasing the diameter the pillars became tapered, especially with nominal diameters of 100 and 50 nm due to degradation of the hard mask (Fig. 54.10).

The results obtained by structuring of the diamond nanopillars were used as a starting point for the fabrication of two-dimensional diamond nanostructures,

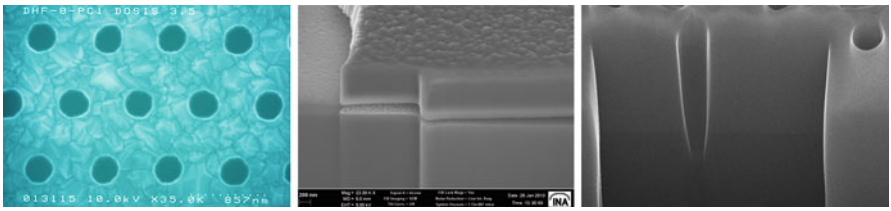

Fig. 54.11 Top-view SEM image of PC in NCD film (*left*), diamond membrane fabricated from NCD (*middle*) and cross-section view of the holes after FIB cut (*right*)

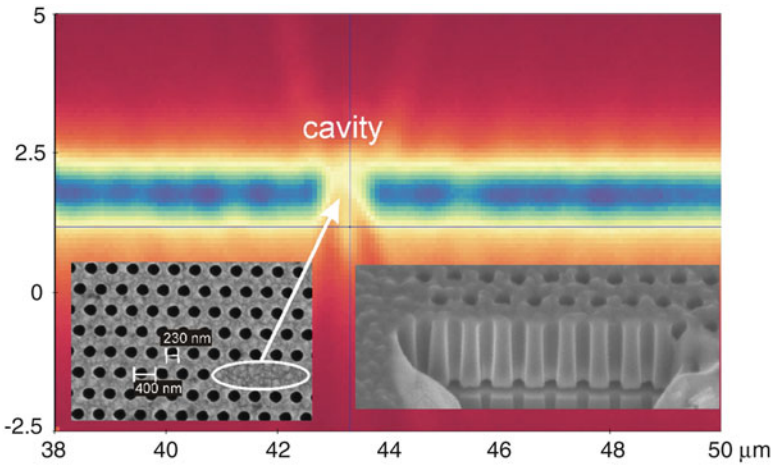

Fig. 54.12 Fluorescence signal of a PC in diamond membrane with a thickness of 750 nm

e.g. photonic crystals (PCs). The integration of NV centers in PCs should increase both the photon emission yield and the collection efficiency of the emitted photons. For this purpose the optimized etching process as described above was also applied for the fabrication of photonic crystals in NCD (Fig. 54.11, left). The process included the deposition of SiO_2 as a hard mask, as the application of gold for this purpose followed by a lift-off step did not give satisfactory results. The PC structure was defined in the resist by EBL followed by RIE of the mask with a mixture of CHF_3 and Ar, and ICP-RIE of the underlaying NCD with oxygen. For the fabrication of a free-standing membrane the NCD film was deposited on sacrificial SiO_2 layers with thicknesses from 150 to 1,000 nm. After opening of holes in the NCD layer using lithography the sacrificial layer was removed by wet chemical etching in NH_4F:HF solution for the formation of the membrane (Fig. 54.11, middle). The cross-sectional SEM images of the holes in NCD reveal smooth and vertical sidewalls with a tilt angle of 2.8° (Fig. 54.11, right). The fabricated PC resonators were optically characterized by fluorescence mapping (Fig. 54.12).

Acknowledgements The authors gratefully acknowledge the German Federal Ministry of Education and Research (BMBF) for the financial support under the Project "Q.com".

References

1. Eckstein JN, Levy J (2013) MRS Bull 38:783
2. Kulisch W (1999) Deposition of superhard diamond-like materials, Springer, tracts on modern physics. Springer, Heidelberg/Berlin
3. Breeding CM, Shigley JE (2009) Gems Gemol 45:96
4. Kulisch W, Popov C (2006) Phys Status Solidi (A) 203:203
5. Nemanich RJ, Glass JT, Lucovsky G, Schroder RE (1988) J Vac Sci Technol A 6:1783
6. Messier R, Badzian AR, Badzian T, Spear KE, Bachman P, Roy R (1987) Thin Solid Films 153:1
7. Zaitzev A (2001) Optical properties of diamond. Springer, Berlin/Heidelberg
8. Doherty MW, Manson NB, Delaney P, Jelezko F, Wrachtrup J, Hollenberg LCL (2013) Phys Rep 528:1
9. Gruber A, Drabenstedt A, Tietz C, Fleury L, Wrachtrup J, von Borczyskowski C (1997) Science 276:2012
10. Balasubramanian G, Chan IY, Kolesov R, Al-Hmoud M, Tisler J, Shin C, Kim C, Wojcik A, Hemmer PR, Krueger A, Hanke T, Leitenstorfer A, Bratschitsch R, Jelezko F, Wrachtrup J (2008) Nature 455:648
11. Maze JR, Stanwix PL, Hodges JS, Hong S, Taylor JM, Cappellaro P, Jiang L, Gurudev Dutt MV, Togan E, Zibrov AS, Yacoby A, Walsworth RL, Lukin MD (2008) Nature 455:644
12. Balasubramanian G, Neumann P, Twitchen D, Markham M, Kolesov R, Mizuoschi N, Isoya J, Achard J, Beck J, Tissler J, Jacques V, Hemmer PR, Jelezko F, Wrachtrup J (2009) Nat Mater 8:383
13. Kurtsiefer C, Mayer S, Zarda P, Weinfurter H (2000) Phys Rev Lett 85:290
14. http://qcvictoria.com/content/download/418/1785/file/SPS%201.01%20prouct%20brochure.pdf
15. Tamarat P, Gaebel T, Rabeau JR, Khan M, Greentree AD, Wilson H, Hollenberg LCL, Prawer S, Hemmer P, Jelezko F, Wrachtrup J (2006) Phys Rev Lett 97:083002
16. Bernien H, Childress L, Robledo L, Markham M, Twitchen D, Hanson R (2012) Phys Rev Lett 108:043604
17. Bernien H, Hensen B, Pfaff W, Koolstra G, Blok MS, Robledo L, Taminiau TH, Markham M, Twitchen D, Childress L, Hanson R (2013) Nature 497:86
18. Hausmann B, Babinec T, Choy J, Hodges J, Hong S, Bulu I, Yacoby A, Lukin M, Lončar M (2011) New J Phys 13:045004
19. Riedrich-Möller J, Kipfstuhl L, Hepp C, Neu E, Pauly C, Mücklich F, Baur A, Wandt M, Wolff S, Fischer M, Gsell S, Schreck M, Becher C (2012) Nat Nanotechnol 7:69
20. Faraon A, Barclay PE, Santori C, Fu KMC, Beausoleil RG (2011) Nat Photonics 5:301
21. Yang Y, Wang X, Ren C, Lu P, Wang P (1999) Diamond Relat Mater 8:1834
22. Leech P, Reeves G, Holland A, Shanks F (2002) Diamond Relat Mater 11:833
23. Leech P, Reeves G, Holland A (2001) J Mater Sci 36:3453
24. Otterbach R, Hilleringmann U (2002) Diamond Relat Mater 11:841
25. Pearton S, Katz A, Ren F, Lothian J (1992) Electron Lett 28:822
26. Karlsson M, Hjort K, Nikolajeff F (2001) Opt Lett 26:1752

Index

P. Petkov et al. (eds.), *Nanoscience Advances in CBRN Agents Detection, Information and Energy Security*, NATO Science for Peace and Security Series A: Chemistry and Biology, DOI 10.1007/978-94-017-9697-2